

Document Version

Final published version

Citation (APA)

de Rooij, S. A. H. (2026). *Quasiparticle Dynamics in Disordered Superconductors*. [Dissertation (TU Delft), Delft University of Technology]. <https://doi.org/10.4233/uuid:4e4a4bc3-c313-4edb-bee5-d5b4dd98026e>

Important note

To cite this publication, please use the final published version (if applicable).
Please check the document version above.

Copyright

In case the licence states "Dutch Copyright Act (Article 25fa)", this publication was made available Green Open Access via the TU Delft Institutional Repository pursuant to Dutch Copyright Act (Article 25fa, the Taverne amendment). This provision does not affect copyright ownership.
Unless copyright is transferred by contract or statute, it remains with the copyright holder.

Sharing and reuse

Other than for strictly personal use, it is not permitted to download, forward or distribute the text or part of it, without the consent of the author(s) and/or copyright holder(s), unless the work is under an open content license such as Creative Commons.

Takedown policy

Please contact us and provide details if you believe this document breaches copyrights.
We will remove access to the work immediately and investigate your claim.

QUASIPARTICLE DYNAMICS IN DISORDERED SUPERCONDUCTORS



Steven de Rooij

QUASIPARTICLE DYNAMICS IN DISORDERED SUPERCONDUCTORS

QUASIPARTICLE DYNAMICS IN DISORDERED SUPERCONDUCTORS

Dissertation

for the purpose of obtaining the degree of doctor
at Delft University of Technology
by the authority of the Rector Magnificus, prof.dr.ir. H. Bijl,
chair of the Board for Doctorates
to be defended publicly on
Monday 23 February 2026 at 17:30.

by

Steven Alexander Hippolytos DE ROOIJ

This dissertation has been approved by the promotors.

Composition of the doctoral committee:

Rector Magnificus	chairperson
Prof.dr.ir. J.J.A. Baselmans	Delft University of Technology / SRON - Space Research Organisation Netherlands, promotor
Dr.ir. P.J. de Visser	Delft University of Technology / SRON - Space Research Organisation Netherlands, copromotor

Independent members:

Prof.dr. Y.V. Nazarov	Delft University of Technology
Prof.dr. L. DiCarlo	Delft University of Technology
Em.prof.dr. J. Aarts	Leiden University
Prof.dr. J. Zmuidzinas	Caltech, USA
Dr. F. Chiodi	CNRS / Université Paris-Saclay, France



Printed by: Ipskamp Printing

Cover design: Curves of the forward transmission (i.e., $|S_{21}|(f)$) of the membrane β -Ta resonator from Chapters 6 and 7 after a photon excitation with a wavelength of 673 nm. Each curve is calculated by shifting and scaling the measured forward transmission in equilibrium via the inductive (θ) and dissipative (δA) response, respectively. The response is measured at 1 MHz, corresponding to $1 \mu\text{s}$ for each curve. The inductive response is multiplied by 30 for visibility. The back shows a similar curve that represents a locally suppressed gap (i.e., $\Delta(x)$) with two quasiparticles that are about to recombine on-site, as hypothesized in Chapter 6.

Copyright © 2026 by S.A.H. de Rooij

ISBN 978-94-6536-040-9

An electronic copy of this dissertation is available at the TU Delft Repository:

<https://doi.org/10.4233/uuid:4e4a4bc3-c313-4edb-bee5-d5b4dd98026e>.

*Der Reiz der Erkenntniss wäre gering,
wenn nicht auf dem Wege zu ihr so viel Scham zu überwinden wäre.*

- Friedrich Nietzsche,
Jenseits von Gut und Böse, Nr. 65

CONTENTS

Summary	xi
Samenvatting	xiii
1. Introduction	1
1.1. The discovery of superconductivity	1
1.2. Adding disorder to superconductors	3
1.3. Quasiparticles in disordered superconductors	5
1.4. A quasiparticle detector	7
1.4.1. Disordered superconductors for MKIDs	7
2. Theory	19
2.1. Electronic response to radiation	19
2.1.1. Normal metals	20
2.1.2. Superconductors: phenomenological	22
2.1.3. Superconductors: microscopic	25
2.2. Microwave resonators	32
2.2.1. Transmission lines	32
2.2.2. Transmission line resonators	34
2.2.3. Hybrid microwave resonators	40
2.2.4. Spurious signal: Two-Level-Systems	42
2.3. Excitations in superconductors	44
2.3.1. Quasi-equilibrium	48
2.3.2. Pair-breaking photon excitations	52
2.3.3. Subgap photons: effects of the microwave probe	62
2.4. Disordered superconductors	65
2.4.1. Suppression of superconductivity: phase transitions	71
2.4.2. Emergent inhomogeneities of the superconducting state	73
2.4.3. Complex conductivity of disordered superconductors	76
3. Methods	95
3.1. Setup	95
3.1.1. Cryogenic and optical setup	95
3.1.2. Microwave setup	97
3.2. Fabrication	101
3.3. Measurements	103
3.3.1. DC measurement	103
3.3.2. S_{21} measurement	105
3.3.3. Noise measurement	107

3.3.4. Single photon pulse measurement	108
4. Strong reduction of quasiparticle fluctuations in a superconductor due to de-coupling of the quasiparticle number and lifetime	113
4.1. Introduction	114
4.2. Methods	115
4.3. Results and discussion	117
4.4. Conclusion	121
Supplementary Information	123
4.A. Device Design and Fabrication	123
4.B. Amplitude, Phase and Cross-Power Spectral Densities	123
4.C. Al Geometry Variations	123
4.C.1. Al Length	123
4.C.2. Al Width	124
4.C.3. Al Thickness	124
4.D. Microwave Readout Power Dependence	128
4.D.1. Peak in Lifetime	128
4.D.2. Creation of Excess Quasiparticles	128
4.E. Responsivity Measurement	129
5. Volume dependence of microwave induced excess quasiparticles in superconducting resonators	139
5.1. Introduction	140
5.2. Device design and measurement	141
5.3. Results and discussion	143
5.3.1. Excess quasiparticles due to dissipated microwave power	144
5.3.2. Limiting MKID sensitivity	146
5.3.3. Microscopic mechanism for excess quasiparticles	146
5.4. Conclusion	148
Supplementary Information	149
5.A. Quasiparticle sensitivity and photon interaction	149
5.B. Bifurcation power estimation	152
5.B.1. Quasiparticle non-linearity	154
5.C. NEP limited by microwave induced excess quasiparticles	156
5.D. Q_i when quasiparticles are redistributed	156
5.E. Pair breaking photon attenuation	156
6. Recombination of localized quasiparticles in disordered superconductors	167
6.1. Introduction	168
6.2. Results	170
6.2.1. Fluctuation measurements	170
6.2.2. Phonon scattering limited quasiparticle relaxation	171
6.2.3. Verification of quasiparticle generation-recombination fluctuations	172
6.2.4. Recombination of localized quasiparticles	173
6.3. Discussion and conclusion	174

6.4. Methods	177
6.4.1. Device design and fabrication	177
6.4.2. Film characterization	177
6.4.3. Setup	179
6.4.4. Fluctuation measurement	179
Supplementary Information	183
6.A. Relaxation time and variance calculations	183
6.A.1. Relaxation time	183
6.A.2. Variance	187
6.B. Characterization of the β -Ta film	191
6.B.1. Resistance versus temperature	191
6.B.2. Hall resistance	192
6.B.3. Upper critical field	192
6.C. TiN data analysis	194
6.D. Fitting the power spectral densities	198
6.E. Fluctuation model for localized quasiparticle recombination	198
6.E.1. Discussion of assumptions and implications of the model	203
6.F. Gap fluctuations and localized states induced by disorder	205
6.G. Estimation of read-out power effects on quasiparticle density and distribution function	206
7. Recombination of non-equilibrium quasiparticles in disordered superconductors excited with single photons	217
7.1. Introduction	218
7.2. Results and discussion	220
7.2.1. Tail decay: localized quasiparticle recombination	220
7.2.2. Initial fast decay: enhanced self-recombination?	224
7.3. Conclusion	233
8. Conclusion	243
A. Phonon transparencies	251
B. Kinetic inductance and microwave loss in β-Ta	257
Acknowledgements	263
Curriculum Vitae	267
List of Publications	269

SUMMARY

In 1911, Heike Kamerlingh Onnes and his research team measured a steep drop to zero in the resistance of mercury when cooling it below 4.2 K: superconductivity was discovered. Forty-six years later, the microscopic theory to describe superconductivity was formulated. It predicts that disorder (the increase of electron scattering due to impurities, defects or other causes), to first order, does not influence the superconducting state. From an application perspective, disordered superconductors are interesting as they have a high kinetic inductance: they strongly - and non-linearly - oppose the change in current due to the inertia of the superconducting charge carriers, which are paired electrons, or Cooper pairs. Therefore, disordered superconductors can be used in superconducting circuits as highly inductive, nonlinear elements to realize, for example, quantum bits, quantum-limited amplifiers and single-photon detectors. In addition, the high normal state resistance of disordered superconductors allows an efficient, broadband absorption of light, which enables single photon counting, energy resolving microwave kinetic inductance detectors (MKIDs) for visible and near-infrared light.

These applications are, however, hindered by an unexplained microwave loss and, for MKID applications, an enhanced decay rate of the elementary excitations in the superconductor. Both these effects become stronger with increasing disorder. The elementary excitations are called quasiparticles and are essentially broken Cooper pairs. Their density decays as they recombine pair-wise into Cooper pairs. Since quasiparticles also induce microwave loss, these observations point towards an effect of disorder on the quasiparticle dynamics. It is however unclear how disorder affects the quasiparticle dynamics exactly.

In this thesis, we measure and describe the quasiparticle dynamics in superconducting films of the pure superconductor Al and the disordered superconductor β -Ta. We probe the superconductor with AC fields, by embedding them in a microwave resonator. From the changes in resonance frequency and quality factor over time, we measure the changes in quasiparticle density, from which we extract the recombination time and quasiparticle density. We vary the bath temperature such that we can compare our results with theoretical models that describe the quasiparticle dynamics. Additionally, we fabricate the superconductor both on a membrane and substrate, such that we probe the effects of the phonons (i.e, lattice vibrations) on the quasiparticle dynamics.

We start by measuring Al resonators in equilibrium, both on substrate and on membrane. From theory and literature, we expect that the quasiparticle recombination scales inversely with quasiparticle density: the higher the density, the higher the chance that two quasiparticles recombine. The membrane should enhance the measured recombination time, as the energy emitted during a recombination event (in the form of a phonon) is trapped and can subsequently break another Cooper-pair. In Chapter 4, we show, however, this theory breaks down at low temperatures. The coupling between

quasiparticle density and recombination time no longer holds at low temperatures, and the effect of the membrane disappears. We link this observation to quasiparticle localization due to a small amount of disorder in the rather pure superconducting Al film. This disorder is likely to be induced by the surface or metal-substrate (or metal-membrane) interface.

By increasing the microwave power used to excite the resonator, we can probe the quasiparticle dynamics in non-equilibrium. As expected from literature, we show in Chapter 5 that the microwave power generates quasiparticles. By changing the Al volume in these resonators we however establish that the creation of quasiparticles is not due to the direct absorption of microwave photons by the quasiparticles, which is usually assumed. The microscopic mechanism of quasiparticle creation is indirect, but acts close to the Al. It is possibly related to two-level-system loss, that heats the Al locally. From this effect, we explain the variation in sensitivity with Al volume in the most sensitive far-infrared MKIDs to date.

We then turn our attention to the disordered superconductor β -Ta. In Chapter 6 we measure the quasiparticle fluctuations in equilibrium and find that the quasiparticle recombination time is governed by phonon scattering, which enhances the recombination. We explain this behavior in terms of disorder-induced quasiparticle localization: quasiparticles are localized and delocalize via phonon scattering. Once mobile, the quasiparticles relax to localization sites, where enhanced ('on-site') recombination takes place. We model this behavior, define different quasiparticle recombination regimes, and predict that quasiparticle recombination is enhanced due to disorder when $ql < 1$ (q is the 2Δ -phonon wavenumber, with 2Δ the binding energy of a Cooper pair, and l the electronic mean free path). We show that this is consistent with literature data on quasiparticle recombination.

Lastly, we probe the β -Ta film in a non-equilibrium situation by exciting it with single photons. From the transient response, we find in Chapter 7 that the quasiparticle density decays non-exponentially and much faster than in Al. By modeling the conventional quasiparticle dynamics, including disorder-induced slow quasiparticle diffusion and phonon dynamics, we conclude that conventional quasiparticle dynamics cannot describe the quasiparticle density decay. We experimentally change both the photon energy and quasiparticle volume, and hypothesize that the non-exponential nature is due to quasiparticle localization effects, where the first part of the decay is governed by on-site recombination of mobile quasiparticles and the second part by recombination of localized quasiparticles.

This thesis shows that the quasiparticle dynamics in a superconductor are strongly influenced by disorder. It induces quasiparticle localization effects, which counterintuitively enhance recombination in the experimentally relevant regimes. At low temperatures, these quasiparticle localization effects might also be able to explain the observed increase of microwave loss in disordered superconductors, although more research is needed to confirm this. Extending the methods presented in this thesis to lower temperatures, lower quasiparticle generation rates, smaller superconducting volumes, and more (types of) disordered superconductors is a promising experimental path to confirm such hypotheses.

SAMENVATTING

In 1911, maten Heike Kamerlingh Onnes en zijn onderzoeksteam een scherpe afname tot nul van de weerstand in kwik toen ze het afkoelde beneden 4.2 K. Dit was de ontdekking van supergeleiding. Pas zesenvestig jaar later werd duidelijk hoe het microscopische mechanisme voor supergeleiding werkte. Die theorie voorspelt dat wanorde (onzuiverheden in het materiaal, afwijkingen in het kristalrooster of een andere reden van botsen van elektronen), in eerste orde geen invloed heeft op de supergeleiding. Wanordelijke supergeleiders hebben interessante toepassingen vanwege hun hoge kinetische inductantie: ze gaan een verandering in stroom sterk tegen door de traagheid van de ladingsdragers. Dat zijn in supergeleiders gepaarde elektronen, Cooper-paren genoemd. Die hoge inductantie is niet-lineair met stroom, wat ervoor zorgt dat wanordelijke supergeleiders gebruikt kunnen worden in kwantumbits, kwantum-gelimiteerde versterkers, en foton detectoren. De hoge weerstand in de normale toestand zorgt er daarnaast voor dat wanordelijke supergeleiders efficiënt en breedbandig licht kunnen absorberen, wat ze geschikt maakt voor het meten van enkele fotonen van infrarode to zichtbare golflengten, inclusief het bepalen van hun energie, door middel van microgolf kinetische inductantie detectoren (MKIDs).

Deze toepassingen worden echter gelimiteerd door onverklaarde microgolfverliezen en een snel verval van de excitaties, die beide sterker worden met wanorde. De elementaire excitaties in een supergeleider zijn gebroken Cooper-paren en worden quasideeltjes genoemd. De dichtheid van quasideeltjes vervalst doordat ze in paren recombineren tot Cooper-paren. Quasideeltjes veroorzaken ook microgolfverliezen. De onverklaarde effecten kunnen dus duiden op een veranderde dynamica van de quasideeltjes in wanordelijke supergeleiders. Hoe wanorde de quasideeltjesdynamica precies beïnvloedt, is echter nog niet duidelijk.

In dit proefschrift meten en beschrijven we de quasideeltjesdynamica in dunne laagjes van de ordelijke supergeleider Al en de wanordelijke supergeleider β -Ta. We meten de response op een wisselstroom in de supergeleider door het te integreren in een microgolfresonator. De veranderingen in resonantiefrequentie en Q-factor geven de veranderingen in de dichtheid van quasideeltjes, waaruit we de quasideeltjes dichtheid en recombinatietijd kunnen afleiden. We leggen de supergeleiders zowel op substraat als op een dun membraan, zodat we de effecten van fononen op de recombinatie kunnen bepalen.

We behandelen eerst ordelijke Al resonatoren in evenwichtstoestand. Vanuit theorie en vorige experimenten verwachten we dat de recombinatietijd omgekeerd evenredig afhangt van de dichtheid van quasideeltjes: hoe meer quasideeltjes er zijn, hoe groter de kans dat ze recombineren. Een membraan zou de recombinatietijd moeten verhogen, omdat het fonon dat ontstaat bij recombinatie gevangen wordt door het membraan en een ander Cooper-paar kan breken. In Chapter 4 zien we echter dat deze theorie niet

meer opgaat bij lage temperaturen. De relatie tussen de quasideeltjes dichtheid en recombinatietijd geldt niet meer en de effecten van het membraan op de recombinatietijd verdwijnen. We koppelen deze observatie aan de lokalisatie van quasideeltjes door een kleine hoeveelheid wanorde in het pure Al laagje. Deze wanorde is waarschijnlijk veroorzaakt door het oppervlak of het raakvlak met het substraat.

Door het microgolffvermogen van het uitleessignaal te verhogen, kunnen we het niet-evenwichtsgedrag van de quasideeltjes meten. In Chapter 5 meten we dat het microgolfsignaal zorgt voor een hogere quasideeltjes dichtheid dan in evenwicht, zoals ook in eerdere studies is aangetoond. Door het volume van het Al te variëren stellen wij echter vast dat de oorzaak hiervan niet ligt in de directe absorptie van microgolffotonen door de quasideeltjes, wat in de literatuur typisch als reden wordt aangevoerd. Het microscopische mechanisme achter de creatie van quasideeltjes door het microgolfsignaal moet indirect zijn, maar werken lokaal bij het Al. Een mogelijkheid is dat tweetoestandsystemen het microgolfsignaal absorberen en zo het Al lokaal opwarmen. Aan de hand van de efficiëntie van dit effect, verklaren we variëteit in gevoeligheid van de huidige, meest gevoelige verre-infrarood MKIDs.

Hierna behandelen we de wanordelijke supergeleider β -Ta. Door het meten van de quasideeltjes fluctuaties in evenwicht, laten we in Chapter 6 zien dat recombinatie in deze wanordelijke supergeleider sneller is dan in een ordelijke supergeleider en gelimiteerd wordt door fononabsorptie. We verklaren dit gedrag door de lokalisatie van quasideeltjes, geïnduceerd door wanorde: quasideeltjes zijn gelokaliseerd en delokaliseren door fononabsorptie. Daarna relaxeren de quasideeltjes naar lokalisatieplekken, waar versnelde recombinatie plaatsvindt. We modelleren dit gedrag en definiëren verschillende regimes van wanorde, waar recombinatie wordt versneld in het regime $ql < 1$ (q is het golfnummer van een fonon met energie gelijk aan de bindingsenergie van een Cooperpaar en l is de vrije weglengte van een elektron). Deze classificatie is consistent met de literatuurdata.

Als laatste meten we de quasideeltjesdynamica in niet-evenwicht door het exciteren van de supergeleider met enkele fotonen. Het transiënte signaal vervalt niet-exponentieel en veel sneller dan in Al. Door het modelleren van de conventionele quasideeltjesdynamica, inclusief de trage diffusie van quasideeltjes door wanorde en de fonon dynamica, concluderen we dat het verval van de quasideeltjes dichtheid niet-conventioneel is. We variëren de foton-energie en het quasideeltjesvolume en beargumenteren dat het niet-exponentiële gedrag door quasideeltjeslokalisatie komt. Het eerste, snelle deel van het verval zou versnelde recombinatie van vrije quasideeltjes in lokalisatieplekken kunnen zijn en het tweede, tragere deel recombinatie van gelokaliseerde quasideeltjes.

Dit proefschrift laat zien dat de quasideeltjesdynamica in supergeleiders sterk wordt beïnvloed door wanorde. Wanorde induceert lokalisatie-effecten van quasideeltjes, wat zorgt voor een snellere recombinatie in de experimenteel relevante regimes. Op lage temperaturen zouden deze lokalisatie-effecten ook de hoge microgolffverliezen van wanordelijke supergeleiders kunnen verklaren, hoewel er meer onderzoek nodig is om dit vast te stellen. Het uitbreiden van de methodes in dit proefschrift naar lagere temperaturen, minder quasideeltjesgeneratie, kleinere supergeleidende volumes en verschillende (typen) wanordelijke supergeleiders, is een veelbelovende experimentele route naar het beter begrijpen van de effecten van wanorde op supergeleiders.

1

INTRODUCTION

1.1 THE DISCOVERY OF SUPERCONDUCTIVITY

From 1908 to 1923, the coldest place on earth was located in the center of Leiden. At the 10th of July 1908 in the laboratory of Leiden University, a team of scientists and engineers led by Heike Kamerlingh Onnes liquefied helium for the first time [1]. He was awarded the Nobel Prize for this work five years later, in 1913. Despite the publication of all experimental details it took 15 years for another lab to do the same. In 1923 John McLennan from Toronto was able to liquefy helium as well, after a visit to the Leiden laboratory [2].

Although these efforts started off as a fundamental investigation of the theory of liquids and gases of Johannes Diderik van der Waals, the technical ability to liquefy helium opened up a completely new range of temperatures to conduct physics experiments. For example, one of the physical questions that Kamerlingh Onnes was interested in was the behavior of metals at temperatures approaching the absolute zero, i.e., 0 K or -273°C . The theory of Paul Drude stated that the movement of electrons in the metal were obstructed by thermal vibrations, and it was therefore expected that the resistance of metal would reduce linearly to zero, when lowering the temperature. However, Lord Kelvin predicted that the resistance would go to infinity close to zero temperature, since every thermal movement would stop and all electrons would stick to their atoms. Kamerlingh Onnes set out to measure this.

He conducted resistance measurements versus temperature on mercury (Hg). This metal could be purified to a large extent, such that the resistance from impurities (i.e., the obstructed movement of electrons by defects or disorder in the metal) was minimized. As three recently discovered letters from Albert Einstein to Kamerlingh Onnes revealed [3], this experimental direction of pure metals was the opposite to what Einstein suggested. Einstein was interested in the effect of disorder on the residual resistance at zero temperature, since this could be influenced by quantum effects as described by the extension of the Drude theory by Arnold Sommerfeld. Disorder is the obstruction of electron movement by sample geometry (typically thickness), impurity concentration, structural defects or other means, and generally leads to an increase of resistance. Later Einstein also suggested reducing the dimensions of the metal to observe quantum effects.

Nevertheless, Kamerlingh Onnes decided to devote his precious helium-time to the pure metal mercury. In 1911, the team in Leiden purified the metal and cooled it down to about 4 K with their unique liquid helium experimental setup. They recorded the resistance versus temperature, which resulted in Fig. 1.1(a). They observed that the resistance indeed goes to 0 at low temperatures, but in an unexpected manner: the resistance drops to zero abruptly at a critical temperature, $T_c = 4.15$ K [4]. At first, Kamerlingh Onnes thought that this was an artifact of the setup, but after several careful checks, the result turned out to be genuine. Moreover, the vanishing resistance was reproducible in other materials which were less pure, like tin ($T_c = 3.8$ K) and lead ($T_c = 7.2$ K). This phenomenon was called 'supraconductivity' by Kamerlingh Onnes and is now known as superconductivity.

Soon after the discovery, it was realized that superconductivity also implied persistent currents: without resistance, currents can run forever in a superconducting coil, or as proposed by Paul Ehrenfest, in a superconducting ring. These persistent currents were measured by Kamerlingh Onnes for the first time in 1914 [6]. Since electrical current generates a magnetic field, superconducting rings can generate very large magnetic fields. This is the basis of many modern applications of superconductivity. For example, MRI (magnetic resonance imaging) scanners use superconductors to generate strong magnetic fields, and the same technique is used in CERN to bend the trajectory of charged particles in the large hadron collider. Small superconducting loops with one or two tiny non-superconducting constrictions in it - a device called a SQUID (superconducting quantum interference device) - are used as the most sensitive magnetic field sensors. Furthermore, superconducting electrical circuits enable physicists to access macroscopic quantum phenomena, for which John Clarke, Michel H. Devoret and John M. Martinis received the Nobel Prize this year. Specifically, the most powerful quantum computers today are built from superconductors [7].

The applications of superconductivity would however be much more widespread if the requirement of cooling the material could be relaxed. A material with a T_c above room temperature would revolutionize electronics, as the dissipation of a superconducting electrical device completely disappears. Energy could be transported with virtually 100% efficiency, which would have a large positive impact on climate change. The value of T_c depends on material. Figure 1.1(b) shows the T_c of different materials, with the year of discovery on the horizontal axis. The highest single-element superconductor is Nb with a critical temperature of $T_c = 9.3$ K, and the metallic compound with the highest critical temperature is MgB_2 with $T_c = 39$ K. High temperature superconductors (HTSC, orange in Fig. 1.1(b)) are compounds with a layered structure of alternating metallic and insulating layers, and the mechanism for superconductivity is fundamentally different from metallic systems [8]. New, unconventional mechanisms for superconductivity keep being predicted and experimentally confirmed, and a future discovery of an ambient (room temperature and atmospheric pressure) superconductor could be possible [5]. Although this is a very exciting and active field of research, we will only consider conventional superconductors in this thesis. As we will see, also for conventional superconductors some aspects are not well understood, especially when introducing

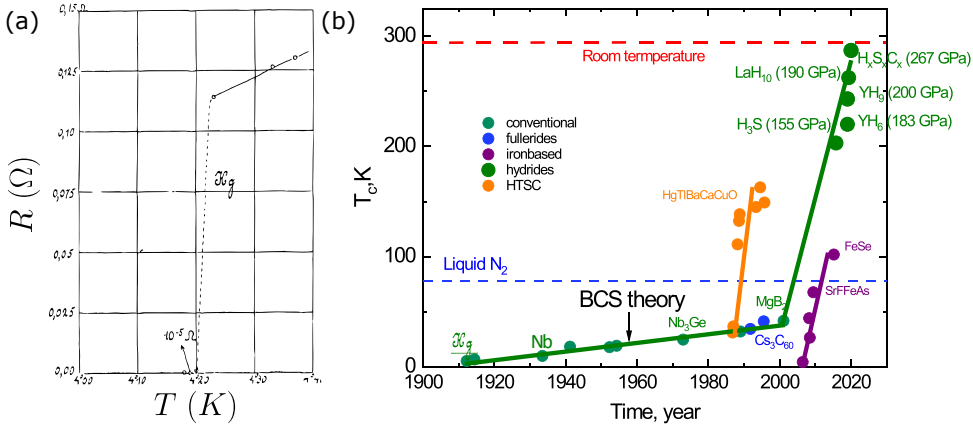


Figure 1.1: The discovery of superconductivity in mercury and other materials. (a): The first measurement of superconductivity by Heike Kamerlingh Onnes [4]. The sharp drop to zero of the resistance is a manifestation of the superconducting transition at $T_c = 4.15$ K. (b): The discovery of other superconducting materials with critical temperature T_c versus discovery year. Different colors indicate the different families/classes of superconductors. HTSC stands for high temperature superconductors, which are also called cuprates, as they contain copper-oxide groups. Image taken from Ref. [5].

disorder to the materials.

1.2 ADDING DISORDER TO SUPERCONDUCTORS

The conventional microscopic theory of superconductivity was put forward 46 years (!) after the discovery of superconductivity, which highlights the completely novel character of the phenomenon. Bardeen, Schrieffer and Cooper (BCS) formulated their theory to explain superconductivity in terms of quantum mechanics [17, 18], which had been developed during the decades before. The core idea is that there is a slight attraction between electrons, mediated by the atomic lattice, which bounds them in pairs at low temperatures. These electron pairs, so-called Cooper-pairs, condense into one macroscopic coherent ground state. This condensate gives rise to zero resistance, and is a purely quantum mechanical phenomenon.

From BCS theory and from experiments, it became clear that the introduction of disorder did not alter the superconducting state [19]. However, the suggestion by Einstein to look into the effect of disorder and dimensionality in metals to find quantum behavior did turn out to be an interesting experimental path. In metals, quantum effects have been found by reducing dimensionality and increasing disorder even in rather large ($\sim \mu\text{m}$) samples, and this has been the birth of a new physics field called mesoscopic physics [20]. Also in superconductors, increasing disorder to a critical value alters the physical state at zero temperature, which is called quantum phase transition. Figure 1.2(a) shows that when tuning disorder in bismuth films with thickness, the low temperature resistance goes from 0 (superconducting) to infinity

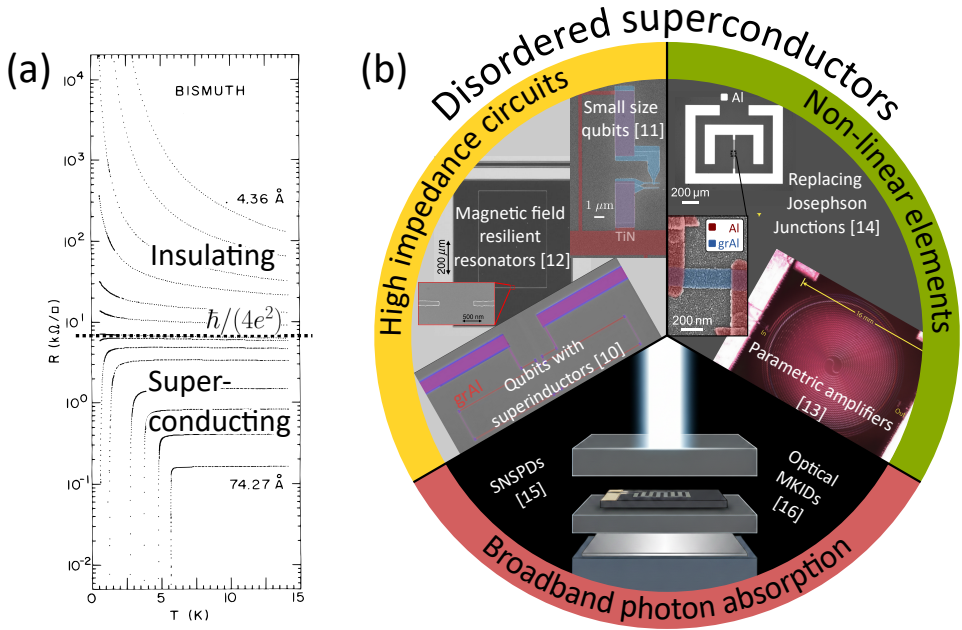


Figure 1.2: Adding disorder to superconductivity. **(a)**: Experiment on bismuth thin films that shows a superconducting to insulating transition at a critical sheet resistance of $\hbar/(4e^2) = 6.5 \text{ k}\Omega/\square$ [9]. **(b)**: Overview of the applications of disordered superconductors. The high kinetic inductance of disordered superconductors can leverage to design high impedance (quantum) circuits [10, 11] that are resilient to magnetic field [12] (yellow), and the non-linearity of the kinetic inductance can be used in parametric amplifiers [13] and qubits [14] (green). The high normal state resistance results in a broadband photon absorption, which can be used in photon detectors, such as SNSPDs [15] and MKIDs [16] (red).

(insulating) when reaching a critical normal state sheet resistance, $R_N \approx \hbar/(4e^2)$ [9]. Here, \hbar is the reduced Planck constant and e is the electronic charge. It turns out that close to the critical sheet resistance, the superconducting state is altered significantly compared to conventional superconductors. These superconductors are called disordered superconductors. They are phenomenologically characterized by a high normal state sheet resistance, R_N .

Conventional BCS theory describes the main consequence of a higher R_N : in the superconducting state, a high R_N results in a high kinetic inductance, L_K . Kinetic inductance is the opposition of the change in current (inductance) due to the inertia of the charge carriers. In normal metals this effect exists as well, but it is very small because the electrons lose their momentum fast due to scattering, which dissipates energy. Only at very high frequencies, exceeding the inverse of the electron scattering time, $\omega > 1/\tau$, the kinetic inductance of normal metals becomes significant. Since the dissipation is zero in superconductors and the charge carriers do not lose their momentum due to scattering, the kinetic inductance is quite

large for superconductors. To be specific, the kinetic inductance for a normal metal is, $L_{k,N} = \tau R_N$, where τ is the average scattering time of an electron. For a superconductor, L_k is enhanced by a factor τ_c/τ , where τ_c is the coherence time of a Cooper-pair, given by $\hbar/(\pi\Delta)$. 2Δ is the binding energy of the Cooper-pair, which is related to the critical temperature according to BCS via, $\Delta = 1.76k_B T_c$, with k_B the Boltzmann constant. This leads to the kinetic inductance of a superconductor of [21, 22],

$$L_k = \frac{\hbar R_N}{\pi\Delta}. \quad (1.1)$$

We see that introducing disorder in a superconductor (i.e., increasing R_N) leads to a proportionally higher kinetic inductance. This high kinetic inductance gives rise to many applications, as shown in Fig. 1.2(b). For example, it allows very small inductive circuit elements, which are resilient to magnetic fields and much more inductive than otherwise possible (highlight in yellow in Fig. 1.2(b)). Besides that, the kinetic inductance has the property that it increases non-linearly when more current is run through. That enables non-linear elements for quantum bits (qubits) and microwave amplifiers with the lowest possible noise (highlight in green in Fig. 1.2(b)). Lastly, the high R_N allows efficient absorption of light with many colors in the superconductor, from which single-photon detectors can benefit (highlight in red in Fig. 1.2(b)). We will discuss the application to single-photon detectors in more detail in Section 1.4.

Apart from the increase of L_k , disorder also affects the superconducting state in ways that cannot be described by conventional BCS theory. For example, Δ can spatially vary due to disorder [23, 24], and when increasing disorder to critical levels, superconductivity can be broken due to different mechanisms [25]. Furthermore, the dynamics of the excitations in the superconductor can be drastically altered, as we will discuss now.

1.3 QUASIPARTICLES IN DISORDERED SUPERCONDUCTORS

A key aspect of the applications and physics described in the previous section are the excitations in a superconductor. In a real device, the superconductor is never in the true ground state, and some Cooper-pairs are broken. This can be due to finite temperature, absorbed radiation and any other form of additional energy to the superconductor. When a Cooper-pair absorbs more than 2Δ energy, two quasiparticles are created. These quasiparticles behave as simple electrons and give rise to dissipation, which is unwanted in most applications.

The combination of quasiparticles and Cooper-pairs can be intuitively modeled by the two fluid model [22, 27], as depicted in Fig. 1.3(a). The response to an alternating current (AC) is given by a parallel resistance due to quasiparticles and a kinetic inductance due to the Cooper-pair condensate. At low frequencies, the current will flow through the inductor (the Cooper-pairs carry the charge), while at higher frequencies, part of the current will flow through the resistor, where the quasiparticles carry the charge and cause dissipation. Therefore, at microwave frequencies, there will be some dissipation (i.e, microwave loss) due to the quasiparticles. The higher

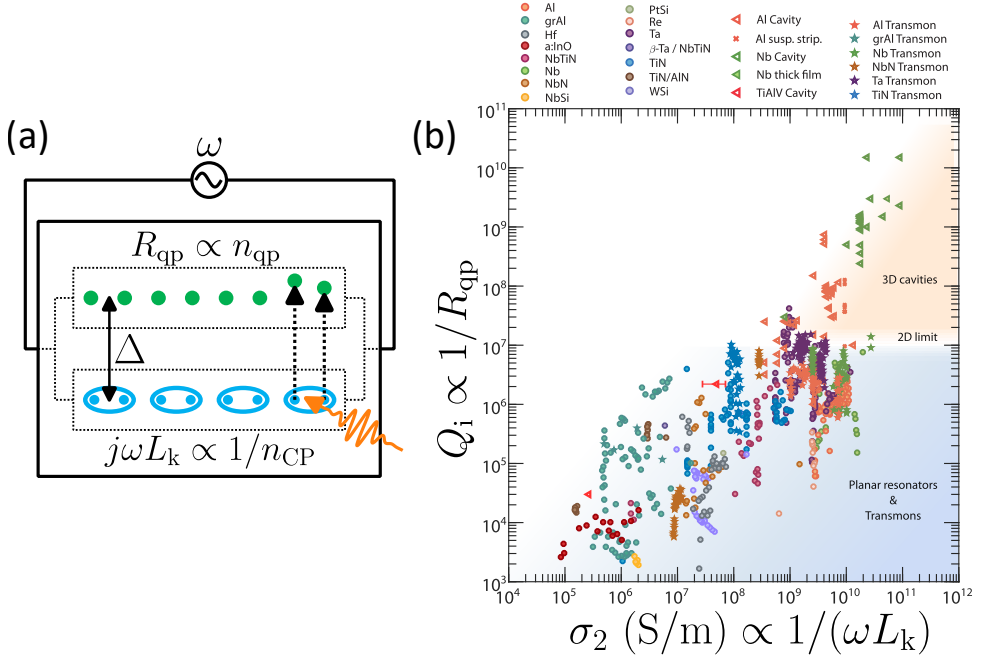


Figure 1.3: The alternating current response of a superconductor and experimentally determined dissipation as a function of kinetic inductance. **(a)**: Diagram of the two-fluid model, with the quasiparticles (green dots) giving rise to resistance (R_{qp}) and the Cooper-pairs (blue pair of dots) giving rise to a parallel inductance (L_k). n_{qp} is the quasiparticle density and n_{CP} the Cooper-pair density. The energy difference between the two is Δ , such that a minimum of 2Δ can break a Cooper-pair into two quasiparticles. When a photon with energy greater than 2Δ hits the superconductor, it can break Cooper-pairs and generate quasiparticles, such that both L_k and R_{qp} change. **(b)**: The measured internal quality factor versus imaginary conductivity of different materials. The internal quality factor is proportional to one over the resistance and the imaginary conductivity to one over the kinetic inductance, such that the lower left corner are disordered superconductors with high dissipation. The correlation shows that disorder may introduce additional quasiparticle loss. Image taken from Ref. [26], see references therein for the individual data points.

the quasiparticle density (n_{qp}), the higher this loss. Therefore, in most applications the quasiparticle density needs to be minimized.

Figure 1.3(b) shows a compilation of many microwave devices where the internal quality factor (Q_i) is measured [26]. Q_i is a measure for the loss in a resonator, which can come from quasiparticles but also from other microwave loss mechanisms inside or close to the resonator. The higher the Q_i , the lower the loss. On the x-axis, the imaginary part of the complex conductivity is shown (i.e., σ_2 in $\sigma = \sigma_1 - j\sigma_2$), which is proportional to one over the kinetic inductance. Therefore, the devices from disordered materials, with high kinetic inductance, are on the left, and ordered, clean materials are on the right. The correlation in the data points shows that

increasing disorder (lower σ_2) results in more microwave loss (lower Q_i). This hinders the implementation of disordered superconductors, and is the main reason that disordered superconductors are not very common in superconducting circuits.

The question is what causes this increased microwave loss in disordered superconductors. One of the options is that the quasiparticles in disordered superconductors behave differently, such that their density is higher. It is argued in Refs. [26, 28] that quasiparticles can get trapped in disordered superconductors due to the local variation of Δ , which is their minimum energy value. However, just from the measurements of the microwave loss (Q_i), this hypothesis cannot be confirmed or rejected. We need to better understand the quasiparticle dynamics in disordered superconductors, for which we need more detailed measurements. We need to measure the evolution of $n_{\text{qp}}(t)$, for different conditions (temperature, environment of the superconductor, etc.) and excitations (photon absorption, microwave drive, etc.). In this thesis, we will provide these measurements with the use of a sensitive probe for quasiparticles within a superconducting volume. This sensitive probe can also be used as a detector of light, as we will discuss now.

1.4 A QUASIPARTICLE DETECTOR

When n_{qp} changes, both L_k and R change, as shown in Fig. 1.3(a). This effect can be used to accurately probe the changes in n_{qp} when the superconductor absorbs some known energy, such as a set temperature or a particle of light (photon) with a known wavelength. When the energy of the excitation is however not known, we can use the changes in L_k and R as principle of detection and measure the excitation energy. Alternatively, when the superconductor is continuously excited with radiation, the changes in L_k and R measure the incoming radiation power.

To be specific, when a photon is absorbed in the superconductor, Cooper-pairs are broken and quasiparticles are generated, as depicted by the orange arrow in Fig. 1.3. This changes both the inductance (L_k) and resistance (R). When we embed the superconductor in a microwave resonator, the changes in L_k and R can be probed very accurately. Such a superconducting photon detector is called a microwave kinetic inductance detector (MKID) [38]. This detector detects light by sensing the quasiparticle density (or equivalently, the Cooper-pair density) in a superconductor. For understanding the detector response, it is therefore crucial to understand the evolution of the quasiparticle density after photon excitation. A number that helps to characterize this evolution is the rate at which the quasiparticle density relaxes to its equilibrium value. The main mechanism for the relaxation is quasiparticle recombination (two quasiparticles from a Cooper-pair), and the effective recombination time is denoted as τ_{qp}^* . For conventional superconductors like Al, this recombination time can be well described by theory [39], and can be as long as a few milliseconds at low temperatures [40, 41].

1.4.1 DISORDERED SUPERCONDUCTORS FOR MKIDS

Having a high kinetic inductance in MKIDs increases the signal, since the fraction of kinetic inductance to the total inductance in the resonator increases, and the

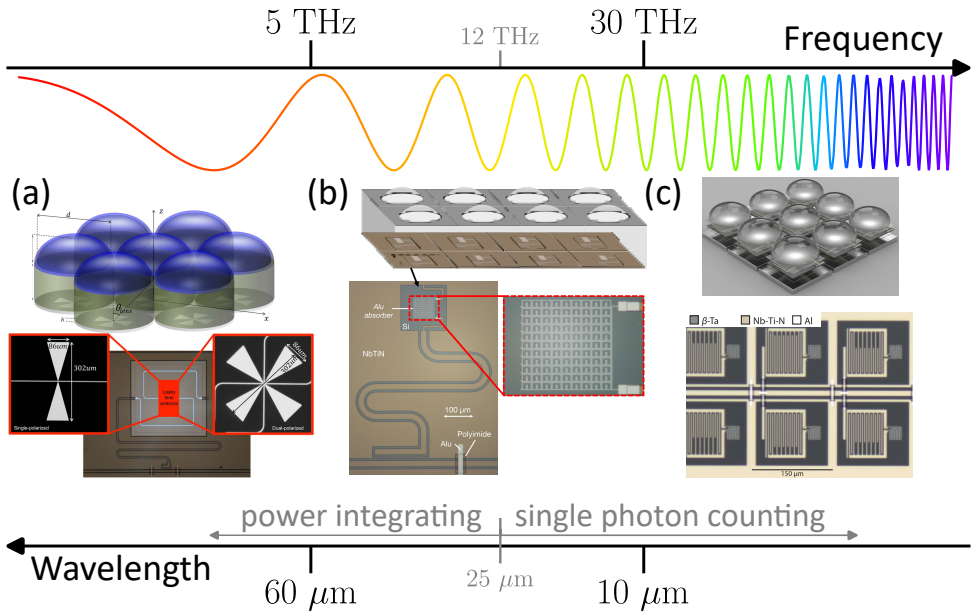


Figure 1.4: Different strategies for absorbing light into an MKID detector as a function of the frequency (top) and wavelength (bottom) of the light. **(a)**: A lens-antenna system, as described in Refs. [29–34]. The lens-antenna couples the light to a superconducting transmission line (highlighted in light blue), where it is absorbed. The lenses with anti-reflection coating (dark blue) are shown at the top and the antenna and MKID are shown at the bottom. The two red-framed insets show single (left) and dual polarized (right) antennae. The images are from Ref. [30]. **(b)**: Lens-absorber system, with a patterned direct absorber below a lens (highlighted in the dashed red box) [35, 36]. The geometry of the absorber can be tuned to maximize absorption efficiency. The image is from Ref. [36] **(c)**: A lens and optical stack geometry (top) to absorb the light directly in a superconducting film of β -Ta, embedded in a lumped-element kinetic inductance detector (LEKID, bottom) [15, 16]. The optical stack consists of two dielectric layers (transparent) with the MKID in between and a mirror at the bottom. The thickness of the dielectric layers can be tuned to maximize absorption efficiency. For wide-band absorption, a disordered superconductor must be used as absorbing film. Top image generated with AI using Google's Gemini 2.5 Pro, with input from the images in Refs. [15, 16, 37]. The bottom image is from Ref. [37].

absorption volume can be designed smaller for the same resonance frequency¹. This is a straight-forward reason to use disordered superconductors in MKIDs [43]. There is however a much more stringent reason to use disordered superconductors for MKIDs, especially for short wavelength light detection. Before going into that reason, we will first shortly review the different kinds of MKIDs, ordered from low to high radiation frequency (see Fig. 1.4).

An MKID can be used for light with photon energies larger than 2Δ , since these

¹The angular resonance frequency is proportional to the square root of the inductance times the capacitance, $\omega_0 \propto 1/\sqrt{LC}$.

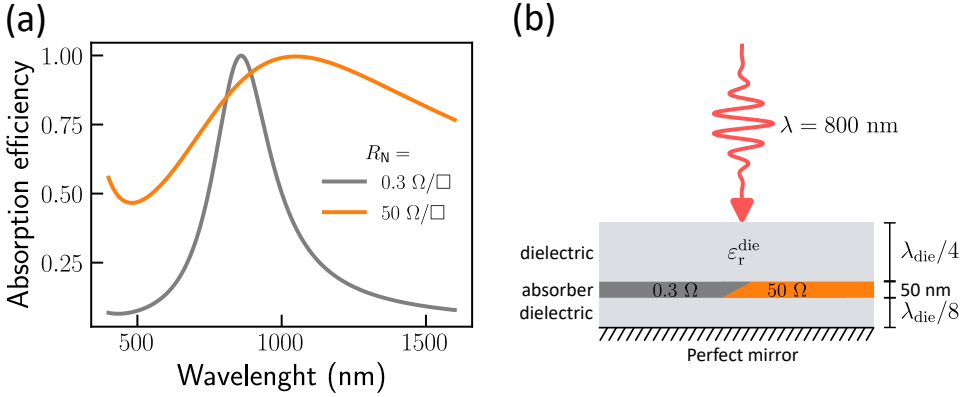


Figure 1.5: Absorption efficiency of a conventional (gray) and disordered (orange) superconducting film in an optical stack. (a): Calculated absorption efficiency versus wavelength. The ABCD-matrix methods presented in Refs. [15, 16, 42] are used to calculate the absorption efficiency, with the structure presented in panel (b). (b): Cross-section of the optical stack. The thickness of the dielectric layers are chosen to be quarter wave (top) and one eighth of the wavelength inside the dielectric (bottom). The structure is optimized with the relative dielectric permittivity of $\epsilon_r^{\text{die}} = 377 \Omega/R_s$, with 377Ω the impedance of free space and $R_s = \sqrt{2\pi c \mu_0 R_N d}/(2\lambda)$ the surface resistance of the absorber, which is considered to be a good conductor, as described in Ref. [42]. μ_0 is the permeability of free space, c is the speed of light, R_N is the normal state sheet resistance (either 0.3Ω or 50Ω), $d = 50 \text{ nm}$ is the sheet thickness and λ is the wavelength in free space which is set to 800 nm .

photons can break Cooper-pairs into quasiparticles². For a superconductor with a $T_c = 1 \text{ K}$, this is light with a frequency of about 74 GHz or a wavelength of 4 mm . For these large wavelengths, lens-antenna systems can be used to couple the light into a superconducting transmission line where the light is absorbed in the superconductor. Such a system is depicted in Fig. 1.4(a). Since the length of the transmission line can be long, a superconductor with low R_N can be used in these systems. Therefore, Al is often chosen as absorbing material, since this results in the best detector performance so far (partly due to the long τ_{qp}^* of Al [45]), and since the superconductor Al is reasonably well understood [46]. When the Al transmission line is designed properly, the absorption efficiency of these detectors is set by the lens-antenna design, and a high absorption efficiency can be achieved over a large frequency range [29, 31].

When the frequency is increased the wavelength decreases, and the alignment and roughness of the lens set a practical limit to the applicability of the lens-antenna systems. At 5 THz or $60 \mu\text{m}$ the required alignment and roughness precision are a few microns (typically one twentieth of the wavelength) and these systems become challenging to fabricate. A solution is to go to absorber systems [35, 36, 47], see Fig. 1.4(b). Using an absorber instead of an antenna relaxes the constraints on the

²Except in the case of very disordered superconductors, where subgap ($< 2\Delta$) absorption of radiation is possible [44].

lens, since the absorption efficiency of an absorber is not dependent on the phase of the incoming light, but only on the amplitude. The absorber can be patterned in a meandering structure to tune the effective sheet impedance for the incoming light. Therefore, the benefits of using Al can still be leveraged in these systems. By using narrow lines and resonant meandering structures the low $R_N \approx 0.5 \Omega/\square$ of Al can be tuned to match the $\sim 100 \Omega$ impedance of the Si lens [36, 47, 48].

When going to even higher frequencies, the patterning of the absorber also becomes unfeasible. At $10 \mu\text{m}$, the patterning must be more accurate than 500 nm (again, $\lambda/20$), at which the nanofabrication process to make these structures becomes increasingly difficult. Therefore, at higher frequencies the light must be absorbed in a superconducting film, and the sheet impedance of the film impacts the absorption efficiency and bandwidth directly. By using a lens, an optical stack of dielectrics and a backing reflector (i.e., a mirror, see Fig. 1.4(c)), the absorption efficiency can be essentially increased to 100% [15, 16]. This can only be optimized for a very limited bandwidth. A high, broadband absorption efficiency is however highly desired for these short wavelength MKIDs, because this would enable a unique feature of these detectors.

For wavelengths shorter than $25 \mu\text{m}$ MKIDs can resolve individual photons [48], which allows a much more sensitive, single photon-counting mode, instead of the power-integrating mode used at longer wavelengths (see Fig. 1.4). In this single photon-counting mode, the amplitude of the single photon signal gives additional information: it gives an estimate of the energy of each incoming photon. Resolving of the energy of single, infrared photons is a unique feature of MKIDs. In order to benefit from this feature, a wide-band absorption is strictly needed.

To achieve a high absorption efficiency for a broad wavelength range, a disordered superconductor is required as absorbing film. The high normal state resistance of disordered superconductors makes it easier to absorb light of different wavelengths. To illustrate this, Fig. 1.5(a) shows the difference in absorption efficiency between an absorbing film of 0.3Ω , which is typical for Al, and 50Ω , which is typical for β -phase Ta as used in the studies in this thesis. Figure 1.5(b) shows a cross-section of the analyzed structure [16, 42]. The higher resistive film (orange) shows a much broader absorption peak in Fig. 1.5(a) and therefore enables the energy resolving capabilities of MKIDs. In contrast, the absorption peak of the lower resistive film is very narrow. Using conventional superconductors in MKIDs therefore eliminates the energy resolving capabilities for wavelengths smaller than $10 \mu\text{m}$. This shows that disordered superconductors are a necessity for energy-resolving, photon-counting MKIDs.

Unfortunately, experiments have shown that it is rather difficult to estimate the photon energy accurately with MKIDs made from disordered superconductors. The metric that measures how well photon energies can be determined is the energy resolving power, and is defined as $R = E/\delta E$ (not to be confused with normal state sheet resistance, R_N), where E is the photon energy and δE is the energy resolution. A high energy resolving power indicates an accurate determination of the photon energy.

Figure 1.6(a) shows that an MKID made from disordered superconductors

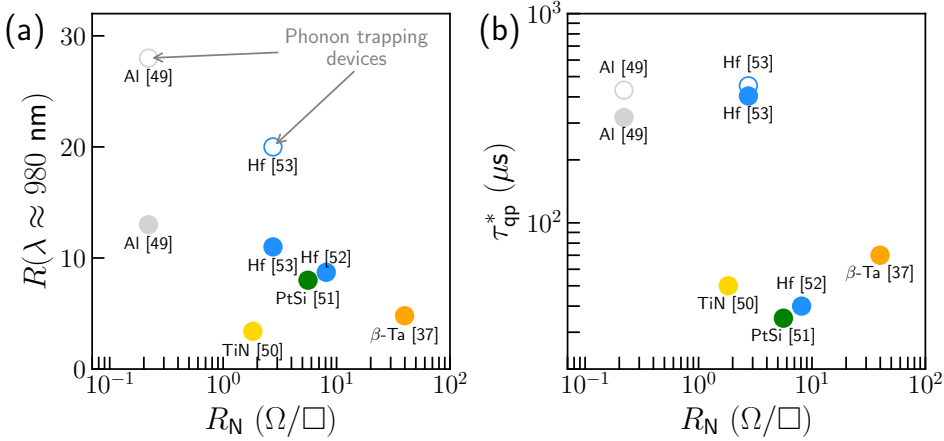


Figure 1.6: Effect of disorder on the energy resolving power (a) and effective quasiparticle recombination time (b). **(a)**: The energy resolving power R at a wavelength of 980 nm for various superconductors as a function of the normal state sheet resistance R_N . The materials are indicated next to the data points, along with references [37, 49–53]. Refs. [49, 53] design the surroundings of the superconductor such, that the energy of the photon stays in the absorbing volume, instead of leaking out via phonon (lattice vibration) excitations. This is called phonon trapping. Those devices have been indicated by open circles. **(b)**: The effective quasiparticle recombination time as a function of normal state sheet resistance, from the same references as in panel (a).

($R_N > 10 \text{ } \Omega/\square$) with a decent resolving power ($R > 10$) has not been realized yet. Obtaining a high absorption efficiency over a broad wavelength range (i.e., having a high R_N) and achieving a high resolving power seems to be excluded by the effects of disorder. From Fig. 1.3(b), we know that the microwave loss in disordered superconductors is higher compared to conventional superconductors. Additionally, from Fig. 1.6(b), we see that also the effective quasiparticle recombination time seems to decrease with disorder. Also when introducing disorder in the conventional Al, the low-temperature value of τ_{qp}^* is observed to decrease [54]. These observations point towards an effect of disorder on the quasiparticle dynamics. It is however not yet clear how exactly disorder affects the quasiparticle dynamics.

In this thesis, we will probe the quasiparticle dynamics in superconductors by measuring the noise and signal in MKIDs. The noise in MKIDs corresponds to fluctuations in the quasiparticle density, and the signal corresponds to a transient change in the quasiparticle density after an excitation. We will particularly focus on the role of disorder on the quasiparticle dynamics. In Chapter 2, we will set out the theoretical background needed to read and understand Chapters 4 to 7. This includes the commonly used theory to predict the response of MKIDs and the effects of disorder on the superconducting state. In Chapter 3, we briefly set out the experimental setup, fabrication of the samples and measurement procedures. In Chapter 4 we will investigate the conventional superconductor Al via quasiparticle

fluctuations. We will show that at low temperatures, the standard theory that describes the relation between τ_{qp}^* and n_{qp} breaks down. This suggests that there are effects of disorder even in a superconductor with low normal state resistance. This chapter also acts as a starting point for the interpretation of the quasiparticle fluctuations in disordered superconductors (Chapter 6).

In Chapter 5 we will measure the effect of the microwave probe power on Al resonators with varying volumes. We show that this power generates quasiparticles at low temperatures and explain the variation in sensitivity with Al volume in the most sensitive MKIDs to date [46]. Contrary to common understanding, we will show that the quasiparticles are generated by an indirect mechanism, instead of direct microwave photon absorption by the quasiparticles.

Chapter 6 deals with the recombination dynamics in the disordered superconductor β -Ta. We will argue in this chapter that disorder causes quasiparticle localization, which alters the recombination dynamics drastically. Counter-intuitively, the effects of localization enhances the recombination rate.

In Chapter 7 we will investigate the β -Ta MKID response to single photons. This response is non-exponential in time, which is usually attributed to an enhanced quasiparticle density due to the photon absorption, that changes over time and space. We will however show that this mechanism alone cannot explain the observations, and argue that localization and non-equilibrium effects should be taken into account to explain the single photon response of disordered superconductors.

REFERENCES

- [1] H. Kamerlingh Onnes. *The Liquefaction of Helium*. In: *KNAW, Proceedings* 11 (1908), pp. 168–185.
- [2] D. Van Delft. *The Liquefaction of Helium*. In: *Europhysics News* 39.6 (2008), pp. 23–25.
- [3] A. Maas and A. J. Kox. *Albert Einstein, Heike Kamerlingh Onnes and the Discovery of Superconductivity*. In: *European Journal of Physics* 46.5 (2025), p. 055805.
- [4] H. K. Onnes and W. H. Keesom. *Further Experiments with Liquid Helium G. On the Electrical Resistance of Pure Metals Etc. VI. On the Sudden Change in the Rate at Which the Resistance of Mercury Disappears*. In: *KNAW, Proceedings* 14.2 (1911), pp. 818–821.
- [5] L. Boeri, R. Hennig, P. Hirschfeld, G. Profeta, A. Sanna, E. Zurek, W. E. Pickett, M. Amsler, R. Dias, M. I. Eremets, C. Heil, R. J. Hemley, H. Liu, Y. Ma, C. Pierleoni, A. N. Kolmogorov, N. Rybin, D. Novoselov, V. Anisimov, A. R. Oganov, C. J. Pickard, T. Bi, R. Arita, I. Errea, C. Pellegrini, R. Requist, E. K. U. Gross, E. R. Margine, S. R. Xie, Y. Quan, A. Hire, L. Fanfarillo, G. R. Stewart, J. J. Hamlin, V. Stanev, R. S. Gonnelli, E. Piatti, D. Romanin, D. Daghero, and R. Valenti. *The 2021 Room-Temperature Superconductivity Roadmap*. In: *Journal of Physics: Condensed Matter* 34.18 (2022), p. 183002.
- [6] D. van Delft and P. Kes. *The Discovery of Superconductivity*. In: *Physics Today* 63.9 (2010), p. 38.
- [7] R. Acharya *et al.* *Quantum Error Correction below the Surface Code Threshold*. In: *Nature* 638.8052 (2025), pp. 920–926.
- [8] X. Zhou, W.-S. Lee, M. Imada, N. Trivedi, P. Phillips, H.-Y. Kee, P. Törmä, and M. Eremets. *High-Temperature Superconductivity*. In: *Nature Reviews Physics* 3.7 (2021), pp. 462–465.
- [9] D. B. Haviland, Y. Liu, and A. M. Goldman. *Onset of Superconductivity in the Two-Dimensional Limit*. In: *Physical Review Letters* 62.18 (1989), pp. 2180–2183.
- [10] L. Grünhaupt, M. Spiecker, D. Gusenkova, N. Maleeva, S. T. Skacel, I. Takmakov, F. Valenti, P. Winkel, H. Rotzinger, W. Wernsdorfer, A. V. Ustinov, and I. M. Pop. *Granular Aluminium as a Superconducting Material for High-Impedance Quantum Circuits*. In: *Nature Materials* 18.8 (8 2019), pp. 816–819.

- [11] J. T. Peltonen, P. C. J. J. Coumou, Z. H. Peng, T. M. Klapwijk, J. S. Tsai, and O. V. Astafiev. *Hybrid Rf SQUID Qubit Based on High Kinetic Inductance*. In: *Scientific Reports* 8.1 (1 2018), p. 10033.
- [12] N. Samkharadze, A. Bruno, P. Scarlino, G. Zheng, D. P. DiVincenzo, L. DiCarlo, and L. M. K. Vandersypen. *High-Kinetic-Inductance Superconducting Nanowire Resonators for Circuit QED in a Magnetic Field*. In: *Physical Review Applied* 5.4 (2016), p. 044004.
- [13] B. Ho Eom, P. K. Day, H. G. LeDuc, and J. Zmuidzinas. *A Wideband, Low-Noise Superconducting Amplifier with High Dynamic Range*. In: *Nature Physics* 8.8 (8 2012), pp. 623–627.
- [14] P. Winkel, K. Borisov, L. Grünhaupt, D. Rieger, M. Spiecker, F. Valenti, A. V. Ustinov, W. Wernsdorfer, and I. M. Pop. *Implementation of a Transmon Qubit Using Superconducting Granular Aluminum*. In: *Physical Review X* 10.3 (2020), p. 031032.
- [15] E. F. C. Driessen, F. R. Braakman, E. M. Reiger, S. N. Dorenbos, V. Zwiller, and M. J. A. de Dood. *Impedance Model for the Polarization-Dependent Optical Absorption of Superconducting Single-Photon Detectors*. In: *The European Physical Journal Applied Physics* 47.1 (1 2009), p. 10701.
- [16] K. Kouwenhoven, I. Elwakil, J. van Wingerden, V. Murugesan, D. J. Thoen, J. J. A. Baselmans, and P. J. de Visser. *Model and Measurements of an Optical Stack for Broadband Visible to Near-Infrared Absorption in TiN MKIDs*. In: *Journal of Low Temperature Physics* 209.5 (2022), pp. 1249–1257.
- [17] J. Bardeen, L. N. Cooper, and J. R. Schrieffer. *Theory of Superconductivity*. In: *Physical Review* 108.5 (1957), pp. 1175–1204.
- [18] J. Bardeen, L. N. Cooper, and J. R. Schrieffer. *Microscopic Theory of Superconductivity*. In: *Physical Review* 106.1 (1957), pp. 162–164.
- [19] P. W. Anderson. *Theory of Dirty Superconductors*. In: *Journal of Physics and Chemistry of Solids* 11.1 (1959), pp. 26–30.
- [20] A. Aronov. *Fourteen Years of Quantum Interference in Disordered Metals*. In: *Physica Scripta* T49A (1993), pp. 28–33.
- [21] M. Tinkham. *Introduction to Superconductivity*. Dover Publications, 2004. 482 pp.
- [22] D. C. Mattis and J. Bardeen. *Theory of the Anomalous Skin Effect in Normal and Superconducting Metals*. In: *Physical Review* 111.2 (1958), pp. 412–417.
- [23] B. Sacépé, C. Chapelier, T. I. Baturina, V. M. Vinokur, M. R. Baklanov, and M. Sanquer. *Disorder-Induced Inhomogeneities of the Superconducting State Close to the Superconductor-Insulator Transition*. In: *Physical Review Letters* 101.15 (2008), p. 157006.
- [24] M. V. Feigel'man and M. A. Skvortsov. *Universal Broadening of the Bardeen-Cooper-Schrieffer Coherence Peak of Disordered Superconducting Films*. In: *Physical Review Letters* 109.14 (2012), p. 147002.

- [25] B. Sacépé, M. Feigel'man, and T. M. Klapwijk. *Quantum Breakdown of Superconductivity in Low-Dimensional Materials*. In: *Nature Physics* 16.7 (7 2020), pp. 734–746.
- [26] T. Charpentier, A. Khvalyuk, L. Ioffe, M. Feigel'man, N. Roch, and B. Sacépé. *Universal Scaling of Microwave Dissipation in Superconducting Circuits*. 2025. URL: <http://arxiv.org/abs/2507.08953>. Pre-published.
- [27] C. J. Gorter and H. Casimir. *The Thermodynamics of the Superconducting State*. In: *Z. tech. Phys* 15 (1934), pp. 539–42.
- [28] L. Grünhaupt, N. Maleeva, S. T. Skacel, M. Calvo, F. Levy-Bertrand, A. V. Ustinov, H. Rotzinger, A. Monfardini, G. Catelani, and I. M. Pop. *Loss Mechanisms and Quasiparticle Dynamics in Superconducting Microwave Resonators Made of Thin-Film Granular Aluminum*. In: *Physical Review Letters* 121.11 (2018), p. 117001.
- [29] A. Neto, N. Llombart, J. J. A. Baselmans, A. Baryshev, and S. J. C. Yates. *Demonstration of The Leaky Lens Antenna at Submillimeter Wavelengths*. In: *IEEE Transactions on Terahertz Science and Technology* 4.1 (2014), pp. 26–32.
- [30] J. Bueno, O. Yurduseven, N. Llombart, S. J. C. Yates, A. Neto, and J. J. A. Baselmans. *Experimental Validation of an MKID Coupled Dual Polarized Leaky Lens Antenna*. In: *2017 42nd International Conference on Infrared, Millimeter, and Terahertz Waves (IRMMW-THz)*. 2017 42nd International Conference on Infrared, Millimeter, and Terahertz Waves (IRMMW-THz). 2017, pp. 1–2.
- [31] S. Hähnle, O. Yurduseven, S. Van Berkel, N. Llombart, J. Bueno, S. J. C. Yates, V. Murugesan, D. J. Thoen, A. Neto, and J. J. A. Baselmans. *An Ultra-Wideband Leaky Lens Antenna for Broadband Spectroscopic Imaging Applications*. In: *IEEE Transactions on Antennas and Propagation* (2020), pp. 1–1.
- [32] L. Ferrari, O. Yurduseven, N. Llombart, S. J. C. Yates, J. Bueno, V. Murugesan, D. J. Thoen, A. Endo, A. M. Baryshev, and J. J. A. Baselmans. *Antenna Coupled MKID Performance Verification at 850 GHz for Large Format Astrophysics Arrays*. In: *IEEE Transactions on Terahertz Science and Technology* 8.1 (2018), pp. 127–139.
- [33] S. J. C. Yates, J. J. A. Baselmans, A. Endo, R. M. J. Janssen, L. Ferrari, P. Diener, and A. M. Baryshev. *Photon Noise Limited Radiation Detection with Lens-Antenna Coupled Microwave Kinetic Inductance Detectors*. In: *Applied Physics Letters* 99.7 (2011), p. 073505.
- [34] P. K. Day, H. G. Leduc, A. Goldin, T. Vayonakis, B. A. Mazin, S. Kumar, J. Gao, and J. Zmuidzinas. *Antenna-Coupled Microwave Kinetic Inductance Detectors*. In: *Nuclear Instruments and Methods in Physics Research Section A: Accelerators, Spectrometers, Detectors and Associated Equipment*. Proceedings of the 11th International Workshop on Low Temperature Detectors 559.2 (2006), pp. 561–563.

- [35] N. Llombart, S. O. Dabironezare, G. Carluccio, A. Freni, and A. Neto. *Reception Power Pattern of Distributed Absorbers in Focal Plane Arrays: A Fourier Optics Analysis*. In: *IEEE Transactions on Antennas and Propagation* 66.11 (2018), pp. 5990–6002.
- [36] S. O. Dabironezare, G. Conenna, D. Roos, D. Lamers, D. P. Capelo, H. M. Veen, D. J. Thoen, V. Anvekar, S. J. C. Yates, W. Jellema, R. Huiting, L. Ferrari, C. Tucker, S. L. van Berkel, P. K. Day, H. G. Leduc, C. M. Bradford, N. Llombart, and J. J. A. Baselmans. *Lens Based Kinetic Inductance Detectors with Distributed Dual Polarised Absorbers for Far Infra-red Space-based Astronomy*. 2025. URL: <http://arxiv.org/abs/2506.03359>. Pre-published.
- [37] K. Kouwenhoven, D. Fan, E. Biancalani, S. A. H. de Rooij, T. Karim, C. S. Smith, V. Murugesan, D. J. Thoen, J. J. A. Baselmans, and P. J. de Visser. *Resolving Power of Visible-To-Near-Infrared Hybrid β -Ta/Nb-Ti-N Kinetic Inductance Detectors*. In: *Physical Review Applied* 19.3 (2023), p. 034007.
- [38] P. K. Day, H. G. LeDuc, B. A. Mazin, A. Vayonakis, and J. Zmuidzinas. *A Broadband Superconducting Detector Suitable for Use in Large Arrays*. In: *Nature* 425.6960 (2003), pp. 817–821.
- [39] S. B. Kaplan, C. C. Chi, D. N. Langenberg, J. J. Chang, S. Jafarey, and D. J. Scalapino. *Quasiparticle and Phonon Lifetimes in Superconductors*. In: *Physical Review B* 14.11 (1976), pp. 4854–4873.
- [40] A. Fyhrie, P. Day, J. Glenn, H. Leduc, C. McKenney, J. Perido, and J. Zmuidzinas. *Decay Times of Optical Pulses for Aluminum CPW KIDs*. In: *Journal of Low Temperature Physics* 199.3 (2020), pp. 688–695.
- [41] P. J. de Visser, J. J. A. Baselmans, P. Diener, S. J. C. Yates, A. Endo, and T. M. Klapwijk. *Number Fluctuations of Sparse Quasiparticles in a Superconductor*. In: *Physical Review Letters* 106.16 (2011), p. 167004.
- [42] D. M. Pozar. *Microwave Engineering, 4th Edition*. Wiley, 2011. 756 pp.
- [43] H. G. Leduc, B. Bumble, P. K. Day, B. H. Eom, J. Gao, S. Golwala, B. A. Mazin, S. McHugh, A. Merrill, D. C. Moore, O. Noroozian, A. D. Turner, and J. Zmuidzinas. *Titanium Nitride Films for Ultrasensitive Microresonator Detectors*. In: *Applied Physics Letters* 97.10 (2010), p. 102509.
- [44] F. Levy-Bertrand, A. Benoît, O. Bourrion, M. Calvo, A. Catalano, J. Goupy, F. Valenti, N. Maleeva, L. Grünhaupt, I. Pop, and A. Monfardini. *Subgap Kinetic Inductance Detector Sensitive to 85-GHz Radiation*. In: *Physical Review Applied* 15.4 (2021), p. 044002.
- [45] B. A. Mazin. *Superconducting Materials for Microwave Kinetic Inductance Detectors*. 2020.
- [46] J. J. A. Baselmans, F. Facchin, A. P. Laguna, J. Bueno, D. J. Thoen, V. Murugesan, N. Llombart, and P. J. de Visser. *Ultra-Sensitive THz Microwave Kinetic Inductance Detectors for Future Space Telescopes*. In: *Astronomy & Astrophysics* 665 (2022), A17.

- [47] A. Monfardini, A. Benoit, A. Bideaud, L. Swenson, A. Cruciani, P. Camus, C. Hoffmann, F. X. Désert, S. Doyle, P. Ade, P. Mauskopf, C. Tucker, M. Roesch, S. Leclercq, K. F. Schuster, A. Endo, A. Baryshev, J. J. A. Baselmans, L. Ferrari, S. J. C. Yates, O. Bourrion, J. Macias-Perez, C. Vescovi, M. Calvo, and C. Giordano. *A Dual-Band Millimeter-Wave Kinetic Inductance Camera for the IRAM 30m Telescope*. In: *The Astrophysical Journal Supplement Series* 194.2 (2011), p. 24.
- [48] P. K. Day, N. F. Cothard, C. Albert, L. Foote, E. Kane, B. H. Eom, R. Basu Thakur, R. M. J. Janssen, A. Beyer, P. M. Echternach, S. van Berkel, S. Hailey-Dunsheath, T. R. Stevenson, S. Dabironezare, J. J. A. Baselmans, J. Glenn, C. M. Bradford, and H. G. Leduc. *A 25-Micrometer Single-Photon-Sensitive Kinetic Inductance Detector*. In: *Physical Review X* 14.4 (2024), p. 041005.
- [49] P. J. de Visser, S. A. H. de Rooij, V. Murugesan, D. J. Thoen, and J. J. A. Baselmans. *Phonon-Trapping-Enhanced Energy Resolution in Superconducting Single-Photon Detectors*. In: *Physical Review Applied* 16.3 (2021), p. 034051.
- [50] S. Meeker, B. Mazin, R. Jensen-Clem, A. Walter, P. Szypryt, M. Strader, and C. Bockstiegel. *Design and Development Status of MKID Integral Field Spectrographs for High Contrast Imaging*. In: *Adaptive Optics for Extremely Large Telescopes 4 – Conference Proceedings* 1.1 (2015).
- [51] P. Szypryt, B. A. Mazin, G. Ulbricht, B. Bumble, S. R. Meeker, C. Bockstiegel, and A. B. Walter. *High Quality Factor Platinum Silicide Microwave Kinetic Inductance Detectors*. In: *Applied Physics Letters* 109.15 (2016), p. 151102.
- [52] N. Zobrist, G. Coiffard, B. Bumble, N. Swimmer, S. Steiger, M. Daal, G. Collura, A. B. Walter, C. Bockstiegel, N. Fruitwala, I. Lipartito, and B. A. Mazin. *Design and Performance of Hafnium Optical and Near-IR Kinetic Inductance Detectors*. In: *Applied Physics Letters* 115.21 (2019), p. 213503.
- [53] N. Zobrist, W. H. Clay, G. Coiffard, M. Daal, N. Swimmer, P. Day, and B. A. Mazin. *Membraneless Phonon Trapping and Resolution Enhancement in Optical Microwave Kinetic Inductance Detectors*. In: *Physical Review Letters* 129.1 (2022), p. 017701.
- [54] R. Barends, S. van Vliet, J. J. A. Baselmans, S. J. C. Yates, J. R. Gao, and T. M. Klapwijk. *Enhancement of Quasiparticle Recombination in Ta and Al Superconductors by Implantation of Magnetic and Nonmagnetic Atoms*. In: *Physical Review B* 79.2 (2009), 020509(R).

2

THEORY

In this chapter, we will provide the theoretical background that is needed to apprehend Chapters 4 to 7. In Section 2.1, we will start with the response of electrons to an alternating electro-magnetic field, such as microwaves in a metallic waveguide or incident radiation on a metallic film. We will extend this description by considering electrons in a zero-resistive (phenomenologically superconducting) state. Then, we will set out the basics of the microscopic description of superconductivity. From this microscopic theory, we obtain an expression for the sheet impedance of a superconducting film, which describes the kinetic inductance (imaginary part of the sheet impedance) and microwave dissipation (the real part of the sheet impedance). In Section 2.2, we will consider a superconducting film that is patterned into a microwave resonator. We will describe the relation between the resonator observables (resonance frequency and Q factor) and the superconducting properties (kinetic inductance and microwave dissipation). We will briefly discuss other mechanisms that change these observables.

Having discussed the basics of superconducting resonators in Sections 2.1 and 2.2, we will deepen this discussion in Section 2.3 by considering a superconducting state that is excited by various mechanisms (thermal fluctuations, pair-breaking photon absorption and subgap photons). Lastly, in Section 2.4, we will describe how the superconducting state and its excitations are altered when disorder is introduced, i.e., when the metal is highly resistive in the normal state.

2.1 ELECTRONIC RESPONSE TO RADIATION

The system that we consider is a superconducting microwave resonator. This means, we probe a superconductor with an alternating current (AC). To understand this system, we thus need a description of the AC response of a superconductor. A superconductor is a metallic conductor that loses its resistance completely when cooled below its critical temperature, T_c , and expels all magnetic flux density in its interior. To understand this, we first need a description of electrical conductance of a normal metal. After that, we will introduce the phenomenological concepts needed to describe the AC response of a superconductor. Then, we will introduce a microscopic framework, which will help to understand the nature of the excitations

in a superconductor.

2.1.1 NORMAL METALS

The simplest way to describe a metal is to consider it as a volume with charged particles that can move freely, where we disregard the atomic lattice and interactions among the electrons completely. Hence, we end up with an ideal electron gas, where all the electrons have a certain position \mathbf{x} and velocity \mathbf{v} . When we consider these electrons as quantum mechanical particles, this is called the Drude-Sommerfeld model. The electron energies only have a kinetic part and have definite, quantized values of $\epsilon(\mathbf{k}) = \hbar^2 |\mathbf{k}|^2 / (2m^*)$. Here, \mathbf{k} is the electronic wave-vector, which is quantized due to the boundary conditions of the volume that the electrons occupy. m^* is the effective mass of an electron within the metal. This effective mass accounts for relatively weak interactions, which are otherwise not included in the model, such as interactions with the lattice and interactions among electrons. That these interactions result in an effective mass can be shown by a Boltzmann equation approach and by Fermi-liquid theory [1].

Since electrons are Fermionic particles (with a spin quantum number of 1/2), they obey the Pauli-exclusion principle and cannot occupy the same state. Therefore, when the temperature T goes to zero and all electrons occupy the lowest possible energy state, there is an occupied, highest energy state with a finite energy. This is called the Fermi energy and given by $\epsilon_F = \hbar^2 k_F^2 / (2m^*)$. Here, k_F is called the Fermi wave-number given by $k_F = (3\pi^2 n)^{1/3}$, where n is the electron number density. See Fig. 2.1(a) for an illustration of the filling of electronic states. The density of states at the Fermi energy for a single spin is given by $N_0 = 3n / (4\epsilon_F)$. The total density of states at the Fermi energy (including spin states) is thus given by $2N_0$. At a finite temperature, T , the electrons close to the Fermi energy will absorb some energy from the thermal bath and move to higher energy states. The distribution of electrons over energy is described by the Fermi-Dirac distribution,

$$f_{\text{FD}}(\epsilon) = \frac{1}{e^{(\epsilon - \epsilon_F) / (k_B T)} + 1}, \quad (2.1)$$

where k_B is the Boltzmann constant. Figure 2.1(a) illustrates this thermal distribution of the electrons close to the Fermi surface.

Because electrons have a charge $-e$, they experience a force in an electric field \mathbf{E} . The average drift velocity of the free electron gas can then be described by,

$$\frac{d\langle \mathbf{v} \rangle}{dt} = -\frac{e}{m^*} \mathbf{E} - \frac{\langle \mathbf{v} \rangle}{\tau}. \quad (2.2)$$

The first term on the right-hand side is Newton's second law of the electrostatic force to the local field \mathbf{E} . The second term is a frictional term that describes the resistance in the metal. τ is the scattering time of the electron, which captures all possible scatterers that cause dissipation, such as impurities and lattice-vibrations (phonons). The mean free path of electrons is given by $l = v_F \tau$, where $v_F = 2\epsilon_F / m^*$ is the Fermi velocity.

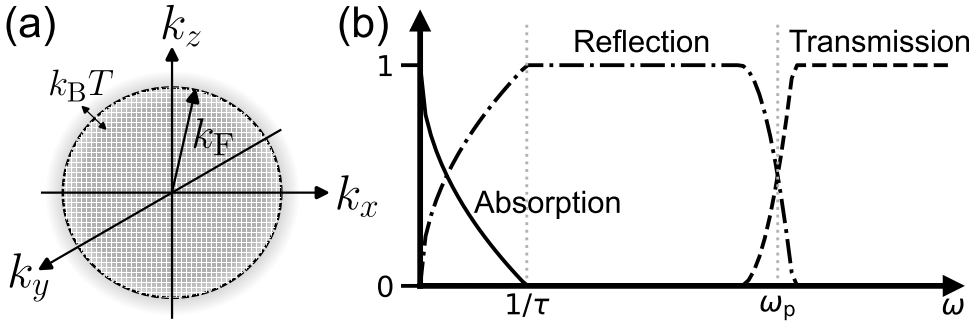


Figure 2.1: (a): Illustration of the quantized electron states in \mathbf{k} -space. The filled states are gray, which forms a Fermi sphere with radius k_F . At $k_B T$, the outermost states are occupied according to the Fermi-Dirac distribution (Eq. (2.1)). (b): Sketch of the high-frequency response of a normal metal, according to the free electron model. At frequencies $\omega < 1/\tau$ radiation is absorbed. For frequencies $1/\tau \ll \omega \ll \omega_p$, the response is inductive and radiation is reflected. For frequencies above the plasma frequency, $\omega \gg \omega_p$, the material supports electro-magnetic waves and the radiation is transmitted.

When we Fourier transform Eq. (2.2) we can solve for the drift velocity as a function of angular frequency ω of the field \mathbf{E} and find the current density,

$$\mathbf{J}(\omega) = -ne \langle \mathbf{v} \rangle = \frac{ne^2 \tau}{m^*} \frac{\mathbf{E}(\omega)}{1 + j\omega\tau} = \sigma(\omega) \mathbf{E}(\omega). \quad (2.3)$$

Here, n is the number density of electrons, $j^2 = -1$ and $\sigma(\omega) = \sigma_1(\omega) - j\sigma_2(\omega)$ is the complex conductivity. If we let $\omega \rightarrow 0$, we obtain the direct current (DC) conductivity of $\sigma_0 = ne^2 \tau / m^*$, which we can also see from the steady state solution of Eq. (2.2). With the expressions for N_0 and v_F given above, we can also express this as,

$$\frac{1}{\rho_N} = \sigma_0 = \frac{ne^2 \tau}{m^*} = 2e^2 N_0 D, \quad (2.4)$$

where $D = l^2 / (3\tau)$ is the electronic diffusion constant and ρ_N is the normal state resistivity, $\rho_N = R_N d$, with d the film thickness and R_N the normal state sheet resistance. Equation (2.4) is an Einstein relation, since it connects the drift and diffusion of the electrons.

For high frequencies, $\omega\tau \gg 1$, the conductivity becomes imaginary and the response becomes inductive. In this situation, the field changes direction faster than the electrons scatter, which changes the dissipative response to an inductive response. Incoming radiation will be reflected instead of absorbed. This is sketched in the low frequency part of Fig. 2.1(b).

With a current density given by Eq. (2.3), we can use the Maxwell equations to find

a wave-equation for the \mathbf{E} -field. The Maxwell equations are,

$$\nabla \cdot \mathbf{E} = \frac{\rho_e}{\epsilon_0}, \quad (2.5a)$$

$$\nabla \cdot \mathbf{B} = 0, \quad (2.5b)$$

$$\nabla \times \mathbf{E} = -\frac{\partial \mathbf{B}}{\partial t}, \quad (2.5c)$$

$$\nabla \times \mathbf{B} = \mu_0 \left(\mathbf{J} + \epsilon_0 \frac{\partial \mathbf{E}}{\partial t} \right). \quad (2.5d)$$

Here, ρ_e is charge density, the \mathbf{B} is the local magnetic flux density, ϵ_0 is the vacuum permittivity and μ_0 is the vacuum permeability, which we assume to be the permeability for all media considered here. When we look for wave solutions with a time-dependent part $e^{j\omega t}$, we find,

$$\nabla \times (\nabla \times \mathbf{E}) = -j\omega(\nabla \times \mathbf{B}) = \left(\frac{\omega}{c} \right)^2 \left(1 - \frac{j\sigma}{\omega\epsilon_0} \right) \mathbf{E}. \quad (2.6)$$

If we assume that the free electron gas is charge neutral, $\nabla \cdot \mathbf{E} = 0$ and the left-hand side of Eq. (2.6) becomes, $\nabla \times (\nabla \times \mathbf{E}) = \nabla(\nabla \cdot \mathbf{E}) - \nabla^2 \mathbf{E} = -\nabla^2 \mathbf{E}$. So, this is a wave equation where the permittivity is given by, $\epsilon = 1 - j\sigma/(\omega\epsilon_0)$. If we take σ from Eq. (2.3) for high frequencies, $\omega\tau \gg 1$, we see that ϵ becomes positive for frequencies above,

$$\omega_p = \sqrt{\frac{ne^2}{\epsilon_0 m^*}}. \quad (2.7)$$

This is called the plasma frequency and above it, electro-magnetic waves can propagate through the metal. This is sketched in the high frequency part of Fig. 2.1(b). To summarize the AC response of a normal metal: for frequencies $\omega \ll 1/\tau$ incoming radiation will be absorbed, for frequencies $1/\tau \ll \omega \ll \omega_p$ incoming radiation will be reflected, and for frequencies $\omega \gg \omega_p$ incoming radiation will be transmitted.

2.1.2 SUPERCONDUCTORS: PHENOMENOLOGICAL

Equation (2.3) describes the local response of a normal metal to an AC electric field, $\mathbf{E}(\omega)$. In an attempt to describe a superconductor, we can naively let the scattering time go to infinity, $\tau \rightarrow \infty$, in these equations. For DC fields, we see that a static field \mathbf{E} results in an accelerating drift velocity (i.e., current density), since the second term in Eq. (2.2) goes to zero,

$$\frac{d\mathbf{J}}{dt} = -\frac{ne^2}{m^*} \mathbf{E}. \quad (2.8)$$

When we take the curl and use the third Maxwell equation (Eq. (2.5c)), we obtain the relation,

$$\frac{\partial}{\partial t} \left(\nabla \times \mathbf{J} + \frac{ne^2}{m^*} \mathbf{B} \right) = 0. \quad (2.9)$$

This equation describes a perfect conductor (with $\tau \rightarrow \infty$). However, a superconductor is more than that: it not only opposes any changing magnetic field applied to it (perfect diamagnetism due to lossless Eddy-currents), it also expels magnetic fields that were already present. The flux density is strictly zero in the interior of a superconductor. This is called the Meissner effect, and can be described phenomenologically by setting expression between the brackets in Eq. (2.9) explicitly to zero. By doing so, we obtain the London equation [2],

$$\nabla \times \mathbf{J} = -\frac{ne^2}{m^*} \mathbf{B}. \quad (2.10)$$

Combining that with the second and fourth Maxwell (Eq. (2.5d)), we obtain,

$$\nabla \times (\nabla \times \mathbf{B}) = -\nabla^2 \mathbf{B} = -\lambda_L^{-2} \mathbf{B}. \quad (2.11)$$

The length scale λ_L is the London penetration depth and is given by,

$$\lambda_L = \sqrt{\frac{m^*}{\mu_0 ne^2}} = \sqrt{\frac{\rho_N l}{\mu_0 v_F}}. \quad (2.12)$$

We see from Eq. (2.11) that the flux density is exponentially suppressed over a length λ_L , i.e. the Meissner effect.

For an AC field, we set $\tau \rightarrow \infty$ in Eqs. (2.2) and (2.3) (or Fourier transform Eq. (2.8)) to obtain a purely imaginary conductivity with, $\sigma_2 = ne^2/(\omega m^*)$. So, we can also write the London penetration depth as $\lambda_L = 1/\sqrt{\mu_0 \omega \sigma_2}$. As a comparison, the skin depth of a normal metal is given by $\delta_N = 1/\sqrt{\mu_0 \omega \sigma_0/2}$ [3].

The penetration depth can be generalized by assuming both lossless charge carriers (with $\tau \rightarrow \infty$) and lossy charge carriers (with finite τ) to be present. This is called the two-fluid model [4]. Then, σ_1 and σ_2 are both finite and the generalized skin depth is given by $\delta = 1/\sqrt{\mu_0 \omega (|\sigma| + \sigma_2)/2}$ [5]. This expression is equal to δ_N when $\sigma \rightarrow 1/\rho_N$ and equal to λ_L when $\sigma \rightarrow -j ne^2/(\omega m^*)$.

Until now, we have assumed that the metal or superconductor responds locally to the fields; we assumed that the charge carriers are point-like particles. In general, however, the response to electro-magnetic fields is non-local, since charge carriers are quantum mechanical particles with a finite coherence length, ξ . The response of the metal at a point \mathbf{r} in space, depends on the field within a coherence length away from \mathbf{r} . Therefore, if the coherence length is much larger than the generalized skin depth, $\xi \gg \delta$, the response is non-local and the penetration depth effectively increases. In the opposite limit, the response is local and the treatment above is valid.

For electrons in a normal metal, the coherence length is given by the mean free path, l . This is usually short compared to the skin depth, $\delta_N \gg l$, so non-locality will only play a role in very good conductors and at very high frequencies [6]. For a superconductor however, the generalized skin depth is equal to λ_L , which is much smaller than δ_N (by a factor $\sqrt{\omega \tau}$). It is therefore likely that in the superconducting state, the non-local character of the response can become important.

Apart from the coherence length of the electrons, the superconducting state has

another coherence length associated with it. This other coherence length can be estimated via the Heisenberg uncertainty principle: $\Delta x \Delta p \geq \hbar/2$, where Δx is the coherence length corresponding to the momentum uncertainty Δp . Since the superconducting state appears at a thermal energy $k_B T_c$, the momentum uncertainty of the electrons around the Fermi level should be on the order of $\Delta p \sim k_B T_c / (2v_F)$. This leads to an estimate of the coherence length, $\xi_P \sim \hbar v_F / (k_B T_c)$, which is called the Pippard coherence length.

Both l and ξ_P constrain the non-local character of the response to the electromagnetic fields. Therefore, a generalized coherence length can be calculated as, $1/\xi = 1/\xi_P + 1/l$. This separates two regimes: $\xi_P \ll l$, where $\xi \approx \xi_P$, which is called the pure limit (also called the clean limit) and $\xi_P \gg l$, where $\xi \approx l$, which is called the dirty limit.

When $\xi < \lambda$, the fields vary only slightly over the coherence length and the local limit applies. To first order, the effective (bulk) penetration depth at low temperatures ($T \ll T_c$) is given by, $\lambda_{\text{eff}} = \lambda_L \sqrt{1 + \xi_P/l}$ [5]. The opposite limit, $l \gg \xi_P \gg \lambda$, is called the extreme anomalous limit, and has an effective penetration depth of $\lambda_{\text{eff}} \approx (\lambda_L \xi_P)^{1/3}$.

For thin films, the mean free path of electrons is limited by the film thickness, d . Therefore, a thin film superconductor is very often in the dirty and local limit and the effective penetration depth for magnetic fields parallel to the film is given by, $\lambda_{\text{eff}} \approx \lambda_L \sqrt{\xi_P/d}$. For perpendicular fields, the penetration depth is increased even more, since when $d < \lambda_{\text{eff}}$, the response is effectively two-dimensional. This is described by the Pearl length, $\lambda_{\perp} = \lambda_{\text{eff}}^2/d$.

In the dirty limit ($l \ll \xi_P$), the electronic motion is diffusive and the coherence length can be estimated as the diffusion length in coherence time, Δt , i.e., $\xi_D = \sqrt{3D\Delta t}$. When we again estimate the coherence time from the Heisenberg uncertainty principle, $\Delta t \Delta E \geq \hbar/2$ and use $\Delta E = k_B T_c$, we obtain $\xi_D \sim \sqrt{\hbar D / (k_B T_c)} \sim \sqrt{\xi_P l}$. So, for thin films in the dirty, local limit, the penetration depth is greatly enhanced (by a factor $\sqrt{\xi_P/d}$ for parallel and a factor $\lambda_L \xi_P^2/d^3$ for perpendicular fields) and the coherence length is reduced (to $\sqrt{\xi_P l}$).

By comparing the penetration depth and coherence length, two types of superconductors can be distinguished. When $\lambda/\xi < 1/\sqrt{2}$ [7], the magnetic field penetrates not further than one coherence length, and the magnetic field is always shielded effectively up until the critical magnetic field where superconductivity is destroyed [5],

$$\mu_0 H_c = \frac{\Phi_0}{2\sqrt{2}\pi\xi\lambda}. \quad (2.13)$$

Here, $\Phi_0 = \pi\hbar/e$ is the magnetic flux quantum. These superconductors are called type I superconductors. Type II superconductors are in the opposite limit, $\lambda/\xi > 1/\sqrt{2}$. The magnetic field can penetrate further than the coherence length into the superconductor and normal state regions can form. These normal state regions are surrounded by circulating currents that shield the rest of the superconductor from the penetrating flux (which is equal to one flux quantum, Φ_0). These objects of a normal region and circulating currents are called Abrikosov vortices [8]. The normal region has a size $\sim \xi$ and the circulating currents decay exponentially over

a distance λ . When these vortices move - for example, by applying current to the superconductor - they will dissipate energy. In real samples however a small amount of disorder in the lattice will pin these vortices at pinning sites, which prevents their movement. Type II superconductors have two critical fields, one where vortices start to enter (H_{c1}), and one where the vortices overlap and superconductivity is broken (H_{c2}). These are given by [9],

$$\mu_0 H_{c1} = \frac{\Phi_0}{4\pi\lambda^2} (\log(\lambda/\xi) + 0.5); \quad \mu_0 H_{c2} = \frac{\Phi_0}{2\pi\xi^2}. \quad (2.14)$$

From the expressions for H_c and H_{c2} , it is clear that the type I and type II are indeed separated by $\lambda/\xi = 1/\sqrt{2}$.

As we have seen above, the perpendicular penetration depth for thin films is greatly enhanced, which means that vortices will form much easier in thin film superconductors. These vortices are called Pearl vortices, and the circulating currents decay over larger distances than Abrikosov vortices ($\propto 1/r^2$ instead of exponential)¹. If these films are patterned into strips, the current is restricted also in the direction parallel to the film. If the width of the strip is much smaller than the Pearl length, $W \ll \lambda_\perp$, the width takes over the role of λ_\perp . The expression for H_{c1} becomes in this case [12, 13],

$$\mu_0 H_{c1} = \frac{2\Phi_0}{\pi W^2} \log(2W/(\pi\xi)). \quad (2.15)$$

2.1.3 SUPERCONDUCTORS: MICROSCOPIC

The above description of superconductivity is purely phenomenological. Questions like: why does τ tend towards infinity?; why does this state appear only at bath temperatures below T_c ?; and what causes the Meissner effect?; remain unanswered. To answer such questions, a microscopic description of superconductivity is needed. In other words, the free electron model (or even the Fermi liquid theory, resulting a m^*) described above lacks physical detail that can explain the superconductive state. For one, it disregards the ionic lattice completely, except for assuming its presence for charge neutrality. Indeed, once the electronic interaction with the ionic lattice is correctly incorporated, superconductivity can be microscopically described, as shown by Bardeen, Cooper and Schrieffer (BCS) [14, 15].

The positively charged ionic lattice responds to electro-magnetic fields as well: when a negative charge is present (e.g. an increased electron density), the ions will be attracted to it. The same happens for the electrons: when a higher ionic density is present, electrons will be attracted to it and screen the effective charge. The difference between these two types of screening is that the ions are much heavier than the electrons. So, when the ions are displaced, the electrons rapidly screen the effective charge, before the ion can return to its original position. This causes an attractive interaction between the electrons. When an electron attracts and displaces

¹These larger scale vortices give rise to stronger vortex-vortex interactions. This enables a Berezinskii-Kosterlitz-Thouless transition [10, 11], where two vortices are paired (one with $+\Phi_0$ flux and one with $-\Phi_0$) below T_{BKT} and unpaired above T_{BKT} .

ions an effective positive charge is created. This is recovered very slowly compared to the movement of electrons. So, when the electrons move away, the positive charge attracts another electrons. This attraction can be stronger than the repulsive Coulomb interactions, since the Coulomb interaction is screened by the electronic motion, which is much faster than the ionic motion. Figure 2.2 illustrates this pairing mechanism.

The collective motion of ions is called a phonon, so this attractive interaction between electrons is phonon-mediated. As long as the energy of the phonon is low enough such that the lattice can host it, the attractive interaction between electrons exists. The highest possible phonon energy in a lattice is the Debye energy, $\hbar\Omega_D$, which corresponds to the wavelength of the collective displacement of two times the lattice spacing.

BCS have described this attractive interaction with a constant potential $-V_{sc}$ for energies up to the Debye energy, and a potential of 0 above it. They only include this attractive potential for electrons with opposite momentum, $\mathbf{k}_2 = -\mathbf{k}_1$, such that a pair of two electrons bound by the attractive interaction has zero momentum. Any other momentum pairing has a total kinetic energy that is higher than zero, and thus is not the ground state. Since the potential is not dependent on the direction of \mathbf{k} , the orbital electronic wave functions are symmetric and the spin wave functions should be antisymmetric under exchange of the two electrons. Thus, the electron spins are in the singlet state: the electrons have opposite spin.

A bound pair of electrons is called a Cooper-pair. In the simplest BCS pairing scenario, the electrons in a Cooper-pair have opposite momentum and spin (see Fig. 2.2). The pairing of electrons into Cooper-pairs is energetically favorable. So, in the ground state, all electrons are paired in Cooper-pairs. The total energy gained by the electron pairing is $N_0\Delta_0^2/2$, where Δ_0 is the superconducting order parameter. The subscript 0 indicates that it is the value at $T \rightarrow 0$.

At finite temperatures, not all electrons are bound in Cooper-pairs and the state is thermally excited (much like the free electron gas in Fig. 2.1(a)). The lowest energy excitation is to break one Cooper-pair, which results in two Bogoliubov quasiparticles, or quasiparticles for short. These quasiparticles are a superposition of an electron and a hole. Their energy is given by $\epsilon_{\mathbf{k}} = \sqrt{E_{\mathbf{k}}^2 + \Delta^2}$, where $E_{\mathbf{k}}$ is the kinetic energy. Thus, they have a minimum energy of Δ , which is therefore also called the gap energy in BCS theory. Quasiparticles with a high kinetic energy behave as free electrons (above the Fermi surface) or holes (below the Fermi surface). The density of quasiparticle states can be obtained by equating the number of quasiparticle states to the number of electronic states, $N_s(\epsilon)d\epsilon = N_n(E)dE$ [5]. Since only the electrons close to the Fermi energy will contribute, we can take $N_n = N_0$ for the (single spin) normal state density of states. We obtain,

$$N_s(\epsilon) = N_0 \operatorname{Re} \left\{ \frac{\epsilon}{\sqrt{\epsilon^2 - \Delta^2}} \right\}. \quad (2.16)$$

The quasiparticle density is then easily calculated as,

$$n_{qp} = \int_{-\infty}^{\infty} 2N_s(\epsilon)f(\epsilon)d\epsilon \approx 2N_0\Delta_0 \sqrt{\frac{2\pi k_B T}{\Delta_0}} e^{-\Delta_0/(k_B T)}. \quad (2.17)$$

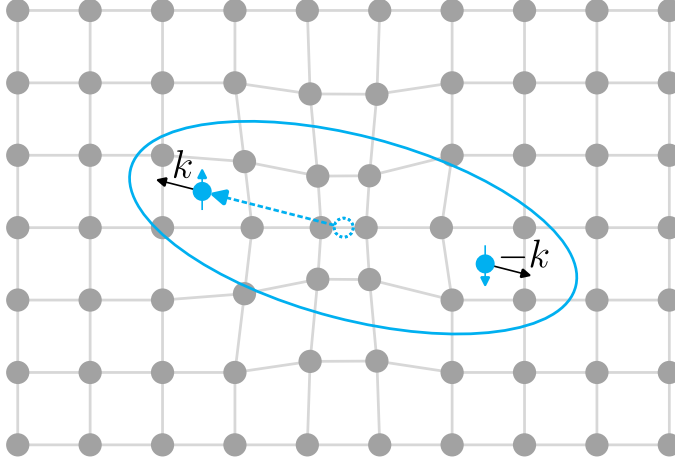


Figure 2.2: Illustration of the Cooper pairing mechanism via electron-phonon interaction. An electron (blue dots) deforms the ionic lattice (connected gray dots) slightly. As it moves away, the lattice restores slowly and the higher positive charge density attracts another electron. In the ground state, the paired electrons have opposite momentum and spin.

In the approximation, we used the Fermi-Dirac distribution (Eq. (2.1)) and approximated $k_B T \ll \Delta_0$. Figure 2.3(a) shows the density of states with the Fermi-Dirac distribution.

The order parameter, Δ , is affected by the presence of quasiparticles. 2Δ can be interpreted as the average binding energy between electrons. When quasiparticles are present, less Cooper-pairs are formed and Δ is suppressed. The temperature dependent order parameter, $\Delta(T)$, can be determined from the self-consistency equation [5],

$$\int_{\Delta(T)}^{\hbar\omega_c} \frac{1 - 2f(\epsilon)}{\sqrt{\epsilon^2 - \Delta^2(T)}} d\epsilon = \frac{1}{N_0 V_{sc}}. \quad (2.18)$$

In thermal equilibrium, the distribution function $f(\epsilon)$ is given by the Fermi-Dirac distribution, $f_{FD}(\epsilon)$ (Eq. (2.1)). The integral upper limit, i.e., the cut-off frequency, is given by $\hbar\omega_c = \sqrt{(\hbar\Omega_D)^2 + \Delta^2(T)} \approx \hbar\Omega_D$. When we take the self-consistency equation to the limit $k_B T \rightarrow 0$, we obtain $\Delta_0 = 2\hbar\Omega_D e^{-1/(N_0 V_{sc})}$, for $N_0 V_{sc} \ll 1$, which is called the weak-coupling limit. When we compare this to the limit $T \rightarrow T_c$ when $\Delta(T) \rightarrow 0$, it can be shown that $2\Delta_0 \approx 3.52 k_B T_c$ [3]. At low temperatures, Δ is fairly constant: $\Delta/\Delta_0 = 1 - n_{qp}/(2N_0\Delta)$, which gives $\Delta \approx 0.9\Delta_0$ at $T = T_c/2$ [16].

For this electron-phonon (BCS) coupling scheme, V_{sc} can be calculated for a clean metal as, $V_{sc} = (\hbar\Omega_D v_F)^2 / (36\hat{\rho}c_L^4)$, where $\hat{\rho}$ is the mass density and c_L is the longitudinal phonon velocity [17].

So, how does this microscopic picture of Cooper-pairs and quasiparticles shed more light onto the superconducting state? Foremost, it answers the question of why the superconducting state appears below T_c . At those temperatures, the Cooper-pairing becomes stronger than the thermal energy and Cooper-pairs are

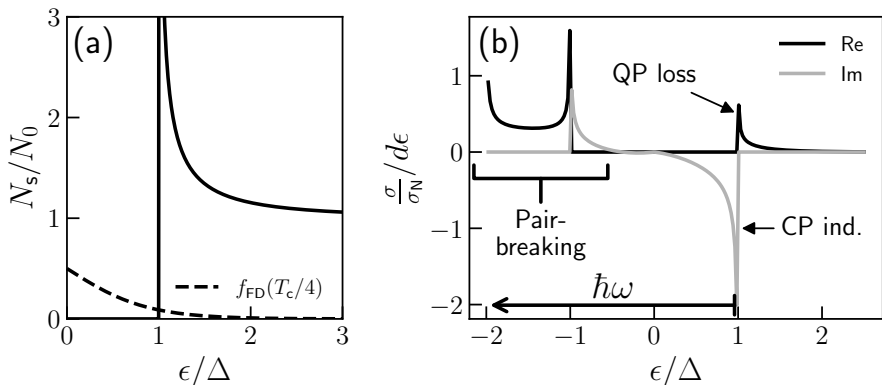


Figure 2.3: **(a)**: BCS density of states (Eq. (2.16)). The dashed line gives the Fermi-Dirac distribution at $T = T_c/4$ (Eq. (2.1)). When this is multiplied by the density of states and integrated, the quasiparticle density is obtained (Eq. (2.17)). **(b)**: The integrand for the complex conductivity (Eq. (2.19)). The parameters are set to $\hbar\omega = 3\Delta$, which results in the pair-breaking term, and $f(\epsilon) = f_{FD}(\epsilon; T_c/4)$ (dashed line in panel (a)), which results in the quasiparticle loss (QP loss) term. The real part describes the dissipation in the metal and the imaginary part describes the (negative of) the reactance. The integral of the imaginary part is negative, which means a net inductive response due to the Cooper-pairs (CP ind.) that is slightly reduced due to the (positive) pair-breaking term.

formed (i.e., $\Delta > 0$ at $T < T_c$). For answering the questions about zero resistance and the Meissner effect, however, one more ingredient is needed. Since Cooper-pairs are bosons (with spin 0 in the singlet state), they can occupy the same state. Therefore, in the ground state all Cooper-pairs will occupy the zero energy state and form a type of Bose-Einstein condensate (BEC), forming one macroscopic coherent state. The BCS condensate differs from a typical BEC, since Cooper-pairs are composite particles and have a finite size. Specifically, the coherence length of a Cooper-pair can be calculated to be $\xi_0 = \hbar v_F / (\pi \Delta_0)$, which was already signaled by Pippards estimate. This coherence length is bigger than the inter-electron spacing $1/k_F \sim \hbar v_F / (\pi \epsilon_F)$, meaning that many Cooper-pairs overlap. This macroscopic coherent state of Cooper-pairs gives rise to the Meissner effect and zero resistance. A scattering event cannot change the state of a single electron within this coherent state. Therefore, to dissipate energy the entire macroscopic state must be changed, which costs a macroscopically large amount of energy [18].

The complex conductivity can be calculated as a sum over all possible ways to absorb radiation that consists of photons with $\hbar\omega$ energy [5]. In the dirty or extremely anomalous limit ($l \ll \xi_0$ or $l \gg \xi_0 \gg \lambda$) the non-local response is determined by dynamics with a smaller length scale than ξ_0 and we can estimate the transition rates as transitions for individual Cooper-pairs and quasiparticles. This

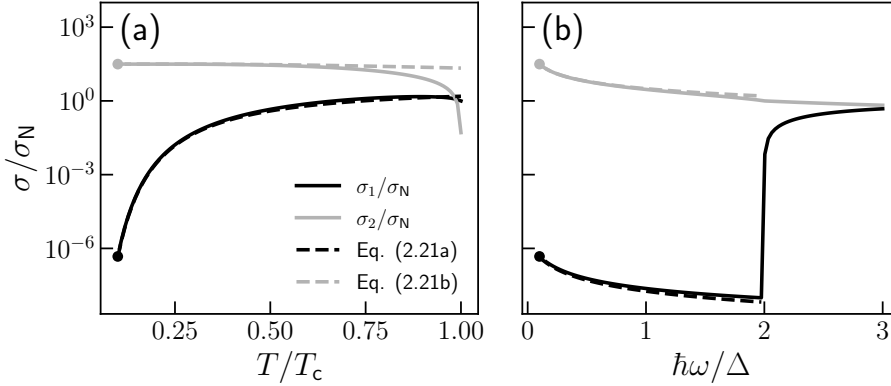


Figure 2.4: **(a)**: The complex conductivity versus temperature calculated with the Mattis-Bardeen equations (Eq. (2.20)), with $\hbar\omega = \Delta/10$. The dashed lines are the low temperature approximations given by Eq. (2.21), with Δ given by the low temperature BSC value, $\Delta_0 = 1.76k_B T_c$. **(b)**: The complex conductivity versus frequency, with $k_B T = k_B T_c/10$. The sharp increase in dissipation (σ_1) at $\hbar\omega = 2\Delta$ is due to the pair-breaking term in Eq. (2.20a). The dots in (a) and (b) indicate that this is the same point in the $(k_B T, \hbar\omega)$ -space.

results in the Mattis-Bardeen equations for the complex conductivity [19],

$$\frac{\sigma}{\sigma_N} = \frac{1}{\hbar\omega} \int_{\Delta-\hbar\omega}^{\infty} \left[1 + \frac{\Delta^2}{\epsilon(\epsilon + \hbar\omega)} \right] \tilde{N}_s(\epsilon) \tilde{N}_s(\epsilon + \hbar\omega) \times [(1 - 2f(\epsilon + \hbar\omega)) H(\Delta - \epsilon) + 2(f(\epsilon) - f(\epsilon + \hbar\omega)) H(\epsilon - \Delta)] d\epsilon. \quad (2.19)$$

The factor in front of the integral ($1/(\hbar\omega)$) ensures normalization to σ_N : when $\Delta \rightarrow 0$, $\sigma/\sigma_N = 1$. The first term in square brackets is the coherence factor, which represents the coherence of the electrons in the Cooper-pair. It has a positive sign before the energy dependence, because we consider the electro-magnetic interaction which is odd with respect to time reversal (i.e., interchanging the electrons in the Cooper-pair) [5]. The functions \tilde{N}_s are the complex density of states normalized to N_0 , $\tilde{N}_s(\epsilon) = \epsilon/\sqrt{\epsilon^2 - \Delta^2}$. $\tilde{N}_s(\epsilon)$ is imaginary for $|\epsilon| < \Delta$, which gives rise to the σ_2 part of the complex conductivity. Together with the distribution functions ($f(\epsilon)$) in the second term in square brackets, the \tilde{N}_s functions give the available initial and final state densities for photon absorption. The distribution functions in the second factor in square brackets give the Cooper-pair (first term) and quasiparticle (second term) response. The Heaviside step functions, $H(x)$, ensure that the Cooper-pair response is active for energies below Δ and the quasiparticle response above Δ . Figure 2.3(b) shows the integrand of Eq. (2.19). The various transitions are indicated.

When we split the real and imaginary parts, $\sigma = \sigma_1 - j\sigma_2$, and write out \tilde{N}_s with the

appropriate signs, we obtain,

$$\begin{aligned} \frac{\sigma_1}{\sigma_N} &= \frac{2}{\hbar\omega} \int_{\Delta}^{\infty} \frac{(f(\epsilon) - f(\epsilon + \hbar\omega))(\epsilon^2 + \Delta^2 + \hbar\omega\epsilon)}{\sqrt{(\epsilon^2 - \Delta^2)((\epsilon + \hbar\omega)^2 - \Delta^2)}} d\epsilon \\ &+ \frac{H(\hbar\omega - 2\Delta)}{\hbar\omega} \int_{\Delta - \hbar\omega}^{-\Delta} \frac{(1 - 2f(\epsilon + \hbar\omega))(\epsilon^2 + \Delta^2 + \hbar\omega\epsilon)}{\sqrt{(\epsilon^2 - \Delta^2)((\epsilon + \hbar\omega)^2 - \Delta^2)}} d\epsilon, \end{aligned} \quad (2.20a)$$

$$\frac{\sigma_2}{\sigma_N} = \frac{1}{\hbar\omega} \int_{\max\{\Delta - \hbar\omega, -\Delta\}}^{\Delta} \frac{(1 - 2f(\epsilon + \hbar\omega))(\epsilon^2 + \Delta^2 + \hbar\omega\epsilon)}{\sqrt{(\Delta^2 - \epsilon^2)((\epsilon + \hbar\omega)^2 - \Delta^2)}} d\epsilon. \quad (2.20b)$$

The second integral of Eq. (2.20a) only contributes when $\hbar\omega > 2\Delta$, as ensured by $H(\hbar\omega - 2\Delta)$. For such high frequencies, a photon can break a Cooper-pair into 2 quasiparticles directly, which induces additional dissipation.

For low temperatures and low frequencies, $(k_B T, \hbar\omega) \ll \Delta$, and assuming a thermal quasiparticle distribution (Eq. (2.1)), the Mattis-Bardeen equations can be approximated by [16],

$$\frac{\sigma_1}{\sigma_N} \approx \frac{4\Delta}{\hbar\omega} e^{-\frac{\Delta}{k_B T}} \sinh(\zeta) K_0(\zeta), \quad (2.21a)$$

$$\frac{\sigma_2}{\sigma_N} \approx \frac{\pi\Delta}{\hbar\omega} \left(1 - 2e^{-\frac{\Delta}{k_B T}} e^{-\zeta} I_0(\zeta) \right), \quad (2.21b)$$

with $\zeta = \hbar\omega/(2k_B T)$ and $I_0(\zeta)$ and $K_0(\zeta)$ and are the zeroth-order modified Bessel functions of the first and second kind, respectively. Together with the low temperature approximations for Δ and n_{qp} , one can derive that to lowest order in $k_B T/\Delta \ll 1$, the change in σ by a change in quasiparticle density is given by [16],

$$\frac{d\sigma_1}{dn_{qp}} = \frac{\sigma_N}{N_0 \hbar\omega} \sqrt{\frac{2\Delta_0}{\pi k_B T}} \sinh(\zeta) K_0(\zeta), \quad (2.22a)$$

$$\frac{d\sigma_2}{dn_{qp}} = -\frac{\sigma_N \pi}{2N_0 \hbar\omega} \left[1 + \sqrt{\frac{2\Delta_0}{\pi k_B T}} e^{-\zeta} I_0(\zeta) \right]. \quad (2.22b)$$

These equations are shown in Fig. 2.5 as the dashed lines. The solid lines give the numerically calculated sensitivities to quasiparticle density changes of the complex conductivity. In Section 6.A.2, we will extend the present discussion by calculating the changes in complex conductivity when the quasiparticle distribution function changes, while the quasiparticle density stays constant. For this, we will introduce a chemical potential, μ , in Eq. (2.1), and keep n_{qp} constant by implicitly changing μ , as is done in Ref. [16].

The complex conductivity (σ) describes the response of the superconducting material to an AC field. For a superconducting thin film, we can describe the response via the sheet impedance, which is a generalization of the DC resistivity and sheet resistance for a normal metal (Eq. (2.4)). In the local limit, the surface impedance of a superconducting thick film ($d \gg \lambda_{\text{eff}}$) is given by $Z_s = \sqrt{j\omega\mu_0/\sigma}$ [20,

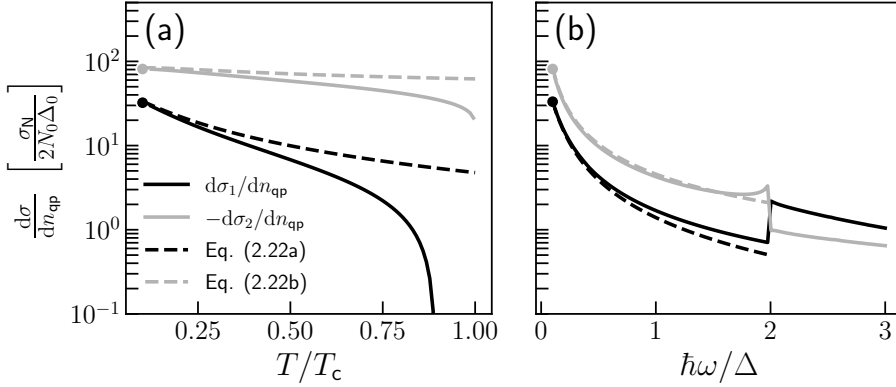


Figure 2.5: **(a)**: The change in complex conductivity when changing quasiparticle density versus temperature numerically calculated with the Mattis-Bardeen equations (Eq. (2.20)), with $\hbar\omega = \Delta/10$. The dashed lines are the low temperature approximations given by Eq. (2.22). **(b)**: The change complex conductivity with changing quasiparticle density versus frequency, with $k_B T = k_B T_c/10$. The dots in (a) and (b) indicate that this is the same point in the $(k_B T, \hbar\omega)$ -space.

21]. This is identical to a normal metal when we set $\sigma \rightarrow \sigma_N$ [22]. We can generalize Z_s for an arbitrary film thickness d , by considering the film as electro-magnetic medium and transforming the impedance from the film to the substrate. When we assume the substrate to have a much higher impedance than the film, we find [21],

$$Z_s = \sqrt{\frac{j\omega\mu_0}{\sigma}} \coth\left(d\sqrt{j\omega\mu_0\sigma}\right) = \sqrt{\frac{j\omega\mu_0}{\sigma_1 - j\sigma_2}} \coth\left(\frac{d}{\lambda_{\text{eff}}}\sqrt{1 + j\frac{\sigma_1}{\sigma_2}}\right). \quad (2.23)$$

In the second expression, we also assumed the dirty limit, in which the effective penetration depth can be expressed as $\lambda_{\text{eff}} = 1/\sqrt{\omega\mu_0\sigma_2}$ [23], with σ_2 from the Mattis-Bardeen equations Eq. (2.20b). In the zero-temperature limit, we obtain $\lambda_{\text{eff}} = \sqrt{\hbar}/(\mu_0\pi\Delta\sigma_N) = \lambda_L\sqrt{\xi_0/l}$, which coincides with the phenomenological description in Section 2.1.2.

When we assume low temperatures and $\hbar\omega < 2\Delta$, such that $\sigma_1 \ll \sigma_2$, we can approximate Z_s as [24],

$$Z_s = R_s + j\omega L_s \approx \mu_0\omega\lambda_{\text{eff}} \coth\left(\frac{d}{\lambda_{\text{eff}}}\right) \left[\zeta \frac{\sigma_1}{2\sigma_2} + j \right], \quad (2.24)$$

with $\zeta = 1 + (2d/\lambda_{\text{eff}})/\sinh(2d/\lambda_{\text{eff}})$, R_s the sheet resistance and L_s the sheet inductance. The factor ζ is 1 for thick films and 2 for thin films. When we interpret $L_s = \mu_0\lambda$ and assume the thin film limit ($d \ll \lambda_{\text{eff}}$), we obtain the Pearl length, $\lambda = \lambda_{\text{eff}}^2/d$. Thus, in the zero-temperature, thin film limit, we obtain with the expression for λ_{eff} from above², $Z_s = j/(d\sigma_2) = j\hbar\omega/(d\pi\Delta\sigma_N)$. More generally, we see

²As a rule of thumb for the kinetic inductance, this formula gives $L_k = (1.38 \text{ pH K}/\Omega) \times R_N/T_c$.

from the second expression of Eq. (2.23) that in the dirty, thin film limit the sheet impedance is simply given by $Z_s = 1/(d\sigma)$ [20].

With the Mattis-Bardeen equations (Eq. (2.20)) and the expression for the sheet impedance (Eq. (2.23)), we now have a microscopic way to describe the AC response of a superconducting film.

2

2.2 MICROWAVE RESONATORS

By probing the surface impedance with an AC field (Eq. (2.24)), we could in principle measure changes in quasiparticle density, via the changes in σ (Eq. (2.22)). The next step is to decide how to couple the fields to the film and how to detect the reflected or transmitted fields. As we will see, the best way to measure the tiny changes in the complex conductivity is to use a superconducting resonator, since these have negligible losses at low temperature ($T < T_c/5$, see σ_1 in Fig. 2.4). This allows for very high quality factors, $Q > 10^5$, such that fractional resonance frequency shifts of $\delta f/f_0 > 10^{-6}$ are easily detected, and fractional complex conductivity changes on the order of $\delta\sigma/\sigma_0 \sim 10^{-6}$ can be measured. In order to understand resonators and how to guide the generated AC fields to them, we first need to discuss waveguides.

2.2.1 TRANSMISSION LINES

To control the AC fields accurately, we can guide them in a waveguide. It is convenient to use a waveguide with two potential defining lines, one of which is kept at zero potential (called the ground) and one of which is excited with an alternating voltage (signal line). This is called a transmission line. The easiest way to create a transmission line with a co-planar waveguide (CPW) structure, which can be created in a single planar metal film, see Fig. 2.6. When we etch two slots in a metal sheet, we obtain a central line and two ground planes on either side. If we ensure that the two ground planes keep the same potential, we can excite a voltage wave on the transmission line by inducing a time dependent voltage on the central conductor. We obtain an even quasi-TEM mode: a wave mode that is approximately transverse in both electric and magnetic fields and has opposite electric fields in the two slots. This is sketched in Fig. 2.6.

Any transmission line can be described by a characteristic impedance, Z_0 and a propagation constant $\gamma = \alpha + j\beta$, with α the attenuation constant and $\beta = \omega/v_{ph} = 2\pi/\lambda$ the wave constant. Here, v_{ph} the phase velocity of the wave and λ the wavelength (not to be confused with the penetration depth). Z_0 and γ are determined by four parameters which characterize the electrical properties of the transmission line: R_l , the series resistance per unit length, L_l the series inductance per unit length, G_l the shunt conductance per unit length and C_l the shunt capacitance per unit length. With these parameters, we have $\gamma = \sqrt{(R_l + j\omega L_l)(G_l + j\omega C_l)}$ and $Z_0 = \sqrt{(R_l + j\omega L_l)/(G_l + j\omega C_l)}$ [22]. When we assume that the attenuation is small ($R_l \ll \omega L_l$, $G_l \ll \omega C_l$), which is valid for superconductors if $\omega < 2\Delta$ (see Fig. 2.4), we obtain to first order $\alpha = R_l/(2Z_0)$, $\beta = \omega\sqrt{L_l C_l}$ and $Z_0 = \sqrt{L_l/C_l}$ [22].

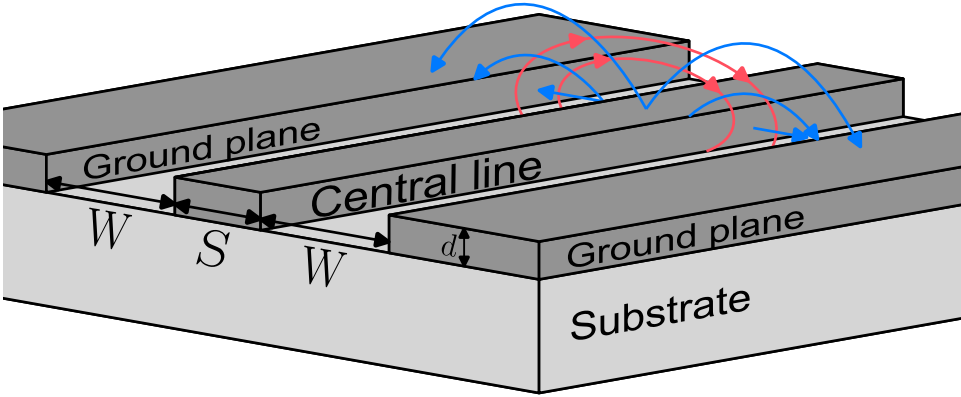


Figure 2.6: Sketch of a co-planar waveguide with a central line width S and with gaps to the ground planes of width W . The \mathbf{E} -field is sketched with blue arrows, when the central line is (locally) positively charged. The \mathbf{B} -field is sketched with red arrows when current flows (locally) to the right.

For the quasi-TEM mode in a CPW structure, we can define an effective permittivity, which combines the effects to the electric field of the vacuum above and dielectric substrate below the metal sheets. The simplest approximation to the permittivity is to take the average between these two, $\epsilon_{\text{eff}} = (1 + \epsilon_{\text{sub}})/2$, where ϵ_{sub} is the relative dielectric permittivity of the substrate. A more accurate method to obtain ϵ_{eff} is to simulate the structure using a numerical solver such as SONNET [25] for 2D structures or Ansys HFSS [26] for 3D, which accounts for the asymmetric field distribution in the substrate and vacuum. With ϵ_{eff} , the geometry of the CPW give a capacitance and inductance per unit length of [27],

$$L_{l,g} = \frac{\mu_0}{4} \frac{K(\sqrt{1-k^2})}{K(k)}, \quad (2.25a)$$

$$C_l = 4\epsilon_0\epsilon_{\text{eff}} \frac{K(k)}{K(\sqrt{1-k^2})}, \quad (2.25b)$$

where $K(x)$ is the complete elliptic integral of the first kind and $k = S/(S+2W)$, i.e the ratio of the central line width to the total CPW width (see Fig. 2.6). In addition to the geometrical contribution to the CPW impedance, the sheet impedance of the metal also results in a contribution. For superconducting sheets, the kinetic inductance resulting from the Cooper-pair condensate dominates the sheet impedance (see Eq. (2.24)). The CPW geometry determines how this sheet impedance contributes to the line impedance. For $d < S/20$ and $k < 0.8$, the central line and ground planes contribute with the respective factors [24, 27–30],

$$g_c = \frac{1}{4S(1-k^2)K^2(k)} \left[\pi + \ln\left(\frac{4\pi S}{d}\right) - k \ln\left(\frac{1+k}{1-k}\right) \right], \quad (2.26a)$$

$$g_g = \frac{k}{4S(1-k^2)K^2(k)} \left[\pi + \ln\left(\frac{4\pi(S+2W)}{d}\right) - \frac{1}{k} \ln\left(\frac{1+k}{1-k}\right) \right]. \quad (2.26b)$$

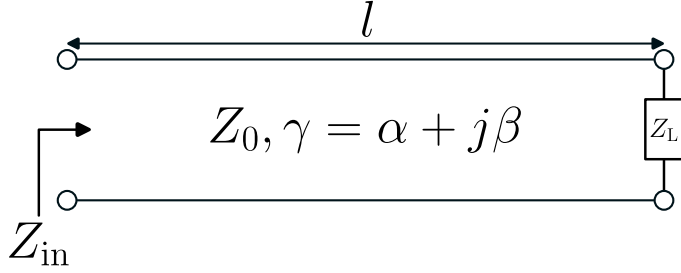


Figure 2.7: Schematic of a transmission line of length l with characteristic impedance Z_0 and propagation constant $\gamma = \alpha + j\beta$. The line is terminated with a load impedance Z_L , which results in an input impedance, Z_{in} , given by Eq. (2.27).

The total kinetic inductance per unit length of the transmission line is then given by, $L_{l,k} = g_c L_{s,c} + g_g L_{s,g}$, where $L_{s,c}$ is the sheet inductance of the central line and $L_{s,g}$ is the sheet inductance of the ground planes, given by Eq. (2.24). The total inductance per unit length of the transmission line is given by $L_l = L_{l,g} + L_{l,k}$. The kinetic inductance fraction is therefore given by, $\alpha_k = L_{l,k}/L_l$, and characterizes how much of the impedance of the transmission line is due to the impedance (i.e., kinetic inductance) of the superconducting sheets. Since we aim to probe superconductivity with the AC response of these structures, this will turn out to be a central parameter in the analysis.

The quasiparticles in the superconducting sheets result in a small attenuation in the transmission line. The resistance per unit length is calculated similarly, $R_l = g_c R_{s,c} + g_g R_{s,g}$, with $R_{s,c}$ and $R_{s,g}$ the sheet resistance for the central line and ground plane, from Eq. (2.24).

With R_l , L_l and C_l , we have the information to predict the propagation of an electro-magnetic wave on a transmission line. With Eq. (2.22), we can interpret the changes in propagation to changes in quasiparticle density in the superconductors. When embedding a transmission line of a finite length in a circuit, it is convenient to characterize the response with the input impedance, Z_{in} . The input impedance of the transmission line of length l , which is terminated by a load impedance Z_L (see Fig. 2.7) is in this case given by [22],

$$Z_{in} = Z_0 \frac{Z_L + Z_0 \tanh \gamma l}{Z_0 + Z_L \tanh \gamma l}. \quad (2.27)$$

With Z_L known, we therefore can interpret the changes in Z_{in} of the finite transmission line as changes in quasiparticle density.

2.2.2 TRANSMISSION LINE RESONATORS

To measure changes in the impedance of a transmission line accurately, we want the electro-magnetic wave to interact with the transmission line as much as possible. We therefore contain the fields in a transmission line of length l , which is weakly coupled to a readout transmission line via a capacitor C_c , see Fig. 2.8. The

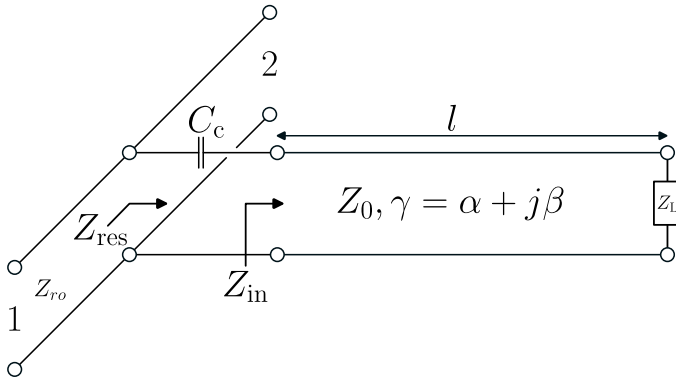


Figure 2.8: Schematic of a capacitively coupled transmission line resonator. The load impedance is either a short ($Z_L = 0$) to make a quarter-waver resonator or an open ($Z_L = \infty$) to make a half-wave resonator. The transmission line is coupled via the coupling capacitor C_c to a readout line with a characteristic impedance Z_{r0} and port 1 as input and port 2 as output.

transmission line is terminated with either a short ($Z_L = 0$) or an open ($Z_L = \infty$), such that the wave is completely reflected. Since we couple capacitively at the readout line side, a shorted termination results in a quarter-wave resonator and an open in an half-wave resonator.

Resonance occurs when the imaginary part of the input impedance of the coupler and terminated transmission line (Z_{res} in Fig. 2.8) goes to zero. This impedance is given by, $Z_{res} = Z_{in} - j/(\omega C_c)$, with Z_{in} from Eq. (2.27) and $Z_L \rightarrow (0 \text{ or } \infty)$.

For the transmission line only, the imaginary part of Z_{in} (Eq. (2.27)) goes to zero at the resonance frequency of $\omega_{TL} = 2\pi m / (l\sqrt{L_1 C_1})$. Here, $m = 1/2$ for a half-wave resonator (with an open termination) and $m = 1/4$ for a quarter-waver resonator (with a shorted termination). Close to this resonance point ($\delta\omega_{TL}/\omega_{TL} \ll 1$, with $\delta\omega_{TL} = \omega - \omega_{TL}$), and with a small attenuation ($\alpha l \ll 1$) the input impedance of the transmission line is to first order [31, 32],

$$Z_{in} \approx \frac{Z_0 Q_i / (\pi m)}{1 + 2jQ_i \frac{\delta\omega_{TL}}{\omega_{TL}}}, \tag{2.28}$$

where $Q_i = \beta / (2\alpha)$ [22] is the internal quality factor, which characterizes the energy lost due to internal dissipation. Using this expression, we find the resonance frequency of the combined coupler and transmission line as the frequency where $\text{Im}(Z_{res}) = 0$. For low internal loss, $Q_i^2 \gg 2\pi m / (\omega C_c Z_0)^2$, this results in a shifted resonance frequency of $\delta\omega_{TL}/\omega_0 = (\omega_{TL} - \omega_0) / \omega_0 \approx Z_0 \omega_{TL} C / (2\pi m)$, where ω_0 is the resonance frequency of the combined coupler and transmission line.

Close to resonance ($\delta\omega/\omega_0 \ll 1$, with $\delta\omega = \omega - \omega_0$) and with a small effect of the coupler ($\delta\omega_{TL}/\omega_0 \ll 1$), the input impedance of the resonator can be approximated

[24],

$$Z_{\text{res}} \approx \frac{1}{\omega_0 C_c} \frac{2Q_i \frac{\delta\omega}{\omega_0} - j}{1 + 2jQ_i \left(\frac{\delta\omega}{\omega_0} - \frac{\delta\omega_{\text{TL}}}{\omega_0} \right)}. \quad (2.29)$$

With this, we can find the transmission through the readout line, from port 1 to port 2 (see Fig. 2.8) as [22],

$$S_{21} = \frac{2}{2 + Z_{\text{ro}}/Z_{\text{res}}} \approx \frac{Q/Q_i + 2jQ \frac{\delta\omega}{\omega_0}}{1 + 2jQ \frac{\delta\omega}{\omega_0}}, \quad (2.30)$$

where Z_{ro} is the characteristic impedance of the readout line and $Q = Q_c Q_i / (Q_c + Q_i)$ is the loaded quality factor. Here, $Q_c = 2\pi m / (\omega_0 C_c \sqrt{Z_0 Z_{\text{ro}}})^2$ is the coupling quality factor, which characterizes the energy lost via the coupler. The approximation is valid for weak coupling to the readout line: $Z_{\text{ro}} \omega_0 C_c \ll 1$. Equation (2.30) as defined by quality factors is generally applicable to any resonator coupled to a readout line [20, 24, 32].

Since we consider superconducting resonators [33], the internal losses are very low in superconductors: $Q_i > 10^5$ at low temperatures, $T/T_c/10$, where Q_i is typically limited by other loss mechanisms than thermal quasiparticle loss. From Eq. (2.30), we see that this gives a dip in S_{21} , which has the value one far away from resonance and Q/Q_i at resonance. The width of the dip is the resonator bandwidth, $\Delta f = \omega_0 / (2\pi Q)$. Q is typically limited by Q_c , such that $Q/Q_i \ll 1$ and the dip is clearly visible. This means that we can place many of these superconducting resonators on one readout line. For example, with $Q \approx Q_c = 50,000$, and $\omega_0 = 2\pi \times 5$ GHz, we obtain a bandwidth of $\Delta f = 100$ kHz, and we can place roughly 4,000 resonators in a 3 to 7 GHz band (placing one resonator every 10 bandwidths). This is why MKIDs, as introduced in Chapter 1, are intrinsically frequency multiplexable and therefore suitable for large arrays.

If we excite port 1 in Fig. 2.8 with a microwave power P_{read} , we can find the absorbed (i.e. dissipated) power at resonance via,

$$P_{\text{abs}} = P_{\text{read}} (1 - |S_{21}|^2 - |S_{11}|^2) = \frac{2Q^2}{Q_i Q_c} P_{\text{read}}, \quad (2.31)$$

where we used $S_{11} = 1 - S_{21}$ [22] and Eq. (2.30). From the absorbed power, we can find the internal power as [20],

$$P_{\text{int}} = \frac{\omega_0 E_{\text{res}}}{4\pi m} = \frac{Q_i P_{\text{abs}}}{4\pi m} = \frac{1}{2\pi m} \frac{Q^2}{Q_c} P_{\text{read}}, \quad (2.32)$$

where we used the definition of the internal quality factor, $Q_i = \omega_0 E_{\text{res}} / P_{\text{abs}}$. The internal power characterizes the energy stored in the resonator when exciting at resonance. This can also be expressed as the number of microwave photons: $\langle n_{\text{phot}} \rangle = E_{\text{res}} / (\hbar\omega_0) = 4\pi m P_{\text{int}} / (\hbar\omega_0^2)$.

Equation (2.30) maps to a circle in the complex S_{21} plane, as is shown in Fig. 2.9(a). This circle can be used as calibration to measure changes in S_{21} . A

coordinate system for this calibration that is often used are polar coordinates with respect to the midpoint of the circle: $x_c = 1 - Q/(2Q_c)$. This way, we can define an amplitude, $A = \sqrt{(\text{Re}(S_{21}) - x_c)^2 + \text{Im}(S_{21})^2}$, and phase, $\theta = \tan(\text{Im}(S_{21}) / (x_c - \text{Re}(S_{21})))$, as indicated in Fig. 2.9(a). The amplitude is often redefined as $\delta A = 1 - A/(1 - x_c)$, such that it is 0 at resonance and normalized to the radius of the resonance circle.

When we probe the resonator at $\omega = \omega_0$, and the quasiparticle density in the superconductor changes, the change in surface impedance will change the resonance frequency (change in L_s) and internal quality factor (change in R_s). This will change the forward transmission via Eq. (2.30).

To first order, the change in resonance frequency can be calculated as,

$$\frac{\delta\omega_0}{\omega_0} \approx -\frac{\alpha_k}{2} \frac{\delta L_s}{L_s} \approx -\frac{\alpha_k \zeta}{2} \frac{\delta \lambda_{\text{eff}}}{\lambda_{\text{eff}}} \approx \frac{\alpha_k \zeta}{4} \frac{\delta \sigma_2}{\sigma_2}, \quad (2.33)$$

where we used $\omega_0 \propto 1/\sqrt{L_l C_l}$ and Eq. (2.24). Similarly, we find the internal quality factor,

$$Q_i = \frac{\beta}{2\alpha} = \frac{\omega L_l}{R_l} = \frac{\omega L_s}{\alpha_k R_s} = \frac{2}{\alpha_k \zeta} \frac{\sigma_2}{\sigma_1}, \quad (2.34)$$

where we again used Eq. (2.24). The change in quality factor is thus,

$$\delta\left(\frac{1}{Q_i}\right) = \frac{\alpha_k \zeta}{2} \frac{\delta \sigma_1}{\sigma_2}, \quad (2.35)$$

where we assumed $\sigma_1 \ll \sigma_2$, which is true for $T/T_c < 0.9$ (see Fig. 2.4). The internal quality factor mentioned here only includes the effect of the quasiparticles. There could be additional dissipation mechanisms in the resonator, which are likely to dominate at low temperatures. These other mechanisms can be characterized by an excess loss internal quality factor, Q_i^{ex} , such that $1/Q_i^{\text{tot}} = 1/Q_i + 1/Q_i^{\text{ex}}$.

With these fractional changes, we can find the responsivity of δA and θ for changes in quasiparticle density,

$$\frac{d\delta A}{dn_{\text{qp}}} \approx 2Q \frac{d(1/Q_i)}{dn_{\text{qp}}} \approx \frac{\alpha_k \zeta Q}{\sigma_2} \frac{d\sigma_1}{dn_{\text{qp}}}, \quad (2.36a)$$

$$\frac{d\theta}{dn_{\text{qp}}} \approx -4Q \frac{d(\delta\omega_0/\omega_0)}{dn_{\text{qp}}} \approx -\frac{\alpha_k \zeta Q}{\sigma_2} \frac{d\sigma_2}{dn_{\text{qp}}}. \quad (2.36b)$$

In the approximations we used Eq. (2.30), keeping only the first order, and assumed Q to be constant with quasiparticle density. This is valid when Q is limited by Q_c or when Q_i is not limited by quasiparticle loss. From these equations, we see that we probe the quasiparticle dissipation (i.e., σ_1) with δA and the Cooper-pair kinetic inductance (i.e., σ_2) with θ .

The responsivity of σ to quasiparticle changes in Eq. (2.36) can be approximated from Eq. (2.22) in the limit $k_B T \ll \hbar\omega \ll 2\Delta$, such that we obtain,

$$\frac{d\delta A}{dn_{\text{qp}}} \approx \frac{\alpha_k \zeta Q}{2N_0 \Delta} \frac{1}{\pi} \sqrt{\frac{2\Delta}{\hbar\omega}}, \quad (2.37a)$$

$$\frac{d\theta}{dn_{\text{qp}}} \approx \frac{\alpha_k \zeta Q}{2N_0 \Delta} \left(1 + \frac{1}{\pi} \sqrt{\frac{2\Delta}{\hbar\omega}}\right). \quad (2.37b)$$

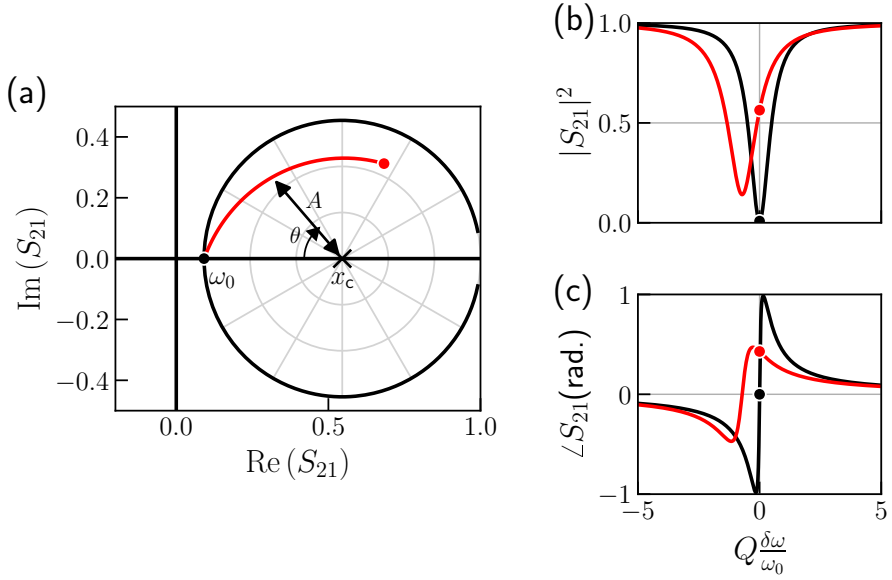


Figure 2.9: Resonance curve and response to quasiparticles. **(a):** Complex S_{21} of the resonance curve (black) and a quasiparticle response when probing the resonator at the resonance frequency ω_0 (red). The resonance curve (black) is calculated with Eq. (2.30), when sweeping $\delta\omega$ from -5 to +5 linewidths (ω_0/Q). The response curve is calculated with Eq. (2.30), with $\omega = \omega_0$ and $\omega_0 \rightarrow \omega_{\text{res}}$ and Q_i given by Eq. (2.34), with n_{qp} increased by photon absorption. The parameters for this calculation are set to $\hbar\omega_0 = \Delta/10$, $\Delta = 1.76k_B \times 0.87$ K, $Q_c = 50.000$, $Q_i^{\text{ex}} = 500.000$, $T/T_c = 0.1$, $\alpha_k = 0.5$ and a 402 nm photon absorbed in a $100 \mu\text{m}^3$ superconducting volume with a pair-breaking efficiency of 0.59 [34, 35]. **(b):** The squared forward transmission given by Eq. (2.30) for the same curves as in panel (a). The red curve is a frequency sweep with the parameters (ω_0 and Q_i) set to the values just after photon absorption, indicated by the red circle in (a). **(c):** The argument of the forward transmission, without photon absorption (black) and just after photon absorption (red).

In the opposite limit, $\hbar\omega \ll k_B T \ll 2\Delta$ we obtain,

$$\frac{d\delta A}{dn_{\text{qp}}} \approx \frac{\alpha_k \zeta Q}{2N_0 \Delta} \frac{1}{\pi} \sqrt{\frac{2\Delta}{\pi k_B T}} \frac{\hbar\omega}{k_B T} \left(\ln\left(\frac{\hbar\omega}{2k_B T}\right) + \gamma_e \right), \quad (2.38a)$$

$$\frac{d\theta}{dn_{\text{qp}}} \approx \frac{\alpha_k \zeta Q}{2N_0 \Delta} \left(1 + \sqrt{\frac{2\Delta}{\pi k_B T}} \right), \quad (2.38b)$$

where $\gamma_e = 0.577$ is Euler's constant.

The response to quasiparticle changes given in Eq. (2.36) are only valid when the changes in the parameters (S_{21} , ω_0 , $1/Q_i$ etc.) are small. In the example of

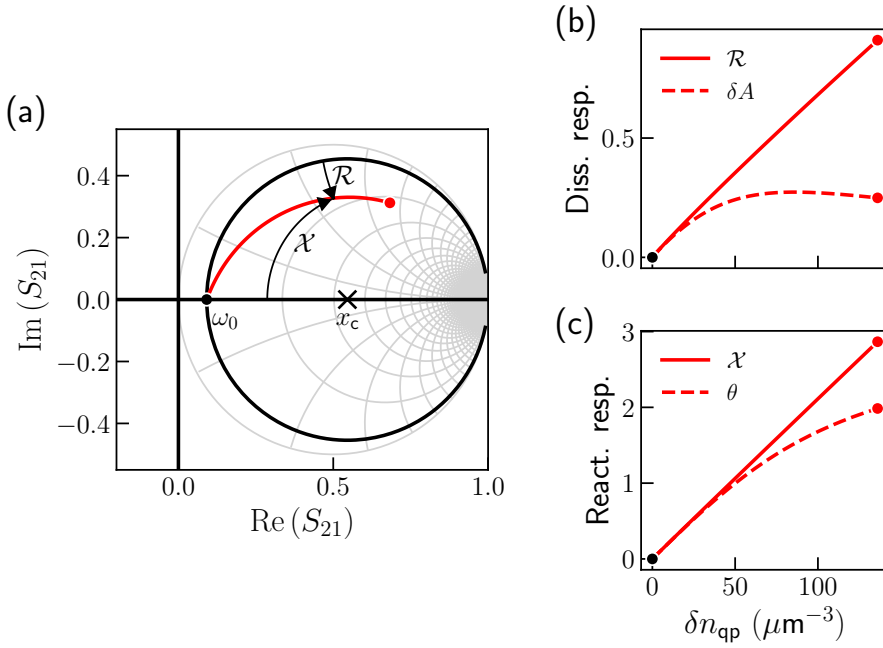


Figure 2.10: Response to a large quasiparticle density change with coordinates that track the input impedance of the resonator ($Z_{\text{res}} \propto \mathcal{R} + j\mathcal{X}$). **(a)**: S_{21} complex plane with the same resonator and response curve as in Fig. 2.9. The gray lines show the $(\mathcal{R}, \mathcal{X})$ -coordinates grid. **(b)** and **(c)**: Dissipative (b) and reactive (c) response to an excess quasiparticle density (δn_{qp}). The solid lines show the response in $(\mathcal{R}, \mathcal{X})$ -coordinates and the dashed line in $(\delta A, \theta)$ -coordinates from Fig. 2.9. The black and red dots correspond to the same points in panel (a).

photon absorption in Fig. 2.9 we clearly see that the change in S_{21} is not small and, consequently, δA and θ become non-linear with the (excess) quasiparticle density. To maintain a linearity in the response to a large change in S_{21} , we can use coordinates that track the input impedance of the resonator directly [36]. From Eq. (2.30), we see that this results in the coordinates,

$$\mathcal{R} = \frac{4Q}{Q_c} \operatorname{Re} \left(\frac{S_{21}}{2 - 2S_{21}} \right) - \frac{2Q}{Q_{i0}}, \quad (2.39a)$$

$$\mathcal{X} = \frac{4Q}{Q_c} \operatorname{Im} \left(\frac{S_{21}}{2 - 2S_{21}} \right). \quad (2.39b)$$

The factors in front and the last term in \mathcal{R} ensure that \mathcal{R} and \mathcal{X} are equal to δA and θ in the small response limit. Q_{i0} is the internal quality factor without response. \mathcal{R} tracks the dissipative part of Z_{res} and \mathcal{X} the reactive part. These coordinates are shown in Fig. 2.10. Panels (b) and (c) show a comparison with the

$(\delta A, \theta)$ -coordinates, which shows that using $(\mathcal{R}, \mathcal{X})$ indeed extends the linearity with n_{qp} much further. For an estimation of the quasiparticle responsivities, we can use Eq. (2.36), since these are valid in the small signal limit where \mathcal{R} and \mathcal{X} are equal to δA and θ .

2.2.3 HYBRID MICROWAVE RESONATORS

Until now, we have assumed that the change in quasiparticle density (e.g. in Eq. (2.36)) was constant over the entire resonator. This is a reasonable assumption in (quasi-)equilibrium, when for example we change the bath temperature of the resonator and the quasiparticle density changes according to Eq. (2.17). However, when we excite the resonator locally, for example with a photon absorption, the quasiparticle density changes locally and is not uniform in the resonator. Since the forward transmission, S_{21} , is sensitive for the changes in dissipation and reactance in the resonator (see Eqs. (2.37) and (2.38)), the local response is weighted by the square of the local current distribution [20, 31]. Therefore, to measure an excitation with high sensitivity, the excited quasiparticles must reside in a volume where the current density is high and uniform³.

Besides that, an excitation with definite energy (e.g. a photon absorption) excites a definite number of quasiparticles, δN_{qp} . Therefore, in order to measure the energy of the excitation with high sensitivity, this number of quasiparticles needs to be contained in a small volume, such that the change in quasiparticle density is high, $\delta n_{\text{qp}} = \delta N_{\text{qp}}/V$.

These considerations lead to the design of a hybrid superconducting resonator [20, 37], see Fig. 2.11. In such a design, the current density is concentrated in an inductive strip. This is realized by making the strip long, narrow and thin and shorting it to the ground plane at one end. The current in the rest of the structure is minimized by patterning the capacitive part in a wide double IDC structure [38]. Additionally, we can select a superconductor with higher normal state resistivity and lower-gap for the inductive strip, such that the sheet kinetic inductance is higher for the inductive strip (see Eq. (2.24)). When we make the inductive strip of a lower-gap superconductor than the capacitive part, the quasiparticles will be trapped in the strip. We can increase the sensitivity for quasiparticles by reducing the inductive strip volume (V in Eq. (2.36)). Furthermore, changes in quasiparticle density in the higher gap superconductor induce a smaller response, since $\delta(\delta A, \theta) \propto \delta n_{\text{qp}}/\sqrt{\Delta}$ (Eq. (2.36)). This ensures that we probe the quasiparticle changes in the inductive strip only⁴.

In this thesis, we will discuss hybrid resonators as shown in Fig. 2.11. The

³In Section 5.A, we will define an effective superconducting volume where the current resides. The ratio between this effective volume and the occupation volume of the excess quasiparticles gives the sensitivity reduction due to current non-uniformities.

⁴In Section 5.A we will quantify the sensitivity to quasiparticles in the capacitive and inductive parts for specific NbTiN-Al hybrid resonators with different Al wire lengths. We find that we are 4.9 to 130 times more sensitive to quasiparticles in the Al, depending on the Al wire length, which is mainly due to the high current density in the Al. We also show in that section that the ratio of the internal power in the inductive and capacitive section is approximately equal to the ratio of the characteristic impedance of each section.

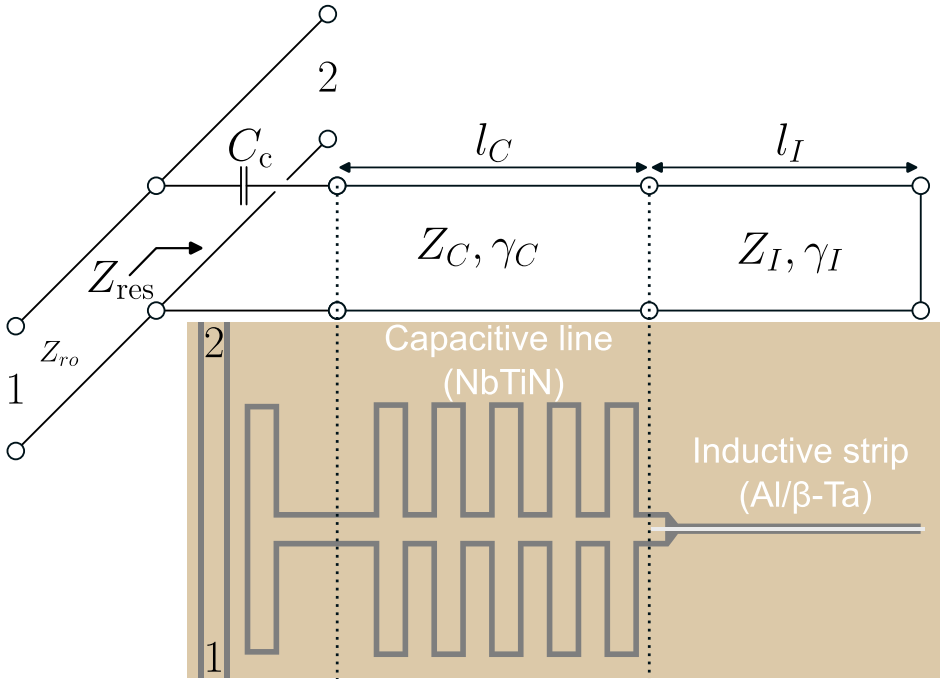


Figure 2.11: Diagram of a transmission line model for a hybrid resonator (top) with a schematic of a co-planar waveguide (CPW) realization (bottom). The hybrid resonator consists of an insensitive capacitive part with a higher gap superconductor and a sensitive inductive part with a lower-gap superconductor. This way, the changes in resonance frequency and internal quality factor are primarily caused by the changes in quasiparticle density in the inductive strip.

capacitive part and ground plane is made of NbTiN, which has a $T_c \sim 14$ K and $1/\sigma_N \sim 160 \mu\Omega\text{cm}$. The sensitive inductive strip consists of either Al ($T_c \sim 1.2$ K, $1/\sigma_N \sim 0.7 \mu\Omega\text{cm}$) or the disordered superconductor β -phase Ta [39], or β -Ta for short, ($T_c \sim 0.8$ K, $1/\sigma_N \sim 200 \mu\Omega\text{cm}$). We tune the coupling quality factor (Q_c) by changing the length and distance to the readout line of the T-coupler⁵. The resonance frequency, we tune with the length of the IDC fingers. The quasiparticle responsivity (Eq. (2.36)) we tune by changing Q_c , the strip volume V and the kinetic inductance fraction, α_k . Here, α_k is the fraction of kinetic inductance of the inductive strip only, $\alpha_k = L_k^1/L_{\text{tot}}$.

With this system, we have a sensitive way to probe the quasiparticle changes in a small superconducting volume, made of material of our choice. When the inductive section of this hybrid superconducting resonator is excited via photon absorption, this device is called a microwave kinetic inductance detector (MKID), as introduced

⁵The length of the T-coupler also changes the total capacitance, which changes the resonance frequency. The resonance frequency is less sensitive to the distance of the T-coupler to the read-out line.

in Chapter 1. In the next chapter, we will discuss what kind of response we would expect from such excitations. We will also discuss the effects of disorder on the superconductor and on the quasiparticles within it.

2

2.2.4 SPURIOUS SIGNAL: TWO-LEVEL-SYSTEMS

Unfortunately, the quasiparticle density is not the only parameter that dictates the input impedance of a superconducting resonator. The loss ($1/Q_i$) and resonance frequency (ω_0) not only depend on the currents in the inductive strip, which probes the superconducting condensate and quasiparticles, but also depend on the electric and magnetic fields in the resonator (see Fig. 2.6). These fields interact with metals and dielectrics in the resonator. When the microscopics of these materials changes, the loss and resonance frequency change as well. The simplest way to model these changes in the material, is to consider a number of two-level systems (TLSs) to be present in the resonator materials [41–43]. Such TLSs can for example be defects with an electric dipole moment in the substrate or surface layers of the metals, that interact with the electric field, or spins of $s = 1/2$ that interact with the magnetic field. Figure 2.12(a) shows various defects that are typically found in superconducting circuits. These defects can introduce TLSs as shown in Fig. 2.12(b). TLSs can absorb a microwave photon and dissipate it through phonon emission, causing an additional loss mechanism. Besides that, the local effective permittivity close to such a defect can differ for the two levels, resulting in a varying capacitance, thereby affecting the resonance frequency, since $\omega_0 \propto 1/\sqrt{LC}$.

A semi-empirical model of many, independent, TLSs can describe the temperature dependence of $\delta\omega_0(T)/\omega_0$ [43] and $1/Q_i(T)$ [44] at low temperatures. The temperature dependence of the resonance frequency is given by [42, 43],

$$\frac{\delta\omega_0}{\omega_0} = -\frac{1}{\pi Q_{i0}^{\text{TLS}}} \left(\text{Re} \left\{ \psi \left(\frac{1}{2} + \frac{1}{2j\pi} \frac{\hbar\omega_0}{k_B T} \right) \right\} - \ln \left(\frac{\hbar\omega_0}{k_B T} \right) \right). \quad (2.40)$$

Here, Q_{i0}^{TLS} is the zero-temperature, low-field limit of the TLS loss, which depends on the field distribution of the resonator and distribution of the TLSs. $\psi(x)$ is the complex digamma function. There is an additional power-dependence in the resonance frequency due to TLS (via Q_{i0}^{TLS}), but this dependence is experimentally found to be weak ($\delta\omega_0 \propto P_{\text{int}}^{0.3}$) [45].

The temperature and power dependence of the TLS loss is given by [42, 44, 46],

$$\frac{1}{Q_i^{\text{TLS}}} = \frac{1}{Q_{i0}^{\text{TLS}}} \frac{\tanh\left(\frac{\hbar\omega_0}{2k_B T}\right)}{\sqrt{1 + (P_{\text{int}}/P_{\text{int}}^c)^{\beta/2}}}, \quad (2.41)$$

where P_{int}^c is the critical internal power where the TLSs saturate and β is typically a fit parameter. Both depend on the spatial field and TLS distributions. For a single layer, CPW resonator with $S/W \approx 2.5$, $\beta \approx 1.6$ [46].

These equations are derived by assuming that resonant, non-interacting TLSs (which have an energy difference between the levels of, $\Delta E = \hbar\omega_0$) dominate the response.

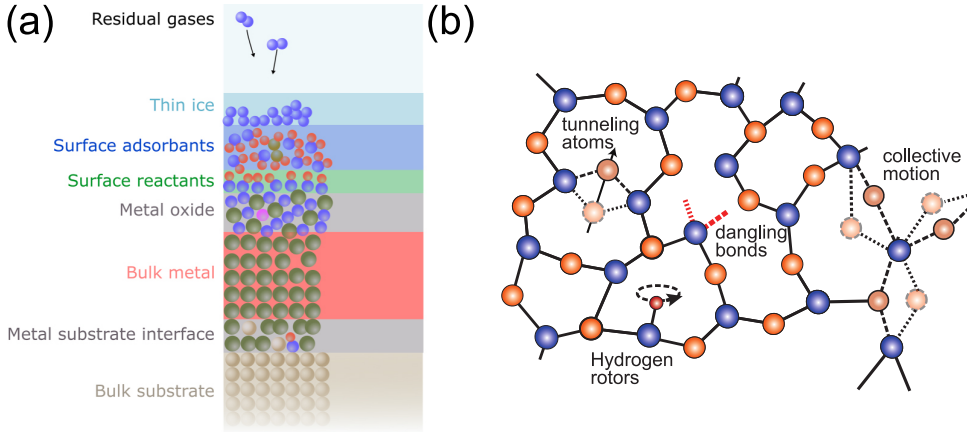


Figure 2.12: Illustration of the microscopic origin of two-level systems (TLSs). (a): Material defects typically introduced when considering a metal layer on substrate surface. Every type of disorder in the atomic structure can cause TLSs. Image from Ref. [40]. (b): Illustration of the TLSs in an amorphous structure of atoms. Image from Ref. [41].

At relatively high temperatures ($T \gtrsim T_c/5$), the quasiparticle response, described by Eqs. (2.20), (2.33) and (2.34), typically dominates the resonance frequency and loss.

The TLSs that affect planar resonant circuits, such as used in this thesis, are experimentally found to be located at the metal and dielectric surfaces [47]. Furthermore, the TLS response is larger when the resonator is surrounded by amorphous dielectric material [48], and the TLSs within the dielectric are likely to be concentrated on the surfaces [49]. Therefore, removing dielectric material that surrounds the resonator [50] and removing surface oxide layers [51] reduces the effects of TLS on the response. Also increasing the total width of a CPW transmission line ($2S+W$ in Fig. 2.6) reduces effects of TLS, since that increases the ratio of the electric field in the vacuum to the electric field in the dielectrics [38, 44, 52]. The ratio of the gap and total width, $W/(2S+W)$, only matters when it is very small (<0.15) or very big (>0.85) [52]. The effects of TLS increase in that case. We therefore design the IDC in Fig. 2.11 to be wide, with $2S+W$ typically $\sim 56 \mu\text{m}$, with a gap ratio of 0.15 to have maximum capacitance per unit length (i.e., a $8-40-8 \mu\text{m}$ geometry).

The TLSs not only result in a temperature dependent response, but also in fluctuations of $1/Q_i$ and ω_0 over time. Since each individual TLS is expected to have a relaxation time τ , many of such independent fluctuators result in a $1/f$ -noise when τ is uniformly distributed [53]. This $1/f$ -noise shows up primarily in phase ($\delta\omega_0/\omega_0$), and scales as [45],

$$S_{\frac{\delta\omega_0}{\omega_0}}(f) = \frac{A}{f} \frac{1}{\sqrt{P_{\text{int}}}} \frac{1}{T^{1+\mu}} \tanh^2\left(\frac{\hbar\omega_0}{k_B T}\right). \quad (2.42)$$

Here, $S_{\frac{\delta\omega_0}{\omega_0}}(f)$ is the noise power spectral density with f the modulation frequency,

A is a constant depending on the geometry and microscopics of the resonator. The $1/f$ character is observed to change to $1/\sqrt{f}$ for high read powers [48, 54]. The term $1/T^{1+\mu}$ is indicative of interaction of the TLSs with other fluctuators at energies lower than $\hbar\omega_0$. μ describes the shape of the density of states of the low energetic TLS [55, 56]. The proportionality of the noise level to $1/\sqrt{P_{\text{int}}}$ is characteristic of TLS noise [57]. It originates from the fact that the TLSs can be saturated in the sense that, at high enough power, they will practically always be in the same, excited state. A common way to limit TLS noise is therefore to maximize P_{int} . However, we will study a wide range of readout powers when we are interested in the effects of readout power on the quasiparticles (Chapter 5), and limit these effects by using a low readout power regimes when studying the quasiparticle relaxation dynamics (Chapters 4, 6 and 7). Therefore, we minimize TLS noise by increasing the capacitive part of the resonator, such that the electric field is distributed over many TLSs and their effect is averaged out [47].

TLS noise in amplitude (i.e., $\delta(1/Q_i)$) follows a similar behavior as Eq. (2.42). In the limit $P_{\text{int}} \rightarrow 0$, the amplitude and phase TLS noise are equal. However, the amplitude TLS noise has an additional factor $1/P_{\text{int}}$ [58], which results in a much lower TLS noise in amplitude at moderate and high readout powers. TLS noise can thus be mitigated for detector applications by considering the amplitude coordinate only [59]. When discriminating between TLS and quasiparticle fluctuations, calculating the correlations between amplitude and phase is useful, since quasiparticles change both the dissipation and kinetic inductance approximately equally (Eq. (2.36)) and TLS is primarily measured in phase [60]. We use this technique in Chapters 4 and 5.

2.3 EXCITATIONS IN SUPERCONDUCTORS

We already dealt with the elemental excitation of the superconducting state in Section 2.1.3, which are quasiparticles. The quasiparticle density in thermal equilibrium exponentially increases with bath temperature, as shown by Eq. (2.17). In Section 2.2, we showed how we can sensitively probe the changes in complex conductivity of the superconductor with a hybrid superconducting resonator (Fig. 2.11). By choosing a coordinate system for the complex forward transmission (S_{21}), we can distinguish between changes in dissipation, σ_1 , and kinetic inductance, σ_2 . From the Mattis-Bardeen equations (Eq. (2.20), Fig. 2.3(b)) we see that these are the dissipative response of quasiparticles and inductive response of the Cooper-pair condensate. We thus have a system that can sensitively probe the superconducting state in real time.

Changes in σ correspond to changes in the quasiparticle distribution function, $f(\epsilon)$, or changes in the density of states, $N_s(\epsilon)$ (see Eq. (2.19)). For changes in $N_s(\epsilon)$, the superconducting condensate must change, which we will come back to in Section 2.4. For changing $f(\epsilon)$, either (a subset of) the quasiparticles must change their energy or the number of quasiparticles must change via quasiparticle generation (Cooper pair-breaking) or recombination. In other words, the quasiparticles must undergo inelastic interactions. In general, a quasiparticle can interact with other quasiparticles (electron-electron interaction) and phonons

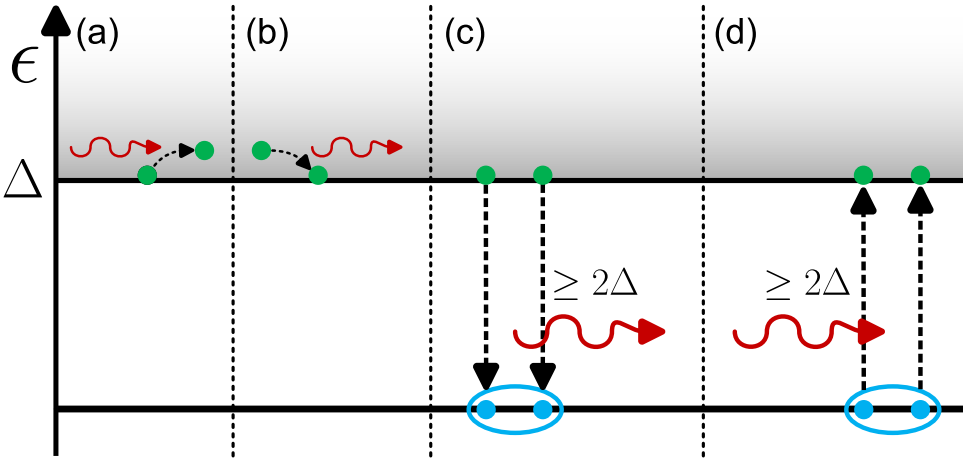


Figure 2.13: Electron-phonon interactions in a superconductor. (a) and (b): Quasiparticle-phonon scattering. The red arrow represents a phonon, which is absorbed (a) or emitted (b) by a quasiparticle (green dots). (c): Quasiparticle recombination, which emits a phonon with energy $\hbar\Omega \geq 2\Delta$. The blue pair of dots represent a Cooper-pair. (d): Quasiparticle generation via a phonon that breaks a Cooper-pair into two quasiparticles.

(electron-phonon interaction). Later, in Sections 2.3.2 and 2.3.3, we will also consider interaction with photons (electron-photon interaction).

The average time between inelastic interactions is called the quasiparticle scattering time, which depends on energy. The scattering time is limited by the smallest interaction time, $\tau(\epsilon) = (1/\tau_{e-e}(\epsilon) + 1/\tau_{e-ph}(\epsilon))^{-1}$. For clean metals, the electron-electron interaction rate is proportional to $\tau_{e-e}^{-1} \propto \epsilon^2/\epsilon_F$ and the electron-phonon interaction is proportional to, $\tau_{e-ph}^{-1} \propto \epsilon^3/(\hbar\Omega_D)$. At energies $\epsilon \lesssim (\hbar\Omega_D)^2/\epsilon_F$ the electron-phonon rate dominates (i.e., τ_{e-ph} is the smallest time). Since quasiparticles have an energy on the order of Δ (see Fig. 2.3(a)), and $\Delta < (\hbar\Omega_D)^2/\epsilon_F$ for most superconductors, the electron-phonon interaction is usually the most important [61]. Only in the case of highly energetic excitations (e.g., absorption of a photon with $\hbar\omega \gg \Delta$) or in the case of very disordered superconductors, electron-electron interaction can start to dominate. We will come back to both these points later in this chapter.

Apart from the conventional scattering events (i.e., exchanging some energy with another particle), quasiparticles can recombine into a Cooper-pair. Therefore, the usual scattering rate in normal metals is split into two rates below T_C : τ_{scat} which conserves quasiparticle number and τ_{rec} which changes quasiparticle number. τ_{rec} is also called the quasiparticle lifetime, since after a recombination event the quasiparticle is annihilated. When two quasiparticles recombine, an energy $\epsilon_1 + \epsilon_2 \geq 2\Delta$ is emitted. If recombination takes place via electron-phonon interaction, this energy is emitted in the form of a phonon. In the opposite process, a phonon with an energy $\epsilon \geq 2\Delta$ breaks a Cooper-pair into two quasiparticles. This is called generation (of quasiparticles). Scattering with a phonon and recombination and

generation of quasiparticles are sketched in Fig. 2.13.

The rates of quasiparticle scattering, recombination and generation are calculated in Ref. [61] for a pure ($ql \gg 1$), 3D ($\xi \ll d$, with d the film thickness) BCS superconductor. Here, $q = \Omega/c_s$ is the phonon wavenumber, with Ω the phonon energy and c_s the sound velocity. In Section 2.4 we will discuss the impure ($ql \ll 1$) and quasi-2D ($\xi \ll d$) limit.

The transition rates can be calculated similar to Eq. (2.19), including coherence factors and initial and final density of states and distribution functions. One obtains [61],

$$\frac{\tau_0}{\tau_{\text{rec}}(\epsilon)} = \frac{\hbar}{(k_B T_C)^3 (1-f(\epsilon))} \int_{\epsilon+\Delta}^{\infty} (\hbar\Omega)^2 \left(1 + \frac{\Delta^2}{\epsilon(\hbar\Omega - \epsilon)}\right) \frac{N_s(\hbar\Omega - \epsilon)}{N_0} \times (n(\hbar\Omega) + 1) f(\hbar\Omega - \epsilon) d\Omega, \quad (2.43a)$$

$$\begin{aligned} \frac{\tau_0}{\tau_{\text{scat}}(\epsilon)} = & \frac{\hbar}{(k_B T_C)^3 (1-f(\epsilon))} \left[\int_0^{\epsilon-\Delta} (\hbar\Omega)^2 \left(1 - \frac{\Delta^2}{\epsilon(\epsilon - \hbar\Omega)}\right) \frac{N_s(\epsilon - \hbar\Omega)}{N_0} \right. \\ & \times (n(\hbar\Omega) + 1) (1 - f(\epsilon - \hbar\Omega)) d\Omega \\ & + \int_0^{\infty} (\hbar\Omega)^2 \left(1 - \frac{\Delta^2}{\epsilon(\hbar\Omega + \epsilon)}\right) \frac{N_s(\hbar\Omega + \epsilon)}{N_0} \\ & \left. \times n(\hbar\Omega) (1 - f(\hbar\Omega + \epsilon)) d\Omega \right]. \end{aligned} \quad (2.43b)$$

Here, $n(\epsilon)$ is the Bose-Einstein distribution function,

$$n(\epsilon) = \frac{1}{e^{\epsilon/(k_B T)} - 1}. \quad (2.44)$$

In Eq. (2.43b), the first term describes phonon emission and the second term describes phonon absorption. For the electron-phonon interaction strength, $\alpha^2(\Omega)$ and the phonon density of states, $F(\Omega)$, it is assumed that $\alpha^2(\Omega)F(\Omega) = b\Omega^2$, such that $\tau_0 = Z'\hbar/(2\pi b(k_B T_C)^3)$. Here, Z' is the Eliashberg renormalization constant [62]. At zero temperature and in the weak-coupling (BCS) limit, this is approximately, $Z' \approx 1 + N_0 V_{sc}$. For clean metals, $b = N_0 V_{sc}/(\hbar\Omega_D)^2$ [17]. For a more realistic estimate of b , neutron scattering data can be used [61]. In general, the approximation $\alpha^2(\Omega)F(\Omega) = b\Omega^2$ is reasonable for small Ω , which dominates Eq. (2.43) if ϵ is on the order of Δ . For higher energies, when ϵ/Ω_D becomes a few percent, the material specific structure of the Eliashberg function $\alpha^2(\Omega)F(\Omega)$ is important.

From the definition of τ_0 , we see that it characterizes the electron-phonon coupling strength. It is proportional to the scattering rate of normal electrons at T_C , $\tau_0 = \frac{7}{4}\Gamma(3)\zeta(3)\tau_s(T_C) = 4.2\tau_s(T_C)$, with $\Gamma(x)$ and $\zeta(x)$ the gamma and Riemann zeta functions [61]. The electron-phonon scattering in a metal film depends on the microscopic structure of the film. Therefore, calculating τ_0 with the clean-limit expression for b given above, or with b from neutron scattering data as done in Ref. [61], only gives an estimate of the actual characteristic electron-phonon scattering time. For Al, this turns out to be accurate within a factor 2.

In thermal equilibrium, $f(\epsilon)$ is given by Fermi-Dirac distribution (Eq. (2.1)) and most quasiparticles have an energy close to Δ . Then, at low temperatures ($k_B T \ll \Delta$), we have,

$$\tau_{\text{rec}}(\Delta; T) = \frac{\tau_0}{\sqrt{\pi}} \left(\frac{k_B T_c}{2\Delta_0} \right)^{5/2} \sqrt{\frac{T_c}{T}} e^{\Delta_0/(k_B T_c)} = \frac{1}{R n_{\text{qp}}}, \quad (2.45a)$$

$$\tau_{\text{scat}}(\Delta; T) = \frac{\tau_0}{\Gamma(\frac{7}{2}) \zeta(\frac{7}{2})} \sqrt{\frac{2\Delta_0}{k_B T_c}} \left(\frac{T_c}{T} \right)^{7/2}. \quad (2.45b)$$

In the second expression for τ_{rec} , we used Eq. (2.17) and defined the recombination constant as $R = 2\Delta_0^2 / ((k_B T_c)^3 N_0 \tau_0)$. For τ_{scat} , only phonon absorption contributes, since a quasiparticle at Δ cannot lose energy and the phonon emission term in Eq. (2.43b) is zero. The quasiparticle interaction times are shown in Fig. 2.14 as a function of temperature (with $\epsilon = \Delta$) and energy (for $T/T_c = 0.1$). The dotted gray line shows the validity of the last equality in Eq. (2.45a).

Ref. [61] also calculated the *phonon* lifetimes against breaking a Cooper-pair (Fig. 2.13(c)) and scattering with a quasiparticle (Fig. 2.13(a)). These are given by,

$$\frac{\tau_0^{\text{ph}}}{\tau_{\text{pb}}(\hbar\Omega)} = \frac{1}{\pi} \int_{\Delta}^{\hbar\Omega - \Delta} \frac{\epsilon(\hbar\Omega - \epsilon) + \Delta^2}{\sqrt{(\epsilon^2 - \Delta^2)((\hbar\Omega - \epsilon)^2 - \Delta^2)}} [1 - f(\epsilon) - f(\hbar\Omega - \epsilon)] d\epsilon, \quad (2.46a)$$

$$\frac{\tau_0^{\text{ph}}}{\tau_{\text{phs}}(\hbar\Omega)} = \frac{1}{\pi} \int_{\Delta}^{\infty} \frac{\epsilon(\hbar\Omega + \epsilon) - \Delta^2}{\sqrt{(\epsilon^2 - \Delta^2)((\hbar\Omega + \epsilon)^2 - \Delta^2)}} [f(\epsilon) - f(\hbar\Omega + \epsilon)] d\epsilon. \quad (2.46b)$$

Here, τ_0^{ph} is the characteristic phonon interaction time, given by, $\tau_0^{\text{ph}} = \hbar N / (4\pi^2 N_0 \langle \alpha^2 \rangle \Delta_0)$, with N the ionic number density and $3 \langle \alpha^2 \rangle = \int_0^{\infty} \alpha^2(\Omega) F(\Omega) d\Omega$. For an order-of-magnitude estimate, the Debye model can be used to find for clean metals, $\langle \alpha^2 \rangle \approx b(\hbar\omega_D)^3/9 \approx N_0 V_{\text{sc}} \hbar\Omega_D/9$ [17, 61], such that $\tau_0^{\text{ph}} \approx 9N / (4\pi^2 N_0^2 V_{\text{sc}} \Omega_D \Delta)$. At low temperatures ($k_B T \ll \Delta$), the 2Δ -phonons will dominate the pair-breaking processes. This is because the phonon occupation above 2Δ is exponentially low (due to $n(\hbar\Omega > 2\Delta) \sim e^{-\hbar\Omega/(k_B T)}$), while the pair-breaking rate only increases linearly with energy. At 2Δ , the pair-breaking time (Eq. (2.46a)) is given by, $\tau_{\text{pb}} = \tau_0^{\text{ph}} \Delta_0 / (\Delta(T)(1 - 2f(\Delta(T))) \approx \tau_0^{\text{ph}}$, where the approximation is valid for low temperatures, $k_B T \ll \Delta$. In practice, we can assume a constant pair-breaking time of phonons of $\tau_{\text{pb}} = \tau_0^{\text{ph}}$ for temperature $T < T_c/2$ with an error less than 10% [61]. On the other hand, the scattering time for phonons grows exponentially at low temperatures, since the distribution functions in between brackets in Eq. (2.46b) go to zero. In other words, phonons are very unlikely to scatter with a quasiparticle at low temperatures, since the quasiparticle density vanishes.

As stated before, electron-electron interaction for quasiparticles is extremely weak, since their energy is usually smaller than $(\hbar\Omega_D)^2/\epsilon_F$. Additionally, electron-electron interaction for quasiparticles scales with the quasiparticle density, which is exponentially small at low temperatures (Eq. (2.17)). For completeness, we mention here the electron-electron inelastic relaxation times of quasiparticles at the gap edge,

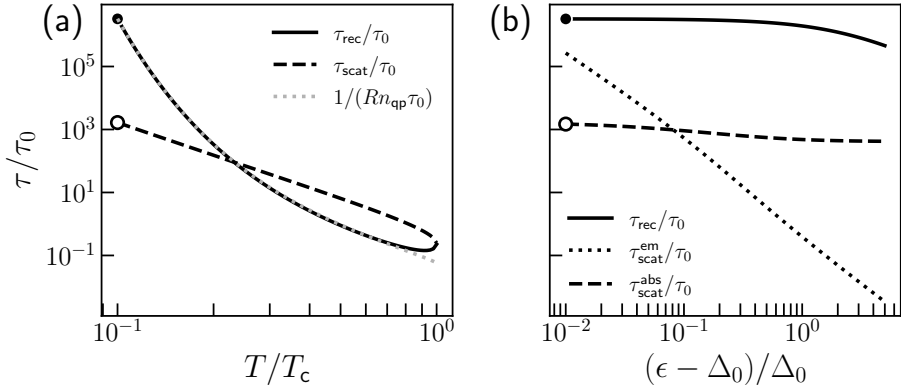


Figure 2.14: Quasiparticle interaction times for scattering and recombination. **(a):** Recombination and scattering times for a quasiparticle at the gap edge ($\epsilon = \Delta$) versus temperature. The gray dotted line is the approximation given in Eq. (2.45a), with $R = 2\Delta_0^2/((k_B T_c)^3 N_0 \tau_0)$. **(b):** Recombination and scattering (phonon emission and absorption) versus energy, for a temperature $T/T_c = 0.1$.

at low temperatures in a clean, 3D superconductor [63],

$$\tau_{\text{rec}}^{\text{e-e},3\text{D}}(\Delta; T) = \frac{\tau_{\text{e-e}}^{3\text{D}}(T)}{(1 + \sqrt{2}/4 + (1 + 5\sqrt{2}/4)(N_0 V_{\text{sc}})^2)} \frac{k_B T}{4\Delta} e^{2\Delta/(k_B T)}, \quad (2.47a)$$

$$\tau_{\text{scat}}^{\text{e-e},3\text{D}}(\Delta; T) = \frac{\tau_{\text{e-e}}^{3\text{D}}(T)}{(1 + 2(1 + (N_0 V_{\text{sc}})^2)/\pi)} \frac{(k_B T)^2}{2\Delta\sqrt{2\pi\Delta k_B T}} e^{\Delta/(k_B T)}, \quad (2.47b)$$

where,

$$\tau_{\text{e-e}}^{3\text{D}}(T) = \left(\frac{64}{\pi^4} \frac{\hbar\epsilon_F}{(k_B T)^2} \frac{k_F}{\sqrt{2N_0 e^2/\epsilon_0}} \right), \quad (2.48)$$

is the normal state electron-electron interaction time [63, 64]. When we compare these expressions to Eq. (2.45), we see an additional factor $e^{\Delta/(k_B T)}$, which is large for low temperatures and reflects the dependence on the quasiparticle density. Therefore, electron-electron scattering is slow compared to electron-phonon scattering.

In quasi-2D, $d \ll \xi_{\text{DL}}$, the rates are slightly enhanced by a factor $\sim \ln(\epsilon_F/\Delta) \sim 10$ due to the electronic confinement [65]. This is similar to the normal metal case. In Section 2.4 we will see that electron-electron scattering is also enhanced when the electrons are confined due to disorder.

2.3.1 QUASI-EQUILIBRIUM

In order to describe the effects of an excitation of the superconductor we make the following simplification. From Fig. 2.13, we see that the change in distribution function is much larger for a generation or recombination event than for a scattering

event. For a scattering event, one quasiparticle changes energy over $\sim k_B T$, while for a generation/recombination 2 quasiparticles of energy $\sim \Delta$ are created/destroyed. Therefore, we are only sensitive for generation-recombination events⁶. Furthermore, at low temperatures, the scattering rate is much faster than the recombination rate (see Fig. 2.14). We therefore assume that the quasiparticles are in quasi-equilibrium: we assume Fermi-Dirac distribution for the quasiparticles and use Eq. (2.45a) for the recombination time. We disregard any further effect of phonon scattering. Then, we can simplify our description by only considering the quasiparticle density, instead of the full, energy-dependent distribution functions. This comes down to counting quasiparticles and 2Δ -phonons and results in the Rothwarf-Taylor equations [66],

$$\frac{dn_{\text{qp}}}{dt} = -2 \frac{Rn_{\text{qp}}^2}{2} + 2 \frac{n_{\text{ph}}}{\tau_{\text{pb}}}, \quad (2.49a)$$

$$\frac{dn_{\text{ph}}}{dt} = \frac{Rn_{\text{qp}}^2}{2} - \frac{n_{\text{ph}}}{\tau_{\text{pb}}} - \frac{n_{\text{ph}} - n_{\text{ph}}^T}{\tau_{\text{esc}}}. \quad (2.49b)$$

Here, $n_{\text{ph}} = N_{\text{ph}}/V$ is the 2Δ -phonon density. The first term in these equations describes quasiparticle recombination (Fig. 2.13(b)), where two quasiparticles are destroyed (with a single particle rate $\tau_{\text{rec}}^{-1} = Rn_{\text{qp}}$, Eq. (2.45a)), and one phonon is emitted. The second term describes quasiparticle generation (Fig. 2.13(c)), where two quasiparticles are created, and one phonon is lost (with a rate $\tau_{\text{pb}}^{-1}(2\Delta) \approx 1/\tau_0^{\text{ph}}$). The last term in Eq. (2.49b) describes the phonon escape to the bath, which has a thermal phonon density of n_{ph}^T . The phonon escape time, τ_{esc} , depends on the thickness and thermal properties of the superconductor and substrate and thermal contact between the two. When we neglect the phonon loss in the bulk superconductor and assume diffusive scattering at the boundary of the superconductor and substrate, we can use the relation [67],

$$\left(1 + \frac{\tau_{\text{esc}}}{\tau_{\text{pb}}}\right) = \frac{4d}{\Lambda_{\text{T,L}}} \frac{1 - (1 - \eta_{\text{T,L}})e^{-2d/\Lambda_{\text{T,L}}}}{\eta_{\text{T,L}}(1 - e^{-2d/\Lambda_{\text{T,L}}})}. \quad (2.50)$$

Here, d is the superconducting film thickness and $\Lambda_{\text{T,L}} = \tau_{\text{pb}} c_{\text{T,L}}$ is the phonon mean free path for either transverse (with a velocity c_{T}) or longitudinal (c_{L}) phonons. $\eta_{\text{T,L}}$ is the phonon transparency, which can be calculated for longitudinal and transverse phonons separately. When the densities and phonon velocities are known, the transparencies can be calculated as set out in Ref. [68]. For a description of these calculations see Appendix A. Usually, the transverse phonon velocity is smaller than the longitudinal phonon velocity, such that $(c_{\text{L}}/c_{\text{T}})^3 \gg 1$, and transverse phonons dominate the electron-phonon interaction [69].

The expression on the left-hand side of Eq. (2.50) is called the phonon trapping factor. In most cases, the phonon interaction times are much shorter than the quasiparticle lifetime, $1/\tau_{\text{pb}} + 1/\tau_{\text{esc}} \gg Rn_{\text{qp}}$, which allows decoupling the two

⁶In Chapter 6 we will explicitly calculate the resistivity for scattering and generation-recombination events and conclude that we are indeed orders of magnitude more sensitive to the generation-recombination process.

differential equations Eq. (2.49)⁷. In this case, we can assume n_{ph} to be in quasi-equilibrium, such that,

$$\frac{dn_{\text{ph}}}{dt} = -\frac{1}{2} \frac{dn_{\text{qp}}}{dt} - \frac{n_{\text{ph}} - n_{\text{ph}}^T}{\tau_{\text{esc}}} \approx 0. \quad (2.51)$$

Solving for n_{ph} and using Eq. (2.49a), we find a single differential equation for n_{qp} ,

$$\frac{dn_{\text{qp}}}{dt} = -\frac{R}{(1 + \tau_{\text{esc}}/\tau_{\text{pb}})} \left(n_{\text{qp}}^2 - (n_{\text{qp}}^T)^2 \right), \quad (2.52)$$

which has a constant pair-breaking term given by the thermal average and where the timescales are renormalized with the phonon trapping factor. We used Eq. (2.49a) in thermal equilibrium to replace the explicit n_{ph}^T dependence.

When we additionally consider only small deviations from thermal equilibrium, such that $n_{\text{qp}}^2 = (n_{\text{qp}}^T + \delta n_{\text{qp}})^2 \approx (n_{\text{qp}}^T)^2 + 2n_{\text{qp}}^T \delta n_{\text{qp}}$ (with n_{qp}^T from Eq. (2.17)), we can solve Eq. (2.52) as,

$$\delta n_{\text{qp}}(t) = \delta n_{\text{qp}}(0) e^{-t/\tau_{\text{qp}}^*}, \quad (2.53)$$

where we defined the effective or bulk quasiparticle recombination time,

$$\tau_{\text{qp}}^* = \tau_{\text{rec}}(1 + \tau_{\text{esc}}/\tau_{\text{pb}})/2, \quad (2.54)$$

with $\tau_{\text{rec}} = 1/(Rn_{\text{qp}}^T)$ (see Eq. (2.45a)).

In addition to the time-dependent solution to the Rothwarf-Taylor equations, a frequency-dependent solution for the fluctuations in n_{qp} and n_{ph} can be found using the framework from Ref. [70]. This is based on a multi-variate master equation approach. We will illustrate the key concepts of this framework here and refer for the details to Ref. [70].

First, we define the levels of interest. In the case of Eq. (2.49), this would be: (1) the quasiparticle level, (2) the 2Δ -phonon level in the superconductor and (3) the phonon bath. Second, we write the transition rates between each level (p_{ij}) with their shot size⁸ (δn_{ij}). This results in,

$$p_{12} = Rn_{\text{qp}}^2/2 \quad \delta n_{12} = 2/V, \quad (2.55a)$$

$$p_{21} = n_{\text{ph}}/\tau_{\text{pb}} \quad \delta n_{21} = 2/V, \quad (2.55b)$$

$$p_{23} = n_{\text{ph}}/\tau_{\text{esc}} \quad \delta n_{23} = 1/V, \quad (2.55c)$$

$$p_{32} = n_{\text{ph}}^T/\tau_{\text{esc}} \quad \delta n_{32} = 1/V. \quad (2.55d)$$

With these transition rates, we can calculate two matrices, $\underline{\underline{M}}$ and $\underline{\underline{B}}$ that describe

⁷For the decoupling to be valid, only one of the two phonon times (τ_{pb} or τ_{esc}) needs to be much shorter than the recombination time.

⁸We here work with density fluctuations, which result in the extra factor $1/V$ for the shot sizes compared to the number fluctuations described in Ref. [70].

the drift and diffusion in the system, respectively. These are calculated by,

$$M_{ij} = \sum_k \delta n_{ik} \left(\frac{\partial p_{ik}}{\partial n_j} - \frac{\partial p_{ki}}{\partial n_j} \right) \Big|_{\{n_i\}=\{n_i^0\}}, \quad (2.56a)$$

$$B_{ii} = \sum_{k \neq i} \delta n_{ik}^2 (p_{ki}^0 + p_{ik}^0), \quad (2.56b)$$

$$B_{ij} = -\delta n_{ij} \delta n_{ji} (p_{ij}^0 + p_{ji}^0), \quad (2.56c)$$

where the superscript 0 indicates steady state. In the case considered here we have, $n_{qp}^0 = n_{qp}^T$ and $n_{ph}^0 = n_{ph}^T$. We find,

$$\underline{\underline{M}} = \frac{1}{V} \begin{pmatrix} 2Rn_{qp}^T & -2/\tau_{pb} \\ -Rn_{qp}^T & 1/\tau_{esc} + 1/\tau_{pb} \end{pmatrix}, \quad (2.57a)$$

$$\underline{\underline{B}} = \frac{R(n_{qp}^T)^2}{V^2} \begin{pmatrix} 4 & -2 \\ -2 & 1 + \tau_{pb}/\tau_{esc} \end{pmatrix}. \quad (2.57b)$$

In expressing $\underline{\underline{B}}$, we used detailed balance: $p_{ij}^0 = p_{ji}^0$, which is valid in equilibrium due to microscopic reversibility and in a system in steady state where the levels are coupled in pairs [70, 71]. With these two matrices known, the cross power spectral density matrix can be calculated as,

$$\underline{\underline{G}}(\omega) = 2 \text{Re} \left\{ (\underline{\underline{M}} + j\omega \underline{\underline{I}})^{-1} \underline{\underline{B}} (\underline{\underline{M}}^T - j\omega \underline{\underline{I}})^{-1} \right\} = \frac{2}{\omega^2} \text{Re} \left\{ (\mathbf{1} + \underline{\underline{M}}/(j\omega))^{-1} \underline{\underline{B}} \right\}, \quad (2.58)$$

where the second equality holds if the system exhibits detailed balance. The superscript T indicates a transpose and the superscript -1 a matrix inversion. The element $G_{11}(\omega)$ gives the power spectral density of the quasiparticle fluctuations,

$$G_{11}(\omega) = S_{n_{qp}}(\omega) = \frac{2\alpha_1 \tau_1 n_{qp}^T/V}{1 + (\omega\tau_1)^2} + \frac{2\alpha_2 \tau_2 n_{qp}^T/V}{1 + (\omega\tau_2)^2}, \quad (2.59)$$

where $1/\tau_1$ and $1/\tau_2$ are the eigenvalues for the matrix $\underline{\underline{M}}$ and,

$$\alpha_1 = 2 \frac{\tau_1 - \tau_{esc}}{\tau_1 - \tau_2} \quad \text{and} \quad \alpha_2 = 2 \frac{\tau_{esc} - \tau_2}{\tau_1 - \tau_2}. \quad (2.60)$$

When we again assume, $1/\tau_{pb} + 1/\tau_{esc} \gg Rn_{qp}^T$, these eigenvalues become,

$$\tau_1 = \frac{(1 + \tau_{esc}/\tau_{pb})}{2Rn_{qp}^T} = \tau_{qp}^* \quad \text{and} \quad \tau_2 = (1/\tau_{esc} + 1/\tau_{pb})^{-1}, \quad (2.61)$$

and $\alpha_1 \approx 2$ and $\alpha_2 \approx 0$, resulting in

$$S_{n_{qp}}(\omega) \approx \frac{4\tau_{qp}^* n_{qp}^T/V}{1 + (\omega\tau_{qp}^*)^2}. \quad (2.62)$$

This is a Lorentzian spectrum, with τ_{qp}^* as timescale and $\langle \delta n_{qp}^2 \rangle = n_{qp}^T/V$ as variance. When expressing the variance in quasiparticle numbers, we see that this

is Poissonian noise, $\langle \delta N_{\text{qp}}^2 \rangle = N_{\text{qp}}^0$. In general, systems that obey detailed balance exhibit Poissonian noise, while driven, non-equilibrium systems can exhibit super- ($\langle \delta N_{\text{qp}}^2 \rangle > N_{\text{qp}}^0$) or sub-Poissonian noise ($\langle \delta N_{\text{qp}}^2 \rangle < N_{\text{qp}}^0$) [70]. This noise source is called generation-recombination (GR) noise and is intrinsic to the superconducting resonator. Since the quasiparticle density fluctuates, this noise is present in both amplitude and phase via Eq. (2.36).

With the time-dependent quasiparticle density from the Rothwarf-Taylor equations (Eq. (2.49)) and the frequency-dependent description of quasiparticle density fluctuations (Eqs. (2.56) and (2.58)), we have two powerful tools to relate our measurements to the quasiparticle dynamics. For example, we can measure the power spectral density of the fluctuations in amplitude and phase and calculate the equivalent quasiparticle density fluctuations with the quasiparticle responsivities (Eq. (2.36)). Then, we can extract the quasiparticle lifetime and density various bath temperatures, by fitting Eq. (2.62) to the measured spectra. In Chapter 4, we use this measurement technique to find that $\tau_{\text{qp}}^* \propto 1/n_{\text{qp}}$ (i.e., Eqs. (2.45a) and (2.54)) breaks down at low temperatures. This results in a strong reduction of the noise level $S_{n_{\text{qp}}} \tau_{\text{qp}}^* n_{\text{qp}}^T$, since τ_{qp}^* saturates for decreasing bath temperature (and thus deviates from Eq. (2.45a)), while n_{qp} stays thermal and exponentially decreases. In Chapter 5, we use this technique to measure the effect of readout power on the excess quasiparticle density at low temperatures.

The Rothwarf-Taylor equations and associated fluctuation framework are also very general: we can add physics to these models simply by adding or removing levels and transition rates. For example, in Chapter 6 we will add a level for localized quasiparticles to explain the temperature dependence of τ_{rec} in disordered superconductors, which differs from Eq. (2.45a). In Chapter 7 we will add diffusion terms to the Rothwarf-Taylor equations and make the quasiparticle and phonon densities position dependent in an attempt to explain the quasiparticle decay after a high-energy excitation.

Above, we addressed thermal equilibrium. These equations can however also describe the dynamics of a driven or excited state by adding a quasiparticle generation term in Eq. (2.49a). As long as the assumption of quasi-equilibrium is correct (i.e., the energy distribution of quasiparticles follow a Fermi-Dirac distribution at each point in time), these equations provide an easy way to model the quasiparticle dynamics. In the next sections, we will discuss different types of excitations and how these equations can be applied. We will also discuss the limitations of the quasi-equilibrium approximation.

2.3.2 PAIR-BREAKING PHOTON EXCITATIONS

The absorption of a photon is probably the most application-relevant excitation of the superconductor. When a photon with an energy⁹ $\hbar\omega_{\text{rad}} \geq 2\Delta$ is absorbed in a superconductor, it will break Cooper-pairs and generate quasiparticles. This can be measured via the forward microwave transmission, resulting in a change in amplitude and phase with a responsivity given by Eq. (2.36). This is the working

⁹We will use $\hbar\omega_{\text{rad}}$ as the photon energy of incoming radiation.

principle of a Microwave Kinetic Inductance Detector, or MKID [72], as introduced in Chapter 1.

MKIDs have two modes of operation: power integrating detection and single photon detection. Power integrating detection is used when the photon count rate is high and the photon energy is low. In that case, the total power absorbed by the detector is integrated over the measurement time and the incoming power is estimated from the statistics of the time trace. Typically, the incoming power is estimated from the calibrated mean, but also the variance or noise level at a modulation frequency can be used.

For single photon detection, the energy of a single photon is enough to produce a measurable signal. In that case, the photon arrival time and photon energy can be estimated from position and amplitude of the single photon peak within a time trace of $(\delta A(t), \theta(t))$.

POWER INTEGRATING RESPONSE

In order to understand the workings and predict the sensitivity of this photon detector, we can use the framework explained above. The continuous generation of quasiparticles can be accounted for in the Rothwarf-Taylor equations by adding a term to the quasiparticle level (assuming $(1/\tau_{\text{pb}} + 1/\tau_{\text{esc}})^{-1} \gg Rn_{\text{qp}}$),

$$\frac{dn_{\text{qp}}}{dt} = -\frac{R}{(1 + \tau_{\text{esc}}/\tau_{\text{pb}})} \left(n_{\text{qp}}^2 - (n_{\text{qp}}^T)^2 \right) + \frac{\eta_{\text{pb}} P_{\text{rad}}^{\text{abs}}}{V\Delta}, \quad (2.63)$$

where $P_{\text{rad}}^{\text{abs}}$ is the absorbed radiation power. This can be expressed as the total radiation power from the source times the absorption efficiency, $P_{\text{rad}}^{\text{abs}} = \eta_{\text{abs}} P_{\text{rad}}$. The absorption efficiency depends on the optical path from source to detector and on the optical efficiency of the absorber, $\eta_{\text{abs}} = \eta_{\text{path}} \eta_{\text{opt}}$. The optical efficiency can be optimized by using antennae for large wavelengths [37], patterned absorbers for medium wavelengths or plane sheet absorbers for small wavelengths, in combination with lenses and anti-reflection layers [73].

Pair-breaking efficiency The pair-breaking efficiency, η_{pb} , describes the efficiency at which an absorbed photon is converted to quasiparticles. This depends on the inelastic interactions within the superconductor. The absorbed photon will excite an electron to an energy $\sim \hbar\omega_{\text{rad}}$ above the Fermi surface. This electron will lose energy to other electrons and phonons via electron-electron and electron-phonon interactions (Eq. (2.43)), which in turn will excite new phonons and electrons. This process is called downconversion [74] and depends on the microscopics of the superconductor, thermal contact with the environment and photon energy. Downconversion is sketched in Fig. 2.18 and at the end of this sections, we will go more into the details of this process.

The calculation of η_{pb} is typically done numerically [34, 35, 76, 77]. The results of calculations from Ref. [34] is shown in Fig. 2.15(a). Figure 2.15(b) shows a comparison with experimental data from Ref. [75]. For a photon with energy $\hbar\omega_{\text{rad}} = 2\Delta$, one photon can create exactly two quasiparticles and no energy is lost,

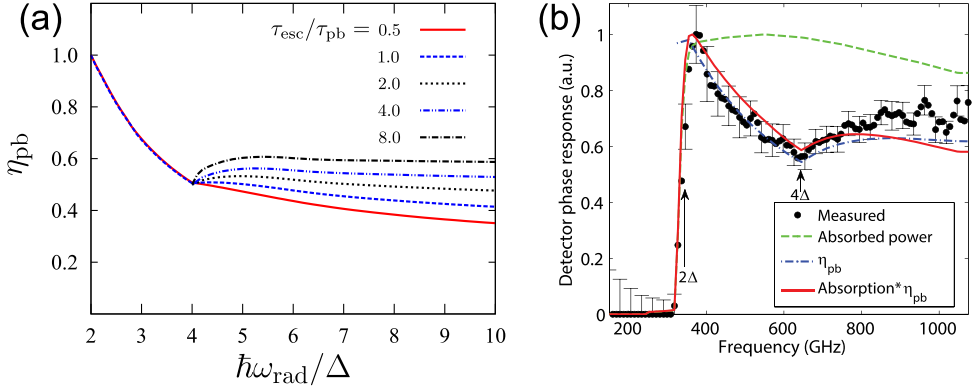


Figure 2.15: Pair-breaking efficiency (η_{pb}) of pair-breaking photons. (a): Numerically calculated η_{pb} as a function of the photon energy, $\hbar\omega_{rad}$. Different lines indicate different phonon escape times, as indicated in the legend. Figure from Ref. [34]. (b): Measured relative pair-breaking efficiency (black dots) compared to the calculated normalized efficiency (red solid line). Figure from Ref. [75].

$\eta_{pb} = 1$ [34, 75]. For a photon with more energy, however, some energy is lost in the form of subgap ($\Omega < 2\Delta$) phonons, which cannot break Cooper-pairs. The conversion to quasiparticles is therefore less efficient. At $\hbar\omega_{rad} = 4\Delta$ the efficiency drops to $\eta_{pb} = 0.5$. Above a photon energy of 4Δ , more than 2 quasiparticles can be generated and η_{pb} increases again. The average efficiency depends on the phonon escape to the bath. When phonon escape is eliminated (i.e., $\tau_{esc} \rightarrow \infty$), the energy lost is equal to the total energy of subgap phonons that are generated in this process. In that case, $\eta_{pb} = 0.59$ [34, 78]. For now, we leave η_{pb} as parameter in our description of the response to radiation.

With η_{pb} known, we find the steady state quasiparticle density from Eq. (2.63),

$$n_{qp}^0 = \sqrt{(n_{qp}^T)^2 + \frac{\eta_{pb} P_{rad}^{abs} (1 + \tau_{esc}/\tau_{pb})}{R\Delta V}} \approx \begin{cases} n_{qp}^T + \frac{\eta_{pb} P_{rad}^{abs} \tau_{qp}^*}{\Delta V} & n_{qp}^T \gg n_{qp}^0 \\ \frac{2\eta_{pb} P_{rad}^{abs} \tau_{qp}^*}{\Delta V} & n_{qp}^T \ll n_{qp}^0 \end{cases} \quad (2.64)$$

with $\tau_{qp}^* = (1 + \tau_{esc}/\tau_{pb})/(2Rn_{qp}^0)$. In the low radiation power approximation (top line in Eq. (2.64)) τ_{qp}^* is constant with P_{rad}^{abs} , since in that case $n_{qp}^0 \approx n_{qp}^T$. Therefore, the excess quasiparticle density varies as $\delta n_{qp} = n_{qp}^0 - n_{qp}^T \propto P_{rad}^{abs}$. However, in the opposite limit (bottom line in Eq. (2.64)), τ_{qp}^* varies with P_{rad}^{abs} , since in that case $n_{qp}^0 \propto \sqrt{P_{rad}^{abs}}$. Therefore, in this high radiation power regime, $\delta n_{qp} \propto \sqrt{P_{rad}^{abs}}$. From the first equality in Eq. (2.64), we find the change in steady-state quasiparticle density with absorbed radiation power [79],

$$\frac{dn_{qp}^0}{dP_{rad}^{abs}} = \frac{\eta_{pb} \tau_{qp}^*}{\Delta V}. \quad (2.65)$$

This increased quasiparticle density will result in an increased GR noise, given by Eq. (2.62) with $n_{\text{qp}}^T \rightarrow n_{\text{qp}}^0$. In addition, the generation mechanism adds noise in this case as well: photons arrive randomly, which induces photon noise. The variance of the photon arrival rate of a thermal source of temperature T_s is given by[80],

$$\langle \delta \dot{N}_\gamma^2 \rangle = 2\dot{N}_\gamma \Delta f (1 + \eta_{\text{abs}} n(\hbar\omega_{\text{rad}}; k_B T_s)), \quad (2.66)$$

with $\dot{N}_\gamma = \eta_{\text{abs}} P_{\text{rad}} / (\hbar\omega_{\text{rad}})$ the photon arrival rate and $n(\epsilon)$ given by Eq. (2.44). Δf is the detector bandwidth, which is given by $\Delta f = 1/(2\pi\tau_{\text{qp}}^*)$ when the quasiparticle recombination time is the longest relaxation time in the system. The factor in parentheses is the photon bunching term, which is relevant when both the absorption efficiency is high and when detecting low frequencies from a hot object ($\hbar\omega_{\text{rad}} < k_B T_s$).

Equation (2.66) results in additional quasiparticle density fluctuations with a variance,

$$\begin{aligned} \langle \delta n_{\text{qp}}^2 \rangle &= \left(\frac{dn_{\text{qp}}^0}{dP_{\text{rad}}^{\text{abs}}} \right)^2 \left\langle \delta \left(P_{\text{rad}}^{\text{abs}} \right)^2 \right\rangle \\ &= \left(\frac{\eta_{\text{pb}}}{\Delta V} \right)^2 \frac{\hbar\omega_{\text{rad}} \tau_{\text{qp}}^*}{\pi} P_{\text{rad}}^{\text{abs}} (1 + \eta_{\text{abs}} n(\hbar\omega_{\text{rad}})). \end{aligned} \quad (2.67)$$

Therefore, the total fluctuation power spectral density is given by,

$$S_{n_{\text{qp}}}(\omega) = \frac{4\tau_{\text{qp}}^*}{V(1 + (\omega\tau_{\text{qp}}^*)^2)} \left(n_{\text{qp}}^0 + P_{\text{rad}}^{\text{abs}} \left(\frac{\eta_{\text{pb}}}{\Delta} \right)^2 \frac{\hbar\omega_{\text{rad}} \tau_{\text{qp}}^*}{\pi} (1 + \eta_{\text{abs}} n(\hbar\omega_{\text{rad}})) \right). \quad (2.68)$$

In the limit $n_{\text{qp}}^T \gg n_{\text{qp}}^0$, this becomes,

$$S_{n_{\text{qp}}}(\omega) \approx \frac{4\tau_{\text{qp}}^*}{V(1 + (\omega\tau_{\text{qp}}^*)^2)} \left(n_{\text{qp}}^T + P_{\text{rad}}^{\text{abs}} \frac{\eta_{\text{pb}} \tau_{\text{qp}}^*}{\Delta} \left(1 + \frac{\eta_{\text{pb}} \hbar\omega_{\text{rad}}}{\pi \Delta V} (1 + \eta_{\text{abs}} n(\hbar\omega_{\text{rad}})) \right) \right), \quad (2.69)$$

and in the opposite limit, $n_{\text{qp}}^T \ll n_{\text{qp}}^0$, this is,

$$S_{n_{\text{qp}}}(\omega) \approx \frac{4(1 + \tau_{\text{esc}}/\tau_{\text{pb}})}{RV(1 + (\omega\tau_{\text{qp}}^*)^2)} \left(2 + \eta_{\text{pb}} \frac{\hbar\omega_{\text{rad}}}{\pi \Delta} (1 + \eta_{\text{abs}} n(\hbar\omega_{\text{rad}})) \right). \quad (2.70)$$

These expressions can be multiplied by the quasiparticle responsivities for amplitude and phase (Eq. (2.36)) to obtain the power spectral densities in δA and θ . From Eq. (2.68), we see that the added noise level is proportional to the absorbed power and we can measure the power of the incoming radiation by recording the noise¹⁰. This is illustrated in Fig. 2.16: for the darker curves (i.e., low radiation power regime) the noise level increases with increasing radiation power. At high absorbed powers, $P_{\text{rad}}^{\text{abs}} > \Delta n_{\text{qp}}^T V / (\eta_{\text{pb}} \tau_{\text{qp}}^*)$, the noise level becomes constant, as also Eq. (2.70) shows. In this regime, the bandwidth of the noise increases with increasing radiation power,

¹⁰In Chapter 4, we will show however that the noise level decreases exponentially with temperature due to an effect of quasiparticle trapping. This compromises this way of measuring the incoming radiation at low temperatures.

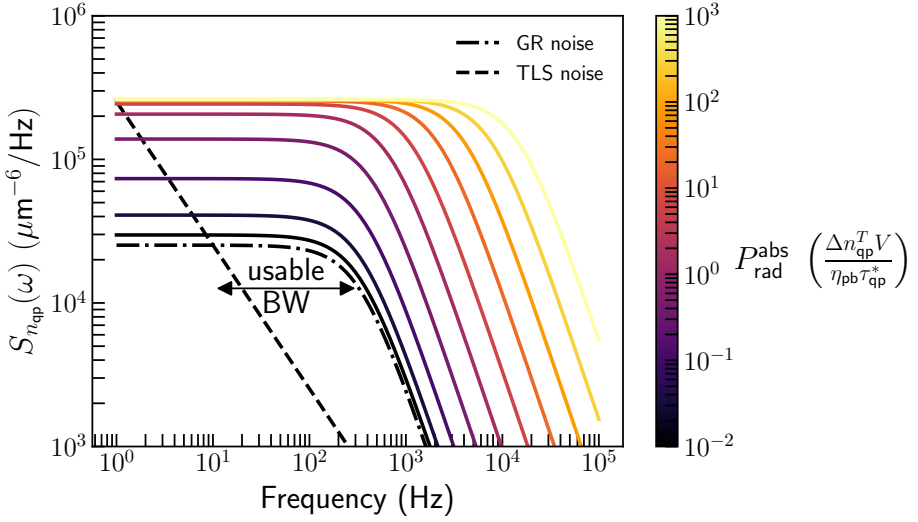


Figure 2.16: Power spectral density of photon noise from Eqs. (2.64) and (2.68), with different absorbed radiation powers indicated by the colors. The dashed line represents TLS noise ($\propto 1/f$ from Eq. (2.42)) and the dashed-dotted line is GR noise (Eq. (2.62)). The arrow indicates the usable bandwidth for the modulation frequency.

since $\tau_{\text{qp}}^* \propto \sqrt{P_{\text{rad}}^{\text{abs}}}$. Therefore, the variance (i.e. area under the curves in Fig. 2.16) and average of $n_{\text{qp}}(t)$ still scale as $\propto \sqrt{P_{\text{rad}}^{\text{abs}}}$. The behavior as described by Eq. (2.68) and Fig. 2.16 is experimentally observed in Ref. [32]. This picture changes when the quasiparticle lifetime and density decouple, that is, when $\tau_{\text{qp}}^* \propto 1/n_{\text{qp}}^0$ does not hold. We will see in Chapter 4 that this will reduce the recombination noise (the first term inside the parentheses in Eq. (2.68)) significantly at low temperatures. Such a situation is also observed in Ref. [81].

The sensitivity of a power integrating detector is expressed in a Noise Equivalent Power (NEP), which describes the equivalent detected power of other noise sources in the detector. For example, the noise equivalent power of GR noise (Eq. (2.62)) is given by,

$$\text{NEP}_{\text{GR}} = \sqrt{S_{n_{\text{qp}}}(\omega) (1 + (\tau_{\text{qp}}^* \omega)^2)} \left(\frac{dn_{\text{qp}}}{dP_{\text{rad}}^{\text{abs}}} \right)^{-1} = \frac{2\Delta}{\eta_{\text{pb}}} \sqrt{\frac{V n_{\text{qp}}^T}{\tau_{\text{qp}}^*}}. \quad (2.71)$$

This expression gives the best NEP possible for a power integrating MKID [82]. The minimal NEP of an actual detector depends on the modulation frequency, $f = \omega/(2\pi)$. This must be smaller than $1/(2\pi\tau_{\text{qp}}^*)$ to have a maximal quasiparticle sensitivity, but larger than the crossing between the TLS noise ($S(\omega) \propto 1/f$, or $S(\omega) \propto 1/\sqrt{f}$, Eq. (2.42)) and GR noise (Eq. (2.71)). This usable bandwidth for the modulation frequency is indicated in Fig. 2.16.

SINGLE PHOTON RESPONSE

When a single photon is absorbed in the superconductor, it will result in a number of excess quasiparticles, $\delta N_{\text{qp}} = \eta_{\text{pb}} \hbar \omega_{\text{rad}} / \Delta$. We can therefore simply add a delta-peak generation term ($\delta(t)$) to Eq. (2.52) and obtain,

$$\frac{dn_{\text{qp}}}{dt} = -\frac{R}{(1 + \tau_{\text{esc}}/\tau_{\text{pb}})} \left(n_{\text{qp}}^2 - (n_{\text{qp}}^T)^2 \right) + \frac{\eta_{\text{pb}} \hbar \omega_{\text{rad}}}{\Delta V} \delta(t). \quad (2.72)$$

We can reformulate this in terms of excess quasiparticles, $\delta n_{\text{qp}}(t) = n_{\text{qp}}(t) - n_{\text{qp}}^T$ and solve the differential equation by separation of variables [83]. We find,

$$\delta n_{\text{qp}}(t) = \frac{2n_{\text{qp}}^T}{(1 + 2n_{\text{qp}}^T/\delta n_{\text{qp}}(0)) e^{t/\tau_{\text{qp}}^*} - 1}, \quad (2.73)$$

where $\delta n_{\text{qp}}(0) = \eta_{\text{pb}} \hbar \omega_{\text{rad}} / (\Delta V)$.

This expression reduces to the quasi-equilibrium simple exponential decay (Eq. (2.53)), when $n_{\text{qp}}^T \gg \delta n_{\text{qp}}(0)$. So, when the photon excitation creates a quasiparticle density that is much lower than the thermal quasiparticle density, the pulse decay is exponential.

In the opposite limit, $\delta n_{\text{qp}}^T \ll \delta n_{\text{qp}}(0)$, the decay follows a $\delta n_{\text{qp}}(t) \propto 1/t$ decay for $t \ll \tau_{\text{qp}}^*$, which gradually goes to an exponential decay for times $t \gtrsim \tau_{\text{qp}}^*$. This is shown in Fig. 2.17.

This faster-than-exponential decay hinders the energy-resolving capabilities of MKIDs. From Fig. 2.17(a) it is clear that for small excitations, the pulse height is proportional to excitation energy. The photon energy can therefore be estimated from the pulse height. A time-stream of δA or θ containing single photon pulses can be analyzed with an optimal filter [84], or a generalized matched filter to suppress noise effects [85]. These methods also give an least-square estimate for the pulse height.

For larger photon energies however, the pulse shape is altered and the information on the photon energy is contained in the first part of the pulse ($t \lesssim \tau_{\text{qp}}^*$). This effect is due to self-recombination of excess quasiparticles: the excess quasiparticles are more likely to recombine with each other than with thermal quasiparticles. This can be mitigated by either increasing the absorption volume (thereby decreasing $\delta n_{\text{qp}}(0)$, Fig. 2.17(a)) or increasing the bath temperature (thereby increasing n_{qp}^T and decreasing τ_{qp}^* , Fig. 2.17(b)).

Equation (2.73) can be used to model the single photon response of MKIDs. It can be multiplied with the quasiparticle responsivities, Eq. (2.36), to obtain the response in $(\delta A, \theta)$. When the response is large in terms of the resonance circle, the coordinates (\mathcal{R}, X) from Eq. (2.39) must be used to ensure linearity with the quasiparticle density.

In addition, the response time of the resonator is set by the bandwidth,

$$\tau_{\text{res}} = \frac{1}{\pi \Delta f} = \frac{2Q}{\omega_0}, \quad (2.74)$$

meaning that for a high- Q resonator (highly responsive and multiplexable), the response time will be slow. For $Q = 50,000$ and $\omega_0 = 2\pi \cdot 5$ GHz, this is $\tau_{\text{res}} \approx 3.2 \mu\text{s}$.

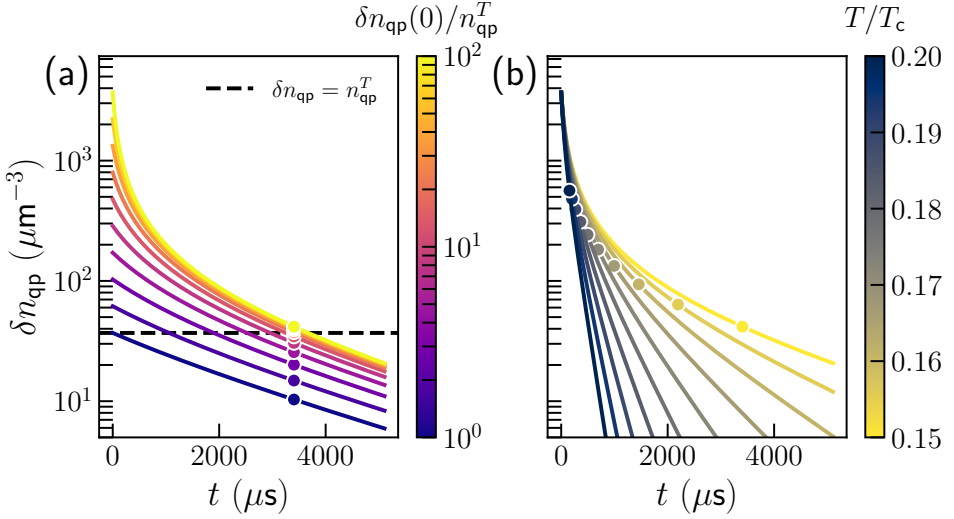


Figure 2.17: Single photon response for various photon energies (a) and bath temperatures (b) from Eq. (2.73). The dots indicate the quasiparticle lifetime, τ_{qp}^* , after which the decay is approximately exponential. The two upper curves (yellow) are the same for (a) and (b). These curves correspond to an excess quasiparticle density created by a 108 nm photon, absorbed in a $10 \mu\text{m}^3$ superconducting volume, with $R = 8 \mu\text{m}^3/\mu\text{s}$, $\Delta = 1.76k_{\text{B}} \times 1.2 \text{ K}$ and at a bath temperature of $T/T_c = 0.15$.

To take this into account, Eq. (2.73) must be convoluted with $e^{-t/\tau_{\text{res}}}/\tau_{\text{res}}$, such that the pulses acquire a rise time of τ_{res} . When the quasiparticle decay is faster than τ_{res} , for example, due to the initial $1/t$ -behavior, the decay is limited to $e^{-t/\tau_{\text{res}}}$.

In Eq. (2.72) we assumed that the excitation causes an increased quasiparticle density that is uniform over the volume V . This is correct when the spatial spread of the excess quasiparticles over the absorption volume is faster than the decay rate. The excess quasiparticles created by the photon diffuse in a BCS superconductor with a diffusion constant given by [86–88],

$$D_{\text{qp}}(\epsilon) = D \sqrt{1 - \left(\frac{\Delta}{\epsilon}\right)^2}, \quad (2.75)$$

where D is the electronic diffusion constant in the normal state (see Section 2.1.1). So, a quasiparticle at the gap edge ($\epsilon = \Delta$), does not diffuse. This is a direct consequence of the dispersion relation of quasiparticles: at $\epsilon = \Delta$ their momentum is zero. The ensemble average diffusion constant in thermal equilibrium ($f(\epsilon) = f_{\text{FD}}(\epsilon)$) and at low temperatures ($k_{\text{B}}T \ll \Delta$) is given by,

$$D_{\text{qp}} = D \sqrt{\frac{2k_{\text{B}}T}{\pi\Delta}}. \quad (2.76)$$

This can be added to the Rothwarf-Taylor equations by making the quasiparticle

density position-dependent ($n_{\text{qp}}(t) \rightarrow n_{\text{qp}}(\mathbf{r}, t)$) and adding a diffusion term: $\nabla \cdot (D_{\text{qp}}(\mathbf{r}) \nabla n_{\text{qp}}(\mathbf{r}, t))$ [89]. We take the diffusion constant to be position-dependent as well, since the effective quasiparticle temperature is dependent on the excess quasiparticle density for large excitations.

A simple estimate of this effect can be found by calculating the time that it takes to diffuse over the full absorber length. For example, a $l = 100 \mu\text{m}$ long Al absorber, with $D = 200 \text{ cm}^2/\text{s}$ and at $T/T_c = 0.1$, takes $t_D = l^2/(2D_{\text{qp}}) = 1.3 \mu\text{s}$. This is much shorter than the typical recombination time at low temperatures, $\tau_{\text{qp}}^* \sim 1 \text{ ms}$ and this effect can mostly be disregarded. For a disordered superconductor, however, diffusion is much slower, since $D \propto 1/\rho_N$. For example, for a β -Ta absorber with $D = 0.75 \text{ cm}^2/\text{s}$, this takes $350 \mu\text{s}$, which is larger than the typical quasiparticle lifetime in β -Ta, $\tau_{\text{qp}}^* \sim 100 \mu\text{s}$. We will come back to the importance of quasiparticle diffusion in disordered superconductors in Chapter 7.

Downconversion of photon energy to quasiparticles Another assumption that we made when writing down Eq. (2.72) is that the photon is instantly converted into quasiparticles with an efficiency η_{pb} . This is a rather crude simplification of the downconversion process from single photon to numerous quasiparticles, especially for a high-energy photon with $\hbar\omega_{\text{rad}} \gg \Delta$. Crucially, this simplification leads to an equal number of excess quasiparticles for each photon with energy $\hbar\omega_{\text{rad}}$. This is contradictory with experimental data, which shows that the pulse height varies for each photon, even though the photon energies are equal (for example, when using a laser source).

To understand this, we have to include the complex dynamics of downconversion. This is intrinsically a non-equilibrium problem, meaning we cannot take $f(\epsilon) = f_{\text{FD}}(\epsilon)$ in this case. When a photon is absorbed in a metal, it will transfer all its energy to a single photo-electron. Then, an energy- and position-dependent interplay between phonons and electrons takes place, collectively called downconversion. This is described in detail in Refs. [74, 78, 91]. Here, we will briefly go over the different stages of downconversion to get an idea of the underlying physics.

After initial creation of an electron-hole pair, three stages can be identified. After these three stages, quasiparticle recombination will dominate the decay, as described by the Rothwarf-Taylor equations Eq. (2.49). The different stages are sketched in Fig. 2.18. Each stage is characterized by a dominant process. At high energies, electron-electron interaction dominates and many more electron-hole pairs are created. These emit phonons, mostly at the Debye energy, $\hbar\Omega_D$. When the typical electron energy is E^* , the phonon emission becomes dominant and the electron-hole pairs are converted into phonons (electron-phonon phase). At this point, the excitation consists phonons with energies close to $\hbar\Omega_D$, which is sometimes called the phonon bubble. These phonons break Cooper-pairs into quasiparticles¹¹, which becomes the dominant process at $\hbar\Omega_1$. At that point, all phonons are converted into quasiparticles (phonon-electron stage). The quasiparticles will relax

¹¹We call the excitation quasiparticles again, since their energy is relatively low. In principle, a very highly energetic quasiparticle is equal to an electron or hole excitation (depending on the direction of the momentum).

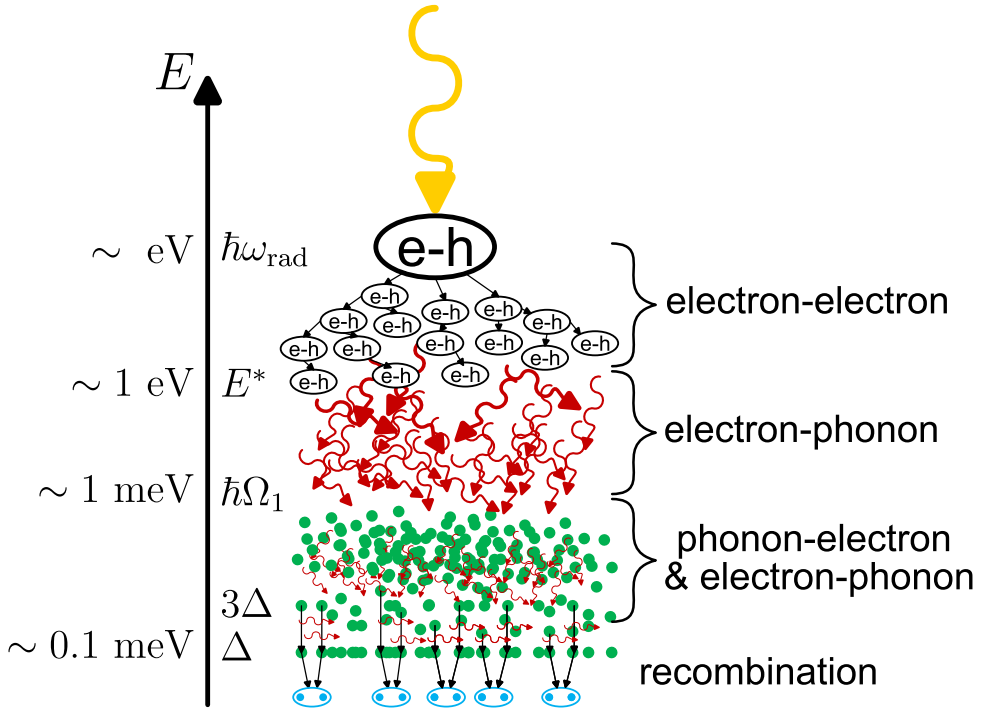


Figure 2.18: Schematic illustration of the downconversion process. The yellow curly arrow represents an incoming photon, which creates a single electron-hole pair (e-h). This decays to many other electron-hole pairs via electron-electron interaction. At the energy E^* , electron-phonon interaction becomes dominant, resulting in many phonons with a maximum energy of $\hbar\Omega_D$. These phonons decay via phonon-electron interaction (i.e. Cooper-pair breaking), which becomes dominant at an energy $\hbar\Omega_1$. At that point, many quasiparticles are created (green dots), until the quasiparticles have a typical energy of 3Δ . After that, the quasiparticles relax further to the gap energy via phonon emission and recombine into Cooper-pairs (paired blue dots). This drawing is a reproduction of Fig. 1 in Ref. [90].

via electron-electron and electron-phonon interactions. Below 3Δ , the quasiparticles cannot emit a phonon with enough energy to break a Cooper-pair. Therefore, when the typical quasiparticle energy is 3Δ , the final number of quasiparticles is reached. These quasiparticles relax further to the gap and recombine with emission of 2Δ phonons.

The duration of the downconversion process is limited by the last (lowest energetic) stage, which is on the order of nanoseconds to microseconds [78, 89]. Quasiparticle diffusion is much faster than phonon diffusion [78], so the width of the spatial distribution of quasiparticles after downconversion can be estimated from the diffusion constant (Eq. (2.75)) to be on the order of microns [78, 89].

With this downconversion picture in mind, we can qualitatively see that the conversion from photon energy to excess quasiparticles is not 1-to-1. Some of the

photon energy goes into phonons with an energy of less than 2Δ , which cannot break Cooper-pairs. The average quasiparticle efficiency turns out to be $\eta_{\text{pb}} = 0.59$ [78], which we discussed earlier in Section 2.3.2 and Fig. 2.15. More importantly for the present discussion: this process is a statistical: starting with the same photon energy, the final number of excess quasiparticles will vary. This variance can be expressed in a Fano factor, $F = \sigma_{\delta N_{\text{qp}}}^2 / \langle \delta N_{\text{qp}} \rangle$. For a BCS superconductor, $F \approx 0.2$ [35, 76, 77]¹². The fact that this is smaller than 1 indicates that the total loss of energy is not a collection of independent stochastic steps (which would result in $F = 1$, i.e. Poissonian noise). Later steps in the downconversion process depend on previous steps, as is also clear from Fig. 2.18. This Fano factor results in a Fano-limited resolving power [91, 92],

$$R_{\text{Fano}} = \frac{E_\gamma}{(\delta E_\gamma)_{\text{FWHM}}} = \frac{1}{2\sqrt{2\ln 2}} \frac{\langle \delta N_{\text{qp}} \rangle}{\sigma_{\delta N_{\text{qp}}}} = 0.425 \sqrt{\frac{\eta_{\text{pb}}^{\text{max}} \hbar \omega_{\text{rad}}}{\Delta F}}, \quad (2.77)$$

where $\eta_{\text{pb}}^{\text{max}} = 0.59$; i.e., the situation for a highly energetic photon when $\tau_{\text{esc}} \rightarrow \infty$. This gives the ultimate resolving power for a BCS superconducting (pair-breaking) single-photon detector. For a superconductor with $T_c = 1$ K this results in an $R = 66$ for a $1 \mu\text{m}$ photon. Improving the resolving power beyond this limit, while keeping T_c constant, would require strict and drastic changes in the phonon density of states or in the energy dependence of the electron-phonon coupling, which are hard to realize [35].

Additionally, the resolving power will be degraded by hot phonon loss. If one of the phonons with an energy $\Omega > 2\Delta$ escapes to the substrate, additional energy is lost. Phonon loss at the start of the downconversion will have a greater effect. This effect can be accounted for by an additional normalized variance, J , such that [90–92],

$$R_{F+J} = 0.425 \sqrt{\frac{\eta_{\text{pb}}^{\text{max}} \hbar \omega_{\text{rad}}}{\Delta(F(1 - \chi_a) + J)}}. \quad (2.78)$$

Here, χ_a is the fraction of the photon energy that escapes as athermal phonons [90]. The values J and $\eta_{\text{pb}} = \eta_{\text{pb}}^{\text{max}}(1 - \chi_a)$ depend on the phonon escape time τ_{esc} , which can be estimated from the framework presented in Appendix A. Placing the absorbing superconductor on a membrane [92] or on a material with a low Debye energy [93] reduces J and increases η_{pb} .

Other effects not related to the downconversion can be expressed in other resolving power contributions, such as the signal-to-noise ratio, R_{SN} [92], or statistical variations in location of photon absorption (both horizontal and vertical), which induce a varying phonon loss or deposition energy [91], R_{abs} . These resolving powers must be added in reciprocal squares to find the total resolving power: $1/R^2 = 1/R_{F+J}^2 + 1/R_{\text{SN}}^2 + 1/R_{\text{abs}}^2 + \dots$, such that proper independent variances are summed. This makes it clear that it is very hard to reach the ultimate resolving power R_{Fano} .

¹²Note that the Fano factor has units of the distribution variable in general. In this case, it is expressed in quasiparticle number, which is unitless.

2.3.3 SUBGAP PHOTONS: EFFECTS OF THE MICROWAVE PROBE

From the above description of superconducting resonators, we expect no effect of subgap photons ($\hbar\omega_{\text{rad}} < 2\Delta$). These photons cannot break Cooper-pairs and therefore are not expected to create quasiparticles and change the resonance frequency or quality factor. However, experiments show that changing the microwave probe power (with typical frequency of $\hbar\omega_{\text{rad}} \approx \Delta/10$) do change the resonator properties. For example, Ref. [60] shows that increasing P_{read} , results in an increased excess quasiparticle density at low temperatures. They find that $n_{\text{qp}}^{\text{ex}} \propto \sqrt{P_{\text{abs}}}$. Conversely, at high temperatures, an increase in superconductivity (T_c , critical current and Δ) is observed at an increasing microwave power [94–96]. Additionally, Refs. [33, 97] show that an increased readout power can also result in a shift in resonance frequency. This shift is dependent on the detuning of the probe frequency with respect to the resonance frequency, which can eventually lead to bifurcation: a bistable state of the resonator.

To understand and predict these observations, we must consider the effect of the microwave probe on the superconductor. This effect is twofold: (1) quasiparticles absorb microwave photons (electron-photon interaction) and gain energy and; (2) the Cooper-pair condensate is accelerated by the AC field. The first mechanism can cause a non-equilibrium distribution of quasiparticles ($f(\epsilon) \neq f_{\text{FD}}(\epsilon)$). The second mechanism results in an adjusted density of states ($N_s(\epsilon) \neq N_s^{\text{BCS}}(\epsilon)$, with $N_s^{\text{BCS}}(\epsilon)$ given by Eq. (2.16)).

QUASIPARTICLE REDISTRIBUTION

To find the non-equilibrium distribution functions of quasiparticles, $f(\epsilon)$, and phonons, $n(\hbar\Omega)$, a (semi-classical) Boltzmann equation approach can be used [99]. The effect of the microwave photons in the resonator can be accounted for by the transition rate given in Refs. [100, 101]. Together with the inelastic relaxation rate for quasiparticles (Eq. (2.43)) and phonons (Eq. (2.46)), this results in the kinetic equations [102]. The structure of these equations is the same as the Rothwarf-Taylor equations (Eq. (2.49)), but is fully energy dependent and includes all electron-phonon and electron-photon inelastic transitions.

These equations can be solved numerically [98] or, in some limits, analytically [103, 104]. The result is sketched in Fig. 2.19. From panel (b), we see that the quasiparticles are pushed away from the gap to higher energies, compared to a Fermi-Dirac distribution. This effect results in two regimes. For high bath temperatures, many quasiparticles are present and main effect is an increase of the average quasiparticle energy. Since the density of states is lower at higher energies, away from the gap, this results in a decrease of microwave loss (see Fig. 2.3). When the temperature is close to T_c and the microwave power is high, this effect results in a measurable enhancement of superconductivity (critical current, critical temperature and gap enhancement). At low bath temperatures, the initial quasiparticle density is low and the dominating effect is the pair-breaking by quasiparticles with an energy $\epsilon > 3\Delta$. These quasiparticles can emit a phonon with $\hbar\Omega > 2\Delta$, which can subsequently break a Cooper-pair and increase the quasiparticle density. This results in an increase of microwave loss. These two regimes are predicted numerically in Ref. [98] and

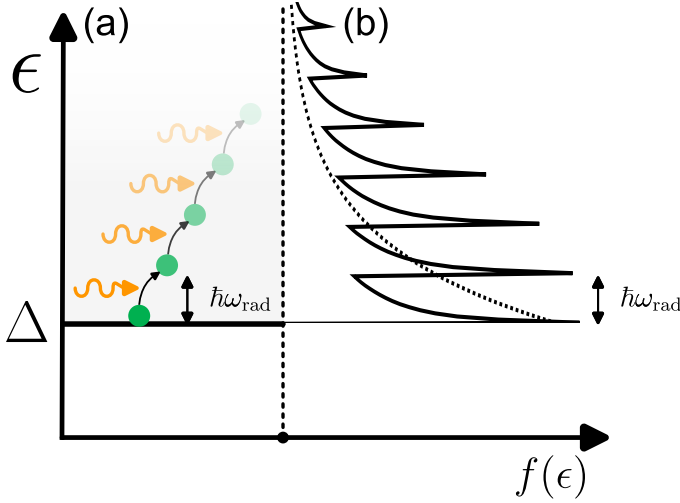


Figure 2.19: Illustration of quasiparticle redistribution due to the microwave probe power. (a): The orange curly arrows represent microwave photons. The quasiparticles (green dots) can absorb these photons and gain an energy $\hbar\omega_{\text{rad}}$. When the inelastic scattering rate is smaller than the photon absorption rate, this results in a non-equilibrium distribution. (b): Sketch of the non-equilibrium quasiparticle distribution function due to microwave photon absorption. The dotted line shows a Fermi-Dirac distribution for comparison (Eq. (2.1)). The curves are copied from Ref. [98], where the $f(\epsilon)$ -axis is multiplied by 10^3 for visibility.

observed in Ref. [105] via a decrease in Q_i at low temperatures and an increase in Q_i at high temperatures when increasing the microwave readout power.

The cross-over temperature between these two regimes has analytically been calculated in Ref. [103] as $(k_B T_*)^3 / (k_B \Delta^2)$ with,

$$\frac{k_B T_*}{\Delta} = \left(\frac{105\pi}{64} \left(\frac{k_B T_c}{\Delta} \right)^3 \frac{\hbar\tau_0}{\Delta^2} c_{\text{phot}}^{\text{qp}} P_{\text{int}} \right)^{1/6}. \quad (2.79)$$

$k_B T_*$ describes the width of the distribution function (see Fig. 2.19(b)) and $c_{\text{phot}}^{\text{qp}}$ describes the quasiparticle-photon interaction strength. This can be derived as the ratio between the photon absorption and the normalized power dissipation by quasiparticles in the resonator,

$$c_{\text{phot}}^{\text{qp}} = \frac{P_{\text{abs}}^{\text{qp}}}{\pi P_{\text{int}}} \frac{\sigma_N / \sigma_1}{2\hbar N_0 V} = \frac{1}{Q_i^{\text{qp}}} \frac{\sigma_N / \sigma_1}{2\hbar N_0 V} \approx \frac{\alpha_k \omega_0}{2\pi N_0 V \Delta}. \quad (2.80)$$

For high photon numbers, $\langle n_{\text{phot}} \rangle \gg 1$ and at low temperatures, $k_B T \ll \Delta$, this expression is equal to the photon-quasiparticle interaction rate originally put forward by Eliashberg [101, 106],

$$\alpha_\omega = \frac{e^2 D A_0^2}{4\hbar} = \langle n_{\text{phot}} \rangle c_{\text{phot}}^{\text{qp}}, \quad (2.81)$$

with A_0 the microwave field strength. Ref. [103] also gives analytical expressions for the internal quality factor, Q_i , and excess quasiparticle density, $n_{\text{qp}}^{\text{ex}}$, in the two regimes. In Chapter 5, we will compare these expressions to experimental data. We will show that the excess quasiparticle density at low temperatures scales with the absorbed power density, $n_{\text{qp}}^{\text{ex}} \propto \sqrt{P_{\text{abs}}/V}$. However, a comparison with the expressions for Q_i and $n_{\text{qp}}^{\text{ex}}$ from Ref. [103] shows that the mechanism that causes $n_{\text{qp}}^{\text{ex}}$ is not direct photon absorption, but an unknown indirect mechanism.

DENSITY OF STATES EFFECTS

Refs. [103, 105] both show that the decrease in resonance frequency with increasing microwave probe power cannot be explained by the excess quasiparticles at low temperatures. The decrease in ω_0 is larger than one would expect from Eq. (2.33), with σ from the solution of the kinetic equations. That is because there is also an inductive, depairing, effect of the microwave drive: the Cooper-pairs are accelerated by the alternating field. This changes the density of states, as is shown in Fig. 2.20. This change in density of state has to be included in the Mattis-Bardeen equations (Eq. (2.20)), which can be done using the generalization by Nam [108–110]. This results in an increased kinetic inductance due to AC current. To first non-zero order [106],

$$L_k(j_0) = L_k(0) \left(1 + 0.069 \left(\frac{j_0}{j_c} \right)^2 \right). \quad (2.82)$$

Here, j_0 is the maximum current density in the wire (which is assumed to be uniform) and j_c is the critical current density, which is given by [111–113],

$$j_c = 0.59 \sqrt{\frac{\pi \Delta^3 N_0}{\hbar \rho_N}}. \quad (2.83)$$

Equation (2.82) coincides with the DC current non-linearity in L_k , with $j_0 \rightarrow \sqrt{2} j_{\text{DC}}$. This is because it is assumed that $\langle n_{\text{phot}} \rangle \ll 2\pi N_0 \Delta V / \alpha_k$ and $k_B T \ll \Delta$, which means that the number of photons must be much lower than the number of Cooper-pairs. Therefore, the effect of each photon averages out over the whole Cooper-pair condensate and only the average kinetic energy of the condensate matters, just as in the DC case [106].

The increased kinetic inductance, leads to a lower resonance frequency as, $\omega_0 \propto 1/\sqrt{L_k}$. This is in addition to any pair-breaking effect due to quasiparticle redistribution. The relative effect can be estimated to be,

$$\frac{\delta\omega|_{L_k}}{\delta\omega|_{\text{qp}}} = 21 \frac{\bar{R} N_0}{\eta_{2\Delta}} \sqrt{\frac{\hbar\Delta}{\omega_0}}, \quad (2.84)$$

as we will show in Section 5.B. Here, $\bar{R} = R/(1 + \tau_{\text{esc}}/\tau_{\text{pb}})$ and $\eta_{2\Delta}$ is quasiparticle generation efficiency of the absorbed microwave power in the resonator (Eq. (2.31)). This is experimentally found to be $\eta_{2\Delta} \sim 10^{-4}$ in Chapter 5, consistent with Ref. [60]. The current in the resonator depends on detuning away from resonance, $j^2 \propto 1/(1 + (Qx)^2)$, with $x = (\omega - \omega_0)/\omega_0$ [97]. Therefore, there exists a read power

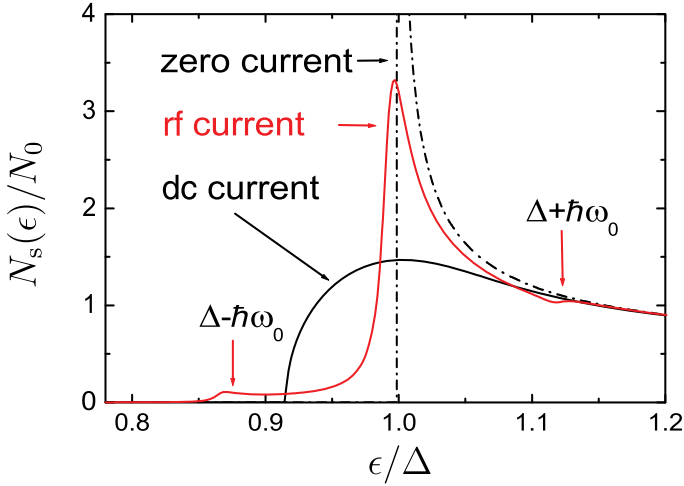


Figure 2.20: The change of the density of states under a microwave drive (rf current). This is compared with zero current (i.e., BCS density of states from Fig. 2.3(a)) and a DC current. Although there is only one subgap peak shown here, there are multiple peaks at $\Delta - n\hbar\omega_0$ with n an integer, which are exponentially suppressed. Figure from Ref. [107].

and frequency range where the resonator becomes bistable, and the transmission depends on the direction of the frequency sweep (hysteresis). This is called bifurcation. In Section 5.B we will derive that this happens for a quarter-wave resonator, with a uniform current in its inductive section (e.g. Fig. 2.11), at,

$$P_{\text{read}}^{\text{bif}} \approx N_0 \Delta^2 \frac{V \omega_0 Q_c}{\alpha_k^2 Q^3}. \quad (2.85)$$

These two non-linearities (quasiparticle redistribution and the effect on the density of states) can be exploited to increase the responsivity to radiation. When slightly negatively detuned and at a large read power (close to $P_{\text{read}}^{\text{bif}}$), a photon absorption will increase the current in resonator. The kinetic inductance effect will amplify this response [97], akin to a parametric amplifier [114]. In addition, the redistribution of quasiparticles will amplify and slow down the recombination of quasiparticles [115–117].

2.4 DISORDERED SUPERCONDUCTORS

The term disorder relates to the structural form of the material. A disordered superconductor has an atomic lattice that differs in some way from the lowest energetic crystalline structure. For example, Fig. 2.21 shows the crystalline, body-centered cubic α -phase of Ta and the disordered β -phase of Ta. In this case, disorder is induced by the deposition of Ta in a meta-stable, higher energetic phase. When depositing Ta at room temperature on a Si or c-Sapphire wafer, the β -Ta forms due to a lattice mismatch between the substrate and the α -phase. Depositing on a

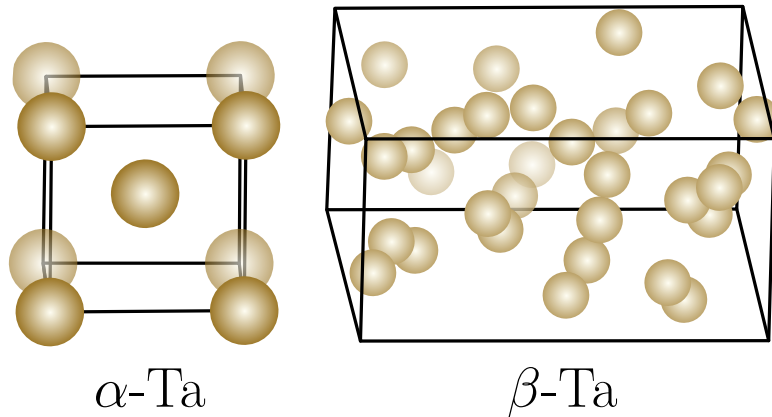


Figure 2.21: Example of structural disorder with a unit cell of Ta in the α -phase (left) and disordered β -phase (right). The β -phase is approximately 10 times more electrically resistive [39, 118]. Picture reproduced from Ref. [119].

heated substrate (400 °C [118]), or on a Nb seed layer [120] will result in the α -phase. Apart from a lattice mismatch, disorder can also be introduced by implanting ions (magnetic or non-magnetic) [121], changing sputtering gas concentrations to introduce impurities or lattice defects (e.g. TiN [122]) and reducing the film thickness [123, 124]. These are all examples of introducing homogeneous disorder. In this case, disorder is increased by increasing the unit cell size (see Fig. 2.21) to the point where the film is completely amorphous (e.g. amorphous InO [125]). Another type of disorder is granular disorder, where the metallic film consists of crystalline grains that are connected via insulating barriers. A famous example of this is granular Al (grAl), which consists of Al grains with amorphous Al-oxide boundaries [126]. In this case, disorder is increased by increasing the oxide content.

Experimentally, an increase in disorder is characterized by a (large) increase in resistivity. Disorder decreases the elastic scattering time of electrons, τ , and therefore decreases the mean free path of the electrons, l . Via Eq. (2.4), this results in a high normal state resistivity, which causes a high kinetic inductance in the superconducting state (Eq. (2.24)).

The fact that the superconducting state is not destroyed by the scattering of electrons can be explained by considering that a Cooper-pair consists of electrons with opposite spin ($s' = -s$, with $s = \pm 1/2$) and opposite momentum ($\mathbf{k}' = -\mathbf{k}$), see Fig. 2.2. An elastic scattering event of one electron changes its momentum to a random direction ($\mathbf{k} \rightarrow \mathbf{q}$, with $|\mathbf{q}| = |\mathbf{k}|$). Since the electron pairing in a BCS superconductor is not dependent on momentum direction ($V_{sc}^{\mathbf{k},\mathbf{k}'} = V_{sc}^{|\mathbf{k}'|=-|\mathbf{k}|}$), this scattered electron can pair with equal amplitude with another electron with momentum $-\mathbf{q}$. In the dirty limit, the electrons scatter many times in one coherence time of a Cooper-pair, $\tau \ll \hbar/\Delta$, which randomizes the electron momenta. Therefore, each momentum direction is present equally (the Fermi surface is isotropic) and scattering does not

change the total pairing amplitude, Δ ¹³. To first order, the superconducting state is therefore not altered by an increase of normal state resistance. This is known as Anderson's theorem [127].

When the scatterers not only change the momentum of the electron, but also spin, the pairing does change upon scattering. This explains why increasing the paramagnetic impurity concentration does reduce the pairing amplitude all the way to zero [128]. This is described by Abrikosov and Gor'kov [129], and leads to a gapless superconductor in an intermediate regime [130]. For weak magnetic scattering, an impurity band of bound (Yu-Shiba-Rusinov [131–133]) states forms in the density of states [134].

To quantify the qualitative effects of disorder, the mean free path, l , must be compared with other length scales. For example, we have already seen that we can compare l with ξ_0 to define a clean ($\xi_0/l \ll 1$) and a dirty ($\xi_0/l \gg 1$) superconductor. As we saw in Section 2.1.2, this results in a reduced coherence length¹⁴, $\xi_{DL} = \sqrt{\xi_0 l}$ and increased penetration depth, $\lambda_{eff} = \lambda_L \sqrt{\xi_0/l}$. A superconductor in the dirty limit is generally not called disordered, since the superconducting properties can still be described by BCS.

Anderson's theorem is valid for dirty superconductors, as long as l does not become shorter than the electron and phonon length scales. As we will see below, we can characterize disorder with respect to the electron-phonon interaction by comparing l to the phonon wavenumber, q . Electronic disorder is characterized by comparing l to the Fermi wavenumber, k_F , which results in the Ioffe-Regel parameter $k_F l$. This changes the electron-electron interaction, as we will discuss after the electron-phonon interaction.

ELECTRON-PHONON INTERACTION

For the electron-phonon interaction, l is to be compared with the phonon wavenumber, $q = 2\pi/\lambda_{ph} = \Omega/c_s$, with λ_{ph} the phonon wave length, Ω its angular frequency and c_s the sound velocity (either longitudinal, c_L or transverse, c_T). When $ql \ll 1$, the metal is in the impure limit, and when $ql \gg 1$, it is in the pure limit. Equations (2.43) and (2.46) give the electron-phonon and phonon-electron scattering rates in the pure limit, respectively. In the impure limit, the electrons scatter on a smaller length scale than the wavelength of a phonon. In that case, the electron-phonon interaction is weakened. Both the rates for phonons scattering on electrons (phonon-electron) [135] and electrons scattering on phonons (electron-phonon) [136] are reduced. Specifically, the longitudinal and transverse

¹³In clean metals, the electron momenta are not randomized and the Fermi surface is anisotropic, in general. Therefore, the anisotropic part of the pairing amplitude can be reduced by scattering.

¹⁴We here use the BCS coherence length, ξ_0 , instead of Pippards phenomenological estimate ξ_p from Section 2.1.2.

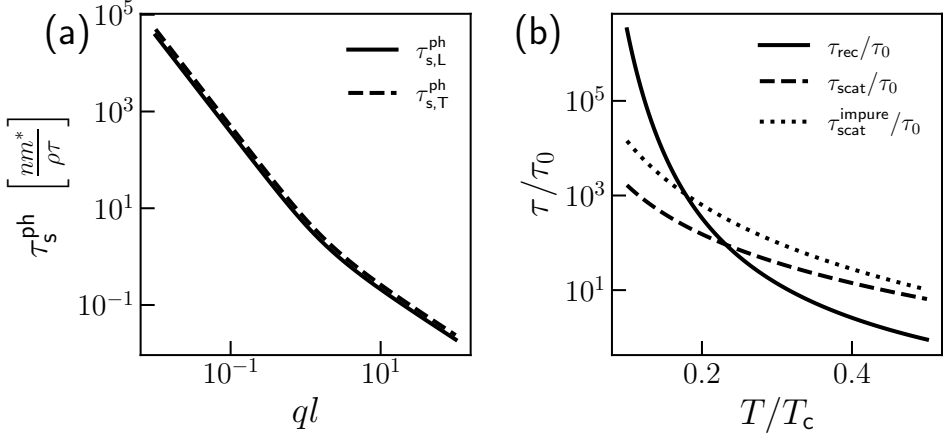


Figure 2.22: Effect of disorder on electron-phonon interaction. **(a):** Phonon scattering times from Eq. (2.86a) as a function of ql , the phonon wavenumber times the electronic mean free path. This parameter describes the amount of disorder in the electron-phonon interaction. $ql \gg 1$ is the pure and $ql \ll 1$ is the impure limit. **(b):** Quasiparticle recombination and scattering times versus temperature. The solid and dashed lines are from Ref. [61] for the pure limit (Eq. (2.45)). The dotted line is the scattering time in the impure limit (Eq. (2.88b)). The resistivity used in the calculation of the impure scattering time is set to the value where the pure and impure the recombination time are equal (i.e., Eq. (2.88a) is equal to Eq. (2.43a)).

phonon-electron scattering rates are [135, 137],

$$\frac{1}{\tau_{s,L}^{\text{ph}}(q_L l)} = \frac{nm^*}{\hat{\rho}\tau} \left(\frac{(q_L l)^2 \tan^{-1}(q_L l)}{3(q_L l - \tan^{-1}(q_L l))} - 1 \right), \quad (2.86a)$$

$$\frac{1}{\tau_{s,T}^{\text{ph}}(q_T l)} = \frac{nm^*}{\hat{\rho}\tau} \left(\frac{1}{\zeta} - 1 \right), \quad (2.86b)$$

$$\text{with } \zeta = \frac{3((1 + (q_T l)^2) \tan^{-1}(q_T l) - q_T l)}{2(q_T l)^3}.$$

Here, $\hat{\rho}$ is the mass density (kg/m^3). The functions in parentheses are plotted in Fig. 2.22(a). For $ql \gg 1$ we see that these functions are proportional to ql , such that $1/\tau_s^{\text{ph}} \approx qnm^* v_F / \hat{\rho}$, which is not dependent on l . However, in the opposite regime, $ql \ll 1$, the factors in parentheses are proportional to $(ql)^2$, which increases the scattering times linearly with decreasing l . Therefore, increasing disorder in the impure limit, will weaken the electron-phonon interaction.

The electron-phonon scattering rates in a normal metal follow the same behavior, since $C_e/\tau_s = C_{\text{ph}}/\tau_s^{\text{ph}}$, where C_e is the electronic heat capacity and C_{ph} is the phononic heat capacity [136]. When taking also static scatterers into account (such

as grain boundaries), the electron-phonon inelastic scattering rate is [69, 138],

$$\frac{1}{\tau_s(T)} = \frac{\pi^4 \beta_L (k_F l) (k_B T)^4}{5 \hbar^4 (k_F c_L)^3} \left(1 + k \frac{3}{2} \left(\frac{c_L}{c_T} \right)^5 \right) + \frac{3\pi^3 \beta_L (k_B T)^2}{2 \hbar^2 (k_F l) (k_F c_L)} (1 - k) \left(1 + 2k \left(\frac{c_L}{c_T} \right)^3 \right), \quad (2.87)$$

with

$$\beta_L = \left(\frac{2\epsilon_F}{3} \right)^2 \frac{N_0}{2\hat{\rho}c_L^2},$$

which describes the electron-phonon coupling with longitudinal phonons. k describes the contribution of vibrating scatterers, with $k = 1$ for completely vibrating scatterers and $k = 0$ completely static scatterers. Hence, the first term in Eq. (2.87) describes scattering on vibrating scatterers and the second term on static scatterers. Scattering with longitudinal phonons is described the first term in the parentheses, which results in two terms of $\tau_s(c_L)$, and transverse phonon scattering is described by the second term in the parentheses, which results in two terms of $\tau_s(c_T)$. Only vibrating scatterers contribute to transverse phonon scattering, as can be seen from the proportionality to k in the second terms in parentheses. When only vibrating scatterers are considered ($k = 1$), the term $k_F l$ in the numerator of the first term shows that increasing disorder (decreasing $k_F l$) causes the scattering time to increase. Static scatterers can drastically change the low temperature behavior and disorder dependence of τ_s : when $k < 1$, the low temperature behavior changes from T^4 to T^2 and an increase of disorder (decrease of $k_F l$) causes a decrease of the scattering time, instead of an increase [69].

In Chapter 6 we will use Eq. (2.86a) to estimate the phonon pair-breaking rate τ_0^{ph} and Eq. (2.87) to estimate the characteristic electron-phonon scattering time τ_0 in β -Ta and TiN.

For superconductors, the scattering and recombination times are proportional to the interaction times in the normal state. Therefore, the scattering and recombination times are also increased in an impure superconductor [136]. Furthermore, the scattering time acquires a steeper temperature dependence ($T^{-9/2}$ instead of $T^{-7/2}$ from Eq. (2.43b)). This results in slightly different expressions for the recombination and scattering times for a quasiparticle at Δ , with $k_B T \ll \Delta$ [136],

$$\tau_{\text{rec}}^{\text{impure}}(\Delta; T) = \frac{\tau_s(T_c)}{4\pi^{5/2}} \left(\frac{k_B T_c}{2\Delta_0} \right)^{7/2} \sqrt{\frac{T_c}{T}} e^{\Delta_0/k_B T}, \quad (2.88a)$$

$$\tau_{\text{scat}}^{\text{impure}}(\Delta; T) = \frac{\tau_s(T_c)}{4\pi^2 \Gamma(9/2) \zeta(9/2)} \sqrt{\frac{2\Delta_0}{k_B T_c}} \left(\frac{T_c}{T} \right)^{9/2}. \quad (2.88b)$$

Figure 2.22(b) shows a comparison between the scattering time in the pure (Eq. (2.45b)) and the impure limit. In the impure limit, scattering is slower for lower temperatures (dotted line is above the dashed line), due to the different temperature dependence. For this comparison, we have chosen the resistivity such that the pre-factor in Eq. (2.88a) equals the one in Eq. (2.45a). In that case, $\tau_{\text{rec}}^{\text{impure}} = \tau_{\text{rec}}$.

Dimensionality Equation (2.88) is for the 3D limit. In general, the effective dimension of a diffusive electron system is reduced, if the motion is restricted by less than the diffusive coherence length in one direction. This diffusive coherence length is given by, $L_\phi = \sqrt{D \min\{\tau_\phi, \hbar/\delta\epsilon\}}$, where τ_ϕ is the phase breaking rate, given by the shortest inelastic relaxation time and $\delta\epsilon$ is the characteristic energy transfer [139, 140]. For superconducting quasiparticles, $\delta\epsilon = \Delta$, and $L_\phi = \sqrt{\hbar D/\Delta} = \xi_{DL} \sqrt{3/\pi}$. So, if the superconducting film has a thickness smaller than ξ_{DL} , $d \ll \xi_{DL}$, the electronic system is quasi-2D. Otherwise, the electronic system is 3D.

For phonons, the dimensionality is reduced if a direction is limited by more than the phonon wavelength. So, if $qd \ll 1$, the film is 2D and if $qd \gg 1$ the film is 3D. The phonon wavenumber depends on energy and phonon mode (transverse or longitudinal). The two relevant energy scales are $k_B T$ for scattering and 2Δ for recombination. In addition, the transverse phonons are usually slower than the longitudinal phonons ($c_T < c_L$), such that they dominate in the electron-phonon interaction. This can be seen from the fact that $(c_L/c_T)^5 \gg 1$ in Eq. (2.87), such that the transverse part dominates.

When the dimensionality in either the electron or phonon systems is reduced, the interaction strengths and temperature dependencies change. For example, for the electron-phonon interaction, the scattering time for impure superconductors changes from a $T^{-9/2}$ power law (Eq. (2.88b)) in 3D (when $q(k_B T)d > 1$) to a $T^{-7/2}$ power law [139] in 2D (when $q(k_B T)d < 1$). In this case, the phonon dimensionality determines the temperature dependence, while the electronic dimensionality determines the disorder dependence (i.e., the pre-factor in Eq. (2.88) or interaction strength). Ref. [139] gives the impure and pure limit repressions for the electron-phonon relaxation times in a superconductor in the 2D limit.

ELECTRON-ELECTRON INTERACTION

To quantify electronic disorder (i.e., how much the electronic behavior is changed due to the elastic scattering), we compare l to the electronic wave length $\lambda_F = 2\pi/k_F$. The parameter $k_F l$ is called the Ioffe-Regel parameter [141] and superconductors with $k_F l \lesssim 10$ are typically called disordered superconductors. This is equivalent to a resistivity of $\rho_N = 3\pi^2 \hbar / (e^2 k_F (k_F l)) \gtrsim 100 \mu\Omega\text{cm}$, where $k_F \approx 2\pi/5 \text{ \AA}^{-1}$, which is approximately correct for most metals [18].

In this strong impurity scattering regime electron-electron interaction is enhanced [140, 142], due to the diffusive motion of electrons. Diffusive motion does not conserve momentum and therefore allows more electron-electron interactions where electrons stay closer together [142, 143]. Besides that, the charge density (n) usually decreases with increasing disorder, which weakens the screening of Coulomb interaction and therefore enhances electron-electron interaction [1].

In disordered superconductors, the electron-electron inelastic scattering time is enhanced compared to Eq. (2.47) due to the diffusive motion of electrons. In 3D

($d \gg \xi_{DL}$), the recombination and scattering rates are given by [144],

$$\tau_{\text{rec}}^{\text{e-e}} = \frac{(\hbar\sqrt{2})^{5/2} (2\pi)^2 N_0 D}{k_B T} \sqrt{\frac{D}{\Delta_0}} \frac{e^{2\Delta_0/(k_B T)}}{(1 + (V_{\text{sc}} N_0)^2)}, \quad (2.89a)$$

$$\tau_{\text{scat}}^{\text{e-e}} = \frac{(\hbar\pi)^{5/2} N_0 D}{6\Delta_0} \sqrt{\frac{D}{k_B T}} e^{4\Delta_0/(5k_B T)}. \quad (2.89b)$$

2

A comparison with Eq. (2.47) shows that the temperature dependence of the recombination time is the same for recombination in a clean 3D superconductor. The scattering time acquires an additional factor $e^{-\Delta/(5k_B T)}$ in the disordered case, which is small for low temperatures. Thus, disorder decreases the quasiparticle-quasiparticle scattering time. The pre-factors in Eq. (2.89) are determined by the diffusion constant, D which reflects the diffusive electronic dynamics.

In quasi-2D, $d \ll \xi_{DL}$, the recombination time has a similar temperature and disorder dependence as Eq. (2.89a). The scattering time however, acquires a contribution from a gapless collective phase mode, with a power law temperature dependence of $T^{-7/2}$, due to the additional confinement by the reduced dimensionality. This phase mode dominates only in very disordered superconductors and at low temperatures ($k_F \xi_{DL} \lesssim 1$ and $k_B T \ll \Delta$) [144]. The superconducting films discussed in this thesis do not reach this level of disorder.

For the measurements presented in this thesis, the electron-phonon recombination time (Eq. (2.88a)) is the most important. As stated in Section 2.3, we are much more sensitive to changes in quasiparticle density (i.e., recombination) than to changes in the quasiparticle distribution function (i.e., scattering). Furthermore, when comparing the electron-electron and electron-phonon recombination times (Eq. (2.89a) and Eq. (2.88a)), the additional factor $e^{\Delta_0/(k_B T)}$ in Eq. (2.89a) results in a much longer electron-electron recombination time at low temperatures. Therefore, we expect to measure a quasiparticle relaxation time given by Eq. (2.88a) when using a disordered film as inductive section.

In Chapter 6, we will see however that for the disordered superconductor β -Ta, we measure a quasiparticle relaxation time given by the electron-phonon scattering time (Eq. (2.88b)), instead. We observe similar behavior for disordered TiN, which has been measured in Refs. [145, 146]. We explain this behavior in terms of disorder-induced inhomogeneities, as we will introduce now.

2.4.1 SUPPRESSION OF SUPERCONDUCTIVITY: PHASE TRANSITIONS

When the electronic mean free path becomes comparable to the electronic wavenumber, $k_F l \sim 1$, localization effects start to play a role. In this regime, electrons scatter on the length of their wavelength, which limits their mobility. When they fully localize this is called Anderson localization [147]. In combination with the increase of electron-electron interactions, electronic disorder can lead to a transition from a metallic state to an insulating state, which is called the Anderson-Mott transition [148]. A precursor of this can be observed as an increase in resistivity when lowering the temperature [149]. Close to this transition (i.e., $k_F l \sim 1$), quantum

interference effects start playing role: as the electronic wavelength is on the order of the scattering length, the phase is not random at each collision and the wave functions interfere. This results in numerous effects [143]. For example, the constructive interference of electron paths that return to their original position leads to less mobile electrons, which is called weak localization [150]. Another example is the fluctuation of the conductance between samples with a size smaller than the diffusion length of an electron over its phase coherence time, $L_\phi = \sqrt{D\tau_\phi}$ [151, 152]. The phase coherence time is given by the smallest inelastic relaxation time (either electron-electron or electron-phonon interaction), which is usually much longer than the elastic scattering time, τ . Therefore, L_ϕ can be large compared to l and the interference of the electronic wave functions can be extended over a large distance¹⁵. As the interference causes the wave functions to sum non-trivially, this results in universal conductance fluctuations, which are of the order $\Delta G \sim e^2/\hbar$. These fluctuations are of the same conductance scale as the Anderson transition (in 2D, the critical conductance is, $G_c = e^2/\hbar$), which shows that the Anderson transition does not occur at exactly $k_F l = 1$.

Remarkably, superconductivity can exist below the $k_F l = 1$ limit. This is because the coherence of Cooper-pairs extends over larger distances than l ($\xi_{DL} = \sqrt{\xi_0 l} > l$) [156]. Therefore, confined electrons can pair and form a coherent state with other, distant, pairs. This implies that for superconductors, there exists a Superconductor-to-Insulator Transition (SIT) [154]. When superconductivity is broken due to a reduction in coupling of the Cooper-pairs, the system goes from a superconducting states (with a globally coherent Cooper-pair condensate) to an insulating state, where electrons and Cooper-pairs are localized, without a globally coherent state. Indeed, a SIT has been observed in Bi where the disorder was tuned by layer thickness [157]. Moreover, there is strong experimental evidence for preformed Cooper-pairs (i.e., Cooper-pairs without superconductivity) [158, 159]. Recently, this transition has been shown to be a (discontinuous) first order quantum phase transition [155].

Breaking superconductivity via weakening of the phase coherent condensate is called the phase-driven or bosonic transition. The other scenario is breaking the pairing amplitude, i.e., $\Delta \rightarrow 0$. This is called the amplitude-driven or fermionic transition. These two scenarios are sketched in Fig. 2.23. In the fermionic scenario, the binding of the Cooper-pairs is weakened due to the increase of repulsive electron-electron interaction, until only single electrons are present. Thus, this results in a Superconductor-to-Metal Transition (SMT). When increasing electron-electron interaction further (due to disorder), the metal can become insulating via the Mott-Anderson transition. In the superconducting state, T_c decreases due to the reduction of Δ , which is described by Finkel'stein as [153, 160],

$$T_c = \frac{\hbar}{k_B} \left(\frac{\sqrt{g} - \sqrt{g_c} + \sqrt{\frac{g_c}{8\pi g}}}{\sqrt{g} + \sqrt{g_c} + \sqrt{\frac{g_c}{8\pi g}}} \right)^{\sqrt{\pi g l^2}}. \quad (2.90)$$

¹⁵These systems, where quantum effects work on macroscopic scales are called mesoscopic.

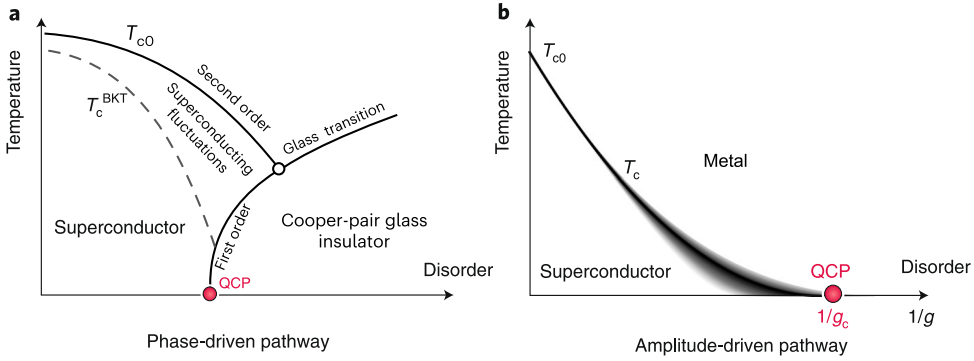


Figure 2.23: Diagrams illustrating the two pathways to break superconductivity. **(a)**: Disorder weakens the phase coherence of the Cooper-pair condensate which leads to a first order phase transition at the quantum critical point (QCP). This is the phase-driven or bosonic scenario. **(b)**: Disorder increases electron-electron interaction, which weakens the Cooper pairing amplitude and decreases T_c via the Finkel'stein mechanism [153]. This is the amplitude-driven, or fermionic scenario. In a superconductor both effects are present. Diagrams are from Ref. [154], with the addition in (a) from Ref. [155].

Here, $g = 2\pi\hbar/(e^2 R_{\square})$ is the conductance normalized to the conductance quantum, $g_c = \ln^2(\hbar/(k_B T_{c0}\tau))/(2\pi)$ is the critical conductance and T_{c0} is the original critical temperature, without reduction by disorder.

2.4.2 EMERGENT INHOMOGENEITIES OF THE SUPERCONDUCTING STATE

Additionally, the universal conductance fluctuations are enhanced due to the strong Coulomb interaction [163]. This gives rise to an inhomogeneous Cooper-pair potential in space, $V_{sc}(\mathbf{r})$ [161], which results in a varying pair-potential, $\Delta(\mathbf{r})$. The average effect of this on the density of states have been calculated by Larkin and Ovchinnikov [164] with use of the Usadel equations [165]. This is sketched in Fig. 2.24(a). Local gap inhomogeneities result in a broadening of the coherence peak, which is identical to the effect of time reversal symmetry breaking (by magnetic impurities, supercurrent or magnetic field) as described by Abrikosov and Gor'kov [129]. In addition, the gap energy is also broadened, which leads to a Lifshitz-type exponential tail in the density of states [164].

Locally, the density of states varies and the sketch in Fig. 2.24(a) is the space-averaged density of states. Local variations in the density of states have been measured in disordered TiN [162, 166] (see Fig. 2.24(b)), NbN [167, 168] and InO_x [158]. The local gap inhomogeneities can be linked directly to the Finkel'stein mechanism of superconductivity suppression [168]. I.e., the enhanced electron-electron interaction causes emergent electron granularity, which suppresses superconductivity locally. In Fig. 2.23(b), this is depicted as a broadening of the T_c curve. Ref. [161] shows that in quasi-2D, $d \ll \xi_{DL}$, the tail and coherence peak broadening in the zero temperature

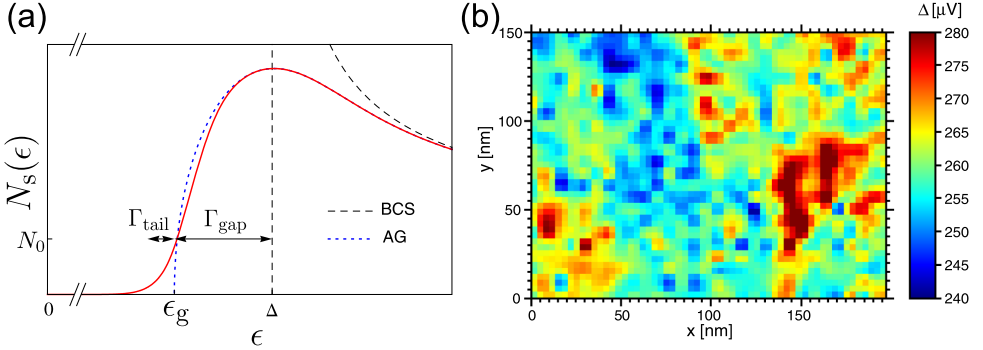


Figure 2.24: Effects of disorder on the global and local density of states. **(a)**: Global (i.e., space-averaged) density of states resulting from a varying Cooper-pair potential in space, $V_{sc}(\mathbf{r})$, which gives rise to a varying gap, $\Delta(\mathbf{r})$. This results in a broadening of the coherence peak (with Γ_{gap}) and a broadening of the energy gap, which leads to a Lifshitz-type exponential tail (with Γ_{tail}). BCS and Abrikosov-Gor'kov (AG) [129] density of states are shown for comparison. Figure from Ref. [161]. **(b)**: Measured local gap variations in TiN (with $k_F l \approx 1.7$, $T_C = 1.3$ K) by fitting the BCS density of states to a scattering tunneling spectroscopy image. Image from [162].

limit are given by,

$$\frac{\Gamma_{\text{tail}}}{\Delta} = \left(\frac{0.47}{g(g - g_c)} \right)^{2/3}, \quad \frac{\Gamma_{\text{gap}}}{\Gamma_{\text{tail}}} = \left(\ln \frac{\Delta}{\Gamma_{\text{tail}}} \right)^{2/3}. \quad (2.91)$$

These broadening parameters are dominated by Coulomb-induced fluctuations because of the additional confinement in quasi-2D [169]. In 3D, the universal conductance fluctuations (without Coulomb enhancement) contribute to additional broadening of the coherence peak [161, 169].

The local gap variations lead to localization of quasiparticles. Quasiparticles that relax to the gap edge, will end up in suppressed gap regions, where they become localized (blue areas in Fig. 2.24(b)). Specifically, the exponential tail in the density of states consists of localized quasiparticle states. Ref. [170] shows that the dynamics of these localized quasiparticles results in an extremely slow recombination when the quasiparticle density is below a critical density. This critical density is on the order of $n_{\text{qp}}^{\text{ex}} \sim 3/(4\pi\xi_{\text{DL}}^3)$; i.e., one quasiparticle per coherence volume.

In Chapter 6 we evaluate the broadening contributions for a β -Ta film to estimate the density of localized quasiparticle states. We modify the Rothwarf-Taylor equations (Eq. (2.49)) to include the recombination dynamics of localized [170] and mobile quasiparticles [66]. We find that in the high temperature regime, localized quasiparticles delocalize via phonon absorption and recombine fast within a localization site. This enhances the recombination rate to the phonon scattering rate (i.e., quasiparticle relaxation goes as Eq. (2.88b) instead of Eq. (2.88a)).

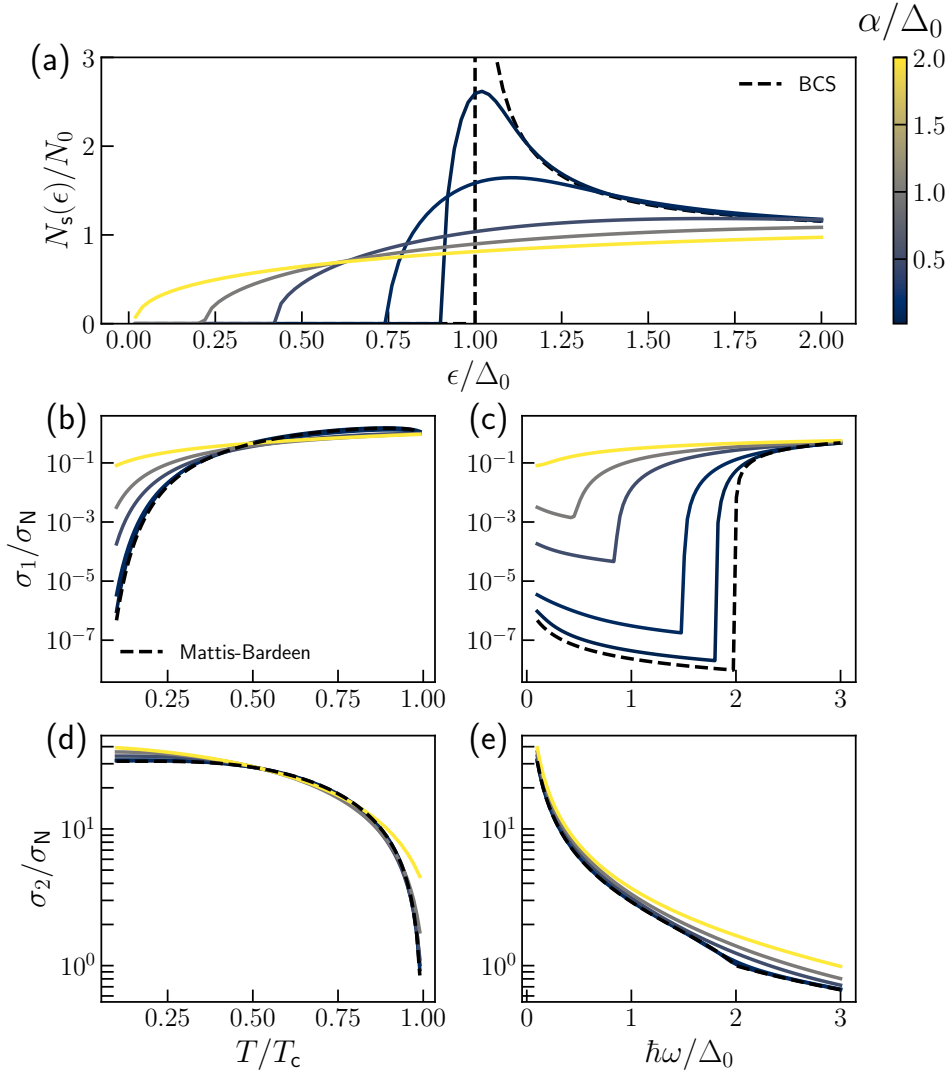


Figure 2.25: Effect of time-reversal symmetry breaking on the density of states and the complex conductivity. **(a)**: Density of states with different pair-breaking parameters, α , indicated by the color. $\Delta_0 = 1.76k_B T_c$ is the BCS order parameter when $\alpha = 0$. T_c is kept constant when varying α , by adjusting T_{c0} with Eq. (2.97). **(b)**: The real part of the complex conductivity versus temperature from Eq. (2.98a), with the pair-breaking parameters indicated by color as in panel (a). The frequency is set to $\hbar\omega = \Delta_0/10$. The dashed line is the Mattis-Bardeen result (Eq. (2.20a) with $\alpha = 0$). **(c)**: The real part of the complex conductivity versus frequency with $T = T_c/100$. **(d)** and **(e)**: same as (b) and (c), but for the imaginary part of the complex conductivity.

2.4.3 COMPLEX CONDUCTIVITY OF DISORDERED SUPERCONDUCTORS

The effect of disorder on the density of states (Fig. 2.24(a)) can also result in a different temperature and frequency dependence of the complex conductivity. That is, the Mattis-Bardeen equations (Eq. (2.20)), should be adjusted for the density of states in Fig. 2.24(a), instead of the BCS density of states.

A full description of the density of states of a disordered superconductor is not available yet. It is possible to numerically average over different inhomogeneous disorder realizations to obtain predictions for the density of states and complex conductivity. For example, Ref. [171] shows with numerical modeling that disorder induces three qualitative differences compared to the Mattis-Bardeen equations: (1) the gap energy is decreased, (2) collective modes can result in additional subgap contributions to the conductivity, and (3) the density of states acquires an additional energy dependence also present above T_c (where N_0 and σ_N are usually taken as a constant). See Fig. 2.26(b) for an illustration of these effects. To predict the effect of disorder on the complex conductivity quantitatively is difficult, since it requires a description of local inhomogeneities of the superconducting states [123].

The decrease of the gap energy (1) and associated effect of the gap broadening (Γ_{gap} in Fig. 2.24(a)) is however relatively simple to include, since this is homogeneous in space. To this end, we can add a pair-breaking term to the Usadel equations [165],

$$i\epsilon \sin\theta + \Delta \cos\theta - \alpha \sin\theta \cos\theta = 0, \quad (2.92)$$

where $\sin\theta$ and $\cos\theta$ are the $\theta(\epsilon)$ -parameterized anomalous and normal Green's functions in the dirty limit and α is the pair-breaking parameter. α describes a general mechanism that breaks time reversal symmetry. It is equivalent to the Abrikosov-Gor'kov model of scattering by magnetic impurities [129] with $\alpha = \hbar/\tau_{\text{ms}}$ (AG in Fig. 2.24(a)), where τ_{ms} is the magnetic scattering time [169, 172]. When we set, $\alpha = 2D(m^* v_s/\hbar)^2$, with v_s the superfluid velocity, it describes the effect of a supercurrent on the density of states [111, 113]. For Coulomb-enhanced conductance fluctuations in 3D with [161, 169],

$$\alpha = \Delta\eta_{3\text{D}} = \frac{2\Delta^2}{\pi^2\hbar D} \left(\frac{\rho_N}{R_Q}\right)^2 \ln\left(\frac{\xi}{l}\right), \quad (2.93)$$

where $R_Q = 2\pi\hbar/e^2 \approx 26 \text{ k}\Omega$ is the resistance quantum. In 2D, α is energy dependent [161]. The broadening parameters in that case are given by Eq. (2.91). By introducing α in Eq. (2.92), the gap energy changes from Δ to,

$$\epsilon_g = (1 - (\alpha/\Delta)^{2/3})^{3/2} \Delta. \quad (2.94)$$

Together with the self-consistency equation (Eq. (2.18) adjusted for the generalized density of states),

$$\Delta(T) = N_0 V_{\text{sc}} \int_0^{\hbar\Omega_D} (1 - 2f(\epsilon; T)) \text{Im}\{\sin\theta\} d\epsilon, \quad (2.95)$$

this gives $\Delta(T)$ and $\theta(\epsilon)$ for a given energy ϵ and temperature T . To solve Eq. (2.95), it is useful to go to the Matsubara representation: $\epsilon \rightarrow j\hbar\omega_n = (2n+1)j\pi k_B T$, with

$n = 0, 1, 2, \dots$. This way, the integral can be evaluated by summing over the pole residuals in $(1 - 2f(\epsilon))$. The self-consistency equation can then be expressed as [134, 173],

$$\Delta \ln \left(\frac{T_{c0}}{T} \right) = 2\pi k_B T \sum_{n=0}^{\infty} \left(\frac{\Delta}{\omega_n} - \sin \theta(\omega_n) \right), \quad (2.96)$$

where T_{c0} is the critical temperature without pair-breaker; i.e., when $\alpha \rightarrow 0$. T_c is reduced due to the pair-breaking, $T_c < T_{c0}$. By taking $\Delta \rightarrow 0$ in Eq. (2.96), we see [134],

$$\ln \left(\frac{T_{c0}}{T_c} \right) = \psi \left(\frac{1}{2} + \frac{\alpha}{2\pi k_B T_c} \right) - \psi \left(\frac{1}{2} \right) = 0. \quad (2.97)$$

Here, $\psi(x)$ is the digamma function. $\Delta(T)$ is obtained by iteratively solving Eqs. (2.92) and (2.96). Then, Eq. (2.92) is solved with the obtained $\Delta(T)$ to find $\theta(\epsilon)$.

With the Green's functions ($\sin \theta$ and $\cos \theta$) known, the density of states can be calculated as, $N_s(\epsilon) = N_0 \text{Re}(\cos \theta(\epsilon))$. This is shown in Fig. 2.25(a). With an increase in α , the density of states broadens and the gap energy is not Δ , but ϵ_g given by Eq. (2.94).

The complex conductivity can be calculated from the generalized Mattis-Bardeen equations (Eq. (2.20)), given by Nam [108–110],

$$\begin{aligned} \frac{\sigma_1}{\sigma_N} &= \frac{2}{\hbar\omega} \int_{\epsilon_g}^{\infty} |g_1(\epsilon, \epsilon + \hbar\omega)| (f(\epsilon) - f(\epsilon + \hbar\omega)) d\epsilon \\ &+ \frac{1}{\hbar\omega} \int_{\epsilon_g - \hbar\omega}^{-\epsilon_g} |g_1(\epsilon, \epsilon + \hbar\omega)| (1 - 2f(\epsilon + \hbar\omega)) d\epsilon, \end{aligned} \quad (2.98a)$$

$$\begin{aligned} \frac{\sigma_2}{\sigma_N} &= \frac{1}{\hbar\omega} \int_{\epsilon_g - \hbar\omega}^{\infty} |g_2(\epsilon, \epsilon + \hbar\omega)| (1 - 2f(\epsilon + \hbar\omega)) d\epsilon \\ &+ \frac{1}{\hbar\omega} \int_{\epsilon_g}^{\infty} |g_2(\epsilon + \hbar\omega, \epsilon)| (1 - 2f(\epsilon)) d\epsilon, \end{aligned} \quad (2.98b)$$

with the generalized coherence factors, g_1 and g_2 , given by,

$$\begin{aligned} g_1(\epsilon_1, \epsilon_2) &= \text{Re}\{\cos \theta(\epsilon_1)\} \text{Re}\{\cos \theta(\epsilon_2)\} \\ &+ \text{Re}\{-j \sin \theta(\epsilon_1)\} \text{Re}\{-j \sin \theta(\epsilon_2)\}, \end{aligned} \quad (2.99a)$$

$$\begin{aligned} g_2(\epsilon_1, \epsilon_2) &= -\text{Im}\{\cos \theta(\epsilon_1)\} \text{Re}\{\cos \theta(\epsilon_2)\} \\ &- \text{Im}\{-j \sin \theta(\epsilon_1)\} \text{Re}\{-j \sin \theta(\epsilon_2)\}. \end{aligned} \quad (2.99b)$$

These equations result in the complex conductivity given in Fig. 2.25(b), (c), (d) and (e)¹⁶. With the increase of α , the loss (σ_1) is increased at lower temperatures and has a weaker temperature dependence. The temperature dependence of σ_2 is slightly stronger at lower temperatures. This fact is used in Ref. [176] to fit α to the resonance

¹⁶A python code that solves the self-consistency (Eq. (2.96)), Usadel (Eq. (2.92)) and Nam equations for arbitrary parameters $\hbar\omega$, α , $k_B T$ is available at [175].

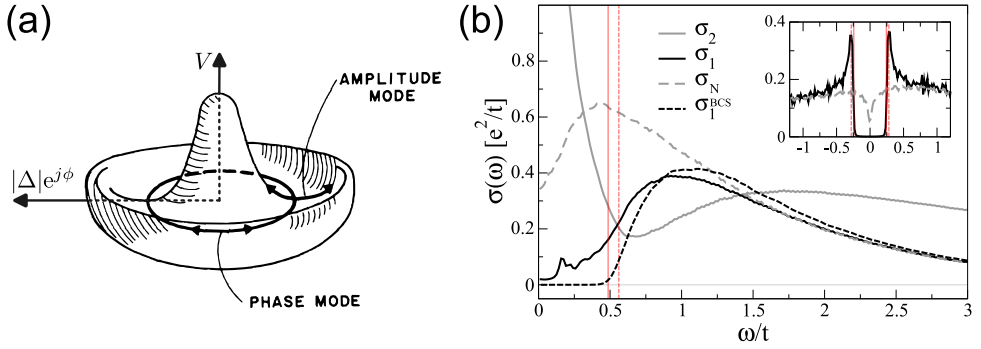


Figure 2.26: Collective modes of the superconducting state and the effects on the complex conductivity. (a): Sketch of the potential energy of the complex order parameter in the superconducting state as described by Ginzberg-Landau theory [7]. Picture from [174]. (b): Numerical study of the complex conductivity obtained from a Hubbard model with site potential energy varying from $-V_0$ to $+V_0$, with $V_0/t=1$, where t is the hopping parameter [171]. The on-site pairing energy is set to $U/t=2$. The solid black (σ_1) and gray (σ_2) lines include the effect of collective modes (the model is gauge-invariant) and a non-constant normal state conductivity (dashed gray line) due to disorder-enhanced electron-electron interaction [140] and a pseudogap [166]. The dashed black line gives σ_1 in the BCS approximation, which only includes quasiparticle excitations. The inset shows the corresponding density of states. The dashed gray line is for the normal state. The red solid line is the gap energy and the red dashed line is the position of the coherence peak. These are also shown in the main panel. Figure taken from Ref. [171].

frequency shift of resonators made from TiN with different degrees of disorder. They found that α is correlated with $k_F l$. The decrease of T_c in these films could be explained by a combination of the Finkel'stein mechanism of electron-electron interaction (Eq. (2.90)) and the pair-breaking parameter α (Eq. (2.97)).

The fitted α in Ref. [176] is, however, orders of magnitude larger than one would expect from the theory of Ref. [161]. Moreover, when measuring the tunneling spectra with Scanning Tunneling Spectroscopy (STS), the density of states was found to significantly differ from the predictions of Eq. (2.92). In particular, the coherence peaks were much more prominent in the spectra than one would expect from Eq. (2.92) at high α (see Fig. 2.25(a)). This means that a time reversal symmetry breaking parameter cannot fully explain the electro-dynamics of disordered superconductors.

COLLECTIVE MODES

One aspect that is not captured by the pair-breaking parameter α is the spatial inhomogeneities of the pairing potential (Fig. 2.24(b)). These inhomogeneities have also been measured with STS in the TiN film of Ref. [123]. Recently, it has been put forward that these inhomogeneities give rise to collective mode excitations of localized Cooper-pairs [177]. This results in a power-law temperature dependence of σ_2 at low temperatures, which has been measured in InO_x [177]. As alternative for

localized quasiparticles, collective modes could potentially be an explanation for the increased loss that is typically observed in disordered superconductors (Fig. 1.3(b)) [178, 179]. We observe a similar power law for the resonance frequency of our β -Ta resonators, which we present in Appendix B.

More generally, collective modes in superconductors are predicted to be more prominent in disordered superconductors [180]. The order parameter can fluctuate in two collective modes: the amplitude (or Higgs) mode, in which $|\Delta|$ fluctuates, and the phase (or Nambu-Goldstone) mode, in which the phase of the superconducting condensate fluctuates [181, 182]. This is sketched in Fig. 2.26(a). In clean superconductors, the frequency of these modes are at 2Δ for the amplitude mode [183], and the plasma frequency for the phase mode (from Eq. (2.7), on the order of ~ 10 eV, much higher than Δ) [184]. Disorder can however bring these frequencies down¹⁷, such that they appear within the gap and become stable [171, 185–188]. Figure 2.26(b) shows the complex conductivity in the presence of disorder, including the effects of collective modes [171]. Compared to BCS, this gives an additional subgap absorption of microwave power. Such behavior has been measured in Ref. [189, 190].

¹⁷One trivial effect is that the plasma frequency is lowered as the charge carrier density decreases with disorder, see Eq. (2.7).

REFERENCES

- [1] S. M. Girvin and K. Yang. *Modern Condensed Matter Physics*. Cambridge University Press, 2019. 720 pp.
- [2] F. London, H. London, and F. A. Lindemann. *The Electromagnetic Equations of the Supraconductor*. In: *Proceedings of the Royal Society of London. Series A - Mathematical and Physical Sciences* 149.866 (1935), pp. 71–88.
- [3] M. L. Cohen and S. G. Louie. *Fundamentals of Condensed Matter Physics*. Cambridge University Press, 2016. 461 pp.
- [4] C. J. Gorter and H. Casimir. *The Thermodynamics of the Superconducting State*. In: *Z. tech. Phys* 15 (1934), pp. 539–42.
- [5] M. Tinkham. *Introduction to Superconductivity*. Dover Publications, 2004. 482 pp.
- [6] R. G. Chambers. *The Anomalous Skin Effect*. In: *Proceedings of the Royal Society of London. Series A, Mathematical and Physical Sciences* 215.1123 (1952), pp. 481–497.
- [7] V. L. Ginzburg and L. D. Landau. *Theory of superconductivity*. In: *Zh. Eksp. Teor. Fiz.; (USSR)* 20:12 (1950).
- [8] A. A. Abrikosov. *On the Magnetic Properties of Superconductors of the Second Group*. In: *Sov. Phys. JETP* 5 (1957), pp. 1174–1182.
- [9] C.-R. Hu. *Numerical Constants for Isolated Vortices in Superconductors*. In: *Physical Review B* 6.5 (1972), pp. 1756–1760.
- [10] J. M. Kosterlitz and D. J. Thouless. *Ordering, Metastability and Phase Transitions in Two-Dimensional Systems*. In: *Journal of Physics C: Solid State Physics* 6.7 (1973), pp. 1181–1203.
- [11] M. R. Beasley, J. E. Mooij, and T. P. Orlando. *Possibility of Vortex-Antivortex Pair Dissociation in Two-Dimensional Superconductors*. In: *Physical Review Letters* 42.17 (1979), pp. 1165–1168.
- [12] E. Bronson, M. P. Gelfand, and S. B. Field. *Equilibrium Configurations of Pearl Vortices in Narrow Strips*. In: *Physical Review B* 73.14 (2006), p. 144501.
- [13] K. K. Likharev. *The Formation of a Mixed State in Planar Semiconductor Films*. In: *Radiophysics and Quantum Electronics* 14.6 (1971), pp. 722–727.
- [14] J. Bardeen, L. N. Cooper, and J. R. Schrieffer. *Theory of Superconductivity*. In: *Physical Review* 108.5 (1957), pp. 1175–1204.
- [15] J. Bardeen, L. N. Cooper, and J. R. Schrieffer. *Microscopic Theory of Superconductivity*. In: *Physical Review* 106.1 (1957), pp. 162–164.

- [16] J. Gao, J. Zmuidzinas, A. Vayonakis, P. Day, B. Mazin, and H. Leduc. *Equivalence of the Effects on the Complex Conductivity of Superconductor Due to Temperature Change and External Pair Breaking*. In: *Journal of Low Temperature Physics* 151.1 (2008), pp. 557–563.
- [17] B. Keck and A. Schmid. *Superconductivity and Electron-Phonon Interaction in Impure Simple Metals*. In: *Journal of Low Temperature Physics* 24.5–6 (1976), pp. 611–629.
- [18] N. W. Ashcroft, N. D. Mermin, and N. D. Mermin. *Solid State Physics*. Holt, Rinehart and Winston, 1976. 868 pp.
- [19] D. C. Mattis and J. Bardeen. *Theory of the Anomalous Skin Effect in Normal and Superconducting Metals*. In: *Physical Review* 111.2 (1958), pp. 412–417.
- [20] J. Gao. *The Physics of Superconducting Microwave Resonators*. California Institute of Technology, 2008.
- [21] R. L. Kautz. *Picosecond Pulses on Superconducting Striplines*. In: *Journal of Applied Physics* 49.1 (1978), pp. 308–314.
- [22] D. M. Pozar. *Microwave Engineering, 4th Edition*. Wiley, 2011. 756 pp.
- [23] R. F. Broom and P. Wolf. *Q Factor and Resonance Amplitude of Josephson Tunnel Junctions*. In: *Physical Review B* 16.7 (1977), pp. 3100–3107.
- [24] R. Barends. *Photon-Detecting Superconducting Resonators*. Delft: Delft University of Technology, 2009.
- [25] J. Rautio. *Sonnet Suites - Sonnet Software*. 2025. URL: <https://www.sonnetsoftware.com/products/sonnet-suites/index.html>.
- [26] *Ansys HFSS | 3D High Frequency Simulation Software*. URL: <https://www.ansys.com/products/electronics/ansys-hfss>.
- [27] R. E. Collin. *Foundations for Microwave Engineering*. Wiley India Pvt. Limited, 2007. 948 pp.
- [28] C. L. Holloway and E. F. Kuester. *A Quasi-Closed Form Expression for the Conductor Loss of CPW Lines, with an Investigation of Edge Shape Effects*. In: *IEEE Transactions on Microwave Theory and Techniques* 43.12 (1995), pp. 2695–2701.
- [29] J. Booth and C. Holloway. *Conductor Loss in Superconducting Planar Structures: Calculations and Measurements*. In: *IEEE Transactions on Microwave Theory and Techniques* 47.6 (1999), pp. 769–774.
- [30] P. J. de Visser. *Quasiparticle Dynamics in Aluminium Superconducting Microwave Resonators*. PhD thesis. Delft: Delft University of Technology, 2014. 222 pp.
- [31] B. A. Mazin. *Microwave Kinetic Inductance Detectors*. PhD thesis. California Institute of Technology, 2005.
- [32] P. J. de Visser, J. J. A. Baselmans, J. Bueno, N. Llombart, and T. M. Klapwijk. *Fluctuations in the Electron System of a Superconductor Exposed to a Photon Flux*. In: *Nature Communications* 5.1 (1 2014), p. 3130.

- [33] J. Zmuidzinias. *Superconducting Microresonators: Physics and Applications*. In: *Annual Review of Condensed Matter Physics* 3.1 (2012), pp. 169–214.
- [34] T. Guruswamy, D. J. Goldie, and S. Withington. *Quasiparticle Generation Efficiency in Superconducting Thin Films*. In: *Superconductor Science and Technology* 27.5 (2014), p. 055012.
- [35] A. Dantuma. *Pushing the Fano Limit*. BA thesis. Delft: Delft University of Technology, 2024.
- [36] N. Zobrist, N. Klimovich, B. Eom, G. Coiffard, M. Daal, N. J. Swimmer, S. Steiger, B. Bumble, H. G. LeDuc, P. K. Day, and B. A. Mazin. *Improving the Dynamic Range of Single Photon Counting Kinetic Inductance Detectors*. In: *Journal of Astronomical Telescopes, Instruments, and Systems* 7.1 (2021), p. 010501.
- [37] S. J. C. Yates, J. J. A. Baselmans, A. Endo, R. M. J. Janssen, L. Ferrari, P. Diener, and A. M. Baryshev. *Photon Noise Limited Radiation Detection with Lens-Antenna Coupled Microwave Kinetic Inductance Detectors*. In: *Applied Physics Letters* 99.7 (2011), p. 073505.
- [38] O. Noroozian, J. Gao, J. Zmuidzinias, H. G. LeDuc, and B. A. Mazin. *Two-level System Noise Reduction for Microwave Kinetic Inductance Detectors*. In: *AIP Conference Proceedings* 1185.1 (2009), pp. 148–151.
- [39] M. H. Read and C. Altman. *A New Structure in Tantalum Thin Films*. In: *Applied Physics Letters* 7.3 (1965), pp. 51–52.
- [40] S. E. de Graaf, S. Un, A. G. Shard, and T. Lindström. *Chemical and Structural Identification of Material Defects in Superconducting Quantum Circuits*. In: *Materials for Quantum Technology* 2.3 (2022), p. 032001.
- [41] C. Müller, J. H. Cole, and J. Lisenfeld. *Towards Understanding Two-Level-Systems in Amorphous Solids: Insights from Quantum Circuits*. In: *Reports on Progress in Physics* 82.12 (2019), p. 124501.
- [42] W. A. Phillips. *Two-Level States in Glasses*. In: *Reports on Progress in Physics* 50.12 (1987), pp. 1657–1708.
- [43] J. Gao, M. Daal, J. M. Martinis, A. Vayonakis, J. Zmuidzinias, B. Sadoulet, B. A. Mazin, P. K. Day, and H. G. Leduc. *A Semiempirical Model for Two-Level System Noise in Superconducting Microresonators*. In: *Applied Physics Letters* 92.21 (2008), p. 212504.
- [44] J. M. Sage, V. Bolkhovsky, W. D. Oliver, B. Turek, and P. B. Welander. *Study of Loss in Superconducting Coplanar Waveguide Resonators*. In: *Journal of Applied Physics* 109.6 (2011), p. 063915.
- [45] S. Kumar, J. Gao, J. Zmuidzinias, B. A. Mazin, H. G. LeDuc, and P. K. Day. *Temperature Dependence of the Frequency and Noise of Superconducting Coplanar Waveguide Resonators*. In: *Applied Physics Letters* 92.12 (2008), p. 123503.

- [46] H. Wang, M. Hofheinz, J. Wenner, M. Ansmann, R. C. Bialczak, M. Lenander, E. Lucero, M. Neeley, A. D. O'Connell, D. Sank, M. Weides, A. N. Cleland, and J. M. Martinis. *Improving the Coherence Time of Superconducting Coplanar Resonators*. In: *Applied Physics Letters* 95.23 (2009), p. 233508.
- [47] J. Gao, M. Daal, A. Vayonakis, S. Kumar, J. Zmuidzinis, B. Sadoulet, B. A. Mazin, P. K. Day, and H. G. Leduc. *Experimental Evidence for a Surface Distribution of Two-Level Systems in Superconducting Lithographed Microwave Resonators*. In: *Applied Physics Letters* 92.15 (2008), p. 152505.
- [48] R. Barends, H. L. Hortensius, T. Zijlstra, J. J. A. Baselmans, S. J. C. Yates, J. R. Gao, and T. M. Klapwijk. *Contribution of Dielectrics to Frequency and Noise of NbTiN Superconducting Resonators*. In: *Applied Physics Letters* 92.22 (2008), p. 223502.
- [49] K. Kouwenhoven, G. P. J. van Doorn, B. T. Buijtenorp, S. A. H. de Rooij, D. Lamers, D. J. Thoen, V. Murugesan, J. J. A. Baselmans, and P. J. de Visser. *Geometry Dependence of Two-Level-System Noise and Loss in a-SiC:H Parallel-Plate Capacitors for Superconducting Microwave Resonators*. In: *Physical Review Applied* 21.4 (2024), p. 044036.
- [50] R. Barends, N. Verduyssen, A. Endo, P. J. de Visser, T. Zijlstra, T. M. Klapwijk, P. Diener, S. J. C. Yates, and J. J. A. Baselmans. *Minimal Resonator Loss for Circuit Quantum Electrodynamics*. In: *Applied Physics Letters* 97.2 (2010), p. 023508.
- [51] A. Bruno, G. de Lange, S. Asaad, K. L. van der Enden, N. K. Langford, and L. DiCarlo. *Reducing Intrinsic Loss in Superconducting Resonators by Surface Treatment and Deep Etching of Silicon Substrates*. In: *Applied Physics Letters* 106.18 (2015), p. 182601.
- [52] J. Wenner, R. Barends, R. C. Bialczak, Y. Chen, J. Kelly, E. Lucero, M. Mariantoni, A. Megrant, P. J. J. O'Malley, D. Sank, A. Vainsencher, H. Wang, T. C. White, Y. Yin, J. Zhao, A. N. Cleland, and J. M. Martinis. *Surface Loss Simulations of Superconducting Coplanar Waveguide Resonators*. In: *Applied Physics Letters* 99.11 (2011), p. 113513.
- [53] S. Kogan. *Electronic Noise and Fluctuations in Solids*. Cambridge: C. University Press, 1996. 354 pp.
- [54] J. Gao, J. Zmuidzinis, B. A. Mazin, H. G. LeDuc, and P. K. Day. *Noise Properties of Superconducting Coplanar Waveguide Microwave Resonators*. In: *Applied Physics Letters* 90.10 (2007), p. 102507.
- [55] J. Burnett, L. Faoro, I. Wisby, V. L. Gurtovoi, A. V. Chernykh, G. M. Mikhailov, V. A. Tulin, R. Shaikhaidarov, V. Antonov, P. J. Meeson, A. Y. Tzalenchuk, and T. Lindström. *Evidence for Interacting Two-Level Systems from the $1/f$ Noise of a Superconducting Resonator*. In: *Nature Communications* 5.1 (1 2014), p. 4119.
- [56] L. Faoro and L. B. Ioffe. *Interacting Tunneling Model for Two-Level Systems in Amorphous Materials and Its Predictions for Their Dephasing and Noise in Superconducting Microresonators*. In: *Physical Review B* 91.1 (2015), p. 014201.

- [57] J. Gao, B. Mazin, M. Daal, P. Day, H. LeDuc, and J. Zmuidzinas. *Power Dependence of Phase Noise in Microwave Kinetic Inductance Detectors*. In: *Millimeter and Submillimeter Detectors and Instrumentation for Astronomy III*. Millimeter and Submillimeter Detectors and Instrumentation for Astronomy III. Vol. 6275. International Society for Optics and Photonics, 2006, p. 627509.
- [58] C. Neill, A. Megrant, R. Barends, Y. Chen, B. Chiaro, J. Kelly, J. Y. Mutus, P. J. J. O'Malley, D. Sank, J. Wenner, T. C. White, Y. Yin, A. N. Cleland, and J. M. Martinis. *Fluctuations from Edge Defects in Superconducting Resonators*. In: *Applied Physics Letters* 103.7 (2013), p. 072601.
- [59] P. J. de Visser, J. J. A. Baselmans, P. Diener, S. J. C. Yates, A. Endo, and T. M. Klapwijk. *Number Fluctuations of Sparse Quasiparticles in a Superconductor*. In: *Physical Review Letters* 106.16 (2011), p. 167004.
- [60] P. J. de Visser, J. J. A. Baselmans, S. J. C. Yates, P. Diener, A. Endo, and T. M. Klapwijk. *Microwave-Induced Excess Quasiparticles in Superconducting Resonators Measured through Correlated Conductivity Fluctuations*. In: *Applied Physics Letters* 100.16 (2012), p. 162601.
- [61] S. B. Kaplan, C. C. Chi, D. N. Langenberg, J. J. Chang, S. Jafarey, and D. J. Scalapino. *Quasiparticle and Phonon Lifetimes in Superconductors*. In: *Physical Review B* 14.11 (1976), pp. 4854–4873.
- [62] G. M. Éliashberg. *Interactions Between Electrons and Lattice Vibrations in a Superconductor*. In: *Journal of Experimental and Theoretical Physics* 38 (1960), pp. 966–976.
- [63] M. Reizer. *Electron-Electron Relaxation in Two-Dimensional and Layered Superconductors*. In: *Physical Review B* 57.2 (1998), pp. 1147–1153.
- [64] J. Rammer and H. Smith. *Quantum Field-Theoretical Methods in Transport Theory of Metals*. In: *Reviews of Modern Physics* 58.2 (1986), pp. 323–359.
- [65] M. Reizer and J. W. Wilkins. *Electron-Electron Relaxation in Heterostructures*. In: *Physical Review B* 55.12 (1997), R7363–R7366.
- [66] A. Rothwarf and B. N. Taylor. *Measurement of Recombination Lifetimes in Superconductors*. In: *Physical Review Letters* 19.1 (1967), pp. 27–30.
- [67] W. Eisenmenger, K. Laßmann, H. J. Trumpp, and R. Krauß. *Quasiparticle Recombination and 2Δ -phonon-trapping in Superconducting Tunneling Junctions*. In: *Applied physics* 11.4 (1976), pp. 307–320.
- [68] S. B. Kaplan. *Acoustic Matching of Superconducting Films to Substrates*. In: *Journal of Low Temperature Physics* 37.3 (1979), pp. 343–365.
- [69] A. Sergeev and V. Mitin. *Electron-Phonon Interaction in Disordered Conductors: Static and Vibrating Scattering Potentials*. In: *Physical Review B* 61.9 (2000), pp. 6041–6047.
- [70] C. M. Wilson and D. E. Prober. *Quasiparticle Number Fluctuations in Superconductors*. In: *Physical Review B* 69.9 (2004), p. 094524.

- [71] K. M. Van Vliet. *Concerning the Theory of Generation-Recombination Noise in Solids*. In: *Physics Letters* 8.1 (1964), pp. 22–24.
- [72] P. K. Day, H. G. LeDuc, B. A. Mazin, A. Vayonakis, and J. Zmuidzinis. *A Broadband Superconducting Detector Suitable for Use in Large Arrays*. In: *Nature* 425.6960 (2003), pp. 817–821.
- [73] K. Kouwenhoven, I. Elwakil, J. van Wingerden, V. Murugesan, D. J. Thoen, J. J. A. Baselmans, and P. J. de Visser. *Model and Measurements of an Optical Stack for Broadband Visible to Near-Infrared Absorption in TiN MKIDs*. In: *Journal of Low Temperature Physics* 209.5 (2022), pp. 1249–1257.
- [74] A. Kozorezov. *Energy Down-Conversion and Thermalization in Metal Absorbers*. In: *Journal of Low Temperature Physics* 167.3 (2012), pp. 473–484.
- [75] P. J. de Visser, S. J. C. Yates, T. Guruswamy, D. J. Goldie, S. Withington, A. Neto, N. Llombart, A. M. Baryshev, T. M. Klapwijk, and J. J. A. Baselmans. *The Non-Equilibrium Response of a Superconductor to Pair-Breaking Radiation Measured over a Broad Frequency Band*. In: *Applied Physics Letters* 106.25 (2015), p. 252602.
- [76] M. Kurakado. *Possibility of High Resolution Detectors Using Superconducting Tunnel Junctions*. In: *Nuclear Instruments and Methods in Physics Research* 196.1 (1982), pp. 275–277.
- [77] N. Rando, A. Peacock, A. van Dordrecht, C. Foden, R. Engelhardt, B. G. Taylor, P. Gare, J. Lumley, and C. Pereira. *The Properties of Niobium Superconducting Tunneling Junctions as X-ray Detectors*. In: *Nuclear Instruments and Methods in Physics Research Section A: Accelerators, Spectrometers, Detectors and Associated Equipment* 313.1 (1992), pp. 173–195.
- [78] A. G. Kozorezov, A. F. Volkov, J. K. Wigmore, A. Peacock, A. Poelaert, and R. den Hartog. *Quasiparticle-Phonon Downconversion in Nonequilibrium Superconductors*. In: *Physical Review B* 61.17 (2000), pp. 11807–11819.
- [79] D. Flanigan, H. McCarrick, G. Jones, B. R. Johnson, M. H. Abitbol, P. Ade, D. Araujo, K. Bradford, R. Cantor, G. Che, P. Day, S. Doyle, C. B. Kjellstrand, H. Leduc, M. Limon, V. Luu, P. Mauskopf, A. Miller, T. Mroczkowski, C. Tucker, and J. Zmuidzinis. *Photon Noise from Chaotic and Coherent Millimeter-Wave Sources Measured with Horn-Coupled, Aluminum Lumped-Element Kinetic Inductance Detectors*. In: *Applied Physics Letters* 108.8 (2016), p. 083504.
- [80] R. W. Boyd. *Photon Bunching and the Photon-Noise-Limited Performance of Infrared Detectors*. In: *Infrared Physics* 22.3 (1982), pp. 157–162.
- [81] J. J. A. Baselmans, F. Facchin, A. P. Laguna, J. Bueno, D. J. Thoen, V. Murugesan, N. Llombart, and P. J. de Visser. *Ultra-Sensitive THz Microwave Kinetic Inductance Detectors for Future Space Telescopes*. In: *Astronomy & Astrophysics* 665 (2022), A17.

- [82] P. J. de Visser, J. J. A. Baselmans, P. Diener, S. J. C. Yates, A. Endo, and T. M. Klapwijk. *Generation-Recombination Noise: The Fundamental Sensitivity Limit for Kinetic Inductance Detectors*. In: *Journal of Low Temperature Physics* 167.3 (2012), pp. 335–340.
- [83] T. S. L. Rutgers. *Quasiparticle Dynamics in Disordered Superconductors*. BA thesis. Delft University of Technology, 2023.
- [84] K. D. Irwin, S. W. Nam, B. Cabrera, B. Chugg, and B. A. Young. *A Quasiparticle-trap-assisted Transition-edge Sensor for Phonon-mediated Particle Detection*. In: *Review of Scientific Instruments* 66.11 (1995), pp. 5322–5326.
- [85] P. J. Rozebraten. *Photon Rate Estimation in MKIDs*. MA thesis. Delft: Delft University of Technology, 2025.
- [86] J. M. Martinis, M. Ansmann, and J. Aumentado. *Energy Decay in Superconducting Josephson-Junction Qubits from Nonequilibrium Quasiparticle Excitations*. In: *Physical Review Letters* 103.9 (2009), p. 097002.
- [87] V. Narayanamurti, R. C. Dynes, P. Hu, H. Smith, and W. F. Brinkman. *Quasiparticle and Phonon Propagation in Bulk, Superconducting Lead*. In: *Physical Review B* 18.11 (1978), pp. 6041–6052.
- [88] J. N. Ullom, P. A. Fisher, and M. Nahum. *Energy-Dependent Quasiparticle Group Velocity in a Superconductor*. In: *Physical Review B* 58.13 (1998), pp. 8225–8228.
- [89] K. P. Syaifoel. *The Impact of Diffusion and Disorder on the Single Photon Response of β -Ta OKIDs*. MA thesis. Delft University of Technology, 2024.
- [90] A. G. Kozorezov, C. Lambert, F. Marsili, M. J. Stevens, V. B. Verma, J. P. Allmaras, M. D. Shaw, R. P. Mirin, and S. W. Nam. *Fano Fluctuations in Superconducting-Nanowire Single-Photon Detectors*. In: *Physical Review B* 96.5 (2017), p. 054507.
- [91] A. G. Kozorezov, J. K. Wigmore, D. Martin, P. Verhoeve, and A. Peacock. *Electron Energy Down-Conversion in Thin Superconducting Films*. In: *Physical Review B* 75.9 (2007), p. 094513.
- [92] P. J. de Visser, S. A. H. de Rooij, V. Murugesan, D. J. Thoen, and J. J. A. Baselmans. *Phonon-Trapping-Enhanced Energy Resolution in Superconducting Single-Photon Detectors*. In: *Physical Review Applied* 16.3 (2021), p. 034051.
- [93] N. Zobrist, W. H. Clay, G. Coiffard, M. Daal, N. Swimmer, P. Day, and B. A. Mazin. *Membraneless Phonon Trapping and Resolution Enhancement in Optical Microwave Kinetic Inductance Detectors*. In: *Physical Review Letters* 129.1 (2022), p. 017701.
- [94] J. E. Mooij and T. M. Klapwijk. *Nonlinear Electrodynamics in Microwave-Stimulated Superconductivity*. In: *Physical Review B* 27.5 (1983), pp. 3054–3057.
- [95] T. M. Klapwijk and J. E. Mooij. *Microwave-Enhanced Superconductivity in Aluminium Films*. In: *Physica B+C* 81.1 (1976), pp. 132–136.

- [96] T. M. Klapwijk and P. J. de Visser. *The Discovery, Disappearance and Re-Emergence of Radiation-Stimulated Superconductivity*. In: *Annals of Physics* (2020), p. 168104.
- [97] L. J. Swenson, P. K. Day, B. H. Eom, H. G. Leduc, N. Llombart, C. M. McKenney, O. Noroozian, and J. Zmuidzinis. *Operation of a Titanium Nitride Superconducting Microresonator Detector in the Nonlinear Regime*. In: *Journal of Applied Physics* 113.10 (2013), p. 104501.
- [98] D. J. Goldie and S. Withington. *Non-Equilibrium Superconductivity in Quantum-Sensing Superconducting Resonators*. In: *Superconductor Science and Technology* 26.1 (2012), p. 015004.
- [99] A. G. Aronov and B. Z. Spivak. *Nonequilibrium Distributions in Superconductors (Review)*. In: *Soviet Journal Low Temperature Physics* 4.11 (1978), pp. 641–660.
- [100] G. M. Éliashberg. *Inelastic Electron Collisions and Nonequilibrium Stationary States in Superconductors*. In: *Soviet Journal of Experimental and Theoretical Physics* 34 (1972), p. 668.
- [101] B. I. Ivlev, S. G. Lisitsyn, and G. M. Eliashberg. *Nonequilibrium Excitations in Superconductors in High-Frequency Fields*. In: *Journal of Low Temperature Physics* 10.3 (1973), pp. 449–468.
- [102] J.-J. Chang and D. J. Scalapino. *Kinetic-Equation Approach to Nonequilibrium Superconductivity*. In: *Physical Review B* 15.5 (1977), pp. 2651–2670.
- [103] P. Fischer and G. Catelani. *Nonequilibrium Quasiparticle Distribution in Superconducting Resonators: An Analytical Approach*. In: *Physical Review Applied* 19.5 (2023), p. 054087.
- [104] P. B. Fischer and G. Catelani. *Nonequilibrium Quasiparticle Distribution in Superconducting Resonators: Effect of Pair-Breaking Photons*. In: *SciPost Physics* 17.3 (2024), p. 070.
- [105] P. J. de Visser, D. J. Goldie, P. Diener, S. Withington, J. J. A. Baselmans, and T. M. Klapwijk. *Evidence of a Nonequilibrium Distribution of Quasiparticles in the Microwave Response of a Superconducting Aluminum Resonator*. In: *Physical Review Letters* 112.4 (2014), p. 047004.
- [106] A. Semenov, I. Devyatov, M. Westig, and T. Klapwijk. *Effect of Microwaves on Superconductors for Kinetic Inductance Detection and Parametric Amplification*. In: *Physical Review Applied* 13.2 (2020), p. 024079.
- [107] A. V. Semenov, I. A. Devyatov, P. J. de Visser, and T. M. Klapwijk. *Coherent Excited States in Superconductors Due to a Microwave Field*. In: *Physical Review Letters* 117.4 (2016), p. 047002.
- [108] S. B. Nam. *Theory of Electromagnetic Properties of Strong-Coupling and Impure Superconductors. II*. In: *Physical Review* 156.2 (1967), pp. 487–493.
- [109] S. B. Nam. *Theory of Electromagnetic Properties of Superconducting and Normal Systems. I*. In: *Physical Review* 156.2 (1967), pp. 470–486.

- [110] I. S. B. Nam. *Theory of Electromagnetic Properties of Superconducting and Normal Systems*. In: *Physical Review B* 2.9 (1970), pp. 3812–3812.
- [111] A. Anthore, H. Pothier, and D. Esteve. *Density of States in a Superconductor Carrying a Supercurrent*. In: *Physical Review Letters* 90.12 (2003), p. 127001.
- [112] J. Romijn, T. M. Klapwijk, M. J. Renne, and J. E. Mooij. *Critical Pair-Breaking Current in Superconducting Aluminum Strips Far below T_c* . In: *Physical Review B* 26.7 (1982), pp. 3648–3655.
- [113] J. R. Clem and V. G. Kogan. *Kinetic Impedance and Depairing in Thin and Narrow Superconducting Films*. In: *Physical Review B* 86.17 (2012), p. 174521.
- [114] B. Ho Eom, P. K. Day, H. G. LeDuc, and J. Zmuidzinas. *A Wideband, Low-Noise Superconducting Amplifier with High Dynamic Range*. In: *Nature Physics* 8.8 (8 2012), pp. 623–627.
- [115] T. Guruswamy, C. N. Thomas, S. Withington, and D. J. Goldie. *Electrothermal Feedback in Kinetic Inductance Detectors*. In: *Superconductor Science and Technology* 30.6 (2017), p. 064006.
- [116] M. Vignati, C. Bellenghi, L. Cardani, N. Casali, I. Colantoni, and A. Cruciani. *Non-Linearity in the System of Quasiparticles of a Superconducting Resonator*. 2021.
- [117] C. Bellenghi, L. Cardani, N. Casali, I. Colantoni, A. Cruciani, G. Pettinari, and M. Vignati. *Pulse Response of a Kinetic Inductance Detector in the Nonlinear Regime*. In: *Journal of Low Temperature Physics* 199.3 (2020), pp. 639–645.
- [118] P. N. Baker. *Preparation and Properties of Tantalum Thin Films*. In: *Thin Solid Films* 14.1 (1972), pp. 3–25.
- [119] M. Magnuson, G. Greczynski, F. Eriksson, L. Hultman, and H. Högborg. *Electronic Structure of β -Ta Films from X-ray Photoelectron Spectroscopy and First-Principles Calculations*. In: *Applied Surface Science* 470 (2019), pp. 607–612.
- [120] D. W. Face and D. E. Prober. *Nucleation of Body-centered-cubic Tantalum Films with a Thin Niobium Underlayer*. In: *Journal of Vacuum Science & Technology A* 5.6 (1987), pp. 3408–3411.
- [121] R. Barends, S. van Vliet, J. J. A. Baselmans, S. J. C. Yates, J. R. Gao, and T. M. Klapwijk. *Enhancement of Quasiparticle Recombination in Ta and Al Superconductors by Implantation of Magnetic and Nonmagnetic Atoms*. In: *Physical Review B* 79.2 (2009), 020509(R).
- [122] H. G. Leduc, B. Bumble, P. K. Day, B. H. Eom, J. Gao, S. Golwala, B. A. Mazin, S. McHugh, A. Merrill, D. C. Moore, O. Noroozian, A. D. Turner, and J. Zmuidzinas. *Titanium Nitride Films for Ultrasensitive Microresonator Detectors*. In: *Applied Physics Letters* 97.10 (2010), p. 102509.
- [123] P. C. J. J. Coumou, E. F. C. Driessen, J. Bueno, C. Chapelier, and T. M. Klapwijk. *Electrodynamic Response and Local Tunneling Spectroscopy of Strongly Disordered Superconducting TiN Films*. In: *Physical Review B* 88.18 (2013), p. 180505.

- [124] E. Gershenson. *Electron-Phonon Interaction in Ultrathin Nb Films*. In: *Zh. Eksp. Teor. Fiz.* 97 (1990), pp. 901–911.
- [125] A. F. Hebard and S. Nakahara. *Structural Phase Transitions of Indium/Indium Oxide Thin-film Composites*. In: *Applied Physics Letters* 41.12 (1982), pp. 1130–1132.
- [126] G. Deutscher, H. Fenichel, M. Gershenson, E. Grünbaum, and Z. Ovadyahu. *Transition to Zero Dimensionality in Granular Aluminum Superconducting Films*. In: *Journal of Low Temperature Physics* 10.1 (1 1973), pp. 231–243.
- [127] P. W. Anderson. *Theory of Dirty Superconductors*. In: *Journal of Physics and Chemistry of Solids* 11.1 (1959), pp. 26–30.
- [128] G. Chanin, E. A. Lynton, and B. Serin. *Impurity Effects on the Superconductive Critical Temperature of Indium and Aluminum*. In: *Physical Review* 114.3 (1959), pp. 719–724.
- [129] A. A. Abrikosov and L. P. Gor'kov. *Contribution to the Theory of Superconducting Alloys with Paramagnetic Impurities*. In: *Zh. Eksp. Teor. Fiz.* 39 (1960), p. 1781.
- [130] J. C. Phillips. *Gapless Superconductivity*. In: *Physical Review Letters* 10.3 (1963), pp. 96–98.
- [131] L. Yu. *Bound State in Superconductors with Paramagnetic Impurities*. In: *Chin. J. Phys. (Peking) (Engl. Transl.)* 21.1 (1965), pp. 75–91.
- [132] H. Shiba. *Classical Spins in Superconductors*. In: *Progress of Theoretical Physics* 40.3 (1968), pp. 435–451.
- [133] A. I. Rusinov. *On the Theory of Gapless Superconductivity in Alloys Containing Paramagnetic Impurities*. In: *Soviet Journal of Experimental and Theoretical Physics* 29 (1969), p. 1101.
- [134] A. V. Balatsky, I. Vekhter, and J.-X. Zhu. *Impurity-Induced States in Conventional and Unconventional Superconductors*. In: *Reviews of Modern Physics* 78.2 (2006), pp. 373–433.
- [135] A. Pippard. *CXXII. Ultrasonic Attenuation in Metals*. In: *The London, Edinburgh, and Dublin Philosophical Magazine and Journal of Science* 46.381 (1955), pp. 1104–1114.
- [136] M. Y. Reizer and A. V. Sergeev. *Electron-Phonon Interaction in Impure Metals and Superconductors*. In: *Zh. Eksp. Teor. Fiz.* 90 (1986), p. 1056.
- [137] C. Kittel. *Quantum Theory of Solids*. Wiley, 1987. 528 pp.
- [138] A. Schmid. *Electron-Phonon Interaction in an Impure Metal*. In: *Zeitschrift für Physik* 259.5 (1973), pp. 421–436.
- [139] T. P. Devereaux and D. Belitz. *Quasiparticle Inelastic Lifetimes in Disordered Superconducting Films*. In: *Physical Review B* 44.9 (1991), pp. 4587–4600.
- [140] B. L. Altshuler and A. G. Aronov. *Electron–Electron Interaction In Disordered Conductors*. In: *Modern Problems in Condensed Matter Sciences*. Ed. by A. L. Efros and M. Pollak. Vol. 10. Electron–Electron Interactions in Disordered Systems. Elsevier, 1985, pp. 1–153.

- [141] A. F. Ioffe and A. R. Regel. *Non-Crystalline, Amorphous, and Liquid Electronic Semiconductors*. In: *PROGRESS IN SEMICONDUCTORS* 4 (1960), pp. 237–291.
- [142] A. Schmid. *On the Dynamics of Electrons in an Impure Metal*. In: *Zeitschrift für Physik* 271.3 (1974), pp. 251–256.
- [143] A. Aronov. *Fourteen Years of Quantum Interference in Disordered Metals*. In: *Physica Scripta* T49A (1993), pp. 28–33.
- [144] M. Reizer. *Electron-Electron Relaxation in Two-Dimensional Impure Superconductors*. In: *Physical Review B* 61.10 (2000), pp. 7108–7117.
- [145] P. C. J. J. Coumou, M. R. Zuiddam, E. F. C. Driessen, P. J. de Visser, J. J. A. Baselmans, and T. M. Klapwijk. *Microwave Properties of Superconducting Atomic-Layer Deposited TiN Films*. In: *IEEE Transactions on Applied Superconductivity* 23.3 (2013), pp. 7500404–7500404.
- [146] A. I. Kardakova, P. C. J. J. Coumou, M. I. Finkel, D. V. Morozov, P. P. An, G. N. Goltsman, and T. M. Klapwijk. *Electron-Phonon Energy Relaxation Time in Thin Strongly Disordered Titanium Nitride Films*. In: *IEEE Transactions on Applied Superconductivity* 25.3 (2015), pp. 1–4.
- [147] P. W. Anderson. *Absence of Diffusion in Certain Random Lattices*. In: *Physical Review* 109.5 (1958), pp. 1492–1505.
- [148] D. Belitz and T. R. Kirkpatrick. *The Anderson-Mott Transition*. In: *Reviews of Modern Physics* 66.2 (1994), pp. 261–380.
- [149] J. H. Mooij. *Electrical Conduction in Concentrated Disordered Transition Metal Alloys*. In: *physica status solidi (a)* 17.2 (1973), pp. 521–530.
- [150] G. Bergmann. *Weak Localization in Thin Films: A Time-of-Flight Experiment with Conduction Electrons*. In: *Physics Reports* 107.1 (1984), pp. 1–58.
- [151] B. L. Altshuler. *Fluctuations in the Extrinsic Conductivity of Disordered Conductors*. In: *Soviet Journal of Experimental and Theoretical Physics Letters* 41 (1985), p. 648.
- [152] P. A. Lee and A. D. Stone. *Universal Conductance Fluctuations in Metals*. In: *Physical Review Letters* 55.15 (1985), pp. 1622–1625.
- [153] A. M. Finkel'stein. *Suppression of Superconductivity in Homogeneously Disordered Systems*. In: *Physica B: Condensed Matter* 197.1 (1994), pp. 636–648.
- [154] B. Sacépé, M. Feigel'man, and T. M. Klapwijk. *Quantum Breakdown of Superconductivity in Low-Dimensional Materials*. In: *Nature Physics* 16.7 (7 2020), pp. 734–746.
- [155] T. Charpentier, D. Perconte, S. Léger, K. R. Amin, F. Blondelle, F. Gay, O. Buisson, L. Ioffe, A. Khvalyuk, I. Poboiko, M. Feigel'man, N. Roch, and B. Sacépé. *First-Order Quantum Breakdown of Superconductivity in an Amorphous Superconductor*. In: *Nature Physics* 21.1 (2025), pp. 104–109.
- [156] M. Ma and P. A. Lee. *Localized Superconductors*. In: *Physical Review B* 32.9 (1985), pp. 5658–5667.

- [157] D. B. Haviland, Y. Liu, and A. M. Goldman. *Onset of Superconductivity in the Two-Dimensional Limit*. In: *Physical Review Letters* 62.18 (1989), pp. 2180–2183.
- [158] B. Sacépé, T. Dubouchet, C. Chapelier, M. Sanquer, M. Ovadia, D. Shahar, M. Feigel'man, and L. Ioffe. *Localization of Preformed Cooper Pairs in Disordered Superconductors*. In: *Nature Physics* 7.3 (3 2011), pp. 239–244.
- [159] K. M. Bastiaans, D. Chatzopoulos, J.-F. Ge, D. Cho, W. O. Tromp, J. M. van Ruitenbeek, M. H. Fischer, P. J. de Visser, D. J. Thoen, E. F. C. Driessen, T. M. Klapwijk, and M. P. Allan. *Direct Evidence for Cooper Pairing without a Spectral Gap in a Disordered Superconductor above T_c* . In: *Science* 374.6567 (2021), pp. 608–611.
- [160] A. M. Finkel'stein. *Superconducting Transition Temperature in Amorphous Films*. In: *Pis'ma Zh. Eksp. Teor. Fiz.* 45.1 (1987), pp. 37–40.
- [161] M. V. Feigel'man and M. A. Skvortsov. *Universal Broadening of the Bardeen-Cooper-Schrieffer Coherence Peak of Disordered Superconducting Films*. In: *Physical Review Letters* 109.14 (2012), p. 147002.
- [162] B. Sacépé, C. Chapelier, T. I. Baturina, V. M. Vinokur, M. R. Baklanov, and M. Sanquer. *Disorder-Induced Inhomogeneities of the Superconducting State Close to the Superconductor-Insulator Transition*. In: *Physical Review Letters* 101.15 (2008), p. 157006.
- [163] M. A. Skvortsov and M. V. Feigel'man. *Superconductivity in Disordered Thin Films: Giant Mesoscopic Fluctuations*. In: *Physical Review Letters* 95.5 (2005), p. 057002.
- [164] A. I. Larkin and Y. N. Ovchinnikov. *Density of States in Inhomogeneous Superconductors*. In: *Soviet Journal of Experimental and Theoretical Physics* 34 (1972), p. 1144.
- [165] K. D. Usadel. *Generalized Diffusion Equation for Superconducting Alloys*. In: *Physical Review Letters* 25.8 (1970), pp. 507–509.
- [166] B. Sacépé, C. Chapelier, T. I. Baturina, V. M. Vinokur, M. R. Baklanov, and M. Sanquer. *Pseudogap in a Thin Film of a Conventional Superconductor*. In: *Nature Communications* 1.1 (1 2010), p. 140.
- [167] Y. Noat, V. Cherkez, C. Brun, T. Cren, C. Carbillet, F. Debontridder, K. Ilin, M. Siegel, A. Semenov, H.-W. Hübers, and D. Roditchev. *Unconventional Superconductivity in Ultrathin Superconducting NbN Films Studied by Scanning Tunneling Spectroscopy*. In: *Physical Review B* 88.1 (2013), p. 014503.
- [168] C. Carbillet, V. Cherkez, M. A. Skvortsov, M. V. Feigel'man, F. Debontridder, L. B. Ioffe, V. S. Stolyarov, K. Ilin, M. Siegel, D. Roditchev, T. Cren, and C. Brun. *Spectroscopic Evidence for Strong Correlations between Local Superconducting Gap and Local Altshuler-Aronov Density of States Suppression in Ultrathin NbN Films*. In: *Physical Review B* 102.2 (2020), p. 024504.

- [169] M. A. Skvortsov and M. V. Feigel'man. *Subgap States in Disordered Superconductors*. In: *Journal of Experimental and Theoretical Physics* 117.3 (2013), pp. 487–498.
- [170] A. Bespalov, M. Houzet, J. S. Meyer, and Y. V. Nazarov. *Theoretical Model to Explain Excess of Quasiparticles in Superconductors*. In: *Physical Review Letters* 117.11 (2016), p. 117002.
- [171] G. Seibold, L. Benfatto, and C. Castellani. *Application of the Mattis-Bardeen Theory in Strongly Disordered Superconductors*. In: *Physical Review B* 96.14 (2017), p. 144507.
- [172] Y. V. Fominov and M. A. Skvortsov. *Subgap States in Disordered Superconductors with Strong Magnetic Impurities*. In: *Physical Review B* 93.14 (2016), p. 144511.
- [173] J. A. Sauls. *Theory of Disordered Superconductors with Applications to Nonlinear Current Response*. In: *Progress of Theoretical and Experimental Physics* (2022).
- [174] P. B. Littlewood and C. M. Varma. *Amplitude Collective Modes in Superconductors and Their Coupling to Charge-Density Waves*. In: *Physical Review B* 26.9 (1982), pp. 4883–4893.
- [175] sahderooij. *Github.Com/Sahderooij/MKID-models*. 2024.
- [176] E. F. C. Driessen, P. C. J. J. Coumou, R. R. Tromp, P. J. de Visser, and T. M. Klapwijk. *Strongly Disordered TiN and NbTiN S-Wave Superconductors Probed by Microwave Electrodynamics*. In: *Physical Review Letters* 109.10 (2012), p. 107003.
- [177] A. V. Khvalyuk, T. Charpentier, N. Roch, B. Sacépé, and M. V. Feigel'man. *Near Power-Law Temperature Dependence of the Superfluid Stiffness in Strongly Disordered Superconductors*. In: *Physical Review B* 109.14 (2024), p. 144501.
- [178] A. G. Moshe, E. Farber, and G. Deutscher. *Granular Superconductors for High Kinetic Inductance and Low Loss Quantum Devices*. In: *Applied Physics Letters* 117.6 (2020), p. 062601.
- [179] T. Charpentier, A. Khvalyuk, L. Ioffe, M. Feigel'man, N. Roch, and B. Sacépé. *Universal Scaling of Microwave Dissipation in Superconducting Circuits*. 2025. URL: <http://arxiv.org/abs/2507.08953>. Pre-published.
- [180] M. V. Feigel'man and L. B. Ioffe. *Microwave Properties of Superconductors Close to the Superconductor-Insulator Transition*. In: *Physical Review Letters* 120.3 (2018), p. 037004.
- [181] R. Shimano and N. Tsuji. *Higgs Mode in Superconductors*. In: *Annual Review of Condensed Matter Physics* 11.1 (2020), pp. 103–124.
- [182] D. Pekker and C. Varma. *Amplitude/Higgs Modes in Condensed Matter Physics*. In: *Annual Review of Condensed Matter Physics* 6.1 (2015), pp. 269–297.
- [183] P. W. Anderson. *Coherent Excited States in the Theory of Superconductivity: Gauge Invariance and the Meissner Effect*. In: *Physical Review* 110.4 (1958), pp. 827–835.

- [184] P. W. Anderson. *Plasmons, Gauge Invariance, and Mass*. In: *Physical Review* 130.1 (1963), pp. 439–442.
- [185] Y. Li and M. Dzero. *Collective Modes in Terahertz Field Response of Disordered Superconductors*. In: *Journal of Physics: Condensed Matter* 37.11 (2025), p. 115602.
- [186] T. Cea, D. Bucheli, G. Seibold, L. Benfatto, J. Lorenzana, and C. Castellani. *Optical Excitation of Phase Modes in Strongly Disordered Superconductors*. In: *Physical Review B* 89.17 (2014), p. 174506.
- [187] T. Cea, C. Castellani, G. Seibold, and L. Benfatto. *Nonrelativistic Dynamics of the Amplitude (Higgs) Mode in Superconductors*. In: *Physical Review Letters* 115.15 (2015), p. 157002.
- [188] M. Silaev. *Nonlinear Electromagnetic Response and Higgs-mode Excitation in BCS Superconductors with Impurities*. In: *Physical Review B* 99.22 (2019), p. 224511.
- [189] F. Levy-Bertrand, A. Benoît, O. Bourrion, M. Calvo, A. Catalano, J. Goupy, F. Valenti, N. Maleeva, L. Grünhaupt, I. Pop, and A. Monfardini. *Subgap Kinetic Inductance Detector Sensitive to 85-GHz Radiation*. In: *Physical Review Applied* 15.4 (2021), p. 044002.
- [190] K. Katsumi, J. Fiore, M. Udina, R. Romero, D. Barbalas, J. Jesudasan, P. Raychaudhuri, G. Seibold, L. Benfatto, and N. P. Armitage. *Revealing Novel Aspects of Light-Matter Coupling by Terahertz Two-Dimensional Coherent Spectroscopy: The Case of the Amplitude Mode in Superconductors*. In: *Physical Review Letters* 132.25 (2024), p. 256903.

3

METHODS

3.1 SETUP

In order to measure the effect of excitations (thermal phonons, subgap photons and pair-breaking photons) in the superconducting resonator, we must cooldown the sample to below the critical temperature. Typically, this means $T < T_c/2$, as for higher temperatures the quasiparticle excitations induce too much loss to be able to measure the changes in resonance frequency and loss accurately¹. For a large responsivity to quasiparticle changes (Eq. (2.36)), a bath temperature of $T \lesssim T_c/10$ is typically needed.

The signal from the quasiparticle excitations must be large compared to the noise produced by other effects or components in the setup. Therefore, the total added noise by the setup itself must be minimized. This is done by a careful microwave design, which we will treat in Section 3.1.2. On top of that, other, uncontrolled, excitations must be limited. This includes magnetic fields, heat from the warm environment (via conduction or radiation), and stray light from unintentional sources (warmer stages, light) that can be absorbed in the superconductor and produce a signal. A proper cryogenic and optical design can mitigate the effects that obscure the signal. We will discuss these first.

3.1.1 CRYOGENIC AND OPTICAL SETUP

To cool the samples we use a dilution refrigerator (SD system from Bluefors [2]) with custom-made sample stage mounted to the mixing chamber stage². This is depicted in Fig. 3.1. Apart from the vacuum can (300 K), 50 K and 4 K thermal shields, the sample is additionally shielded from stray light by a box-in-a-box setup based on the design of Ref. [4]. This entails a light-tight enclosure of the sample-holder and a light-tight enclosure of the sample itself. Stray light is prevented from passing through the sides of the removable parts (lids, flanges etc.) by use of labyrinths that

¹Specifically, $Q \approx Q_i(\hbar\omega = \Delta_0/10, T = T_c/2) \sim 10^2$ (Eqs. (2.20) and (2.34)) deteriorates the responsivity to excitations (Eq. (2.36)) too much to have a decent signal-to-noise ratio.

²We use this specific setup for the measurements in Chapters 6 and 7. The measurements presented in Chapters 4 and 5 are performed in an adiabatic demagnetization refrigerator (ADR) with a similar microwave setup. The details for that setup can be found in Ref. [3].

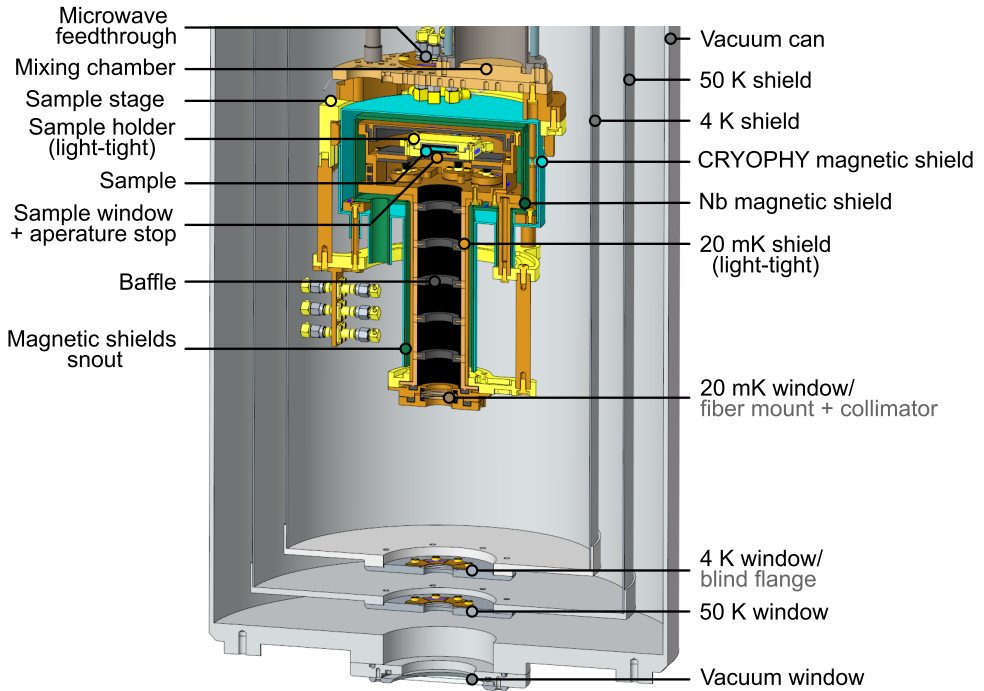


Figure 3.1: Render of the cryogenic setup. Several critical components are indicated. The setup as displayed is for external irradiation on to the sample. Each window can additionally also host radiation filters (low pass, high pass, band pass filters) to limit heat load and stray light onto the sample [1]. Alternatively, the 4 K window can be replaced by a blind flange, the 20 mK window can be replaced by a fiber mount and collimator (both named in gray) and a fiber is connected from the 20 mK sample stage to outside via proper feedthroughs.

are coated by carbon-loaded epoxy, embedded with SiC grains of 1 mm diameter for additional scattering [4, 5]. Magnetic fields can induce frequency shifts of the resonator and induce additional loss [6]. To limit this, the sample is shielded from magnetic fields with the use of two shields: a CRYOPHY[®] shield (a Mn-Cr-Ni-Fe alloy with a high magnetic permeability) that attenuates magnetic fields and a superconducting Nb shield that opposes any changing magnetic field. This leads to a simulated shielding of a factor $\sim 10^6$ for time dependent magnetic fields and a factor ~ 70 for static fields (limited by vertically orientated fields; horizontal static fields are suppressed by a factor $\sim 10^3$). The vertical static earth magnetic field in the Netherlands is approximately $40 \mu\text{T}$ [7]. This is attenuated to $0.6 \mu\text{T}$ by the CRYOPHY[®] magnetic shield. To check if this shielding is adequate, Table 3.1 shows the typical critical fields for the materials studied in this thesis. For Al and NbTiN the shielding is clearly sufficient to prevent vortices³. In a large area film of $\beta\text{-Ta}$,

³Al is close to the type I regime ($\lambda/\xi < 1/\sqrt{2}$) for 3D superconductors with these values. However, since the thickness is much smaller than the coherence length ($d \ll \xi$), the film is in the quasi-2D limit. Therefore, when $\lambda/\xi < 1/\sqrt{2}$, the critical field is reduced by a factor $\sqrt{d/\xi}$ [8], and will be

vortices could be induced. However, the maximum strip width that we use is $10\ \mu\text{m}$, which is much smaller than the Pearl length. This increases $\mu_0 H_{c1}$ to $77\ \mu\text{T}$ (see Eq. (2.15)), and we expect the shielding to prevent nucleation of vortices in the β -Ta structures as well.

In order to excite the resonators on the sample with electro-magnetic radiation, two methods can be used. The first is to use an external source, which is located below the cryostat. Radiation is coupled to the chip via windows in each shield, as indicated in Fig. 3.1. These windows include appropriate filters to block thermal radiation and other stray light from warmer stages [1]. Since this requires an opening in the sample stage, the magnetic shields are designed with a snout. In the interior of this snout is an optical baffle with carbon-loaded side walls, to limit the angles of incident radiation on the chip.

The second method is to use an optical fiber (SMF-28e+ 1260–1620 nm) that is fed through the different stages. This fiber is connected to a collimator at the bottom of the sample stage, such that it radiates upwards. The lid with fiber mount and collimator is also designed to be light-tight, by use of labyrinths, coated with carbon-loaded epoxy. The 4 K window is in this case replaced by a blind flange to limit the heat load on the sample stage, as indicated in gray in Fig. 3.1. This setup is also used for dark measurements, when we do not couple light to the fiber.

With these two methods, optical light from a laser source (Thorlabs MCLS1, with 402 nm, 673 nm, 986 nm and 1545 nm lasers) can be coupled to the chip. To attenuate the (\sim mW) radiation power from the laser source, we use mechanical variable attenuators (OZ Optics BB-100-11 for each specific wavelength) and a digital variable attenuator (OZ Optics DA-100-11-1550-9), such that we are left with \sim 100 photons per second (\sim aW). Alternatively, with the external source method, we can use a monochromator (custom Oriol Cornerstone 260) with a spectral range from 200 to 1400 nm [1]. For lower frequencies of order THz (i.e., smaller than the average frequency of photon from the 300 K environment, which is \sim 22 THz), a third method is to mount a black body radiator on the inside of the 4 K blind flange. With the use of proper filters pass-band can be selected, and with controlling the temperature of the black body the radiation power can be tuned [3, 10].

3.1.2 MICROWAVE SETUP

The measurement that we perform is a homodyne microwave measurement. We retrieve the forward scattering parameter S_{21} of a superconducting resonator (see Eq. (2.30) in Section 2.2). This entails a generated signal at a frequency f , that is split to two microwave lines. One of these lines is connected through the sample to the intermediate frequency (IF) port of an IQ-mixer. The other line is connected to the local-oscillator (LO) port of the IQ-mixer. The in-phase (I) and quadrature (Q) outputs of the IQ-mixer are proportional to the real and imaginary parts of S_{21} . Higher order mixing products are disregarded with a low-pass filter (LPF) and the I and Q outputs are digitized with an analog-to-digital converter (ADC). A full schematic of the microwave setup is given in Fig. 3.2.

lower than H_{c2} , which stays the same in the quasi-2D regime [9]. Therefore, the Al film can be considered to be well in the type II regime.

Table 3.1.: Typical parameters of the superconducting films used in this thesis: thickness, Pearl length, dirty limit coherence length, and lower and upper critical fields. These values are calculated with the equations in Section 2.1.2, and the film parameters mentioned in Chapters 5 and 6.

Material	d (nm)	λ_{\perp} (nm)	ξ_{DL} (nm)	$\mu_0 H_{c1}$ (μT)	$\mu_0 H_{c2}$ (μT)
Al	40	2.1×10^2	2.6×10^2	1.0×10^3	4.7×10^3
β -Ta	40	6.5×10^4	19	0.32	9.4×10^5
NbTiN	150	5.7×10^2	4.5	2.7×10^3	1.6×10^7

3

A calibration is performed by warming up the sample to $T \approx 0.6T_c$, such that the resonators do not influence the transmission of the sample much. The NbTiN transmission line is practically not affected by this higher temperature, due to the much higher critical temperature (~ 15 K versus ~ 1.2 K for Al and 0.8 K for β -Ta). A full S_{21} -versus-frequency curve (magnitude and phase) is recorded and taken as calibration (a microwave thru calibration). This calibration is checked against a reference measurement to exclude issues with broken lines or shorts in the cold, which are otherwise hard to detect due to the enormous dynamic range of the measurement setup. Differences in measured S_{21} and the calibration are interpreted as the S_{21} of the resonator.

In order to have a high signal-to-noise ratio, the noise contribution of all components in the setup must be minimized. Every microwave component adds noise, each with a different noise spectrum. These spectra can typically be described by a $1/f$ -spectrum at low frequencies and a white noise floor at higher frequencies. For our measurements, the $1/f$ of TLS noise in the resonator (Section 2.2.4) usually dominates the low frequency noise spectrum.

A white noise floor can be characterized by a noise temperature. This temperature corresponds to the Nyquist shot noise produced by a matched resistance of temperature T_n [11]. The voltage fluctuations from such a resistor is given by, $V_n = \sqrt{k_B T_n R \Delta f}$, with Δf the bandwidth and R the resistance of the element. The noise power spectral density is therefore given by $k_B T_n$. This thermal noise is due to the shot noise of black body radiation photons in 1 dimension and in the Rayleigh-Jeans (long wavelength) limit [11].

Passive components add this type of thermal noise. The output noise temperature of an attenuator with a gain $G < 1$ is $T_n = T_a(1-G)$, where T_a is the physical temperature of the attenuator [12]. For $G \ll 1$, an attenuator thus adds thermal noise equal to the physical temperature.

The white noise of active components (amplifiers, signal generators) can also be characterized by an effective noise temperature. Since all components in the microwave chain are matched, we can add all the noise temperatures of the individual components, while keeping track of the attenuation and amplification of each noise contribution. This way, we find the system noise temperature as,

$$T_{\text{sys}} = T_1 + \sum_{i=0}^N \frac{T_i}{\prod_{j=1}^{i-1} G_j} = T_1 + \frac{T_2}{G_1} + \frac{T_3}{G_1 G_2} + \dots, \quad (3.1)$$

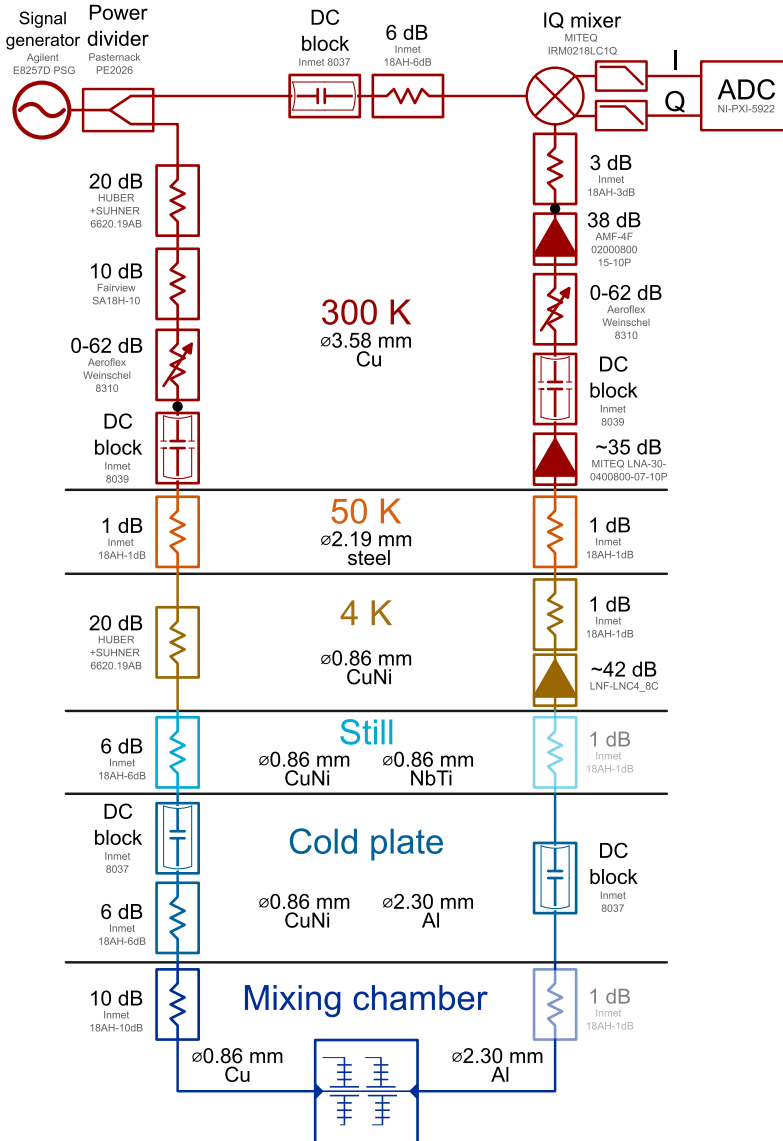


Figure 3.2: Overview of the microwave setup. All components are named and temperature stages are indicated in color. The 1 dB attenuators after the chip are half-transparent as they are taken out in some measurements to reduce the system noise. The cabling is indicated below the stage names (left and right if input and output cabling differs). The black dots indicate the point where the top homodyne setup can be replaced by a VNA (Keysight N5230A PNA-L), for quick frequency sweeps to find resonators and for the S_{21} -measurement (Section 3.3.2).

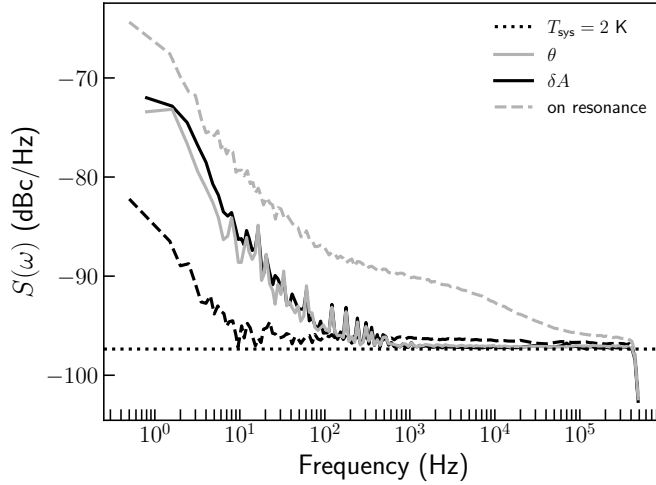


Figure 3.3: The noise power spectral density in amplitude (δA) and phase (θ). The solid lines are measured off resonance (5 bandwidths away from resonance) and are a measure of the system noise. The dotted horizontal line gives the system noise floor for $T_{\text{sys}} = 2$ K from Eq. (3.2). These spectra have been measured with $P_{\text{read}} = -92$ dBm, with a resonator with $Q_i = 5.6 \times 10^5$ and $Q_c = 12 \times 10^3$.

where T_i is the effective output noise temperature of component i and G_i is its gain. To obtain the highest signal-to-noise ratio, the noise before the sample must be attenuated and the signal after the sample must be amplified with as little added noise as possible. For this we use the microwave chain as shown in Fig. 3.2. At the input side of the sample, the microwave signal is attenuated on each temperature stage to minimize thermal noise. DC blocks are added to help thermalize the cold wires and to prevent low frequency ground loops [12]. With the variable attenuators on the input and output, the microwave readout power at the sample, P_{read} , can be set, while keeping the power at the ADC approximately constant. At the output side of the sample, the signal is amplified by a cold low-noise amplifier at the 4 K stage, with noise temperature of ~ 1.8 K. The cables before this amplifier are superconducting, such that $G = 1$ and these components do not add noise. The 4 K amplifier dominates the system noise floor, since it is added just after the sample. The signal is further amplified at room temperature, before it is mixed with the original signal and digitized with the ADC. The total noise temperature of this setup is $T_{\text{sys}} = 2.7$ K [1]. This can be translated to a noise power spectral density in amplitude or phase as [12],

$$S_{\text{sys}}(\omega) = \frac{k_B T_{\text{sys}}}{r_c^2 P_{\text{read}}}, \quad (3.2)$$

where $r_c = Q/(2Q_c)$ is the radius of the resonance circle (see Fig. 2.9). The 1 dB attenuators after the sample are added to prevent reflections from the amplifier. They do however increase the noise floor significantly. When these are removed,

the system noise is reduced to ~ 2 K [1]. Figure 3.3 shows a measurement of the noise power spectral density in amplitude and phase, both on (dashed lines) and off resonance (solid lines). The 1 dB attenuators are removed in this measurement. The white noise floor is dominant at high frequencies (> 1 kHz) and corresponds to a system noise temperature of approximately $T_{\text{sys}} \approx 2$ K. At lower frequencies, the $1/f$ -noise dominates. The system noise $1/f$ visible in the off-resonance spectrum is generated at the input side of the sample. It is therefore attenuated by the resonator when on resonance. Specifically, from Eq. (2.30), we see that it is attenuated by, $S_{21,\text{min}} = Q/Q_i$ which is -33 dB for the resonator used in Fig. 3.3. Therefore, on resonance (dashed lines), TLS noise dominates the low frequency part (Section 2.2.4). At intermediate frequencies ($100 \text{ Hz} < f < 20 \text{ kHz}$) either generation-recombination noise (Section 2.3.1) or photon noise (Section 2.3.2) dominates, which shows a roll-off with the quasiparticle lifetime, τ_{qp}^* , around $1/(2\pi\tau_{\text{qp}}^*) \approx 20$ kHz. For higher frequencies, the system white noise floor dominates.

The microwave coax cables used in this setup can introduce high frequency photons into the box-in-box setup and induce stray light and elevated electron temperatures in the sample [4]. Adequate filtering is therefore necessary. In Section 5.E, we will analyze the effect of pair-breaking photons originating as thermal radiation from the attenuators on warmer stages and from the signal generator on the quasiparticle density in the resonator. We will find that the effects are negligible for the setup used.

3.2 FABRICATION

The samples are created via sputter deposition and standard contact-lithography patterning techniques. The microwave resonators are designed in a co-planar waveguide (CPW) geometry, as introduced in Section 2.2. This geometry is chosen because it is relatively simple to fabricate: it can be realized with deposition, pattern and etching only one layer. However, as we increase the sensitivity to excitations by using a hybrid microwave resonator, we require one more layer. In addition, we only want to excite the differential mode of the CPW (see Fig. 2.6). We therefore add bridges to the through-line that connect the two ground planes on either side of the central line. This brings the number of layers to three. The fabrication of these three layers is shown in Fig. 3.4(a), (b) and (c).

Before initial deposition of the first layer (NbTiN), the wafer is cleaned with Piranha ($\text{H}_2\text{SO}_4:\text{H}_2\text{O}_2$ (3:1), at 95°C for 10 minutes) and oxides are removed with a dilute (10%) HF solution (10 seconds). Then, the NbTiN is sputter deposited until a typical thickness of 150 nm has been reached. A shuttle deposition and rectangular NbTi target is used to enhance the uniformity of the film [13]. Then, a photo-resist (ECI3012) is spun, exposed with a hard contact mask (aligned with a Karl Suss MA6 mask aligner) and developed (with 17% AZ351B). The NbTiN film is etched with an SF_6 reactive ion etch (RIE), with additional oxygen for an isotropic etch. This results in a sloped edge of the NbTiN for 60 degrees to facilitate galvanic contact with the Al layer later (see Fig. 3.4(a)). After the RIE etch, an oxygen plasma is used to remove reactants and to ease the removing of the resist, which is done with AZ 100 remover

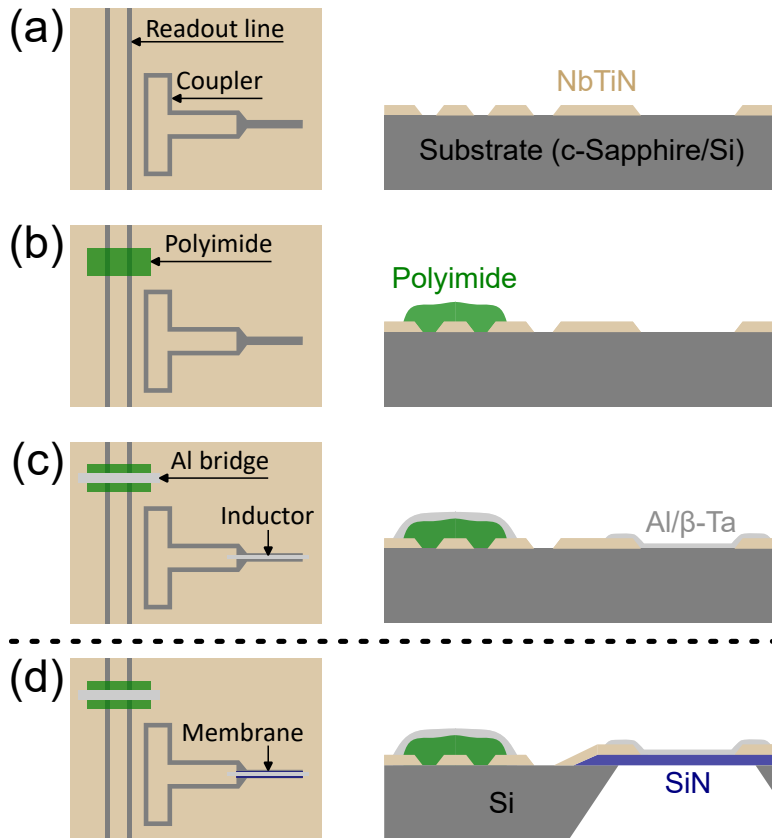


Figure 3.4: Overview of the fabrication of the devices. **(a)**: NbTiN is deposited and etched on a silicon or c-sapphire wafer. **(b)**: Polyimide is deposited and patterned to form a bridge over the through-line. **(c)**: The lower-gap superconductor (either Al or β -Ta) is deposited and patterned as the inductive section of the hybrid resonator and as top section of the bridge to connect the ground planes. **(d)**: Optionally, this process is performed on a Si wafer with a 150 nm thick SiN dielectric, which is first patterned to form patches under the inductive sections. After the processing steps ((a), (b) and (c)), the backside of the Si wafer is etched away with KOH, to form a SiN membrane under the inductive section.

and acetone.

For the second layer, polyimide (LTC9305) is spin-coated on the wafer and baked at 100°C for 3 minutes. This layer is exposed, developed (with HTRD2), cleaned with an oxygen plasma and cured in a vacuum oven (at 20 mbar at N₂) with a 250°C bake for 3 hours. The result is sketched in Fig. 3.4(b).

For the last layer, the wafer is cleaned with an oxygen plasma and surface oxides are removed with dilute (10%) HF, to ensure galvanic contact between the NbTiN and the lower-gap superconductor. Then, the lower-gap superconductor is sputter deposited, while shuttling the wafer, to a typical thickness of 40 nm. For β -Ta, this

layer is patterned in the same way as the NbTiN layer. For Al, the wafer is baked at 110°C for two minutes to remove remnant water, and (AZ 1518) resist is spin-coated on the wafer. The resist is patterned, developed (AZ developer) and hard baked at 125°C for 75 seconds. Then, the wafer is cleaned with an oxygen plasma for 15 seconds, before the Al is wet-etched. The resist is removed with acetone. The result is sketched in Fig. 3.4(c).

Finally, the wafer is spin-coated with resist (AZ 6632) and soft baked (110°C for two minutes) for protection, and the individual chips on the wafer are diced.

Optionally, the lower-gap superconducting inductive section is suspended on a membrane (Fig. 3.4(d)). To this end, the process is performed on a Si wafer with a 150 nm thick SiN dielectric layer on both sides, deposited using low pressure chemical vapor deposition (LPCVD) with a Si rich, low tensile stress (~ 150 MPa) recipe. These layers are first patterned with a similar process as the NbTiN etch. This forms SiN patches with sloped edges, that are located under the inductive sections on the front side, and an etch mask on the backside for the later KOH etch. After the processing of the three layers described above (NbTiN, polyimide, and Al/ β -Ta), the individual chips are placed in a holder that allows contact with a solution only on one side of the chip. Parts of the Si wafer are etched from the back side with KOH (25%, at 75°C), until the SiN layer on the front side has been reached. Leftover particles of the Si are removed with RCA2/SC2 at 70°C for 10 minutes.

3.3 MEASUREMENTS

The basic measurement we want to perform is to excite the inductive section of the superconducting resonator and interpret the change in transmission of the resonator in terms of this excitation. To interpret the change in transmission in terms of superconductor excitations, we need to know some basic properties of the superconductor and resonator. The superconductor is characterized with a DC measurement, which we will set out first. The resonator is characterized with an S_{21} measurement which we will treat in Section 3.3.2. After that, we will explain the excitation measurements of thermal excitations (generation-recombination noise described in Section 2.3.1) and a single photon excitation as described in Section 2.3.2.

3.3.1 DC MEASUREMENT

In order to characterize a superconductor in the BCS framework (Sections 2.1.2 and 2.1.3), the critical temperature, T_c , normal state resistivity, ρ_N , (single spin) density of states at the Fermi level, N_0 and Fermi wave number, k_F are sufficient. With these parameters, all electronic length scales can be calculated (penetration depth, λ , coherence length ξ and mean free path, l), which set the disorder and dimensionality regimes for electrons (Section 2.4). To characterize the electron-phonon interactions, the phonon velocities (transverse, c_T and longitudinal, c_L) and mass density, $\hat{\rho}$, are needed as well.

The critical temperature and normal state resistivity are measured in a DC measurement. These values can change significantly per fabrication run, depending

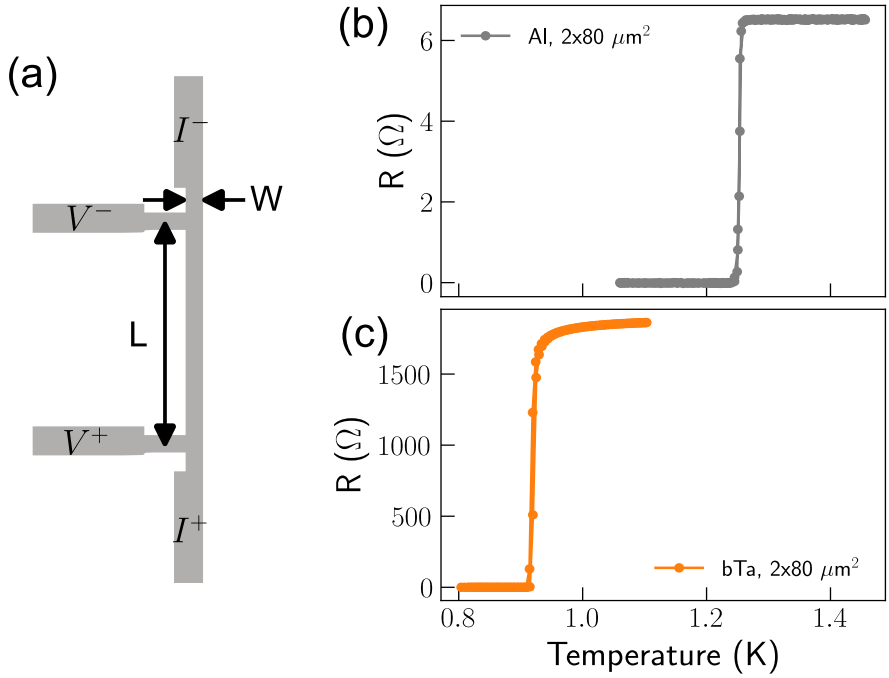


Figure 3.5: DC measurement for normal state resistivity and critical temperature. **(a)**: Structure used for 4-point probe measurements. The resistance is measured as the voltage difference ($V^+ - V^-$) divided by the induced current (from I^+ to I^-), over a strip with length L and width W . **(b)** and **(c)**: Resulting two-way resistance curves versus bath temperature for Al **(b)** and β -Ta **(c)**, for strips with $(W \times L) = 2 \times 80 \mu\text{m}^2$.

on type of substrate, substrate condition, etch type, resist type, previous and subsequent fabrication steps (such as resist baking, stripping, surface cleaning etc.) and more. We therefore measure T_c and ρ_N for each fabrication run, with a dedicated DC sample on the same wafer. The phonon parameters (c_T , c_L and $\hat{\rho}$) and Fermi surface parameters (N_0 and k_F), we typically get from literature (Refs. [14, 15] for β -Ta and Refs. [16, 17] for Al).

Figure 3.5(a) shows the structure that is used for the DC measurement. This is a 4-point probe structure, that uses separate leads for voltage measurements and current excitations to eliminate contact resistances. We measure the resistance with a Lakeshore 372 AC resistance bridge. The DC sample is mounted on a separate stage that is weakly thermally connected to the mixing chamber. It has a temperature sensor and resistor mounted to it to measure and control the temperature of the sample. We sweep the temperature up and down and record the resistance of the 4-point probe structure at each temperature. An example of the results are shown in Fig. 3.5(b) and (c) for Al and β -Ta. By doing a two-way measurement (temperature going up and down), we measure the hysteresis induced by Joule heating due to the

current excitation in the normal state. In Fig. 3.5(b) and (c) these curves overlap and this effect is minimized.

We extract the normal state resistance, R_N from these curves as the maximum. The resistance per square is given by $R_{\square} = R_N W/L$, where L is the strip length and W is the strip width (see Fig. 3.5(a)). The normal state resistivity is found by $\rho_N = R_{\square} d$, with d the film thickness. We extract T_c as the temperature where the resistance is half that of the normal state resistance: $R(T_c) = R_N/2$. With these values, we have the basic characteristics of the superconductor.

Ideally, we would measure the Fermi surface parameters (N_0 and k_F) and phonon parameters (c_T , c_L and $\hat{\rho}$) as well, since these also are likely to vary for each fabrication run. Unfortunately, we do not have such capabilities in our lab. We did however conduct measurements on β -Ta for N_0 and k_F in collaboration with the Jan Aarts group in Leiden University. With the capability to measure 4-point probe structures in a magnetic field of a few Tesla, N_0 and k_F can be extracted from an upper critical field measurement versus temperature ($H_{c2}(T)$) and a Hall resistance measurement versus magnetic field ($R_{\text{Hall}}(B)$). These measurements are detailed in Chapter 6.

3.3.2 S_{21} MEASUREMENT

In order to relate the change in transmission to the properties of the excitations in the superconducting inductive section, we must characterize the resonator with respect to these excitations. For quasiparticle excitations, this comes down to knowing the amplitude and phase responsivities to quasiparticle changes; i.e., $d(\delta A)/dn_{\text{qp}}$ and $d\theta/dn_{\text{qp}}$ given in Eq. (2.36). To this end, we measure the change in resonance frequency and internal quality factor when changing the bath temperature. Then, we relate this to the change in quasiparticle density when changing the bath temperature from Eq. (2.17). The responsivities are found this way by,

$$\frac{d(\delta A)}{dn_{\text{qp}}} = 2Q(T) \frac{d(1/Q_i)(T)}{dn_{\text{qp}}(T)}, \quad (3.3a)$$

$$\frac{d\theta}{dn_{\text{qp}}} = -4Q(T) \frac{d(\delta\omega_0/\omega_0)(T)}{dn_{\text{qp}}(T)}. \quad (3.3b)$$

We measure $Q(T)$, $(1/Q_i)(T)$ and $(\delta\omega_0/\omega_0)(T)$ in the S_{21} measurement. $n_{\text{qp}}(T)$ is taken from Eq. (2.17) with the material parameters from the DC measurement.

From Eq. (3.3), we see that we need the quality factors and resonance frequency versus temperature. To obtain this, we measure the (calibrated) forward transmission versus frequency at different bath temperatures. An example of this measurement is given in Fig. 3.6(a). To extract the resonance frequency and quality factors we fit a Lorentzian resonance curve (Eq. (2.30)) to the data. This is shown for the lowest temperature curve as the gray dashed line in Fig. 3.6(a). The resulting quality factors and resonance frequencies versus temperature are shown in Fig. 3.6(b) and (c). From the high temperature data (usually $T > T_c/5$) we determine the last factors in Eq. (3.3), such that the changes in Q_i and ω_0 are dominated by quasiparticle changes and not by TLS (Section 2.2.4) or other effects.

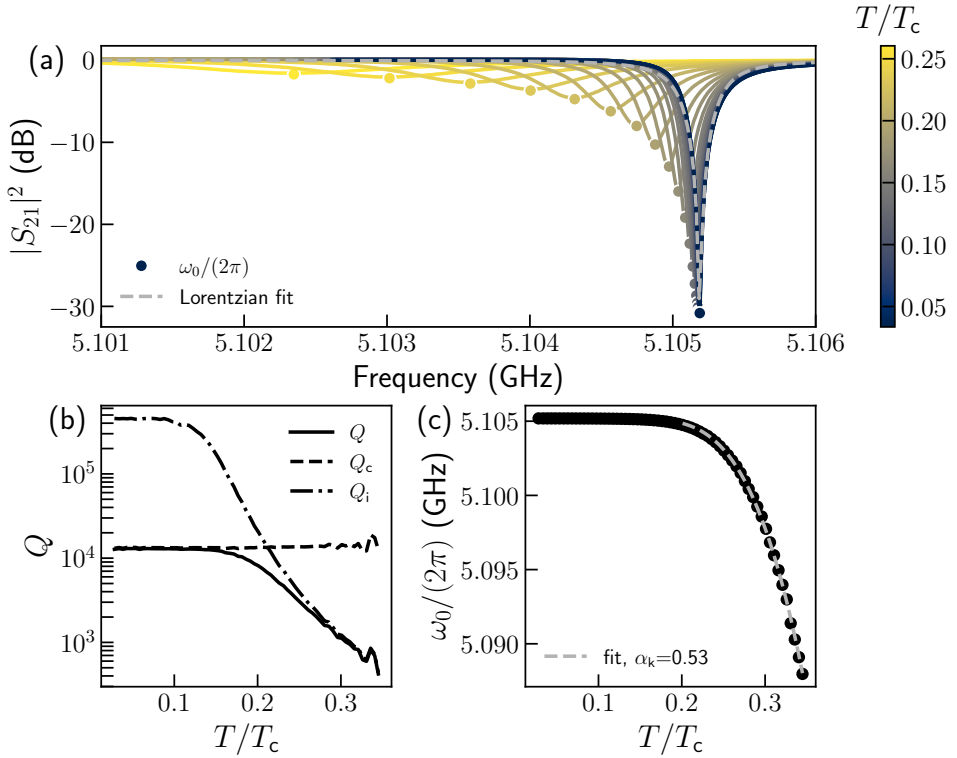


Figure 3.6: An example for an S_{21} measurement with extracted parameters. (a): The magnitude squared of the forward transmission versus frequency. Each curve is for a different bath temperature, as indicated by the color. Half of the measured curves and the highest temperature points are left out for visibility. The gray dashed line is a fit to Eq. (2.30) for the lowest temperature point. From this fit, the Q factors and resonance frequency are extracted. (b): Q factors extracted from each fit versus temperature. (c): Resonance frequency extracted from each fit. The gray dashed line gives a fit to Eq. (3.4), to extract the kinetic inductance fraction.

The responsivity factors from Eq. (3.3) give us the ability to translate the measured δA and θ to changes in quasiparticle density in the superconductor. For large excitations, we can use these factors in combination with the $(\mathcal{R}, \mathcal{X})$ -coordinates introduced in Section 2.2. As long as the resonator Q factor does not change during the excitation and the superconductor does not enter a non-linear regime (i.e., the effective quasiparticle temperature stays below $T_{\text{eff}} \lesssim T_c/2$), this will correctly predict the quasiparticle change in the superconductor.

Kinetic inductance fraction The S_{21} measurement gives us the quality factors (Q_i and Q_c) and resonance frequency (ω_0) versus temperature. Apart from the responsivity (Eq. (3.3)), we can also extract the kinetic inductance fraction, α_k ,

from this. Since $\omega_0 \propto 1/\sqrt{L_k/\alpha_k}$, an increase in temperature induces a decrease in resonance frequency via⁴,

$$\left(\frac{L_k(T)}{L_{k0}} - 1\right)\alpha_k = \left(\frac{\omega_{00}}{\omega_0(T)}\right)^2 - 1, \quad (3.4)$$

where ω_{00} and L_{k0} are the original (low temperature) values and $\omega_0(T)$ and $L_k(T)$ are the new (higher temperature) values. When $\sigma_1 \ll \sigma_2$ (i.e., $\hbar\omega < 2\Delta$ and $T \lesssim 0.9T_c$ see Fig. 2.4) and in the dirty limit, the kinetic inductance is proportional to $L_k \propto \lambda_{\text{eff}} \coth(d/\lambda_{\text{eff}})$, with $\lambda_{\text{eff}} = 1/\sqrt{\mu_0\omega(T)\sigma_2(T)}$ (see Section 2.1.3). We calculate $\sigma_2(T)$ from the Mattis-Bardeen equations (Eq. (2.20)) and take the angular frequency in this expression as the measured resonance frequency, $\omega(T) = \omega_0(T)$. Then, we obtain α_k from a fit to Eq. (3.4). An example is shown in Fig. 3.6(c) as the dashed gray line.

In the thin film, local limit, and taking only first order changes in ω_0 and σ_2 , Eq. (3.4) becomes,

$$\frac{\delta\omega_0(T)}{\omega_{00}} = \frac{\alpha_k}{2 - \alpha_k} \frac{\delta\sigma_2(T)}{\sigma_{20}}, \quad (3.5)$$

with σ_{20} the low temperature value of σ_2 .

3.3.3 NOISE MEASUREMENT

To study the quasiparticle fluctuations (generation-recombination noise [18], see Section 2.3.1), we measure time traces of δA and θ . These are shown in blue in Fig. 3.7(a) and (b). We subtract a second order polynomial fit to correct for drift. To eliminate the effect of cosmic rays [19, 20] and radioactivity [21], we split the time stream in 32 segments and reject segments that contain points above 6 times the minimal standard deviation of all the segments (see Fig. 3.7(a) and (b)). For each remaining segment, we estimate the power spectral density from a periodogram with a Hamming window (Wiener-Khinchin theorem), which we then average. To reduce data size, we measure two time streams, one with 50 kHz sample frequency and one with 1 MHz sample frequency, and stitch⁵ the two resulting spectra at 20 kHz. Finally, the spectra are down-sampled to contain 30 points per decade for visibility. This results in a noise power spectral density for amplitude and phase, as shown in Fig. 3.7(c). In addition, we compute the cross power spectral density in the same manner. When generation-recombination noise is clearly visible in both amplitude and phase spectra, the real, negative part of the cross power spectral density gives an accurate estimate of the generation-recombination noise, since a generation or recombination event changes the dissipation (δA) and kinetic inductance (θ) simultaneously [22]. The cross power spectral density, $S_{\delta A, \theta}(\omega)$ is also shown in Fig. 3.7(c) as the green curve.

⁴We denote α_k here as the low temperature limit of the kinetic inductance fraction, $\alpha_k = L_{k0}/L_{\text{tot}}$. When the central line of the inductive section is a lower T_c material (Fig. 2.11), this method gives the kinetic inductance fraction of that section, $\alpha_k = \alpha_{k0}^1 = L_{k0}^1/L_{\text{tot}}$.

⁵To optimize the frequency information in the resulting spectrum, we use Welch's method with a Hamming window of length 10 μs when computing the individual spectra of the high frequency segments, instead of a periodogram.

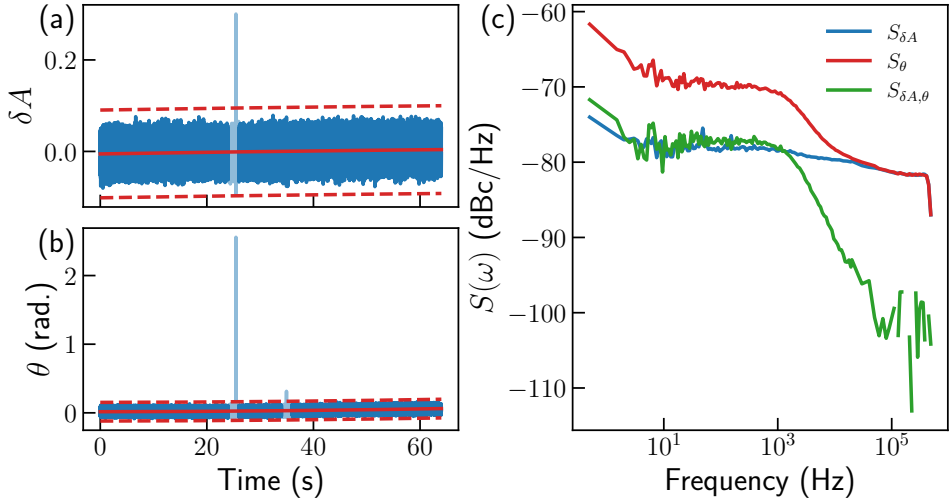


Figure 3.7: Noise power spectral density measurement. **(a)** and **(b)**: Time traces of amplitude (a) and phase (b) at 50 kHz sample speed for an Al device as presented in Chapter 4. The solid red line gives a second order polynomial fit that is subtracted from the data. The dashed red lines give the threshold for rejection of the data segment. If the segment is rejected, it is shown in light blue. **(c)**: Resulting power spectral densities for amplitude, phase and cross correlations (the negative values for the real part), as indicated by the legend.

Together with the quasiparticle responsivities, Eq. (3.3), these spectra can be fitted with Eq. (2.62) to extract the quasiparticle density, n_{qp} , and effective recombination time τ_{qp}^* . This is the basis of the measurements presented in Chapters 4 to 6. A measurement of the resonator response to an incoming photon flux is similar. Instead of the dark environment used in the noise measurement, a black body radiator is mounted on the 4 K stage and heated to achieve a desired radiation power. With a proper filter stack in between the black body and the sample, a frequency for the incoming can be selected (see also Section 3.1.1).

3.3.4 SINGLE PHOTON PULSE MEASUREMENT

Apart from thermal fluctuations (i.e., phonon excitations) and THz radiation (i.e., low frequency photon excitations), we can also excite the superconductor with shorter wavelength photons (few μm to 402 nm). To this end, we either use the fiber mount and collimator on the sample stage (see gray text in Fig. 3.1) or we use a light source from outside such as a monochromator and windows in each shield (Fig. 3.1). These shorter wavelength photons have enough energy to produce a measurable pulse excitation in the resonator. The decay time and pulse shape give information on the relaxation of the excess quasiparticle density in the superconductor (see Section 2.3.2).

To measure the single photon pulse response, we illuminate the sample with a

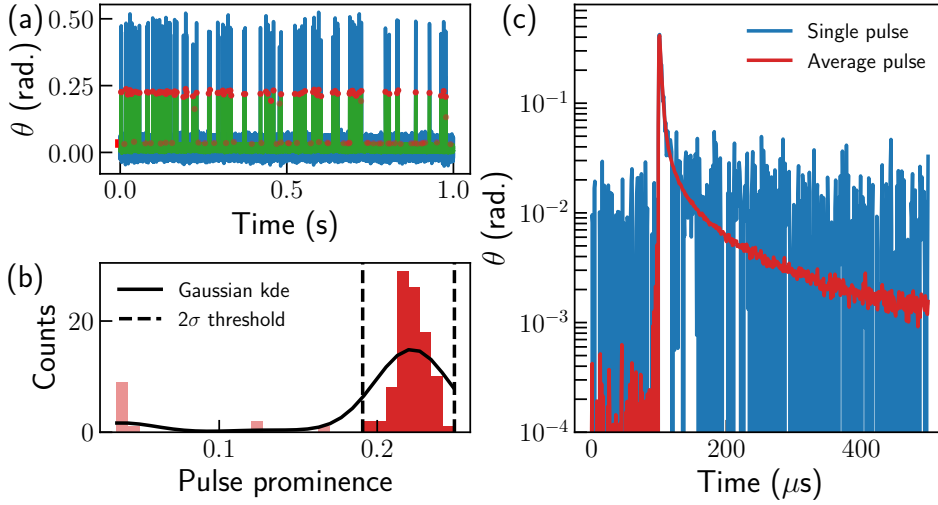


Figure 3.8: Single photon pulse measurement via pulse detection and averaging. **(a)**: Time stream of phase which includes many single photon pulses. Blue is the raw data and green is the filtered data with a moving average with a window of 10 samples. The red dots indicate the identified pulses via a prominence method. The minimum prominence is set to 7 times the estimated standard deviation of the noise and is indicated by the red bar on the left. The transparent red dots indicate pulses that are excluded from the average. **(b)**: Histogram of the prominence of the identified pulses. A Gaussian kernel density estimate (KDE) is shown as the solid black line. The dashed vertical lines give the maximum and minimum prominence for the pulses to be used in the average, which is chosen to be two times the standard deviation of the Gaussian distribution with the highest KDE. The data outside of this range is not used for the average and shown as transparent red bars. **(c)**: Resulting average single photon pulse in red. In blue, a single photon pulse is shown for comparison.

continuous source of a single wavelength. We attenuate the power to about 100 photons per second, such that there are not so many overlapping pulses. We record amplitude (δA) and phase (θ) data with a sampling frequency of 1 MHz. This sampling frequency must be larger than twice the resonator ring time, τ_{res} in Eq. (2.74), to be able to determine the photon arrival time with an uncertainty that is better than 1 sample. To capture the height of the pulse accurately, the sample frequency must be larger than the decay time, just after photon absorption. From Fig. 2.17, we see that this decay time can be significantly faster than τ_{qp}^* , when the equilibrium quasiparticle density is much smaller than the excess quasiparticle density induced by the photon. Typically, we record 40 separate time streams of one second to limit read and write time of the data. An example of such a one-second time stream of phase data is shown in blue in Fig. 3.8(a). The blue data in Fig. 3.8(c) is a single photon pulse extracted from this data.

To increase the signal-to-noise ratio of the single photon pulse, we average hundreds of them. Since this averaging process can induce biases in the resulting

single photon pulse (for example, a longer decay time due to overlapping pulses or a longer rise time due to misalignment of individual pulses in time), we select the pulses for the final average in several steps. First, we detect all significant pulses in the phase data stream by applying a moving average with a window size of approximately $\tau_{qp}^*/10$ and using the *find_peaks* function from the *scipy.signal* module with the prominence option⁶. We set the prominence threshold to 7 times the standard deviation of the noise. We estimate the standard deviation of the noise as the difference between the 16th and 50th percentile of the data stream. That is, we assume Gaussian distributed noise and look at the lower half of the data to estimate the width of the distribution. The moving average of the data and identified pulses are shown in Fig. 3.8(a) as the green curve and red dots. The prominence threshold is shown as the red bar on the left.

To select single photon pulses only, we disregard pulses that have a distance to neighboring pulses that is smaller than the pulse window of the final average. This pulse window is set to approximately 10 times τ_{qp}^* . About 20% of this pulse window is used for capturing the noise just before the photon arrival. In the example of Fig. 2.17, the pulse window is 500 μs and the duration of the noise before the pulse is 100 μs . Once we have selected only single pulses in this pulse window, we select the single photon pulses by looking at the prominence of the individual pulses. We make a histogram of all the found prominences and set an upper and lower limit to it of two times the standard deviation of the maximal likely Gaussian distribution. This is shown in Fig. 3.8(b).

Finally, we align all the pulses in time (x-axis) by the pulse start, which we identify by the point with the maximum increase in phase after one τ_{res} (Eq. (2.74)). This way, the pulses are aligned on the time point τ_{res} after the photon is absorbed. We align the pulses in phase (y-axis) by subtracting the average of the data in the pulse window that is more than 5 times τ_{res} earlier than the pulse start. We average all selected and aligned pulses to obtain the single photon pulse with a higher signal-to-noise ratio. This average pulse is shown in orange in Fig. 3.8(c).

This method is used in Chapter 7 to study the non-equilibrium quasiparticle dynamics after photon absorption in the disordered superconductor $\beta\text{-Ta}$.

⁶Prominence is a measure of how much one data point stands out from its surrounding data points. See [23] for a definition.

REFERENCES

- [1] K. Kouwenhoven. *Visible to Near-Infrared Kinetic Inductance Detectors*. PhD thesis. Delft: Delft University of Technology, 2024.
- [2] *SD Dilution Refrigerator Measurement System*. Bluefors.com. 2024. URL: <https://bluefors.com/products/dilution-refrigerator-measurement-systems/sd-dilution-refrigerator-measurement-system/>.
- [3] P. J. de Visser. *Quasiparticle Dynamics in Aluminium Superconducting Microwave Resonators*. PhD thesis. Delft: Delft University of Technology, 2014. 222 pp.
- [4] J. J. A. Baselmans, S. J. C. Yates, P. Diener, and P. J. de Visser. *Ultra Low Background Cryogenic Test Facility for Far-Infrared Radiation Detectors*. In: *Journal of Low Temperature Physics* 167.3 (2012), pp. 360–366.
- [5] R. Barends, J. Wenner, M. Lenander, Y. Chen, R. C. Bialczak, J. Kelly, E. Lucero, P. O'Malley, M. Mariani, D. Sank, H. Wang, T. C. White, Y. Yin, J. Zhao, A. N. Cleland, J. M. Martinis, and J. J. A. Baselmans. *Minimizing Quasiparticle Generation from Stray Infrared Light in Superconducting Quantum Circuits*. In: *Applied Physics Letters* 99.11 (2011), p. 113507.
- [6] C. Song, T. W. Heitmann, M. P. DeFeo, K. Yu, R. McDermott, M. Neeley, J. M. Martinis, and B. L. T. Plourde. *Microwave Response of Vortices in Superconducting Thin Films of Re and Al*. In: *Physical Review B* 79.17 (2009), p. 174512.
- [7] B. G. Survey. *An Overview of the Earth's Magnetic Field*. 2020. URL: http://www.geomag.bgs.ac.uk/education/earthmag.html#_Toc2075549.
- [8] A. L. Fetter and P. C. Hohenberg. *The Mixed State of Thin Superconducting Films in Perpendicular Fields*. In: *Physical Review* 159.2 (1967), pp. 330–343.
- [9] M. Tinkham. *Effect of Fluxoid Quantization on Transitions of Superconducting Films*. In: *Physical Review* 129.6 (1963), pp. 2413–2422.
- [10] W. Ras. In: (2025).
- [11] H. Nyquist. *Thermal Agitation of Electric Charge in Conductors*. In: *Physical Review* 32.1 (1928), pp. 110–113.
- [12] R. Barends. *Photon-Detecting Superconducting Resonators*. Delft: Delft University of Technology, 2009.
- [13] D. J. Thoen, B. G. C. Bos, E. A. F. Haalebos, T. M. Klapwijk, J. J. A. Baselmans, and A. Endo. *Superconducting NbTiN Thin Films With Highly Uniform Properties Over a 100 Mm Wafer*. In: *IEEE Transactions on Applied Superconductivity* 27.4 (2017), pp. 1–5.

- [14] M. Magnuson, G. Greczynski, F. Eriksson, L. Hultman, and H. Högberg. *Electronic Structure of β -Ta Films from X-ray Photoelectron Spectroscopy and First-Principles Calculations*. In: *Applied Surface Science* 470 (2019), pp. 607–612.
- [15] G. Abadias, J. J. Colin, D. Tingaud, Ph. Djemia, L. Belliard, and C. Tromas. *Elastic Properties of α - and β -Tantalum Thin Films*. In: *Thin Solid Films* 688 (2019), p. 137403.
- [16] S. B. Kaplan, C. C. Chi, D. N. Langenberg, J. J. Chang, S. Jafarey, and D. J. Scalapino. *Quasiparticle and Phonon Lifetimes in Superconductors*. In: *Physical Review B* 14.11 (1976), pp. 4854–4873.
- [17] S. B. Kaplan. *Acoustic Matching of Superconducting Films to Substrates*. In: *Journal of Low Temperature Physics* 37.3 (1979), pp. 343–365.
- [18] P. J. de Visser, J. J. A. Baselmans, P. Diener, S. J. C. Yates, A. Endo, and T. M. Klapwijk. *Number Fluctuations of Sparse Quasiparticles in a Superconductor*. In: *Physical Review Letters* 106.16 (2011), p. 167004.
- [19] K. Karatsu, A. Endo, J. Bueno, P. J. de Visser, R. Barends, D. J. Thoen, V. Murugesan, N. Tomita, and J. J. A. Baselmans. *Mitigation of Cosmic Ray Effect on Microwave Kinetic Inductance Detector Arrays*. In: *Applied Physics Letters* 114.3 (2019), p. 032601.
- [20] E. Yelton, C. P. Larson, V. Iaia, K. Dodge, G. La Magna, P. G. Baity, I. V. Pechenezhskiy, R. McDermott, N. A. Kurinsky, G. Catelani, and B. L. T. Plourde. *Modeling Phonon-Mediated Quasiparticle Poisoning in Superconducting Qubit Arrays*. In: *Physical Review B* 110.2 (2024), p. 024519.
- [21] L. Cardani, F. Valenti, N. Casali, G. Catelani, T. Charpentier, M. Clemenza, I. Colantoni, A. Cruciani, G. D’Imperio, L. Gironi, L. Grünhaupt, D. Gusenkova, F. Henriques, M. Lagoin, M. Martinez, G. Pettinari, C. Rusconi, O. Sander, C. Tomei, A. V. Ustinov, M. Weber, W. Wernsdorfer, M. Vignati, S. Pirro, and I. M. Pop. *Reducing the Impact of Radioactivity on Quantum Circuits in a Deep-Underground Facility*. In: *Nature Communications* 12.1 (1 2021), p. 2733.
- [22] P. J. de Visser, J. J. A. Baselmans, S. J. C. Yates, P. Diener, A. Endo, and T. M. Klapwijk. *Microwave-Induced Excess Quasiparticles in Superconducting Resonators Measured through Correlated Conductivity Fluctuations*. In: *Applied Physics Letters* 100.16 (2012), p. 162601.
- [23] *Peak_prominences — SciPy v1.16.0 Manual*. URL: https://docs.scipy.org/doc/scipy-1.16.0/reference/generated/scipy.signal.peak_prominences.html.

4

STRONG REDUCTION OF QUASIPARTICLE FLUCTUATIONS IN A SUPERCONDUCTOR DUE TO DECOUPLING OF THE QUASIPARTICLE NUMBER AND LIFETIME

We measure temperature dependent quasiparticle fluctuations in a small Al volume, embedded in a NbTiN superconducting microwave resonator. The resonator design allows for read-out close to equilibrium. By placing the Al film on a membrane, we enhance the fluctuation level and separate quasiparticle from phonon effects. When lowering the temperature, the recombination time saturates and the fluctuation level reduces a factor ~ 100 . From this we deduce that the number of free quasiparticles is still thermal. Therefore, the theoretical, inverse relation between quasiparticle number and recombination time is invalid in this experiment. This is consistent with quasiparticle trapping, where on-trap recombination limits the observed quasiparticle lifetime.

This chapter was published as S. A. H. de Rooij, J. J. A. Baselmans, V. Murugesan, D. J. Thoen, and P. J. de Visser. *Strong Reduction of Quasiparticle Fluctuations in a Superconductor Due to Decoupling of the Quasiparticle Number and Lifetime*. In: *Physical Review B* 104.18 (2021), p. L180506.

4.1 INTRODUCTION

In a superconductor well below its critical temperature, most electrons are bound together in Cooper pairs, while the number of unpaired electrons, quasiparticles, exponentially decreases with decreasing temperature. The recombination time of quasiparticles is inversely proportional to the quasiparticle number and therefore increases exponentially towards lower temperature. At a constant, finite temperature, the quasiparticle number fluctuates around its average value due to random generation and recombination events [2]. In Ref. [3], a measurement of these fluctuations showed that the quasiparticle number and recombination time are indeed inversely proportional, and as a consequence the quasiparticle fluctuation level is *constant* as a function of temperature. Both observations are consistent with direct recombination of free quasiparticles with emission of a phonon [4], see Fig. 4.1(a). Also in the presence of excess quasiparticles at low temperature, which often occur in superconducting devices in varying conditions [5–10], the relation between the number of quasiparticles and their recombination time is maintained [3].

In this chapter we show experimentally that the intimate relation between the free quasiparticle number and recombination time is broken when quasiparticles are first trapped and then recombine as depicted in Fig. 4.1(b).

Impurities and disorder in superconductors are known to reduce the recombination time at low temperatures [11, 12] and can fundamentally change the relation between quasiparticle number and recombination time. The low-temperature recombination time is typically limited to tens of microseconds [12, 13] to milliseconds [3, 14], depending on the material. However, these experiments only measure the recombination time from a non-equilibrium pulse decay, or suffer from excess quasiparticles. Moreover, in tunnel junction devices, including qubits, only non-equilibrium, local quasiparticle properties can be measured directly. Understanding the reduced recombination time at low temperatures and close to thermal equilibrium, and in particular its relation to the quasiparticle density, has been hindered by the lack of a sensitive probe of quasiparticle dynamics.

We measure quasiparticle fluctuations in a small Al volume ($27 \mu\text{m}^3$), embedded in a NbTiN superconducting resonator. This design allows for read-out at low microwave

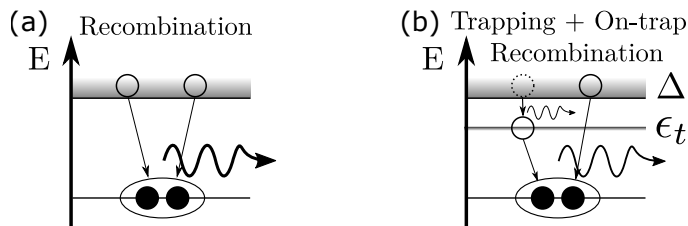


Figure 4.1: Schematic representations of simple recombination (a) and trapping with subsequent on-trap recombination (b) of two quasiparticles. Δ is the superconducting energy gap and ϵ_t the trap energy. Curved arrows represent emitted phonons, with thickness indicating their relative energy.

powers, minimizing the creation of excess quasiparticles [10]. By placing the Al volume on a membrane, we enhance the fluctuation level and separate quasiparticle from phonon effects.

We observe a strong reduction in the quasiparticle fluctuation level by a factor ~ 100 when lowering the bath temperature from 350 to 200 mK, together with a saturation of the recombination time. Hence, the inverse proportionality between quasiparticle number and recombination time must be broken, and the recombination time is not limited by excess quasiparticles as we observed before [3, 10]. Together, our observations are in qualitative agreement with quasiparticle trapping and subsequent on-trap recombination.

Our methodology is well suited to better understand the quasiparticle dynamics in devices where quasiparticle trap structures [15, 16] and vortices [17] are introduced deliberately, to reduce the excess quasiparticle density in critical regions of a device.

4.2 METHODS

In thermal equilibrium and at low temperatures ($T \ll \Delta/k_B$), the number of quasiparticles in a superconducting volume V , is given by [18],

$$N_{\text{qp}}(T) = 2VN_0\sqrt{2\pi k_B T \Delta} e^{-\Delta/k_B T}, \quad (4.1)$$

where N_0 is the single spin density of states at the Fermi-level (we use $N_0 = 1.72 \times 10^4 \mu\text{eV}^{-1} \mu\text{m}^{-3}$, for Al), k_B is the Boltzmann constant and $\Delta = 1.76k_B T_c$ is the superconducting gap energy, with T_c the critical temperature. The intrinsic quasiparticle lifetime with respect to recombination (hereafter called 'the quasiparticle lifetime') is given by [4],

$$\tau_{\text{qp}}(T) = \frac{\tau_0 N_0 V (k_B T_c)^3}{2\Delta^2 N_{\text{qp}}(T)} = \frac{V}{RN_{\text{qp}}(T)}, \quad (4.2)$$

where τ_0 is a material dependent characteristic time for the electron-phonon coupling. For Al, we take $\tau_0 = 0.44 \mu\text{s}$ [4]. In the last equality, all the material dependent parameters are combined into the recombination constant, R .

In experiments, the relaxation of an ensemble of quasiparticles is typically probed. As the recombination of two quasiparticles into a Cooper-pair is a pair-wise process and the emitted phonon can subsequently break a Cooper-pair [19], the *apparent* quasiparticle lifetime is given by,

$$\tau_{\text{qp}}^* = \tau_{\text{qp}}(1 + \tau_{\text{esc}}/\tau_{\text{pb}})/2. \quad (4.3)$$

Here, τ_{esc} is the phonon escape time, τ_{pb} is the phonon pair-breaking time and the factor in parentheses is called *the phonon trapping factor*. Equation (4.3) is valid when, $\tau_{\text{esc}}, \tau_{\text{pb}} \ll \tau_{\text{qp}}$, which is typically the case [20]. We take $\tau_{\text{pb}} = 0.28\text{ns}$ for Al [4]. τ_{esc} can experimentally be tuned [21, 22], for instance with the use of a membrane, which we use here to distinguish phonon effects from intrinsic quasiparticle processes.

Fluctuations in the quasiparticle number occur randomly. Starting from a master

equation approach [2], the Power Spectral Density (PSD) of these fluctuations can be calculated to be,

$$S_{N_{\text{qp}}}(\omega) = \frac{4\tau_{\text{qp}}^* N_{\text{qp}}}{1 + (\omega\tau_{\text{qp}}^*)^2}. \quad (4.4)$$

This is a Lorentzian spectrum, with a constant level with temperature (since $\tau_{\text{qp}}^* \propto 1/N_{\text{qp}}$) and a roll-off frequency of $\omega = 1/\tau_{\text{qp}}^*$.

The device under study is shown in Fig. 4.2. Four NbTiN-Al hybrid [23] resonators are capacitively coupled to a read-out line patterned around them. The capacitive part is a NbTiN double-sided interdigitated capacitor (IDC)[24] and the inductive part is a NbTiN co-planar waveguide with an Al central line. For details see Section 4.A.

4

The resonator response is only sensitive to quasiparticle - Cooper-pair fluctuations within the Al ($V = 27 \mu\text{m}^3$ and $T_c = 1.26$ K), as we measure at $T \ll T_{c,\text{NbTiN}} = 15.6$ K and the current density is much higher in the Al section due to the IDC design. Furthermore, as $\Delta_{\text{Al}} \ll \Delta_{\text{NbTiN}}$, quasiparticles are confined to the Al volume.

The resonators are mounted in a pulse tube pre-cooled adiabatic demagnetization refrigerator, surrounded by a CRYOPHY[®] and a superconducting magnetic shield, and isolated from stray light by a 'box-in-a-box' configuration [25]. The forward microwave transmission, S_{21} , is recorded at an on-chip read power, $P_{\text{read}} = -99$ dBm. In the following, we present the results for two resonators, of which one has its sensitive volume on a membrane and one on the substrate, see Fig. 4.2(c,d).

We translate the complex S_{21} to an amplitude (δA) and phase (θ) to distinguish changes in dissipation (δA) and kinetic inductance (θ). These variables are defined relative to the resonance circle, which is measured for each temperature before the fluctuation measurement. The responsivity is given by $dX/dN_{\text{qp}} = 2\alpha_k Q \kappa_X / V$, where X is either δA or θ and α_k is the fraction of kinetic inductance over the total inductance. κ_X describes the change in complex conductivity with respect to a change in quasiparticle density, which is only weakly dependent on temperature [26]. Q is the loaded quality factor and measured to be 4.3×10^4 and 3.5×10^4 at 50 mK, for the membrane and substrate resonator, respectively. The resonators are designed to have the same volume and kinetic inductance fraction.

We measure 40 s time streams at 50 kHz of δA and θ , at temperatures ranging from 50 to 400 mK. We filter pulses caused by cosmic rays [8] or other external sources and calculate the cross-PSD, $S_{\delta A, \theta}(\omega)$, as explained in detail in Section 3.3.3. By using the cross-PSD, we extract the dissipation - kinetic inductance (i.e., quasiparticle - Cooper-pair) fluctuations and suppress uncorrelated noise sources such as amplifier and TLS noise [10]. We determine the spectrum of the quasiparticle fluctuations via,

$$S_{N_{\text{qp}}}(\omega) = S_{\delta A, \theta} (1 + (\omega\tau_{\text{res}})^2)^{-1} \left(\frac{d\delta A d\theta}{dN_{\text{qp}}^2} \right)^{-1}, \quad (4.5)$$

where $\tau_{\text{res}} = Q/\pi f_0$ is the resonator ring time (f_0 is the resonance frequency), typically a few μs . This implies $(\omega\tau_{\text{res}})^2 \ll 1$ for frequencies below 100 kHz, and we therefore neglect this factor. The last factor in Eq. (4.5) is the multiplication of the amplitude and phase responsivities, which we determine from a measurement of

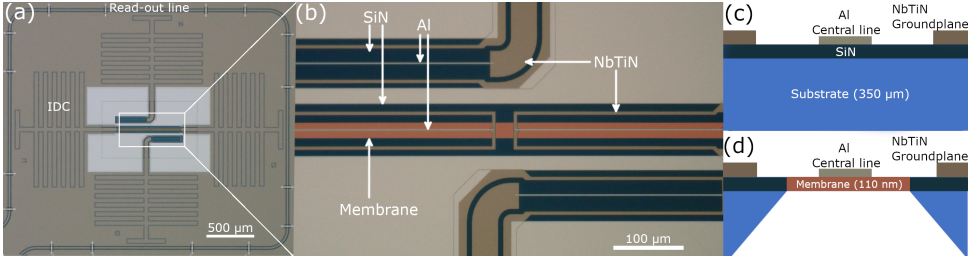


Figure 4.2: **(a)**: Micrograph of the resonators studied. **(b)**: Zoom-in on the Al inductive parts of the resonators, of which two are on a 110 nm thick SiN membrane (highlighted in orange). **(c,d)**: Schematic cross-sections (not to scale) of the inductive (Al) part of a substrate and membrane resonator, respectively. The CPW dimensions are such, that only the Al central line is suspended by the membrane.

$S_{21}(\omega; T)$, for $T > 250$ mK, see Section 4.E.

4.3 RESULTS AND DISCUSSION

The central result of this paper is presented in Fig. 4.3. Figures 4.3(a,b) show the measured cross-PSDs and Figures 4.3(c,d) show the extracted apparent quasiparticle lifetime and fluctuation level from Lorentzians fits to these spectra (Eq. (4.4)). For high temperatures (≥ 300 mK), we observe a higher level and τ_{qp}^* for the membrane resonator compared to the substrate resonator. This is expected from Eqs. (4.3) and (4.4), as the membrane effectively increases τ_{esc} . The dashed lines in Fig. 4.3(c,d) are fits to Eqs. (4.2) and (4.3) for temperatures ≥ 300 mK, with τ_{esc} as only free parameter, resulting in $\tau_{esc} = 5.6 \pm 0.4$ ns and 0.09 ± 0.02 ns for the membrane and substrate resonator respectively. These intervals only indicate uncertainties from the fitting procedure. Equivalently, the phonon trapping factors (Eq. (4.3)) are 21 and 1.3 from which we would expect a 12 dB higher fluctuation level for the membrane resonator. This is indeed observed in Fig. 4.3(d). The dashed lines give the expected level from Eq. (4.4), where the fitted τ_{esc} is used. A detailed analysis of the effects of the membrane on phonon statistics and energy resolution will be published elsewhere [27].

The fluctuation levels expected from Eq. (4.4) (dashed lines in Fig. 4.3(d)) are constant with changing temperature. In sharp contrast, we here observe a strongly decreasing level when lowering the temperature. At temperatures 190 mK, no Lorentzian spectrum (Eq. (4.4)) can be identified. The individual amplitude and phase PSDs show this behavior as well, see Section 4.B. As the responsivity factor in Eq. (4.5) is constant in this temperature range (Section 4.E), this result should be interpreted as a strong reduction of $S_{N_{qp}}$.

We calculate N_{qp} from $S_{N_{qp}}$ by dividing the level by $4\tau_{qp}^*$, which is shown in Fig. 4.4. The number of quasiparticles follows a thermal dependence for both the substrate and membrane resonator. Therefore, we conclude that the lifetime saturation is not

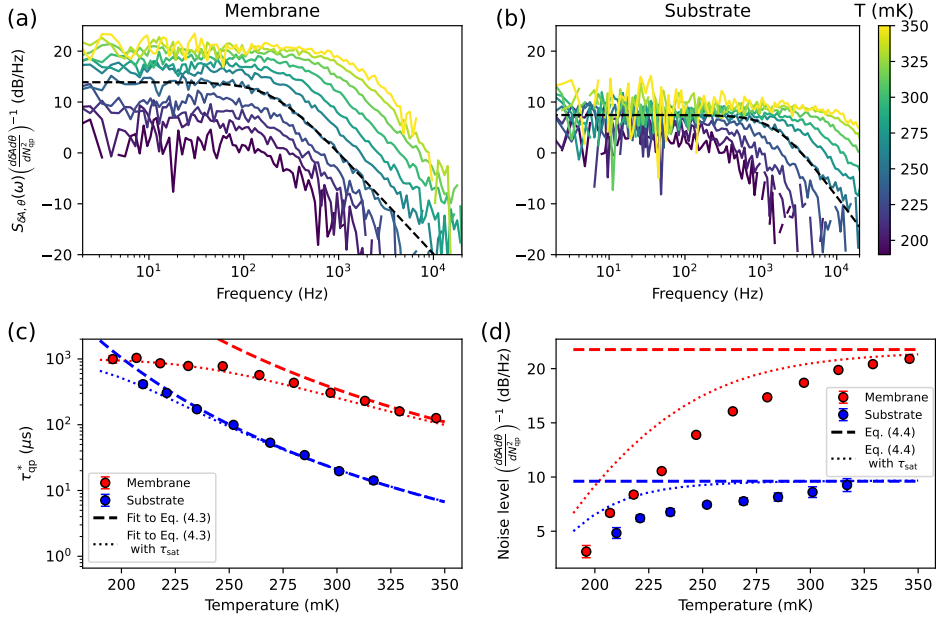


Figure 4.3: **(a, b)**: Measured quasiparticle fluctuations for a resonator on membrane (a) and on substrate (b). The quasiparticle fluctuations are determined from the measured cross-PSD, using the measured responsivities and Eq. (4.5). The measurements are performed at -99 dBm read-out power. The dashed black lines give examples of the Lorentzian fits (Eq. (4.4)). **(c, d)**: Lifetimes (c) and noise levels (d) from Lorentzian fits (Eq. (4.4)) to the spectra in (a, b). The error bars indicate statistical uncertainties from the fitting procedure. Only fits with a relative fitting uncertainty lower than 13.5% in lifetime are displayed. The dashed lines in the lifetime plot are fits to Eqs. (4.2) and (4.3) for temperatures ≥ 300 mK, with τ_{esc} as free parameter. The dashed lines in the level plot are calculated from Eq. (4.4), with Eqs. (4.1) and (4.3) and the same τ_{esc} . The dotted lines are calculated in the same way, but with $\tau_{\text{qp}}^* \rightarrow \left((\tau_{\text{qp}}^*)^{-1} + (\tau_{\text{sat}})^{-1} \right)^{-1}$, with $\tau_{\text{sat}} = 1$ ms.

caused by excess quasiparticles, in contrast to the observations in Ref. [3]. On top of that, the lifetimes observed for membrane and substrate resonators, saturate at a similar level despite the 16 times stronger phonon trapping in the membrane. Therefore, the lifetime saturation must originate from an effect that directly interacts with the quasiparticle system.

The design of the NbTiN-Al hybrid resonators enables read-out low microwave powers (P_{read}), which minimizes the creation of excess quasiparticles. When we increase P_{read} , we eventually observe excess quasiparticles without a level reduction, equivalent to a higher, P_{read} -induced, effective temperature. The results of Refs. [3, 10] are thus recovered in the high P_{read} -regime, as shown in Section 4.D

To verify that the lifetime saturation without creation of excess quasiparticles results in a level reduction, we calculated the lifetimes and fluctuation levels with Eq. (4.4),

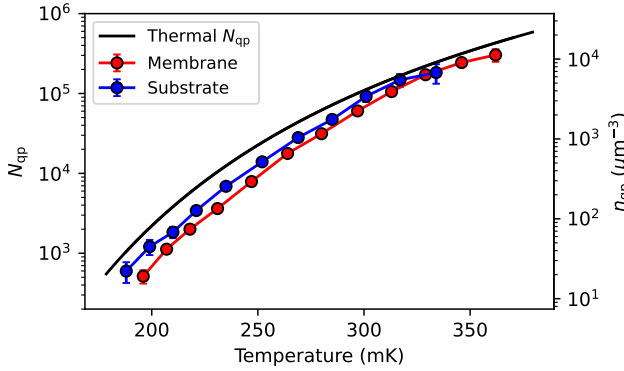


Figure 4.4: Number of quasiparticles and quasiparticle density (right axis) within the Al volume, calculated from the Lorentzian fits in Fig. 4.3(c,d). Error bars indicate propagated fitting uncertainties. The solid black line is from Eq. (4.1).

but with an alteration to Eq. (4.3):

$$\frac{1}{\tau_{qp}^*} = \frac{2}{\tau_{qp}(1 + \tau_{esc}/\tau_{pb})} + \frac{1}{\tau_{sat}}, \quad (4.6)$$

with τ_{sat} the saturation lifetime. For both membrane and substrate, τ_{sat} is set to 1 ms, based on τ_{qp}^* from the membrane resonator. The results are plotted in Fig. 4.3(c,d) as the dotted lines, which follow the measured τ_{qp}^* very well and shows a decrease in fluctuation level, for both resonators. The deviations of level in Fig. 4.3(d), are likely caused by the responsivity measurement method (Section 4.E).

A possible cause of a lifetime saturation without excess quasiparticles is *quasiparticle trapping*. From theory, it is known that magnetic [28–34] and non-magnetic [35–37] impurities can cause subgap electronic states [38] and disorder, which can result in local variations of Δ [39, 40]. Thickness variations [41] and unpaired surface spins [42] due to native oxide [43] may induce Δ -variations as well. Quasiparticles can be trapped at these suppressed Δ -regions [44, 45] by inelastic scattering, resulting in a background number of trapped quasiparticles, N_t . At low temperatures, N_{qp} (Eq. (4.1)) inevitably becomes comparable to N_t , leading to dominating quasiparticle trapping behavior even for low impurity concentrations, weak disorder or other effects that lead to small variations in Δ [44, 46, 47].

At that point, the quasiparticle lifetime is no longer limited by free quasiparticle recombination, but by *on-trap* recombination events, where a free quasiparticle recombines with a trapped one. Trapping itself does not change the number of Cooper-pairs and therefore is not observable in our experiments. This is in contrast to experiments where the free quasiparticle density near a junction is measured, in which case trapping dominates the low temperature behavior [48, 49]. The trapping states we conjecture are dissipative, as the amplitude and phase PSDs show the same

temperature behavior (Section 4.B), in contrast to what is observed for disordered TiN [12, 50].

Analogous to Eqs. (4.2) and (4.3), the saturation lifetime due to on-trap recombination can be written, $\tau_{\text{sat}} = V/2R_{\text{t}}N_{\text{t}}$, with R_{t} the on-trap recombination constant [46]. The phonon that is emitted during an on-trap recombination event has an energy $\Omega < 2\Delta$ and is therefore unable to break a Cooper-pair into two free quasiparticles. *On-trap* pair-breaking (a subgap phonon breaking a Cooper-pair into a trapped and free quasiparticle) is far less likely because the density of trapping states is assumed to be small [51]. Therefore, τ_{sat} is independent of phonon trapping, which is consistent with the observation that the substrate and membrane resonator show the same τ_{sat} . To investigate where quasiparticle traps could be located in our system, we conducted the same experiment with different geometries of the Al strip. Width (0.6 to 1.5 μm) and length (0.12 to 1.4 mm) variations did not affect the saturation lifetime, which implies the traps are not located at the NbTiN-Al interface or the sides of the Al central line. τ_{sat} increases from 0.7 to 3.1 ms with increasing the film thickness from 25 to 150 nm, respectively, and the reduction in fluctuation level is not observed for the thickest film. The experimental data of these geometry variations is presented in Section 4.C. This suggests that the trap density (N_{t}/V) decreases for thicker films and the location of the traps is either at the Al-substrate interface or the top surface. The top surface might contain unpaired surface spins from native Al oxide [11, 43]. Further progress in understanding the trapping mechanism will require identification of the microscopic origin of the traps.

We here analyzed the lifetime saturation phenomenologically using Eq. (4.6). A more detailed model of the fluctuations comprises multi-variable rate equations for quasiparticles and phonons, including quasiparticle trapping and on-trap recombination terms [2, 46]. Only non-equilibrium experiments [17, 49, 52] were conducted previously ($\delta N_{\text{qp}} \gg N_{\text{qp}}$), which allows neglecting the generation terms and feedback from the phonon system, in contrast to our near-equilibrium ($\delta N_{\text{qp}} \ll N_{\text{qp}}$) experiment. We have studied several such models [53], but without satisfactory results due to the number of (unknown) input parameters. However, we can constrain such a model to follow our experimental data.

Quasiparticle trapping could decrease the low-temperature responsivity of superconducting tunnel junction detectors [48], cause long-lived excitations in granular Al resonators [52] and lead to anomalous electrodynamic response of disordered TiN resonators [12, 50]. However, for single-photon detection using MKIDs [54, 55], the quasiparticle trapping effects can be beneficial. The fluctuation level reduction results in a higher signal-to-noise ratio when generation-recombination noise is the dominant noise source and the responsivity stays the same, as we observe (see Section 4.E and Ref. [27]). This means, somewhat counter-intuitively, that single-photon detector performance can be improved at low temperatures, by introducing quasiparticle traps, compared to a quasiparticle number saturation [10].

4.4 CONCLUSION

In conclusion, at high temperatures (≥ 300 mK), quasiparticle lifetimes in Al superconducting resonators are well described by simple recombination in thermal equilibrium [4]. At low temperatures, the lifetime is limited to < 1 ms, independent of phonon trapping, while the quasiparticle number exponentially decreases with temperature. This results in a strong reduction of quasiparticle fluctuations. Quasiparticle trapping with subsequent on-trap recombination is consistent with our observations. Variations in the Al strip geometry (width, length and thickness) showed that the traps are likely located at top or bottom surfaces.

Data and code availability All presented data and used analysis scripts are available at: <https://doi.org/10.5281/zenodo.4580356>.

SUPPLEMENTARY INFORMATION

4.A DEVICE DESIGN AND FABRICATION

The capacitive part is a (8-40-8)- μ *textm* co-planar waveguide (CPW) with interdigitated capacitors (IDC) on both sides [24, 56], patterned in a 200 nm thick NbTiN film [57] (normal state resistivity, $\rho_N = 245.6 \mu\Omega\text{cm}$, $T_c = 15.6$ K, residual resistance ratio, $RRR = 0.93$). The large width of the IDC suppresses TLS noise, as the electric field is distributed over a larger area [58, 59]. The capacitive fingers increase the device capacitance, allowing a resonator with a much lower total inductance for the same resonant frequency ($f_0 \propto 1/\sqrt{LC}$). The resulting quality factors are shown in Section 4.A

The sensitive part is a (23-1.73-23) μm CPW, with an Al ($\rho_N = 1.6 \mu\Omega\text{cm}$, $T_c = 1.26$ K, $RRR = 4.0$) central line, which is 312 μm long, 50 nm thick and shorted to the NbTiN ground plane to make a quarter-wave resonator.

The NbTiN and Al films are sputtered on a 350 μm thick Si wafer with a 150 nm SiN film on top, deposited with low pressure chemical vapor deposition. A backside KOH etch is used to release the SiN membrane, which supports two of the four Al sections as seen in Fig. 4.2. The final membrane thickness is 110 nm due to over-etching. The SiN beneath the capacitive part is etched away to suppress two level system (TLS) noise.

4.B AMPLITUDE, PHASE AND CROSS-POWER SPECTRAL DENSITIES

The complete fluctuation data set is presented in Fig. 4.B.1, and the resulting fits for the lifetime and noise level are shown in Fig. 4.B.2.

4.C AL GEOMETRY VARIATIONS

In the following sections, measurements of different devices will be discussed, which have not been presented. The measurement procedure and data analysis is the same. Table 4.C.1 shows an overview of the different parameters of the devices.

4.C.1 AL LENGTH

We measured the quasiparticle fluctuation in device B1, which Al strip length variations from 0.12 to 1.4 mm. The results are shown in Fig. 4.C.1.

We do not see a clear dependence of the saturation lifetime on Al length. The

Table 4.A.1.: The internal (Q_i), coupling (Q_c), loaded (Q) quality-factors and resonance frequency (f_0) at 50 mK, measured from S_{21} curves. An on-chip microwave power of -99 dBm was used to probe the resonators.

	Membrane	Substrate
Q_i	5.8×10^5	1.0×10^6
Q_c	4.6×10^4	3.6×10^4
Q	4.2×10^4	3.5×10^4
f_0	4.3 GHz	4.5 GHz

Table 4.C.1.: An overview of the devices, including the Al geometry from thickness, d , width, W , and length L , with their electrical properties. The results presented are from device A1 and A2.

Device	Substrate	d (nm)	W (μm)	L (mm)	T_c (K)	ρ_N ($\mu\Omega\text{cm}$)	RRR
A1	SiN membrane	50	1.73	0.31	1.26	1.6	4.0
A2	SiN/Si	50	1.73	0.31	1.26	1.6	4.0
A3	SiN membrane	25	1.73	0.31	1.35	2.4	2.7
B1	c-Sapphire	40	0.6	0.12 - 1.4	1.2 ^a	0.7 ^a	5.2 ^a
B2	c-Sapphire	40	1.5	0.12 - 1.4	1.2 ^a	0.7 ^a	5.2 ^a
C	c-Sapphire	150	0.92	0.53	1.12	0.4	9.3

^aMeasured on the same Al film, but on a strip of 100 μm wide, instead of the Al strip width of the resonator.

increase in noise level with longer strip length, can partly be explained by noting that $S_{N_{\text{qp}}}(\omega) \propto V$. Figure 4.C.1(c) shows the noise levels when divided by Al volume.

4.C.2 AL WIDTH

In Fig. 4.C.2, we show a comparison in lifetime and noise levels, when the Al width is varied. Although the lifetimes for the 1.5 μm strip are a bit higher (possibly due to a higher phonon escape time), no difference in saturation lifetime can be observed. The offset in noise levels can be explained by the larger Al volume, as Fig. 4.C.2(c) shows.

4.C.3 AL THICKNESS

The same device as in Fig. 4.2 is also fabricated with an Al thickness of 25 nm (device A3). A comparison of lifetime and noise level for the membrane resonators is given in Fig. 4.C.3(a,b). Only a slight difference in saturation lifetime can be observed. We would expect shorter lifetimes for device A3 than for A1, as the phonon escape time should be shorter. However, the 25 nm film has a higher T_c (as theoretically predicted in Ref. [41]), which also increases the lifetime (Eq. (4.2)). This diminishes the difference in lifetime we would expect from phonon trapping.

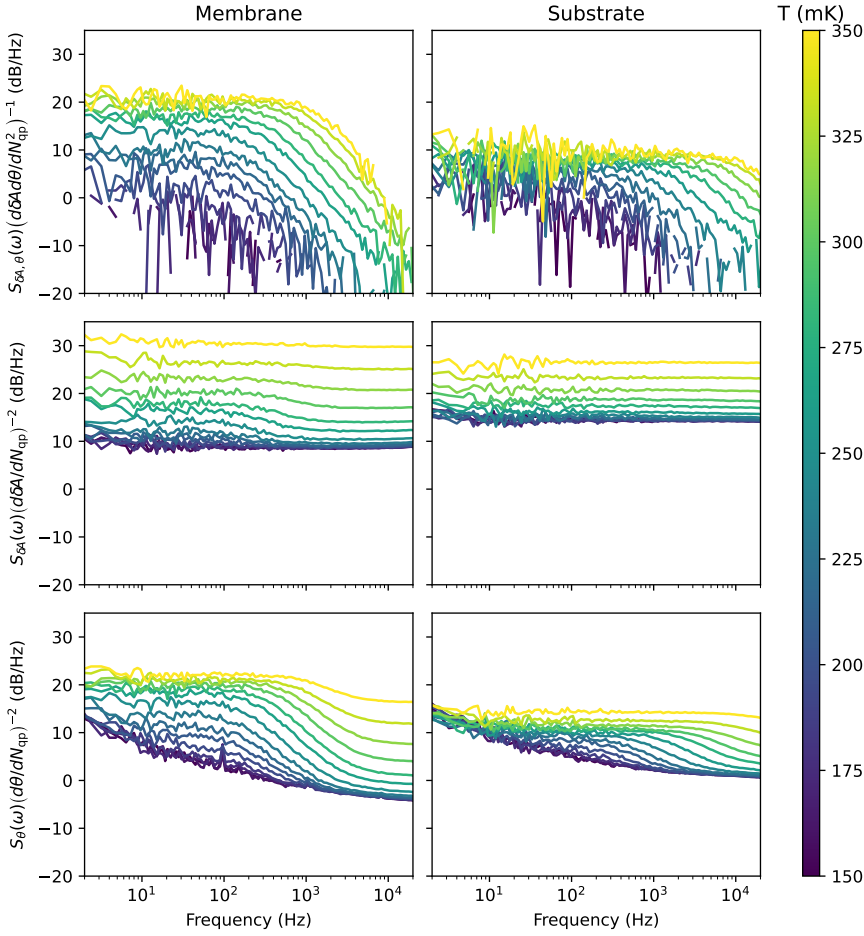


Figure **4.B.1**: Cross-, amplitude and phase Power Spectral Densities (PSDs) for the membrane and substrate resonators (see titles) and different temperatures (see colour scale). The top two panels are equivalent to Fig. 4.3(a,b). The noise levels are divided by the appropriate responsivities (c.f. Eq. (4.5)), as indicated in the y-axis labels.

To be precise, the phonon trapping factor is calculated to be 21 and 11 and the T_C is measured to be 1.255 K and 1.35 K for the 50 nm and 25 nm resonators, respectively. The 8 dB/Hz difference in noise level can only partly be explained by the larger Al volume (3 dB/Hz). Differences in critical temperature (c.f. 1.255K and 1.35 K) and resistivity (c.f. $1.6 \mu\Omega\text{cm}$ and $2.4 \mu\Omega\text{cm}$, for the 50 nm and 25 nm, respectively) influences τ_0 [4], while τ_0 is taken constant here. This could be the cause for the large difference in noise level.

We also include the lifetimes and noise levels from a different resonator, which has

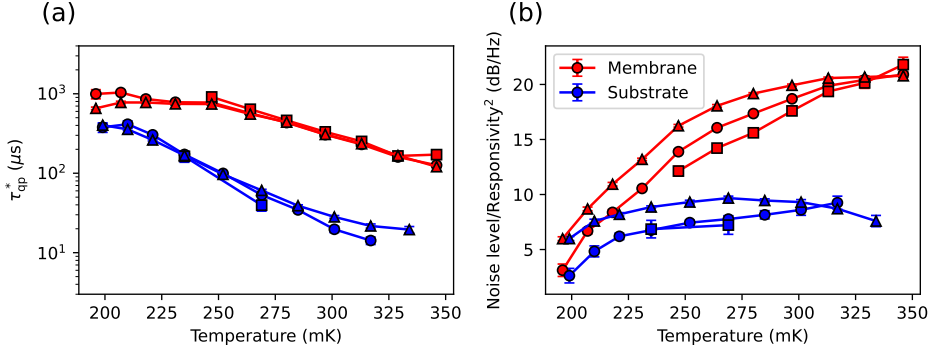


Figure 4.B.2: Lifetime (a) and noise level (b) from Lorentzian fits (Eq. (4.4)) to the spectra of Fig. 4.B.1. Red (blue) curves are for the membrane (substrate) resonator. The markers show which spectrum is fitted: (O) is the cross-PSD ($S_{\delta A, \theta}(\omega)$), (□) is the amplitude PSD ($S_{\delta A}(\omega)$) and (Δ) is the phase PSD ($S_{\theta}(\omega)$). Error bars indicate the uncertainty from the fitting procedure and only fits with a relative uncertainty of less than 16% in lifetime are displayed. Before fitting to $S_{\theta}(\omega)$ and $S_{\delta A}(\omega)$, the level at 18 kHz is subtracted from the spectrum, to eliminate amplifier noise.

4

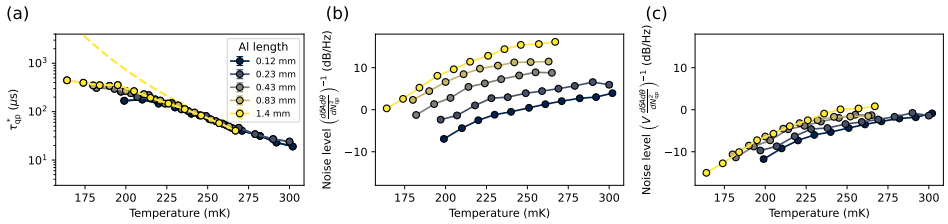


Figure 4.C.1: Lifetime (a) and noise levels (b,c) for device B1, from δA - θ cross-PSDs and responsivities (see Eq. (4.5)) fitted with Eq. (4.4), for different Al strip lengths given by the legend. Only fits with a relative error of $> 13\%$ in lifetime are shown, and the error bars include statistical fitting uncertainties only. The dashed line is a fit to Eq. (4.3) for the 1.4 mm data, with a fitted value $\tau_{esc} = 0.14$ ns. Panel (c) shows the same noise levels as (b), but divided by the Al volume. Read-out powers vary from -110 to -113 dBm

a Al thicknesses of 150 nm. In Fig. 4.C.3(c,d), we observe a high saturation lifetime for the lowest read power (≥ 3 ms) and, interestingly, the reduction of noise level is not observed in this thicker resonator. This suggests that the cause of the noise level reduction is located either on the Al-substrate interface or the top surface, for example, by unpaired surface spins from native Al oxide, which is supported by the results of Ref. [11]. In contrast, the results of Ref. [14] show higher τ_{sat} for decreasing Al thickness.

The lifetime saturation that is still present, is most likely due to read power induced creation of excess quasiparticles as observed in Refs. [3, 10], and supported by the

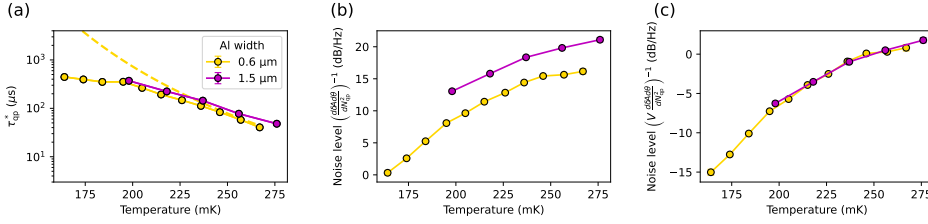


Figure 4.C.2: Lifetime (a) and noise levels (b,c) from δA - θ cross-PSDs and responsivities (see Eq. (4.5)) fitted with Eq. (4.4), for different Al strip widths given by the legend (devices B1 and B2). Only fits with a relative error of 11% in lifetime are shown, and the error bars include statistical fitting errors only. The 0.6 μm data and dashed line are the same as in Fig. 4.C.1. Panel (c) shows the noise levels divided by Al volume.

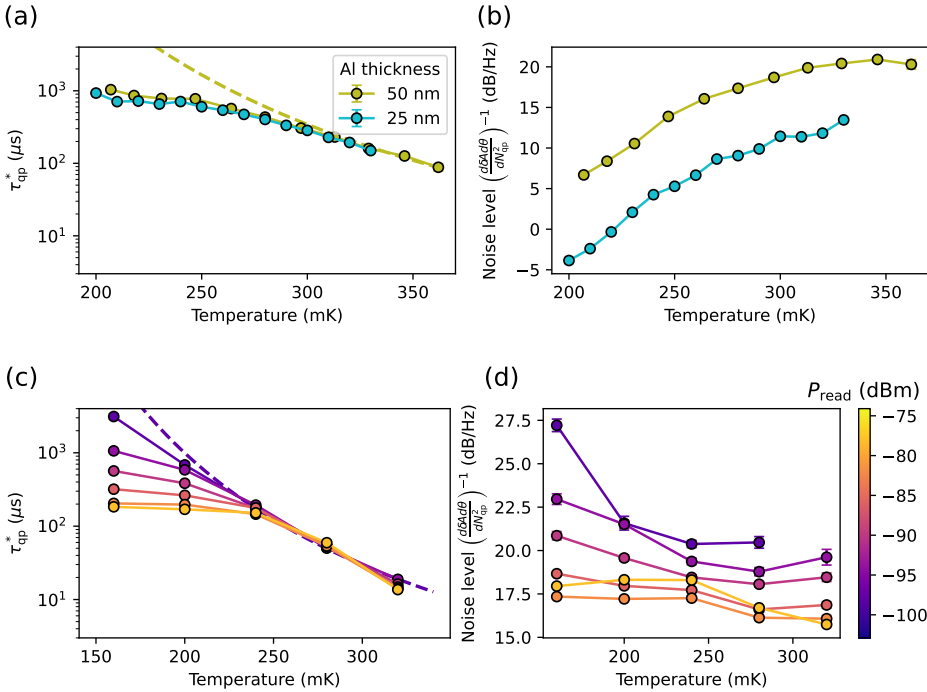


Figure 4.C.3: Lifetime (a,c) and noise level (b,d) from a fit of Eq. (4.4), to the cross-PSD divided by responsivity squared (Eq. (4.5)). (a,b): Green curves are from Fig. 4.3(c,d) (device A1) and the blue curves are for device A3 at -97 dBm read power. (c,d): Lifetime and noise levels measured for device C, for a large variety of read powers, see colour scale. The dashed lines are fits of Eq. (4.3), to the lowest read power data, only for temperatures > 240 mK.

fact that τ_{sat} decreases with increasing read power. Note that here, the read power is

increased ~ 25 dB with respect to the other data presented up to this point.

4.D MICROWAVE READOUT POWER DEPENDENCE

In the measurements of Fig. 4.3, we selected low read powers to limit read-out power effects, such as creation of excess quasiparticles [10], redistribution of quasiparticles [60] and non-linear kinetic inductance [61, 62], which was recently reviewed in Ref. [63]. Here, we analyse the effect of increasing the read-out power.

4

4.D.1 PEAK IN LIFETIME

Figure 4.D.1 shows how the results change when the read power is increased. In Fig. 4.D.1(a,b) we observe a peak in lifetime around 230 mK appearing at higher read power. This is also observed in Ref. [11], where also trapping states are deemed to be the cause. We notice that τ_{sat} is now temperature dependent, implying that N_t increases with decreasing temperature. From Fig. 4.D.1(c), we see that this increase in read power does not result in excess (free) quasiparticles.

4.D.2 CREATION OF EXCESS QUASIPARTICLES

Figure 4.D.1(d-f) shows the noise behavior at even larger read powers, measured in device B2. Upon increasing read power, the onset of the noise level reduction occurs to lower temperatures, after which it disappears. The saturation lifetime still decreases as read power increases, consistent with the creation of excess quasiparticles [10, 60], also observed in Fig. 4.D.1(f). Indeed, we see that more excess quasiparticles are created when increasing the readout power from -98 to -78 dBm. Interestingly, we see that increasing the read power from -78 to -74 dBm, does not increase the amount of non-equilibrium quasiparticles, but does lower the saturation lifetime and noise level. This may be caused by a microwave redistribution effect on the responsivity [64], which we do not account for.

We conclude from these observations that a lifetime saturation can be caused by two phenomena. At high readout powers, excess quasiparticles are created, which saturates the free quasiparticle number (N_{qp} in Eq. (4.1)), and therefore also τ_{qp} (Eq. (4.2)). The quasiparticle lifetime is then limited by recombination events. This is consistent with Refs. [3, 10]. At low readout powers, the creation of excess quasiparticles is suppressed and the trapped quasiparticle number (N_t) becomes significant compared to N_{qp} . This limits the quasiparticle lifetime to *on-trap* recombination events, while the free quasiparticle number (N_{qp}) stays thermal. These two phenomena can be distinguished by calculating N_{qp} from the noise levels, as done in Fig. 4.D.1(c,f) and Fig. 4.4.

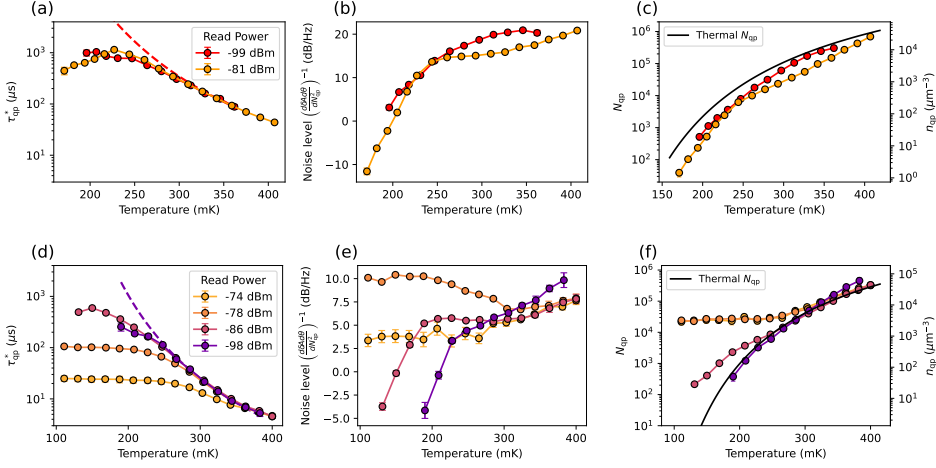


Figure 4.D.1: Lifetime (a,d), noise level (b,e) and calculated quasiparticle number (c,f) from a fit of Eq. (4.4) to the cross-PSD divided by responsivity squared (Eq. (4.5)) at various read powers (see legend), for device A1 (a-c) and device B2 (d-f). The red curves in (a-c) are the same as in Fig. 4.3 and Fig. 4.4. The dashed lines are fits of Eq. (4.3), to the lowest read power data with τ_{esc} as fitting parameter.

4.E RESPONSIVITY MEASUREMENT

We determine the amplitude and phase responsivities in a separate measurement of S_{21} as a function of temperature, as also explained in Section 3.3.2. We fit Lorentzian curves to the $|S_{21}|^2$ dips to determine the resonance frequency (f_0) and the internal and coupling quality factor for each temperature and read power. We then linearly fit $1/Q_i(T)$ and $\delta f_0(T)/f_0(0)$ to $N_{\text{qp}}(T)$ at high temperatures (> 250 mK), where quasiparticle loss dominates. Here, $\delta f_0 = f_0(T) - f_0(0)$, where $f_0(0)$ is the resonance frequency at 50 mK and $N_{\text{qp}}(T)$ is calculated from Eq. (4.1). The amplitude and phase responsivities are calculated as $d\delta A/dN_{\text{qp}} = -2Q(T) \frac{d(1/Q_i)}{dN_{\text{qp}}}$ and $d\theta/dN_{\text{qp}} = 4Q(T) \frac{d(\delta f_0/f_0(0))}{dN_{\text{qp}}}$, respectively [64]. This method does not take read power effects into account, but it is executed at the same read power as the noise measurement.

Figure 4.E.1(a) shows the calculated responsivities along with a different method to calculate the responsivity. This second method is based on the single photon response of the resonator, which is used as an MKID [54]. When a photon is absorbed in the Al, it will break thousands of Cooper-pairs, resulting in an excess quasiparticle number, δN_{qp} , and therefore a measurable signal in δA and θ . The responsivity is calculated as,

$$\frac{dX}{dN_{\text{qp}}} = X_{\text{max}} (\delta N_{\text{qp}})^{-1} = X_{\text{max}} \left(\eta_{\text{pb}} \frac{\hbar\omega_{\gamma}}{\Delta} \right)^{-1},$$

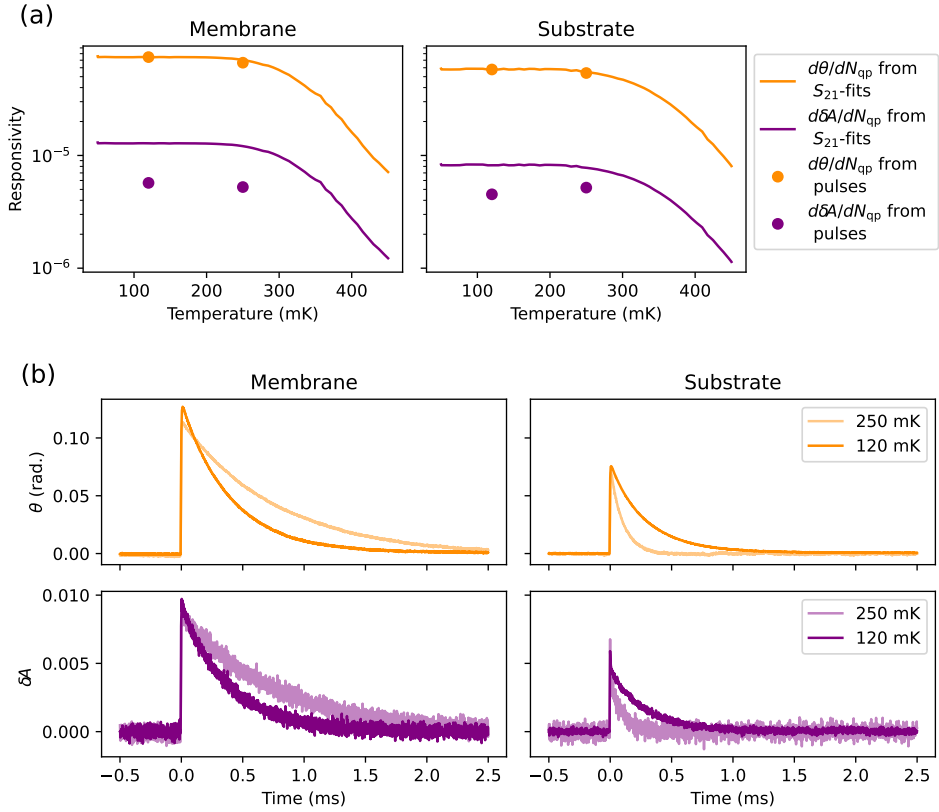


Figure 4.E.1: (a): Amplitude and phase responsivities determined by two methods: from S_{21} -fits as explained in the text and from a single photon (1545 nm) response pulse height. (b): Average amplitude and phase pulse response for a 1545 nm photon.

where X is either θ or δA and X_{\max} is the maximum measured value. η_{pb} is the pair-breaking efficiency, which we here set to 0.40 and 0.31 for the membrane and substrate resonator respectively [27]. These values are chosen such that the two calculation methods coincide for the phase variable at 120 mK and should be compared to the theoretical maximum value of 0.59 [65]. $\hbar\omega_\gamma$ is the 1545 nm-photon energy, i.e. 0.8 eV. For Δ , we use the BSC-relation $2\Delta = 3.52k_{\text{B}}T_{\text{c}}$.

Experimentally, a 1545 nm light source illuminates the middle part of the chip. The laser is attenuated to the point where single photon absorption events can be detected, without much overlap. A time stream of 40 s is measured at 1 MHz, with a read frequency equal to the resonance frequency of the resonator and power $P_{\text{read}} = -85$ dBm and -83 dBm for on and off membrane, respectively. The I and Q signals from the IQ -mixer are translated to δA and θ with the use of the resonance circle, which is measured earlier.

The average of multiple (typically a thousand) single photon pulses is presented in Fig. 4.E.1(b). A detailed description of the experiment and results of phonon trapping effects to the pulse amplitudes will be published separately [27].

In Fig. 4.E.1(a) both methods show that the responsivity does not decrease over the temperature range where the noise level reduction is observed (c.f. Fig. 4.3(c,d)). We conclude that the noise level reduction is caused by quasiparticle dynamics, and not by a reduction in responsivity (i.e. by $S_{N_{qp}}$ and not by the last factor in Eq. (4.5)).

REFERENCES

- [1] S. A. H. de Rooij, J. J. A. Baselmans, V. Murugesan, D. J. Thoen, and P. J. de Visser. *Strong Reduction of Quasiparticle Fluctuations in a Superconductor Due to Decoupling of the Quasiparticle Number and Lifetime*. In: *Physical Review B* 104.18 (2021), p. L180506.
- [2] C. M. Wilson and D. E. Prober. *Quasiparticle Number Fluctuations in Superconductors*. In: *Physical Review B* 69.9 (2004), p. 094524.
- [3] P. J. de Visser, J. J. A. Baselmans, P. Diener, S. J. C. Yates, A. Endo, and T. M. Klapwijk. *Number Fluctuations of Sparse Quasiparticles in a Superconductor*. In: *Physical Review Letters* 106.16 (2011), p. 167004.
- [4] S. B. Kaplan, C. C. Chi, D. N. Langenberg, J. J. Chang, S. Jafarey, and D. J. Scalapino. *Quasiparticle and Phonon Lifetimes in Superconductors*. In: *Physical Review B* 14.11 (1976), pp. 4854–4873.
- [5] J. M. Martinis, M. Ansmann, and J. Aumentado. *Energy Decay in Superconducting Josephson-Junction Qubits from Nonequilibrium Quasiparticle Excitations*. In: *Physical Review Letters* 103.9 (2009), p. 097002.
- [6] D. Rainis and D. Loss. *Majorana Qubit Decoherence by Quasiparticle Poisoning*. In: *Physical Review B* 85.17 (2012), p. 174533.
- [7] R. Barends, J. Wenner, M. Lenander, Y. Chen, R. C. Bialczak, J. Kelly, E. Lucero, P. O'Malley, M. Mariantoni, D. Sank, H. Wang, T. C. White, Y. Yin, J. Zhao, A. N. Cleland, J. M. Martinis, and J. J. A. Baselmans. *Minimizing Quasiparticle Generation from Stray Infrared Light in Superconducting Quantum Circuits*. In: *Applied Physics Letters* 99.11 (2011), p. 113507.
- [8] K. Karatsu, A. Endo, J. Bueno, P. J. de Visser, R. Barends, D. J. Thoen, V. Murugesan, N. Tomita, and J. J. A. Baselmans. *Mitigation of Cosmic Ray Effect on Microwave Kinetic Inductance Detector Arrays*. In: *Applied Physics Letters* 114.3 (2019), p. 032601.
- [9] L. Cardani, F. Valenti, N. Casali, G. Catelani, T. Charpentier, M. Clemenza, I. Colantoni, A. Cruciani, G. D'Imperio, L. Gironi, L. Grünhaupt, D. Gusenkova, F. Henriques, M. Lagoin, M. Martinez, G. Pettinari, C. Rusconi, O. Sander, C. Tomei, A. V. Ustinov, M. Weber, W. Wernsdorfer, M. Vignati, S. Pirro, and I. M. Pop. *Reducing the Impact of Radioactivity on Quantum Circuits in a Deep-Underground Facility*. In: *Nature Communications* 12.1 (1 2021), p. 2733.
- [10] P. J. de Visser, J. J. A. Baselmans, S. J. C. Yates, P. Diener, A. Endo, and T. M. Klapwijk. *Microwave-Induced Excess Quasiparticles in Superconducting Resonators Measured through Correlated Conductivity Fluctuations*. In: *Applied Physics Letters* 100.16 (2012), p. 162601.

- [11] R. Barends, S. van Vliet, J. J. A. Baselmans, S. J. C. Yates, J. R. Gao, and T. M. Klapwijk. *Enhancement of Quasiparticle Recombination in Ta and Al Superconductors by Implantation of Magnetic and Nonmagnetic Atoms*. In: *Physical Review B* 79.2 (2009), 020509(R).
- [12] J. Gao, M. R. Vissers, M. O. Sandberg, F. C. S. da Silva, S. W. Nam, D. P. Pappas, D. S. Wisbey, E. C. Langman, S. R. Meeker, B. A. Mazin, H. G. Leduc, J. Zmuidzinas, and K. D. Irwin. *A Titanium-Nitride near-Infrared Kinetic Inductance Photon-Counting Detector and Its Anomalous Electrodynamics*. In: *Applied Physics Letters* 101.14 (2012), p. 142602.
- [13] R. Barends, H. L. Hortensius, T. Zijlstra, J. J. A. Baselmans, S. J. C. Yates, J. R. Gao, and T. M. Klapwijk. *Contribution of Dielectrics to Frequency and Noise of NbTiN Superconducting Resonators*. In: *Applied Physics Letters* 92.22 (2008), p. 223502.
- [14] A. Fyhrie, P. Day, J. Glenn, H. Leduc, C. McKenney, J. Perido, and J. Zmuidzinas. *Decay Times of Optical Pulses for Aluminum CPW KIDs*. In: *Journal of Low Temperature Physics* 199.3 (2020), pp. 688–695.
- [15] R.-P. Riwar, A. Hosseinkhani, L. D. Burkhardt, Y. Y. Gao, R. J. Schoelkopf, L. I. Glazman, and G. Catelani. *Normal-Metal Quasiparticle Traps for Superconducting Qubits*. In: *Physical Review B* 94.10 (2016), p. 104516.
- [16] N. A. Court, A. J. Ferguson, R. Lutchyn, and R. G. Clark. *Quantitative Study of Quasiparticle Traps Using the Single-Cooper-pair Transistor*. In: *Physical Review B* 77.10 (2008), 100501(R).
- [17] C. Wang, Y. Y. Gao, I. M. Pop, U. Vool, C. Axline, T. Brecht, R. W. Heeres, L. Frunzio, M. H. Devoret, G. Catelani, L. I. Glazman, and R. J. Schoelkopf. *Measurement and Control of Quasiparticle Dynamics in a Superconducting Qubit*. In: *Nature Communications* 5.1 (2014), p. 5836.
- [18] M. Tinkham. *Introduction to Superconductivity*. Dover Publications, 2004. 482 pp.
- [19] A. Rothwarf and B. N. Taylor. *Measurement of Recombination Lifetimes in Superconductors*. In: *Physical Review Letters* 19.1 (1967), pp. 27–30.
- [20] S. B. Kaplan. *Acoustic Matching of Superconducting Films to Substrates*. In: *Journal of Low Temperature Physics* 37.3 (1979), pp. 343–365.
- [21] K. Rostem, P. J. de Visser, and E. J. Wollack. *Enhanced Quasiparticle Lifetime in a Superconductor by Selective Blocking of Recombination Phonons with a Phononic Crystal*. In: *Physical Review B* 98.1 (2018), p. 014522.
- [22] T. A. Puurtinen, K. Rostem, P. J. de Visser, and I. J. Maasilta. *A Composite Phononic Crystal Design for Quasiparticle Lifetime Enhancement in Kinetic Inductance Detectors*. In: *Journal of Low Temperature Physics* 199.3–4 (2020), pp. 577–584.

- [23] S. J. C. Yates, J. J. A. Baselmans, A. Endo, R. M. J. Janssen, L. Ferrari, P. Diener, and A. M. Baryshev. *Photon Noise Limited Radiation Detection with Lens-Antenna Coupled Microwave Kinetic Inductance Detectors*. In: *Applied Physics Letters* 99.7 (2011), p. 073505.
- [24] O. Noroozian, J. Gao, J. Zmuidzinas, H. G. LeDuc, and B. A. Mazin. *Two-level System Noise Reduction for Microwave Kinetic Inductance Detectors*. In: *AIP Conference Proceedings* 1185.1 (2009), pp. 148–151.
- [25] J. J. A. Baselmans, S. J. C. Yates, P. Diener, and P. J. de Visser. *Ultra Low Background Cryogenic Test Facility for Far-Infrared Radiation Detectors*. In: *Journal of Low Temperature Physics* 167.3 (2012), pp. 360–366.
- [26] J. Gao, J. Zmuidzinas, A. Vayonakis, P. Day, B. Mazin, and H. Leduc. *Equivalence of the Effects on the Complex Conductivity of Superconductor Due to Temperature Change and External Pair Breaking*. In: *Journal of Low Temperature Physics* 151.1 (2008), pp. 557–563.
- [27] P. J. de Visser, S. A. H. de Rooij, V. Murugesan, D. J. Thoen, and J. J. A. Baselmans. *Phonon-Trapping-Enhanced Energy Resolution in Superconducting Single-Photon Detectors*. In: *Physical Review Applied* 16.3 (2021), p. 034051.
- [28] A. A. Abrikosov and L. P. Gor'kov. *Theory of Superconducting Alloys. I. The Electrodynamics of Alloys at Absolute Zero*. In: *Sov. Phys. - JETP (Engl. Transl.); (United States)* 8.6 (1959), pp. 1090–1098.
- [29] A. A. Abrikosov and L. P. Gor'kov. *Superconducting Alloys at Finite Temperatures*. In: *Sov. Phys. - JETP (Engl. Transl.); (United States)* 9.1 (1959), pp. 220–221.
- [30] E. Müller-Hartmann and J. Zittartz. *Kondo Effect in Superconductors*. In: *Physical Review Letters* 26.8 (1971), pp. 428–432.
- [31] L. Yu. *Bound State in Superconductors with Paramagnetic Impurities*. In: *Chin. J. Phys. (Peking) (Engl. Transl.)* 21.1 (1965), pp. 75–91.
- [32] H. Shiba. *Classical Spins in Superconductors*. In: *Progress of Theoretical Physics* 40.3 (1968), pp. 435–451.
- [33] A. I. Rusinov. *On the Theory of Gapless Superconductivity in Alloys Containing Paramagnetic Impurities*. In: *Soviet Journal of Experimental and Theoretical Physics* 29 (1969), p. 1101.
- [34] Ya. V. Fominov, M. Houzet, and L. I. Glazman. *Surface Impedance of Superconductors with Weak Magnetic Impurities*. In: *Physical Review B* 84.22 (2011), p. 224517.
- [35] A. B. Kaiser. *Effect of Non-Magnetic Localized States in Superconducting Alloys*. In: *Journal of Physics C: Solid State Physics* 3.2 (1970), p. 410.
- [36] A. Ghosal, M. Randeria, and N. Trivedi. *Inhomogeneous Pairing in Highly Disordered S-Wave Superconductors*. In: *Physical Review B* 65.1 (2001), p. 014501.

- [37] A. Bespalov, M. Houzet, J. S. Meyer, and Y. V. Nazarov. *Density of States in Gapped Superconductors with Pairing-Potential Impurities*. In: *Physical Review B* 93.10 (2016), p. 104521.
- [38] A. A. Bespalov. *Impurity-Induced Subgap States in Superconductors with Inhomogeneous Pairing*. In: *Physical Review B* 100.9 (2019), p. 094507.
- [39] A. I. Larkin and Y. N. Ovchinnikov. *Density of States in Inhomogeneous Superconductors*. In: *Soviet Journal of Experimental and Theoretical Physics* 34 (1972), p. 1144.
- [40] M. V. Feigel'man and M. A. Skvortsov. *Universal Broadening of the Bardeen-Cooper-Schrieffer Coherence Peak of Disordered Superconducting Films*. In: *Physical Review Letters* 109.14 (2012), p. 147002.
- [41] P. N. Chubov, V. V. Eremenko, and Y. A. Pilipenko. *Dependence of the Critical Temperature and Energy Gap on the Thickness of Superconducting Aluminum Films*. In: *SOV PHYS JETP* 28.3 (1969), pp. 389–395.
- [42] L. Faoro and L. B. Ioffe. *Microscopic Origin of Low-Frequency Flux Noise in Josephson Circuits*. In: *Physical Review Letters* 100.22 (2008), p. 227005.
- [43] P. Kumar, S. Sendelbach, M. A. Beck, J. W. Freeland, Z. Wang, H. Wang, C. C. Yu, R. Q. Wu, D. P. Pappas, and R. McDermott. *Origin and Reduction of 1/f Magnetic Flux Noise in Superconducting Devices*. In: *Physical Review Applied* 6.4 (2016), 041001(R).
- [44] A. Bespalov, M. Houzet, J. S. Meyer, and Y. V. Nazarov. *Theoretical Model to Explain Excess of Quasiparticles in Superconductors*. In: *Physical Review Letters* 117.11 (2016), p. 117002.
- [45] J. S. Meyer, M. Houzet, and Y. V. Nazarov. *Dynamical Spin Polarization of Excess Quasiparticles in Superconductors*. In: *Physical Review Letters* 125.9 (2020), p. 097006.
- [46] A. G. Kozorezov, A. A. Golubov, J. K. Wigmore, D. Martin, P. Verhoeve, R. A. Hijmering, and I. Jerjen. *Inelastic Scattering of Quasiparticles in a Superconductor with Magnetic Impurities*. In: *Physical Review B* 78.17 (2008), p. 174501.
- [47] A. G. Kozorezov, A. A. Golubov, J. K. Wigmore, D. Martin, P. Verhoeve, R. A. Hijmering, and I. Jerjen. *The Effect of Magnetic Impurities on the Response of Superconducting Photon Detectors*. In: *IEEE Transactions on Applied Superconductivity* 19.3 (2009), pp. 440–444.
- [48] A. G. Kozorezov, J. K. Wigmore, A. Peacock, A. Poelaert, P. Verhoeve, R. den Hartog, and G. Brammertz. *Local Trap Spectroscopy in Superconducting Tunnel Junctions*. In: *Applied Physics Letters* 78.23 (2001), pp. 3654–3656.
- [49] A. G. Kozorezov, R. A. Hijmering, G. Brammertz, J. K. Wigmore, A. Peacock, D. Martin, P. Verhoeve, A. A. Golubov, and H. Rogalla. *Dynamics of Nonequilibrium Quasiparticles in Narrow-Gap Superconducting Tunnel Junctions*. In: *Physical Review B* 77.1 (2008), p. 014501.

- [50] J. Bueno, P. J. de Visser, S. Doyle, and J. J. A. Baselmans. *Study on Optical Filter Heating in Background Limited Detector Experiments*. In: *Journal of Low Temperature Physics* 176.5 (2014), pp. 1089–1095.
- [51] A. G. Kozorezov, J. K. Wigmore, D. Martin, P. Verhoeve, and A. Peacock. *Phonon Noise in Thin Metal Films in an Advanced Energy Down-Conversion Stage*. In: *Journal of Low Temperature Physics* 151.1 (2008), pp. 51–57.
- [52] L. Grünhaupt, N. Maleeva, S. T. Skacel, M. Calvo, F. Levy-Bertrand, A. V. Ustinov, H. Rotzinger, A. Monfardini, G. Catelani, and I. M. Pop. *Loss Mechanisms and Quasiparticle Dynamics in Superconducting Microwave Resonators Made of Thin-Film Granular Aluminum*. In: *Physical Review Letters* 121.11 (2018), p. 117001.
- [53] S. A. H. de Rooij. *Quasiparticle Dynamics in Optical MKIDs: Single Photon Response and Temperature Dependent Generation-Recombination Noise*. MA thesis. Delft: Delft University of Technology, 2020.
- [54] P. K. Day, H. G. LeDuc, B. A. Mazin, A. Vayonakis, and J. Zmuidzinas. *A Broadband Superconducting Detector Suitable for Use in Large Arrays*. In: *Nature* 425.6960 (2003), pp. 817–821.
- [55] J. Zmuidzinas. *Superconducting Microresonators: Physics and Applications*. In: *Annual Review of Condensed Matter Physics* 3.1 (2012), pp. 169–214.
- [56] J. J. A. Baselmans, F. Facchin, A. P. Laguna, J. Bueno, D. J. Thoen, V. Murugesan, N. Llombart, and P. J. de Visser. *Ultra-Sensitive THz Microwave Kinetic Inductance Detectors for Future Space Telescopes*. In: *Astronomy & Astrophysics* 665 (2022), A17.
- [57] D. J. Thoen, B. G. C. Bos, E. A. F. Haalebos, T. M. Klapwijk, J. J. A. Baselmans, and A. Endo. *Superconducting NbTiN Thin Films With Highly Uniform Properties Over a 100 Mm Wafer*. In: *IEEE Transactions on Applied Superconductivity* 27.4 (2017), pp. 1–5.
- [58] J. Gao, M. Daal, A. Vayonakis, S. Kumar, J. Zmuidzinas, B. Sadoulet, B. A. Mazin, P. K. Day, and H. G. LeDuc. *Experimental Evidence for a Surface Distribution of Two-Level Systems in Superconducting Lithographed Microwave Resonators*. In: *Applied Physics Letters* 92.15 (2008), p. 152505.
- [59] H. Wang, M. Hofheinz, J. Wenner, M. Ansmann, R. C. Bialczak, M. Lenander, E. Lucero, M. Neeley, A. D. O’Connell, D. Sank, M. Weides, A. N. Cleland, and J. M. Martinis. *Improving the Coherence Time of Superconducting Coplanar Resonators*. In: *Applied Physics Letters* 95.23 (2009), p. 233508.
- [60] P. J. de Visser, D. J. Goldie, P. Diener, S. Withington, J. J. A. Baselmans, and T. M. Klapwijk. *Evidence of a Nonequilibrium Distribution of Quasiparticles in the Microwave Response of a Superconducting Aluminum Resonator*. In: *Physical Review Letters* 112.4 (2014), p. 047004.

- [61] L. J. Swenson, P. K. Day, B. H. Eom, H. G. Leduc, N. Llombart, C. M. McKenney, O. Noroozian, and J. Zmuidzinas. *Operation of a Titanium Nitride Superconducting Microresonator Detector in the Nonlinear Regime*. In: *Journal of Applied Physics* 113.10 (2013), p. 104501.
- [62] F. Valenti, F. Henriques, G. Catelani, N. Maleeva, L. Grünhaupt, U. von Lüpke, S. T. Skacel, P. Winkel, A. Bilmes, A. V. Ustinov, J. Goupy, M. Calvo, A. Benoît, F. Levy-Bertrand, A. Monfardini, and I. M. Pop. *Interplay Between Kinetic Inductance, Nonlinearity, and Quasiparticle Dynamics in Granular Aluminum Microwave Kinetic Inductance Detectors*. In: *Physical Review Applied* 11.5 (2019), p. 054087.
- [63] C. N. Thomas, S. Withington, Z. Sun, T. Skyrme, and D. J. Goldie. *Nonlinear Effects in Superconducting Thin Film Microwave Resonators*. In: *New Journal of Physics* 22.7 (2020), p. 073028.
- [64] P. J. de Visser. *Quasiparticle Dynamics in Aluminium Superconducting Microwave Resonators*. PhD thesis. Delft: Delft University of Technology, 2014. 222 pp.
- [65] T. Guruswamy, D. J. Goldie, and S. Withington. *Quasiparticle Generation Efficiency in Superconducting Thin Films*. In: *Superconductor Science and Technology* 27.5 (2014), p. 055012.

5

VOLUME DEPENDENCE OF MICROWAVE INDUCED EXCESS QUASIPARTICLES IN SUPERCONDUCTING RESONATORS

The presence of quasiparticles typically degrades the performance of superconducting microwave circuits. The readout signal can generate non-equilibrium quasiparticles, which lead to excess microwave loss and decoherence. To understand this effect quantitatively, we measure quasiparticle fluctuations and extract the quasiparticle density across different temperatures, readout powers, and resonator volumes. We find that microwave power generates a higher quasiparticle density as the active resonator volume is reduced and show that this effect sets a sensitivity limit on kinetic inductance detectors. We compare our results with theoretical models of direct microwave photon absorption by quasiparticles and conclude that an unknown, indirect mechanism plays a dominant role in quasiparticle generation. These results provide a route to mitigate quasiparticle generation due to readout power in superconducting devices.

This chapter was published as S. A. H. de Rooij, J. J. A. Baselmans, J. Bueno, V. Murugesan, D. J. Thoen, and P. J. de Visser. *Volume Dependence of Microwave-Induced Excess Quasiparticles in Superconducting Resonators*. In: *Physical Review Applied* 24.2 (2025), p. 024007.

5.1 INTRODUCTION

Superconducting devices have found numerous applications, ranging from advanced quantum circuits to the most sensitive radiation detectors. Quasiparticles (i.e., broken Cooper pairs) generally degrade the performance of these devices as they introduce microwave loss, decoherence [2] and reduced detector sensitivity [3]. The quasiparticle density exponentially decreases with decreasing bath temperature, but is typically observed to saturate at low temperatures [4, 5]. Multiple sources of quasiparticle generation have been identified and mitigated, including cosmic rays [6, 7], radioactivity [8], and stray light [9].

We focus on the quasiparticle generation by the microwave signal used to read out the superconducting devices [10]. The on-chip power of this readout signal (P_{read}) induces two nonlinear effects. The first is a nonlinear kinetic inductance effect. The kinetic inductance increases quadratically when the current becomes a significant fraction of the critical current. This nonlinear inductance is used in parametric amplifiers [11] and tunable resonators [12]. It is an effect of the acceleration of the Cooper pair condensate. The second effect is the absorption of microwave photons by quasiparticles [13, 14], resulting in a redistribution to higher energies [15, 16]. At low temperatures, this can lead to an increased quasiparticle density. Direct pair-breaking by microwave photons is not possible because their energy ($\hbar\omega_0$) is much smaller than the gap energy (2Δ). However, when the quasiparticle relaxation rate is small compared to the photon absorption rate, quasiparticles can absorb multiple microwave photons. As a result, redistributed quasiparticles with energies $> 3\Delta$ can emit phonons of $> 2\Delta$ to break Cooper pairs. This leads to an excess quasiparticle density at low bath temperatures, which increases with P_{read} [10].

Superconducting resonators are particularly sensitive to both these effects, since P_{read} accumulates to an internal power, $P_{\text{int}} \propto QP_{\text{read}}$, where Q is the quality factor. The quality factor is typically limited by the coupling quality factor, Q_c , which is usually greater than 10^4 . Resonators are widely used in quantum circuits and as ultrasensitive radiation detectors spanning millimeter-wave to visible wavelengths, known as Microwave Kinetic Inductance Detectors (MKIDs) [17]. To reduce Two Level System noise (TLS), MKIDs are typically operated at a high P_{int} [18], just below the bifurcation power, $P_{\text{int}}^{\text{bif}}$. At $P_{\text{int}}^{\text{bif}}$ the nonlinear kinetic inductance causes hysteresis in the resonance curve [19]. At such high P_{int} , we expect quasiparticle redistribution effects to become important as well.

Another common approach to improve the sensitivity of MKIDs is reducing the absorption volume [20]. However, in Ref. [21] it is observed that decreasing V by a factor 7 does not increase the sensitivity when driving close to $P_{\text{int}}^{\text{bif}}$. At the same time, the quasiparticle recombination time is observed to decrease with decreasing volume. That points towards a volume-dependent excess quasiparticle density, since the quasiparticle lifetime and density are inversely related. This raises the question: how are the excess quasiparticle density, MKID sensitivity, readout power and the resonator volume interrelated?

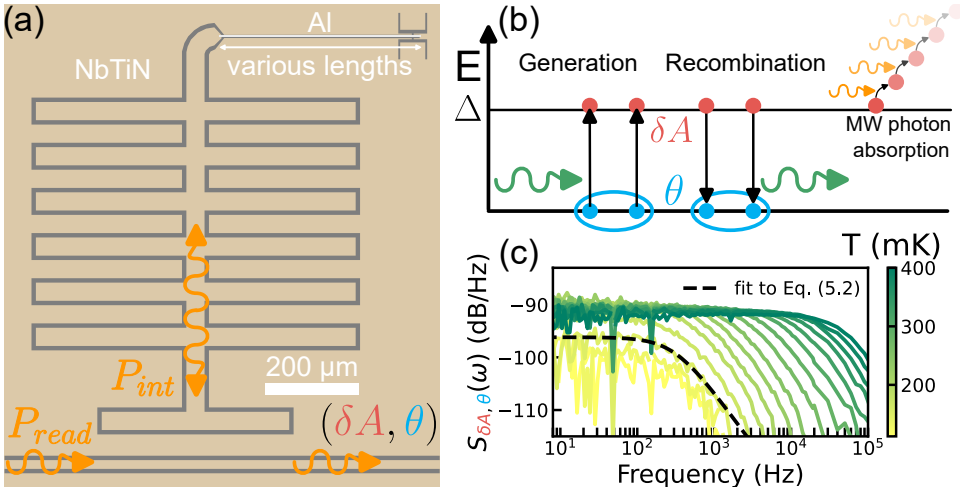


Figure 5.1.1: Generation-recombination noise measurement on hybrid superconducting resonators. (a) Diagram of one of the resonators studied. The central line of the inductive part is a narrow ($1.7 \mu\text{m}$) Al line of various lengths. At the end of the inductive section, a twin-slot antenna is patterned in the NbTiN, which is not used in the measurement. The gaps to the NbTiN ground plane are $2 \mu\text{m}$ for the inductive section. The NbTiN shunt capacitive part has a $40 \mu\text{m}$ wide central line and $8 \mu\text{m}$ wide gaps. We measure the forward transmission and calibrate it to the resonance curve to obtain δA and θ . (b) Energy diagram of the relevant processes regarding quasiparticles (red), Cooper pairs (blue), phonons (green) and microwave photons (orange). By analyzing correlations in δA and θ , we extract information about the quasiparticle generation-recombination process. (c) Measured cross power spectral densities for one of the resonators, at different bath temperatures. From a fit (dashed line), we obtain the quasiparticle density and effective lifetime.

5.2 DEVICE DESIGN AND MEASUREMENT

To answer this question, we measure the quasiparticle density in Al sections of different volumes, which are embedded in a NbTiN microwave resonator, see Fig. 5.1.1(a). The NbTiN (normal state resistivity $\rho_N = 158 \mu\Omega\text{cm}$, critical temperature $T_c = 14.6 \text{ K}$, thickness $d = 110 \text{ nm}$) [23] is sputtered on a c-Sapphire substrate and patterned using a reactive ion etch as a large shunt interdigitated capacitor (IDC) [24] to decrease the impedance of that section. By changing the length of the IDC fingers we set the resonance frequency, $\omega_0/(2\pi)$, between 4.5 and 6.5 GHz. The resonator is capacitively coupled to the transmission line with a coupling bar, which sets Q_c between 30,000 and 100,000 for the resonators studied here. The inductive section is a co-planar waveguide with a sputtered and wet etched Al central line ($\rho_N = 0.7 \mu\Omega\text{cm}$, $T_c = 1.18 \text{ K}$, $d = 40 \text{ nm}$), which is shorted at the end to make a quarter wave resonator.

In our analysis, we assume that we effectively probe an Al resonator with a volume equal to the volume of the Al strip. This is justified by the fact that the sensitivity to quasiparticles in the Al is significantly greater than for quasiparticles in the

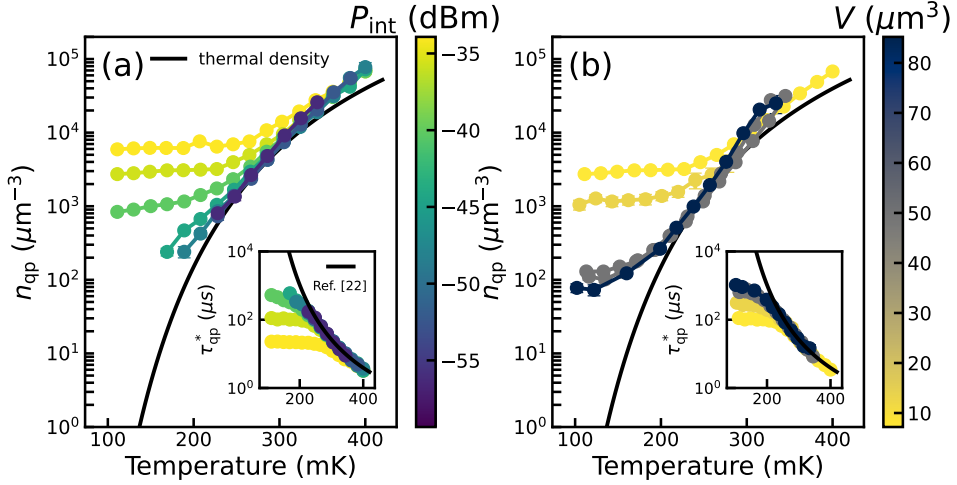


Figure 5.1.2: Results of the noise measurements for (a) the smallest Al volume resonator at various internal signal powers and (b) for various Al volumes when the microwave signal power is close to the bifurcation point. Error bars indicate statistical fit errors (see Fig. 5.3.1(c)) and are smaller than the data points for most data points. The insets show the results for the effective quasiparticle lifetime, obtained from the same measurements. The black line in the insets is a fit to $\tau_{qp}^*(T) = \tau_{qp}(T)(1 + \tau_{\text{esc}}/\tau_{\text{pb}})/2$, with $\tau_{\text{esc}} = 0.42 \pm 0.07$ ns as only free fit parameter. The error indicates the spread in fit results for the different resonators. We get τ_{pb} and $\tau_{qp}(T)$ for Al from [22].

NbTiN, since the current density in the Al is uniform and much greater than in the NbTiN. The quasiparticles in the Al are confined in the strip, because of the larger gap energy of NbTiN. Furthermore, the microwave photons in the resonator mainly interact with the quasiparticles in the Al, because of the high impedance of the Al line and small Al volume compared to the NbTiN volume [25]. See Section 5.A for an estimate of the quasiparticle sensitivity and photon interaction in the Al versus the NbTiN.

We probe the resonator at its resonance frequency with P_{read} , resulting in an internal power [26],

$$P_{\text{int}} = \frac{\hbar\omega_0^2}{\pi} \langle n_{\text{ph}} \rangle = \frac{2Q^2}{\pi Q_c} P_{\text{read}}, \quad (5.1)$$

where $\langle n_{\text{ph}} \rangle$ represents the average number of photons in the resonator. $Q = (1/Q_c + 1/Q_i)^{-1}$ the loaded quality factor, with Q_i the internal quality factor. We measure the forward transmission and calibrate it with respect to the resonance circle in the IQ-plane, to obtain the normalized amplitude (δA) and phase (θ) [27]. δA corresponds to changes in the dissipation (i.e. $\delta(1/Q_i)$), induced by the quasiparticles, and θ to changes in the kinetic inductance (i.e. $\delta\omega_0$), induced by Cooper pairs, see Fig. 5.1.1(b). We record noise in δA and θ at different bath temperatures and calculate the cross power spectral density, shown in Fig. 5.1.1(c) [10]. As we select for correlated changes in δA and θ , we effectively probe the

generation-recombination process [10]. This process is characterized by a Lorentzian spectrum [5, 28],

$$S_{\delta A, \theta}(\omega) = \frac{4 \langle \delta N_{\text{qp}}^2 \rangle \tau_{\text{qp}}^*}{1 + (\omega \tau_{\text{qp}}^*)^2} \left[\frac{d\delta A}{dN_{\text{qp}}} \frac{d\theta}{dN_{\text{qp}}} \right]. \quad (5.2)$$

Here, N_{qp} is the average number of quasiparticles inside the Al volume and τ_{qp}^* is the effective quasiparticle recombination time. We measure the term inside the brackets, i.e. the amplitude and phase responsivities to changes in quasiparticle number, independently, by sweeping the bath temperature for $T > T_c/5$ and recording the change in resonance frequency (ω_0) and internal quality factor (Q_i) [29]. From the same measurement, we obtain the kinetic inductance fraction, α_k [30], which is between 2 and 8% for the devices studied here. With the responsivities known, we fit Eq. (5.2) to the data to obtain τ_{qp}^* and $\langle \delta N_{\text{qp}}^2 \rangle$. An example fit is shown in Fig. 5.1.1(c).

The quasiparticle fluctuation variance is given by $\langle \delta N_{\text{qp}}^2 \rangle = 2\bar{R}N_{\text{qp}}^2\tau_{\text{qp}}^*/V$ [31], where $\bar{R} = 2\Delta^2/((k_B T_c)^3 N_0 \bar{\tau}_0)$ is the recombination constant renormalized for phonon trapping (indicated by the bar). Here, k_B is the Boltzmann constant and $N_0 = 1.72 \times 10^4 \mu\text{eV}^{-1} \mu\text{m}^{-3}$ is the single spin density of states at the Fermi level for Al [22]. For Δ , we use the BCS result, $2\Delta = 3.52k_B T_c$. $\bar{\tau}_0 = \tau_0(1 + \tau_{\text{esc}}/\tau_{\text{pb}})$ is the renormalized electron-phonon time constant, with $\tau_0 = 438$ ns describing the electron-phonon coupling strength and $\tau_{\text{pb}} = 0.28$ ns the phonon pair-breaking time in Al [22]. τ_{esc} is the phonon escape time, which we get from a fit to the high temperature data of $\tau_{\text{qp}}^* = \tau_{\text{qp}}(1 + \tau_{\text{esc}}/\tau_{\text{pb}})/2$, with $\tau_{\text{qp}} = 1/(2Rn_{\text{qp}}^T)$, where n_{qp}^T is the thermal quasiparticle density (black line in Fig. 5.1.2(a)). The fit is shown in the insets of Fig. 5.1.2 and results in $\tau_{\text{esc}} = 0.42 \pm 0.07$ ns. From an analytical calculation of the phonon transparency of the Al-Sapphire interface [32, 33] we find $\tau_{\text{esc}} = 0.40$ ns, which is consistent. Combining these results, we can extract the quasiparticle density, $n_{\text{qp}} = N_{\text{qp}}/V$ from the measured variance.

The expression we use for the variance has been recently calculated in Ref. [31] and includes the effects of quasiparticle generation by microwave readout power. When phonons dominate the quasiparticle generation, it results in $\langle N_{\text{qp}}^2 \rangle = N_{\text{qp}}$, because in this regime $\tau_{\text{qp}}^* = 1/(2\bar{R}n_{\text{qp}})$ [28]. When microwave power dominates, however, an excess quasiparticle density absorbs more microwave power, which results in a higher variance of $\langle N_{\text{qp}}^2 \rangle = 2N_{\text{qp}}$, and $\tau_{\text{qp}}^* = 1/(\bar{R}n_{\text{qp}})$.

5.3 RESULTS AND DISCUSSION

Fig. 5.1.2(a) shows n_{qp} obtained in this way, for one resonator and various P_{int} . At high temperatures n_{qp} is equal to the thermal quasiparticle density, which verifies the method we use to extract n_{qp} . At high P_{int} and low temperatures, n_{qp} saturates at a value that increases with increasing P_{int} . The inset shows the results for τ_{qp}^* from the same fits, which saturates for low temperatures at lower values for higher P_{int} . This aligns with Ref. [10], confirming that the microwave power induces excess quasiparticles.

Fig. 5.1.2(b) shows n_{qp} for various Al volumes when P_{int} is close to $P_{\text{int}}^{\text{bif}}$, i.e. in the

high microwave power regime. We estimate the bifurcation power for the kinetic inductance nonlinearity as,

$$P_{\text{int}}^{\text{bif}} = 0.64 N_0 \Delta^2 \frac{V \omega_0}{Q \alpha_k^2}. \quad (5.3)$$

This expression is derived in Section 5.B for a quarter wave resonator with uniform current density.

We observe from Fig. 5.1.2(b) that the excess quasiparticle density is higher and the effective quasiparticle lifetime decreases for the smaller Al volumes. We conclude that the quasiparticle generation by microwave readout power is more effective at small Al volumes.

5.3.1 EXCESS QUASIPARTICLES DUE TO DISSIPATED MICROWAVE POWER

To quantify this statement, we compare these results to theory. In Ref. [15], the authors numerically study the kinetic equations describing the phonon and quasiparticle distribution functions in a non-equilibrium state [35]. The readout power effects are included via a microwave drive term [13, 14], which is proportional to the quasiparticle-photon coupling constant $c_{\text{phot}}^{\text{qp}}$. The authors of Ref. [15] implicitly determine $c_{\text{phot}}^{\text{qp}}$ by equating the absorbed power by the quasiparticles ($P_{\text{abs}}^{\text{qp}}$) to the power lost due to inelastic scattering (both quasiparticle-phonon scattering and recombination). They take $P_{\text{abs}}^{\text{qp}}$ as input parameter in the model. The dissipated power density in a resonator can be calculated as [26]

$$\frac{P_{\text{abs}}}{V} = \frac{2Q^2}{Q_i Q_c} \frac{P_{\text{read}}}{V} = \frac{\pi P_{\text{int}}}{Q_i V}. \quad (5.4)$$

If Q_i is dominated by quasiparticle losses (i.e. $Q_i = Q_i^{\text{qp}}$), $P_{\text{abs}}^{\text{qp}}$ is equal to P_{abs} and can be obtained from measurements. The power lost due to inelastic scattering is obtained from the numerical calculations.

This results in two regimes. At high bath temperatures, thermal quasiparticles are redistributed to higher energies due to $P_{\text{abs}}^{\text{qp}}$, away from Δ , and Q_i increases ('redistribution regime'). At low bath temperatures, $P_{\text{abs}}^{\text{qp}}$ induces excess quasiparticles and Q_i decreases ('quasiparticle creation regime'). These two regimes are experimentally observed in Ref. [16]. The dependence of ω_0 on P_{int} was observed to be much stronger than expected from the excess quasiparticle density [16]. This was later identified as a nonlinear kinetic inductance effect [36, 37].

Here, we focus on the quasiparticle creation regime. In Fig. 5.3.1(a), we show the excess quasiparticle density, $n_{\text{qp}}^{\text{ex}} = n_{\text{qp}} - n_{\text{qp}}^{\text{T}}$, from Fig. 5.1.2(b) as a function of the absorbed power density (P_{abs}/V , see Eq. (5.4)).

In the quasiparticle creation regime, the excess quasiparticle density is predicted to be [15],

$$n_{\text{qp}}^{\text{ex}} = \sqrt{\eta_{2\Delta} \frac{\pi P_{\text{int}}}{Q_i V} \frac{8(1 + \tau_{\text{esc}}/\tau_{\text{pb}}) N_0^2 \Delta k_B}{\Sigma_s}}, \quad (5.5)$$

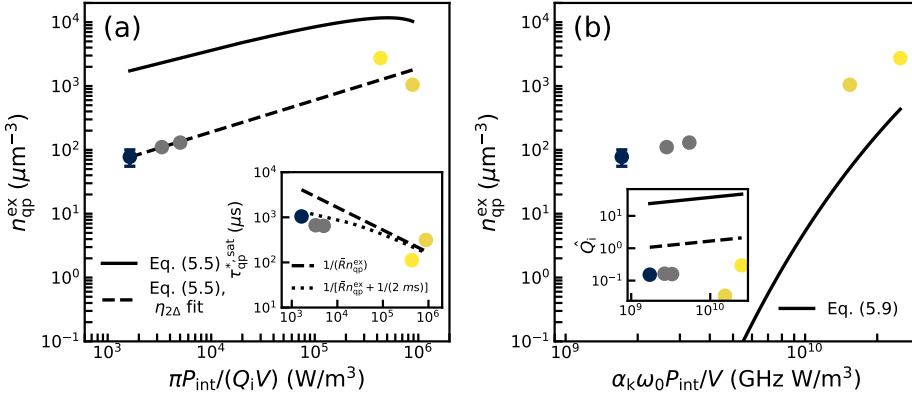


Figure 5.3.1: Excess quasiparticle density due to microwave power compared to kinetic equation calculations. (a) Comparison with the numerical study of Ref.[15] (Eq. (5.5)). The solid line is Eq. (5.5) with $\eta_{2\Delta}$ from Ref. [34] for Al. The dashed line is with $\eta_{2\Delta} = 4 \times 10^{-4}$ as a fit parameter. The data points are the low temperature data of Fig. 5.1.2(b) using the same colour coding for the device volume and with the error bars given by the standard deviation of the 3 lowest temperature points. The x-axis is P_{abs}/V (see Eq. (5.4)) with Q_i from measurement. The inset shows the saturated effective quasiparticle lifetime from Fig. 5.1.2(b) on the same x-axis as the main panel, compared to the expected effective lifetime from $\tau_{qp}^* = 1/(\bar{R}n_{qp}^{ex})$ with $\eta_{2\Delta} = 4 \times 10^{-4}$ as the dashed line. The dotted line includes an additional relaxation channel with a time constant of 2 ms. (b) Comparison with the analytical description in Ref. [25] (Eq. (5.9)) without fit parameter. The main difference is that in Ref. [25], the authors use an analytical expression for the quasiparticle-photon coupling constant, allowing P_{int} as parameter, as opposed to P_{abs}^{qp} in Ref. [15]. The data points are the same as in (a), but on a different x-axis. The inset shows the internal quality factor normalized to the quasiparticle density and resonator properties, $\hat{Q}_i = Q_i \alpha_k \hbar \omega_0 n_{qp}^{ex} / (2N_0 \Delta^2)$, on the same x-axis as the main panel. The dots are measured values, including Q_i from a separate measurement and n_{qp}^{ex} from the main panel. The solid line is the prediction for the quasiparticle creation regime and the dashed line for the redistribution regime, both from Ref. [25]. As the measured values are consistently lower, a process different from quasiparticle dissipation is likely to limit Q_i .

where $\Sigma_s = 3.4 \times 10^{10} \text{ W}/\text{m}^3/\text{K}$ for Al [15], which describes the power flow density from the quasiparticles to the phonons. If only recombination (and no phonon scattering) would be taken into account, this would equal $\Sigma_s^{rec} = 2\pi k_B (2N_0 \Delta)^2 R = 2.7 \times 10^{10} \text{ W}/\text{m}^3/\text{K}$, see Section 5.B for a derivation. The parameter $\eta_{2\Delta}$ in Eq. (5.5) is the fraction of the phonons with an energy $> 2\Delta$, which can be interpreted as a pair-breaking efficiency for the absorbed microwave power in the quasiparticle system. It has been numerically calculated in Ref. [34]. For Al in our P_{abs}/V regime we get $\eta_{2\Delta} = 0.20 - 0.013$, which results in the black line in Fig. 5.3.1(a). This prediction clearly does not describe the measured quasiparticle density. If we use $\eta_{2\Delta}$ as fit parameter, we obtain $\eta_{2\Delta} = 4 \times 10^{-4}$, shown by the dashed line in Fig. 5.3.1(a). This value for $\eta_{2\Delta}$ is comparable to the values found in

Ref. [10] (where this parameter is defined as η_{read}). This description satisfactorily explains the data and we thus conclude that the excess quasiparticle density follows the dependence $n_{\text{qp}}^{\text{ex}} \propto \sqrt{P_{\text{abs}}/V}$.

This dependence results in a quasiparticle lifetime scaling as, $\tau_{\text{qp}}^* \propto 1/n_{\text{qp}} \propto \sqrt{P_{\text{abs}}/V}$. We verify this in the inset of Fig. 5.3.1(a). The dashed line is given by $1/(\bar{R}n_{\text{qp}}^{\text{ex}})$, with $n_{\text{qp}}^{\text{ex}}$ from Eq. (5.5) with $\eta_{2\Delta} = 4 \times 10^{-4}$. The deviation from the dashed line at low P_{abs}/V could be due to additional quasiparticle relaxation channels, such as recombination in impurities [38, 39] or disorder-induced gap inhomogeneities [40, 41]. To account for that, we included a saturation lifetime of 2 ms in the dotted line, which is a typical value for Al [39]. The dotted line describes the data well, which supports our conclusion that $n_{\text{qp}}^{\text{ex}} \propto \sqrt{P_{\text{abs}}/V}$.

5.3.2 LIMITING MKID SENSITIVITY

The sensitivity of a power-integrating MKID is measured as the Noise Equivalent Power (NEP). This is ultimately limited by the fluctuations of quasiparticles in the absorber volume [3], $\text{NEP}_{\text{GR}} = 2\Delta/\eta_{\text{pb}} \sqrt{n_{\text{qp}} V/\tau_{\text{qp}}^*}$, where η_{pb} is the pair-breaking efficiency of pair-breaking photons [42]. In the quasiparticle creation regime, this is thus limited by the excess quasiparticles generated by the microwave probe. To suppress other noise sources such as TLS and amplifier noise, typically a high probe power is chosen. If we assume the internal microwave power to be the maximum before bifurcation, $P_{\text{int}} = P_{\text{int}}^{\text{bif}}$ (Eq. (5.3)), the internal quality factor is limited by quasiparticles, $Q_i = Q_i^{\text{qp}}$, and $k_B T \ll (\Delta, \hbar\omega_0)$, we can estimate this to be (see Section 5.C),

$$\text{NEP}_{\text{GR}}^{\text{bif}} = 0.3 \frac{\eta_{2\Delta}}{\eta_{\text{pb}}} \sqrt{\frac{\Delta^3}{\hbar R} \frac{\sqrt{V\omega_0}}{Q\alpha_k}}. \quad (5.6)$$

Filling in $\eta_{2\Delta} = 4 \times 10^{-4}$, $\eta_{\text{pb}} = 0.37$ [21, 42] and the material and resonator parameters from Ref. [21], we obtain $1.8 \times 10^{-20} \text{ W}/\sqrt{\text{Hz}}$. Ref. [21] measured a similar value $3.1 \times 10^{-20} \text{ W}/\sqrt{\text{Hz}}$ for all resonators, while the design parameters (V , ω_0 , Q and α_k) vary significantly. According to Eq. (5.6) the quasiparticle-limited NEP should vary as $\sqrt{V\omega_0}/(Q\alpha_k)$. This factor is approximately constant for all resonators in Ref. [21], which suggests that fluctuations of the microwave-induced excess quasiparticles limit the NEP of small volume MKIDs driven at high readout powers. This limit can be relaxed by decreasing the factor $\sqrt{V\omega_0}/(Q\alpha_k)$ in the MKID design. However, this will decrease the maximum internal power, since $P_{\text{int}}^{\text{bif}} \propto V\omega_0/(Q\alpha_k^2)$ (Eq. (5.3)), and in turn increase TLS noise [43]. Therefore, to improve the NEP of MKIDs further, both the factor $\sqrt{V\omega_0}/(Q\alpha_k)$ and TLS noise must be reduced simultaneously.

5.3.3 MICROSCOPIC MECHANISM FOR EXCESS QUASIPARTICLES

From Fig. 5.3.1(a), we concluded that P_{abs}/V generates excess quasiparticles with an efficiency $\eta_{2\Delta}$. However, it is not clear which microscopic mechanism is

responsible for this. The authors of Ref. [25] pursued an analytical approach to solving the kinetic equations, preserving the microscopic nature of direct photon absorption. They explicitly calculate the quasiparticle-photon coupling constant [44] for $\langle n_{\text{ph}} \rangle \gg 1$ as the ratio between the photon absorption and the normalized power dissipation in the resonator,

$$c_{\text{phot}}^{\text{qp}} = \frac{P_{\text{abs}}^{\text{qp}}}{\pi P_{\text{int}}} \frac{\sigma_N / \sigma_1}{2\hbar N_0 V} = \frac{1}{Q_i^{\text{qp}}} \frac{\sigma_N / \sigma_1}{2\hbar N_0 V} \approx \frac{\alpha_k \omega_0}{2\pi N_0 V \Delta}, \quad (5.7)$$

where the last approximation is valid for, $k_B T_{\text{eff}} \ll \Delta$, which introduces a maximum error of 7% for our measurements. With $c_{\text{phot}}^{\text{qp}}$ known explicitly, they derive a temperature $(k_B T_*)^3 / (k_B \Delta^2)$, that separates the redistribution from the quasiparticle creation regime when compared to the bath temperature. $k_B T_*$ characterizes the width of the quasiparticle distribution function and is given by,

$$\frac{k_B T_*}{\Delta} = \left(\frac{105\pi}{64} \left(\frac{k_B T_c}{\Delta} \right)^3 \frac{\hbar \tau_0}{\Delta^2} c_{\text{phot}}^{\text{qp}} P_{\text{int}} \right)^{1/6}. \quad (5.8)$$

Assuming $\hbar \omega_0 \ll k_B T_* \lesssim \Delta$ and that the non-equilibrium phonons with energies below 2Δ have little effect on the quasiparticle distribution (both valid for Al at the microwave powers considered here), they come to an explicit expression for the excess quasiparticle number at low temperatures,

$$n_{\text{qp}}^{\text{ex}} = 0.42 \frac{\tau_{\text{esc}}}{\tau_{\text{pb}}} N_0 \Delta \left(\frac{k_B T_*}{\Delta} \right)^{9/2} \times \exp \left[-\sqrt{\frac{14}{5}} \left(\frac{k_B T_*}{\Delta} \right)^{-3} \right]. \quad (5.9)$$

This expression depends on experimental parameter P_{int} as opposed Eq. (5.5), which depends on the estimated parameter $P_{\text{abs}}^{\text{qp}}$. We compare Eq. (5.9) to the data in Fig. 5.3.1(b), without fit parameters. The variable on the x-axis combines the resonator-dependent variables in Eqs. (5.7) and (5.8).

We observe a much higher excess quasiparticle density at low microwave power densities than predicted by Eq. (5.9). A similar discrepancy is observed in Ref. [25], when comparing $Q_i(P_{\text{int}})$ to the measurements of Ref. [16]. This suggests that the quasiparticle generation at low temperature and readout powers involves a different mechanism than direct photon absorption. From Fig. 5.3.1(a) we know that such a mechanism should be readout power dependent, with an efficiency of only 4×10^{-4} with respect to the absorbed power.

The authors of Ref. [31] proposed pair-breaking photons generated by the signal generator as additional mechanism. In Section 5.E, we exclude this hypothesis by measuring the attenuation of several microwave components in the setup at frequencies above the gap frequency of the Al, which results in a total attenuation on the order of -300 dB. We also exclude pair-breaking photons radiated from other parts of the microwave chain. Therefore, the pair-breaking mechanism is likely to be related to the microscopics of the resonator.

To identify possible pair-breaking mechanisms in the resonator, we show the measured Q_i , normalized to quasiparticle density and resonator properties, in the inset of Fig. 5.3.1(b). The solid black line is the prediction of Ref. [25] for Q_1^{qp} in the quasiparticle creation regime and the dashed line is for the redistribution regime. The expressions are given in Section 5.D. Both these predictions are higher than the measured Q_i , which implies that the Q_i is not limited by quasiparticles (i.e. $Q_i \neq Q_1^{\text{qp}}$), but by another dissipation mechanism. This could for example be TLS loss in the inductor, which would locally heat the Al and, indirectly, generate quasiparticles. Further study on different quasiparticle generation mechanisms, both theoretical and experimental, is needed to identify such a mechanism.

Apart from this, the kinetic inductance nonlinearity could also play a role. Effects of the condensate are more likely to dominate at low quasiparticle densities [45]. Physically, the microwave drive broadens the coherence peak and creates an exponential-like tail in the density of states [36, 37]. This causes the sharply peaked non-equilibrium distribution function to be broadened as well. A theory incorporating both the non-equilibrium density of states and redistribution effects is still lacking.

5.4 CONCLUSION

To conclude, we have shown that microwave readout power generates a higher excess quasiparticle density in resonators with a smaller active volume, which scales as $n_{\text{qp}}^{\text{ex}} \propto \sqrt{P_{\text{int}}/(Q_i V)}$. The generated quasiparticles limit the sensitivity of MKIDs, which can only be mitigated by simultaneously reducing $\sqrt{V\omega_0}/(Q\alpha_k)$ in the MKID design and the TLS noise. The microscopic mechanism for the quasiparticle generation is unknown, but acts local at the active resonator volume. A complete microscopic understanding needs a treatment of the non-equilibrium effects of multiple microwave power absorption channels.

Data and code availability All data and analysis scripts presented and used in this work are openly available at [10.5281/zenodo.14999891](https://zenodo.org/record/14999891).

SUPPLEMENTARY INFORMATION

5.A QUASIPARTICLE SENSITIVITY AND PHOTON INTERACTION

Since we probe a hybrid NbTiN-Al superconducting resonator, we are in principle sensitive to quasiparticle density changes in both the NbTiN and Al sections. In this section we will show, however, that we are only sensitive to quasiparticles in the Al section. Additionally, we will show that the photons in the resonator effectively only interact with the quasiparticle in the Al. This justifies the simplification to regard the resonator as a pure Al resonator, with a volume equal to the volume of the Al inductive strip.

To the lowest order in temperature and resonance frequency ($k_B T \ll \hbar\omega \ll \Delta$) the quasiparticle sensitivity of the amplitude, δA and phase θ for thin films (with a thickness much smaller than the penetration depth) is proportional to [29, 47]⁴,

$$\frac{d(\delta A, \theta)}{dn_{\text{qp}}} \propto \frac{\alpha_k Q}{\pi N_0 \Delta} \sqrt{\frac{2\Delta}{\hbar\omega}} \propto \frac{\alpha_k}{N_0 \sqrt{\Delta}}. \quad (5.10)$$

In the last expression, we only kept the material dependent parameters. The denominator, $N_0 \sqrt{\Delta}$, is a factor ~ 7.0 bigger for NbTiN, since $\Delta \approx 1.76 k_B T_c$ and $N_0^{\text{NbTiN}} = 3.7 \times 10^4 \mu\text{eV}^{-1} \mu\text{m}^{-3}$ [48] and $N_0^{\text{Al}} = 1.7 \times 10^4 \mu\text{eV}^{-1} \mu\text{m}^{-3}$ [22]. The kinetic induction fraction, α_k , can be obtained from simulation in the following way. We first simulate the full resonator and find the resonance frequency, f_{res} . We set the sheet kinetic inductance to their nominal values, $L_{k,s} = \hbar R_N / (\pi \Delta)$ [49], where R_N is the normal state resistance. Then, we set the sheet kinetic inductance of the NbTiN or Al to 0 and find the resonance frequency for that case, f_{res}^0 . We obtain the kinetic induction fraction is by $\alpha_k = 1 - (f_{\text{res}} / f_{\text{res}}^0)^2$. We simulate the resonators with longest and shortest Al sections with SONNET [46]. The resulting current density (with nominal kinetic inductance) is plotted in Fig. 5.A.1. We find $\alpha^{\text{NbTiN}} = 0.12$ and $\alpha_k^{\text{Al}} = 0.094$ for the long Al resonator and $\alpha_k^{\text{NbTiN}} = 0.11$ and $\alpha_k^{\text{Al}} = 0.024$ for the short one. These Al kinetic induction fractions are consistent with the measured values from the change in resonance frequency [30], which range from 2 to 8 % for the short and long Al section resonators, respectively. Comparing the NbTiN and Al values, the kinetic induction fraction of NbTiN is at maximum a factor ~ 5 higher. The total sensitivity (Eq. (5.10)) is a factor 5.5 to 1.5 higher for Al.

Furthermore, the sensitivity to the quasiparticle density is dependent on the squared current at that location $I^2(x)$ [26, 50]. To take this into account, we square the simulated current density from SONNET (Fig. 5.A.1) and sum the NbTiN and Al

⁴In the opposite limit, $\hbar\omega \ll k_B T \ll \Delta$, the first proportionality is slightly adjusted, but the second proportionality (keeping the material parameters only) still holds.

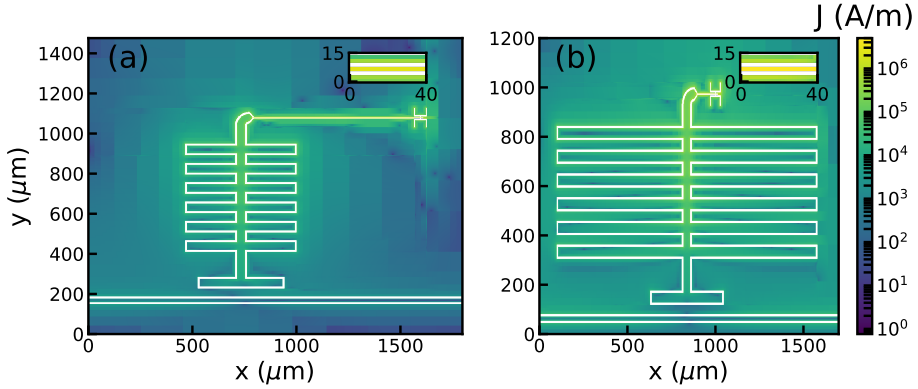


Figure 5.A.1: Current density at resonance from a simulation using SONNET [46] for the longest (a) and shortest (b) Al sections. The insets show a zoom-in of the inductive section. The color bar relates to both panels.

5

parts individually. The squared current density is a factor 22 higher in the long Al section and a factor 3.2 higher in the short one, compared to the current density in the NbTiN. Thus, we are more sensitive to quasiparticle density changes in the Al than the NbTiN, by a factor 130 for the long Al section resonator and a factor 4.9 for the short one.

Within the Al wire, the current will be non-uniform over the wire length, since the wire has some capacitance in addition to the inductance and therefore electrical length. When we assume a sinusoidal current distribution over the wire, we can determine an effective quasiparticle volume as,

$$\begin{aligned} \frac{V_{\text{eff}}}{V} &= \frac{v_{\text{ph}}}{\omega_0 L} \int_{\pi/2 - \omega_0 L/v_{\text{ph}}}^{\pi/2} \sin^2(x) dx \\ &= \frac{1}{2} + \frac{\sin(2\omega_0 L/v_{\text{ph}})}{4\omega_0 L/v_{\text{ph}}}, \end{aligned} \quad (5.11)$$

where L is the inductor length, $\omega_0 = 2\pi f_0$ is the angular resonance frequency and v_{ph} is the phase velocity of the hybrid NbTiN-Al co-planar waveguide (CPW) transmission line. The integration limits go from the phase at the NbTiN connection to the short (with a current maximum, so a phase of $\pi/2$). We obtain v_{ph} from a SONNET simulation of just the inductive CPW line. For the resonator with the longest Al section, this results in a fraction $V_{\text{eff}}/V \approx 0.95$. This is consistent with the simulation shown in Fig. 5.A.1(a), where the current density squared on the left side of the Al strip is $\sim 95\%$ of the current on the right side. Therefore, we ignore this effect and assume that the current in the Al wire is uniform, such that we are equally sensitive to all quasiparticles in the Al.

Additionally, the photons in the resonator will interact mainly with the quasiparticles in the Al. The relative photon occupation in the NbTiN capacitive

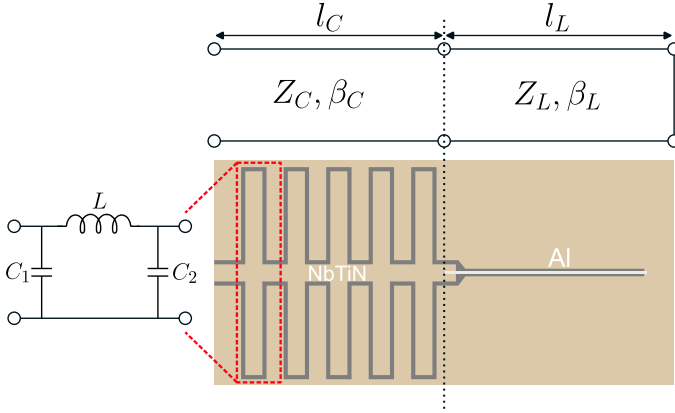


Figure 5.A.2: Transmission line model for the hybrid NbTiN-Al resonator. The NbTiN capacitive and Al inductive parts are modeled by a transmission line with lengths l_C and l_L , characteristic impedances, Z_C and Z_L , and phase constants, $\beta_C = \omega/v_{\text{ph}}^C$ and $\beta_L = \omega/v_{\text{ph}}^L$. The inductive part is shorted to make a quarter-wave resonator. The physical structure of the transmission lines is shown below. The characteristic impedances and phase velocities are obtained from a simulation in SONNET. For the inductive Al line this results in $Z_L = 83 \Omega$ and $v_{\text{ph}}^L = 1.0 \times 10^8$ m/s. For the NbTiN capacitive part this is done by simulating one element (highlighted in the dashed red line) and extracting the PI-model parameters as shown on the left. This way, $Z_C = \sqrt{L/(C_1 + C_2)}$ and $v_{\text{ph}} = l'/\sqrt{L(C_1 + C_2)}$, where l' is the length of the element. This results in $Z_C = 17 - 25 \Omega$ and $v_{\text{ph}}^C = 2.5 - 4.0 \times 10^7$ m/s, varying with capacitive finger length, see Fig. 5.A.1.

part and the Al inductive part can be estimated by considering the resonator as two connected transmission lines (Fig. 5.A.2). We disregard the effect of the coupler, since the coupling is weak ($Q_c > 30.000$). The ratio of internal power is given by $P_{\text{int}}^C/P_{\text{int}}^L = Z_L|V_C^+|^2/(Z_C|V_L^+|^2)$ [29, 51], with V_C^+ and V_L^+ the voltage wave amplitudes in the capacitive and inductive part respectively. The voltage on the connecting point of the two transmission lines (black dashed line in Fig. 5.A.2) must be the same, $2V_C^+ \cos(\beta_C l_C) = -2jV_L^+ \sin(\beta_L l_L)$. On resonance, the sum of the input impedance from the dashed line looking to the left and looking to the right, should be 0 (transverse resonance technique [51]), $jZ_C/\tan(\beta_C l_C) = jZ_L \tan(\beta_L l_L)$. Combining these two equations gives,

$$\frac{P_{\text{int}}^C}{P_{\text{int}}^L} = \frac{Z_C}{Z_L} \left(\frac{\cos(\beta_L l_L)}{\sin(\beta_C l_C)} \right)^2 \approx \frac{Z_C}{Z_L}. \quad (5.12)$$

The last approximation holds if most of the electrical length is in the capacitive section. This is the case for the resonators considered here, since for the longest Al section, $(\cos(\beta_L l_L)/\sin(\beta_C l_C))^2 \approx 1.2$. This results in a fraction $P_{\text{int}}^C/P_{\text{int}}^L \approx 0.24$, meaning that most of the photon occupation is in the inductive Al section.

Furthermore, the quasiparticle-photon interaction is much stronger in the Al section. As mentioned in the main text, the interaction strength can be estimated by,

$c_{\text{phot}}^{\text{qp}} \approx \alpha_k \omega_0 / (2\pi N_0 \Delta V)$ [25]. This expression has the same dependence on α_k , N_0 and Δ as Eq. (5.10), which slightly favors interaction with the Al quasiparticles. However, there is an additional factor V in the expression for $c_{\text{phot}}^{\text{qp}}$. This is the volume that the quasiparticles occupy, which is much larger for NbTiN (see Fig. 5.A.1). Therefore, a photon is much more likely to interact with a quasiparticle in the Al than with a quasiparticle in the NbTiN.

These two conclusions - the photon occupation is larger and the photon-quasiparticle interaction is stronger in the Al section compared to the NbTiN section - justify the simplification of considering the resonator as purely Al when applying the photon-quasiparticle physics described in Refs. [15, 25, 31].

5.B BIFURCATION POWER ESTIMATION

When a superconducting microwave resonator is driven above a certain power, the transmission curve becomes hysteretic [19, 52]. A resonator in this state is called to be bifurcated and the internal power at which this start to happen we call the bifurcation power or $P_{\text{int}}^{\text{bif}}$.

This behavior can be modeled as a classical Duffing oscillator, with a nonlinearity parameter a that describes the resonance frequency shift in number of line widths when driving at resonance. For $a > 4\sqrt{3}/9 = 0.77$ the resonator is bifurcated [19, 52]. For the kinetic inductance nonlinearity, a depends on the ratio of the current density in the resonator over the critical current density in the superconductor: j_0/j_c where j_0 is the maximum current density in one cycle. We will first find j_0 as a function of internal microwave power, P_{int} .

The internal power is given by [26],

$$P_{\text{int}} = \frac{\omega_0 E_{\text{res}}}{4\pi m} = \frac{1}{2\pi m} \frac{Q^2}{Q_c} P_{\text{read}}, \quad (5.13)$$

with $m = 1/4$ for a quarter-wave resonator (and lumped-element resonator) and $m = 1/2$ for a half-wave. ω_0 is the angular resonance frequency, $Q = (1/Q_c + 1/Q_i)^{-1}$ is the loaded quality factor with Q_c the coupling quality factor and Q_i the internal quality factor. E_{res} is the energy stored in the resonator, which can be expressed as,

$$E_{\text{res}} = \langle n_{\text{ph}} \rangle \hbar \omega_0 = \frac{1}{2} L I_0^2, \quad (5.14)$$

with $\langle n_{\text{ph}} \rangle$ the average number of photons in the resonator, \hbar the reduced Planck constant, L the total inductance and I_0 the maximum current in the inductor over one cycle. In this equation, we assumed the current to be constant over the inductor wire and that all inductive energy in the resonator can be described by a single lumped element inductor with inductance L (see previous section). If we consider a completely distributed resonator, i.e. a transmission line of finite length, there would be an additional factor 1/2 in Eq. (5.14). For now, we consider a quarter-wave resonator and set $m = 1/4$.

Combining Eqs. (5.13) and (5.14), we see,

$$j_0 = \sqrt{\frac{2\pi P_{\text{int}}}{L\omega_0(dw)^2}}, \quad (5.15)$$

where $j_0 = I_0/(dw)$ is the current density, d is the wire thickness and w is the wire width. The total inductance can be calculated via,

$$L = \frac{L_k}{\alpha_k} = \frac{L_{k,s}}{\alpha_k} \frac{l}{w}, \quad (5.16)$$

with l the wire length, α_k the kinetic inductance fraction, L_k the total kinetic inductance and $L_{k,s}$ the sheet kinetic inductance. In the thin film, local limit we have $L_{k,s} = 1/(d\sigma_2\omega_0)$ [26] and at low temperatures, $k_B T \ll \Delta$, the imaginary part of the complex conductivity equals, $\sigma_2 = \pi\Delta/(\hbar\omega_0\rho_N)$ [49], with ρ_N the normal state resistivity. Putting this together, we find,

$$j_0 = \sqrt{\frac{4\pi^2}{\rho_N} \frac{\Delta}{\hbar\omega_0} \frac{\alpha_k P_{\text{int}}}{V}}. \quad (5.17)$$

The critical current density is given by [53, 54]²,

$$j_c = 0.59 \sqrt{\frac{\pi\Delta^3 N_0}{\hbar\rho_N}} = 0.59 j_*, \quad (5.18)$$

where j_* is defined as the square-root term by convention. Because we assume that the current density is uniform over the wire, this critical current is given by the depairing current. If the wire would not be straight, but would have constrictions, sharp turns, or would be wider than the penetration depth, the critical current would be reduced [54, 55].

To first order, the kinetic inductance changes with (uniform) current as, $L_k(j) = L_k(0)(1 + 0.069(j/j_c)^2)$ [36, 37] under AC field, which coincides with the DC case when we take $j_{\text{rms}} = j_0/\sqrt{2} \rightarrow j_{\text{DC}}$ [37, 53]. This results in a fractional frequency shift compared to the zero current case¹,

$$\begin{aligned} \left. \frac{\delta\omega}{\omega_0} \right|_{L_k} &= -\frac{\alpha_k}{2} \frac{\delta L_k}{L_k(0)} \\ &= -0.035\alpha_k \left(\frac{j_0}{j_c} \right)^2 \\ &= -1.2 \frac{\alpha_k^2 P_{\text{int}}}{N_0 V \Delta^2 \omega_0}. \end{aligned} \quad (5.19)$$

²This equation is derived with via the Usadel equations, which holds for $T \ll T_c$ as opposed to the derivations using the Ginzburg-Landau equations, $j_c = 1.54 j_*$ [54]

¹Ref. [36] omitted a factor α_k as pointed out by Ref. [31]. However, an additional factor 0.16 is omitted in the derivation of $\delta\omega/\omega_0$ in Ref. [36]. Since the resonator studied there have a α_k close to 0.16, these errors approximately cancel. Eq. (5.19) is consistent with Ref. [36], when these two errors are taken into account and considering that P_0 in Ref. [36] can also be expressed as $P_0 = 2N_0 V \Delta^2 \omega_0 / \alpha_k$ for a distributed, half-wave resonator.

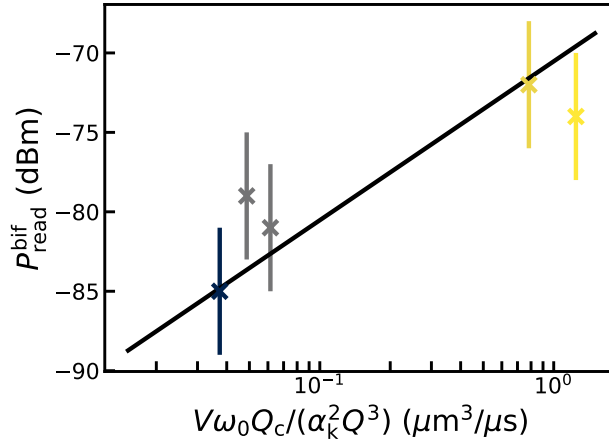


Figure 5.B.1: Verification of Eq. (5.21) with the resonators presented in Fig. 5.1.1. $P_{\text{read}}^{\text{bif}}$ is measured by visually checking the transmission curves at $T = 100$ mK with 4 dB steps in read power, which is indicated by the error bars. The black line is Eq. (5.21) without fit parameters, with Q_c and Q from a Lorentzian fit to the same transmission curves. α_k is obtained from transmission curves at higher bath temperatures [30].

Finally, bifurcation occurs when $\delta\omega/\omega_0 = -0.77/Q$ [19, 52], which results in

$$P_{\text{int}}^{\text{bif}} = 0.64N_0\Delta^2 \frac{V\omega_0}{\alpha_k^2 Q}, \quad (5.20)$$

and for the microwave power on the read-out line (see Eq. (5.13)),

$$P_{\text{read}}^{\text{bif}} = N_0\Delta^2 \frac{V\omega_0 Q_c}{\alpha_k^2 Q^3}. \quad (5.21)$$

This equation agrees closely with the resonator data, see Fig. 5.B.1.

5.B.1 QUASIPARTICLE NON-LINEARITY

Apart from the kinetic inductance non-linearity discussed above, the quasiparticle redistribution effects of read power also introduce a non-linearity in resonance frequency [15, 25, 31]. We can estimate this via the excess quasiparticle density, as $\delta\omega/\omega_0 = -\alpha_k n_{\text{qp}}^{\text{ex}}/(4N_0\Delta)$. The corrections for the reduced gap energy and quasiparticle distribution shape for this expression are of order unity [31]; approximately a factor 1.7 for the powers close to bifurcation in the resonators considered here.

We can take $n_{\text{qp}}^{\text{ex}}$ from Eq. (5.5), if we know Q_i and Σ_s in terms of superconductor

and resonator properties. We can approximate,

$$Q_i^{\text{qp}} = \frac{\sigma_2}{\alpha_k \sigma_1} \approx \frac{2\pi N_0 \Delta}{\alpha_k n_{\text{qp}}} \sqrt{\frac{\hbar \omega_0}{2\Delta}}, \quad (5.22)$$

which holds for $k_B T \ll (\Delta, \hbar \omega_0)$ [49].

If we assume that for Σ_s the power flow from quasiparticle to phonon system is via recombination only, we can equate,

$$\frac{P_{\text{abs}}}{V} = \frac{\Delta n_{\text{qp}}}{\eta_{2\Delta} \tau_{\text{qp}}^*} = \frac{\Sigma_s^{\text{rec}} \tau_0 (k_B T_c)^3}{16\pi \eta_{2\Delta} N_0 \Delta^3 k_B} \frac{n_{\text{qp}}}{\tau_{\text{qp}}^*}, \quad (5.23)$$

where the last expression is from Ref. [15]. $\eta_{2\Delta}$ is the fraction of pair-breaking phonons in the non-equilibrium phonon distribution function [15]. Solving for Σ_s^{rec} gives,

$$\Sigma_s^{\text{rec}} = 2\pi k_B (2N_0 \Delta)^2 R, \quad (5.24)$$

where $R = 2\Delta^2 / ((k_B T_c)^3 N_0 \tau_0)$. For Al, this results in 2.7×10^{10} W/m³/K, which is close to the value of 3.4×10^{10} W/m³/K from numerical calculations [15]. Combining the analytical expression for Σ_s^{rec} , Q_i^{qp} and Eq. (5.5) results in,

$$n_{\text{qp}}^{\text{ex}} = \frac{\alpha_k P_{\text{int}}}{2N_0 \Delta V} \sqrt{\frac{2\Delta}{\hbar \omega_0}} \frac{\eta_{2\Delta}}{\pi \Delta \bar{R}}. \quad (5.25)$$

Here, $\bar{R} = R / (1 + \tau_{\text{esc}} / \tau_{\text{pb}})$, with τ_{esc} the phonon escape time, τ_{pb} the phonon pair-breaking time and τ_0 the electron-phonon characteristic interaction time. Combining these expressions results in a resonance frequency shift due to the quasiparticle nonlinearity,

$$\left. \frac{\delta \omega}{\omega_0} \right|_{\text{qp}} = - \frac{\alpha_k^2 P_{\text{int}}}{N_0 V \Delta^2} \frac{\eta_{2\Delta}}{8\pi \bar{R} N_0 \Delta} \sqrt{\frac{2\Delta}{\hbar \omega_0}}. \quad (5.26)$$

From Eqs. (5.19) and (5.26) we thus find the ratio of the frequency shift due to kinetic inductance effects and quasiparticle redistribution effects to be,

$$\frac{\delta \omega|_{L_k}}{\delta \omega|_{\text{qp}}} = 21 \frac{\bar{R} N_0}{\eta_{2\Delta}} \sqrt{\frac{\hbar \Delta}{\omega_0}}. \quad (5.27)$$

When filling in $\eta_{2\Delta} = 4 \times 10^{-4}$, the measured Al properties, $\tau_{\text{esc}} = 0.35$ ns and the resonance frequencies of the resonators studied here, we obtain 5.1–6.1 for this ratio. This implies the two nonlinear effects are of the same order of magnitude and the measured bifurcation is caused by the kinetic inductance nonlinearity that is described by Eqs. (5.20) and (5.21).

In Eq. (5.22), we also assumed a thermal quasiparticle distribution. However, the quasiparticle distribution is generally not thermal when microwave photon absorption is considered [15, 16, 25]. The non-thermal distribution increases Q_i , which favors the kinetic inductance nonlinearity. See Section 3 for a quantitative description of this effect.

5.C NEP LIMITED BY MICROWAVE INDUCED EXCESS QUASIPARTICLES

We can estimate the NEP from quasiparticle fluctuations as [3]

$$\text{NEP}_{\text{GR}} = \frac{2\Delta}{\eta_{\text{pb}}} \sqrt{\frac{n_{\text{qp}} V}{\tau_{\text{qp}}^*}} = \frac{2\Delta}{\eta_{\text{pb}}} n_{\text{qp}} \sqrt{\tilde{R}V}, \quad (5.28)$$

where we used that, in the quasiparticle creation regime, the effective quasiparticle lifetime is given by, $\tau_{\text{qp}}^* = 1/(\tilde{R}n_{\text{qp}})$ [31]. If we use Eq. (5.25), i.e. assume $k_{\text{B}}T \ll (\Delta, \hbar\omega_0)$, and assume $P_{\text{int}}^{\text{bif}}$ from Eq. (5.20) for P_{int} , we arrive at

$$\text{NEP}_{\text{GR}}^{\text{bif}} = 0.29 \frac{\eta_{2\Delta}}{\eta_{\text{pb}}} \sqrt{\frac{\Delta^3}{\hbar\tilde{R}}} \frac{\sqrt{V\omega_0}}{\alpha_{\text{k}}Q}. \quad (5.29)$$

5.D Q_i WHEN QUASIPARTICLES ARE REDISTRIBUTED

Eq. (62) from [25] gives for the redistributed quasiparticle Q_i in the quasiparticle creation regime,

$$\begin{aligned} Q_i^{\text{qp,red.}} \Big|_{\text{crea}} &= \frac{19.3}{\alpha_{\text{k}}} \frac{\Delta}{\hbar\omega_0} \frac{\tau_{\text{pb}}}{\tau_{\text{esc}}} \left(\frac{\Delta}{k_{\text{B}}T_*} \right)^3 e^{\sqrt{14/5}(\Delta/k_{\text{B}}T_*)^3} \\ &= \frac{91.9}{\alpha_{\text{k}}} \frac{\Delta}{\hbar\omega_0} \frac{2N_0\Delta}{n_{\text{qp}}^{\text{ex}}} \left(\frac{k_{\text{B}}T_*}{\Delta} \right)^{3/2}, \end{aligned} \quad (5.30)$$

where we used Eq. (5.9) in the last equality.

In the redistribution regime, Q_i is predicted to follow Eq. (63) of [25],

$$Q_i^{\text{qp,red.}} \Big|_{\text{red.}} = \frac{4.1}{\alpha_{\text{k}}} \frac{\Delta}{\hbar\omega_0} \frac{2N_0\Delta}{n_{\text{qp}}} \left(\frac{k_{\text{B}}T_*}{\Delta} \right)^{3/2}. \quad (5.31)$$

This equation should also hold when n_{qp} is non-thermal due to another pair-breaking process, when setting $n_{\text{qp}} \rightarrow n_{\text{qp}}^{\text{ex}}$ [31].

5.E PAIR BREAKING PHOTON ATTENUATION

From Fig. 5.3.1(b), we concluded that the measured excess quasiparticle density cannot be explained by direct microwave photon absorption by quasiparticles only. This is a similar conclusion as the authors of Ref. [25] when comparing their explicit expression for $Q_i(P_{\text{int}})$ with the data from Ref. [16]. There must be an additional quasiparticle generation effect.

Since we observe that the excess quasiparticle density increases with increasing read power (Fig. 5.E.3(a)), as is observed in Ref. [16], this additional generation mechanism must increase with increasing read power. In Ref. [31], the authors propose a *pair-breaking* photon occupation number that is read power dependent as this additional generation mechanism. They show that they can fit the data of

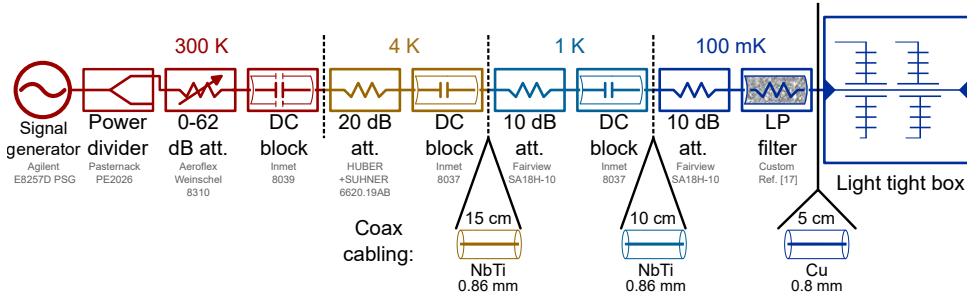


Figure 5.E.1: Diagram showing the measured components in the microwave chain from signal generator to chip.

Ref. [16] when they assume a pair-breaking photon occupation in the resonator, that is a factor 10^{-9} of the microwave photon occupation, i.e. -90 dBc.

The origin of these pair-breaking photons is not clear. Two possible sources are higher harmonics of the signal generator, also mentioned in [31], and heating of the 10 dB attenuator on the 100 mK stage (see Fig. 5.E.1). We show in this section that these hypotheses cannot explain the measured quasiparticle densities.

To estimate the effect of high harmonics generated by the signal generator, we measured the attenuation of pair-breaking radiation by several components in our setup, see Fig. 5.E.1. We used a Keysight-Agilent N5242A microwave network analyzer and two Anritsu 3740A-EW modules for frequency up-conversion to the 75-110 GHz band, with adapters to go from WR-10 to SMA. We calibrated the setup with a THRU calibration, including adapters, and measured each component in Fig. 5.E.1 individually. The combined results of these measurements are presented in Fig. 5.E.2. The main contributions to the attenuation are the variable attenuator at 300 K and the custom-made low-pass powder filter [9] at 100 mK. We measured an attenuation of -70 dB at most frequencies for these components, which is the noise floor of the setup. The actual attenuation is therefore likely to be higher.

On the other hand, the measured shown in Fig. 5.E.2 are performed at room temperature, while the components in the setup are cooled to the temperature specified in Fig. 5.E.1. We therefore disregard the losses in the superconducting NbTi wires. For the copper wire, we divide the attenuation (in dB) by the residual resistance ratio (RRR), which we assume to be 40. By doing this, we disregard losses in the dielectric of the coax cables, which might be significant at these frequencies. These corrections therefore lead to a conservative estimate of the attenuation in the wires. The attenuation of the low-pass filter is induced primarily by eddy currents in the metal powder dielectric, which is a bronze-Stycast mixture [9]. This attenuation has only a weak temperature dependence [56]. To account for this, we assume a RRR of bronze of 3 and divide the measured attenuation by the square root of that, as the skin depth in the metal grains scales with the square root of the resistance. These corrections are included in Fig. 5.E.2.

The signal generator is specified to generate less than -55 dBc in higher harmonics [57]. The average measured attenuation in the setup is $-117 \text{ dBc} \pm 10 \text{ dB}$, see

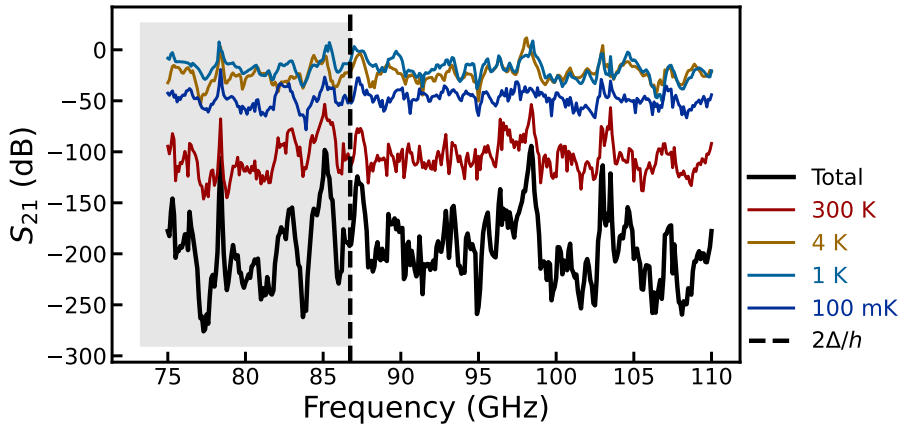


Figure 5.E.2: Measured forward transmission of the total combined microwave chain (black) and the components of the various temperature stages, indicated by the colors. The gap frequency of the Al is indicated by the black dashed line.

Fig. 5.E.2. The pair-breaking photon occupation at the chip is thus at maximum -162 dBc. This is much lower than the required -90 dBc [31] to explain the data from Ref. [16].

For the measurement presented in Fig. 5.1.2, we estimate the excess quasiparticle density generated by this pair-breaking photon occupation via [31],

$$n_{\text{qp}}^{\text{ex}} = 2N_0\Delta\sqrt{\frac{\pi}{4}\langle n_{\text{pb}}\rangle c_{\text{phot,pb}}^{\text{qp}}\tau_0\frac{\xi}{\Delta}\left(\frac{k_{\text{B}}T_{\text{c}}}{\Delta}\right)^3}. \quad (5.32)$$

$c_{\text{phot,pb}}^{\text{qp}} = \alpha_{\text{k}}\hbar\omega_{\text{pb}}^2/(2\pi N_0\Delta^2V)$ [31] is the quasiparticle-photon coupling constant for pair-breaking photons with energy $\hbar\omega_{\text{pb}}$. $\langle n_{\text{pb}}\rangle$ is the pair-breaking photon occupation and $\xi = 2\Delta - \hbar\omega_{\text{pb}}$.

If we take for $\langle n_{\text{pb}}\rangle = \chi P_{\text{read}}/(\hbar\omega_{\text{pb}}^2)$, with $\chi = 10^{-16.2}$, or -162 dB, the on-chip ratio of readout power and pair-breaking photons and $\hbar\omega_{\text{pb}} = 2.8\Delta$ [31], we come to $n_{\text{qp}}^{\text{ex}} \approx 10^{-3} \mu\text{m}^{-3}$. This is 5 orders of magnitude lower than measured at these read powers, see Fig. 5.E.3(a). We therefore exclude the signal generator as pair-breaking photon source.

Another possible source pair-breaking photons is radiation coming from the 10 dB attenuator at the 100 mK stage, see Fig. 5.E.1. We consider this the only relevant component for heating effects, since the read power must significantly heat the component to obtain the read power dependence of $n_{\text{qp}}^{\text{ex}}$ (Fig. 5.E.3(a)).

We estimate the on-chip pair-breaking power coming from the 10 dB attenuator as 1D black-body radiation (i.e. Johnson-Nyquist noise [58]) that is attenuated by the

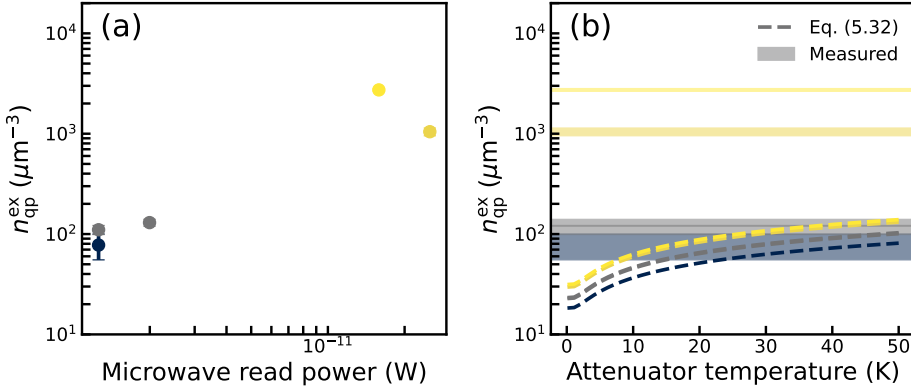


Figure 5.E.3: Estimation for excess quasiparticle density due to read out power heating of the 10 dB attenuator at 100 mK. **(a)**: The measured excess quasiparticle density from Fig. 5.3.1, with the used on-chip read power on the x-axis. This shows that the quasiparticle density does increase with increasing read power. **(b)**: Estimation of the excess quasiparticle density from Eq. (5.32) [31], when assuming a heated temperature for the 10 dB attenuator given by the x-axis. Different colors indicate the different resonators, like in Figs. 5.1.2 and 5.B.1. The colored areas are the measured values from (a). Since these are much larger than the predicted values (dashed lines), we conclude that this effect is too small to explain the measured excess quasiparticle densities.

low-pass powder filter,

$$P_{\text{chip}} = \int_{2\Delta/h}^{\infty} \left[\frac{hf}{e^{hf/k_B T_{\text{att}}} - 1} + \frac{hf}{2} \right] e^{-f/f_c} df, \quad (5.33)$$

where $h = 2\pi\hbar$ is the Planck constant, T_{att} is the temperature of the 10 dB attenuator and $f_c = 10$ GHz is the cut-off frequency of the filter [9]. This filter shape has been confirmed up to 10 GHz. At 80 GHz this would be a attenuation of -45 dB, where we measured it to be at least -70 dB. Thus, the filter attenuates more at higher frequencies than we assume here.

We calculate the average photon energy as,

$$\langle E_{\text{ph}} \rangle = P_{\text{chip}} / \int_{2\Delta/h}^{\infty} \left[\frac{1}{e^{hf/k_B T} - 1} + \frac{1}{2} \right] e^{-f/f_c} df, \quad (5.34)$$

which results in $\xi = 0.22$. Using $\langle n_{\text{pb}} \rangle = hP_{\text{chip}} / \langle E_{\text{ph}} \rangle^2$ in Eq. (5.32), we obtain the dashed lines in Fig. 5.E.3(b). The different lines correspond to the different resonators. We deem it extremely unlikely that the attenuator at 100 mK is heated to 50 K or more, since it has a stainless steel body that is connected directly to the cryostat 100 mK stage. Moreover, we here did not consider the coupling of pair-breaking photon from transmission line to the Al section of the resonator. That would give an additional attenuation of -32 dB, as estimated from a simulation

of the resonator in SONNET. When taking this coupling into account, the dashed lines in Fig. 5.E.3(b) shift more than an order of magnitude downwards. We therefore conclude that also this mechanism is not the cause of the measured excess quasiparticle density.

REFERENCES

- [1] S. A. H. de Rooij, J. J. A. Baselmans, J. Bueno, V. Murugesan, D. J. Thoen, and P. J. de Visser. *Volume Dependence of Microwave-Induced Excess Quasiparticles in Superconducting Resonators*. In: *Physical Review Applied* 24.2 (2025), p. 024007.
- [2] L. Glazman and G. Catelani. *Bogoliubov Quasiparticles in Superconducting Qubits*. In: *SciPost Physics Lecture Notes* (2021), p. 031.
- [3] P. J. de Visser, J. J. A. Baselmans, P. Diener, S. J. C. Yates, A. Endo, and T. M. Klapwijk. *Generation-Recombination Noise: The Fundamental Sensitivity Limit for Kinetic Inductance Detectors*. In: *Journal of Low Temperature Physics* 167.3 (2012), pp. 335–340.
- [4] J. M. Martinis, M. Ansmann, and J. Aumentado. *Energy Decay in Superconducting Josephson-Junction Qubits from Nonequilibrium Quasiparticle Excitations*. In: *Physical Review Letters* 103.9 (2009), p. 097002.
- [5] P. J. de Visser, J. J. A. Baselmans, P. Diener, S. J. C. Yates, A. Endo, and T. M. Klapwijk. *Number Fluctuations of Sparse Quasiparticles in a Superconductor*. In: *Physical Review Letters* 106.16 (2011), p. 167004.
- [6] J. M. Martinis. *Saving Superconducting Quantum Processors from Decay and Correlated Errors Generated by Gamma and Cosmic Rays*. In: *npj Quantum Information* 7.1 (1 2021), pp. 1–9.
- [7] M. McEwen, L. Faoro, K. Arya, A. Dunsworth, T. Huang, S. Kim, B. Burkett, A. Fowler, F. Arute, J. C. Bardin, A. Bengtsson, A. Bilmes, B. B. Buckley, N. Bushnell, Z. Chen, R. Collins, S. Demura, A. R. Derk, C. Erickson, M. Giustina, S. D. Harrington, S. Hong, E. Jeffrey, J. Kelly, P. V. Klimov, F. Kostritsa, P. Laptev, A. Locharla, X. Mi, K. C. Miao, S. Montazeri, J. Mutus, O. Naaman, M. Neeley, C. Neill, A. Opremcak, C. Quintana, N. Redd, P. Roushan, D. Sank, K. J. Satzinger, V. Shvarts, T. White, Z. J. Yao, P. Yeh, J. Yoo, Y. Chen, V. Smelyanskiy, J. M. Martinis, H. Neven, A. Megrant, L. Ioffe, and R. Barends. *Resolving Catastrophic Error Bursts from Cosmic Rays in Large Arrays of Superconducting Qubits*. In: *Nature Physics* 18.1 (2022), pp. 107–111.
- [8] L. Cardani, F. Valenti, N. Casali, G. Catelani, T. Charpentier, M. Clemenza, I. Colantoni, A. Cruciani, G. D’Imperio, L. Gironi, L. Grünhaupt, D. Gusenkova, F. Henriques, M. Lagoin, M. Martinez, G. Pettinari, C. Rusconi, O. Sander, C. Tomei, A. V. Ustinov, M. Weber, W. Wernsdorfer, M. Vignati, S. Pirro, and I. M. Pop. *Reducing the Impact of Radioactivity on Quantum Circuits in a Deep-Underground Facility*. In: *Nature Communications* 12.1 (1 2021), p. 2733.

- [9] J. J. A. Baselmans, S. J. C. Yates, P. Diener, and P. J. de Visser. *Ultra Low Background Cryogenic Test Facility for Far-Infrared Radiation Detectors*. In: *Journal of Low Temperature Physics* 167.3 (2012), pp. 360–366.
- [10] P. J. de Visser, J. J. A. Baselmans, S. J. C. Yates, P. Diener, A. Endo, and T. M. Klapwijk. *Microwave-Induced Excess Quasiparticles in Superconducting Resonators Measured through Correlated Conductivity Fluctuations*. In: *Applied Physics Letters* 100.16 (2012), p. 162601.
- [11] M. Esposito, A. Ranadive, L. Planat, and N. Roch. *Perspective on Traveling Wave Microwave Parametric Amplifiers*. In: *Applied Physics Letters* 119.12 (2021), p. 120501.
- [12] M. R. Vissers, J. Hubmayr, M. Sandberg, S. Chaudhuri, C. Bockstiegel, and J. Gao. *Frequency-Tunable Superconducting Resonators via Nonlinear Kinetic Inductance*. In: *Applied Physics Letters* 107.6 (2015), p. 062601.
- [13] G. M. Éliashberg. *Inelastic Electron Collisions and Nonequilibrium Stationary States in Superconductors*. In: *Soviet Journal of Experimental and Theoretical Physics* 34 (1972), p. 668.
- [14] B. I. Ivlev, S. G. Lisitsyn, and G. M. Eliashberg. *Nonequilibrium Excitations in Superconductors in High-Frequency Fields*. In: *Journal of Low Temperature Physics* 10.3 (1973), pp. 449–468.
- [15] D. J. Goldie and S. Withington. *Non-Equilibrium Superconductivity in Quantum-Sensing Superconducting Resonators*. In: *Superconductor Science and Technology* 26.1 (2012), p. 015004.
- [16] P. J. de Visser, D. J. Goldie, P. Diener, S. Withington, J. J. A. Baselmans, and T. M. Klapwijk. *Evidence of a Nonequilibrium Distribution of Quasiparticles in the Microwave Response of a Superconducting Aluminum Resonator*. In: *Physical Review Letters* 112.4 (2014), p. 047004.
- [17] P. K. Day, H. G. LeDuc, B. A. Mazin, A. Vayonakis, and J. Zmuidzinis. *A Broadband Superconducting Detector Suitable for Use in Large Arrays*. In: *Nature* 425.6960 (2003), pp. 817–821.
- [18] J. Gao, J. Zmuidzinis, B. A. Mazin, H. G. LeDuc, and P. K. Day. *Noise Properties of Superconducting Coplanar Waveguide Microwave Resonators*. In: *Applied Physics Letters* 90.10 (2007), p. 102507.
- [19] L. J. Swenson, P. K. Day, B. H. Eom, H. G. Leduc, N. Llombart, C. M. McKenney, O. Noroozian, and J. Zmuidzinis. *Operation of a Titanium Nitride Superconducting Microresonator Detector in the Nonlinear Regime*. In: *Journal of Applied Physics* 113.10 (2013), p. 104501.
- [20] S. Hailey-Dunsheath, R. M. J. Janssen, J. Glenn, C. M. Bradford, J. Perido, J. Redford, and J. Zmuidzinis. *Kinetic Inductance Detectors for the Origins Space Telescope*. In: *Journal of Astronomical Telescopes, Instruments, and Systems* 7.1 (2021), p. 011015.

- [21] J. J. A. Baselmans, F. Facchin, A. P. Laguna, J. Bueno, D. J. Thoen, V. Murugesan, N. Llombart, and P. J. de Visser. *Ultra-Sensitive THz Microwave Kinetic Inductance Detectors for Future Space Telescopes*. In: *Astronomy & Astrophysics* 665 (2022), A17.
- [22] S. B. Kaplan, C. C. Chi, D. N. Langenberg, J. J. Chang, S. Jafarey, and D. J. Scalapino. *Quasiparticle and Phonon Lifetimes in Superconductors*. In: *Physical Review B* 14.11 (1976), pp. 4854–4873.
- [23] D. J. Thoen, B. G. C. Bos, E. A. F. Haalebos, T. M. Klapwijk, J. J. A. Baselmans, and A. Endo. *Superconducting NbTiN Thin Films With Highly Uniform Properties Over a 100 Mm Wafer*. In: *IEEE Transactions on Applied Superconductivity* 27.4 (2017), pp. 1–5.
- [24] O. Noroozian, J. Gao, J. Zmuidzinas, H. G. LeDuc, and B. A. Mazin. *Two-level System Noise Reduction for Microwave Kinetic Inductance Detectors*. In: *AIP Conference Proceedings* 1185.1 (2009), pp. 148–151.
- [25] P. Fischer and G. Catelani. *Nonequilibrium Quasiparticle Distribution in Superconducting Resonators: An Analytical Approach*. In: *Physical Review Applied* 19.5 (2023), p. 054087.
- [26] J. Gao. *The Physics of Superconducting Microwave Resonators*. California Institute of Technology, 2008.
- [27] R. Barends. *Photon-Detecting Superconducting Resonators*. Delft: Delft University of Technology, 2009.
- [28] C. M. Wilson and D. E. Prober. *Quasiparticle Number Fluctuations in Superconductors*. In: *Physical Review B* 69.9 (2004), p. 094524.
- [29] P. J. de Visser. *Quasiparticle Dynamics in Aluminium Superconducting Microwave Resonators*. PhD thesis. Delft: Delft University of Technology, 2014. 222 pp.
- [30] J. Gao, J. Zmuidzinas, B. A. Mazin, P. K. Day, and H. G. Leduc. *Experimental Study of the Kinetic Inductance Fraction of Superconducting Coplanar Waveguide*. In: *Nuclear Instruments and Methods in Physics Research Section A: Accelerators, Spectrometers, Detectors and Associated Equipment*. Proceedings of the 11th International Workshop on Low Temperature Detectors 559.2 (2006), pp. 585–587.
- [31] P. B. Fischer and G. Catelani. *Nonequilibrium Quasiparticle Distribution in Superconducting Resonators: Effect of Pair-Breaking Photons*. In: *SciPost Physics* 17.3 (2024), p. 070.
- [32] S. B. Kaplan. *Acoustic Matching of Superconducting Films to Substrates*. In: *Journal of Low Temperature Physics* 37.3 (1979), pp. 343–365.
- [33] W. Eisenmenger, K. Laßmann, H. J. Trumpp, and R. Krauß. *Quasiparticle Recombination and 2Δ -phonon-trapping in Superconducting Tunneling Junctions*. In: *Applied physics* 11.4 (1976), pp. 307–320.

- [34] T. Guruswamy, D. J. Goldie, and S. Withington. *Nonequilibrium Superconducting Thin Films with Sub-Gap and Pair-Breaking Photon Illumination*. In: *Superconductor Science and Technology* 28.5 (2015), p. 054002.
- [35] J.-J. Chang and D. J. Scalapino. *Kinetic-Equation Approach to Nonequilibrium Superconductivity*. In: *Physical Review B* 15.5 (1977), pp. 2651–2670.
- [36] A. V. Semenov, I. A. Devyatov, P. J. de Visser, and T. M. Klapwijk. *Coherent Excited States in Superconductors Due to a Microwave Field*. In: *Physical Review Letters* 117.4 (2016), p. 047002.
- [37] A. Semenov, I. Devyatov, M. Westig, and T. Klapwijk. *Effect of Microwaves on Superconductors for Kinetic Inductance Detection and Parametric Amplification*. In: *Physical Review Applied* 13.2 (2020), p. 024079.
- [38] A. G. Kozorezov, A. A. Golubov, J. K. Wigmore, D. Martin, P. Verhoeve, R. A. Hijmering, and I. Jerjen. *Inelastic Scattering of Quasiparticles in a Superconductor with Magnetic Impurities*. In: *Physical Review B* 78.17 (2008), p. 174501.
- [39] R. Barends, S. van Vliet, J. J. A. Baselmans, S. J. C. Yates, J. R. Gao, and T. M. Klapwijk. *Enhancement of Quasiparticle Recombination in Ta and Al Superconductors by Implantation of Magnetic and Nonmagnetic Atoms*. In: *Physical Review B* 79.2 (2009), 020509(R).
- [40] S. A. H. de Rooij, J. J. A. Baselmans, V. Murugesan, D. J. Thoen, and P. J. de Visser. *Strong Reduction of Quasiparticle Fluctuations in a Superconductor Due to Decoupling of the Quasiparticle Number and Lifetime*. In: *Physical Review B* 104.18 (2021), p. L180506.
- [41] S. A. H. de Rooij, R. Fermin, K. Kouwenhoven, T. Coppens, V. Murugesan, D. J. Thoen, J. Aarts, J. J. A. Baselmans, and P. J. de Visser. *Recombination of Localized Quasiparticles in Disordered Superconductors*. In: *Nature Communications* 16.1 (2025), p. 8465.
- [42] T. Guruswamy, D. J. Goldie, and S. Withington. *Quasiparticle Generation Efficiency in Superconducting Thin Films*. In: *Superconductor Science and Technology* 27.5 (2014), p. 055012.
- [43] J. Gao, M. Daal, J. M. Martinis, A. Vayonakis, J. Zmuidzinas, B. Sadoulet, B. A. Mazin, P. K. Day, and H. G. Leduc. *A Semiempirical Model for Two-Level System Noise in Superconducting Microresonators*. In: *Applied Physics Letters* 92.21 (2008), p. 212504.
- [44] G. Catelani and D. M. Basko. *Non-Equilibrium Quasiparticles in Superconducting Circuits: Photons vs. Phonons*. In: *SciPost Physics* 6.1 (2019), p. 013.
- [45] T. M. Klapwijk and P. J. de Visser. *The Discovery, Disappearance and Re-Emergence of Radiation-Stimulated Superconductivity*. In: *Annals of Physics* (2020), p. 168104.
- [46] J. Rautio. *Sonnet Suites - Sonnet Software*. 2025. URL: <https://www.sonnetsoftware.com/products/sonnet-suites/index.html>.

- [47] J. Gao, J. Zmuidzinas, A. Vayonakis, P. Day, B. Mazin, and H. Leduc. *Equivalence of the Effects on the Complex Conductivity of Superconductor Due to Temperature Change and External Pair Breaking*. In: *Journal of Low Temperature Physics* 151.1 (2008), pp. 557–563.
- [48] M. Sidorova, A. D. Semenov, H.-W. Hübers, S. Gyger, S. Steinhauer, X. Zhang, and A. Schilling. *Magnetoconductance and Photoresponse Properties of Disordered NbTiN Films*. In: *Physical Review B* 104.18 (2021), p. 184514.
- [49] D. C. Mattis and J. Bardeen. *Theory of the Anomalous Skin Effect in Normal and Superconducting Metals*. In: *Physical Review* 111.2 (1958), pp. 412–417.
- [50] B. A. Mazin. *Microwave Kinetic Inductance Detectors: The First Decade*. In: *AIP Conference Proceedings* 1185.1 (2009), pp. 135–142.
- [51] D. M. Pozar. *Microwave Engineering, 4th Edition*. Wiley, 2011. 756 pp.
- [52] J. Zmuidzinas. *Superconducting Microresonators: Physics and Applications*. In: *Annual Review of Condensed Matter Physics* 3.1 (2012), pp. 169–214.
- [53] A. Anthore, H. Pothier, and D. Esteve. *Density of States in a Superconductor Carrying a Supercurrent*. In: *Physical Review Letters* 90.12 (2003), p. 127001.
- [54] J. R. Clem and V. G. Kogan. *Kinetic Impedance and Depairing in Thin and Narrow Superconducting Films*. In: *Physical Review B* 86.17 (2012), p. 174521.
- [55] J. R. Clem and K. K. Berggren. *Geometry-Dependent Critical Currents in Superconducting Nanocircuits*. In: *Physical Review B* 84.17 (2011), p. 174510.
- [56] F. P. Milliken, J. R. Rozen, G. A. Keefe, and R. H. Koch. *50Ω Characteristic Impedance Low-Pass Metal Powder Filters*. In: *Review of Scientific Instruments* 78.2 (2007), p. 024701.
- [57] *E8257D PSG Microwave Analog Signal Generator*. Keysight Technologies, Inc.
- [58] H. Nyquist. *Thermal Agitation of Electric Charge in Conductors*. In: *Physical Review* 32.1 (1928), pp. 110–113.

6

RECOMBINATION OF LOCALIZED QUASIPARTICLES IN DISORDERED SUPERCONDUCTORS

Disordered superconductors offer new impedance regimes for quantum circuits, enable a pathway to protected qubits, and can improve superconducting detectors due to their high kinetic inductance and sheet resistance. The performance of these devices can be limited, however, by quasiparticles - the fundamental excitations of a superconductor. While experiments have shown that disorder affects the relaxation of quasiparticles drastically, the microscopic mechanisms are still not understood. We address this issue by measuring quasiparticle relaxation in a disordered β -Ta film, which we pattern as the inductor of a microwave resonator. We observe that quasiparticle recombination is governed by the phonon scattering time, which is faster than conventional recombination in ordered superconductors. We interpret the results as recombination of localized quasiparticles, induced by disorder, which first delocalize via phonon absorption. We analyze quasiparticle relaxation measurements on superconductors with different degrees of disorder and conclude that this phenomenon is inherent to disordered superconductors.

This chapter was published as S. A. H. de Rooij, R. Fermin, K. Kouwenhoven, T. Coppens, V. Murugesan, D. J. Thoen, J. Aarts, J. J. A. Baselmans, and P. J. de Visser. *Recombination of Localized Quasiparticles in Disordered Superconductors*. In: *Nature Communications* 16.1 (2025), p. 8465.

6.1 INTRODUCTION

Disordered superconductors have a high resistance in their normal state, leading to a competition between electronic localization effects and the global phase coherence of superconductivity. A large amount of disorder can induce electronic granularity, pre-formed Cooper-pairs, ultimately causing a superconductor-to-insulator phase transition [8, 9].

Localization effects weaken the superfluid stiffness, thereby increasing the kinetic inductance (L_k) of the superconductor. This enables new regimes in high impedance quantum circuits and the development of protected qubits [10], as well as highly non-linear elements for parametric amplification [11]. For superconducting single-photon detectors [12, 13], the high normal state resistance of disordered superconductors increases the broadband photon absorption efficiency [14, 15] and photon responsivity [16, 17].

Quasiparticles, the elementary excitations in a superconductor, play a central role in these applications. In quantum circuits, quasiparticles cause decoherence and microwave loss. Considerable efforts have been made to mitigate excess quasiparticles [18–22] and to explain the non-vanishing quasiparticle density at low temperatures [2, 23–25]. For superconducting radiation detectors, the relaxation of photon-generated quasiparticles dictates the detector performance [26].

As disorder increases, the limiting relaxation time at low temperatures becomes shorter [27]. In contrast, quasiparticle relaxation times on the order of seconds have been measured in granular Al, which is highly disordered due to oxidized grain boundaries [28]. Furthermore, when exciting disordered superconductors with electromagnetic radiation, an anomalous quasiparticle response has been measured [29, 30] and microwave loss typically increases with L_k [31]. This hinders the use of disordered superconductors in quantum circuits and superconducting radiation detectors. These observations suggest that disorder affects quasiparticle relaxation, but the underlying mechanisms remain poorly understood.

In this work, we demonstrate that localization effects govern the relaxation of quasiparticles in disordered superconductors. Disorder induces local gap inhomogeneities that serve as localization sites where quasiparticles rapidly recombine. Consequently, the relaxation process is not governed by recombination of mobile quasiparticles, as in ordered superconductors (Fig. 6.1.1(c)), but rather by delocalization and subsequent on-site recombination with a localized quasiparticle (Fig. 6.1.1(d)). This leads to a shorter relaxation time with a weaker temperature dependence than in the absence of localization effects. Such a short relaxation time will help to mitigate excess quasiparticles in quantum circuits [18]. On the other hand, at low temperatures and quasiparticle generation rates, a background of localized quasiparticles may induce additional microwave loss [28] and limit the response of superconducting detectors [29, 30].

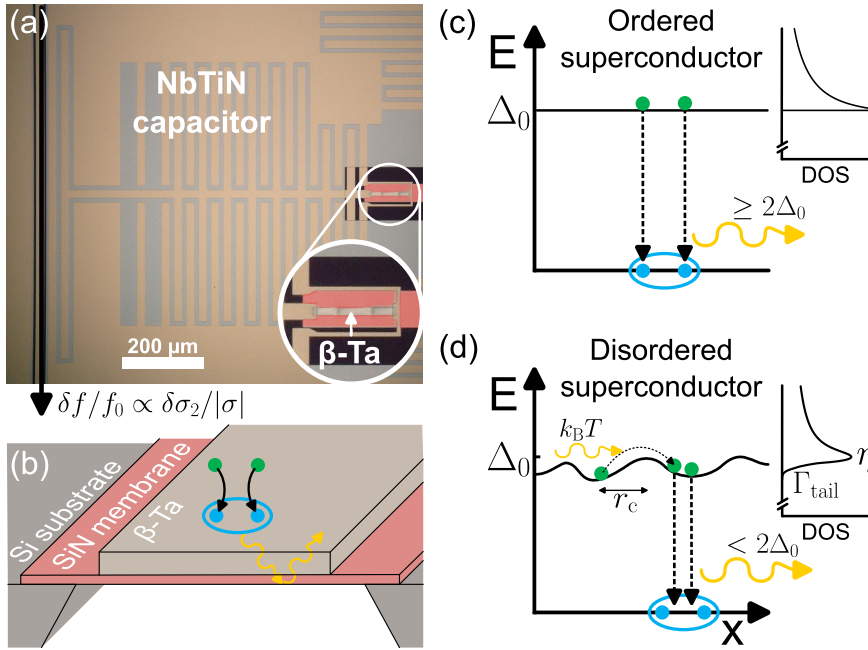


Figure 6.1.1: **Quasiparticle fluctuation measurement and the inferred effect of disorder on quasiparticle recombination.** (a): Micrograph of the microwave resonator consisting of a NbTiN capacitor and β -Ta inductor on a membrane, which is highlighted in red. Inside the white circle the figure is two times enlarged. We measure fluctuations in resonance frequency (δf), which are proportional to complex conductivity fluctuations ($\delta\sigma_2$). (b): Sketch of the β -Ta inductor on the 110 nm thick SiN membrane. When two quasiparticles (green) recombine into a Cooper-pair (blue), a phonon is emitted (yellow curly arrows). A change in the number of quasiparticles or Cooper-pairs changes σ_2 , which we measure. The emitted phonon is trapped by the membrane, as indicated. We measure two resonators: one with the inductor on a SiN membrane (as sketched) and one with the SiN patch on solid Si substrate. (c): Sketch of traditional quasiparticle recombination with emission of a phonon with energy $\geq 2\Delta_0$, which can subsequently break a Cooper-pair. The BCS density of state (DOS) is sketched on the right, which has the same energy y-axis. (d): Sketch of quasiparticle recombination in disordered superconductors. Disorder can suppress the gap locally, inducing quasiparticle localization at a typical length scale of $r_c \sim \xi$ [2]. Quasiparticles can delocalize via absorption of a phonon, after which they relax and rapidly recombine on-site, emitting a phonon with less than $2\Delta_0$ energy. Since phonon absorption is slow in disordered superconductors [3, 4] and subsequent on-site recombination is fast [2, 5], delocalization limits this process. On the right, the position-averaged DOS is sketched with a broadened coherence peak, parameterized by η , and a sub-gap tail consisting of localized states, parameterized by Γ_{tail} [6, 7].

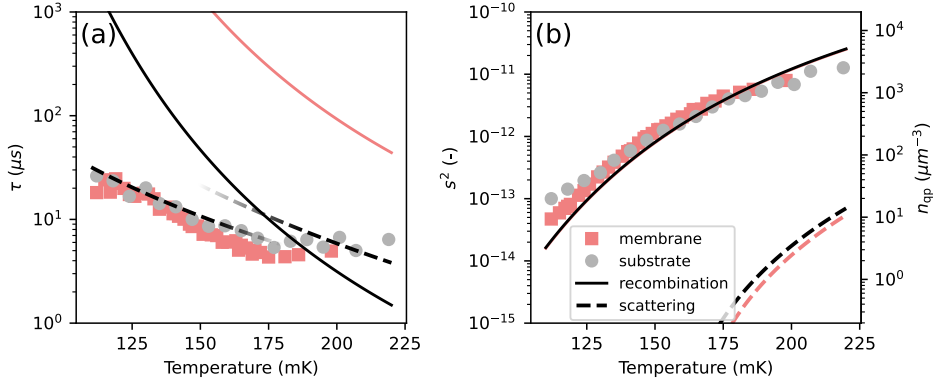


Figure 6.2.1: Measured relaxation time and variance compared with quasiparticle fluctuation theory. The gray circles and red squares are determined from a fit to the measured fluctuation spectra (Fig. 6.4.1), which gives the relaxation time (a) and variance (b) of the quasiparticle fluctuation. The red squares are for the inductor on a SiN membrane (see Fig. 6.1.1(b)) and the gray circles on a SiN/Si solid substrate, as indicated by the legend. Error bars from statistical fit errors are smaller than the data points. The dashed lines in (a) are calculations for electron-phonon scattering time, Eq. (6.3), which is 2D for $T < 165$ mK [32] and 3D for higher temperatures [3]. The dashed lines in (b) are the variance of quasiparticle fluctuations for scattering events. The solid lines are for recombination. The red solid line in (a) includes the expected increase in relaxation time due to phonon trapping by the membrane (Fig. 6.1.1(b)). These curves are calculated with the parameters in Table 6.4.1 without fit parameters. The right axis in (b) gives the quasiparticle density corresponding to the variance of recombination events (the solid line).

6.2 RESULTS

6.2.1 FLUCTUATION MEASUREMENTS

We measure the quasiparticle relaxation time (τ) and density (n_{qp}) in a 40 nm thick disordered β -Ta film [33], which is patterned as the inductor in a microwave resonator. The device is shown in Fig. 6.1.1(a) and the film parameters are given in Table 6.4.1. This β -Ta film is disordered as the Ioffe-Regel parameter, $k_F l$, is close to one, with k_F the Fermi wave number and l the electronic mean free path. We therefore expect localization effects to become important. Moreover, ql is much smaller than unity, with q the phonon wave number of a phonon with energy $2\Delta_0$, which is the BCS superconducting gap energy at low temperatures. This means the film is disordered with respect to electron-phonon interactions [3]. The characterization of the film is outlined in the Methods section.

We cool the resonators to bath temperatures ranging from 20 mK to 300 mK. For each bath temperature, we drive the resonator at its resonance frequency and measure time streams of the complex microwave transmission in a homodyne setup (see Methods). From that, we extract the Power Spectral Density (PSD) of the fluctuations in σ_2 , $S_{\delta\sigma_2/|\sigma|}(\omega)$, where $\sigma = \sigma_1 - i\sigma_2$ is the complex conductivity. This

is equivalent to measuring the resonator frequency noise. These fluctuations are characterized by a Lorentzian spectrum [34], as is visible in the measured PSDs in Fig. 6.4.1. We fit a Lorentzian spectrum and extract the variance, s^2 , and relaxation time, τ , as described in the Methods section.

The measured τ and s^2 are shown in Fig. 6.2.1(a) and (b). For higher and lower bath temperatures than shown in Fig. 6.2.1, the quasiparticle fluctuations were obscured by other noise sources such as $1/f$ and amplifier noise.

6.2.2 PHONON SCATTERING LIMITED QUASIPARTICLE RELAXATION

We compare these measured values to the theory for quasiparticle relaxation. At low temperatures, $k_B T \ll \Delta_0$ with T the bath temperature and k_B the Boltzmann constant, τ is governed by electron-phonon interactions, because n_{qp} is low compared to the normal state carrier density [35]. As a check, we compared the electron-electron and electron-phonon interaction times [36] and find that the electron-phonon interaction has the shortest relevant timescales in our system, as outlined in the Section 6.A.

There are two inelastic electron-phonon processes that contribute to the relaxation of quasiparticles: recombination and scattering.

During a recombination event, two quasiparticles recombine into a Cooper-pair and emit a phonon with energy $\Omega \geq 2\Delta_0$, as illustrated in Fig. 6.1.1(c). Quasiparticle generation is the same process, but time-reversed. The recombination time, τ_{rec} , is proportional to $1/n_{qp}$, which exponentially decreases with temperature, i.e. [3, 35]

$$\tau_{rec}(T) = \tau_0^{rec} \sqrt{\frac{T_c}{T}} e^{\Delta_0/k_B T}. \quad (6.1)$$

T_c is the critical temperature and τ_0^{rec} is a proportionality constant that does not depend on temperature, but does depend on disorder and dimensionality (see Methods).

In our experiment, we probe the entire inductor volume and therefore measure the relaxation of an ensemble of quasiparticles. The bulk recombination time is given by [37],

$$\tau_{rec}^* = \tau_{rec}(1 + \tau_{esc}/\tau_{pb})/2, \quad (6.2)$$

where τ_{esc} is the escape time and τ_{pb} is the pair-breaking time of a $2\Delta_0$ phonon. The last division by two in Eq. (6.2) describes the pair-wise nature of recombination. The factor in parenthesis is the phonon trapping factor and takes into account that the emitted $2\Delta_0$ -phonon can subsequently break another pair. Quasiparticles in an ordered superconductor, like Al and α -Ta with $ql \gg 1$, relax with a relaxation time given by Eq. (6.2), which increases when phonon trapping is enhanced [27, 35, 38].

For the substrate case, with β -Ta on a SiN/Si substrate, we estimate the phonon trapping factor to be 2.0 from the acoustic mismatch theory set out in Ref. [39, 40]. Using the parameters of the film (Table 6.4.1), which are independently measured without fitting to the data, we obtain the solid black line in Fig. 6.2.1(a). Details on the calculation of the curves in Fig. 6.2.1 are presented in Section 6.A.

We increase τ_{esc} experimentally by etching the Si under the SiN patch of the

resonators, such that the β -Ta inductor is suspended on a 110 nm thick membrane. This is shown in Fig. 6.1.1(b). Via a simple geometric calculation (Section 6.A), we estimate that the membrane results in an increase of τ_{esc} by factor 58 compared to the substrate case. That would increase τ_{rec}^* by a factor 29, which is shown in Fig. 6.2.1(a) as the red solid line. We observe that the quasiparticle relaxation time is identical for both the substrate and membrane case, which is not in agreement with conventional quasiparticle recombination. Moreover, the temperature dependence of the relaxation time is much weaker than the conventional exponential temperature dependence (Eq. (6.2)).

The dashed lines in Fig. 6.2.1(a) are for quasiparticle-phonon scattering. During a scattering event, a quasiparticle absorbs a thermal phonon of energy $\sim k_B T$. The inelastic time related to scattering, τ_{scat} , is proportional to the phonon occupation and therefore follows a power law versus temperature,

$$\tau_{\text{scat}}(T) = \tau_0^{\text{scat}} \left(\frac{T}{T_C} \right)^{-n}, \quad (6.3)$$

with $2 \leq n \leq 9/2$. n and τ_0^{scat} depend on disorder and the electron and phonon dimensionality [3, 32, 35, 41]. In our film, thermal phonons are 2D for $T \lesssim 165$ mK and 3D for higher temperatures. This changes the exponent n from 9/2 in 3D [3] to 7/2 in 2D [32]. Using the parameters from Table 6.4.1 results in the dashed lines in Fig. 6.2.1(a). We divide Eq. (6.3) by a factor 2 in Fig. 6.2.1(a) to account for pair-wise recombination after the phonon scattering event, similar to Eq. (6.2).

The agreement between the measured quasiparticle relaxation time and the power-law temperature dependence of phonon scattering, indicates that quasiparticle relaxation is governed by phonon scattering. This is the main experimental result of this work and is in sharp contrast to ordered superconductors, such as Al and α -Ta [27, 38].

6.2.3 VERIFICATION OF QUASIPARTICLE GENERATION-RECOMBINATION FLUCTUATIONS

To examine which relaxation process we observe, we compare the measured variance to the calculated variance of quasiparticle generation-recombination and scattering fluctuations in σ_2 . This is shown in Fig. 6.2.1(b). We calculate the generation-recombination noise variance with $s^2 = (n_{\text{qp}}/V)(d(\sigma_2/|\sigma|)/dn_{\text{qp}})^2$ [34], where V is the β -Ta volume and the factor in parentheses is the responsivity of the complex conductivity to changes in the quasiparticle density. This results in the solid line in Fig. 6.2.1(b). This variance is equal for the membrane and substrate case, because it does not depend on phonon trapping. The responsivity factor is approximately constant with temperature (< 2 % deviation in our measurement regime) and known from theory [42, 43], which allows us to directly measure the quasiparticle density from the variance [44]. The right axis of Fig. 6.2.1(d) gives the quasiparticle density corresponding to the variance.

The dashed lines in Fig. 6.2.1(b) give the variance for scattering interactions. It is orders of magnitude lower than the variance for recombination events, because the

energy difference of a scattering event is much less than that of a recombination event, $k_B T \ll \Delta_0$. The variance of the fluctuations clearly corresponds to the recombination of thermal quasiparticles [34]. We attribute the small deviation from the thermal line at low temperatures to microwave read-out power effects [23], see also Fig. 6.4.3.

We performed the same analysis to the measured dissipative fluctuations, $\delta\sigma_1$, which are shown in Fig. 6.4.2. The results show the same phenomenology as Fig. 6.2.1: a relaxation time governed by phonon scattering and a generation-recombination noise variance. This shows that we measure quasiparticle recombination events [34, 44].

To summarize the above, we observe that the quasiparticle relaxation in this disordered film is governed by fast quasiparticle recombination with a timescale given by phonon scattering, which is not affected by phonon trapping. This is in sharp contrast to ordered superconductors [38].

6.2.4 RECOMBINATION OF LOCALIZED QUASIPARTICLES

We explain these observations by localized quasiparticles that delocalize via phonon absorption. A delocalized quasiparticle relaxes again to another localization site and subsequently recombines on-site (Fig. 6.1.1(d)). Phonon absorption is relatively slow in a disordered ($ql \ll 1$) metal [4] and the subsequent on-site recombination is fast, since the quasiparticles relax to the same location [2]. Therefore, phonon absorption limits the relaxation time, as observed in Fig. 6.2.1(a). Even in the membrane case, where recombination should be slow due to phonon trapping, phonon absorption limits the relaxation time. The reason for this could be the following. The phonon that is emitted during on-site recombination has an energy below $2\Delta_0$, since the delocalized quasiparticle relaxes further into a localization site (Fig. 6.1.1(d)). The chance for such a phonon to break a Cooper-pair is very low, because the density of localized states with $E < \Delta_0$ is very low (inset of Fig. 6.1.1(d)). Therefore, the phonon trapping effect for on-site recombination should be largely reduced [5]. This is consistent with Fig. 6.2.1, where we observe the relaxation time to be equal to the scattering time for both the membrane and substrate case.

To support this interpretation of the results, we modeled the quasiparticle fluctuations with the master equation approach described in Ref. [34]. We describe the quasiparticles as localized such that their recombination rate depends on the average distance between two quasiparticles, as set out in Ref. [2]. For vanishing temperatures, this results in an exponentially long relaxation time and an excess quasiparticle density [2]. We however measure at a finite temperature where quasiparticles can delocalize via inelastic phonon scattering. We therefore include a second quasiparticle level to describe mobile quasiparticles, and set the delocalization time to τ_{scat} from Eq. (6.3). We assume the localization time to be much shorter, such that the mobile quasiparticle density is small. We include an on-site recombination term, where a mobile quasiparticle relaxes and recombines on-site with a localized quasiparticle (Fig. 6.1.1(d)). We set the characteristic time for on-site recombination, τ_0^{os} c.f. τ_0^{rec} in Eq. (6.1), such that on-site recombination is much faster than localization.

The resulting fluctuation spectra for the total number of quasiparticles are shown in Fig. 6.4.1(c) and (d). These calculated spectra follow the observed behavior. When analytically examining this model, we see that in the limit of fast on-site recombination, the quasiparticle relaxation time is given by $\tau_{\text{scat}}/2$ (the dashed lines in Fig. 6.2.1(a)) and the variance is equal to n_{qp} (black line in Fig. 6.2.1(b)). For details on the model calculations, see Section 6.E.

The proposed origin of the localized states is local gap variations induced by disorder. This is described by the theory of Refs. [6, 45], which extends the Larkin-Ovchinnikov inhomogeneous pairing theory [7]. Such gap variations have been measured in highly disordered TiN [46]. The effect of inhomogeneous pairing on the density of states is two-fold: (1) the coherence peak is broadened with a pair-breaking parameter η , which is equivalent to the Abrikosov-Gor'kov description of magnetic impurities [47], and (2) the density of states acquires an exponential subgap tail of localized states, characterized by Γ_{tail} . This is sketched in the inset of Fig. 6.1.1(d). The values of η and Γ_{tail} depend on the strength of the local gap variations.

Because the thickness of our β -Ta film is on the order of the coherence length, ξ (see Methods), we take both Coulomb induced mesoscopic fluctuations and finite thickness effects into account and obtain $\eta \approx 2.4 \times 10^{-5}$ [6]. To estimate Γ_{tail} , we consider our film quasi-2D, in which case Coulomb-enhanced mesoscopic fluctuations dominate and give $\Gamma_{\text{tail}}/\Delta_0 \approx 1.5 \times 10^{-4}$ [6]. Quasiparticle states in this subgap tail overlap and quasiparticles in these states will relax further. The effective localization radius at which this process stops can be estimated from Γ_{tail} and η and is on the order of ξ [2]. With the values mentioned above, $r_c \approx 3.5\xi \approx 65$ nm. This gives an estimate of density of localized quasiparticle states of $\tilde{n}_{\text{qp}}^{\text{loc}} = 3/(4\pi r_c^3) \approx 8.5 \times 10^2 \mu\text{m}^{-3}$. For details see Section 6.F.

Comparing this number to the right axis of Fig. 6.2.1(b) we conclude that the thermally generated quasiparticles localize due to gap variations for temperatures $T < 178$ mK. This leads to the situation in Fig. 6.1.1(d). For higher temperatures, the thermal quasiparticle density is larger than the density of localized states. This alters the quasiparticle localization dynamics and might be related to the plateau we observe in Fig. 6.2.1(a) for $T > 175$ mK.

6.3 DISCUSSION AND CONCLUSION

Following the same line of reasoning, we expect to see the same phenomenology in other disordered superconductors. Indeed, a weak temperature dependence of the quasiparticle relaxation time is also observed in TiN for different levels of disorder [48], which was not understood before. The electron-phonon scattering time at T_c has also been measured for these films [49], which provides an accurate estimate of τ_0^{scat} and τ_0^{rec} in Eqs. (6.1) and (6.3). We analyzed those results and find that static scatterers cause a power law temperature dependence of the phonon scattering time with $n = 2$ [41]. Taking this into account, the relaxation times for these TiN films follow both the temperature and disorder dependence of electron-phonon scattering, similar to Fig. 6.2.1(a), see Section 6.C. With $r_c \sim \xi^{\text{TiN}}$ [2] these films are in the same

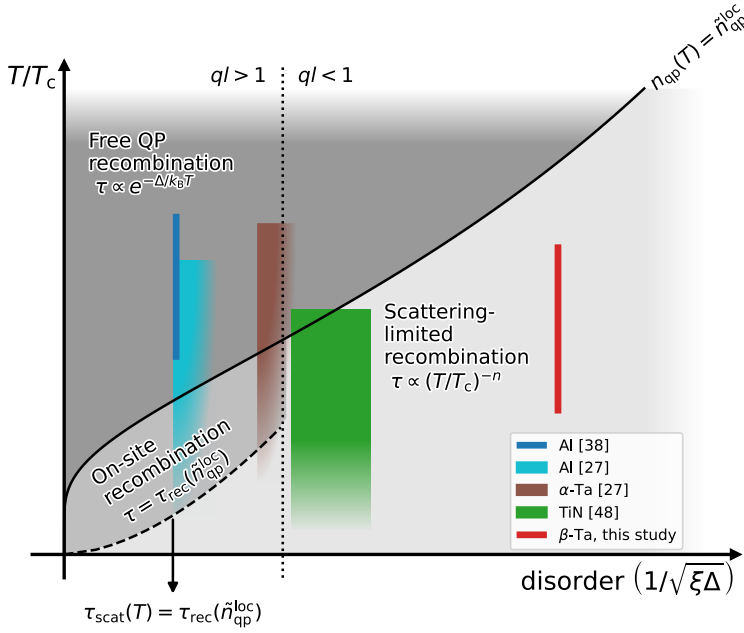


Figure 6.3.1: Different regimes of quasiparticle recombination as a function of temperature and disorder. Each regime (indicated in a shade of gray) is characterized by a different temperature dependence of the quasiparticle (QP) relaxation time. The x-axis is chosen such that the dotted vertical line, $ql = 1$ for $2\Delta_0$ phonons, is approximately on the same point for different superconductors. For simplicity, we take ql for $2\Delta_0$ phonons only in this sketch, such that on the right side of the $ql = 1$ dotted line both recombination and scattering interactions are disordered. The solid line gives the values at which the thermal quasiparticle number equals the number of localized quasiparticle states, which we estimate as $\tilde{n}_{\text{qp}}^{\text{loc}} = 3/(4\pi\xi^3)$. Below this solid line, quasiparticles will localize and recombine on-site. Below the dashed line the scattering time, Eq. (6.3), is longer than the recombination time, Eq. (6.1), at a quasiparticle density equal to $\tilde{n}_{\text{qp}}^{\text{loc}}$, i.e. $\tau_{\text{rec}}(\tilde{n}_{\text{qp}}^{\text{loc}})$ [3, 35]. In that regime, delocalization via phonon absorption limits quasiparticle recombination (Fig. 6.1.1(d)), which is indicated in light gray. For $ql < 1$ (the right side of the dotted line), phonon absorption is always slower than recombination at $\tilde{n}_{\text{qp}}^{\text{loc}}$. The colored areas give the experimental conditions of Refs. [27, 38, 48] and Fig. 6.2.1. The fade at lower temperatures for Refs. [27, 48] are added because these are measurements via a pulsed excitation, which does not give information on the quasiparticle temperature. In Ref. [27], disorder is increased by implanting ions. There is however no data on how much $1/\sqrt{\xi\Delta}$ increased in these films, which we indicated by an additional fade to higher disorder. The recombination regimes are consistent with the observed temperature dependence of the relaxation time in the respective experiments.

regime as β -Ta, where $n_{\text{qp}}(T) < \tilde{n}_{\text{qp}}^{\text{loc}}$ and $ql < 1$. Therefore, also in these films thermal quasiparticles localize and the recombination process is limited to delocalization via phonon absorption (Fig. 6.1.1(d)).

Even in an ordered superconductor a small amount of disorder could induce

quasiparticle localization at low temperatures [2]. In Ref. [38], we observed for Al that there is no effect of phonon trapping on the relaxation time in the saturation regime at low temperatures. We explained that by the presence of an excess number of localized quasiparticles. We estimate that the density of localized quasiparticle states for the quasi-2D Al film is given by, $\bar{n}_{\text{qp}}^{\text{loc}} \approx 1/(\pi r_c^2 d) \approx 160 \mu\text{m}^{-3}$, where we take $r_c \sim \xi^{\text{Al}} \approx 200 \text{ nm}$. If all these states are filled due to a non-equilibrium generation process, the quasiparticle density corresponds to the observed saturation time of 1 ms in Ref. [38]. An increase in disorder increases the number of localized quasiparticle states and decreases this saturation time. This is experimentally shown in [27] for Al and α -Ta. Furthermore, the most disordered Al film in Ref. [27] shows a weaker temperature dependence of τ , which points towards the same phenomenology as observed in Fig. 6.2.1(a).

In Fig. 6.3.1, we sketch these different quasiparticle recombination regimes. Above the solid line the thermal quasiparticle density is larger than the density of localized quasiparticle states. In that regime, the relaxation time follows the free quasiparticle recombination time, $\tau_{\text{rec}}^*(T)$ given by Eqs. (6.1) and (6.2) and shown in Fig. 6.1.1(c). Below the solid line, quasiparticles recombine within a localization site. The relaxation time saturates to the recombination time at a quasiparticle density equal to the number of localization sites, $\bar{n}_{\text{qp}}^{\text{loc}}$, as observed in Refs. [27, 38]. However, if the phonon scattering time is longer than this saturation time, quasiparticle localization via phonon absorption limits the relaxation and the temperature dependence of the relaxation time is altered to the power-law of τ_{scat} , Eq. (6.3). This regime is indicated as the light gray area in Fig. 6.3.1. The results of Refs. [27, 38, 48], which were previously unexplained, and Fig. 6.2.1 are shown in the appropriate disorder and temperature regimes and are consistent with the observed temperature dependence of the measured relaxation times.

A saturation of the quasiparticle relaxation time requires a non-equilibrium quasiparticle generation process such as microwave readout power [23], cosmic rays [20], radioactivity [22] and stray light [21]. In Fig. 6.3.1, this can be viewed as a saturation of T/T_c , when T is an effective quasiparticle temperature. We assume that there is a number of excess quasiparticles present in our experiment due to the continuous microwave read-out [23], which is small compared to the thermal quasiparticle density. To verify this, we show the results for τ and s^2 obtained in the same way, but for higher read-out powers in Fig. 6.4.3. We observe that the excess quasiparticle generated by read-out power is minimized at a read-out power equivalent to a number of photons in the resonator of $\bar{n}_{\text{ph}} \approx 6 \times 10^4$, which was used to obtain Fig. 6.2.1 (see Section 6.G for an estimation of the read-out power effects at this read-out power). If we reduced the bath temperature and minimize this generation process further, quasiparticles could become fully localized, which enhances the relaxation time exponentially [2]. For example, a relaxation time in granular Al on the order of seconds has been measured with $\bar{n}_{\text{ph}} \approx 1 - 300$ at 25 mK [28]. This relaxation time decreases with increasing \bar{n}_{ph} , indicating a saturated excess quasiparticle density that is sustained by microwave power. To verify that this originates from the localized quasiparticle dynamics presented in Ref. [2], an experiment that independently probes both the relaxation rate and the quasiparticle

effective temperature is needed. Such an experiment would be similar to this work, but at much lower temperatures and generation rates.

During the review process of this Article some related studies became available, which we reference here for completeness [50–52].

To conclude, we showed that quasiparticle relaxation in a disordered superconductor (with $ql < 1$) is governed by quasiparticle localization. After delocalization via phonon absorption, quasiparticles relax and recombine rapidly on-site (Fig. 6.1.1(d)), which enhances the relaxation rate. This impacts the performance of superconducting devices. For radiation detectors that measure the presence of photon-generated quasiparticles, the signal will be reduced as a result of the faster relaxation time. This presents a trade-off between photon absorption efficiency (increasing with disorder) and signal (decreasing with disorder). In quantum circuits, the short relaxation time will help eliminate excess quasiparticles at critical elements such as Josephson junctions, thereby improving coherence [53]. At low temperatures and small quasiparticle generation rates, localized quasiparticles could however increase microwave loss [7, 28]. Therefore, the fundamentally different quasiparticle dynamics presented in this work must be considered when implementing disordered superconductors in quantum circuits and radiation detectors.

6.4 METHODS

6.4.1 DEVICE DESIGN AND FABRICATION

The capacitive part of the resonator is an interdigitated capacitor (IDC), with $20\ \mu\text{m}$ wide fingers and $10\ \mu\text{m}$ wide gap. It is patterned using a SF_6 Reactive Ion Etch (RIE) in a $150\ \text{nm}$ thick NbTiN film [55] with a critical temperature of $14.0\ \text{K}$ and resistivity of $260\ \mu\Omega\text{cm}$. This design minimizes noise from Two Level Systems (TLS) [56, 57] and ensures that resonance frequency is highly sensitive to changes in the inductive β -Ta section, where the current density is high. The inductor is a strip of β -Ta, see Table 6.4.1, patterned with a SF_6 RIE etch. We place the β -Ta film on a SiN patch, which serves as a membrane for one of the resonators after the Si wafer is etched away from the backside using KOH, see Fig. 6.2.1(a) and (b). The inductor is shorted at the end to the NbTiN ground plane to make a quarter wave resonator. Quasiparticles in the β -Ta are confined to the inductor volume due to the higher superconducting gap of the NbTiN.

The resonance frequency is $5.1\ \text{GHz}$ for the membrane resonator and $5.3\ \text{GHz}$ for the substrate resonator, which is set by the finger lengths of the IDC. We set the coupling quality factor, Q_c , to $\sim 10,000$ by tuning the length of the coupling bar next to the read-out line. The internal quality factor, Q_i , at $20\ \text{mK}$ is approximately $400,000$.

6.4.2 FILM CHARACTERIZATION

To obtain a measure of disorder and electron and phonon dimensionalities, we performed a measurement of the resistance versus temperature, which provides the normal state resistivity, ρ_N , and T_c , the Hall resistance at $1\ \text{K}$, which provides the

Table 6.4.1.: **Geometry, electronic properties and phonon properties for β -Ta.** The electronic properties are obtained via a resistance versus temperature, a Hall resistance versus magnetic field and an upper critical field versus temperature measurement, as set out in Section 6.B.

Geometry			Measured electronic properties					
d	W	L	T_c	$\rho_N(T = 1 \text{ K})$	D	n_e	RRR	$k_F l$
(nm)	(μm)	(μm)	(K)	($\mu\Omega\text{cm}$)	(cm^2/s)	(μm^{-3})		
40	10	90	0.87	206	0.74	9.3×10^{10}	1.03	4.2

Phonon properties from Ref. [54]			
$\hat{\rho}$	c_L	c_T	T_D
(g/cm^3)	(km/s)	(km/s)	(K)
16.6	4.34	1.73	221

charge carrier density, n_e , and the upper critical field as a function of temperature, which provides the diffusion constant, D . The results can be found in Table 6.4.1 and the details of these measurements are given in Section 6.B. The Ioffe-Regel parameter, $k_F l$, with k_F the Fermi wavenumber and l the electron mean free path, is of order unity. Therefore, the film is electronically disordered and we expect localization effects become important. Refs. [6, 45] describe what electronic disorder does to the superconducting state: it introduces a broadening of the density of states and a subgap tail, consisting of localized quasiparticle states (see Fig. 6.1.1(d)).

For phonon-mediated superconductivity, disorder is characterized with respect to the electron-phonon interaction, i.e. ql , with q the phonon wave number. We calculate ql at two phonon energies: $2\Delta_0$, corresponding to recombination phonons and $k_B T$, typical phonon energies for scattering. We use the mass density, $\hat{\rho}$, and the longitudinal and transverse phonon velocities, c_L and c_T , from Ref. [54], see Table 6.4.1. We only consider transverse phonons because these are the fastest the relaxation rates in our case, as $(c_T/c_L)^3 \ll 1$ [3, 41]. With that, we calculate $q(2\Delta_0)l = 0.070$ and $q(0.2 \text{ K})l = 0.0046$: both much smaller than 1 so the film is disordered with respect to electron-phonon interactions. We therefore use quasiparticle relaxation time calculations of Reizer and Sergeev [3] and Devereaux and Belitz [32] which are in the disordered limit ($ql \ll 1$), instead of the widely used pure limit ($ql \gg 1$) results of Kaplan et al. [35]. The main difference is that the scattering time (Eq. (6.3)) has a steeper temperature dependence in the disordered case ($n \rightarrow n+1$) and the proportionality constants in Eqs. (6.1) and (6.3), τ_{rec}^0 and τ_{scat}^0 , become proportional to $1/\rho_N$, which reflects the weakening of the electron-phonon coupling as disorder increases [4].

For electronic dimensionality, the dirty limit coherence length divided by the film thickness is, $\xi/d = \sqrt{l\xi_0}/d = 0.39 < 1$, with $l = 0.30 \text{ nm}$ and $\xi_0 = 0.79 \mu\text{m}$, the Pippard coherence length. Therefore, the β -Ta film is a 3D superconductor, although it is close to 2D.

For the phonon dimensionality, we compare the phonon wavenumbers to the film thickness, qd . For recombination phonons, the film is 3D ($q(2\Delta_0)d = 9.3 > 1$) and

we can use the results of Ref. [3] for τ_{rec}^0 . For scattering phonons, the film is 2D for $T < 165$ mK (when $q(k_B T)d \leq 1/2$) and 3D for higher temperatures. The phonon dimensionality dictates the temperature dependence, while the electronic dimensionality dictates the disorder dependence [32]. We therefore use the 2D results of Ref. [32] with $n = 7/2$ for the low temperature regime and the 3D result of Ref. [3] with $n = 9/2$ for the high temperatures.

6.4.3 SETUP

The sample is cooled in a dilution refrigerator, shielded from stray light with a box-in-a-box setup [21]. Magnetic interference is reduced by a factor 10^{-6} by a CRYOPHY and superconducting niobium shield. The forward transmission measurement is performed in a homodyne setup. The microwave signal is attenuated at each temperature stage before it reaches the sample. After the signal passed the sample, it is amplified by a HEMT amplifier at 3 K and by a room temperature amplifier before it is mixed with the original microwave signal by an IQ mixer. For details on all the components see Ref. [58].

6.4.4 FLUCTUATION MEASUREMENT

Before each fluctuation measurement, we sweep the probe frequency to find the resonance frequency, f_0 , and calibrate the complex forward transmission to an amplitude, δA , and phase, θ , with respect to the resonance circle [58]. We set the microwave power of the on-chip probe tone relatively low at -98 dBm to limit non-equilibrium effects such as quasiparticle redistribution [23] (see Fig. 6.4.3). We measure θ during 40 s at 50 kHz sampling frequency and 1 s at 1 MHz. We disregard parts of the time traces that contain pulses from cosmic rays and calculate the Power Spectral Densities (PSDs) [38] and stitch the two PSDs from the 50 kHz and 1 MHz data at 20 kHz and downsample the spectrum to 30 points per decade to obtain $S_\theta(\omega)$ for a single bath temperature. The fluctuations in σ_2 , f_0 and θ are related via,

$$\begin{aligned} S_{\delta\sigma_2/|\sigma|}(\omega) &= \left(\frac{4}{\alpha_k\beta}\right)^2 S_{\delta f/f_0}(\omega) \\ &= \left(\frac{1}{\alpha_k\beta Q}\right)^2 S_\theta(\omega). \end{aligned} \quad (6.4)$$

Here, $\sigma = \sigma_1 - i\sigma_2$ the complex conductivity and $|\sigma|$ is the absolute, mean, value at the set bath temperature. At low temperatures ($k_B T \ll \Delta_0$) $|\sigma| \approx \sigma_2$. $Q = (1/Q_i + 1/Q_c)^{-1}$ is the loaded quality factor and $\alpha_k = L_k/L_{\text{tot}}$ is the kinetic inductance fraction of the β -Ta volume with respect to the entire resonator. β is a correction factor for the film thickness, which we set to 2 since we are in the thin film limit ($\lambda \gg d$, with $\lambda \approx 1.6 \mu\text{m}$, the penetration depth) [58].

Q and α_k are measured in a separate measurement where we sweep the probe frequency to get the resonance curve at each bath temperature. We fit a Lorentzian resonance dip to those curves and extract f_0 , Q_i and Q_c versus temperature. From $f_0(T)$ we determine α_k [58], which in our case is $\alpha_k \approx 0.44$.

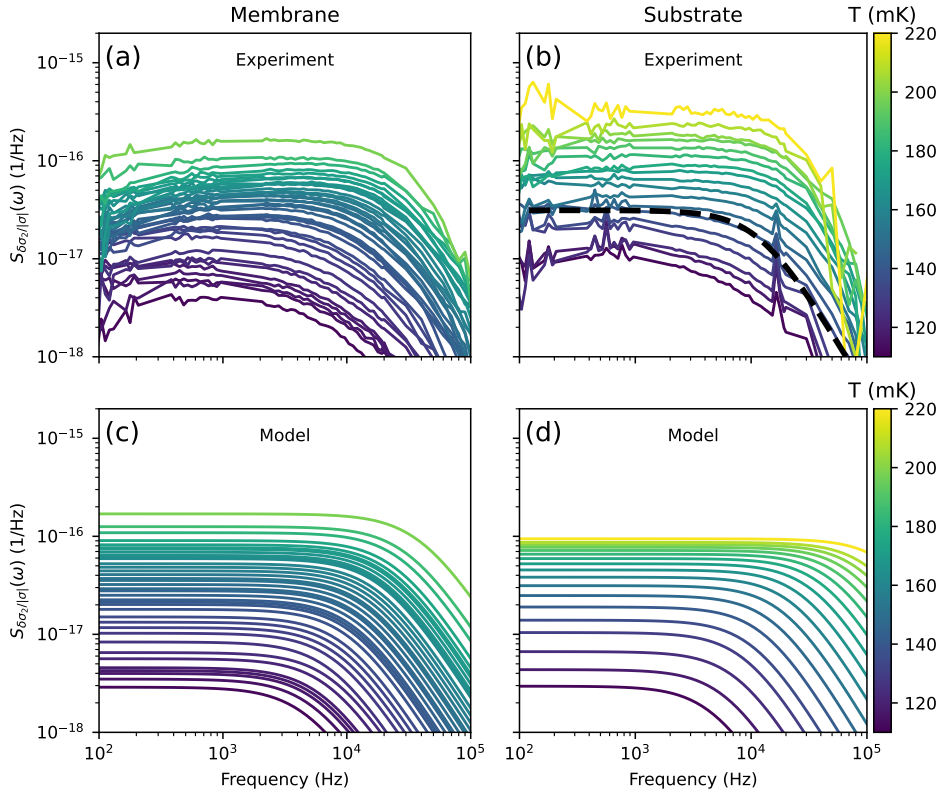


Figure 6.4.1: Measured and simulated power spectral densities of the complex conductivity. Different colors are for different bath temperatures, as indicated by the colorbar. Other noise sources, such as amplifier noise and $1/f$ -noise have been subtracted from the measured spectra in (a) and (b), as explained in the Section 6.D. The dashed black line in (b) is an example fit using Eq. (6.5). (c) and (d) are calculated power spectral densities for quasiparticle fluctuations at the same bath temperatures as the measurements. The quasiparticle fluctuation spectra are calculated with the framework described in Ref. [34], including the localized quasiparticle dynamics described in Ref. [2]. The quasiparticle density fluctuations are analytically converted to $\sigma_2/|\sigma|$ -fluctuations. For details on the model and calculations, see Section 6.F.

We disregard the 50 Hz, amplifier and $1/f$ noise contributions in the PSD, see Section 6.D. After that, we fit a Lorentzian spectra to $S_{\delta\sigma_2/|\sigma|}(\omega)$ via,

$$S_{\text{fit}}(\omega) = \frac{4s^2\tau}{1 + (\omega\tau)^2}, \quad (6.5)$$

to extract the variance s^2 and relaxation time τ from the fluctuations.

The resonance frequencies and quality factors result in a resonator bandwidth of $\Delta f = f_0/(2Q) \approx 0.3$ MHz (or equivalently, a resonator ring time of ~ 0.6 μs), which is

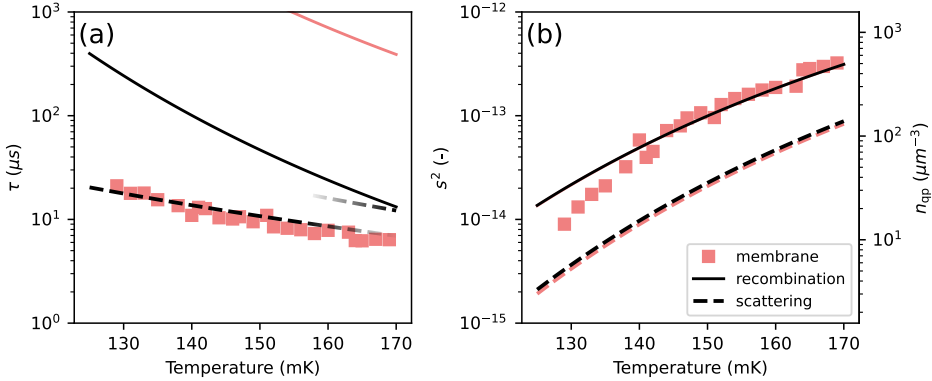


Figure 6.4.2: **Fluctuation measurement of σ_1 .** Quasiparticle relaxation time (a) and the variance (b) are obtained the same way as in Fig. 6.2.1, but from the fluctuations of the dissipative part of the complex conductivity, $\delta\sigma_1$. Error bars indicating statistical fit errors are smaller than the data points. The quasiparticle signal in σ_1 is a few times lower than in σ_2 [43], which results in a smaller usable temperature range. For the substrate resonator we did not observe any Lorentzian signatures in the PSDs of σ_1 .

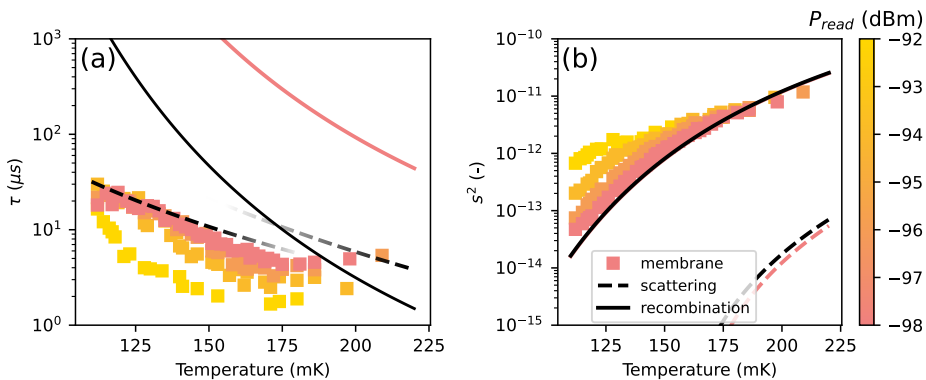


Figure 6.4.3: **Read-out power dependence of the relaxation time and variance.** (a): Relaxation time versus temperature for the membrane resonator at different on-chip read-out powers, indicated by the colors. The red data points and theory lines are the same as in Fig. 6.2.1. (b): Corresponding variances extracted from the same fits to σ_2 -fluctuations. Error bars indicating the statistical fit errors are smaller than the data points, for both panels. A higher read-out power, leads to a larger variance and smaller lifetime, which is consistent with microwave power induced excess quasiparticles [23]. To limit these effects, we set the read-out power to the minimal value in this figure (red data set) and obtain the data in Fig. 6.2.1. See Section 6.G for an estimation of the read-out power effects at this lowest read-out power.

outside the frequency range used for the fits. We therefore do not consider effects of the resonator roll-off on the PSDs.

The datasets for membrane and substrate have been measured at two different times, in the same setup and experimental conditions.

Data and code availability All data and analysis scripts used in this study have been deposited in the Zenodo database under accession code 13380277: [10.5281/zenodo.13380277](https://doi.org/10.5281/zenodo.13380277).

SUPPLEMENTARY INFORMATION

6.A RELAXATION TIME AND VARIANCE CALCULATIONS

Here we describe how the theory lines in Fig. 6.2.1(a) and (b) are calculated. The fluctuation spectrum is given by a Lorentzian, $S(\omega) = 4s^2\tau/(1 + (\omega\tau)^2)$, with τ the relaxation time and s^2 the variance. We will first go over the relaxation time calculations (Fig. 6.2.1(a)), including the phonon trapping effect for the β -Ta on substrate and membrane, and then explain how we calculated the variances (Fig. 6.2.1(b)).

6.A.1 RELAXATION TIME

ELECTRON-PHONON INTERACTION

First, we recall that the β -Ta film is disordered with respect to electron-phonon interactions, i.e. $q(\Omega)l < 1$ with $q(\Omega)$ the phonon wave number and l the electronic mean free path, for both thermal ($\Omega = k_B T$) and recombination ($\Omega = 2\Delta_0$) phonons. k_B is the Boltzmann constant, T is the bath temperature and $2\Delta_0$ is the superconducting gap energy at low temperatures and when there is no disorder present.

Second, the film is 2D for $T < 165$ mK thermal phonons ($qd < 1/2$, with d the film thickness) and 3D for higher temperatures and for recombination phonons. We take the values for quasiparticle energy Δ_0 , by which we assume that the quasiparticles are in thermal equilibrium and are all relaxed to the gap energy.

Recombination The 3D case of the recombination time for disordered superconductors is given in Ref. [3], Eq. (61),

$$\tau_{\text{rec}}^{\text{e-ph}}(T) = \frac{\tau_s(T_c)}{4\pi^{5/2}} \left(\frac{k_B T_c}{2\Delta_0} \right)^{7/2} \sqrt{\frac{T_c}{T}} e^{\Delta_0/k_B T}, \quad (6.6)$$

where $\tau_s(T_c)$ is the electron-phonon scattering time in the normal metal at $T = T_c$. This is given in Eq. (31) of Ref. [3] or Eq. (51) of Ref. [41] with $k = 1$:

$$\tau_s(T_c) = \frac{5\hbar^4}{\pi^4} \frac{(k_F c_L)^3}{(k_F l)(k_B T_c)^4 \beta_L \left(1 + \frac{3}{2} \left(\frac{c_L}{c_T} \right)^5 \right)}, \quad (6.7)$$

with,

$$\beta_L = \left(\frac{2E_F}{3} \right)^2 \frac{N_0}{2\hat{\rho}c_L^2}. \quad (6.8)$$

Here, \hbar is the reduced Planck constant, E_F is the Fermi energy, k_F is the Fermi wavenumber, c_L and c_T are the longitudinal and transverse sound velocities, $\hat{\rho}$ is the mass density, T_c is the critical temperature and N_0 is the single spin density of states at the Fermi energy. We use the parameters from Table 6.4.1 and calculate N_0 from the Einstein relation, $N_0 = 1/(2e^2 \rho_N D)$, with e the electronic charge, ρ_N the normal state resistivity and D the diffusion constant. For Δ_0 we take the zero temperature BCS value, $\Delta_0 = 1.76 k_B T_c$, which is correct up to 0.1%, since we measure at $T < T_c/4$. We assume the free electron model, so we take $k_F = (3\pi^2 n_e)^{1/3}$, where n_e is the charge density, and $E_F = k_F^3/(4\pi^2 N_0)$. We determine n_e from a Hall resistance measurement and D from an upper critical field measurement, which are explained in the section *Characterization of the β -Ta film*.

Scattering For scattering, we need to distinguish between the 2D and 3D phonon case. The 2D case (for $T > 165$ mK) can be found in Ref. [32], Eq. (4.8a), bottom row:

$$\tau_{\text{scat}}^{\text{e-ph, 2D}} = \frac{16}{\sqrt{2}} \frac{Z'}{\Gamma(7/2)\zeta(7/2)} \left(\frac{E_F}{\Delta_0} \right)^2 \frac{c_T \hat{\rho} d}{\Delta_0 k_F^3} \frac{\rho_N e^2}{d\hbar} \frac{c_T^3}{v_F^3} \frac{1}{1 + (c_T/c_L)^4} \left(\frac{\Delta_0}{k_B T} \right)^{7/2}, \quad (6.9)$$

where Z' is the Eliashberg renormalization constant for the 3D clean limit, $Z' = 1 + N_0 (k_B T_D)^2 v_F^2 / (36 \hat{\rho} c_L^4)$ [59], with T_D the Debye temperature, see Table 6.4.1. v_F is the Fermi velocity, Γ is the gamma function and ζ is the Riemann zeta function. The 3D case can be found in Ref. [3], Eq. (62),

$$\tau_{\text{scat}}^{\text{e-ph, 3D}} = \frac{\tau_s(T_c)}{4\pi^2 \Gamma(9/2)\zeta(9/2)} \sqrt{\frac{2\Delta_0}{k_B T_c}} \left(\frac{T_c}{T} \right)^{9/2}, \quad (6.10)$$

with $\tau_s(T_c)$ given by Eq. (6.7).

ELECTRON-ELECTRON INTERACTION

Electron-electron interactions can be enhanced in disordered metals [60]. However, in a superconductor the normal state charge carrier density is exponentially suppressed, such that the electron-phonon interaction become more favorable. To quantify that statement, we calculate the electron-electron interactions times here as well.

Our β -Ta film is in the dirty (or impure) regime since, $\xi/l = 62$. l is 0.30 nm and ξ is the dirty limit coherence length, 18 nm. The electron-electron rates in the dirty regime are calculated in Ref. [36], both for 2D and 3D. This is an extension of the theory in Ref. [32] to include gapless collective phase mode in 2D, which occurs when $k_F \xi \lesssim 1$. This collective mode has a power law temperature dependence with $n = 7/2$. In our case, $k_F \xi \approx 262$ so we are not in that regime. Besides that, $\xi/d = 0.47$, so we are not in the 2D but 3D regime. Therefore, the observed power law in Fig. 6.2.1 cannot be this gapless phase mode.

All other interaction channels for the electron-electron interaction are gapped and have a exponential temperature dependence. From Ref. [36], Eq. (48), the 3D case,

we have,

$$\tau_{\text{rec}}^{\text{e-e}} = \frac{(\hbar\sqrt{2})^{5/2}(2\pi)^2 N_0 D}{k_B T} \sqrt{\frac{D}{\Delta_0}} \frac{e^{2\Delta_0/k_B T}}{(1 + (V_{\text{sc}} N_0)^2)}. \quad (6.11)$$

V_{sc} is the BCS attractive potential energy. We calculate this via the BCS gap equation at zero temperature, $1/V_{\text{sc}} = N_0 \int_{\Delta_0}^{k_B T_D} dE / \sqrt{E^2 - \Delta_0^2} = 1.2 \times 10^5 \mu\text{eV}^{-1} \mu\text{m}^{-3}$.

For scattering, we have from Ref. [36], Eq. (47),

$$\tau_{\text{scat}}^{\text{e-e}} = \frac{(\pi\hbar)^{5/2} N_0 D}{6\Delta_0} \sqrt{\frac{D}{k_B T}} e^{4\Delta_0/5k_B T}. \quad (6.12)$$

In Fig. 6.A.1 the recombination and scattering lifetimes for electron-phonon and electron-electron interactions are shown. $\tau_{\text{rec}}^{\text{e-e}}$ is an order of magnitude longer than $\tau_{\text{rec}}^{\text{e-ph}}$ due to the additional factor $e^{\Delta_0/k_B T}$, which reflects the 3 particle nature of electron-electron recombination instead of 2 quasiparticle electron-phonon recombination.

The electron-electron scattering time is the shortest in this temperature regime. However, this process conserves quasiparticle number and does not change the total energy stored in the quasiparticle system. It only changes the distribution function to the thermal Fermi-Dirac distribution on the timescale of $\tau_{\text{scat}}^{\text{e-e}}$. As we calculated for electron-phonon scattering, the variance on the kinetic inductance for changes in distribution function are very low (see Fig. 6.2.1(b)) and this is not visible in our experiment.

PHONON TRAPPING FACTOR

The phonons that are emitted during a recombination event can break other Cooper-pairs, which enhances the measured bulk quasiparticle lifetime. This effect is captured by the phonon trapping factor, $(1 + \tau_{\text{esc}}/\tau_{\text{pb}})$ in Eq. (6.2) [34, 37]. We experimentally tune τ_{esc} by measuring the β -Ta on substrate and on a thin membrane. We will first estimate τ_{esc} for β -Ta on a SiN substrate and then estimate the enhanced phonon trapping by the membrane.

We assume that phonon scattering on the film boundaries is diffusive. The SiN is etched by a reactive ion etch when patterning the NbTiN before deposition of β -Ta, which makes the interface rough. We only take transverse phonons into account (since $(c_T/c_L)^3 \ll 1$) and neglect phonon loss in the bulk. We then use Eq. (51) of Ref. [40],

$$(1 + \tau_{\text{esc}}/\tau_{\text{pb}}) = \frac{4d}{\Lambda_T} \frac{1 - (1 - \eta_T)e^{-2d/\Lambda_T}}{\eta_T(1 - e^{-2d/\Lambda_T})}. \quad (6.13)$$

Λ_T is the transverse phonon mean free path against pair breaking, which is given by, $\Lambda_T = c_T \tau_{\text{pb}}^T$, with c_T from Table 6.4.1 and τ_{pb}^T the pair breaking time for transverse phonons. We estimate τ_{pb}^T as the inelastic scattering time of phonons in a metal [4, 61],

$$\frac{1}{\tau_{\text{pb}}^T} = \frac{n_e m^*}{\hat{\rho} \tau} \left(\frac{1}{\zeta} - 1 \right), \quad (6.14)$$

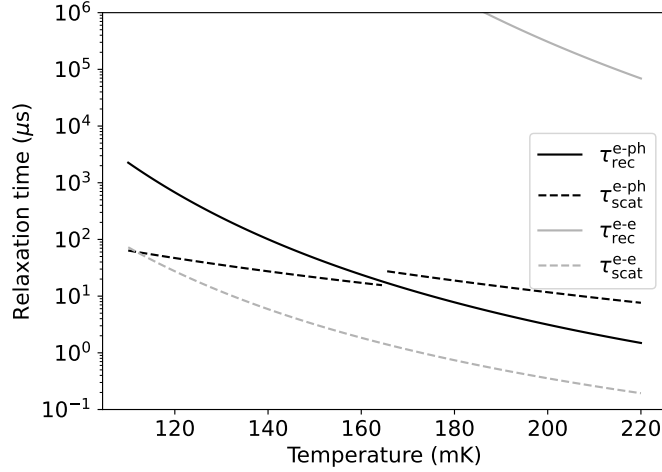


Figure 6.A.1: Electron-phonon and electron-electron relaxation rates from Eqs. (6.6) and (6.9) to (6.12). The temperature range is chosen to match our measurement regime. The electron-phonon times (black solid and dashed lines) are the same as in Fig. 6.2.1(a).

6

with $\zeta = 3[(1 + (ql)^2) \tan^{-1} ql - ql]/2(ql)^3$, where $q = 2\Delta_0/(\hbar c_T)$ is the recombination phonon wave number. n is the charge density, m^* is the effective electron mass, $m^* = 2\hbar^2 N_0 \pi^2 / k_F$ and τ_e is the Drude elastic scattering time, $\tau_e = l/v_F$. This gives $\tau_{pb}^T = 37$ ns, which is relatively long due to disorder, $ql \ll 1$ [4]. Thus, $\Lambda_T = 65$ μm is also large. For example, τ_{pb}^T in Al is 0.12 ns and Λ_T is 0.39 μm .

η_T in Eq. (6.13) is the transmission efficiency for transverse phonons. We calculate it via the acoustic mismatch model from Ref. [39]. The code to calculate the phonon transparencies for an arbitrary interface is available at Zenodo (10.5281/zenodo.13380277).

We use the values from Table 6.4.1 for the β -Ta phonon properties and $\hat{\rho} = 3.1$ g/cm³, $c_T = 6.2$ km/s and $c_L = 10.3$ km/s for SiN [62, 63]. That gives $\eta_T = 0.054$, which results in a phonon trapping factor, from Eq. (6.13), of $(1 + \tau_{esc}/\tau_{pb}) = 2.0$.

To estimate the effect of the membrane, we use a geometrical calculation as shown in Fig. 6.A.2. The $2\Delta_0$ -phonon wavelength is 27 nm, which is smaller but close to $2d = 80$ nm, so a purely geometrical calculation is somewhat justified. We will come back to this point at the end of this section.

We calculate the transverse phonon transparency from SiN to β -Ta in the same way as explained above. This results in $\eta'_T = 0.80$. We use the out- and in-going transparencies (η_T and η'_T , respectively) to scale the thickness of the two layers, see Fig. 6.A.2(b). With these effective thicknesses, we take the phonon transparencies in the new geometry, Fig. 6.A.2(b), to be 1, so we can consider it as one geometrical volume. We assume scattering on the sides is diffusive, such that all the angle dependencies are averaged out. We therefore only consider the escape angles as measured from the center of the geometrical volume. This is slightly different for

the membrane compared to the substrate case, see Fig. 6.A.2(b).

For the substrate case we assume a phonon is lost when it enters the SiN. This results in the escape angle θ in Fig. 6.A.2(b). For the membrane case, we consider the phonon to be lost when it leaves the volume beneath the β -Ta, which results in an escape angle of $2\theta'$ in Fig. 6.A.2(b). The effect of the membrane is given by the ratio of the these two escape angles, $\theta/(2\theta')$, when we also compensate for the time that the phonon is in the SiN membrane via the effective thicknesses and transverse sound velocities,

$$\frac{\tau_{\text{esc}}^{\text{mem}}}{\tau_{\text{esc}}^{\text{sub}}} = \frac{\theta}{2\theta'} \frac{d/(\eta_T c_T^{\beta\text{-Ta}})}{d_{\text{SiN}}/(\eta'_T c_T^{\text{SiN}})} + d/(\eta_T c_T^{\beta\text{-Ta}}) = 60 \times 0.96 = 58. \quad (6.15)$$

This gives a phonon trapping factor of $(1 + \tau_{\text{esc}}^{\text{mem}}/\tau_{\text{pb}}) = 59$. The black line in Fig. 6.2.1(c) is given by $\tau_{\text{rec}}^* = \tau_{\text{rec}}^{\text{e-ph}}(1 + \tau_{\text{esc}}/\tau_{\text{pb}})/2$ (Eq. (6.2)), where $\tau_{\text{rec}}^{\text{e-ph}}$ is the solid black line in Fig. 6.A.1 and $(1 + \tau_{\text{esc}}/\tau_{\text{pb}}) = 2.0$. The red line in Fig. 6.2.1 is the same, but with $(1 + \tau_{\text{esc}}/\tau_{\text{pb}}) = 59$.

As a check, we perform the exact same calculation for Al on SiN and compare it with Ref. [38]. We come to a phonon trapping factor on SiN substrate of 3.2 and on membrane 17.6. So, a factor 5.5 longer lifetimes are expected. The measurement in Ref. [38] shows an increase in lifetime of a factor 16. Therefore, the assumption of a purely geometric effect of the membrane has limited applicability. For Al, the $2\Delta_0$ -phonon wavelength is 37 nm, while the film thickness is 50 nm. For higher energetic phonons (i.e. shorter wavelengths) generated by single photon absorption events, such a geometric model is consistent with the data [64]. We therefore expect that the low energetic $2\Delta_0$ -phonons are trapped more effectively by the membrane than the geometrical calculation predicts. Therefore, we can interpret the above geometric calculation as minimum for the phonon trapping effect of the membrane.

6.A.2 VARIANCE

The theory lines for the variance in Fig. 6.2.1(d) are calculated as,

$$s^2 = \langle \delta(\sigma_2/|\sigma|)^2 \rangle = \langle \delta(k_B T)^2 \rangle \left(\frac{d(\sigma_2/|\sigma|)}{dk_B T} \right)^2, \quad (6.16)$$

where the first factor is the variance of the thermal fluctuations and the second is the responsivity to temperature changes. We will calculate these factors for scattering and recombination separately.

THERMAL FLUCTUATIONS

In equilibrium, thermal fluctuations have a variance of $\langle \delta(k_B T)^2 \rangle = k_B^3 T^2 / C$, where $C = dU/dT$ is the heat capacity, with U the internal energy [65].

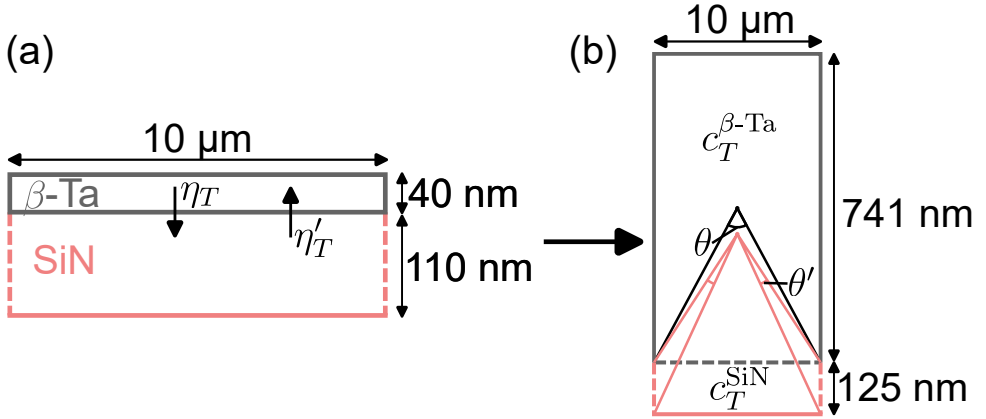


Figure 6.A.2: Illustration of the geometrical calculation to estimate the effect of the membrane on the phonon escape time, τ_{esc} . (a): Situation of the β -Ta film (gray) on the SiN membrane (pink). The physical thicknesses are indicated. The dashed lines indicate that it is not a physical boundary of the material, but only of the volume considered. η_T is the transverse phonon transparency from β -Ta to SiN and η'_T vice versa. (b): Effective film thicknesses d/η_T and d_{SiN}/η'_T , with the phonon escape angles for the substrate case (θ) and the membrane case ($2\theta'$) as indicated.

6

Recombination For recombination, C is given by the change in quasiparticle number, δN_{qp} , with energy Δ_0 . That gives a heat capacity [66],

$$\begin{aligned}
 C_{\text{qp}} &= \frac{dU}{dT} = \frac{d}{dT} \left(4N_0 V \int_{\Delta_0}^{\infty} \frac{E^2 f(E; k_B T)}{\sqrt{E^2 - \Delta_0^2}} dE \right) \\
 &\approx \frac{d}{dT} (2N_0 V \Delta_0^2 [K_0(\Delta_0/k_B T) + K_2(\Delta_0/k_B T)]) \\
 &\approx \frac{d}{dT} (\Delta_0 N_{\text{qp}}) \\
 &\approx \frac{N_{\text{qp}} \Delta_0^2}{k_B T^2}.
 \end{aligned} \tag{6.17}$$

$K_n(x)$ is the n -th modified Bessel function of the second kind. The first approximation is valid for $f(E; k_B T) \approx e^{-E/k_B T}$. The other two are valid for $k_B T \ll \Delta_0$, which automatically satisfies the first. From this we see that to first order in $k_B T/\Delta_0$, the internal energy is changed mainly by the change in quasiparticle number and not by the change in distribution function.

If we use this heat capacitance, we come to a variance of

$$\langle \delta(k_B T)^2 \rangle_{\text{rec}} = \frac{(k_B T)^4}{N_{\text{qp}} \Delta_0^2}. \tag{6.18}$$

If we multiply this variance with $(dN_{\text{qp}}/dk_B T)^2 \approx (N_{\text{qp}} \Delta_0)^2 / (k_B T)^4$, we get N_{qp} , which is the variance of quasiparticle number fluctuations ($\langle \delta N_{\text{qp}}^2 \rangle = N_{\text{qp}}$). Thus, this

is the variance of the temperature fluctuations due to recombination.

Scattering For scattering, we can do something similar as Ref. [43]: we implicitly introduce a chemical potential μ^* to keep N_{qp} constant, while changing $k_{\text{B}}T$. In this case, we need the higher orders in the Bessel functions $K_0(\Delta_0/k_{\text{B}}T)$ and $K_2(\Delta_0/k_{\text{B}}T)$, to get the first order in explicit temperature dependence of U . So,

$$\begin{aligned} U &= N_0 V \Delta_0 \sqrt{2\pi k_{\text{B}} T \Delta_0} e^{-\frac{\Delta_0}{k_{\text{B}}T}} \left(1 + \frac{k_{\text{B}}T}{\Delta_0} \right) \\ &= \Delta_0 N_{\text{qp}} \left(1 + \frac{k_{\text{B}}T}{\Delta_0} \right). \end{aligned} \quad (6.19)$$

Now,

$$C_{\text{rec}} = \frac{\partial U}{\partial N_{\text{qp}}} \frac{dN_{\text{qp}}}{dT} = \frac{N_{\text{qp}} \Delta_0^2}{k_{\text{B}} T^2}, \quad (6.20)$$

and

$$C_{\text{scat}} = \frac{\partial U}{\partial T} = k_{\text{B}} N_{\text{qp}}. \quad (6.21)$$

The total variance can be written,

$$\langle \delta(k_{\text{B}}T)^2 \rangle = \frac{k_{\text{B}}^3 T^2}{C_{\text{rec}} + C_{\text{scat}}} \approx \frac{(k_{\text{B}}T)^4}{N_{\text{qp}} \Delta_0^2} \left[1 - \left(\frac{k_{\text{B}}T}{\Delta_0} \right)^2 \right], \quad (6.22)$$

where the approximation is valid for $k_{\text{B}}T \ll \Delta_0$. This shows that scattering only gives a small negative correction to the variance of the temperature fluctuations. It is a negative correction, as the change in $k_{\text{B}}T$ enhances the heat capacity.

If the number of quasiparticles stays constant, $C_{\text{rec}} = 0$ and we would be left with,

$$\langle \delta(k_{\text{B}}T)^2 \rangle_{\text{scat}} = \frac{k_{\text{B}}^3 T^2}{C_{\text{scat}}} = \frac{(k_{\text{B}}T)^2}{N_{\text{qp}}}. \quad (6.23)$$

This is larger than $\langle \delta(k_{\text{B}}T)^2 \rangle_{\text{rec}}$ by a factor $(\Delta_0/k_{\text{B}}T)^2$, which is $\sim 10^2$ in our measurement, see Fig. 6.A.3(a). We use Eq. (6.23) for the variance of scattering events. It is however only valid when the number of quasiparticles stays constant. This is true when $\tau_{\text{scat}} \ll \tau_{\text{rec}}$, which is valid for $T \lesssim 130$ mK in our case, see Fig. 6.A.1. When this condition is not satisfied, the variance will be governed by recombination events. Therefore, Eq. (6.23) can be viewed as an upper limit for the complete measurement range.

RESPONSIVITIES

The second factor in Eq. (6.16) is the temperature responsivity of $\sigma_2/|\sigma|$ squared. We calculate this factor for recombination and scattering separately. We use the methods of Ref. [43] to calculate these responsivities from the Mattis-Bardeen equations [42]. For completeness, we show the calculations for both σ_1 and σ_2 .

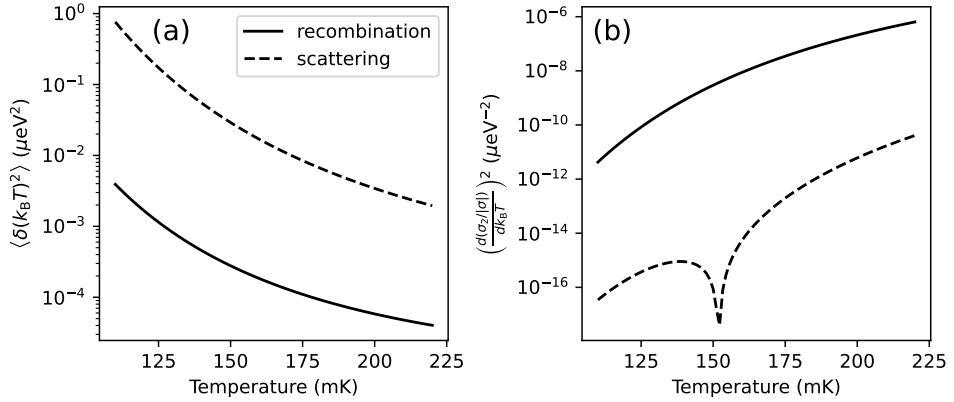


Figure 6.A.3: Contributions to the variance calculations. **(a)**: Thermal fluctuation variance for recombination, Eq. (6.18), and scattering, Eq. (6.23). **(b)**: Temperature responsivity of $\sigma_2/|\sigma|$ from Eq. (6.26). The legend is applicable to (a) and (b). For the calculations we set $\omega_0/2\pi = 5$ GHz and use the properties of β -Ta from Table 6.4.1. The multiplication of the curves in (a) and (b) give the theory lines in Fig. 6.2.1(b).

6

For recombination, we assume that the temperature is constant, while the number of quasiparticle changes with the use of a chemical potential. We can use Eqs. (18) and (19) from Ref. [43] and multiply by

$$\frac{dn_{\text{qp}}}{dk_B T} \approx \frac{n_{\text{qp}} \Delta_0}{(k_B T)^2}. \quad (6.24)$$

The approximation is valid for low temperatures, $k_B T \ll \Delta_0$. This results in,

$$\begin{aligned} \left. \frac{d\sigma_1}{dk_B T} \right|_{\text{rec}} &= \frac{\sigma_n n_{\text{qp}}}{N_0 \hbar \omega} \sqrt{\frac{2\Delta_0^3}{\pi(k_B T)^5}} [\sinh(\chi) K_0(\chi)] \\ \left. \frac{d\sigma_2}{dk_B T} \right|_{\text{rec}} &= -\frac{\sigma_n n_{\text{qp}}}{N_0 \hbar \omega} \sqrt{\frac{\pi\Delta_0^3}{2(k_B T)^5}} \left[\sqrt{\frac{\pi k_B T}{2\Delta_0}} + e^{-\chi} I_0(\chi) \right], \end{aligned} \quad (6.25)$$

with, $\chi = \hbar\omega_0/2k_B T$. $I_0(\chi)$ is the zero-order modified Bessels function of the first kind. ω_0 is the angular resonance frequency of the resonator.

For scattering, we assume that the number of quasiparticles is constant, but $k_B T$ changes. We take Eqs. (16) and (17) from Ref. [43] and differentiate with respect to $k_B T$ to find:

$$\begin{aligned} \left. \frac{d\sigma_1}{dk_B T} \right|_{\text{scat}} &= \frac{\sigma_n n_{\text{qp}}}{N_0 \hbar \omega} \sqrt{\frac{\Delta_0}{2\pi(k_B T)^3}} [2\chi (\sinh(\chi) K_1(\chi) - \cosh(\chi) K_0(\chi)) - \sinh(\chi) K_0(\chi)] \\ \left. \frac{d\sigma_2}{dk_B T} \right|_{\text{scat}} &= \frac{\sigma_n n_{\text{qp}}}{N_0 \hbar \omega} \sqrt{\frac{\pi\Delta_0}{8(k_B T)^3}} [e^{-\chi} (I_0(\chi) + 2\chi (I_1(\chi) - I_0(\chi)))]. \end{aligned} \quad (6.26)$$

We divide Eqs. (6.25) and (6.26) by $|\sigma(T)| = |\sigma_1 - i\sigma_2|$, which we calculate $\sigma(T)$ from the Mattis-Bardeen equations [42]. When we square the result, we get for $\sigma_2/|\sigma|$ the values plotted in Fig. 6.A.3(b), for $\omega_0/2\pi = 5$ GHz and the material parameters for β -Ta from Table 6.4.1.

The responsivity for scattering events is ~ 5 orders of magnitude lower than for recombination. This can also be seen from the curves in Fig. 1 of Ref. [43]: to first order, the scattering responsivity of σ_1 and σ_2 is equal to the difference of the thermal and excess quasiparticle responsivity curves. This is very small, but grows for higher temperatures.

The dip around 150 mK in Fig. 6.A.3(b) is at the point where $\chi \approx 0.79$, or $k_B T \approx 0.63\hbar\omega_0$. At that value of χ , the term in square brackets in the lower equations of Eq. (6.26) vanishes.

The curves in Fig. 6.2.1(b) are the multiplication of the curves in Fig. 6.A.3(a) and (b), but with the actual resonance frequencies. The variance of thermal fluctuations is ~ 2 order of magnitude higher but the responsivity is ~ 5 orders of magnitude lower. Therefore, the variance of σ_2 -fluctuations is ~ 3 orders of magnitude lower for scattering events, which is shown in Fig. 6.2.1(b).

As the substrate and membrane resonator have a slightly different resonance frequency the dip in Fig. 6.A.3(b) is at a different location. That results in the difference for the variance of σ_2 -fluctuations for scattering events in Fig. 6.2.1(b).

6.B CHARACTERIZATION OF THE β -TA FILM

We characterize the β -Ta film in three ways: (1) a resistance versus temperature measurement; (2) a Hall resistance versus magnetic field and (3) a upper critical field measurement versus temperature. The first is measured in the same setup as the measurements presented in Fig. 6.2.1, but at a different, thermally weakly coupled, stage. The resistance measurements are done with a Lakeshore model 372 AC resistance bridge.

The Hall resistance and upper critical field measurement are performed in a different setup, which includes a superconducting coil to apply a magnetic field up to 6 T, which is orientated in the out-of-plane direction with respect to the β -Ta film. In this setup, the resistance measurements are performed with a SynkTek MCL1-540 lock-in amplifier.

The 4-probe and Hall bar structures used for these measurements are fabricated on the same wafer as the devices presented in Fig. 6.1.1. The geometries are shown in the insets of Fig. 6.B.1.

6.B.1 RESISTANCE VERSUS TEMPERATURE

The resistance measurement is shown in Fig. 6.B.1(a). From this measurement, we get a critical temperature of $T_c = 0.87$ K shown by the dashed line. We choose T_c as the temperature where the resistance is approximately half the normal state resistance. We measure the normal state resistance to be $R_N = 661 \Omega$ at 1.0 K, which equals a normal state resistivity $\rho_N = 206 \mu\Omega\text{cm}$ when taking the geometry in Fig. 6.B.1(a) into account.

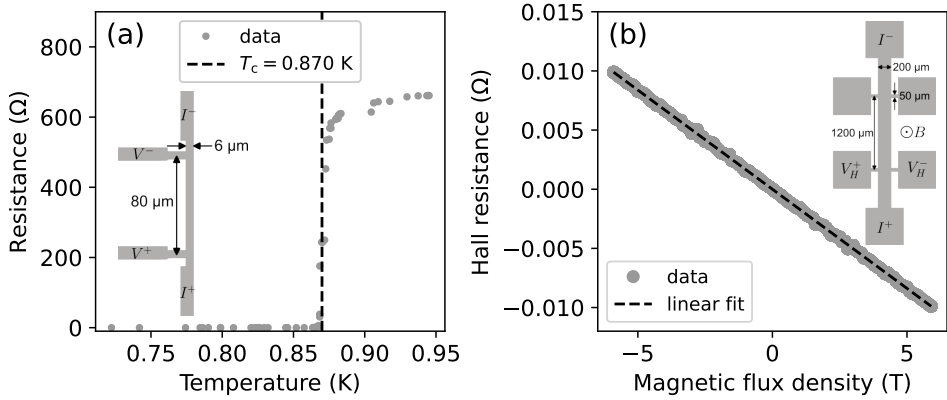


Figure 6.B.1: Transport measurements characterizing the β -Ta film. (a): Resistance measurement versus temperature in the absence of magnetic field. The dashed line gives the critical temperature we use in the analysis. The inset shows the geometry which is used for the measurement. (b): Anti-symmetrized Hall resistance (V_H/I) measurement, performed at 1 K. The standard deviation for each data point is smaller than the marker size, for both panels. The dashed line gives a linear fit with a slope of $dR_H/dB = 1.68 \times 10^{-3} \Omega/T$. The inset shows the Hall bar geometry and contacts used for the measurement. The measurement in (a) is performed with a different setup than the measurement in (b). The devices are from the same wafer as the devices shown in Fig. 6.2.1(a).

6

6.B.2 HALL RESISTANCE

The Hall resistance measurement is performed at 1.0 K bath temperature and with the geometry shown in the inset of Fig. 6.B.1(b). The dashed line shows a linear fit to the data, with $dR_H/dB = 1.68 \times 10^{-3} \Omega/T$. The raw resistance measurement data is anti-symmetrized with respect to the magnetic field ($R_{\text{Hall}} = (R_T(B) - R_T(-B))/2$) to eliminate of any longitudinal resistance component. From the fitted slope we can find the charge carrier density,

$$n_e = \frac{1}{ed} \left(\frac{dR_{\text{Hall}}}{dB} \right)^{-1} = 9.3 \times 10^{28} \text{ m}^{-3}, \quad (6.27)$$

where e is the electron charge and d is the film thickness. Assuming the free electron model to hold, we can calculate the Fermi wavenumber as, $k_F = (3\pi^2 n_e)^{1/3} = 14 \text{ nm}^{-1}$. The Ioffe-Regel parameter is given by, $k_F l = \hbar(3\pi^2)^{2/3} / (n_e^{1/3} e^2 \rho_N) = 4.2$. This also gives the electron mean free path, $l = 0.30 \text{ nm}$.

6.B.3 UPPER CRITICAL FIELD

The only other parameter missing for the calculations of the scattering times and variance is the single spin density of states at the Fermi level, N_0 . We use the Einstein relation, $N_0 = 1/(2e^2 \rho_N D)$ to calculate N_0 from the diffusion constant D . This can be measured in superconductors from the temperature dependence of the

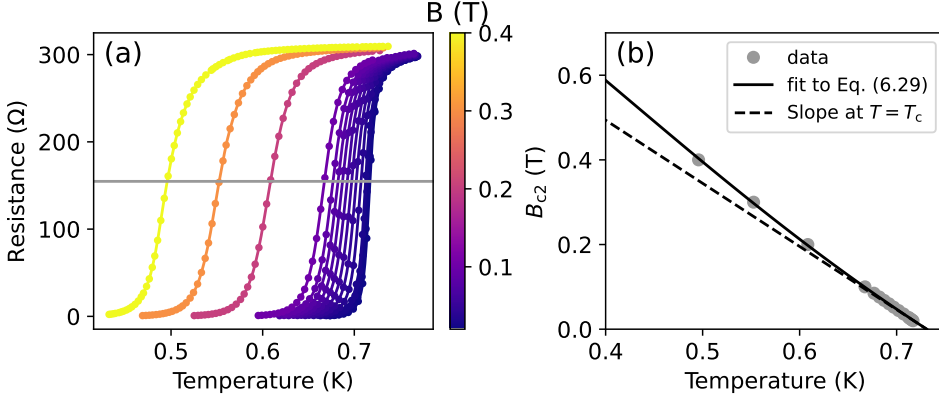


Figure 6.B.2: Upper critical field measurement versus temperature. (a): Resistance versus temperature at different magnetic flux densities, see the color bar. The dots are data points and the solid lines are cubic spline fits for each value of B . The gray line indicates where we chose to define B_{c2} , which is arbitrary for our analysis as long as it is in the transition. The measured device is depicted in the inset of Fig. 6.B.1(b), where we measure the resistance over two lateral contacts. (b): The gray dots are the extracted upper critical field from the intersection of the gray line and the individual spline fits in (a). The black solid line is a fit to Eq. (6.29), with $B_{c2}(0)$ and T_{c0} as free parameters. The dashed line gives the slope at T_{c0} , $dB_{c2}/dT|_{T=T_c} = -2.0$ T/K.

upper critical field, $H_{c2}(T)$. Specifically [67, 68],

$$D = \frac{4k_B}{\pi e} \left(\left. \frac{d(\mu_0 H_{c2})}{dT} \right|_{T=T_{c0}} \right)^{-1}. \quad (6.28)$$

T_{c0} is the critical temperature at zero field. To determine the slope of $B_{c2}(T) = \mu_0 H_{c2}(T)$ at T_{c0} , we measure resistance versus temperature curves for different applied fields, as shown in Fig. 6.B.2(a). We use the same Hall bar geometry as shown in the inset of Fig. 6.B.1(b) to measure the longitudinal resistance. We determine the critical temperature for a given magnetic field as the temperature where the resistance is 50% of the normal state resistance, and invert that to get $B_{c2}(T)$. The result is shown in Fig. 6.B.2(b).

To account for a slight non-linearity of $B_{c2}(T)$ at T_{c0} , we fit $B_{c2}(T)$ to the function [69],

$$B_{c2}(T) = B_{c2}(0) \left(\frac{1 - (T/T_{c0})^2}{1 + (T/T_{c0})^2} \right), \quad (6.29)$$

where $B_{c2}(0)$ is the upper critical flux density at $T = 0$. We use both $B_{c2}(0)$ and T_{c0} as fit parameters and we are interested in ratio, which gives the slope of $B_{c2}(T)$ at T_{c0} . The fit is shown in Fig. 6.B.2(b) as the solid black line together with the slope at T_{c0} as dashed line, which is $dB_{c2}/dT|_{T=T_{c0}} = -1.5$ T/K.

This slope gives from Eq. (6.28) $D = 0.74$ cm^2/s , and $N_0 = 2.1 \times 10^4$ $\mu eV^{-1} \mu m^{-3}$,

which is comparable to the value $3.1 \times 10^4 \mu\text{eV}^{-1} \mu\text{m}^{-3}$ from Ref. [70]. These values result in a Ginzburg-Landau coherence length of $\xi_{\text{GL}} = 16 \text{ nm}$.

Surprisingly, we find from Fig. 6.B.2(b) $T_{c0} = 0.72 \text{ K}$, while we found $T_c = 0.87 \text{ K}$ in Fig. 6.B.1(a). We verified this lower T_c for the Hall bar structure in the setup without magnetic field which was used to obtain the data in Fig. 6.2.1. The 4-probe and Hall bar structures are patterned in the same deposited film and close together on the wafer. The main difference is the width of the structures: $6 \mu\text{m}$ versus $200 \mu\text{m}$, see the insets of Fig. 6.B.2(a) and (b). Why this would change the T_c is not known, although it could be related to the stress in the film that might change the electron-phonon coupling for different widths. Nonetheless, we use the Hall bar geometry to extract normal state electronic properties only, namely the diffusion constant and the carrier charge density. For the diffusion constant, $D \propto T_c/B_{c2}$ with, in the dirty limit, $B_{c2} \propto 1/\xi_{\text{GL}}^2 \propto 1/\xi_0 \propto T_c$, where ξ_0 the BCS coherence length. From this, we see that the diffusion constant does not depend on T_c to first order. The carrier charge density is extracted in the normal state. Therefore, we expect that the different T_c of the Hall bar does not have an effect on the extracted properties.

We take $T_c = 0.87 \text{ K}$ for the inductors, as they are $10 \mu\text{m}$ wide, which similar to the 4-probe structure width. We verify this T_c by comparing the measured fractional resonance frequency shift versus temperature, $\delta f(T)/f_0$, to the calculated curves from Mattis-Bardeen [42] with $T_c = 0.72 \text{ K}$ and $T_c = 0.87 \text{ K}$ as input. We used a kinetic induction fraction of $\alpha_k^{\text{sim}} = 0.66$ from a simulation, since the measurement of $\alpha_k = 0.44$ assumes that $T_c = 0.87 \text{ K}$. This comparison is shown in Fig. 6.B.3, from which we conclude that the inductors have a T_c of 0.87 K . The small deviations from the solid line are most likely due to the disorder in the film, as the complex sheet impedance of disordered superconductors is slightly different from the prediction by standard Mattis-Bardeen theory [71, 72].

6.C TiN DATA ANALYSIS

The electron-phonon scattering time has a weak power-law temperature dependence (Eq. (6.3)), which contrasts the exponential temperature dependence of conventional quasiparticle recombination (Eq. (6.1)). This weak temperature dependence has also been measured with TiN resonators in Ref. [48]. There, the relaxation time is measured as the decay time of a pulsed excitation, which is either generated by a (high photon number) LED pulse, or a microwave pulse applied to the read-out line of the resonators. The normal state electron-phonon times of these 3 films have been measured in Ref. [49], where they suppress T_c using a magnetic field. The results of these measurements are shown in Fig. 6.C.1. In this section, we analyze the three films from Ref. [48], C, D and E, in the same manner as we analyzed the β -Ta film.

The parameters used for the calculations are shown in Table 6.C.1. The first 6 columns are from Refs. [48, 49] and give us the electronic properties. From the $k_F l$ values we see that these films are indeed disordered, but somewhat less than the β -Ta film. To estimate the rest of the electronic properties, we need N_0 as well. This has been measured in Ref. [73] for similar films. We compare the thickness of each

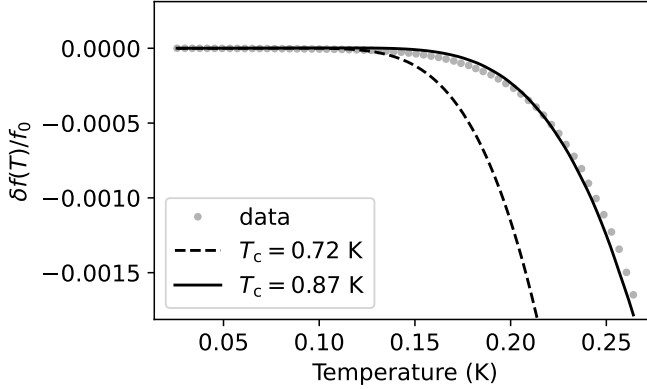


Figure 6.B.3: Fractional frequency shift with temperature of the membrane resonator compared to Mattis-Bardeen theory [42] to verify the critical temperature of $T_c = 0.87$ K. The dashed and solid lines are calculated with the parameters in Table 6.4.1, $\alpha_k^{\text{sim}} = 0.66$ from simulation and T_c as indicated by the legend.

film and estimate N_0 to be the values in Table 6.C.1. With these values, we calculate $\xi/d \lesssim 0.25$. So, these are 3D superconducting films.

We estimate the phonon properties of the TiN films in the following way. The mass density we get from Ref. [74], for TiN film with similar thickness. The Debye temperature we get from Ref. [75]. The transverse and longitudinal sound velocities, we estimate from a fit to the data for Ref. [49]. This is procedure is also set out in Ref. [76]. We assume $c_T = c_L/2$ and let c_L be a free fit parameter. This relation seems to be correct for many materials [35]. The results do not change if we assume $c_T < c_L/2$, since the relaxation times are then limited by transverse phonon scattering and we are left with only one sound velocity. To fit the measured electron-phonon relaxation times, we use the theory of Ref. [41], which includes statics scatterers when $k \leq 1$. We use Eq. (51) of [41],

$$\frac{1}{\tau_s(T)} = \frac{\pi^4 \beta_L (k_F l) (k_B T)^4}{5 \hbar^4 (k_F c_L)^3} \left(1 + k \frac{3}{2} \left(\frac{c_L}{c_T} \right)^5 \right) + \frac{3\pi^3 \beta_L (k_B T)^2}{2 \hbar^2 (k_F l) (k_F c_L)} (1 - k) \left(1 + 2k \left(\frac{c_L}{c_T} \right)^3 \right). \quad (6.30)$$

β_L is defined in Eq. (6.8). These measurements are performed at a finite temperature, above T_c , where the electrons distributed in energy around the Fermi surface with a width of $k_B T$. The measured signal is an average of all these electrons. So, the measured $\tau_s^{\text{meas.}}$, is given by [76, 77],

$$\frac{1}{\tau_s^{\text{meas.}}(T)} = \frac{3(n+2)\Gamma(n+2)\zeta(n+2)}{2\pi^2(2-2^{1-n})\Gamma(n)\zeta(n)} \frac{1}{\tau_s(T)}. \quad (6.31)$$

For n we use the values from [49], see Table 6.C.1. We use Eq. (6.31) to fit the the

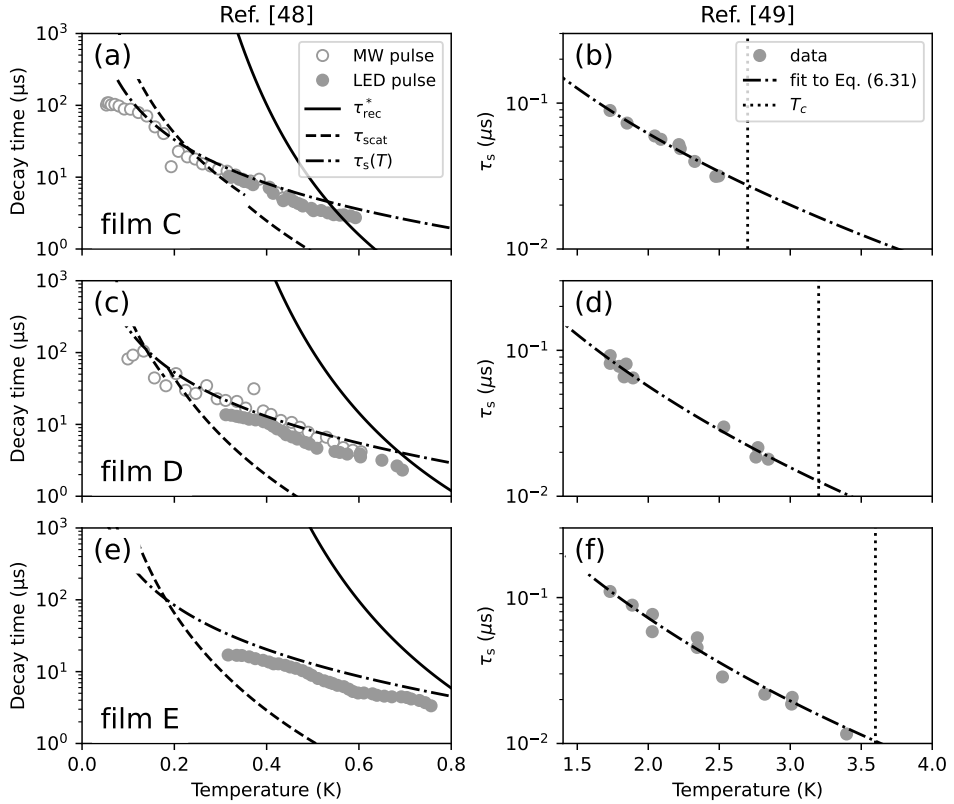


Figure 6.C.1: Relaxation times of three different TiN films from Refs. [48, 49], compared to disorder theory of Refs. [3, 32, 41]. (a), (c) and (e): Decay times of a pulse response from Ref. [48]. Solid gray dots are for a LED pulse and the open grey circles are for a microwave pulse applied at the resonator read-out line. The solid line is given by Eq. (6.2), with τ_{rec} given by Eq. (6.6) and the phonon trapping factor given by Eq. (6.13). The dashed lines are from Eq. (6.9) for low temperatures ($T < \hbar c_T / (2dk_B)$) and from Eq. (6.10) for high temperatures ($T > \hbar c_T / (2dk_B)$). (b), (d) and (f): The electron-phonon scattering time as measured in [49], for the same films as (a), (c) and (e), respectively. The dotted vertical line indicates the critical temperature. The dashed-dotted black line is a fit to Eq. (6.31), with k and c_L as free parameters and assuming $c_T = c_L/2$. The dashed-dotted lines in (a), (b) and (c) are the same, but without correction factor (Eq. (6.31)). The legends are applicable to all the figures in the same column. We used the parameters from Table 6.C.1 to calculate the theoretical lines.

data of [49], as shown in Fig. 6.C.1(b), (d) and (f). The fit results are given in the two right columns of Table 6.C.1.

With also the sound velocities available, we can estimate the phonon dimensionality via qd and disorder via ql . For thermal phonons, we find that $q(k_B T)d = 1/2$ at 0.36 K, 0.18 K and 0.11 K, for film C, D and E respectively. Below these temperatures, the thermal phonons are 2D, above, they are 3D. Recombination phonons are 3D,

Table 6.C.1.: Parameters for the TiN films from Refs. [48, 49], with additional parameters estimated from Refs. [73–75]. N_0 and $\hat{\rho}$ are estimated from similar films taking the thickness into account. n is the power of the temperature dependence of τ_s , as measured in [49]. c_L and k are the results of the fits in Fig. 6.C.1(b), (d) and (f), using Eq. (6.31) and assuming $c_T = c_L/2$.

Film	d (nm)	From Refs. [48, 49]				n	Ref. [73] N_0 ($\mu\text{eV}^{-1}\mu\text{m}^{-3}$)
		T_c (K)	ρ_N ($\mu\Omega\text{cm}$)	$k_F l$			
C	22	2.7	253	4.6	2.8	6.2×10^4	
D	45	3.2	187	6.1	3.1	6.0×10^4	
E	89	3.6	120	8.6	3.3	5.9×10^4	

Film	Ref. [74]	Ref. [75]	Fit Ref. [49] to Eq. (6.31)	
	$\hat{\rho}$ (g/cm^3)	T_D (K)	c_L (km/s)	k
C	5.7	579	4.0	0.993
D	5.0	579	4.2	0.995
E	5.0	579	5.1	0.995

$q(2\Delta_0)d \geq 13$ for all films.

Electron phonon interaction is disordered, since both $q(2\Delta_0)l \leq 0.46$ and $q(0.8 \text{ K})l \leq 0.03$ are smaller than one. We therefore use the same equations as for β -Ta, namely Eq. (6.6) for recombination and Eqs. (6.9) and (6.10) for scattering.

We calculate the phonon trapping factor in the same manner as for β -Ta, i.e. Eq. (6.13), but with the parameters in Table 6.C.1. The substrate is in this case Si, for which we use: $\hat{\rho} = 2.33 \text{ g}/\text{cm}^3$, $c_L = 8.98 \text{ km}/\text{s}$ and $c_T = 5.34 \text{ km}/\text{s}$ [39]. The diffuse scattering assumption is in this case justified by the presence of a native oxide layer between the TiN and the Si. Furthermore, the TiN films are poly-crystalline with a grain size smaller than 42 nm [78]. We get from Eq. (6.13) a phonon trapping factor of 29, 96 and 193 for films C, D and E, respectively. As an example, for film D the pair breaking time is on the order of 2 ns and phonon escape time on the order of 200 ns.

The resulting scattering and recombination times are shown in Fig. 6.C.1(a), (c) and (e) by the dashed and solid lines. The measured quasiparticle relaxation times have an even weaker temperature dependence than the phonon scattering time, $n < 9/2$. However, the theory of Refs. [3, 32] do not take static scattering into account, while we see from the fit results in Table 6.C.1 that $k < 1$ for all films. A theory for inelastic electron-phonon scattering in superconductors that includes static scatterers is still lacking. Nonetheless, we can compare the quasiparticle relaxation times to the normal state scattering time, $\tau_s(T)$. From Eq. (6.30) we see that static scatters cause a $n = 2$ power-law when $k < 1 - (k_B T l / (\hbar c_T))^2 < 0.999$ [41], which is satisfied in all experimental regimes in Fig. 6.C.1(a), (c) and (e). We plotted $\tau_s(T)$ from Eq. (6.30) with the same film parameters and no fit parameter. We omitted the averaging factor in Eq. (6.31), as the quasiparticles in a superconductor all have an energy very close to Δ_0 due to the gap in the density of states.

We observe that the relaxation times follow the same $n = 2$ temperature dependence for all film. The disorder dependence of the relaxation rate is also captured by Eq. (6.30), since the difference between the data and Eq. (6.30) is constant for the variation in disorder in the different films. We therefore conclude that also in TiN, the quasiparticle relaxation is enhanced and governed by the phonon scattering time. It also shows that this phenomenology is not limited to the β -Ta film, but is present in different disordered superconductors.

If we take $\xi^{\text{TiN}} \approx 6$ nm as localization length, we get a density of localized quasiparticle states of $n_{\text{qp}}^{\text{loc}} = 3/(4\pi(\xi^{\text{TiN}})^3) \approx 1 \times 10^6 \mu\text{m}^{-3}$. The thermal quasiparticle density at the maximum measured temperatures in Fig. 6.C.1(a), (c) and (e) is $n_{\text{qp}}^T \approx 7 \times 10^3 \mu\text{m}^{-3}$. This shows we are in the same regime as the β -Ta film: the thermally excited quasiparticles localize and recombine after delocalization by electron-phonon scattering. The values mentioned are based on the parameters in Table 6.C.1 and are the same within a factor 2 for all three films.

6.D FITTING THE POWER SPECTRAL DENSITIES

Figure 6.D.1(a) shows 5 examples of measured power spectral densities (PSDs) for the substrate resonator. Contributions from 50 Hz interference, $1/f$ fluctuators and the 4 K HEMT amplifier are clearly visible in the PSDs. To minimize the effects from these noise sources to the Lorentzian fit, we first disregard the data points in the gray shaded regions in Fig. 6.D.1(a). Second, we take the maximum value between 250 kHz and 500 kHz as the amplifier noise contribution and subtract that from the PSD. This value is shown by the gray dashed line. Third, we fit the function, A/f^γ , from 3 Hz to 100 Hz with A and γ as fit parameters. The fit is shown as the gray solid line, which is also subtracted from the PSD. The resulting PSDs are shown in Fig. 6.D.1(b). We fit Eq. (6.5) to these PSDs, which results in the gray dashed lines and gives us τ and s^2 in Fig. 6.2.1(a) and (b).

6.E FLUCTUATION MODEL FOR LOCALIZED QUASIPARTICLE RECOMBINATION

From Fig. 6.2.1, we observe that the measured complex conductivity fluctuations can be interpreted as quasiparticle number fluctuations [44], but with a lifetime of $\tau_{\text{scat}}/2$, instead of the conventional τ_{rec}^* (Eq. (6.2)). We conclude that the recombination of two quasiparticles must be preceded with a phonon absorption event. We explain this by recombination of localized quasiparticles, that first delocalize via phonon absorption, see Fig. 6.E.1(c) and (d). In this section, we model the quasiparticle fluctuations with the master equation approach as described in Refs. [34, 79], including the localized quasiparticle dynamics described in Ref. [2]. At the end of this section, we will discuss the assumptions and implications of the model.

To capture the observed phenomenology, we use the following rate equations for

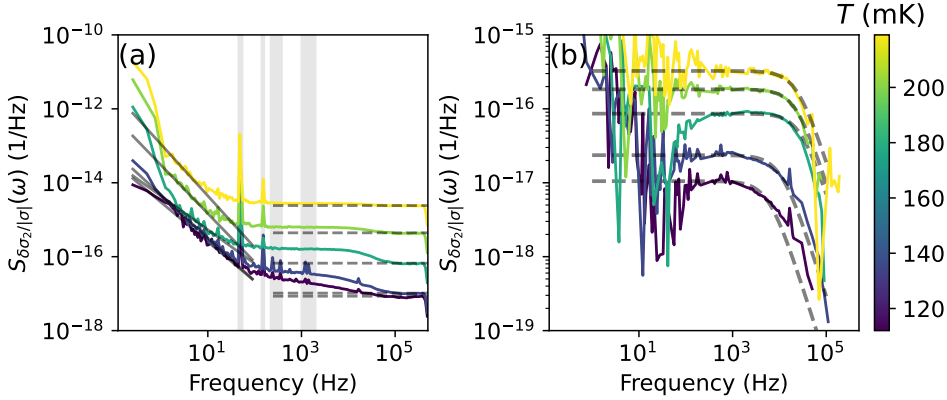


Figure **6.D.1**: Example of the subtraction of other noise sources and fitting of the measured kinetic inductance fluctuation power spectral density (PSD). **(a)**: Measured raw PSD as solid lines for the substrate resonator at different temperatures, indicated by the colors. The gray shaded vertical areas indicate the frequency ranges that we disregard to limit the influence of 50 Hz spikes. The dashed gray lines give the maxima of the solid lines between 250 kHz and 500 kHz, which we subtract as amplifier noise. The solid gray lines give a A/f^γ -fit, with A and γ as fit parameters, which we subtract to limit the effects of $1/f$ noise. **(b)**: Resulting PSDs when the other noise contributions are subtracted. The dashed gray lines give the Lorentzian fit, Eq. (6.5), from which we extract the quasiparticle lifetime and variance (Fig. 6.2.1(a) and (b)).

mobile and localized quasiparticle densities,

$$\begin{aligned} \frac{dn_m}{dt} &= -\Gamma_1 n_m + \Gamma_d n_l - 2R_{os} (n_m n_l - n_m^0 n_l^0) \\ \frac{dn_l}{dt} &= -2R_1 n_l^2 + 2\Gamma_{pb} + \Gamma_1 n_m - \Gamma_d n_l. \end{aligned} \quad (6.32)$$

Here, n_m is the mobile quasiparticle density and n_l is the localized quasiparticle density. The first two terms in the rate equation for n_l (second line) are the *localized* quasiparticle recombination (Fig. 6.E.1(a)) and generation terms described in Ref. [2]. We assume that the localized recombination and pair-breaking are in detailed balance ($2R_1 n_l^2 = 2\Gamma_{pb}$), as we do for all other transitions, since we are in equilibrium [34]. The main evidence for this is that the fluctuation variance equals the variance of a thermal quasiparticle density (Fig. 6.2.1(b)).

We set the generation rate equal to the pair-breaking rate of thermal phonons, $\Gamma_{pb} = R (n_{qp}^T)^2 / 2$, since we measure at a relatively high bath temperatures. R is the conventional recombination constant, $R = (2\Delta_0 / (k_B T_C))^3 / (4N_0 \Delta \tau_0^{\text{rec}})$, with $\tau_0^{\text{rec}} = 21$ ns for β -Ta [3, 35] (see Section 6.A). The thermal quasiparticle density is given by,

$$n_{qp}^T = 2N_0 \Delta_0 \sqrt{\frac{2\pi k_B T}{\Delta_0}} e^{-\Delta_0 / k_B T}. \quad (6.33)$$

The recombination rate for localized quasiparticles (Fig. 6.E.1(a)) depends on the average distance between quasiparticles, $2r$ [2],

$$R_l = \begin{cases} \frac{R}{2} \left(\frac{4\pi}{3C_p} \right)^2 b \left(\frac{r}{r_c} \right)^{\beta+3} e^{-r/r_c} & r/r_c > 3 \\ \frac{R}{2(1 + \tau_{\text{esc}}/\tau_{\text{pb}})} & r/r_c < 3 \end{cases}. \quad (6.34)$$

Here, $b = 0.008$ and $\beta = 0.41$ [2]. In Section 6.F, we estimate the critical quasiparticle distance to be $r_c \approx 3.5\xi = 65$ nm. We obtain r from numerically solving the equation [2],

$$b \left(\frac{r}{r_c} \right)^{\beta-3} e^{-r/r_c} = \frac{\Gamma_{\text{pb}} r_c^6}{R}. \quad (6.35)$$

Since Γ_{pb} is temperature dependent, this results in a temperature dependent quasiparticle density, $n_{\text{qp}} = C_p/(4\pi/3r^3)$. For $r/r_c \lesssim 3.0$, the quasiparticle density should be equal to the thermal number of quasiparticles, $n_{\text{qp}}(r/r_c < 3) \approx n_{\text{qp}}^T$ [2]. Therefore, we set $R_l = R/(1 + \tau_{\text{esc}}/\tau_{\text{pb}})$ when $r/r_c < 3$ in Eq. (6.34). We include the effect of phonon trapping for $r < 3r_c$ and omit it for $r > 3r_c$, since the quasiparticles are likely to have an energy close to Δ_0 only at higher temperatures. Furthermore, we set the quasiparticle packing coefficient $C_p = 0.54$, such that $n_{\text{qp}}(r/r_c = 3) = n_{\text{qp}}^T$. This is slightly smaller than the value $C_p = 0.61$ mentioned in Ref. [2]. With these parameters, we obtain a cross-over temperature for $r/r_c = 3$ of $T \approx 124$ mK. For lower temperatures we expect an excess number of quasiparticles due to localization. For higher bath temperatures, we expect a thermal quasiparticle density, which is consistent with the measured variance in Fig. 6.2.1(b) (see also Fig. 6.E.2(b)).

If we would only include the localized quasiparticle recombination (R_l) and thermal generation (Γ_{pb}) terms, as is considered in Ref. [2], we would obtain the conventional quasiparticle fluctuations in our measurement regime, with a thermal quasiparticle density as variance and τ_{rec}^* as relaxation time. We expect however that quasiparticles can delocalize due to inelastic phonon scattering at these relatively high bath temperatures. This enables a second, faster recombination mechanism: *on-site* recombination (Fig. 6.E.1(d)). To include this in the model, we introduce a mobile quasiparticle level and localization and delocalization terms in Eq. (6.32), see Fig. 6.E.1(b) and (c). We set the delocalization rate to the reciprocal of the inelastic phonon scattering time, $\Gamma_d = 1/\tau_{\text{scat}}$, which is the time it takes to absorb a thermal phonon (Fig. 6.E.1(c)). Since we assume that we are in equilibrium, localization and delocalization obey detailed balance and the steady state values are given by,

$$\begin{aligned} n_l^0 &= n_{\text{qp}} \\ n_m^0 &= n_{\text{qp}} \frac{\Gamma_d}{\Gamma_l}, \end{aligned} \quad (6.36)$$

We set the localization rate (Fig. 6.E.1(b)) much higher than the delocalization rate, $\Gamma_d \ll \Gamma_l = 10^2/\tau_{\text{scat}}$, such that the mobile quasiparticle density is low and the total

density is close to n_{qp} . We omit the conventional mobile-mobile recombination, since these rates are very low at a low mobile quasiparticle density.

The last term in Eq. (6.32), first line, describes the relaxation of a mobile quasiparticle and subsequent *on-site* recombination with a localized quasiparticle (Fig. 6.E.1(d)). The rate depends on both the mobile and localized quasiparticle density, n_m and n_l , and we include the $n_m^0 n_l^0$ term to ensure that detailed balance is satisfied. The on-site recombination constant is given by $R_{\text{os}} = (2\Delta / (k_B T_c))^3 / (4N_0 \Delta \tau_0^{\text{os}})$, with τ_0^{os} the characteristic on-site recombination time. This is likely to be short, since the mobile and localized quasiparticles relax to the same location [2]. We choose this characteristic time to be $\tau_0^{\text{os}} = 10^{-4} \tau_0^{\text{rec}}$, such that on-site recombination is faster than localization and delocalization over our entire measurement regime. Any shorter characteristic time gives the same results when comparing it to our measurements. We disregard the phonon trapping effect for on-site recombination (Fig. 6.E.1(d)), since this is a multistep relaxation process and the individual phonons emitted have less energy than $2\Delta_0$ and are unlikely to break a Cooper-pair [5].

To obtain the quasiparticle fluctuation spectra, we calculate the two matrices $\underline{\underline{M}}$ and $\underline{\underline{B}}$, that describe the drift and diffusion in the (n_m, n_l) -space, respectively [34]. From Eq. (6.32), we read off the transition probabilities, p , and shot sizes, δn ,

$$\begin{aligned}
 p_{12} &= \Gamma_1 n_m & \delta n_{12} &= 1/V \\
 p_{13} &= R_{\text{os}} n_m n_l & \delta n_{13} &= 2/V \\
 p_{21} &= \Gamma_d n_l & \delta n_{21} &= 1/V \\
 p_{23} &= R_l n_l^2 & \delta n_{23} &= 2/V \\
 p_{31} &= R_{\text{os}} n_m^0 n_l^0 & \delta n_{31} &= 2/V \\
 p_{32} &= \Gamma_{\text{pb}} & \delta n_{31} &= 2/V,
 \end{aligned} \tag{6.37}$$

where the index 1 denotes the mobile quasiparticle level, 2 the localized quasiparticle level and 3 the Cooper-pair level. From this, we can directly calculate the matrices with [34]

$$\begin{aligned}
 M_{ij} &= \sum_k \delta n_{ik} \left(\frac{\partial p_{ik}}{\partial n_j} - \frac{\partial p_{ki}}{\partial n_j} \right) \Big|_{\{n_i\}=\{n_i^0\}} \\
 B_{ii} &= \sum_{k \neq i} \delta n_{ik}^2 (p_{ki}^0 + p_{ik}^0) \\
 B_{ij} &= -\delta n_{ij} \delta n_{ji} (p_{ij}^0 + p_{ji}^0).
 \end{aligned} \tag{6.38}$$

Using these equations results in,

$$\begin{aligned}
 \underline{\underline{M}} &= \frac{1}{V} \begin{bmatrix} \Gamma_1 + 2R_{\text{os}} n_l^0 & -\Gamma_d + 2R_{\text{os}} n_m^0 \\ -\Gamma_1 & \Gamma_d + 4R_l n_l^0 \end{bmatrix} \\
 \underline{\underline{B}} &= \frac{2n_l^0}{V^2} \begin{bmatrix} \Gamma_d + 4R_{\text{os}} n_m^0 & -\Gamma_d \\ -\Gamma_d & \Gamma_d + 4R_l n_l^0 \end{bmatrix},
 \end{aligned} \tag{6.39}$$

where we used the principle of detailed balance (i.e. $p_{ij}^0 = p_{ji}^0$) in the expression for $\underline{\underline{B}}$.

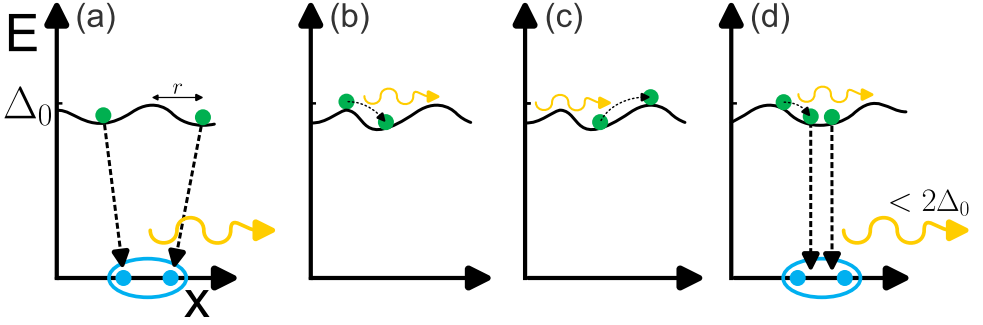


Figure 6.E.1: Sketches of the different transitions in the rate equations, Eq. (6.32). (a): Localized quasiparticle recombination, as described in Ref. [2]. The recombination rate depends on the distance between two quasiparticles, $2r$. The emitted phonon has less than $2\Delta_0$ energy at low temperatures, but can be $\geq 2\Delta_0$ for higher temperatures when the quasiparticles are not fully relaxed into the localized states. (b): Quasiparticle localization with emission of a phonon. (c): Quasiparticle delocalization via absorption of a phonon. (d): On-site recombination, where a mobile quasiparticle relaxes to a localized quasiparticle in the same localization site. This process emits multiple phonons with energy $< 2\Delta_0$. Phonons are depicted with curvy yellow arrows, quasiparticles with green dots and Cooper-pairs with blue, grouped dots.

6

The eigenvalues of the matrix \underline{M} give the fluctuation rates. In the limit of slow localized recombination and fast on-site recombination, $R_1 n_1^0 \ll \Gamma_d \ll \Gamma_1 \ll R_{os} n_m^0$, the smallest fluctuation rate is $1/\tau = 2\Gamma_d = 2/\tau_{scat}$. This corresponds to the temperature regime $T < 175$ mK in Fig. 6.2.1, where recombination is slow (black line) and we observe $2/\tau_{scat}$ (dashed line) as relaxation rate. The factor two in the relaxation rate reflects the pair-wise nature of recombination.

The variance matrix in equilibrium can be calculated as $\underline{s}^2 = \underline{M}^{-1} \underline{B} / 2$ [34]. We compare the sum of the matrix entries to the experimental measured variance ($s^2 = \sum_{i,j} s_{ij}^2$) since we are sensitive to both localized and mobile quasiparticles. This results in $s^2 = (n_1^0 + n_m^0) / V \approx n_{qp} / V$, which is equal to n_{qp}^T / V in our measurement regime. To summarize this analytical argument, we expect quasiparticle fluctuations with a relaxation time of $\tau = \tau_{scat} / 2$ and a variance $s^2 = n_{qp}^T / V$, which we observe from the experiment in Fig. 6.2.1.

Figure 6.E.2 shows the numerically calculated relaxation time and variance from this model. For this, we used the parameters as previously mentioned: $\Gamma_1 = 10^2 \Gamma_d = 10^2 / \tau_{scat}$, $\tau_0^{os} = 10^{-4} \tau_0^{rec} = 10^{-4} \cdot 21$ ns and R_1 from Eq. (6.34). This describes the data accurately, except for temperatures above 175 mK. In that regime, the average distance between quasiparticles is larger than the critical distance, $r > r_c$. Therefore, a significant fraction of quasiparticles will be mobile, which is not included in our model. That suggests that the plateau in relaxation time we observe for $T > 175$ mK might be a cross-over regime from localized to mobile quasiparticle dynamics.

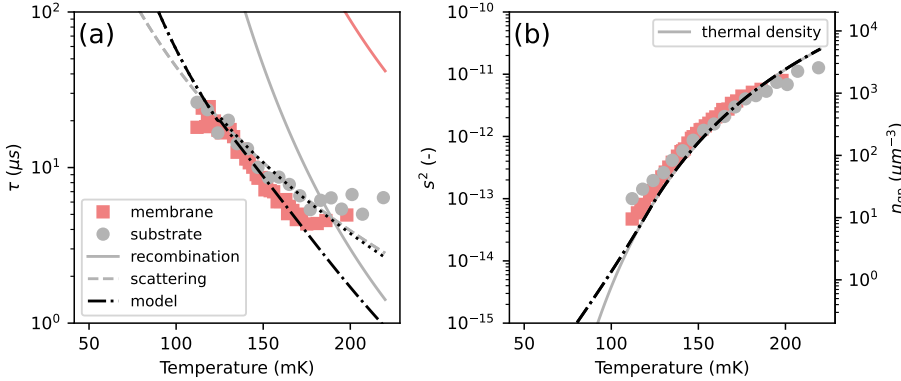


Figure 6.E.2: Calculated relaxation time and variance from the fluctuation model, compared to the measured data. **(a)**: The solid lines give the localized recombination time ($1/(4R_1n_1^0)$), which corresponds to conventional recombination in this regime. The gray solid line is for the substrate resonator and the red line is for the membrane resonator. The gray dashed line is the delocalization time ($\tau_{\text{scat}}/2$). The solid and dashed lines are identical to the lines in Fig. 6.2.1(a). The black dashed-dotted lines are the model prediction for the substrate resonator. This is given by the reciprocal of the smallest eigenvalue of $\underline{\underline{M}}$. The dotted black line is for the membrane case. This follows $\tau_{\text{scat}}/2$ to much higher temperatures than in the substrate case, since the localized recombination is much slower (red solid line). **(b)**: The solid gray line corresponds to the thermal quasiparticle density (Eq. (6.33)). The dashed-dotted line is calculated from the model as the sum of the elements of $\underline{\underline{s}}^2 = \underline{\underline{M}}^{-1}\underline{\underline{B}}/2$. This is equal to $n_{\text{qp}}/V = C_p/(4\pi V/3r^3)$, with r from Eq. (6.35). For temperatures $T > 124$ mK, this equals n_{qp}^T/V from Eq. (6.33). For lower temperatures, the deviation of the dashed-dotted line from the thermal density shows that quasiparticle localization effects cause an excess quasiparticle density as predicted in Ref. [2]. The gray dots and red squares in both panels are the same data points as in Fig. 6.2.1.

The full power spectral density matrix can be calculated with [34],

$$\underline{\underline{G}}(\omega) = \frac{2}{\omega^2} \text{Re} \left[\left(\mathbf{1} + \underline{\underline{M}}/(i\omega) \right)^{-1} \underline{\underline{B}} \right]. \quad (6.40)$$

Here, ω is the angular frequency of the fluctuations and $\mathbf{1}$ is the identity matrix. Taking the sum of all matrix elements ($G(\omega) = \sum_{i,j} G_{ij}(\omega)$) results in the power spectral densities as shown in Fig. 6.4.1(c) and (d). These resemble the data accurately and also show the features $\tau = \tau_{\text{scat}}/2$ and a variance $s^2 = n_{\text{qp}}^T/V$.

6.E.1 DISCUSSION OF ASSUMPTIONS AND IMPLICATIONS OF THE MODEL

At this point, we like to make some remarks about the assumptions in the model. First, we assumed that the delocalization time is given by the inelastic phonon scattering time (τ_{scat} from Eq. (6.9)). This scattering time [3, 35] is for quasiparticles

with energy Δ_0 and a BCS density of states. Since these quasiparticles cannot lose energy (the density of states below Δ_0 energy in a BCS superconductor is 0), the only contribution to this inelastic interaction time is phonon absorption. This justifies the choice $\Gamma_d = 1/\tau_{\text{scat}}$.

Secondly, for the same reason as mentioned above, the scattering rate for phonon emission is zero for quasiparticles in BCS superconductor with Δ_0 energy. For disordered superconductors, with a slightly altered density of states, it is thus likely that phonon emission by a mobile quasiparticle is very slow. We assumed however a much higher localization rate than delocalization, since that is required for most quasiparticles to be localized. It is not clear what causes this fast relaxation. Electron-electron interaction could be responsible for this, since it is enhanced in disordered metals and superconductors (see Fig. 6.A.1). For a proper analysis however, these interaction times should be calculated with the full density of states that is affected by disorder.

Thirdly, since the density of states is much larger close to Δ_0 (see Fig. 6.1.1(d)), thermal phonons are more likely to generate mobile quasiparticles. We however included this term (Γ_{pb}) in the localized quasiparticle level, to ensure detailed balance with the localized recombination (R_l). The conventional (mobile) quasiparticle dynamics coincides with these localized recombination and generation terms, since the localized quasiparticle density is high ($r < 3r_c$, see Eq. (6.34) and Ref. [2]). Therefore, the conventional generation-recombination quasiparticle dynamics are also captured in this model, when fast localization is assumed (see second discussion point above).

Fourthly, we modeled the on-site recombination as a rate that only affects the mobile quasiparticle density, while it would be more intuitive to include it in both the localized and mobile rate equations (see Fig. 6.E.1(d)). In fact, we could divide the R_{os} term in Eq. (6.32) by 2 and add the same term to the n_l -rate equation. This results in a relaxation time of $\tau_{\text{scat}}/4$ and a variance of $n_{\text{qp}}/(2V)$, i.e., both missing a factor 2 compared to the measurements. The reason for that is that the pair-wise nature of on-site recombination is not captured in the model that way. It is not clear how to include such a multi-level, pair-wise transition in the framework of Ref. [34]. That is why we choose to include the on-site recombination term in the n_m -level only.

In a more rigorous treatment of the localization and recombination dynamics (Fig. 6.E.1), the effects of the local variations should be included. For example, position-dependent quasiparticle densities, $n_m(\mathbf{r})$ and $n_l(\mathbf{r})$, and a diffusion term in the mobile quasiparticle rate equation could be added. In that way, the localized and on-site recombination terms (Fig. 6.E.1(a) and (d)) could be combined in one recombination term that is dependent on the local quasiparticle density. This could give a microscopic reasoning for the fast on-site recombination characteristic time, which we here have set to $\tau_0^{\text{os}} = 10^{-4} \tau_0^{\text{rec}}$. Such position-dependent models are much more complicated to solve, and we therefore do not treat them here. However, similar models have been developed in the context of fluctuations in semiconductors [79, 80]. In semiconductors, Shockley-Read-Hall trap-assisted recombination [81, 82] of electrons and holes cause a similar enhanced recombination rate.

Lastly, we would like to comment on the low-temperature behavior of the model. For the quasiparticle density, the model follows the predictions of Ref. [2]: when the distance between the localized quasiparticles becomes larger than $6r_c$ localized recombination (R_l) slows down and causes an excess quasiparticle density (Fig. 6.E.2(b)). At some point, the pair-breaking rate of thermal phonons will be smaller than another pair-breaking mechanism such as cosmic rays, radioactivity or stray light. For our measurement, it is likely that the microwave read-out power is the dominating pair-breaking processes at low temperatures [83], see also Fig. 6.4.3. At low temperatures, the quasiparticle density will therefore saturate completely. Additionally, the on-site recombination slows down at low temperatures as n_{qp} decreases. Therefore, a delocalized quasiparticle will be more likely to localize again, instead of recombine on-site. In the limit $\Gamma_l \ll R_{os} n_1^0$, relaxation is dominated by localized recombination (Fig. 6.E.1(a)) instead of on-site recombination (Fig. 6.E.1(d)). Localized recombination is more-than exponentially slow at low quasiparticle densities, with a relaxation time $\tau = 1/(4R_l n_1^0)$ [2]. This could explain the measurements of Ref. [28], where relaxation times on the order of seconds have been measured in disordered grAl.

6.F GAP FLUCTUATIONS AND LOCALIZED STATES INDUCED BY DISORDER

To estimate the density of localized quasiparticle states, we need an estimate for η and Γ_{tail} , which parameterize the disorder-induced broadening and exponential subgap tail of the density of states (see Fig. 6.1.1). Since $\xi/d = 0.39$ (see *Film characterization* in the *Methods section*) is close to 1, we calculate η and Γ_{tail} both for the mesoscopic fluctuations in 3D, and Coulomb induced mesoscopic fluctuations in quasi-2D [45]. For η the 3D contribution is given by [6],

$$\eta_{3D} = \frac{2\Delta_0}{\pi^2 \hbar D} \left(\frac{\rho_N}{R_Q} \right)^2 \ln \left(\frac{\xi}{l} \right), \quad (6.41)$$

where $R_Q = 2\pi\hbar/e^2 = 25.8 \text{ k}\Omega$ is the resistance quantum. For the β -Ta film, this results in $\eta_{3D} = 1.5 \times 10^{-5}$ and a gap broadening of $\Gamma_{gap}^{3D}/\Delta_0 = 1 - (1 - \eta_{3D}^{2/3})^{3/2} = 8.9 \times 10^{-4}$. The subgap tail in the density of states is due to the local variations of Δ [6, 7]. In quasi-2D, homogeneously disordered films, it is always dominated by Coulomb-induced fluctuations [6, 45], which is given by,

$$\frac{\Gamma_{tail}^{2D}}{\Delta_0} = \left(\frac{0.47}{g(g - g_c)} \right)^{2/3}, \quad (6.42)$$

where $g = R_Q d / \rho_N$ and $g_c = \ln^2(\hbar / (k_B T_{c0} \tau_*)) / (2\pi)$, with $\tau_* = \max\{\tau_e, \tau_e(d/l)^2\}$. Here, T_{c0} is the critical temperature without the presence of disorder. For the β -Ta film, we take $T_{c0} \approx T_c$. This is a reasonable approximation, since in that case $g \approx 500$ is much larger than $g_c \approx 0.0058$ and T_c only degrades significantly near the fermionic

quantum critical point [84]. We obtain $\Gamma_{\text{tail}}^{2\text{D}}/\Delta_0 = 1.5 \times 10^{-4}$.

The mesoscopic fluctuations in 3D without Coulomb interaction are given by [7, 45],

$$\frac{\Gamma_{\text{tail}}^{3\text{D}}}{\Delta_0} = \left(\frac{5}{6^{1/4} (8\pi N_0 \Delta_0 \xi^3)^2} \right)^{5/4} \left(1 - \frac{\Gamma_{\text{gap}}^{3\text{D}}}{\Delta_0} \right), \quad (6.43)$$

which results in 1.0×10^{-6} for the β -Ta film. This is much smaller than the quasi-2D Coulomb contribution, and we therefore take $\Gamma_{\text{tail}} = \Gamma_{\text{tail}}^{2\text{D}}$.

With $\Gamma_{\text{tail}}^{2\text{D}}$, we can calculate the quasi-2D, Coulomb contribution to the gap broadening, which is given by [6],

$$\eta_{2\text{D}} = \left(1 - \left(1 - \frac{\Gamma_{\text{tail}}^{2\text{D}}}{\Delta_0} \ln^{2/3} \left(\frac{\Delta_0}{\Gamma_{\text{tail}}^{2\text{D}}} \right) \right)^{2/3} \right)^{3/2}. \quad (6.44)$$

This results in $\eta_{2\text{D}} = 9.0 \times 10^{-6}$, which is comparable to $\eta_{3\text{D}}$. We therefore take, $\eta = \eta_{2\text{D}} + \eta_{3\text{D}}$ [2], which results in $\Gamma_{\text{gap}}/\Delta_0 = 1.2 \times 10^{-3}$.

The coherence peak energy Δ differs less than 0.1% from Δ_0 with this amount of disorder, which we calculated by numerically solving the Usadel equations with η as pair-breaking parameter [71, 85]. That justifies the use of Δ_0 in these calculations.

The density of states is thus altered by disorder which is parameterized by η and Γ_{tail} , which we estimated above. Quasiparticles generated at Δ_0 are mobile and relax to lower energies $\Delta - \Gamma_{\text{gap}} - \Gamma_{\text{tail}}$, where they localize [2]. At this energy, the length scale of the gap variations is $L_T = 0.9\xi (\Gamma_{\text{tail}}/\Delta_0)^{-1/4} \approx 9\xi$ and within a volume L_T^3 the number of overlapping localized states is $N_T \approx 0.46 N_0 \Delta_0 \xi^3 (\Gamma_{\text{tail}}/\Delta_0)^{3/4} (\Delta_0/\Gamma_{\text{gap}})$. Therefore, the quasiparticles will relax further until there is approximately one quasiparticle state per localization volume. The average distance between quasiparticles at this point is given by [2],

$$2r_c \approx 0.92\xi \left(\frac{\Gamma_{\text{tail}}}{\Delta_0} \right)^{-1/4} (\ln N_T)^{-1/5}. \quad (6.45)$$

This results in $r_c \approx 3.5\xi = 65$ nm for the β -Ta film and we estimate the number of localized quasiparticles states as $\tilde{n}_{\text{qp}}^{\text{loc}} = 3/(4\pi r_c^3) \approx 8.5 \times 10^2 \mu\text{m}^{-3}$. How many of these states are filled, depends on the (possibly non-equilibrium) agent that supports the localized quasiparticle density [2]. In our measurement, the dominating pair-breaking mechanism is thermal phonon absorption, see Section 6.E.

6.G ESTIMATION OF READ-OUT POWER EFFECTS ON QUASIPARTICLE DENSITY AND DISTRIBUTION FUNCTION

In all the calculations above, we assumed that the quasiparticles are in equilibrium with the thermal bath. This is supported by the observation that the measured variance in Fig. 6.2.1(b) corresponds to thermal quasiparticle density fluctuations (the black line in Fig. 6.2.1(b)). The continuous excitation with read-out power can however cause a non-equilibrium quasiparticle density at low bath temperatures

[83, 86, 87] and a non-thermal quasiparticle distribution over energy at higher bath temperature [23, 86, 87]. Figure 6.4.3 shows the read-out power dependence of the relaxation time and variance. This is qualitatively consistent with the creation of excess quasiparticles: the relaxation time decreases and variance increases with increasing read-out power.

To limit these effects, we select the lowest read-out power at which we still have signal-to-noise ratio high enough to extract the relaxation time and variance (see Section 6.D). This read-out power is the red data set in Fig. 6.4.3, which is the same as the membrane data in Fig. 6.2.1. We can estimate the bath temperature below which excess quasiparticles are expected from Eq. (35) of Ref. [87],

$$T_B^* = \frac{(k_B T_*)^3}{k_B \Delta_0^2}, \quad (6.46)$$

where $k_B T_*$ is a measure for the width of the distribution function and is given by [87],

$$\frac{k_B T_*}{\Delta_0} = \left(\frac{105\pi}{64} \left(\frac{k_B T_c}{\Delta_0} \right)^3 \frac{\hbar \tau_0}{\Delta_0^2} c_{\text{phot}}^{\text{qp}} P_{\text{int}} \right)^{1/6}. \quad (6.47)$$

Here, $c_{\text{phot}}^{\text{qp}} = \alpha_k \omega_0 / (2\pi N_0 V \Delta_0)$ is the photon-quasiparticle coupling constant and $P_{\text{int}} = 2Q^2 P_{\text{read}} / (\pi Q_c)$ is the internal microwave power in the resonator, with $Q \approx 9.7 \times 10^3$ the loaded quality factor and $Q_c \approx 10.0 \times 10^3$ the coupling quality factor. With an on-chip read-out power of $P_{\text{read}} = -98$ dBm, this results in $T_B^* = 19$ mK. For the substrate resonator (which we measure at $P_{\text{read}} = -100$ dBm), the same calculation results in $T_B^* = 16$ mK. Since we measure at bath temperatures of $T > 100$ mK, we do not expect excess quasiparticles generated by read-out power for the main data set (Fig. 6.2.1).

The distribution function of the quasiparticles has the equilibrium Fermi-Dirac shape for energies larger than $E_* = \Delta_0 + k_B T_* \sqrt{T_*/T}$ [87]. In our measurement regime, we obtain $E_* = 1.3\Delta_0$ and $1.4\Delta_0$ for the highest and lowest bath temperatures. For lower energies than E_* , the quasiparticle distribution function could deviate from the thermal distribution, and the average quasiparticle energy could be slightly higher than Δ_0 (when a BCS density of states is assumed, as is done in these calculations). At the same time, we calculated the recombination and scattering times for a quasiparticle at Δ_0 in Eqs. (6.6), (6.9) and (6.10). A higher quasiparticle energy of $1.4\Delta_0$ (which is a strict upper limit to the average quasiparticle energy) will however only result in a faster recombination time by less than a factor 2 [35] and the exponential temperature dependence ($\tau_{\text{rec}} \propto 1/n_{\text{qp}}$) is preserved in the case of a non-equilibrium distribution[86].

Moreover, the enhanced electron-electron inelastic relaxation due to disorder (see Fig. 6.A.1) will result in a more thermal shape of the distribution function than calculated by Refs. [86, 87], which only consider electron-phonon interactions. Additionally, the broadened density of states due to disorder (see Section 6.F) will also result in a broadening of the non-equilibrium peaks in the distribution function and thus diminish the read-out power effects on the distribution function.

Therefore, at these low read-out powers, we expect a thermal quasiparticle density and an approximately thermal shape for the distribution function, with an average quasiparticle energy close to the gap energy. This justifies the relaxation time calculations in Section 6.A.

REFERENCES

- [1] S. A. H. de Rooij, R. Fermin, K. Kouwenhoven, T. Coppens, V. Murugesan, D. J. Thoen, J. Aarts, J. J. A. Baselmans, and P. J. de Visser. *Recombination of Localized Quasiparticles in Disordered Superconductors*. In: *Nature Communications* 16.1 (2025), p. 8465.
- [2] A. Bespalov, M. Houzet, J. S. Meyer, and Y. V. Nazarov. *Theoretical Model to Explain Excess of Quasiparticles in Superconductors*. In: *Physical Review Letters* 117.11 (2016), p. 117002.
- [3] M. Y. Reizer and A. V. Sergeev. *Electron-Phonon Interaction in Impure Metals and Superconductors*. In: *Zh. Eksp. Teor. Fiz.* 90 (1986), p. 1056.
- [4] A. Pippard. *CXXII. Ultrasonic Attenuation in Metals*. In: *The London, Edinburgh, and Dublin Philosophical Magazine and Journal of Science* 46.381 (1955), pp. 1104–1114.
- [5] A. G. Kozorezov, A. A. Golubov, J. K. Wigmore, D. Martin, P. Verhoeve, R. A. Hijmering, and I. Jerjen. *Inelastic Scattering of Quasiparticles in a Superconductor with Magnetic Impurities*. In: *Physical Review B* 78.17 (2008), p. 174501.
- [6] M. V. Feigel'man and M. A. Skvortsov. *Universal Broadening of the Bardeen-Cooper-Schrieffer Coherence Peak of Disordered Superconducting Films*. In: *Physical Review Letters* 109.14 (2012), p. 147002.
- [7] A. I. Larkin and Y. N. Ovchinnikov. *Density of States in Inhomogeneous Superconductors*. In: *Soviet Journal of Experimental and Theoretical Physics* 34 (1972), p. 1144.
- [8] B. Sacépé, M. Feigel'man, and T. M. Klapwijk. *Quantum Breakdown of Superconductivity in Low-Dimensional Materials*. In: *Nature Physics* 16.7 (7 2020), pp. 734–746.
- [9] K. M. Bastiaans, D. Chatzopoulos, J.-F. Ge, D. Cho, W. O. Tromp, J. M. van Ruitenbeek, M. H. Fischer, P. J. de Visser, D. J. Thoen, E. F. C. Driessen, T. M. Klapwijk, and M. P. Allan. *Direct Evidence for Cooper Pairing without a Spectral Gap in a Disordered Superconductor above T_c* . In: *Science* 374.6567 (2021), pp. 608–611.
- [10] L. Grünhaupt, M. Spiecker, D. Gusenkova, N. Maleeva, S. T. Skacel, I. Takmakov, F. Valenti, P. Winkel, H. Rotzinger, W. Wernsdorfer, A. V. Ustinov, and I. M. Pop. *Granular Aluminium as a Superconducting Material for High-Impedance Quantum Circuits*. In: *Nature Materials* 18.8 (8 2019), pp. 816–819.

- [11] M. Esposito, A. Ranadive, L. Planat, and N. Roch. *Perspective on Traveling Wave Microwave Parametric Amplifiers*. In: *Applied Physics Letters* 119.12 (2021), p. 120501.
- [12] P. K. Day, H. G. LeDuc, B. A. Mazin, A. Vayonakis, and J. Zmuidzinas. *A Broadband Superconducting Detector Suitable for Use in Large Arrays*. In: *Nature* 425.6960 (2003), pp. 817–821.
- [13] G. N. Gol'tsman, O. Okunev, G. Chulkova, A. Lipatov, A. Semenov, K. Smirnov, B. Voronov, A. Dzardanov, C. Williams, and R. Sobolewski. *Picosecond Superconducting Single-Photon Optical Detector*. In: *Applied Physics Letters* 79.6 (2001), pp. 705–707.
- [14] K. Kouwenhoven, I. Elwakil, J. van Wingerden, V. Murugesan, D. J. Thoen, J. J. A. Baselmans, and P. J. de Visser. *Model and Measurements of an Optical Stack for Broadband Visible to Near-Infrared Absorption in TiN MKIDs*. In: *Journal of Low Temperature Physics* 209.5 (2022), pp. 1249–1257.
- [15] R. Ma, Q. Huan, J. Huang, X. Zhang, Y. Xiao, H. Xu, H. Han, X. Liu, W. Peng, H. Li, X. Zhang, and L. You. *Disorder Enhanced Relative Intrinsic Detection Efficiency in NbTiN Superconducting Nanowire Single Photon Detectors at High Temperature*. In: *Applied Physics Letters* 124.7 (2024), p. 072601.
- [16] H. G. Leduc, B. Bumble, P. K. Day, B. H. Eom, J. Gao, S. Golwala, B. A. Mazin, S. McHugh, A. Merrill, D. C. Moore, O. Noroozian, A. D. Turner, and J. Zmuidzinas. *Titanium Nitride Films for Ultrasensitive Microresonator Detectors*. In: *Applied Physics Letters* 97.10 (2010), p. 102509.
- [17] M. Sidorova, A. D. Semenov, I. Charaev, M. Gonzalez, A. Schilling, S. Gyger, and S. Steinhauer. *Phonon Heat Capacity and Disorder: New Opportunities for Performance Enhancement of Superconducting Devices*. 2023. URL: <http://arxiv.org/abs/2308.12090>. Pre-published.
- [18] J. M. Martinis. *Saving Superconducting Quantum Processors from Decay and Correlated Errors Generated by Gamma and Cosmic Rays*. In: *npj Quantum Information* 7.1 (1 2021), pp. 1–9.
- [19] R.-P. Riwar and G. Catelani. *Efficient Quasiparticle Traps with Low Dissipation through Gap Engineering*. In: *Physical Review B* 100.14 (2019), p. 144514.
- [20] K. Karatsu, A. Endo, J. Bueno, P. J. de Visser, R. Barends, D. J. Thoen, V. Murugesan, N. Tomita, and J. J. A. Baselmans. *Mitigation of Cosmic Ray Effect on Microwave Kinetic Inductance Detector Arrays*. In: *Applied Physics Letters* 114.3 (2019), p. 032601.
- [21] J. J. A. Baselmans, S. J. C. Yates, P. Diener, and P. J. de Visser. *Ultra Low Background Cryogenic Test Facility for Far-Infrared Radiation Detectors*. In: *Journal of Low Temperature Physics* 167.3 (2012), pp. 360–366.

- [22] L. Cardani, F. Valenti, N. Casali, G. Catelani, T. Charpentier, M. Clemenza, I. Colantoni, A. Cruciani, G. D’Imperio, L. Gironi, L. Grünhaupt, D. Gusenkova, F. Henriques, M. Lagoin, M. Martinez, G. Pettinari, C. Rusconi, O. Sander, C. Tomei, A. V. Ustinov, M. Weber, W. Wernsdorfer, M. Vignati, S. Pirro, and I. M. Pop. *Reducing the Impact of Radioactivity on Quantum Circuits in a Deep-Underground Facility*. In: *Nature Communications* 12.1 (1 2021), p. 2733.
- [23] P. J. de Visser, D. J. Goldie, P. Diener, S. Withington, J. J. A. Baselmans, and T. M. Klapwijk. *Evidence of a Nonequilibrium Distribution of Quasiparticles in the Microwave Response of a Superconducting Aluminum Resonator*. In: *Physical Review Letters* 112.4 (2014), p. 047004.
- [24] A. P. Vepsäläinen, A. H. Karamlou, J. L. Orrell, A. S. Dogra, B. Loer, F. Vasconcelos, D. K. Kim, A. J. Melville, B. M. Niedzielski, J. L. Yoder, S. Gustavsson, J. A. Formaggio, B. A. VanDevender, and W. D. Oliver. *Impact of Ionizing Radiation on Superconducting Qubit Coherence*. In: *Nature* 584.7822 (7822 2020), pp. 551–556.
- [25] R. Barends, J. Wenner, M. Lenander, Y. Chen, R. C. Bialczak, J. Kelly, E. Lucero, P. O’Malley, M. Mariani, D. Sank, H. Wang, T. C. White, Y. Yin, J. Zhao, A. N. Cleland, J. M. Martinis, and J. J. A. Baselmans. *Minimizing Quasiparticle Generation from Stray Infrared Light in Superconducting Quantum Circuits*. In: *Applied Physics Letters* 99.11 (2011), p. 113507.
- [26] A. V. Sergeev and M. Yu. Reizer. *Photoresponse Mechanisms of Thin Superconducting Films and Superconducting Detectors*. In: *International Journal of Modern Physics B* 10.06 (1996), pp. 635–667.
- [27] R. Barends, S. van Vliet, J. J. A. Baselmans, S. J. C. Yates, J. R. Gao, and T. M. Klapwijk. *Enhancement of Quasiparticle Recombination in Ta and Al Superconductors by Implantation of Magnetic and Nonmagnetic Atoms*. In: *Physical Review B* 79.2 (2009), 020509(R).
- [28] L. Grünhaupt, N. Maleeva, S. T. Skacel, M. Calvo, F. Levy-Bertrand, A. V. Ustinov, H. Rotzinger, A. Monfardini, G. Catelani, and I. M. Pop. *Loss Mechanisms and Quasiparticle Dynamics in Superconducting Microwave Resonators Made of Thin-Film Granular Aluminum*. In: *Physical Review Letters* 121.11 (2018), p. 117001.
- [29] J. Gao, M. R. Vissers, M. O. Sandberg, F. C. S. da Silva, S. W. Nam, D. P. Pappas, D. S. Wisbey, E. C. Langman, S. R. Meeker, B. A. Mazin, H. G. Leduc, J. Zmuidzinas, and K. D. Irwin. *A Titanium-Nitride near-Infrared Kinetic Inductance Photon-Counting Detector and Its Anomalous Electrodynamics*. In: *Applied Physics Letters* 101.14 (2012), p. 142602.
- [30] J. Bueno, P. J. de Visser, S. Doyle, and J. J. A. Baselmans. *Study on Optical Filter Heating in Background Limited Detector Experiments*. In: *Journal of Low Temperature Physics* 176.5 (2014), pp. 1089–1095.
- [31] A. G. Moshe, E. Farber, and G. Deutscher. *Granular Superconductors for High Kinetic Inductance and Low Loss Quantum Devices*. In: *Applied Physics Letters* 117.6 (2020), p. 062601.

- [32] T. P. Devereaux and D. Belitz. *Quasiparticle Inelastic Lifetimes in Disordered Superconducting Films*. In: *Physical Review B* 44.9 (1991), pp. 4587–4600.
- [33] M. H. Read and C. Altman. *A New Structure in Tantalum Thin Films*. In: *Applied Physics Letters* 7.3 (1965), pp. 51–52.
- [34] C. M. Wilson and D. E. Prober. *Quasiparticle Number Fluctuations in Superconductors*. In: *Physical Review B* 69.9 (2004), p. 094524.
- [35] S. B. Kaplan, C. C. Chi, D. N. Langenberg, J. J. Chang, S. Jafarey, and D. J. Scalapino. *Quasiparticle and Phonon Lifetimes in Superconductors*. In: *Physical Review B* 14.11 (1976), pp. 4854–4873.
- [36] M. Reizer. *Electron-Electron Relaxation in Two-Dimensional Impure Superconductors*. In: *Physical Review B* 61.10 (2000), pp. 7108–7117.
- [37] A. Rothwarf and B. N. Taylor. *Measurement of Recombination Lifetimes in Superconductors*. In: *Physical Review Letters* 19.1 (1967), pp. 27–30.
- [38] S. A. H. de Rooij, J. J. A. Baselmans, V. Murugesan, D. J. Thoen, and P. J. de Visser. *Strong Reduction of Quasiparticle Fluctuations in a Superconductor Due to Decoupling of the Quasiparticle Number and Lifetime*. In: *Physical Review B* 104.18 (2021), p. L180506.
- [39] S. B. Kaplan. *Acoustic Matching of Superconducting Films to Substrates*. In: *Journal of Low Temperature Physics* 37.3 (1979), pp. 343–365.
- [40] W. Eisenmenger, K. Laßmann, H. J. Trumpp, and R. Krauß. *Quasiparticle Recombination and 2Δ -phonon-trapping in Superconducting Tunneling Junctions*. In: *Applied physics* 11.4 (1976), pp. 307–320.
- [41] A. Sergeev and V. Mitin. *Electron-Phonon Interaction in Disordered Conductors: Static and Vibrating Scattering Potentials*. In: *Physical Review B* 61.9 (2000), pp. 6041–6047.
- [42] D. C. Mattis and J. Bardeen. *Theory of the Anomalous Skin Effect in Normal and Superconducting Metals*. In: *Physical Review* 111.2 (1958), pp. 412–417.
- [43] J. Gao, J. Zmuidzinas, A. Vayonakis, P. Day, B. Mazin, and H. Leduc. *Equivalence of the Effects on the Complex Conductivity of Superconductor Due to Temperature Change and External Pair Breaking*. In: *Journal of Low Temperature Physics* 151.1 (2008), pp. 557–563.
- [44] P. J. de Visser, J. J. A. Baselmans, P. Diener, S. J. C. Yates, A. Endo, and T. M. Klapwijk. *Number Fluctuations of Sparse Quasiparticles in a Superconductor*. In: *Physical Review Letters* 106.16 (2011), p. 167004.
- [45] M. A. Skvortsov and M. V. Feigel'man. *Subgap States in Disordered Superconductors*. In: *Journal of Experimental and Theoretical Physics* 117.3 (2013), pp. 487–498.
- [46] B. Sacépé, C. Chapelier, T. I. Baturina, V. M. Vinokur, M. R. Baklanov, and M. Sanquer. *Disorder-Induced Inhomogeneities of the Superconducting State Close to the Superconductor-Insulator Transition*. In: *Physical Review Letters* 101.15 (2008), p. 157006.

- [47] A. A. Abrikosov and L. P. Gor'kov. *Contribution to the Theory of Superconducting Alloys with Paramagnetic Impurities*. In: *Zh. Eksp. Teor. Fiz.* 39 (1960), p. 1781.
- [48] P. C. J. J. Coumou, M. R. Zuiddam, E. F. C. Driessen, P. J. de Visser, J. J. A. Baselmans, and T. M. Klapwijk. *Microwave Properties of Superconducting Atomic-Layer Deposited TiN Films*. In: *IEEE Transactions on Applied Superconductivity* 23.3 (2013), pp. 7500404–7500404.
- [49] A. I. Kardakova, P. C. J. J. Coumou, M. I. Finkel, D. V. Morozov, P. P. An, G. N. Goltsman, and T. M. Klapwijk. *Electron–Phonon Energy Relaxation Time in Thin Strongly Disordered Titanium Nitride Films*. In: *IEEE Transactions on Applied Superconductivity* 25.3 (2015), pp. 1–4.
- [50] P. B. Fischer and G. Catelani. *Excess Quasiparticles and Their Dynamics in the Presence of Subgap States*. In: *Physical Review B* 112.10 (2025), p. L100507.
- [51] E. Gurra, D. A. Bennett, S. M. Duff, M. R. Vissers, and J. N. Ullom. *Can Slow Recombination in Ordered Superconductors Explain the Excess Quasiparticle Population?* 2025. URL: <http://arxiv.org/abs/2507.03217>. Pre-published.
- [52] T. Charpentier, A. Khvalyuk, L. Ioffe, M. Feigel'man, N. Roch, and B. Sacépé. *Universal Scaling of Microwave Dissipation in Superconducting Circuits*. 2025. URL: <http://arxiv.org/abs/2507.08953>. Pre-published.
- [53] J. M. Martinis, M. Ansmann, and J. Aumentado. *Energy Decay in Superconducting Josephson-Junction Qubits from Nonequilibrium Quasiparticle Excitations*. In: *Physical Review Letters* 103.9 (2009), p. 097002.
- [54] G. Abadias, J. J. Colin, D. Tingaud, Ph. Djemia, L. Belliard, and C. Tromas. *Elastic Properties of α - and β -Tantalum Thin Films*. In: *Thin Solid Films* 688 (2019), p. 137403.
- [55] D. J. Thoen, B. G. C. Bos, E. A. F. Haalebos, T. M. Klapwijk, J. J. A. Baselmans, and A. Endo. *Superconducting NbTiN Thin Films With Highly Uniform Properties Over a 100 Mm Wafer*. In: *IEEE Transactions on Applied Superconductivity* 27.4 (2017), pp. 1–5.
- [56] J. Gao, M. Daal, A. Vayonakis, S. Kumar, J. Zmuidzinas, B. Sadoulet, B. A. Mazin, P. K. Day, and H. G. Leduc. *Experimental Evidence for a Surface Distribution of Two-Level Systems in Superconducting Lithographed Microwave Resonators*. In: *Applied Physics Letters* 92.15 (2008), p. 152505.
- [57] H. Wang, M. Hofheinz, J. Wenner, M. Ansmann, R. C. Bialczak, M. Lenander, E. Lucero, M. Neeley, A. D. O'Connell, D. Sank, M. Weides, A. N. Cleland, and J. M. Martinis. *Improving the Coherence Time of Superconducting Coplanar Resonators*. In: *Applied Physics Letters* 95.23 (2009), p. 233508.
- [58] P. J. de Visser. *Quasiparticle Dynamics in Aluminium Superconducting Microwave Resonators*. PhD thesis. Delft: Delft University of Technology, 2014. 222 pp.
- [59] B. Keck and A. Schmid. *Superconductivity and Electron-Phonon Interaction in Impure Simple Metals*. In: *Journal of Low Temperature Physics* 24.5–6 (1976), pp. 611–629.

- [60] A. Schmid. *On the Dynamics of Electrons in an Impure Metal*. In: *Zeitschrift für Physik* 271.3 (1974), pp. 251–256.
- [61] C. Kittel. *Quantum Theory of Solids*. Wiley, 1987. 528 pp.
- [62] T. Kühn, D. V. Anghel, J. P. Pekola, M. Manninen, and Y. M. Galperin. *Heat Transport in Ultrathin Dielectric Membranes and Bridges*. In: *Physical Review B* 70.12 (2004), p. 125425.
- [63] K. Petersen. *Silicon as a Mechanical Material*. In: *Proceedings of the IEEE* 70.5 (1982), pp. 420–457.
- [64] P. J. de Visser, S. A. H. de Rooij, V. Murugesan, D. J. Thoen, and J. J. A. Baselmans. *Phonon-Trapping-Enhanced Energy Resolution in Superconducting Single-Photon Detectors*. In: *Physical Review Applied* 16.3 (2021), p. 034051.
- [65] L. D. Landau and E. M. Lifshitz. *Statistical Physics: Volume 5*. Elsevier, 2013. 563 pp.
- [66] C. N. Thomas, S. Withington, and D. J. Goldie. *Electrothermal Model of Kinetic Inductance Detectors*. In: *Superconductor Science and Technology* 28.4 (2015), p. 045012.
- [67] E. Gershenson. *Electron-Phonon Interaction in Ultrathin Nb Films*. In: *Zh. Eksp. Teor. Fiz.* 97 (1990), pp. 901–911.
- [68] P. H. Kes and C. C. Tsuei. *Two-Dimensional Collective Flux Pinning, Defects, and Structural Relaxation in Amorphous Superconducting Films*. In: *Physical Review B* 28.9 (1983), pp. 5126–5139.
- [69] M. Tinkham. *Introduction to Superconductivity*. Dover Publications, 2004. 482 pp.
- [70] M. Magnuson, G. Greczynski, F. Eriksson, L. Hultman, and H. Högberg. *Electronic Structure of β -Ta Films from X-ray Photoelectron Spectroscopy and First-Principles Calculations*. In: *Applied Surface Science* 470 (2019), pp. 607–612.
- [71] E. F. C. Driessen, P. C. J. J. Coumou, R. R. Tromp, P. J. de Visser, and T. M. Klapwijk. *Strongly Disordered TiN and NbTiN S-Wave Superconductors Probed by Microwave Electrodynamics*. In: *Physical Review Letters* 109.10 (2012), p. 107003.
- [72] A. V. Khvalyuk, T. Charpentier, N. Roch, B. Sacépé, and M. V. Feigel'man. *Near Power-Law Temperature Dependence of the Superfluid Stiffness in Strongly Disordered Superconductors*. In: *Physical Review B* 109.14 (2024), p. 144501.
- [73] A. Kardakova, M. Finkel, D. Morozov, V. Kovalyuk, P. An, C. Dunscombe, M. Tarkhov, P. Mauskopf, T. M. Klapwijk, and G. Goltsman. *The Electron-Phonon Relaxation Time in Thin Superconducting Titanium Nitride Films*. In: *Applied Physics Letters* 103.25 (2013), p. 252602.
- [74] K. Hansen, M. Cardona, A. Dutta, and C. Yang. *Plasma Enhanced Atomic Layer Deposition of Plasmonic TiN Ultrathin Films Using TDMATi and NH₃*. In: *Materials* 13.5 (2020), p. 1058.

- [75] D. Chen, J. Chen, Y. Zhao, B. Yu, C. Wang, and D. Shi. *Theoretical Study of the Elastic Properties of Titanium Nitride*. In: *Acta Metallurgica Sinica (English Letters)* 22.2 (2009), pp. 146–152.
- [76] M. Sidorova, A. Semenov, H.-W. Hübers, K. Ilin, M. Siegel, I. Charaev, M. Moshkova, N. Kaurova, G. N. Goltsman, X. Zhang, and A. Schilling. *Electron Energy Relaxation in Disordered Superconducting NbN Films*. In: *Physical Review B* 102.5 (2020), p. 054501.
- [77] K. S. Il'in, N. G. Ptitsina, A. V. Sergeev, G. N. Gol'tsman, E. M. Gershenzon, B. S. Karasik, E. V. Pechen, and S. I. Krasnosvobodtsev. *Interrelation of Resistivity and Inelastic Electron-Phonon Scattering Rate in Impure NbC Films*. In: *Physical Review B* 57.24 (1998), pp. 15623–15628.
- [78] P. C. J. J. Coumou, E. F. C. Driessen, J. Bueno, C. Chapelier, and T. M. Klapwijk. *Electrodynamic Response and Local Tunneling Spectroscopy of Strongly Disordered Superconducting TiN Films*. In: *Physical Review B* 88.18 (2013), p. 180505.
- [79] K. M. Van Vliet and J. R. Fasset. *Fluctuation Phenomena in Solids*. Vol. 19. Pure and Applied Physics. Academic Press, 1965. 414 pp.
- [80] K. M. Van Vliet and J. Blok. *Electronic Noise in Semiconductors*. In: *Physica* 22.1 (1956), pp. 231–242.
- [81] W. Shockley and W. T. Read. *Statistics of the Recombinations of Holes and Electrons*. In: *Physical Review* 87.5 (1952), pp. 835–842.
- [82] R. N. Hall. *Electron-Hole Recombination in Germanium*. In: *Physical Review* 87.2 (1952), p. 387.
- [83] P. J. de Visser, J. J. A. Baselmans, S. J. C. Yates, P. Diener, A. Endo, and T. M. Klapwijk. *Microwave-Induced Excess Quasiparticles in Superconducting Resonators Measured through Correlated Conductivity Fluctuations*. In: *Applied Physics Letters* 100.16 (2012), p. 162601.
- [84] A. M. Finkel'stein. *Superconducting Transition Temperature in Amorphous Films*. In: *Pis'ma Zh. Eksp. Teor. Fiz.* 45.1 (1987), pp. 37–40.
- [85] P. C. J. J. Coumou. *Electrodynamics of Strongly Disordered Superconductors*. PhD thesis. Delft University of Technology, 2015.
- [86] D. J. Goldie and S. Withington. *Non-Equilibrium Superconductivity in Quantum-Sensing Superconducting Resonators*. In: *Superconductor Science and Technology* 26.1 (2012), p. 015004.
- [87] P. Fischer and G. Catelani. *Nonequilibrium Quasiparticle Distribution in Superconducting Resonators: An Analytical Approach*. In: *Physical Review Applied* 19.5 (2023), p. 054087.

7

RECOMBINATION OF NON-EQUILIBRIUM QUASIPARTICLES IN DISORDERED SUPERCONDUCTORS EXCITED WITH SINGLE PHOTONS

In order to improve the photon absorption efficiency of microwave kinetic inductance detectors (MKIDs) over a broad frequency band in the visible/near-infrared, disordered superconductors are needed as sensitive element. A high resolving power ($R > 10$ at $1 \mu\text{m}$) has not been reached yet with these devices, and the single photon response decays much faster than in Al MKIDs. We investigate this fast pulse decay by measuring the single photon response of β -Ta MKIDs as a function of temperature, photon energy, and photon absorption volume. The pulses are characterized by an initial non-exponential decay and a subsequent exponential tail. By comparing the tail decay time to the measurement of the quasiparticle relaxation time (Chapter 6), we conclude that this part of the pulse decay is likely to be governed by localized quasiparticles. A comparison between the dissipative and inductive response, indicates that the occupied localized states are non-dissipative at low temperatures. To understand the initial non-exponential decay, we model the pulse decay with conventional recombination, including phonon dynamics and quasiparticle diffusion. We conclude that the non-exponential decay is not caused by conventional recombination dynamics. We argue that the non-equilibrium character of the quasiparticle localization process after photon absorption may cause the non-exponential decay.

The work presented in this chapter was done in collaboration with Kian Syaifoel, Thomas Rugers, Kevin Kouwenhoven, Tonny Coppens, David J. Thoen, Jochem J.A. Baselmans and Pieter J. de Visser.

7.1 INTRODUCTION

Microwave kinetic inductance detectors (MKIDs) [1] have matured over the past decade as sensitive and efficient radiation detectors suitable for large arrays. In the far-infrared regime, careful detector design in combination with efficient radiation absorption with a lens-antenna [2, 3], or lens-absorber [4, 5] system has led to a noise-equivalent power (NEP) of $\sim 3 \times 10^{-20} \text{ W}/\sqrt{\text{Hz}}$ [5, 6] using Al based detectors. This has made the MKID technology sensitive enough for astronomical observations of the far-infrared in space based missions [7, 8].

For wavelengths from $25 \mu\text{m}$ [5] and shorter, MKIDs act as single photon counting, energy resolving detectors. Combining this with the frequency-multiplexability of MKIDs results in an integral field spectrograph, which can perform imaging spectroscopy [9–11]. For astronomical applications such as low light, space-based exoplanet imaging [12], the MKID technology must be improved further [13, 14]. Apart from demonstrating large arrays ($> 1,000$ pixels) with sufficient yield ($> 90\%$), the individual pixels must be improved in two ways: a high absorption efficiency, $\eta_{\text{abs}} > 0.50$ from 400 nm to $1.8 \mu\text{m}$ must be reached and energy resolving power R must be as high as 100 at $1 \mu\text{m}$ [15]¹.

For wavelengths below ten micron, it is not feasible to use lithographically patterned Al as antenna or absorber, since the required features become too small. Therefore, improving η_{abs} over a large bandwidth must be realized by combining MKIDs with highly resistive absorbers and structures, such as lenses [16] and anti-reflection layers [17–19]. Thus, this naturally leads to the implementation of disordered superconductors for MKIDs. Because disordered superconductors also have a large kinetic inductance, the MKID responsivity is boosted as well [20].

Unfortunately, an MKID with a disordered superconductor absorber (normal state resistivity $\rho_N > 100 \mu\Omega\text{cm}$) that also has a decent resolving power ($R > 10$ at $\lambda = 1 \mu\text{m}$) has not been realized yet. An overview of the measured resolving power at approximately 980 nm as a function of the normal state resistance is shown in Fig. 7.1.1(a). Reaching the top-right corner of this plot seems very challenging, while the exact reason for this is still unknown.

One of the limiting factors of R is the signal-to-noise ratio of the single photon pulses. If the noise is high compared to the pulse, the excess quasiparticle density created by the photon cannot be estimated well. In Fig. 7.1.1(b) we plot the averaged single photon pulse response of Al and β -Ta. The pulse decay of the β -Ta absorber is much faster than for Al. Therefore, the total signal of a single photon, measured by the area under the curve, in β -Ta is much less than in Al, while the noise is comparable. A similar fast single photon pulse decay has also been measured in other disordered superconductors, such as PtSi [22], Hf [23] and TiN [27]. In Fig. 7.1.1(b), we see that the β -Ta pulse decay is strongly non-exponential. We separate two regimes in time, via the exponential tail decay time, τ_{tail} (see black line in Fig. 7.1.1(b)). The separation of these regimes is indicated in Fig. 7.1.1(b) with the orange dashed line. Both regimes show a much faster decay than the single exponential decay of the Al pulse. Such a fast, non-exponential pulse shape is highly

¹With only $R=30$ and $\eta_{\text{abs}}=0.95$ for a 10% bandwidth at 600 nm , a speed-up in exoplanet detector can already be reached [13].

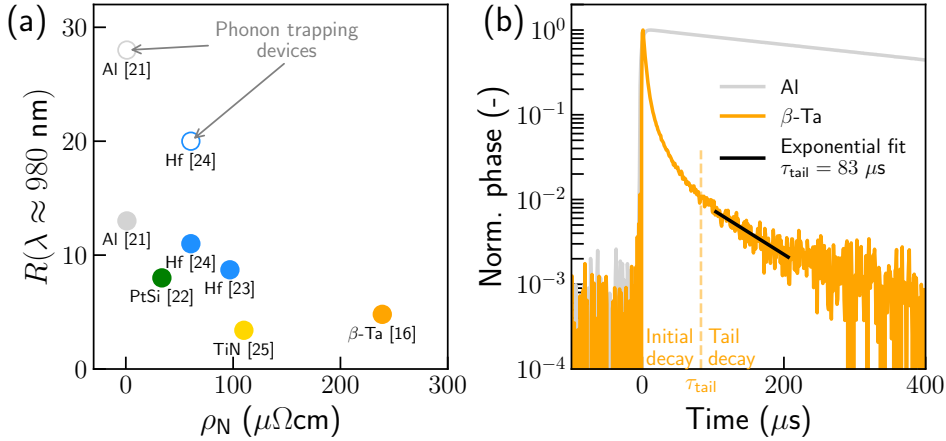


Figure 7.1.1: Comparison of resolving power and single photon pulses of different materials. **(a)**: Resolving power measured in Refs. [16, 21–25] at $\lambda \approx 980 \text{ nm}$, as a function of normal state resistivity. The circles are devices that implement phonon trapping to limit hot phonon loss during photon energy downconversion [26], either with a thin SiN membrane [21] or with an additional layer with low Debye temperature [24]. **(b)**: Comparison of the Al (gray) and β -Ta (orange) phase response to a 673 nm single photon. The pulses are normalized to their maximum. The bath temperature is set to 120 mK and read-out power is minimized, while maintaining a decent signal-to-noise (-89 dBm for Al and -100 dBm for β -Ta). The pulses are averages of a few thousand single photon pulses to suppress noise. The Al data is from the same device as presented in Chapter 4 and the β -Ta device is the same as in Chapter 6. Both absorbers are on a membrane. The black line shows an exponential fit to the β -Ta tail decay. The fit range is the start and end of the black line (see main text for details on how this is set). The orange dashed line is located at the fitted time constant, τ_{tail} , after the pulse start. The region before this line we call the initial decay, and after that we call it the tail decay.

undesired, since it reduces the signal-to-noise ratio of the single photon response. The question we would like to answer is thus: what causes the fast, non-exponential single photon pulse decay in disordered superconductors?

In this chapter, we analyze both the initial decay and the tail decay regimes. We compare the tail decay time to the steady-state relaxation time from quasiparticle fluctuations presented in Chapter 6. Since these times overlap for higher temperatures, we conclude that the tail decay is governed by localized recombination, as we have shown in Chapter 6. Additionally, from the non-equilibrium measurements in this chapter, we show that the localized states are non-dissipative at low temperatures. To understand the initial fast decay, we compare the measurement data to a model of conventional recombination dynamics. We include quasiparticle diffusion, as we expect this to be slow for disordered superconductors. We estimate the parameters in this conventional model from theory and experimentally vary the photon energy and quasiparticle occupation volume. From the qualitative differences between the model and

measurement data, we conclude that the non-exponential behavior is not caused by conventional recombination dynamics. This implies that, in addition to the equilibrium quasiparticle dynamics, disorder significantly changes the recombination of non-equilibrium quasiparticles as well.

7.2 RESULTS AND DISCUSSION

We measure the single photon response of hybrid β -Ta/NbTiN MKIDs on a SiN membrane (the same as presented in Chapter 6)² by recording the complex forward transmission at resonance at a sampling rate of 1 MHz, while illuminating the chip with single photons from a laser source. We translate the complex forward transmission to the dissipative part (δA , amplitude) and inductive part (θ , phase) via a pre-recorded frequency sweep, which traces out a resonance circle in the complex transmission plane. We vary the photon energy by using four different wavelength lasers: 402 nm, 673 nm, 986 nm and 1545 nm, and we attenuate the laser to absorb approximately 100 photons per second in the β -Ta inductor. We record 40 time streams of 1 s, such that we obtain a few thousand single photon pulses. We select the single photon pulses based on their height in phase³ and align baselines and rising edges. An example of an average pulse obtained this way is shown in Fig. 7.1.1(b). To obtain physically relevant trends, we vary the bath temperature (from 20 mK to 180 mK, above which the signal becomes too weak) and microwave read-out power (from the bifurcation power to -8 dB below that, where the signal-to-noise ratio typically deteriorates). For details on the experimental setup and measurement of the average single photon response see Chapter 3 and for the MKID design see Chapter 6.

7

7.2.1 TAIL DECAY: LOCALIZED QUASIPARTICLE RECOMBINATION

We fit an exponential decay to the tail of the pulse. The end of the fit range is chosen as the first data point that is below the standard deviation (1σ) of the noise after the pulse start, as estimated from the data $100 \mu\text{s}$ before the pulse start. This ensures we are not biased to longer decay times due to small secondary peaks in the tail. The beginning of the fit range is chosen halfway between the pulse start to the end time point. An example of this fit is shown in Fig. 7.1.1(b) as the black line, which spans the fit range. After the fit, we check if the beginning of the fit range is later than τ_{tail} after the pulse start to ensure that the fit range does not include a part of the initial decay.

The resulting tail decay time is shown in Fig. 7.2.1(a) as a function of temperature. For the temperature variations, we only use the 673 nm laser source. We measure the response to all four laser sources at 20 mK and 100 mK. We compare the obtained decay times to the relaxation times obtained from quasiparticle fluctuation measurements, which are the gray squares (see Chapter 6). The recombination time, phonon scattering time and electron-electron scattering time from theory, without

²We measured the substrate resonator as well, and found no difference in the pulse response.

³We set the prominence threshold to 7 times the standard deviation of the noise, see Section 3.3.4

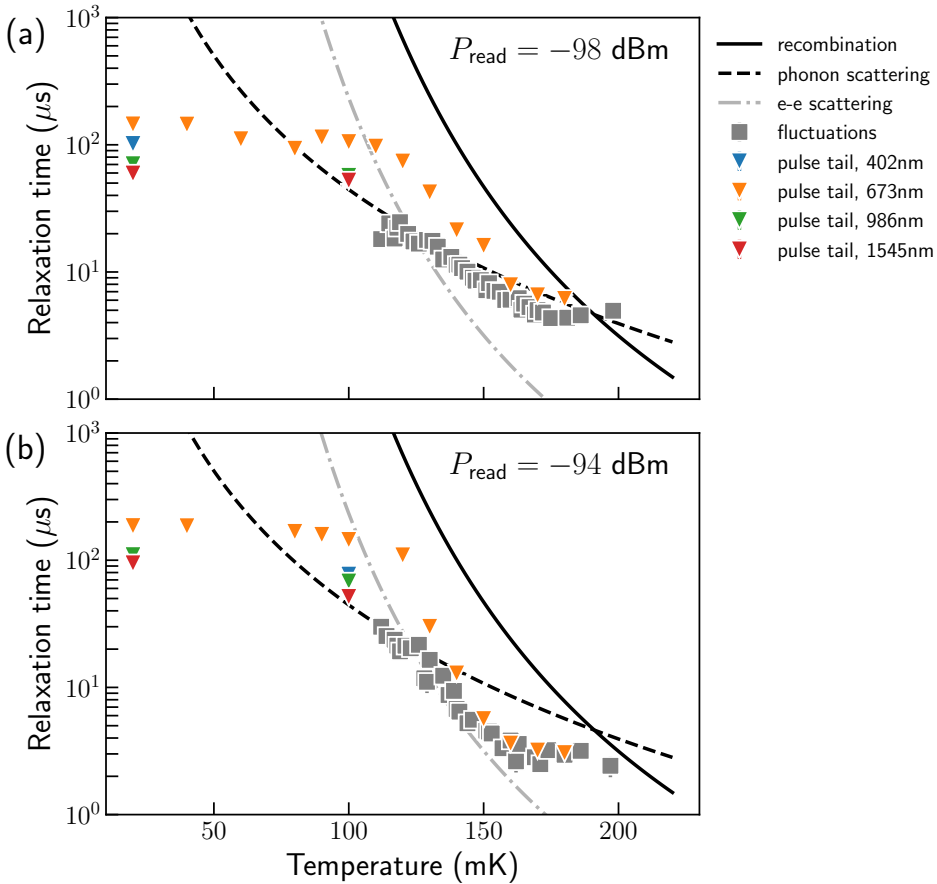


Figure 7.2.1: Quasiparticle relaxation time versus temperature measured from quasiparticle fluctuations and an exponential fit to the tail decay of a single photon excitation (see Fig. 7.1.1(b)). The fluctuation results are the same as the membrane resonator in Chapter 6. The pulse lifetimes are measured from the phase decay in the same device and same read-out power (-98 dBm for panel (a) and -94 dBm for panel (b)). The data from $\lambda = 673$ nm photons are measured in the same cooldown as the fluctuation data, the other wavelength in a different cooldown. Error bars indicating the statistical fit errors are smaller than the data points and not shown. The black solid and dashed lines are from theory without fit parameters, for quasiparticle recombination and (2D) phonon absorption (scattering), respectively [28, 29]. The gray dash-dotted line is for electron-electron scattering [30]. See Chapter 6 for details on the device and theory lines.

fit parameters, are indicated by the black solid, dashed and gray dashed-dotted line, respectively. See Chapter 6 for details on these calculations. We observe that the pulse tail decay time (orange triangles) aligns with the relaxation time obtained from quasiparticle fluctuation measurements (gray squares) for high temperatures

(> 130 mK). This is expected based on the fluctuation-dissipation theorem [31], which states that the dissipative (i.e., transient) relaxation time close to equilibrium equals the relaxation time of the fluctuations. This has also been confirmed in aluminum superconducting resonators, in which the quasiparticle relaxation time is given by the recombination time [32]. Here, we observe that the quasiparticle relaxation time is given by the phonon scattering time, which we explained in Chapter 6 as the recombination of localized quasiparticles.

At lower temperatures (< 130 mK), the pulse tail decay time is significantly longer than the relaxation time extracted from quasiparticle fluctuations. The reason for this is not clear, but could be related to the non-equilibrium, transient nature of the pulse measurement. The average quasiparticle energy could still be higher in the tail of the pulse decay than in equilibrium, which would favor conventional recombination dynamics (black solid line in Fig. 7.2.1) over localized quasiparticle dynamics (black dashed line in Fig. 7.2.1). When exciting the superconductor with a lower photon energy (green and red triangles at 100 mK in Fig. 7.2.1), the relaxation time is closer to the dashed black line. This might indicate that for a lower photon energy, the average quasiparticle energy is lower in the tail of the pulse decay. The higher photon energy (blue triangles) is also closer to the black dashed line. This could be caused by a heating effect, since these measurements typically require a larger laser power to obtain the same photon count rate due to a non-uniform illumination. Such a heating effect would result in a faster relaxation time.

When we increase read-out power, the average quasiparticle energy increases in steady state, as opposed to the transient non-equilibrium effects discussed above. A continuous absorption of read-out microwave photons can result in non-equilibrium quasiparticle distribution function, as has been shown for aluminum resonators [33–35]. Since disorder generally reduces the electron-phonon coupling (Chapter 6), this effect could be enhanced in β -Ta compared to Al. Figure 7.2.1(b) shows the relaxation times from the tail decay (triangles) and fluctuation measurements (gray squares) for a 4 dB higher read-out power. For temperatures below 130 mK, the tail decay times (orange triangles) deviate more from the timescale obtained via the quasiparticle fluctuation measurement (gray squares), compared to the lower read-out power (Fig. 7.2.1(a)). This could indicate that the deviations of the tail decay time from the quasiparticle fluctuation timescale are induced by non-equilibrium effects, which are enhanced by read power. That is, both a transient (single pair-breaking photon) and a steady-state effect (continuous microwave photons) increase the average quasiparticle energy.

Interestingly, for higher temperatures (> 130 mK) and the higher read-out power (Fig. 7.2.1(b)), both the tail decay time and the quasiparticle fluctuation timescale seem to follow the electron-electron scattering relaxation time (gray dashed-dotted line). This scattering time dictates the relaxation rate of quasiparticle distribution, while the quasiparticle number is constant. This could indicate that the recombination of quasiparticles at these temperatures is limited by the inelastic electron-electron relaxation of the non-equilibrium distribution function, after which on-site recombination occurs much faster (see Chapter 6 for details on the on-site recombination hypothesis).

Below 100 mK, the tail decay time saturates to approximately 100 μ s. This saturation time is constant for different read-out powers, but varies slightly for different photon energies.

AMPLITUDE RESPONSE: NON-DISSIPATIVE, LOW ENERGETIC LOCALIZED STATES

At low temperatures (< 100 mK) and at low read-out powers (< -94 dBm), we observe the tail decay in phase (the inductive response) only, and not in amplitude (the dissipative response). This is shown in Fig. 7.2.2. For the amplitude response, we only observe the fast initial decay in this regime. When increasing either temperature or read-out power, the tail decay reappears in amplitude and the difference between amplitude and phase disappears.

Similar observations have been made in the dissipative and inductive response of disordered TiN resonators [27]. This suggests that there are non-dissipative quasiparticle bound states inside the gap at low energies. For these states to be non-dissipative, microwave photon absorption must be forbidden, or at least highly suppressed. This implies that there is a subgap band, akin to a Yu-Shiba-Rusinov band [36–39], that is occupied by quasiparticles with an energy at least $\hbar\omega_0$ lower than the continuum ($< \Delta - \hbar\omega_0$), with ω_0 the angular resonance frequency. In that case, the quasiparticle dissipation (σ_1 , the real part of the complex conductivity) is reduced [40], since transitions to states with $\hbar\omega_0$ more energy are suppressed. When the temperature is increased, the average quasiparticle energy increases and these transitions might become possible again. At high temperatures, the amplitude tail response therefore reappears (Fig. 7.2.2(a)). When increasing read-out power, the amplitude tail decay also reappears (Fig. 7.2.2(c)), which also indicates a higher average quasiparticle energy. An Eliashberg-type non-equilibrium scenario [33, 34, 41] can not cause this, since the photon absorption is reduced. However, as we have shown in Chapter 5 for Al, the read-out power induced heating does not follow the Eliashberg-type non-equilibrium scenario. A different mechanism that simply increases of the effective quasiparticle temperature by the read-out power might be present here as well. Thus, the phenomenology as presented in Fig. 7.2.2 may be explained by localized states that are isolated from the continuum by at least $\hbar\omega_0$. A higher read-out power or bath temperature heats the quasiparticle system, allowing dissipative transitions and the reappearing of the tail decay in the amplitude response.

Localization bands inside the gap typically occur in superconductors with a moderate concentration of pair-breaking magnetic impurities. For our sample, a small concentration of magnetic impurities might reside in the native Ta-oxide layer [42]. Electronic disorder in the form of an inhomogeneous pairing potential additionally introduces broadening of these bands and the coherence peak [43], and enhance the localization effects [44].

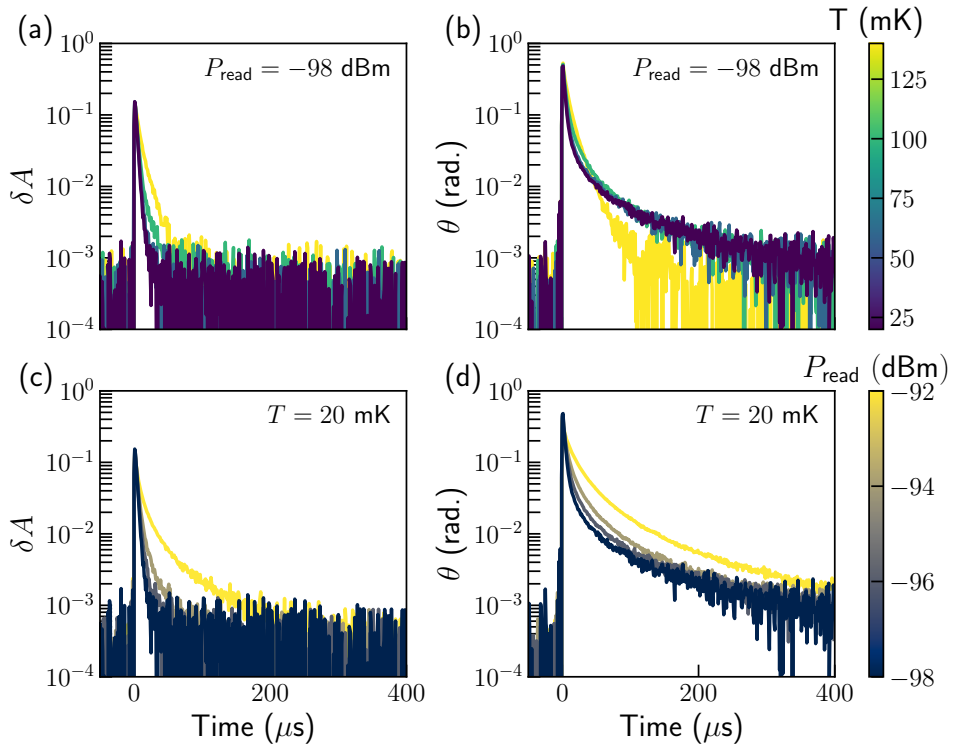


Figure 7.2.2: Averaged amplitude ((a) and (c)) and phase ((b) and (d)) response to a 673 nm single photon, for varying temperature ((a) and (b)) and read-out power ((c) and (d)). The darkest curves in (a) and (b) are identical to the dark curves in (c) and (d). The data is from the same MKID as in Fig. 7.2.1.

7.2.2 INITIAL FAST DECAY: ENHANCED SELF-RECOMBINATION?

MASTER EQUATIONS FOR QUASIPARTICLE RECOMBINATION

We now turn to the non-exponential, fast initial decay of the single photon response (see Fig. 7.1.1(b)). We will only consider the phase response for simplicity. Usually, non-exponential behavior in the pulse decay is attributed to self-recombination: the excess quasiparticle density generated by the photon, δn_{qp} , significantly exceeds the equilibrium quasiparticle density, n_{qp}^0 , and the excess quasiparticles are more likely to recombine with each other than with equilibrium quasiparticles. This decreases the recombination time, as $\tau_{\text{rec}} \propto 1/n_{\text{qp}}$, where $n_{\text{qp}} = n_{\text{qp}}^0 + \delta n_{\text{qp}}$. When the quasiparticle density is close to the equilibrium quasiparticle density ($n_{\text{qp}} \approx n_{\text{qp}}^0$), the recombination time is given by $\tau_{\text{rec}} \approx \tau_{\text{qp}} = 1/(2Rn_{\text{qp}}^0)$. Here, $R = 2\Delta_0^2 / ((k_{\text{B}}T_{\text{c}})^3 N_0 \tau_0)$ is the recombination constant, with $2\Delta_0 = 3.52k_{\text{B}}T_{\text{c}}$ the superconducting gap energy, k_{B} the Boltzmann constant, T_{c} the critical temperature, N_0 the density of states at the Fermi energy and τ_0 the characteristic electron-phonon scattering time [45].

Self-recombination leads to a $1/t$ -like time dependence of the decay in the limit $n_{\text{qp}} \approx \delta n_{\text{qp}} \gg n_{\text{qp}}^0$, which gradually transitions to an exponential decay with τ_{qp} when the quasiparticle density becomes close to the equilibrium value again [46–50].

When the quasiparticle recombination is faster than the phonon pair-breaking time, τ_{pb} and phonon escape time, τ_{esc} , the phonon dynamics will limit the decay of the photon excitation. This is called a phonon bottleneck. The fast recombination emits phonons with an energy larger than $2\Delta_0$, which can subsequently break Cooper-pairs. If this is faster than pair-breaking and phonon escape ($1/\tau_{\text{rec}} \gg 1/\tau_{\text{pb}} + 1/\tau_{\text{esc}}$), the quasiparticle density is reduced by a factor $1/(\tau_{\text{pb}}/\tau_{\text{rec}} + 1)$ and the decay time is limited to $2\tau_{\text{esc}}$. When recombination is slower than the phonon dynamics ($1/\tau_{\text{rec}} \ll 1/\tau_{\text{pb}} + 1/\tau_{\text{esc}}$), which is typically the case, the photon energy is converted to quasiparticles and the decay time is enhanced by a factor, $\tau_{\text{qp}}^* = \tau_{\text{qp}}(1 + \tau_{\text{esc}}/\tau_{\text{pb}})$, which is called the phonon trapping factor [47, 50–52].

If we assume that all quasiparticles are relaxed to the gap edge, we can ignore the energy dependence of the scattering times (i.e., take $\tau_{\text{qp}}(\Delta_0)$, $\tau_{\text{ph}}(2\Delta_0)$ and $\tau_{\text{esc}}(2\Delta_0)$) and simply count the quasiparticles and the phonons. In this case, the dynamics of self-recombination and the phonon trapping are described by the Rothwarf-Taylor equations [47],

$$\frac{d\delta n_{\text{qp}}}{dt} = -\frac{\delta n_{\text{qp}}}{\tau_{\text{qp}}} - R(\delta n_{\text{qp}})^2 + 2\frac{\delta n_{\text{ph}}}{\tau_{\text{pb}}}, \quad (7.1a)$$

$$\frac{d\delta n_{\text{ph}}}{dt} = \frac{\delta n_{\text{qp}}}{2\tau_{\text{qp}}} + \frac{R(\delta n_{\text{qp}})^2}{2} - \left(\frac{1}{\tau_{\text{pb}}} + \frac{1}{\tau_{\text{esc}}}\right)\delta n_{\text{ph}}. \quad (7.1b)$$

In these equations, δn_{ph} is the excess phonon density. On the right-hand side, the first terms describe equilibrium recombination, the second terms describe self-recombination and the third term describe the phonon dynamics. This is the starting point for our model to describe the single photon pulse decay in β -Ta. In Chapter 6 we estimate the phonon trapping factor to be 2 for our β -Ta film on a SiN/Si substrate. Since we did not observe any difference between the substrate and membrane devices for the quasiparticle fluctuation and pulse measurements, we will use the substrate values and set $\tau_{\text{esc}} = \tau_{\text{pb}}$. We estimate the pair-breaking time to be $\tau_{\text{pb}}(2\Delta_0) = \tau_{\text{ph}}^0 = 0.82$ ns. This is based on Eq. (30) of Ref. [45], with the electron-phonon interaction strength and phonon density of states, $\alpha^2(\Omega)F(\Omega)$, calculated from Ref. [53] using the materials parameters given in Chapter 6 and $N = 5.5 \times 10^{10} \mu\text{m}^{-3}$ as ion density [54]⁴. R and τ_{qp} are calculated with the same parameters and with $\tau_0 = 81$ ns. We estimate this from a comparison of the recombination times calculated in Ref. [45] for the pure case and in Ref. [28] for the impure (disordered) case. Choosing the value of $\tau_0 = 81$ ns in Ref. [45], gives the same result for the recombination time as Ref. [28].

⁴In Chapter 6, we estimated τ_{pb} from the transverse ultrasonic attenuation constant for metals from Refs. [55, 56], which resulted in a much longer $\tau_{\text{pb}} = 37$ ns. This however does not change the phonon trapping factor by more than a factor 2, since the mean free path of a 2Δ -phonon against pair-breaking is much longer than the β -Ta film thickness.

With only this conventional recombination model in mind, there would be no obvious reason why self-recombination is more prominent in disordered superconductors. We do however observe a large difference between Al and β -Ta in Fig. 7.1.1(b). The only parameter that changes the contribution of self-recombination in this model is the ratio $\delta n_{\text{qp}}/n_{\text{qp}}^0$. Since the excitation energy is the same for both MKIDs, and the geometry and the gap energy are similar, we expect δn_{qp} to be the same. Therefore, n_{qp}^0 should be much lower for β -Ta than for Al. The steady-state quasiparticle density at low temperatures is proportional to $n_{\text{qp}}^0 \propto P_{\text{gen}}\tau_{\text{qp}}^*/(\Delta_0 V)$, with P_{gen} the quasiparticle generation power (the thermal bath, stray light, microwave power, cosmic rays, and radioactivity among others) and V the quasiparticle occupation volume, see Section 2.3.2. Since both V and P_{gen} are comparable for the Al and β -Ta MKIDs, this leaves the bulk quasiparticle lifetime as possible difference. Indeed, we measure a factor 10 lower τ_{qp}^* for β -Ta at low temperatures (see Chapters 4 and 6), which could be related to disorder [57]. From Chapter 6, we know that this is related to the localized quasiparticle dynamics. We include the on-site recombination here by adding a term $-\delta n_{\text{qp}}/\tau_{\text{tail}}$ to Eq. (7.1a). We fit τ_{tail} separately from the tail of the phase decay (see Fig. 7.1.1(b)). We omit a similar term in the phonon evolution (Eq. (7.1b)), since the enhanced on-site recombination of localized quasiparticles emits a phonon with less than $2\Delta_0$ energy (see Chapter 6).

Apart from this, another key difference between disordered β -Ta and Al is the resistivity (see Fig. 7.1.1(a)). This is a factor 100 higher for β -Ta, which makes electronic diffusion approximately a factor 100 slower. Specifically, in the Al used in Fig. 7.1.1(b) and at 120 mK bath temperature, it takes 2 μs for an impulsive point source of quasiparticles to diffusive over 100 μm , while in β -Ta that takes 240 μs . Comparing those numbers to the timescales of the pulses, we conclude that the spacial distribution of quasiparticles after photon excitation is non-uniform in β -Ta, while for Al it is approximately uniform. This effect enhances self-recombination as well, as the local quasiparticle density is enhanced in β -Ta compared to Al.

To account for quasiparticle diffusion, we make the excess quasiparticle and phonon densities position dependent ($\delta n_{\text{qp}}(\mathbf{r})$ and $\delta n_{\text{ph}}(\mathbf{r})$) and add a diffusion term to Eq. (7.1a). This results in,

$$\frac{d\delta n_{\text{qp}}(\mathbf{r})}{dt} = -\frac{\delta n_{\text{qp}}(\mathbf{r})}{\tau_{\text{qp}}} - R(\delta n_{\text{qp}}(\mathbf{r}))^2 + 2\frac{\delta n_{\text{ph}}(\mathbf{r})}{\tau_{\text{pb}}} - \frac{\delta n_{\text{qp}}(\mathbf{r})}{\tau_{\text{tail}}} + D_{\text{qp}}\nabla^2 n_{\text{qp}}(\mathbf{r}), \quad (7.2a)$$

$$\frac{d\delta n_{\text{ph}}(\mathbf{r})}{dt} = \frac{\delta n_{\text{qp}}(\mathbf{r})}{2\tau_{\text{qp}}} + R\frac{(\delta n_{\text{qp}}(\mathbf{r}))^2}{2} - \left(\frac{1}{\tau_{\text{pb}}} + \frac{1}{\tau_{\text{esc}}}\right)\delta n_{\text{ph}}(\mathbf{r}) + D_{\text{ph}}\nabla^2 n_{\text{ph}}(\mathbf{r}), \quad (7.2b)$$

where we also included the on-site, localized quasiparticle recombination with the τ_{tail} -term. We set the quasiparticle diffusion constant to [58–60],

$$D_{\text{qp}} = D\sqrt{\frac{2k_{\text{B}}T_{\text{eff}}}{\pi\Delta_0}}, \quad (7.3)$$

where $D = 0.74 \text{ cm}^2/\text{s}$ is the normal state diffusion constant in β -Ta (as measured via the temperature dependence of the upper critical field, see Section 6.B.3) and

T_{eff} is the effective electronic temperature. We set $T_{\text{eff}} = 100$ mK, since the relaxation times saturate at that bath temperature, see Fig. 7.2.1. The definition of an effective temperature is only valid if the thermalization of the distribution function is faster than the observed dynamics. The electron-electron and electron-phonon scattering is however considerably slow in disordered superconductors at low temperatures (see Fig. 7.2.1). Nevertheless, we use a T_{eff} for simplicity and we will come back to this point in the discussion section.

We also include phonon diffusion in Eq. (7.2b), and we estimate the phonon diffusion constant from the mean free path of diffusive scattering on the volume walls to be $D_{\text{ph}} = 0.65 \text{ cm}^2/\text{s}$ [61]. The mean phonon scattering time on the walls is approximately $3D_{\text{ph}}/\nu_s^2 \approx 50$ ps, with ν_s the properly averaged sound velocity. This is shorter than the phonon-electron inelastic scattering times, which is given by $\tau_{\text{pb}} \approx 0.82$ ns for pair-breaking and much longer than that for scattering [45]. We therefore neglect phonon-electron interactions in the estimation of D_{ph} . We also ignore any position dependence of D_{qp} and D_{ph} . Including a position dependent effective quasiparticle temperature based on the local quasiparticle density, and therefore make D_{qp} position dependent, is possible, but does not alter the results significantly [61].

A sketch of the model is presented in Fig. 7.2.3. We set the initial condition such that $\delta n_{\text{qp}} + 2\delta n_{\text{ph}} = \eta_{\text{pb}} E_\gamma / (\Delta_0 V)$, integrated over the volume. Here, η_{pb} is the pair-breaking efficiency, which we set to the theoretical maximum of $\eta_{\text{pb}} = 0.59$ [62, 63], and E_γ is the phonon energy. When the phonon pair-breaking time is much faster than the recombination time, this results in $\delta n_{\text{ph}} \ll \delta n_{\text{qp}} \approx \eta_{\text{pb}} E_\gamma / (\Delta_0 V)$. As we will see later, this accurately describes the pulse height for all four laser wavelengths. We set the phonon and quasiparticle initial spacial distribution to a Gaussian distribution with a standard deviation of $0.67 \text{ }\mu\text{m}$. This estimate is based on the phonon and quasiparticle diffusion length during the last two stages of the downconversion process. When the photon is absorbed by the superconductor, a cascade of electron-electron, electron-phonon and phonon-electron interactions sets off, which is collectively called downconversion Refs. [64–67]. Different stages can be identified, characterized by which interaction dominates. The duration of the downconversion process is controlled by the last stages, since the average particle energy goes down as the downconversion progresses and therefore the interaction times go up. In the last two stages the photon energy is primarily contained in the phonon and quasiparticle systems, respectively. The phonon stage duration is given by $t_{\text{I}} \approx 2\tau_{\text{pb}}(\Omega_1) = 0.66$ ns, where $\hbar\Omega_1 = \sqrt{3(k_{\text{B}} T_{\text{c}})^3 / (\pi\Delta_0\tau_{\text{ph}}^0)}$ [64]. We calculate $\tau_{\text{pb}}(\Omega)$ from Eq. (27) of Ref. [45] and use $T_{\text{eff}} = 100$ mK. The quasiparticle stage duration can be estimated as $t_{\text{II}} = \tau_{\text{scat}}(4.5\Delta_0) \approx 0.77$ ns [64], where we use Eq. (8) of Ref. [45] with $\tau_0 = 81$ ns. This leads to a total diffusion length in two dimensions during downconversion of, $\sqrt{4D_{\text{ph}}t_{\text{I}}} + \sqrt{4D_{\text{qp}}t_{\text{II}}} = 0.67 \text{ }\mu\text{m}$.

COMPARISON WITH DATA: CHANGING PHOTON ENERGY AND ABSORPTION VOLUME

With the parameters and initial condition known, we solve Eq. (7.2) numerically in one spacial dimension, as outlined in Ref. [61]. Diffusion in the other two dimensions reaches the metal boundaries within $1.3 \text{ }\mu\text{s}$, for the width, and 3.3 fs,

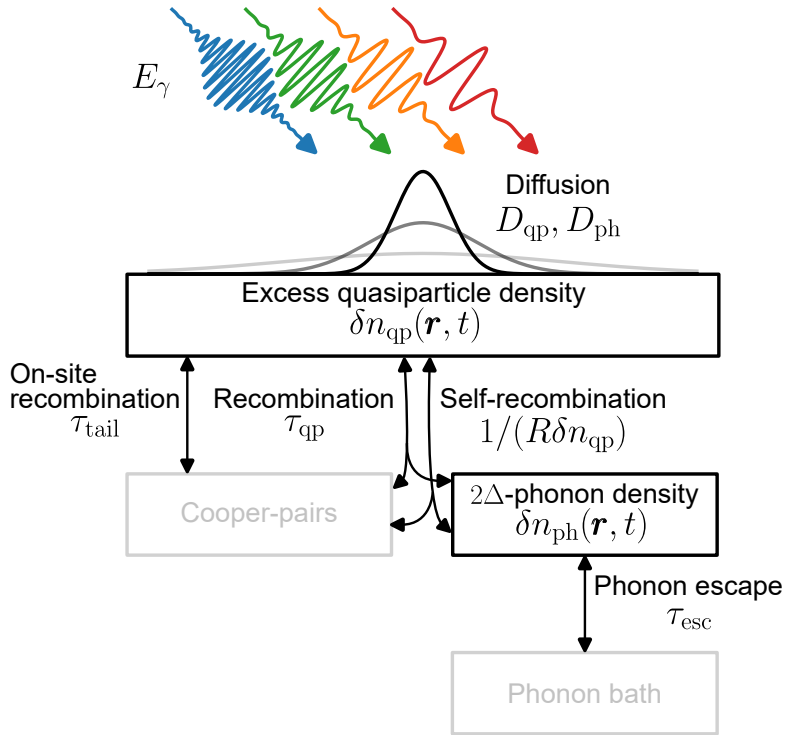


Figure 7.2.3: Schematic illustrating the different levels and transitions included in the model. The gray boxes are levels that are implicitly included, and the black boxes are the two levels described by Eq. (7.2). The initial condition is given by $\delta n_{\text{qp}} + 2\delta n_{\text{ph}} = \eta_{\text{pb}} E_{\gamma} / (\Delta_0 V)$, which is solved with Eq. (7.2) in steady state. E_{γ} is the phonon energy corresponding to the four laser wavelengths of 402, 673, 986, and 1545 nm, as illustrated by the blue, green, orange and red curvy arrow at the top.

7

for the thickness, which we therefore neglect⁵. We convolve the resulting solution for $\delta n_{\text{qp}}(t)$ with $e^{-t/\tau_{\text{res}}}/\tau_{\text{res}}$, where $\tau_{\text{res}} = Q/(\pi f_0)$ is the resonator ring time. This accounts for the response time of the resonator. We measure the quality factors (internal Q_i , coupling Q_c and loaded $Q = Q_i Q_c / (Q_i + Q_c)$) and resonance frequency (f_0) separately, by sweeping the frequency and fitting a Lorentzian resonance curve. We extend this measurement to different bath temperatures to obtain the quasiparticle responsivities, $d\delta A/dn_{\text{qp}}$ and $d\theta/dn_{\text{qp}}$, see Section 3.3.2 for details. We multiply the convoluted solution $\delta n_{\text{qp}}(t)$ with this responsivity to compare the solution to the data.

The result is shown in Fig. 7.2.4(b) as the solid lines. These curves can be compared with the measured single photon phase response in Fig. 7.2.4(a). It is clear that the

⁵Diffusion in the width direction can be taken into account by changing the diffusion dynamics in the first 1.3 μs as projected 2D diffusion on the 1D domain. This does however not change the results much [61].

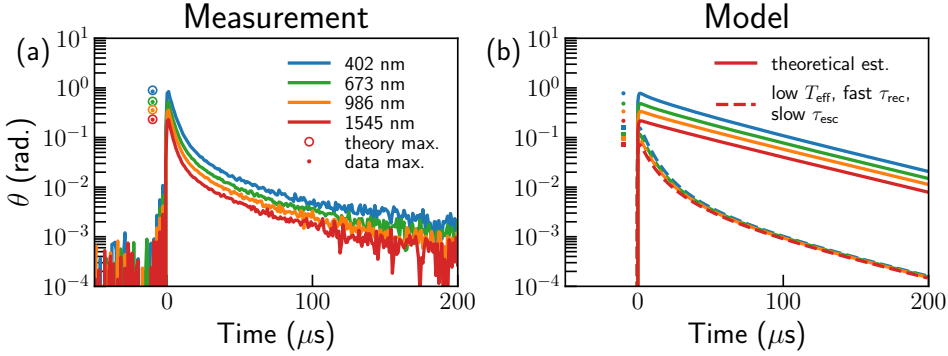


Figure 7.2.4: Measurement (a) and model (b) of the single photon phase response to four different photon energies, indicated by their color. The data is from the same MKID as Fig. 7.2.2 and Fig. 7.1.1(b), at a read-out power of -99 dBm and at 20 mK bath temperature. The circles in (a) give the theoretical maximum for the pulse height, given by $\theta_{\max} = (d\theta/dn_{\text{qp}})\eta_{\text{pb}}E_{\gamma}/(V\Delta_0)$, with $\eta_{\text{pb}} = 0.59$ [62, 63]. The dots in (a) give the measured maximum. The solid lines in (b) are model curves with the theoretical estimates given in the main text. The dashed lines are with adjusted parameters: $T_{\text{eff}} = T_{\text{bath}}$, $\tau_0 \rightarrow 10^{-6}\tau_0$ and τ_{esc} given by the initial decay time as obtained from an exponential fit to the δA response. The points on the left of the pulses give the pulses give the maxima for the parameters from theory (dots) and adjusted parameters (squares).

model, with the parameters estimated above, does not predict the non-exponential decay as observed in the data. The exponential τ_{tail} -term quickly dominates over the quadratic term R -term, which results in a single exponential.

In an attempt to describe the data, we can tune the parameters of this model. To increase the non-exponential behavior, we can try to decrease n_{qp}^0 by setting $T_{\text{eff}} = T_{\text{bath}} = 20$ mK and increasing R by a factor 10^6 (or, equivalently setting $\tau_0 \rightarrow 10^{-6}\tau_0$). Tuning the diffusion constant, D_{qp} , does not influence the solution with estimated parameters as much, since $\delta n_{\text{qp}}(t)/n_{\text{qp}}^0$ only grows as $1/\sqrt{D_{\text{qp}}}$, while this ratio grows exponentially with decreasing T_{eff} . We would therefore have to decrease D_{qp} by multiple orders of magnitude, as well as increasing R , which we deem less likely than changing T_{eff} to the bath temperature.

Additionally, we observe in the measured curves in Fig. 7.2.4(a), that the first part of the initial decay does not exactly follow a pure $1/t$ -decay, but a slower exponential-like decay (see also Ref. [50]). In terms of conventional recombination dynamics, this could be understood as a phonon bottleneck [47, 68]: recombination is faster than the phonon escape and pair-breaking, resulting in a quasiparticle decay that is limited by $2\tau_{\text{esc}}$. In an attempt to describe this, we therefore set $\tau_{\text{esc}} = 2.8 \mu\text{s}$, which is half of the decay time fitted to amplitude pulse (which lacks the tail decay at these low temperatures, see Fig. 7.2.2)⁶. The resulting solutions are shown in

⁶To be consistent with the observation that the membrane and substrate resonators show the same pulse decay, the presumed phonon bottleneck should not be altered by the introduction of the membrane. This seems unlikely, but we will continue with this assumption for now.

Fig. 7.2.4(b) as the dashed lines.

This attempt recovers qualitatively the measured pulse shapes, but fails to fully describe the data. We observe two discrepancies: (1) the pulse height is lower in the model pulses, and (2) the tail decays overlap in the model, while in the data the entire pulse height scales with photon energy. The first discrepancy is a consequence of the fast recombination and slow phonons. Part of the photon energy is stored in the phonon system, which only later (when recombination becomes slower than phonon pair-breaking) is converted into quasiparticles. The dots and circles in Fig. 7.2.4(a) indicate the measured pulse height (maximum) and theoretical estimate, respectively. This estimate is calculated as $\theta_{\max} = (d\theta/dn_{\text{qp}})\eta_{\text{pb}}E_{\gamma}/(V\Delta_0)$, with $\eta_{\text{pb}} = 0.59$, which is the theoretical maximum. Since the dots and circles align, we conclude that approximately all available photon energy is converted to quasiparticles and not to phonons. This implies that recombination is always slower than pair-breaking by phonons, and increasing R by a factor 10^6 is not physically correct. The recombination dynamics is at least as slow as the resonator ring time of $0.56 \mu\text{s}$ during the entire decay. Additionally, we conclude that there is no major hot phonon loss, as this would bring down η_{pb} [62].

The second discrepancy is an important observation that brings us to one of our main conclusions. A consequence of conventional self-recombination is that the pulse shape is always dependent on the photon energy. A higher photon energy gives more excess quasiparticles, which enhances the self-recombination. Since we observe that the measured pulse response scales with photon energy and its shape is not dependent on photon energy, we conclude that the non-exponential behavior is not caused by conventional self-recombination. More generally, we can conclude that the non-linearity that results in the non-exponential decay is intrinsic in the superconductor and not caused by the excitation; when we increase the excitation, the non-linearity is not changed.

To gain more insight into the quasiparticle diffusion and recombination dynamics, we perform a separate experiment, where we constrain the volume that the excess quasiparticle can occupy, V_{qp} , by adding NbTiN barriers to the β -Ta inductor. An image of these devices is shown in Fig. 7.2.5(a). Due to the larger gap of NbTiN ($T_c = 14 \text{ K}$, while β -Ta has $T_c = 0.87 \text{ K}$) the quasiparticles are trapped in the β -Ta superconducting volumes. We vary these volumes per MKID, such that we can observe the effect of the constrained movement on the single photon response. The total β -Ta volume is kept approximately constant. We choose the quasiparticle volumes such, that the quasiparticles do not reach the end of the β -Ta wire for the largest volume (yellow curves), while they occupy the smallest volume (dark blue) within $1 \mu\text{s}$. We design these MKIDs as half-wave resonators to ensure that the current in the relatively long β -Ta wire remains uniform. The measurement results are shown in Fig. 7.2.5(c) and the model predictions are shown in panel (d).

Also in this case, we see that the model does not describe the data. However, a trend in the model can also be observed in the data. In both the data and the model, the initial decay is faster when the quasiparticle volume is decreased. This indicates that the initial decay becomes faster when self-recombination is increased. For the larger quasiparticle volumes, we expect from the model a more

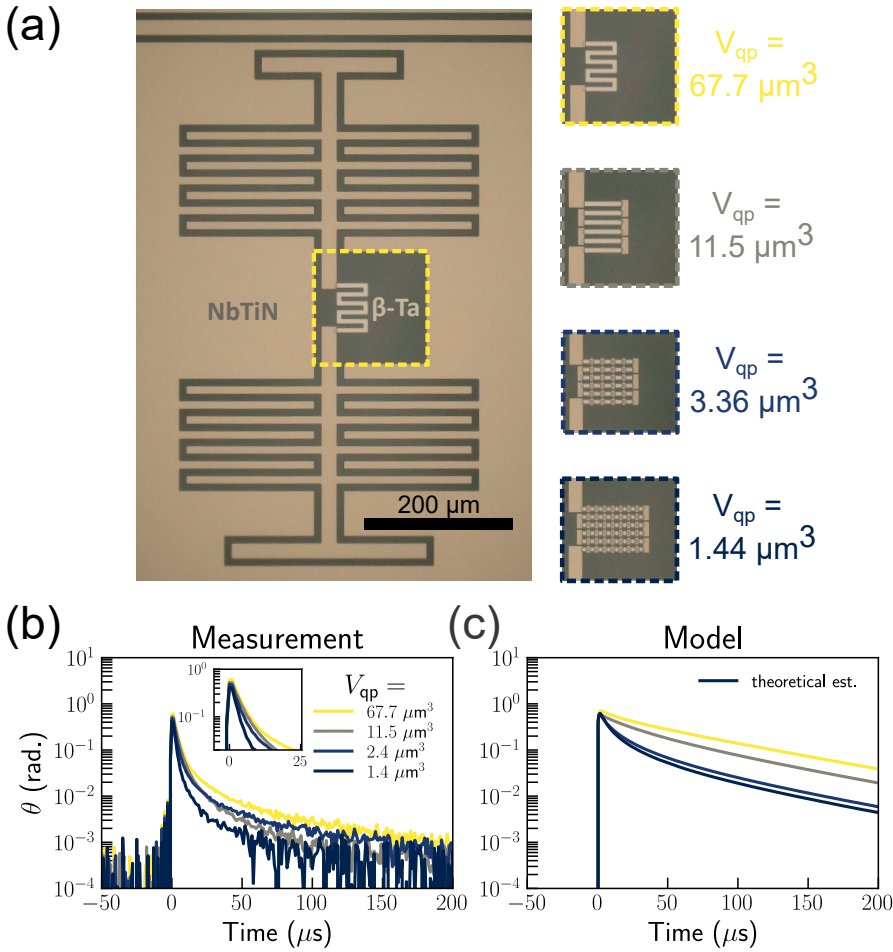


Figure 7.2.5: Experiment with constrained excess quasiparticle volume (V_{qp}) via NbTiN barriers at various distances. (a): Micrograph of the device with the largest quasiparticle volume. On the right, the β -Ta inductor of the other devices are shown. The width of the β -Ta is $6 \mu\text{m}$, the thickness is 44 nm and the total length is approximately $270 \mu\text{m}$. The dashed boxes correspond to the different quasiparticle volumes given by the color bar of panel (c). (b): Measured average single photon phase response for different quasiparticle volumes, indicated by the color. The inset shows a zoom-in of the initial decay. The photon wavelength is 402 nm , the read-out power is around -100 dBm , such that the internal power in the MKIDs does not vary more than 2.5 dB . The resonance frequencies are between 8.0 GHz and 8.8 GHz and the coupling quality factors are between $10,000$ and $20,000$. The internal quality factors are typically 1×10^5 to 5×10^5 . (c): Model curves with the parameters as estimated in the text.

exponential-like decay: the onset of the exponential tail is earlier. We do not observe this in the measurement data. Therefore, the non-exponential behavior of the single

photon response of β -Ta MKIDs cannot be described by conventional recombination dynamics, as we concluded before. However, the initial decay does become faster when self-recombination is induced by limiting the quasiparticle volume. This indicates that the initial decay is governed by a recombination process that is dependent on the local quasiparticle density. In addition, we observe the same pulse response for the substrate resonator (not shown here), similar to the fluctuation results of Chapter 6 and the low temperature fluctuation results of Chapter 5. This might indicate that the initial decay is governed by on-site recombination of mobile quasiparticles.

DISCUSSION: NON-EQUILIBRIUM, LOCALIZATION EFFECTS?

The non-exponential behavior may be related to the localization dynamics. The gradual transition from initial fast decay to tail decay, may be due to a transition from enhanced mobile (higher energetic) quasiparticle recombination within localization sites, to the delocalization and subsequent on-site recombination of localized (lower energetic) quasiparticles. The initial mobile quasiparticle recombination would be dependent on the local quasiparticle density, which is consistent with the observations in Fig. 7.2.5(b).

The model used here (Eq. (7.2)) is similar to model used in Ref. [69], where the authors investigate the non-exponential single photon decay for MKIDs with disordered TiN as absorber⁷. The authors of Ref. [69] use the quasiparticle diffusion constant, D_{qp} , and η_{pb} as fit parameters, and find a much lower D_{qp} and higher (temperature dependent) η_{pb} than predicted by theory. In particular, the fitted D_{qp} is three orders of magnitude lower than Eq. (7.3) predicts. They attribute this to quasiparticle localization. In an attempt to model this, they calculate the localized quasiparticle density as the occupied states below Δ from a broadened density of states with a pair-breaking parameter estimated from a fit to the resonance frequency versus temperature, similar to Ref. [70]. In this way, they calculate an effective diffusion constant that is on the same order as the fitted D_{qp} . However, localized quasiparticle states reside in the exponential subgap tail [71–73], not in the broadened coherence peak. The subgap tail spans a much smaller area and has been omitted in their analysis and the resonance frequency fits [70].

In this chapter, we additionally vary the photon energy and quasiparticle volume experimentally. Crucially, we observed that the single photon pulse shape is not dependent on photon energy, which directly contradicts the predictions from conventional recombination theory (Eq. (7.1)). From this, we concluded that the single photon pulse decay in a disordered superconductor cannot be explained by conventional dynamics. This includes slow diffusion due to quasiparticle localization, as hypothesized in Ref. [69] and described by Eq. (7.1). We believe that a detailed modeling of the localization dynamics is needed to expand on the hypothesis of localization. Since the variations in quasiparticle volume (Fig. 7.2.5) indicates that the first part of the decay is governed by mobile quasiparticles, the localization

⁷In Ref. [69], the authors use a pulsed laser excitation, which gives additional excitations to a direct single photon absorption via non-direct hits. They correct for this post-processing, but this inevitably introduces uncertainties in the exact single photon pulse shape.

presumably takes place only later in the decay. This would make the quasiparticle energy-dependence of the localization and recombination rates important, which requires non-equilibrium modeling. This would entail setting up kinetic equations, including a local varying density of states, and solving them in time (to describe a transient response), space (to account for the local character of the localization dynamics) and energy (to account for the non-equilibrium effects).

7.3 CONCLUSION

The single photon pulse shape of disordered β -Ta is highly non-exponential, in sharp contrast to Al MKIDs in similar measurement conditions. The decay is characterized by a fast initial decay followed by a slower tail decay. The tail decay times correspond to the fluctuation relaxation times at high temperatures, which follow the electron-phonon scattering times from theory. Therefore, the tail decay is likely to be related to the delocalization and on-site recombination of localized quasiparticles. From the absence of the tail in the amplitude response, we conclude that the low-energetic localized states are non-dissipative. By modeling quasiparticle recombination, including quasiparticle diffusion, self-recombination and phonon dynamics, we conclude that the initial fast decay is not due to conventional (self-)recombination. Specifically, the measured photon pulse is proportional to the photon energy and the shape is constant, which is in sharp contrast to the model predictions for conventional self-recombination. When we experimentally enhance the excess quasiparticle density by decreasing the quasiparticle volume, the initial decay rate is increased. This indicates that the initial decay is governed by recombination of mobile quasiparticles, which could be on-site recombination due to localization effects.

Data and code availability All data and analysis scripts used in this study have been deposited in the Zenodo database under accession code 17376007: [zenodo.17376007](https://zenodo.org/record/17376007).

REFERENCES

- [1] P. K. Day, H. G. LeDuc, B. A. Mazin, A. Vayonakis, and J. Zmuidzinas. *A Broadband Superconducting Detector Suitable for Use in Large Arrays*. In: *Nature* 425.6960 (2003), pp. 817–821.
- [2] S. J. C. Yates, J. J. A. Baselmans, A. Endo, R. M. J. Janssen, L. Ferrari, P. Diener, and A. M. Baryshev. *Photon Noise Limited Radiation Detection with Lens-Antenna Coupled Microwave Kinetic Inductance Detectors*. In: *Applied Physics Letters* 99.7 (2011), p. 073505.
- [3] S. Hähnle, O. Yurduseven, S. Van Berkel, N. Llombart, J. Bueno, S. J. C. Yates, V. Murugesan, D. J. Thoen, A. Neto, and J. J. A. Baselmans. *An Ultra-Wideband Leaky Lens Antenna for Broadband Spectroscopic Imaging Applications*. In: *IEEE Transactions on Antennas and Propagation* (2020), pp. 1–1.
- [4] S. O. Dabironezare, G. Conenna, D. Roos, D. Lamers, D. P. Capelo, H. M. Veen, D. J. Thoen, V. Anvekar, S. J. C. Yates, W. Jellema, R. Huiting, L. Ferrari, C. Tucker, S. L. van Berkel, P. K. Day, H. G. Leduc, C. M. Bradford, N. Llombart, and J. J. A. Baselmans. *Lens Based Kinetic Inductance Detectors with Distributed Dual Polarised Absorbers for Far Infra-red Space-based Astronomy*. 2025. URL: <http://arxiv.org/abs/2506.03359>. Pre-published.
- [5] P. K. Day, N. F. Cothard, C. Albert, L. Foote, E. Kane, B. H. Eom, R. Basu Thakur, R. M. J. Janssen, A. Beyer, P. M. Echternach, S. van Berkel, S. Hailey-Dunsheath, T. R. Stevenson, S. Dabironezare, J. J. A. Baselmans, J. Glenn, C. M. Bradford, and H. G. Leduc. *A 25-Micrometer Single-Photon-Sensitive Kinetic Inductance Detector*. In: *Physical Review X* 14.4 (2024), p. 041005.
- [6] J. J. A. Baselmans, F. Facchin, A. P. Laguna, J. Bueno, D. J. Thoen, V. Murugesan, N. Llombart, and P. J. de Visser. *Ultra-Sensitive THz Microwave Kinetic Inductance Detectors for Future Space Telescopes*. In: *Astronomy & Astrophysics* 665 (2022), A17.
- [7] S. Hailey-Dunsheath, R. M. J. Janssen, J. Glenn, C. M. Bradford, J. Perido, J. Redford, and J. Zmuidzinas. *Kinetic Inductance Detectors for the Origins Space Telescope*. In: *Journal of Astronomical Telescopes, Instruments, and Systems* 7.1 (2021), p. 011015.
- [8] J. Glenn, M. Meixner, C. M. Bradford, K. Pontoppidan, A. Pope, T. Kataria, J. Rocca, E. Luthman, L. Armus, J. Baselmans, C. Battersby, A. Bolatto, D. Burgarella, W. Chen, L. Ciesla, P. Day, A. D. Giorgio, M. DiPirro, C. D. Dowell, P. Echternach, T. Essinger-Hileman, M. Foote, C. Gruppioni, B. Hensley, T. Henning, W. Jellema, M. Johnson, A. Kogut, O. Krause, J. McGuire, E. Mills, A. Moullet, M. Rodgers, M. Sauvage, J. D. Smith, R. Somerville, J. Staguhn,

- T. Stevenson, C. Tucker, S. Unwin, J. Ziemer, M. Cannella, and R. Dissly. *PRIMA Mission Concept*. In: *Journal of Astronomical Telescopes, Instruments, and Systems* 11.3 (2025), p. 031628.
- [9] B. Mazin, J. Bailey, J. Bartlett, C. Bockstiegel, B. Bumble, G. Coiffard, T. Currie, M. Daal, K. Davis, R. Dodkins, N. Fruitwala, N. Jovanovic, I. Lipartito, J. Lozi, J. Males, D. Mawet, S. Meeker, K. O'Brien, M. Rich, J. Smith, S. Steiger, N. Swimmer, A. Walter, N. Zobrist, and J. Zmuidzinas. *MKIDs in the 2020s*. In: *Vol. 51, Issue 7 (Astro2020 APC White Papers)* 51.7 (2019).
- [10] S. R. Meeker, B. A. Mazin, A. B. Walter, P. Strader, N. Fruitwala, C. Bockstiegel, P. Szypryt, G. Ulbricht, G. Coiffard, B. Bumble, G. Cancelo, T. Zmuda, K. Treptow, N. Wilcer, G. Collura, R. Dodkins, I. Lipartito, N. Zobrist, M. Bottom, J. C. Shelton, D. Mawet, J. C. van Eyken, G. Vasisht, and E. Serabyn. *DARKNESS: A Microwave Kinetic Inductance Detector Integral Field Spectrograph for High-contrast Astronomy*. In: *Publications of the Astronomical Society of the Pacific* 130.988 (2018), p. 065001.
- [11] B. A. Mazin, B. Bumble, S. R. Meeker, K. O'Brien, S. McHugh, and E. Langman. *A Superconducting Focal Plane Array for Ultraviolet, Optical, and near-Infrared Astrophysics*. In: *Optics Express* 20.2 (2012), pp. 1503–1511.
- [12] NASA Science | *Habitable Worlds Observatory Homepage - NASA Science*. 2023. URL: <https://science.nasa.gov/astrophysics/programs/habitable-worlds-observatory/>.
- [13] S. Steiger, L. Pueyo, E. H. Por, P. Chen, R. Soummer, R. Pourcelot, I. Laginja, and V. P. Bailey. *Simulated Performance of Energy-Resolving Detectors towards Exoplanet Imaging with the Habitable Worlds Observatory*. In: *Space Telescopes and Instrumentation 2024: Optical, Infrared, and Millimeter Wave*. Space Telescopes and Instrumentation 2024: Optical, Infrared, and Millimeter Wave. Vol. 13092. SPIE, 2024, pp. 603–614.
- [14] A. R. Howe, C. C. Stark, and J. E. Sadleir. *Scientific Impact of a Noiseless Energy-Resolving Detector for a Future Exoplanet-Imaging Mission*. In: *Journal of Astronomical Telescopes, Instruments, and Systems* 10.2 (2024), p. 025008.
- [15] B. J. Rauscher, E. R. Canavan, S. H. Moseley, J. E. Sadleir, and T. Stevenson. *Detectors and Cooling Technology for Direct Spectroscopic Biosignature Characterization*. In: *Journal of Astronomical Telescopes, Instruments, and Systems* 2.4 (2016), p. 041212.
- [16] K. Kouwenhoven, D. Fan, E. Biancalani, S. A. H. de Rooij, T. Karim, C. S. Smith, V. Murugesan, D. J. Thoen, J. J. A. Baselmans, and P. J. de Visser. *Resolving Power of Visible-To-Near-Infrared Hybrid β -Ta/Nb-Ti-N Kinetic Inductance Detectors*. In: *Physical Review Applied* 19.3 (2023), p. 034007.
- [17] K. Kouwenhoven, I. Elwakil, J. van Wingerden, V. Murugesan, D. J. Thoen, J. J. A. Baselmans, and P. J. de Visser. *Model and Measurements of an Optical Stack for Broadband Visible to Near-Infrared Absorption in TiN MKIDs*. In: *Journal of Low Temperature Physics* 209.5 (2022), pp. 1249–1257.

- [18] A. E. Lita, A. J. Miller, and S. W. Nam. *Counting Near-Infrared Single-Photons with 95% Efficiency*. In: *Optics Express* 16.5 (2008), pp. 3032–3040.
- [19] D. Rosenberg, S. W. Nam, A. J. Miller, A. Salminen, E. Grossman, R. E. Schwall, and J. M. Martinis. *Near-Unity Absorption of near-Infrared Light in Tungsten Films*. In: *Nuclear Instruments and Methods in Physics Research Section A: Accelerators, Spectrometers, Detectors and Associated Equipment*. Proceedings of the 10th International Workshop on Low Temperature Detectors 520.1 (2004), pp. 537–540.
- [20] H. G. Leduc, B. Bumble, P. K. Day, B. H. Eom, J. Gao, S. Golwala, B. A. Mazin, S. McHugh, A. Merrill, D. C. Moore, O. Noroozian, A. D. Turner, and J. Zmuidzinas. *Titanium Nitride Films for Ultrasensitive Microresonator Detectors*. In: *Applied Physics Letters* 97.10 (2010), p. 102509.
- [21] P. J. de Visser, S. A. H. de Rooij, V. Murugesan, D. J. Thoen, and J. J. A. Baselmans. *Phonon-Trapping-Enhanced Energy Resolution in Superconducting Single-Photon Detectors*. In: *Physical Review Applied* 16.3 (2021), p. 034051.
- [22] P. Szypryt, B. A. Mazin, G. Ulbricht, B. Bumble, S. R. Meeker, C. Bockstiegel, and A. B. Walter. *High Quality Factor Platinum Silicide Microwave Kinetic Inductance Detectors*. In: *Applied Physics Letters* 109.15 (2016), p. 151102.
- [23] N. Zobrist, G. Coiffard, B. Bumble, N. Swimmer, S. Steiger, M. Daal, G. Collura, A. B. Walter, C. Bockstiegel, N. Fruitwala, I. Lipartito, and B. A. Mazin. *Design and Performance of Hafnium Optical and Near-IR Kinetic Inductance Detectors*. In: *Applied Physics Letters* 115.21 (2019), p. 213503.
- [24] N. Zobrist, W. H. Clay, G. Coiffard, M. Daal, N. Swimmer, P. Day, and B. A. Mazin. *Membraneless Phonon Trapping and Resolution Enhancement in Optical Microwave Kinetic Inductance Detectors*. In: *Physical Review Letters* 129.1 (2022), p. 017701.
- [25] S. Meeker, B. Mazin, R. Jensen-Clem, A. Walter, P. Szypryt, M. Strader, and C. Bockstiegel. *Design and Development Status of MKID Integral Field Spectrographs for High Contrast Imaging*. In: *Adaptive Optics for Extremely Large Telescopes 4 – Conference Proceedings* 1.1 (2015).
- [26] A. G. Kozorezov, A. A. Golubov, J. K. Wigmore, D. Martin, P. Verhoeve, R. A. Hijmering, and I. Jerjen. *Inelastic Scattering of Quasiparticles in a Superconductor with Magnetic Impurities*. In: *Physical Review B* 78.17 (2008), p. 174501.
- [27] J. Gao, M. R. Vissers, M. O. Sandberg, F. C. S. da Silva, S. W. Nam, D. P. Pappas, D. S. Wisbey, E. C. Langman, S. R. Meeker, B. A. Mazin, H. G. Leduc, J. Zmuidzinas, and K. D. Irwin. *A Titanium-Nitride near-Infrared Kinetic Inductance Photon-Counting Detector and Its Anomalous Electrodynamics*. In: *Applied Physics Letters* 101.14 (2012), p. 142602.
- [28] M. Y. Reizer and A. V. Sergeev. *Electron-Phonon Interaction in Impure Metals and Superconductors*. In: *Zh. Eksp. Teor. Fiz.* 90 (1986), p. 1056.

- [29] T. P. Devereaux and D. Belitz. *Quasiparticle Inelastic Lifetimes in Disordered Superconducting Films*. In: *Physical Review B* 44.9 (1991), pp. 4587–4600.
- [30] M. Reizer. *Electron-Electron Relaxation in Two-Dimensional Impure Superconductors*. In: *Physical Review B* 61.10 (2000), pp. 7108–7117.
- [31] R. Kubo. *The Fluctuation-Dissipation Theorem*. In: *Reports on Progress in Physics* 29.1 (1966), pp. 255–284.
- [32] P. J. de Visser, J. J. A. Baselmans, P. Diener, S. J. C. Yates, A. Endo, and T. M. Klapwijk. *Number Fluctuations of Sparse Quasiparticles in a Superconductor*. In: *Physical Review Letters* 106.16 (2011), p. 167004.
- [33] P. J. de Visser, D. J. Goldie, P. Diener, S. Withington, J. J. A. Baselmans, and T. M. Klapwijk. *Evidence of a Nonequilibrium Distribution of Quasiparticles in the Microwave Response of a Superconducting Aluminum Resonator*. In: *Physical Review Letters* 112.4 (2014), p. 047004.
- [34] D. J. Goldie and S. Withington. *Non-Equilibrium Superconductivity in Quantum-Sensing Superconducting Resonators*. In: *Superconductor Science and Technology* 26.1 (2012), p. 015004.
- [35] P. Fischer and G. Catelani. *Nonequilibrium Quasiparticle Distribution in Superconducting Resonators: An Analytical Approach*. In: *Physical Review Applied* 19.5 (2023), p. 054087.
- [36] L. Yu. *Bound State in Superconductors with Paramagnetic Impurities*. In: *Chin. J. Phys. (Peking) (Engl. Transl.)* 21.1 (1965), pp. 75–91.
- [37] H. Shiba. *Classical Spins in Superconductors*. In: *Progress of Theoretical Physics* 40.3 (1968), pp. 435–451.
- [38] A. I. Rusinov. *On the Theory of Gapless Superconductivity in Alloys Containing Paramagnetic Impurities*. In: *Soviet Journal of Experimental and Theoretical Physics* 29 (1969), p. 1101.
- [39] A. V. Balatsky, I. Vekhter, and J.-X. Zhu. *Impurity-Induced States in Conventional and Unconventional Superconductors*. In: *Reviews of Modern Physics* 78.2 (2006), pp. 373–433.
- [40] Ya. V. Fominov, M. Houzet, and L. I. Glazman. *Surface Impedance of Superconductors with Weak Magnetic Impurities*. In: *Physical Review B* 84.22 (2011), p. 224517.
- [41] G. M. Éliashberg. *Inelastic Electron Collisions and Nonequilibrium Stationary States in Superconductors*. In: *Soviet Journal of Experimental and Theoretical Physics* 34 (1972), p. 668.
- [42] S. Arabi, Q. Li, R. Dhundhwal, D. Fuchs, T. Reisinger, I. M. Pop, and W. Wulfhökel. *Magnetic Bound States Embedded in Tantalum Superconducting Thin Films*. In: *Applied Physics Letters* 126.11 (2025), p. 114001.
- [43] Y. V. Fominov and M. A. Skvortsov. *Subgap States in Disordered Superconductors with Strong Magnetic Impurities*. In: *Physical Review B* 93.14 (2016), p. 144511.

- [44] A. A. Bespalov. *Impurity-Induced Subgap States in Superconductors with Inhomogeneous Pairing*. In: *Physical Review B* 100.9 (2019), p. 094507.
- [45] S. B. Kaplan, C. C. Chi, D. N. Langenberg, J. J. Chang, S. Jafarey, and D. J. Scalapino. *Quasiparticle and Phonon Lifetimes in Superconductors*. In: *Physical Review B* 14.11 (1976), pp. 4854–4873.
- [46] K. E. Gray. *Steady State Measurements of the Quasiparticle Lifetime in Superconducting Aluminium*. In: *Journal of Physics F: Metal Physics* 1.3 (1971), pp. 290–308.
- [47] A. Rothwarf and B. N. Taylor. *Measurement of Recombination Lifetimes in Superconductors*. In: *Physical Review Letters* 19.1 (1967), pp. 27–30.
- [48] P. J. de Visser. *Quasiparticle Dynamics in Aluminium Superconducting Microwave Resonators*. PhD thesis. Delft: Delft University of Technology, 2014. 222 pp.
- [49] A. Fyhrie, J. Zmuidzinas, J. Glenn, P. Day, H. G. LeDuc, and C. McKenney. *Progress towards Ultra Sensitive KIDs for Future Far-Infrared Missions: A Focus on Recombination Times*. In: *Millimeter, Submillimeter, and Far-Infrared Detectors and Instrumentation for Astronomy IX*. Millimeter, Submillimeter, and Far-Infrared Detectors and Instrumentation for Astronomy IX. Vol. 10708. International Society for Optics and Photonics, 2018, 107083A.
- [50] T. S. L. Rugers. *Quasiparticle Dynamics in Disordered Superconductors*. BA thesis. Delft University of Technology, 2023.
- [51] K. Gray, ed. *Nonequilibrium Superconductivity, Phonons, and Kapitza Boundaries*. Nato Science Series B: Springer US, 1981.
- [52] C. M. Wilson and D. E. Prober. *Quasiparticle Number Fluctuations in Superconductors*. In: *Physical Review B* 69.9 (2004), p. 094524.
- [53] B. Keck and A. Schmid. *Superconductivity and Electron-Phonon Interaction in Impure Simple Metals*. In: *Journal of Low Temperature Physics* 24.5–6 (1976), pp. 611–629.
- [54] G. Abadias, J. J. Colin, D. Tingaud, Ph. Djemia, L. Belliard, and C. Tromas. *Elastic Properties of α - and β -Tantalum Thin Films*. In: *Thin Solid Films* 688 (2019), p. 137403.
- [55] A. Pippard. CXXII. *Ultrasonic Attenuation in Metals*. In: *The London, Edinburgh, and Dublin Philosophical Magazine and Journal of Science* 46.381 (1955), pp. 1104–1114.
- [56] C. Kittel. *Quantum Theory of Solids*. Wiley, 1987. 528 pp.
- [57] R. Barends, S. van Vliet, J. J. A. Baselmans, S. J. C. Yates, J. R. Gao, and T. M. Klapwijk. *Enhancement of Quasiparticle Recombination in Ta and Al Superconductors by Implantation of Magnetic and Nonmagnetic Atoms*. In: *Physical Review B* 79.2 (2009), 020509(R).
- [58] J. M. Martinis, M. Ansmann, and J. Aumentado. *Energy Decay in Superconducting Josephson-Junction Qubits from Nonequilibrium Quasiparticle Excitations*. In: *Physical Review Letters* 103.9 (2009), p. 097002.

- [59] V. Narayanamurti, R. C. Dynes, P. Hu, H. Smith, and W. F. Brinkman. *Quasiparticle and Phonon Propagation in Bulk, Superconducting Lead*. In: *Physical Review B* 18.11 (1978), pp. 6041–6052.
- [60] J. N. Ullom, P. A. Fisher, and M. Nahum. *Energy-Dependent Quasiparticle Group Velocity in a Superconductor*. In: *Physical Review B* 58.13 (1998), pp. 8225–8228.
- [61] K. P. Syaifoel. *The Impact of Diffusion and Disorder on the Single Photon Response of β -Ta OKIDs*. MA thesis. Delft University of Technology, 2024.
- [62] T. Guruswamy, D. J. Goldie, and S. Withington. *Quasiparticle Generation Efficiency in Superconducting Thin Films*. In: *Superconductor Science and Technology* 27.5 (2014), p. 055012.
- [63] P. J. de Visser, S. J. C. Yates, T. Guruswamy, D. J. Goldie, S. Withington, A. Neto, N. Llombart, A. M. Baryshev, T. M. Klapwijk, and J. J. A. Baselmans. *The Non-Equilibrium Response of a Superconductor to Pair-Breaking Radiation Measured over a Broad Frequency Band*. In: *Applied Physics Letters* 106.25 (2015), p. 252602.
- [64] A. G. Kozorezov, A. F. Volkov, J. K. Wigmore, A. Peacock, A. Poelaert, and R. den Hartog. *Quasiparticle-Phonon Downconversion in Nonequilibrium Superconductors*. In: *Physical Review B* 61.17 (2000), pp. 11807–11819.
- [65] A. G. Kozorezov, J. K. Wigmore, D. Martin, P. Verhoeve, and A. Peacock. *Electron Energy Down-Conversion in Thin Superconducting Films*. In: *Physical Review B* 75.9 (2007), p. 094513.
- [66] A. Kozorezov. *Energy Down-Conversion and Thermalization in Metal Absorbers*. In: *Journal of Low Temperature Physics* 167.3 (2012), pp. 473–484.
- [67] A. G. Kozorezov, C. Lambert, F. Marsili, M. J. Stevens, V. B. Verma, J. P. Allmaras, M. D. Shaw, R. P. Mirin, and S. W. Nam. *Fano Fluctuations in Superconducting-Nanowire Single-Photon Detectors*. In: *Physical Review B* 96.5 (2017), p. 054507.
- [68] M. Johnson. *Direct Real Time Measurement of Quasiparticle Lifetimes in a Superconductor*. In: *Physical Review Letters* 67.3 (1991), pp. 374–377.
- [69] J. Hu, J.-M. Matin, P. Nicaise, F. Boussaha, C. Chaumont, M. Piat, V. D. Pham, and P. Bonifacio. *Investigation of Quasi-Particle Relaxation in Strongly Disordered Superconductor Resonators*. In: *Superconductor Science and Technology* 37.5 (2024), p. 055014.
- [70] E. F. C. Driessen, P. C. J. J. Coumou, R. R. Tromp, P. J. de Visser, and T. M. Klapwijk. *Strongly Disordered TiN and NbTiN S-Wave Superconductors Probed by Microwave Electrodynamics*. In: *Physical Review Letters* 109.10 (2012), p. 107003.
- [71] A. Bespalov, M. Houzet, J. S. Meyer, and Y. V. Nazarov. *Theoretical Model to Explain Excess of Quasiparticles in Superconductors*. In: *Physical Review Letters* 117.11 (2016), p. 117002.

- [72] M. V. Feigel'man and M. A. Skvortsov. *Universal Broadening of the Bardeen-Cooper-Schrieffer Coherence Peak of Disordered Superconducting Films*. In: *Physical Review Letters* 109.14 (2012), p. 147002.
- [73] M. A. Skvortsov and M. V. Feigel'man. *Subgap States in Disordered Superconductors*. In: *Journal of Experimental and Theoretical Physics* 117.3 (2013), pp. 487–498.

8

CONCLUSION

In Chapter 1 we saw that disordered superconductors promise to push the boundaries of superconducting circuits. The high kinetic inductance of disordered superconductors offers unexplored impedance regimes and novel non-linear elements for quantum circuits, while the high normal state resistance offers an efficient, broadband photon absorption for superconducting detectors.

However, disordered superconductors have not fulfilled this promise yet. They show a higher microwave loss and lower photon energy resolving power. Despite the strong implications for the applications, the physical reasons for these experimental facts are not known.

In this thesis, we have shown that the quasiparticle dynamics in disordered superconductors are strongly altered by disorder. In Chapter 6 we have argued that the localization of quasiparticles due to disorder [1, 2] enhances the recombination rate at moderately low temperatures ($T_c/10 < T < T_c/4$). Localization confines the quasiparticle movement to specific localization sites, and enhances recombination as they relax to the same positions. This is qualitatively the same picture as the trap-assisted recombination of electron-hole pairs in semiconductors, described by Shockley-Read theory [3].

The disorder in the superconducting film does not have to be strong for these effects to play a role. Even the quasiparticle dynamics in an ordered superconductor show effects of disorder as we have shown for Al in Chapter 4. In this case, disorder is likely located at the surface or at the film-substrate interface.

Also in non-equilibrium conditions, the effects of disorder on the quasiparticle dynamics have become evident. For example, a continuous microwave excitation generates quasiparticles in Al, which cannot be explained by direct photon absorption by quasiparticles (Chapter 5). In this case, disorder is to be interpreted as the introduction of defects, either on the surface or substrate interface of the Al, or in the surrounding dielectrics. These defects can induce additional two-level systems, which can absorb microwave photons and heat the superconductor locally to generate quasiparticles.

Furthermore, when exciting an intrinsically disordered superconductor with a visible or near infrared photon, the quasiparticle density decays non-exponentially to equilibrium, as shown in Chapter 7. This behavior cannot be described by

conventional quasiparticle dynamics, even when we include the slow diffusion of quasiparticles in disordered superconductors. Moreover, the low temperature dissipative (quasiparticle) response is reduced compared to the inductive (Cooper-pair condensate) response close to equilibrium. This suggests that the localized quasiparticle states are isolated in energy (at least one microwave photon below the gap energy), which does not align with the theory of suppressed gap regions due to disorder [1, 2]. Although the analysis of this theory in Chapter 6 is consistent with the observations, we needed to assume an unexplained, fast inelastic relaxation to the localized states. An effect of (magnetic) impurities, additional to disorder, that gives rise to isolated localized states could explain this as well [4].

To conclude, the application of disordered superconductors in superconducting circuits is hindered by the effects of disorder on the quasiparticle dynamics. This includes quasiparticle localization and possibly an increase of the number of two-level systems in or close to the superconductor. These effects lead to an increased microwave loss and enhanced recombination rate.

OPEN QUESTIONS

Together with this conclusion, there are still many open questions. We list a few of these here.

1. How does a locally varying density of states affect the non-equilibrium quasiparticle dynamics? Although the locally varying density of states in disordered superconductors has been theoretically described [1, 5–9] and measured using scanning tunneling spectroscopy [10–13], the effects on the non-equilibrium quasiparticle dynamics (both transient and steady state) are not completely clear. For this, a numerical approach of the kinetic equations [14, 15] could be set up, including a spatially varying quasiparticle density and density of states, which would improve the modeling in Chapters 6 and 7.
2. What role do magnetic surface impurities play in the microscopic quasiparticle dynamics? In Chapter 7, we hypothesized that in addition to homogeneous disorder, surface magnetic impurities may also induce localized states that are more isolated in space. Recently, more evidence pointing towards such states has emerged [16, 17], and an investigation into how these states affect the quasiparticle dynamics in disordered superconductors is needed.
3. Is the increase in microwave loss in disordered superconductors due to localized quasiparticles, two-level systems or collective modes? In Chapter 1, we argued that the increased microwave loss in disordered superconductors (Fig. 1.3(b)) points towards an effect of disorder on the quasiparticle dynamics. In Chapters 4, 6 and 7, we showed how disorder affects the quasiparticle dynamics, in particular via localization. Indeed, in Ref. [18] the authors argue that localized quasiparticles induce the enhanced microwave loss in disordered superconductors. However, a recent theoretical study on the dynamics of the localized quasiparticles concludes that the subgap states cannot influence the total density significantly [19], which has also been argued in an experimental

study [20]. This modeling and conclusion is very similar to the observation in Chapter 6 that the localization effects do not affect the quasiparticle density in experimentally accessible regimes. Other options for the increased microwave loss would be two-level-system loss [21–23] or disorder-induced collective modes [24–26]. This open issue can potentially be resolved by extending the methods presented in this thesis to lower temperatures and quasiparticle generation rates, such that the predicted effects of localization on the quasiparticle density can be verified and quantified.

4. What microscopic mechanism causes the microwave power induced excess quasiparticles at low temperatures? In Chapter 5, we excluded the commonly assumed mechanism of direct microwave photon absorption [15, 27], and concluded that this mechanism is indirect and acts close to the sensitive Al volume. That implies a photon absorption mechanism, possibly two-level-systems, that locally heat the superconductor. To confirm this hypothesis, more experiments are needed. A direction for these experiments could be to focus on the correlation between the quasiparticle generation efficiency of the microwave power and the density of the two-level-systems close to the superconductor.
5. How does disorder affect the energy resolving power of MKIDs? Although we showed in Chapter 7 that the pulse decay of a single photon is likely to be drastically enhanced by disorder, the effect on the energy resolving power has not yet been addressed. Apart from the negative impact of the fast decay on the signal-to-noise ratio, disorder could also affect the downconversion of the photon energy to quasiparticles [28, 29]. A thorough analysis of the resolving power for various degrees of disorder - using the same methods as presented in Chapter 7 - could shed new light on this question.
6. How does granular disorder influence the quasiparticle dynamics? In this thesis, we have considered homogeneous disorder. For granular disorder (such as in granular Al [30, 31]), completely different microscopic mechanisms may induce other effects on the quasiparticle dynamics [32, 33]. By using the methods presented in this thesis (Chapters 6 and 7) on granular disordered superconductors, new insights into the quasiparticles in these systems could be obtained.

IMPACT ON APPLICATIONS

As these questions remain unanswered for now, low microwave loss and high resolving power applications of disordered superconductors require more work. For superconducting circuits where microwave loss limits the performance, this implies that high kinetic inductance elements must be realized differently. This can be done with Josephson junction arrays [34–36] and might be possible in the future with 2D superconducting materials, like magic angle twisted bilayer graphene [37, 38] or niobium diselenide [39, 40].

For microwave kinetic inductance detectors (MKIDs), the effects of disorder seem to

be detrimental to their photon energy resolving capabilities (Fig. 1.6(a)). Selecting a moderately disordered material that compromises between broadband photon absorption efficiency and energy resolving power is an educated engineering solution. This compromise can be based on the disorder effects on the quasiparticle dynamics, as sketched in Fig. 6.3.1, and might already be realized in hafnium devices [41, 42]. To surpass such a compromise, it may be required to separate the photon absorption and detection (i.e., quasiparticle generation) mechanisms, similar to antenna-coupled (longer wavelength) MKIDs [43, 44]. To realize this, bilayer inductors consisting of a top disordered superconductor (for efficient photon absorption) and a bottom pure superconductor with slow recombination dynamics (for detection), could be investigated.

REFERENCES

- [1] M. V. Feigel'man and M. A. Skvortsov. *Universal Broadening of the Bardeen-Cooper-Schrieffer Coherence Peak of Disordered Superconducting Films*. In: *Physical Review Letters* 109.14 (2012), p. 147002.
- [2] A. Bespalov, M. Houzet, J. S. Meyer, and Y. V. Nazarov. *Theoretical Model to Explain Excess of Quasiparticles in Superconductors*. In: *Physical Review Letters* 117.11 (2016), p. 117002.
- [3] W. Shockley and W. T. Read. *Statistics of the Recombinations of Holes and Electrons*. In: *Physical Review* 87.5 (1952), pp. 835–842.
- [4] A. A. Bespalov. *Impurity-Induced Subgap States in Superconductors with Inhomogeneous Pairing*. In: *Physical Review B* 100.9 (2019), p. 094507.
- [5] A. V. Khvalyuk and M. V. Feigel'man. *Distribution of the Order Parameter in Strongly Disordered Superconductors: An Analytic Theory*. In: *Physical Review B* 104.22 (2021), p. 224505.
- [6] M. A. Skvortsov and M. V. Feigel'man. *Superconductivity in Disordered Thin Films: Giant Mesoscopic Fluctuations*. In: *Physical Review Letters* 95.5 (2005), p. 057002.
- [7] M. A. Skvortsov and M. V. Feigel'man. *Subgap States in Disordered Superconductors*. In: *Journal of Experimental and Theoretical Physics* 117.3 (2013), pp. 487–498.
- [8] J. S. Meyer and B. D. Simons. *Gap Fluctuations in Inhomogeneous Superconductors*. In: *Physical Review B* 64.13 (2001), p. 134516.
- [9] A. I. Larkin and Y. N. Ovchinnikov. *Density of States in Inhomogeneous Superconductors*. In: *Soviet Journal of Experimental and Theoretical Physics* 34 (1972), p. 1144.
- [10] B. Sacépé, C. Chapelier, T. I. Baturina, V. M. Vinokur, M. R. Baklanov, and M. Sanquer. *Disorder-Induced Inhomogeneities of the Superconducting State Close to the Superconductor-Insulator Transition*. In: *Physical Review Letters* 101.15 (2008), p. 157006.
- [11] P. C. J. J. Coumou, E. F. C. Driessen, J. Bueno, C. Chapelier, and T. M. Klapwijk. *Electrodynamic Response and Local Tunneling Spectroscopy of Strongly Disordered Superconducting TiN Films*. In: *Physical Review B* 88.18 (2013), p. 180505.

- [12] C. Carbillet, V. Cherkez, M. A. Skvortsov, M. V. Feigel'man, F. Debontridder, L. B. Ioffe, V. S. Stolyarov, K. Ilin, M. Siegel, D. Roditchev, T. Cren, and C. Brun. *Spectroscopic Evidence for Strong Correlations between Local Superconducting Gap and Local Altshuler-Aronov Density of States Suppression in Ultrathin NbN Films*. In: *Physical Review B* 102.2 (2020), p. 024504.
- [13] G. Lemarié, A. Kamlapure, D. Bucheli, L. Benfatto, J. Lorenzana, G. Seibold, S. C. Ganguli, P. Raychaudhuri, and C. Castellani. *Universal Scaling of the Order-Parameter Distribution in Strongly Disordered Superconductors*. In: *Physical Review B* 87.18 (2013), p. 184509.
- [14] J.-J. Chang and D. J. Scalapino. *Kinetic-Equation Approach to Nonequilibrium Superconductivity*. In: *Physical Review B* 15.5 (1977), pp. 2651–2670.
- [15] D. J. Goldie and S. Withington. *Non-Equilibrium Superconductivity in Quantum-Sensing Superconducting Resonators*. In: *Superconductor Science and Technology* 26.1 (2012), p. 015004.
- [16] I. Tamir, M. Trahms, F. Gorniaczyk, F. von Oppen, D. Shahar, and K. J. Franke. *Direct Observation of Intrinsic Surface Magnetic Disorder in Amorphous Superconducting Films*. In: *Physical Review B* 105.14 (2022), p. L140505.
- [17] S. Arabi, Q. Li, R. Dhundhwal, D. Fuchs, T. Reisinger, I. M. Pop, and W. Wulfhekkel. *Magnetic Bound States Embedded in Tantalum Superconducting Thin Films*. In: *Applied Physics Letters* 126.11 (2025), p. 114001.
- [18] T. Charpentier, A. Khvalyuk, L. Ioffe, M. Feigel'man, N. Roch, and B. Sacépé. *Universal Scaling of Microwave Dissipation in Superconducting Circuits*. 2025. URL: <http://arxiv.org/abs/2507.08953>. Pre-published.
- [19] P. B. Fischer and G. Catelani. *Excess Quasiparticles and Their Dynamics in the Presence of Subgap States*. In: *Physical Review B* 112.10 (2025), p. L100507.
- [20] E. Gurra, D. A. Bennett, S. M. Duff, M. R. Vissers, and J. N. Ullom. *Can Slow Recombination in Ordered Superconductors Explain the Excess Quasiparticle Population?* 2025. URL: <http://arxiv.org/abs/2507.03217>. Pre-published.
- [21] C. R. H. McRae, H. Wang, J. Gao, M. R. Vissers, T. Brecht, A. Dunsworth, D. P. Pappas, and J. Mutus. *Materials Loss Measurements Using Superconducting Microwave Resonators*. In: *Review of Scientific Instruments* 91.9 (2020), p. 091101.
- [22] S. Frasca, I. Arabadzhiev, S. B. de Puechredon, F. Oppliger, V. Jouanny, R. Musio, M. Scigliuzzo, F. Minganti, P. Scarlino, and E. Charbon. *NbN Films with High Kinetic Inductance for High-Quality Compact Superconducting Resonators*. In: *Physical Review Applied* 20.4 (2023), p. 044021.
- [23] C. Müller, J. H. Cole, and J. Lisenfeld. *Towards Understanding Two-Level-Systems in Amorphous Solids: Insights from Quantum Circuits*. In: *Reports on Progress in Physics* 82.12 (2019), p. 124501.
- [24] A. V. Khvalyuk, T. Charpentier, N. Roch, B. Sacépé, and M. V. Feigel'man. *Near Power-Law Temperature Dependence of the Superfluid Stiffness in Strongly Disordered Superconductors*. In: *Physical Review B* 109.14 (2024), p. 144501.

- [25] M. V. Feigel'man and L. B. Ioffe. *Microwave Properties of Superconductors Close to the Superconductor-Insulator Transition*. In: *Physical Review Letters* 120.3 (2018), p. 037004.
- [26] A. V. Khvalyuk and M. V. Feigel'man. *Dissipation Due to Bulk Localized Low-Energy Modes in Strongly Disordered Superconductors*. 2025. URL: <http://arxiv.org/abs/2512.11636>. Pre-published.
- [27] P. J. de Visser, D. J. Goldie, P. Diener, S. Withington, J. J. A. Baselmans, and T. M. Klapwijk. *Evidence of a Nonequilibrium Distribution of Quasiparticles in the Microwave Response of a Superconducting Aluminum Resonator*. In: *Physical Review Letters* 112.4 (2014), p. 047004.
- [28] A. G. Kozorezov, A. A. Golubov, J. K. Wigmore, D. Martin, P. Verhoeve, R. A. Hijmering, and I. Jerjen. *The Effect of Magnetic Impurities on the Response of Superconducting Photon Detectors*. In: *IEEE Transactions on Applied Superconductivity* 19.3 (2009), pp. 440–444.
- [29] A. G. Kozorezov, C. Lambert, F. Marsili, M. J. Stevens, V. B. Verma, J. P. Allmaras, M. D. Shaw, R. P. Mirin, and S. W. Nam. *Fano Fluctuations in Superconducting-Nanowire Single-Photon Detectors*. In: *Physical Review B* 96.5 (2017), p. 054507.
- [30] G. Deutscher, H. Fenichel, M. Gershenson, E. Grünbaum, and Z. Ovadyahu. *Transition to Zero Dimensionality in Granular Aluminum Superconducting Films*. In: *Journal of Low Temperature Physics* 10.1 (1 1973), pp. 231–243.
- [31] L. Grünhaupt, M. Spiecker, D. Gusenkova, N. Maleeva, S. T. Skacel, I. Takmakov, F. Valenti, P. Winkel, H. Rotzinger, W. Wernsdorfer, A. V. Ustinov, and I. M. Pop. *Granular Aluminium as a Superconducting Material for High-Impedance Quantum Circuits*. In: *Nature Materials* 18.8 (8 2019), pp. 816–819.
- [32] L. Grünhaupt, N. Maleeva, S. T. Skacel, M. Calvo, F. Levy-Bertrand, A. V. Ustinov, H. Rotzinger, A. Monfardini, G. Catelani, and I. M. Pop. *Loss Mechanisms and Quasiparticle Dynamics in Superconducting Microwave Resonators Made of Thin-Film Granular Aluminum*. In: *Physical Review Letters* 121.11 (2018), p. 117001.
- [33] A. G. Moshe, E. Farber, and G. Deutscher. *Granular Superconductors for High Kinetic Inductance and Low Loss Quantum Devices*. In: *Applied Physics Letters* 117.6 (2020), p. 062601.
- [34] M. Watanabe, D. B. Haviland, and R. L. Kautz. *Control of the Electromagnetic Environment for Single Josephson Junctions Using Arrays of Dc SQUIDs*. In: *Superconductor Science and Technology* 14.10 (2001), p. 870.
- [35] L. Planat, E. Al-Tavil, J. P. Martínez, R. Dassonneville, F. Froughi, S. Léger, K. Bharadwaj, J. Delaforce, V. Milchakov, C. Naud, O. Buisson, W. Hasch-Guichard, and N. Roch. *Fabrication and Characterization of Aluminum SQUID Transmission Lines*. In: *Physical Review Applied* 12.6 (2019), p. 064017.

- [36] R. Kuzmin, R. Mencia, N. Grabon, N. Mehta, Y.-H. Lin, and V. E. Manucharyan. *Quantum Electrodynamics of a Superconductor–Insulator Phase Transition*. In: *Nature Physics* 15.9 (2019), pp. 930–934.
- [37] Y. Cao, V. Fatemi, S. Fang, K. Watanabe, T. Taniguchi, E. Kaxiras, and P. Jarillo-Herrero. *Unconventional Superconductivity in Magic-Angle Graphene Superlattices*. In: *Nature* 556.7699 (2018), pp. 43–50.
- [38] A. Banerjee, Z. Hao, M. Kreidel, P. Ledwith, I. Phinney, J. M. Park, A. Zimmerman, M. E. Wesson, K. Watanabe, T. Taniguchi, R. M. Westervelt, A. Yacoby, P. Jarillo-Herrero, P. A. Volkov, A. Vishwanath, K. C. Fong, and P. Kim. *Superfluid Stiffness of Twisted Trilayer Graphene Superconductors*. In: *Nature* 638.8049 (2025), pp. 93–98.
- [39] R. F. Frindt. *Superconductivity in Ultrathin NbSe₂ Layers*. In: *Physical Review Letters* 28.5 (1972), pp. 299–301.
- [40] M. Kreidel, X. Chu, J. Balgley, A. Antony, N. Verma, J. Ingham, L. Ranzani, R. Queiroz, R. M. Westervelt, J. Hone, and K. C. Fong. *Measuring Kinetic Inductance and Superfluid Stiffness of Two-Dimensional Superconductors Using High-Quality Transmission-Line Resonators*. In: *Physical Review Research* 6.4 (2024), p. 043245.
- [41] N. Zobrist, G. Coiffard, B. Bumble, N. Swimmer, S. Steiger, M. Daal, G. Collura, A. B. Walter, C. Bockstiegel, N. Fruitwala, I. Lipartito, and B. A. Mazin. *Design and Performance of Hafnium Optical and Near-IR Kinetic Inductance Detectors*. In: *Applied Physics Letters* 115.21 (2019), p. 213503.
- [42] N. Zobrist, W. H. Clay, G. Coiffard, M. Daal, N. Swimmer, P. Day, and B. A. Mazin. *Membraneless Phonon Trapping and Resolution Enhancement in Optical Microwave Kinetic Inductance Detectors*. In: *Physical Review Letters* 129.1 (2022), p. 017701.
- [43] P. K. Day, H. G. Leduc, A. Goldin, T. Vayonakis, B. A. Mazin, S. Kumar, J. Gao, and J. Zmuidzinas. *Antenna-Coupled Microwave Kinetic Inductance Detectors*. In: *Nuclear Instruments and Methods in Physics Research Section A: Accelerators, Spectrometers, Detectors and Associated Equipment*. Proceedings of the 11th International Workshop on Low Temperature Detectors 559.2 (2006), pp. 561–563.
- [44] S. J. C. Yates, J. J. A. Baselmans, A. Endo, R. M. J. Janssen, L. Ferrari, P. Diener, and A. M. Baryshev. *Photon Noise Limited Radiation Detection with Lens-Antenna Coupled Microwave Kinetic Inductance Detectors*. In: *Applied Physics Letters* 99.7 (2011), p. 073505.

A

PHONON TRANSPARENCIES

Ref. [1] sets out how the phonons in a medium are transmitted (refracted) or reflected on the interface with another medium. The transmission efficiency of longitudinal and transverse phonons (η_L and η_T) can be calculated from the media densities (ρ) and longitudinal and transverse sound velocities (c_L and c_T). There are three phonon modes: 2 transverse and 1 longitudinal. The transverse modes are shear displacements, and either horizontal (SH) or vertical (SV). The longitudinal is compressive displacement and indicated with L. Since the SH mode has no displacement perpendicular to the interface plane, this mode will only reflect or refract on the interface, without mode conversion. The L and SV modes, however, have perpendicular components and will convert into one another. This is shown in Fig. A.1. The refractions and reflections obey Snell's law:

$$\frac{\sin \theta_1}{c_{L1}} = \frac{\sin \theta_2}{c_{L2}} = \frac{\sin \gamma_1}{c_{T1}} = \frac{\sin \gamma_2}{c_{T2}}. \quad (\text{A.1})$$

The general method to calculate the transmission efficiencies is the following. First, the incoming and outgoing waves are described as plane wave in displacement vectors. Second, the amplitudes of these waves are related to each other via the boundary conditions: the normal and tangent components of the displacement vectors and stress tensor should be continuous at the interface (4 equations in total). Third, energy conservation of the incoming and outgoing waves is considered, which are combined with the boundary equations by using Snell's law (Eq. (A.1)) and geometrical identities. This results in a phonon transmission efficiency (going from medium 1 to medium 2), that depends on the incident angle. Lastly, this expression is integrated over all angles, weighted by the size of the solid angle. This procedure must be executed for the three different modes separately to obtain η_{SH} , η_L and η_{SV} . We will mention the results of Ref. [2] for the SH mode and L mode and present a similar calculation for the SV mode to complement Ref. [2]. With these equations, the phonon transparency can be calculated for an arbitrary interface between two media, when the phonon velocities and densities are known. A Python code that implements these calculations can be found at [3].

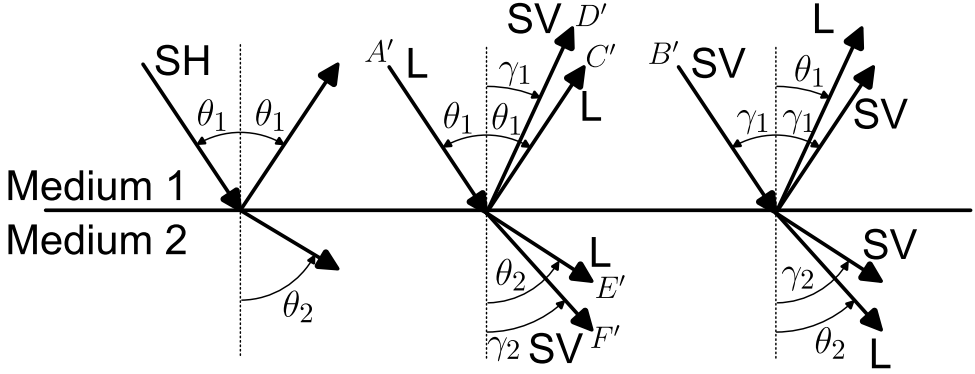


Figure A.1: Schematic of the three different phonon modes incident on an interface between two media. The angles are indicated as used in the calculation for the phonon transmission efficiency. The letters indicate the complex wave amplitudes as used in the calculations.

SH mode The SH mode can only be refracted or reflected to form another SH mode. Therefore, two of the four boundary conditions are trivial and a system of 2 equations needs to be solved. This results in,

$$\eta_{SH}(\gamma_1) = \frac{4x}{(1+x)^2}, \text{ with } x = \frac{\rho_2 c_{T2} \cos \gamma_2}{\rho_1 c_{T1} \cos \gamma_1}. \quad (\text{A.2})$$

The total transverse transmission for this mode is obtained via,

$$\eta_{SH} = 2 \int_0^{\theta_c} \eta_{SH}(\gamma_1) \sin \gamma_1 \cos \gamma_1 d\gamma_1, \quad (\text{A.3})$$

where the critical angle for total internal reflection is $\theta_c = \sin^{-1}(c_{T1}/c_{T2})$. The conversion between γ_1 , γ_2 and θ_1 can be done via Snell's law (Eq. (A.1)).

L mode Incoming L and SV waves will result in four outgoing waves and thus 4 coupled equations that need to be solved to obtain the outgoing complex wave amplitudes (C' , D' , E' and F'), in terms of the incoming amplitude (A')

$$\begin{aligned} -\alpha_1(A' - C') + \sigma D' &= -\alpha_2 E' + \sigma F', \\ \sigma(A' + C') - \beta_1 D' &= \sigma E' + \beta_2 F', \\ \rho_1 c_{T1}^2 ((A' + C')(\cot^2 \gamma_1 - 1) + 2D' \cot \gamma_1) &= \rho_2 c_{T2}^2 (E'(\cot^2 \gamma_2 - 1) - 2F' \cot \gamma_1), \\ \rho_1 c_{T1}^2 (-2(A - C') \cot \theta_1 + D'(1 - \cot^2 \gamma_1)) &= \rho_2 c_{T2}^2 (-2E' \cot \theta_2 + F'(1 - \cot^2 \gamma_2)). \end{aligned} \quad (\text{A.4})$$

Here, $\sigma = \omega \sin \theta_1 / c_{L1}$, with ω the angular wave frequency. When adding energy conservation to these equations,

$$1 = \frac{|C'|^2}{|A'|^2} + \frac{c_{L1}|D'|^2 \cos \gamma_1}{c_{T1}|A'|^2 \cos \theta_1} + \frac{\rho_2 c_{L1}|E'|^2 \cos \theta_2}{\rho_1 c_{L2}|A'|^2 \cos \theta_1} + \frac{\rho_2 c_{T1}|F'|^2 \cos \gamma_2}{\rho_1 c_{T2}|A'|^2 \cos \theta_1}, \quad (\text{A.5})$$

the angle dependent phonon transmission can be found as the last two terms of this expression,

$$\eta_L(\theta_1) = \frac{\rho_2 c_{L1} |E'|^2 \cos \theta_2}{\rho_1 c_{L2} |A'|^2 \cos \theta_1} + \frac{\rho_2 c_{L1} |F'|^2 \cos \gamma_2}{\rho_1 c_{T2} |A'|^2 \cos \theta_1}, \quad (\text{A.6})$$

where γ_2 and θ_2 can be expressed in θ_1 using Snell's law.

The total phonon transmission can be found as,

$$\begin{aligned} \eta_L &= 2 \int_0^{\pi/2} \eta_L(\theta_1) \sin \theta_1 \cos \theta_1 \, d\theta_1 \\ &= 2 \left(\int_0^{\theta_{c1}} \left[\frac{\rho_2 c_{L1} |E'|^2 \cos \theta_2}{\rho_1 c_{L2} |A'|^2 \cos \theta_1} + \frac{\rho_2 c_{L1} |F'|^2 \cos \gamma_2}{\rho_1 c_{T2} |A'|^2 \cos \theta_1} \right] \sin \theta_1 \cos \theta_1 \, d\theta_1 \right. \\ &\quad \left. + \int_{\theta_{c1}}^{\theta_{c2}} \frac{\rho_2 c_{L1} |F'|^2 \cos \gamma_2}{\rho_1 c_{T2} |A'|^2 \cos \theta_1} \sin \theta_1 \cos \theta_1 \, d\theta_1 \right) \end{aligned} \quad (\text{A.7})$$

with the critical angles, $\theta_{c1} = \sin^{-1}(c_{L1}/c_{L2})$ and $\theta_{c2} = \sin^{-1}(c_{L1}/c_{T2})$.

SV mode Similar to the L mode in Ref. [1], we start with the plane wave representations of the velocity potentials ϕ and ψ ,

$$\begin{aligned} \phi_1 &= \phi_{\text{refl}} = C' e^{i(\alpha_1 z + \sigma x - \omega t)} \\ \phi_2 &= \phi_{\text{trans}} = E' e^{i(-\alpha_2 z + \sigma x - \omega t)} \\ \psi_1 &= \psi_{\text{inc}} + \psi_{\text{refl}} = B' e^{i(-\beta_1 z + \sigma x - \omega t)} + D' e^{i(\beta_1 z + \sigma x - \omega t)} \\ \psi_2 &= \psi_{\text{trans}} = F' e^{i(-\beta_2 z + \sigma x - \omega t)} \end{aligned} \quad (\text{A.8})$$

Then, applying the boundary condition equations,

$$\begin{aligned} \alpha_1 C' + \sigma(D' + B') &= -\alpha_2 E' + \sigma F', \\ \sigma C' - \beta_1(D' - B') &= \sigma E' + \beta_2 F', \\ \rho_1 c_{T1}^2 (C'(\cot^2 \gamma_1 - 1) + 2(D' - B') \cot \gamma_1) &= \rho_2 c_{T2}^2 (E'(\cot^2 \gamma_2 - 1) - 2F' \cot \gamma_1), \\ \rho_1 c_{T1}^2 (2C' \cot \theta_1 + (D' + B')(1 - \cot^2 \gamma_1)) &= \rho_2 c_{T2}^2 (-2E' \cot \theta_2 + F'(1 - \cot^2 \gamma_2)), \end{aligned} \quad (\text{A.9})$$

In the last two equations, we divided by σ^2 on both sides and used geometrical identities as well as Snell's law to come to this form. We see that these equations very much resemble Eq. (A.4). In fact, we can define one matrix where we put $A' = 0$ to solve for the SV mode and $B' = 0$ for the L mode. The critical angles are given,

$$\begin{aligned} \gamma_1 &> \sin^{-1}(c_{T1}/c_{L2}) \rightarrow E' = 0 \\ \gamma_1 &> \sin^{-1}(c_{T1}/c_{T2}) \rightarrow F' = 0 \\ \gamma_1 &> \sin^{-1}(c_{T1}/c_{L1}) \rightarrow C' = 0 \end{aligned} \quad (\text{A.10})$$

The energy flux of the incoming SV mode phonon is given

$$\text{energy flux} = \rho_1 \omega^2 |B'|^2 \cos \gamma_1 / (2c_{T1}) \quad (\text{A.11})$$

A

So, energy conservation requires that

$$1 = \frac{|D'|^2}{|B'|^2} + \frac{c_{t1}|C'|^2 \cos \theta_1}{c_{t1}|B'|^2 \cos \gamma_1} + \frac{\rho_2 c_{t1}|E'|^2 \cos \theta_2}{\rho_1 c_{t2}|B'|^2 \cos \gamma_1} + \frac{\rho_2 c_{t1}|F'|^2 \cos \gamma_2}{\rho_1 c_{t2}|B'|^2 \cos \gamma_1}. \quad (\text{A.12})$$

Again, the last two terms form $\eta_{\text{SV}}(\gamma_1)$, which can again be integrated over the angles to find η_{SV} .

Finally, the transverse phonon transparency for all polarizations can be calculated via, $\eta_{\text{T}} = (\eta_{\text{SV}} + \eta_{\text{SH}})/2$.

REFERENCES

- [1] S. B. Kaplan. *Acoustic Matching of Superconducting Films to Substrates*. In: *Journal of Low Temperature Physics* 37.3 (1979), pp. 343–365.
- [2] S. B. Kaplan, C. C. Chi, D. N. Langenberg, J. J. Chang, S. Jafarey, and D. J. Scalapino. *Quasiparticle and Phonon Lifetimes in Superconductors*. In: *Physical Review B* 14.11 (1976), pp. 4854–4873.
- [3] sahderooij. *Github.Com/Sahderooij/MKID-models*. 2024.

B

KINETIC INDUCTANCE AND MICROWAVE LOSS IN β -TA

In disordered superconductors, the change in kinetic inductance with temperature is often observed to deviate from Mattis-Bardeen [1] (i.e., BCS [2, 3]) theory. For example, in Ref. [4] the authors use of the Usadel [5] and Nam [6, 7] equations to fit an additional pair-breaking parameter, α , to the frequency shift of TiN and NbTiN resonators with various amounts of disorder. They find that α scales with the disorder parameter $1/(k_F l)$, where k_F is the Fermi wavenumber and l is the mean free path of the electrons. In a subsequent study, using scanning tunneling microscopy (STM) [8], the authors find however that the broadening by α does not accurately describe the density of states. The coherence peak at Δ is much more pronounced than predicted by the Usadel equation that includes a pair-breaking term with α . The value of Δ is however observed to vary with position.

In a more recent study [9] the low temperature behavior of the resonance frequency of amorphous InO_x resonators is found to behave as a power law, $\delta f/f_0 = (T/T_0)^n$. The power is found to be approximately $n = 1.6 - 1.7$ for various amounts of disorder (the normal state resistance ranges from $R_N = 1.45$ to 7.47 k Ω and the critical temperature from $T_c = 3.2$ to 1.4 K, respectively), and T_0 is found to scale linearly with $1/L_k$, with L_k the kinetic inductance. The authors developed a model based on a spatially varying order parameter, Δ , [10, 11] that induces localized Cooper-pairs that can tunnel to neighboring sites [12] (quasiparticles are not considered in the model). This model can approximately reproduce such a power law, although the predicted values of n and T_0 differed from the observed values. Specifically, the model predicts $1.6 < n < 3$ for large disorder (n decreases with increasing disorder) and $T_0 \sim \Delta/k_B$, while a 5 to 10 times higher T_0 was observed.

Here, we show that β -Ta resonators show a similar power-law behavior at low temperatures. Figure B.1(a) shows the fractional resonance frequency shift of the substrate resonator described in Chapter 6. The dashed-dotted line shows the prediction from Mattis-Bardeen theory (see Section 2.1.3), which deviates strongly at low temperatures. The dashed line shows a power law with $T_0 = 3.6$ K and $n = 3.5$, and the solid line is the sum of the power law and the Mattis-Bardeen result. As

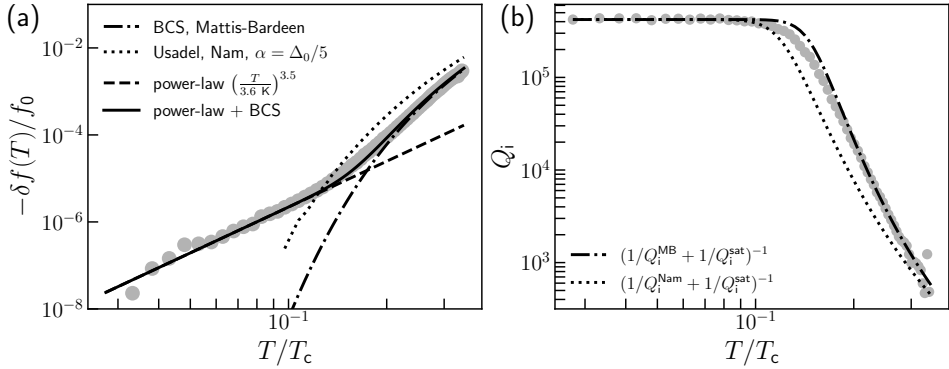


Figure **B.1**: Temperature dependence of the resonance frequency and internal quality factor of the substrate resonator described in Chapter 6, measured at -96 dBm on-chip read power. **(a)**: The fractional resonance frequency shift with temperature, $\delta f(T)/f_0$. This is proportional to the fractional shift in kinetic inductance. Here, $\delta f(T) = f_{\text{res}} - f_0$ and f_0 is the resonance frequency at the lowest temperature, which is 23 mK. The BCS and Usadel theory lines are calculated as set out in Chapter 2, with a kinetic induction fraction of $\alpha_k = 0.44$, which was obtained from a BCS fit to the high temperature data (see also Section 3.3.2). The solid line is a combination of the power law and the BCS, Mattis-Bardeen calculation. **(b)**: Internal quality factor obtained in the same measurement. The theory lines are from the same calculation as in panel (a). I.e., Q_i^{MB} is obtained from the BCS, Mattis-Bardeen equations and Q_i^{Nam} is obtained from the Usadel and Nam equations. We included a saturation value, Q_i^{sat} , which is set to the value at the lowest temperature point.

a comparison, we added the predictions from a broadened density of states by the Usadel and Nam equations by the dotted line, with a pair-breaking parameter of $\alpha = \Delta_0/5$ (see Section 2.4.3).

We observe a considerably higher $n = 3.5$ that predicted in [9], which could be consistent with the moderate disorder in β -Ta compared to the InO_x films. As a comparison, $L_k = 0.082$ nH/ \square for our β -Ta film, while $L_k = 0.63 - 7.4$ nH/ \square for the InO_x films in Ref. [9]. The observed $T_0 = 3.6$ for our β -Ta film is of the same order of magnitude as $\Delta_0/k_B = 1.53$. Therefore, this behavior could be seen as an additional indication of a locally varying Δ .

We also show the internal quality factor (Q_i) from the same measurement in Fig. B.1(b). Apart from a slight deviation close to the saturation temperature ($T \approx T_c/10$), the temperature dependence can be well described by Mattis-Bardeen (see Eq. (2.34)), when a saturation value is included. The nature of this saturation in Q_i is not clear. From the resonance frequency shift (Fig. B.1(a)), we can however exclude a quasiparticle density saturation, since that would also induce a resonance frequency saturation. In that case, we would expect the curve in Fig. B.1(a) to drop to zero faster than the Mattis-Bardeen prediction, which we do not observe. Therefore, opposite to what is argued in Ref. [13] (i.e., Fig. 1.3(b)), the saturation in microwave loss for this resonator is more likely to be caused by two-level-systems

(TLS) [14, 15] or disorder induced collective modes [9, 16]. The fact that the Q_i saturation and power law in $\delta f/f_0$ start at approximately the same temperature, may indicate that they are caused by the same mechanism. This would favor the collective mode hypothesis [9, 16]. When we compare the values of $Q_i = 4.2 \times 10^5$ and $\sigma_2 = 9.7 \times 10^6$ with the literature data in Fig. 1.3(b) (i.e., Ref. [13]), we see that Q_i is in the same order of magnitude of the apparent maximum Q_i . Only a TiN [17] and a few granular Al films [18] have significantly higher Q_i ($\sim 5 \times 10^6$) at this σ_2 . Therefore, it is likely that the Q_i of our β -Ta film is determined by the same limiting mechanism, while it stays unclear what the exact mechanism is.

REFERENCES

- [1] D. C. Mattis and J. Bardeen. *Theory of the Anomalous Skin Effect in Normal and Superconducting Metals*. In: *Physical Review* 111.2 (1958), pp. 412–417.
- [2] J. Bardeen, L. N. Cooper, and J. R. Schrieffer. *Microscopic Theory of Superconductivity*. In: *Physical Review* 106.1 (1957), pp. 162–164.
- [3] J. Bardeen, L. N. Cooper, and J. R. Schrieffer. *Theory of Superconductivity*. In: *Physical Review* 108.5 (1957), pp. 1175–1204.
- [4] E. F. C. Driessen, P. C. J. J. Coumou, R. R. Tromp, P. J. de Visser, and T. M. Klapwijk. *Strongly Disordered TiN and NbTiN S-Wave Superconductors Probed by Microwave Electrodynamics*. In: *Physical Review Letters* 109.10 (2012), p. 107003.
- [5] K. D. Usadel. *Generalized Diffusion Equation for Superconducting Alloys*. In: *Physical Review Letters* 25.8 (1970), pp. 507–509.
- [6] S. B. Nam. *Theory of Electromagnetic Properties of Strong-Coupling and Impure Superconductors. II*. In: *Physical Review* 156.2 (1967), pp. 487–493.
- [7] S. B. Nam. *Theory of Electromagnetic Properties of Superconducting and Normal Systems. I*. In: *Physical Review* 156.2 (1967), pp. 470–486.
- [8] P. C. J. J. Coumou, E. F. C. Driessen, J. Bueno, C. Chapelier, and T. M. Klapwijk. *Electrodynamic Response and Local Tunneling Spectroscopy of Strongly Disordered Superconducting TiN Films*. In: *Physical Review B* 88.18 (2013), p. 180505.
- [9] A. V. Khvalyuk, T. Charpentier, N. Roch, B. Sacépé, and M. V. Feigel'man. *Near Power-Law Temperature Dependence of the Superfluid Stiffness in Strongly Disordered Superconductors*. In: *Physical Review B* 109.14 (2024), p. 144501.
- [10] A. V. Khvalyuk and M. V. Feigel'man. *Distribution of the Order Parameter in Strongly Disordered Superconductors: An Analytic Theory*. In: *Physical Review B* 104.22 (2021), p. 224505.
- [11] M. Feigel'man, L. Ioffe, V. Kravtsov, and E. Cuevas. *Fractal Superconductivity near Localization Threshold*. In: *Annals of Physics* 325.7 (2010), pp. 1390–1478.
- [12] M. Ma and P. A. Lee. *Localized Superconductors*. In: *Physical Review B* 32.9 (1985), pp. 5658–5667.
- [13] T. Charpentier, A. Khvalyuk, L. Ioffe, M. Feigel'man, N. Roch, and B. Sacépé. *Universal Scaling of Microwave Dissipation in Superconducting Circuits*. 2025. URL: <http://arxiv.org/abs/2507.08953>. Pre-published.

- [14] H. Wang, M. Hofheinz, J. Wenner, M. Ansmann, R. C. Bialczak, M. Lenander, E. Lucero, M. Neeley, A. D. O'Connell, D. Sank, M. Weides, A. N. Cleland, and J. M. Martinis. *Improving the Coherence Time of Superconducting Coplanar Resonators*. In: *Applied Physics Letters* 95.23 (2009), p. 233508.
- [15] J. Gao, M. Daal, J. M. Martinis, A. Vayonakis, J. Zmuidzinas, B. Sadoulet, B. A. Mazin, P. K. Day, and H. G. Leduc. *A Semiempirical Model for Two-Level System Noise in Superconducting Microresonators*. In: *Applied Physics Letters* 92.21 (2008), p. 212504.
- [16] A. V. Khvalyuk and M. V. Feigel'man. *Dissipation Due to Bulk Localized Low-Energy Modes in Strongly Disordered Superconductors*. 2025. URL: <http://arxiv.org/abs/2512.11636>. Pre-published.
- [17] S. Ohya, B. Chiaro, A. Megrant, C. Neill, R. Barends, Y. Chen, J. Kelly, D. Low, J. Mutus, P. J. J. O'Malley, P. Roushan, D. Sank, A. Vainsencher, J. Wenner, T. C. White, Y. Yin, B. D. Schultz, C. J. Palmström, B. A. Mazin, A. N. Cleland, and J. M. Martinis. *Room Temperature Deposition of Sputtered TiN Films for Superconducting Coplanar Waveguide Resonators*. In: *Superconductor Science and Technology* 27.1 (2013), p. 015009.
- [18] C. Roy, S. Frasca, and P. Scarlino. *Study of Magnetic Field Resilient High Impedance High-Kinetic Inductance Superconducting Resonators*. 2025. URL: <http://arxiv.org/abs/2503.13321>. Pre-published.

ACKNOWLEDGEMENTS

Somehow, the image of science has always been very individualistic. We cherish the stereotypical view of a brilliant scientist, whose superior intellect solely pushes the boundaries of our understanding of nature. Nothing could be further from the truth. A more realistic view of advancements in science would be like the superconducting phase transition: only when individual particles pair up and form a collective coherent state, a fundamentally new view of nature arises. It is impossible to truthfully ascribe scientific advances to individuals. By acknowledging the efforts of colleagues and friends in this section, I hope to give an impression of the collective efforts that gave rise to this thesis and the scientific experiences that I gained.

First and foremost, I mention the tireless efforts of **Pieter** to guide me in becoming a scientist. Thank you for the countless proofreads of draft papers and chapters, in record response times and with record comment counts. Thank you for asking questions on my work that I did not dare to ask at first, thank you for showing me how to be an experimentalist with fundamental interests, and thank you for the amusing 'speculaas' about physics. But most of all, thank you for trusting me and letting me explore; I'm sure that without that, I wouldn't be where I am now.

Jochem, you are the living proof to me that deep, intrinsic motivation can bring one further than anyone would dare to predict in any point in time. How you bring together all aspects of the Experimental Astronomy research group (fabrication, measurements, at least three subjects of science and four kinds of state-of-the-art technology) while understanding each nitty-gritty detail within half a sentence, is truly inspiring. Thank you for being open and willing to go to bottom of things together, despite the fact that you have probably been there several times already.

The other members of the Experimental Astronomy and Terahertz Sensing group have also played a pivotal role in this thesis journey. **Kevin**, thank you for building a bridge with me between physics and electrical engineering, even when that meant we had to go to the depths of the chasm first. **Wilbert**, thank you for your wonder and our brainstorming on what could explain our latest measurement results. **Louis**, thank you for the long evidence-based, metaphysical discussions and your physics-based engineering approach. **Leon**, thank you for your combination of a down-to-earth mindset and genuine amazement; it is as magical as nanofabrication itself. **Arend**, thank you for your contagious interest in fundamental physics and mathematics. **Sander, Alexandros, Alexandra** and **Daan**, thank you for sharing the office space with me, and with that, sharing all banalities, stupidities, twist and turns that revolve around a PhD project. **Akira**, thank you for showing me how to combine fundamental interests with a drive to push technology, even when these might only be connected far in the future. **Kenichi**, thank you for showing me that hard experimental work and thorough understanding of lab equipment will always pay off. **Shahab**, from you I learned that cynicism can be an entertaining way to

deepen one's critical thinking. **Bruno**, you showed me how to stay honest and humble in a world full of experts. **Juan**, thank you for your patience and expertise in cryogenics, high frequency measurements, superconducting detectors and your world-class word-plays. **Andrea** and **Nuria**, thank you for cultivating and growing the Terahertz Sensing group and **Everdine**, **Sophie** and **Esther** thank you for nurturing it.

The people and environment in SRON have been instrumental in my PhD journey as well. **Rianne**, thank you for your curiosity, which made mine grow as well, and **Michiel**, thank you showing me that things become easier and more fun, if you take the work and yourself just a bit less serious. **Henk**, thank you for the trust and for the opportunity to conduct this predominantly fundamental research in the applied institute SRON.

At this point, I would like to stop this enumeration for a bit and acknowledge the major influence of the nanofabrication team in SRON. This entire thesis would not exist without this team being so effective as they are. This team in itself is an example of how collective efforts and knowledge can be much greater than the sum of their individual members. As part of this collective, the individual members deserve much more credit than an occasional co-authorship of a paper. **Tonny**, thank you for your observant patience. **Dani**, thank you for your punctilious efforts. **Vishal**, thank you for your kind openness. **Dimitry**, thank you for your astonishingly broad and deep skill set (including your sense of humor). **Martijn**, thank you for always having more solutions than problems (including alcohol solutions). **Vignesh**, thank you for your great legacy in nanofabrication, which is still intertwined with the (nano/litho)fabrication team in SRON. And last but not least, thank you **David**, for driving this team, for explaining anything that I would like to know about nanofabrication, for giving me intuition on when to cut corners and when not to, for preventing stupid mistakes by slowing me down ('with half the pace, you get things done three times faster'), but most of all, thank you for advocating freedom and responsibility in our work, as this makes people flourish.

Guiding of students in their projects has motivated me greatly and I am grateful for their dedication. **Yannic**, you showed me that any research project should be flexible, both adjusting to the scientific output and interest of the people involved. **Thomas**, thank you for your enthusiasm, which made me realize that motivation grows strongly when it is mutually amplified. Thank you, **Roland**, for your eagerness to get to the bottom of things, which showed me that being pragmatic does not have to be about focusing on goals and results. **Douwe**, thank you for your wholeheartedness and for showing me that a well-defined engineering problem can be immensely motivating. **Ditto**, with your astonishing independence, you showed me that the right focus can bring you much further than a broad interest in everything. Finally, **Kian**, thank you for your inexhaustible perseverance. From you I learned that planning research only works when you update the planning at every new step.

Lastly, I had the opportunity to characterize our samples with a magnetic field cryogenic setup in Leiden University. For the opportunity to get to know the LION institute, I would like to thank **Jan** and **Kaveh**. This has led me to continue research as a postdoc in this institute. **Remko**, thank you for welcoming me warm-heartedly to the measurement hall, working with me on these measurements and proofreading the draft manuscript. I enjoyed our collaboration; pairing-up felt very natural.

During the years of my PhD, I've been part of a collective, constituted by the people

mentioned above and many more. It was only because of this collective that this thesis exists in the present form. Many contributions are still invisible and will always be due to the nature of research. Therefore, I urge the reader to look further than the names on a paper, and not to cherish the individual scientists, but the fruitful collectives and stimulating environments.

Mijn sociale omgeving heeft ook bijgedragen aan deze thesis, door mij te ondersteunen, mij genoeg ruimte te geven en mij genoeg af te leiden.

Voor de afleiding wil ik in de eerste plaats wil ik dan ook **JC Aurum** bedanken, voor de onredelijk vanzelfsprekende vriendschappen. Ik verheug me op het voorzetten van deze vriendschappen tijdens de komende, veranderende levensfasen van ons. In het bijzonder, **Christos**, bedankt voor de analytische gesprekken over de totaal irrationale diersoort waartoe wij behoren. Ondanks het grote aantal van deze gesprekken, heb ik het idee dat we er nog maar net aan zijn begonnen. **Rogier**, bedankt voor de levendige discussies die mij laten inzien dat de dingen soms minder duidelijk zijn dan ik ze voor ogen heb. **Thomas**, bedankt voor het mogen meeliften op jouw kennis en vindingrijkheid in onze gezamenlijke interesses en humor. **Kenneth**, dank voor de onveranderlijke en onbeperkte vriendschap, terwijl ondertussen onze levens aldoor veranderen en meer beperkingen kennen.

Ook de boze (oud)huisgenoten hebben mij nuttig en vermakelijk afgeleid tijdens mijn promotie, waarvoor mijn grote dank aan **Piep** (nét goed genoeg is het efficiëntst), **Ket** (geluk hoeft niet ingewikkelder te zijn dan een lekker biertje of een pizza tonno), **Mims** (beter te weinig lachen om een grap, dan te weinig grappen om te lachen), **Lex** (eerst kopen, ervan balen komt later wel) en **Cru** (nog maar een discussie voeren dan?).

Mochten deze groepen niet voor genoeg afleiding zorgen, dan deden de wereldkampioenen van **Nuna9** dat wel. Dank voor jullie teamgevoel, wat tegenwoordig getransformeerd is naar vrijblijvende vriendschap. Mijn dank gaat ook uit naar de leden **Raad van Toezicht** van de Nuna-stichting, die mijn (nu al) starre en verouderde blik maandelijks proberen te verjongen.

De ondersteuning en ruimte kwam van mijn familie, waarvoor ik hen zeer dankbaar ben. **Moeders**, aan jou heb ik eigenlijk alles te danken; vroeger de zorgeloosheid van een kind, nu de vrijheid om te doen wat ik leuk vind. **Helen**, dank voor het delen van ons leven, dat - ondanks dat het zoveel van elkaar verschilt - heel vertrouwd en dichtbij voelt. **Pap**, het doet mij verdriet dat je mijn promotie niet hebt kunnen meemaken; het geeft me hoop dat jouw honger naar kennis ook in mij zit.

Gijs en **Femke**, dank voor het zachte en warme onthaal in jullie gezin, en **Anjoke** en **Maarten**, dank voor het open en innige welkom in dat van jullie.

Sarah, dank voor je ondersteuning, liefdevolle oprechtheid, kinderlijk plezier en onbegrensde medeleven. Ik kan niet wachten om samen meer van onze toekomst mee te maken.

CURRICULUM VITAE

Steven Alexander Hippolytos DE ROOIJ

Date of birth: 7th of March, 1995

Place of birth: Rotterdam, The Netherlands


- 2007 - 2013 *Atheneum, Natuur en Techniek*
Dongemond College, Raamsdonksveer
- 2013 - 2016 *Bachelor Applied Physics*
Delft University of Technology
Honours Programme (additional 20 ECTS)
minor: theoretical physics
thesis: NV Centres in Diamond Membranes
- 2018 - 2020 *Master Applied Physics, Quantum Nanoscience*
Delft University of Technology
thesis: Quasiparticle dynamics in optical MKID
- 2020 - 2021 *Assistant instrument scientist*
SRON, Space Research Organisation Netherlands
- 2021 - 2025 *PhD Candidate*
SRON, Space Research Organisation Netherlands
Delft University of Technology
thesis: Quasiparticle dynamics in disordered superconductors
promotor: Prof. dr. ir. Jochem Baselmans
supervisor: Dr. ir. Pieter de Visser
- 2025 > *Postdoctoral researcher*
Leiden University
Bhattacharyya lab - Quantum transport in 2D materials

LIST OF PUBLICATIONS

6. S. A. H. de Rooij, R. Fermin, K. Kouwenhoven, T. Coppens, V. Murugesan, D. J. Thoen, J. Aarts, J. J. A. Baselmans, and P. J. de Visser. *Recombination of Localized Quasiparticles in Disordered Superconductors*. In: *Nature Communications* 16.1 (2025), p. 8465
5. S. A. H. de Rooij, J. J. A. Baselmans, J. Bueno, V. Murugesan, D. J. Thoen, and P. J. de Visser. *Volume Dependence of Microwave-Induced Excess Quasiparticles in Superconducting Resonators*. In: *Physical Review Applied* 24.2 (2025), p. 024007
4. K. Kouwenhoven, G. P. J. van Doorn, B. T. Buijtenorp, S. A. H. de Rooij, D. Lamers, D. J. Thoen, V. Murugesan, J. J. A. Baselmans, and P. J. de Visser. *Geometry Dependence of Two-Level-System Noise and Loss in α -SiC:H Parallel-Plate Capacitors for Superconducting Microwave Resonators*. In: *Physical Review Applied* 21.4 (2024), p. 044036
3. K. Kouwenhoven, D. Fan, E. Biancalani, S. A. H. de Rooij, T. Karim, C. S. Smith, V. Murugesan, D. J. Thoen, J. J. A. Baselmans, and P. J. de Visser. *Resolving Power of Visible-To-Near-Infrared Hybrid β -Ta/Nb-Ti-N Kinetic Inductance Detectors*. In: *Physical Review Applied* 19.3 (2023), p. 034007
2. S. A. H. de Rooij, J. J. A. Baselmans, V. Murugesan, D. J. Thoen, and P. J. de Visser. *Strong Reduction of Quasiparticle Fluctuations in a Superconductor Due to Decoupling of the Quasiparticle Number and Lifetime*. In: *Physical Review B* 104.18 (2021), p. L180506
1. P. J. de Visser, S. A. H. de Rooij, V. Murugesan, D. J. Thoen, and J. J. A. Baselmans. *Phonon-Trapping-Enhanced Energy Resolution in Superconducting Single-Photon Detectors*. In: *Physical Review Applied* 16.3 (2021), p. 034051

SUPERVISED THESES

6. *Single photon response in microwave kinetic inductance detectors*
- BSc thesis Applied Physics, Yannic Alkemade
5. *Quasiparticle dynamics in disordered superconductors: modeling the single photon response*
- BSc thesis Applied Physics, Thomas Rugers,
4. *Dissipation in superconductors subject to both alternating and direct currents*
- BSc thesis Applied Physics, Roland Stolk,
3. *Modeling superconducting filters using ABCD matrices to verify Debye conductivity*
- BSc thesis Applied Physics, Douwe Brogtrop
2. *Pushing the Fano limit: improving Fano-limited single photon counting MKIDs*
- BSc thesis Applied Physics, Aaron Dantuma
1. *The impact of diffusion and disorder on the single photon response of β -Ta OKIDs*
- MSc thesis Applied Physics, Kian P. Syaifoel



ISBN: 978-94-6536-040-9